

**Final Report**  
**Grant No. N00014-91-J-4164**  
**September 15, 1991 - September 15, 1994**

**ENVIRONMENTALLY ASSISTED CRACKING OF HIGH  
STRENGTH BETA TITANIUM ALLOYS**

**Submitted to:**

**Dr. A. John Sedriks**  
**Materials Division, Code 1131M**  
**Office of Naval Research**  
**800 N. Quincy Street**  
**Arlington, VA 22217-5660**

**DTIC**  
**ELECTE**  
**DEC 28 1994**  
**C**

**Submitted by:**

**Richard P. Gangloff**  
**Professor**

**John R. Scully**  
**Assistant Professor**

**Robert G. Kelly**  
**Assistant Professor**

**Report No. UVA/525461/MSE95/102**  
**November 1994**

**EXEMPTED FROM AUTOMATIC DOWNGRADING AND DECLASSIFICATION**  
**Approved for public release**  
**Distribution Unlimited**

**DEPARTMENT OF MATERIALS SCIENCE AND ENGINEERING**

**SCHOOL OF**  
**ENGINEERING**   
**& APPLIED SCIENCE**

**University of Virginia**  
**Thornton Hall**  
**Charlottesville, VA 22903**

**DTIC QUALITY CONTROLLED**

**19941227 001**

**UNIVERSITY OF VIRGINIA**  
**School of Engineering and Applied Science**

The University of Virginia's School of Engineering and Applied Science has an undergraduate enrollment of approximately 1,500 students with a graduate enrollment of approximately 600. There are 160 faculty members, a majority of whom conduct research in addition to teaching.

Research is a vital part of the educational program and interests parallel academic specialties. These range from the classical engineering disciplines of Chemical, Civil, Electrical, and Mechanical and Aerospace to newer, more specialized fields of Applied Mechanics, Biomedical Engineering, Systems Engineering, Materials Science, Nuclear Engineering and Engineering Physics, Applied Mathematics and Computer Science. Within these disciplines there are well equipped laboratories for conducting highly specialized research. All departments offer the doctorate; Biomedical and Materials Science grant only graduate degrees. In addition, courses in the humanities are offered within the School.

The University of Virginia (which includes approximately 2,000 faculty and a total of full-time student enrollment of about 17,000), also offers professional degrees under the schools of Architecture, Law, Medicine, Nursing, Commerce, Business Administration, and Education. In addition, the College of Arts and Sciences houses departments of Mathematics, Physics, Chemistry and others relevant to the engineering research program. The School of Engineering and Applied Science is an integral part of this University community which provides opportunities for interdisciplinary work in pursuit of the basic goals of education, research, and public service.

A Final Report  
Grant No. N00014-91-J-4164  
September 15, 1991 - September 15, 1994

**ENVIRONMENTALLY ASSISTED CRACKING OF HIGH  
STRENGTH BETA TITANIUM ALLOYS**

Submitted to:

Dr. A. John Sedriks  
Materials Division, Code 1131M  
Office of Naval Research  
800 N. Quincy Street  
Arlington, VA 22217-5660

Submitted by:

Richard P. Gangloff  
Professor

John R. Scully  
Assistant Professor

Robert G. Kelly  
Assistant Professor

|                    |                                     |
|--------------------|-------------------------------------|
| Accession For      |                                     |
| NTIS CRA&I         | <input checked="" type="checkbox"/> |
| DTIC TAB           | <input type="checkbox"/>            |
| Unannounced        | <input type="checkbox"/>            |
| Justification      |                                     |
| By <i>Per Hts.</i> |                                     |
| Distribution /     |                                     |
| Availability Codes |                                     |
| Dist               | Avail and/or Special                |
| <i>A-1</i>         |                                     |

Department of Materials Science and Engineering  
SCHOOL OF ENGINEERING AND APPLIED SCIENCE  
UNIVERSITY OF VIRGINIA  
CHARLOTTESVILLE, VIRGINIA  
22903-2442

Report No. UVA/525461/MSE95/102  
November 1994

Copy No. \_\_\_\_\_

# REPORT DOCUMENTATION PAGE

Form Approved  
OMB No. 0704-0188

Public reporting burden for the collection of information is estimated to average 1 hour per response, including the time for reviewing instructions, searching existing data sources, gathering and maintaining the data needed, and completing and reviewing the collection of information. Send comments regarding this burden estimate or any other aspect of this collection of information, including suggestions for reducing this burden to Washington Headquarters Services, Directorate for Information Operations and Reports, 1215 Jefferson Davis Highway, Suite 1294, Arlington, VA 22202-4302, and to the Office of Management and Budget, Paperwork Reduction Project (0704-0188), Washington, DC 20503.

1. AGENCY USE ONLY (Leave Blank)

2. REPORT DATE  
November 1994

3. REPORT TYPE AND DATES COVERED  
Final 09/15/91 - 09/15/94

4. TITLE AND SUBTITLE

Environmentally Assisted Cracking of High Strength Beta Titanium Alloys

5. FUNDING NUMBERS

N00014-91-J-4164

6. AUTHOR(S)

R. P. Gangloff  
J. R. Scully and R. G. Kelly

7. PERFORMING ORGANIZATION NAME(S) AND ADDRESS(ES)

Department of Materials Science and Engineering  
School of Engineering and Applied Science  
University of Virginia  
Thornton Hall  
Charlottesville, VA 22903-2442

8. PERFORMING ORGANIZATION  
REPORT NUMBER

UVA/525461/MSE95/102

9. SPONSORING MONITORING AGENCY NAME(S) AND ADDRESS(ES)

Office of Naval Research  
800 North Quincy Street  
Arlington, VA 22217-5660

10. SPONSORING/MONITORING  
AGENCY REPORT NUMBER

11. SUPPLEMENTARY NOTES

12a. DISTRIBUTION/AVAILABILITY STATEMENT

12b. DISTRIBUTION CODE

13. ABSTRACT (Maximum 200 words)

## RESEARCH GOALS

The objective of this integrated research program is to define the conditions under which high strength  $\beta$ -titanium alloys resist environmentally assisted cracking (EAC) in marine environments. Specific goals are to: (1) characterize EAC for metallurgical, chemical and mechanical conditions that could destabilize crack tip passive films to promote local dissolution and hydrogen uptake, (2) test the hydrogen embrittlement mechanism for EAC, and (3) develop a mechanism-based model of EAC by integrating crack chemistry, surface dissolution and repassivation kinetics, hydrogen uptake to trap sites, and crack tip process zone micromechanics and damage.

This final report presents a summary of the results and includes papers published during the period of this grant from September, 1991 to September, 1994.

14. SUBJECT TERMS

Titanium alloys, hydrogen embrittlement, stress corrosion cracking, mechanical properties, intergranular cracking, microstructure, hydrides, passive film, beta titanium alloys, fracture threshold, fracture mechanics

15. NUMBER OF PAGES  
8

16. PRICE CODE

17. SECURITY CLASSIFICATION  
OF REPORT

Unclassified

18. SECURITY CLASSIFICATION  
OF THIS PAGE

Unclassified

19. SECURITY CLASSIFICATION  
OF ABSTRACT

Unclassified

20. LIMITATION OF ABSTRACT

Unlimited



## TABLE OF CONTENTS

|  |   |
|--|---|
| I. Summary of Results .....  | 1 |
| II. Appendix A - Publications from ONR Grant No. N00014-91-J-4164 .....  | 8 |
| <ol style="list-style-type: none"> <li>1. L.M. Young, G.A. Young Jr., J.R. Scully and R.P. Gangloff, "Aqueous Environmental Crack Propagation in High Strength Beta Titanium Alloys," <i>Metall. Trans. A</i>, in press, 1994.</li> <li>2. L.M. Young and R.P. Gangloff, "Hydrogen Environment Embrittlement of Beta Titanium Alloys," in <u>Titanium '92, Science and Technology</u>, Vol. 3, F.H. Froes and I.L. Caplan, eds., TMS-AIME, Warrendale, PA, pp. 2209-221, 1993.</li> <li>3. B.P. Somerday, J.A. Grandle and R.P. Gangloff, "Yield Strength and Solution Composition Effects on Aqueous Environmental Cracking of Ti-8V-6Cr-4Zr-4Mo-3Al (Beta C)," in <u>Proc. of the Tri-Service Conference on Corrosion</u>, Materials Laboratory, Wright Patterson Air Force Base, OH, in press, 1994.</li> <li>4. D.G. Kolman and J.R. Scully, "Electrochemistry and Passivity of a Ti-15Mo-3Nb-3Al Beta-Titanium Alloy in Ambient Temperature Aqueous Chloride Solutions," <i>J. Electrochem. Soc.</i>, Vol. 140, No. 10, pp. 2771-2779, 1993.</li> <li>5. D.G. Kolman and J.R. Scully, "Electrochemistry and Passivity of Ti-15V-3Cr-3Al-3Sn <math>\beta</math>-Titanium Alloy in Ambient Temperature Aqueous Chloride Solutions," <i>J. Electrochem. Soc.</i>, Vol. 141, No. 10, pp. 2633-2641, 1994.</li> <li>6. D.G. Kolman and J.R. Scully, "Limitations of Potentiostatic Repassivation Techniques and Their Relationship to the Applicability of the High Field Approximation to the Repassivation of Titanium," <i>J. Electrochem. Soc.</i>, in review, October 1994.</li> <li>7. G.A. Young and J. R. Scully, "Effects of Hydrogen on the Mechanical Properties of a Ti-Mo-Nb-Al Alloy," <i>Scripta Metall.</i>, Vol. 28, pp. 507-512, 1993.</li> <li>8. G.A. Young and J. R. Scully, "Internal Hydrogen Embrittlement of Solution Heat Treated and Aged Ti-15V-3Cr-3Al-3Sn and Ti-15Mo-3Nb-3Al," <i>Corrosion J.</i>, in press, 1994.</li> <li>9. G.A. Young and J. R. Scully, "The Effects of Hydrogen on the Room Temperature Mechanical Properties of Ti-15V-3Cr-3Al-3Sn and Ti-15Mo-3Nb-3Al," in <u>Beta Titanium Alloys in the 1990's</u>, D. Eylon, R.R. Boyer and D.A. Koss, eds., TMS, Warrendale, PA, pp. 147-158, 1993.</li> <li>10. M.A. Gaudett and J.R. Scully, "Hydrogen Interactions and Embrittlement in Metastable Beta Ti-3Al-8V-6Cr-4Mo-4Zr", to be submitted for publication, 1994.</li> <li>11. R.P. Gangloff and R.G. Kelly, "Microbe Enhanced Environmental Fatigue Crack Propagation in HY130 Steel," <i>Corrosion</i>, Vol. 50, No. 5, pp. 345-354, 1994.</li> <li>12. R.P. Gangloff, "Corrosion Fatigue Cracking," in <u>Manual on Corrosion Tests and Standards: Application and Interpretation</u>, R. Baboian, Ed., ASTM, Philadelphia, PA, in press, 1994.</li> </ol> |   |

## RESULTS

Rising load fracture mechanics experiments with solution treated and peak aged Ti-15-3 (Ti-15V-3Cr-3Al-3Sn; wt%) and Beta 21S (Ti-15Mo-3Nb-3Al; wt%) in aqueous NaCl solution lead to the following conclusions: (L.M. Young, G.A. Young Jr., J.R. Scully and R.P. Gangloff, "Aqueous Environmental Crack Propagation in High Strength Beta Titanium Alloys," *Metall. Trans. A*, in press, 1994.)

- oo The STA condition of Beta-21S is susceptible to environment assisted cracking (EAC) in aqueous NaCl at  $-600 \text{ mV}_{\text{SCE}}$  when subjected to rising stress intensity. The threshold for subcritical crack propagation ( $K_{\text{TH}} = 39 \text{ to } 46 \text{ MPa}\sqrt{\text{m}}$ ) is reduced significantly compared to the plane strain fracture toughness ( $K_{\text{ICi}}$ ) of  $66 \text{ MPa}\sqrt{\text{m}}$ . Average subcritical crack growth rates are on the order of  $10 \mu\text{m}/\text{sec}$ , and EAC is intergranular for Beta-21S in chloride compared to microvoid-based for moist air.
- oo For STA Ti-15-3,  $K_{\text{ICi}}$  ( $57 \text{ to } 64 \text{ MPa}\sqrt{\text{m}}$ ) and transgranular microvoid fracture processes are unaffected by aqueous chloride exposure for several slow loading rates and applied electrode potentials. Intergranular EAC in STA Ti-15-3 is promoted by increased solution treatment temperature and/or time.
- oo Intergranular EAC in STA Beta-21S (as well as in resolution treated and aged Ti-15-3) correlates with  $\alpha$ -colonies precipitated at  $\beta$  grain boundaries and with localized planar slip; the governing causal factor is not defined. Both features are promoted by high temperature-long time solution treatment. The relative importance of these features and other alloy-dependent factors is not established; however, hydrogen trapping at  $\alpha/\beta$  interfaces coupled with stress and strain localization near  $\beta$  grain boundaries may be important.
- oo EAC in peak aged Beta-21S is not produced during static loading, for times similar to the deleterious rising load case, and average subcritical EAC growth rates decrease with decreasing crack tip strain rate.
- oo EAC in STA Beta-21S is eliminated by applied cathodic polarization at  $-1000 \text{ mV}_{\text{SCE}}$ , and occurs, but is not exacerbated during anodic polarization at  $-150 \text{ mV}_{\text{SCE}}$ .
- oo EAC in STA Beta-21S may proceed by hydrogen environment embrittlement. The beneficial effects of cathodic polarization and stagnant crack tip strain rate are speculatively traced to reduced hydrogen production at the occluded crack tip for the former, and to increased crack tip passive film stability or reduced dislocation transport of process zone hydrogen for the latter.

- oo The 25°C chloride EAC resistance of STA  $\beta$ -titanium alloys can be superior to that of quenched and tempered martensitic steels at similar high strengths, certainly for cathodic polarization and short term static loading. Beta titanium alloys are not, however, immune to chloride EAC; thermomechanical processing must be controlled for cracking resistance.

The following conclusions were established based on rising load fracture mechanics experiments with solution treated and peak aged Beta C (Ti-8V-6Cr-4Zr-4Mo-3Al; wt%) in aqueous NaCl and aqueous NaCl with sulfur-species additions. (B.P. Somerday, J.A. Grandle and R.P. Gangloff, "Yield Strength and Solution Composition Effects on Aqueous Environmental Cracking of Ti-8V-6Cr-4Zr-4Mo-3Al (Beta C)," in Proc. of the Tri-Service Conference on Corrosion, Materials Laboratory, Wright Patterson Air Force Base, OH, in press, 1994.)

- oo The high-strength  $\beta/\alpha$  titanium alloy, STA Beta C, is embrittled by loading in neutral aqueous NaCl solution at 25°C, given an occluded crack, active strain rate and electrode potentials near free corrosion. This behavior is analogous to that of STA Beta 21S.
- oo STA Beta C resists crack propagation in NaCl under static load/displacement or cathodic polarization, at least for short-term experiments. This behavior is analogous to that of STA Beta 21S.
- oo Moderate strength, single phase ( $\beta$ ) ST Beta C is immune to chloride EAC at the free corrosion potential and under short-term rising displacement. Sulfur-species and acid additions to NaCl that embrittle ferritic steels do not promote intergranular EAC in ST Beta C.
- oo EAC in STA Beta C is intergranular; the contributions of grain boundary  $\alpha$  precipitation, locally intense planar slip and impurity segregation are not yet defined. Moist air fracture of the STA and ST conditions, as well as ST fracture in chloride-sulfur-species solutions, are by transgranular microvoid rupture.
- oo The rising CMOD method an effective characterization of EAC, but requires instrumentation and analysis of  $da/dt$  as a function of K and crack tip strain rate.
- oo Alternating slow-rapid EAC propagation rate in Beta C and Beta 21S is speculatively attributed to coupled K- and crack tip strain rate-control, and specimen compliance-induced changes in these driving force parameters.

The electrochemistry, passivity, and repassivation kinetics of a Mo/Nb stabilized  $\beta$ -titanium alloy (Beta 21S) was investigated. (D.G. Kolman and J.R. Scully, "The Passivity and Electrochemistry of a Ti-Mo-Nb  $\beta$ -Titanium Alloy in Ambient Temperature Aqueous Sodium Chloride Solution," *J. Electrochem. Soc.*, Vol. 140, No. 10, pp. 2771-2779, 1993.)

- oo There are no major electrochemical differences between Beta 21S exposed to 0.6 M NaCl and pH 1, 0.6 M NaCl in its STA and ST forms, although ST Beta 21S almost always yielded the largest passive current density.
- oo Significant electrochemical differences do not exist between either the model precipitate (grade 6 Ti) or commercially pure Ti (grade 2 Ti) and Beta 21S in the NaCl solutions, which suggests that there is minimal galvanic interaction between the matrix and precipitates in STA Beta 21S in the NaCl environments.
- oo All of the alloys were spontaneously passive in the NaCl solutions examined and no pitting potentials were observed up to 2.1V vs. SCE.
- oo Experiments in deaerated 5M HCl reveal an active/passive transition for all alloys except ST Beta 21S, which was spontaneously passive, indicating that the  $\alpha$  precipitates in STA Beta 21S have a deleterious effect upon passivity and that galvanic coupling between the  $\alpha$  and  $\beta$  phases may possibly occur. Both the anodic and cathodic kinetics were affected by the Mo/Nb additions in Beta 21S. Rotating disk electrode experiments confirmed that Beta 21S is indeed passive in a 5M HCl environment.
- oo Similarity of hydrogen evolution kinetics, the lack of observed alloying addition oxidation peaks on anodic polarization scans, and AES and XPS studies indicate limited incorporation of alloying additions into the passive film in the NaCl solutions. AES and XPS studies indicate the passive film on all Ti alloys was predominantly  $\text{TiO}_2$  with lesser amounts of oxidized Mo, Nb and Al contained in the oxides on Beta 21S. The small quantity of alloying additions within the passive film may account for the similar passive electrochemical behaviors observed among the studied alloys.
- oo All of the alloys in this study yielded peak current densities that were too low solely to account for crack growth rates observed in separate studies, even after crack tip acidification, suggesting that passive film must be mechanically destabilized in order to account for these crack growth rates, regardless of the exact mechanism.

Studies of the electrochemistry, passivity, and repassivation kinetics of  $\beta$ -titanium alloy Ti-15-3 lead to the following conclusions: (D.G. Kolman and J.R. Scully, "Electrochemistry and Passivity of Ti-15V-3Cr-3Al-3Sn  $\beta$ -Titanium Alloy in Ambient Temperature Aqueous Chloride Solutions," *J. Electrochem. Soc.*, Vol. 141, No. 10, pp. 2633-2641, 1994.)

- oo No major electrochemical differences were observed between ST Ti-15-3, STA Ti-15-3, commercially pure (grade 2) Ti, and grade 6 Ti, which approximates the composition of the  $\alpha$  precipitates present in STA Ti-15-3.
- oo Similar open circuit potentials between grade 6 Ti and the  $\beta$ -titanium alloys indicates

that little galvanic coupling occurs between the  $\alpha$  precipitates and the  $\beta$  matrix in the STA alloy.

- oo All of the alloys were found to be spontaneously passive in all of the NaCl solutions examined, as confirmed by EIS, and no pitting was observed on these alloys up to 1.7V vs. SCE. However, active/passive transitions were observed on all four materials in 5M HCl.
- oo Ti-15-3 and grade 6 Ti oxide thicknesses were found to increase linearly with potential, as found with commercially pure grade 2 Ti, suggesting comparable oxide growth mechanisms.
- oo Similar passive electrochemical behaviors amongst the four alloys is explained by the fact that the oxides on these materials are quite close in composition. Ex-situ AES sputter depth profiles show that the oxide on ST Ti-15-3 is predominantly  $\text{TiO}_2$  and contains less than stoichiometric concentrations of alloying additions. Ex-situ XPS tests indicate little difference between the oxide on ST and STA Ti-15-3. Oxide similarity was also confirmed by comparable hydrogen evolution kinetics.
- oo The peak dissolution rates of the  $\beta$ -titanium alloys were found to be too low to solely account for EAC. Therefore, mechanical destabilization of the passive film is required in order to obtain observed crack growth rates, even after crack tip cation hydrolysis and acidification, regardless of the exact mechanism of EAC.

The repassivation behavior of fractured pure titanium thin films has been examined in order to determine the bare surface electrode kinetics indicative of a crack tip following a film rupture event. (D.G. Kolman and J.R. Scully, "Limitations of Potentiostatic Repassivation Techniques and Their Relationship to the Applicability of the High Field Approximation to the Repassivation of Titanium," *J. Electrochem. Soc.*, in review, October 1994.)

- oo Current densities as large as 75 - 100 A/cm<sup>2</sup> ( $E_{\text{app}} = -0.6V_{\text{SCE}}$ , 0.6M NaCl) can be obtained on titanium in the first microseconds following film rupture. Although orders of magnitude larger than any current density previously observed on titanium, the current density is still too low to account for the fastest crack growth rates observed (90  $\mu\text{m/s}$ ) by a dissolution-based EAC mechanism, which would require 245 A/cm<sup>2</sup> ( $E_{\text{app}} = -0.6V_{\text{SCE}}$ ). This suggests that some mechanism other than a dissolution-based mechanism (e.g., a hydrogen mechanism) controls cracking in these alloys.

The following conclusions were reached based on internal hydrogen embrittlement (IHE) studies of solution treated and aged  $\beta$ -21S and Ti-15-3: (G.A. Young, J.R. Scully, "The Influence of Hydrogen on the Mechanical Properties of a Ti-Mo-Nb Alloy," *Scripta Metall.*, Vol. 23, pp. 507-512,



1993, and G.A. Young, J.R. Scully, "Internal Hydrogen Embrittlement of Solution Heat Treated and Aged Ti-15V-3Cr-3Al-3Sn and Ti-15Mo-3Nb-3Al," *Corrosion J.*, in press, 1994).

- oo An embrittlement threshold of approximately 1000 wt. ppm total hydrogen was observed for blunt circumferentially notched specimens of peak aged  $\beta$ -21S. A threshold was not observed for Ti-15-3, however approximately the same degree of embrittlement was obtained gradually as the hydrogen concentrations was increased from 100 to 3800 wt. ppm.
- oo Solutionized  $\beta$ -21S and Ti-15-3 were not embrittled by hydrogen up to concentrations of 3000 wt. ppm.
- oo Reduction in the maximum longitudinal tensile stress and plastic strain developed in re-solution annealed Ti-15-3 at hydrogen concentrations < 2900 wt. ppm suggest that the  $\beta$  phase can be intrinsically embrittled by hydrogen, especially when deformation occurs by localized planar slip.
- oo Embrittlement is a function of hydrogen concentration, constraint, and yield strength for alloys which have a susceptible microstructure. Susceptible microstructures are caused by high solution treatment temperatures and long times which remove heterogeneous nucleation sites from grain interiors to promote grain boundary  $\alpha$  formation, delay intragranular  $\alpha$  precipitation and promote planar slip. In aged alloys it is speculated that fine  $\alpha$  precipitates may be sheared by dislocations to promote planar slip, concentrate hydrogen along planar slip bands and transport hydrogen to grain boundaries. Alternatively, planar slip may promote deformation induced trap site formation at the  $\alpha/\beta$  interfaces or near  $\beta$  grain boundaries.
- oo Hydriding of a large volume fraction of the  $\alpha$  and  $\beta$  phases is not required for hydrogen embrittlement to occur in these high strength  $\beta$  titanium alloys. Hydriding was only observed when surface connected  $\alpha$  was exposed to electrochemical reactions. The internal hydrogen preferentially partitions to the  $\beta$  matrix. The possibility exists for deformation assisted or highly localized hydriding of  $\alpha$ - $\beta$  interfaces in STA material.
- oo The relationships between microstructure, deformation mode and speculated hydrogen transport behavior can account for the observed cracking in  $\beta$  titanium which was precharged with hydrogen and slowly strained in air as well as simultaneously polarized and slowly strained in aqueous chloride solution. This correlation supports a hydrogen embrittlement/dislocation transport mechanism for aqueous saltwater stress corrosion cracking of metastable  $\beta$  titanium alloys.

The following conclusions were reached based on IHE studies and thermal desorption spectroscopy (TDS) performed on solutionized (ST) and solutionized and peak aged (STA) Beta-C: (M.A. Gaudett, J.R. Scully, "Hydrogen Interactions and Embrittlement in Metastable

Beta Ti-3Al-8V-6Cr-4Mo-4Zr", to be submitted for publication, 1993).

- oo The STA material shows a large decrease in the maximum longitudinal stress at hydrogen concentrations of approximately 1500 wt. ppm. The evolution of fracture mode with increased hydrogen concentration progresses from transgranular microvoid coalescence, ductile slip line fracture and a less ductile transgranular fracture, to intergranular fracture at 1500 wt. ppm. At higher concentrations a granulated fracture surface appears followed by cleavage fracture observed at 3000 wt. ppm.
- oo The ST material shows a decrease in the maximum longitudinal stress above a concentration of approximately 2600 wt. ppm. The fracture mode is characterized by microvoid coalescence at low concentrations and a less ductile transgranular fracture with increasing hydrogen. Ductile slip line fracture appears at 4100 wt. ppm hydrogen. Cleavage fracture is observed at approximately 6900 wt. ppm.
- oo Internal hydriding of a large volume of charged material was not detected by x-ray diffraction (XRD) in either the ST or STA condition and therefore is not required to observe embrittlement in Beta-C.
- oo The similarity of  $T_{\max}$  for the high temperature peak in the thermal desorption spectra of both the ST and STA condition indicate a microstructural trap site common to both conditions. The concentration associated with this site is consistent with the O or N content of this alloy, implicating interstitials as a trap site.
- oo The microstructural trap sites for hydrogen detected by TDS remain unidentified as yet. However, calculations indicate the following:
  - (1) Measured hydrogen concentrations are too large to be associated with trapping at the oxide/metal interface.
  - (2) The concentrations measured by XRD are consistent with the concentration associated with peak #2 in the ST desorption spectrum.
  - (3) Although bulk hydriding in the STA material was not detected with x-ray diffraction, the concentrations measured are on the order of that calculated assuming the decomposition of a small amount of hydride during TDS (<2 vol.%). Also, the concentrations in the  $\beta$  lattice determined by XRD can account for peak #1 or #2 in the STA desorption spectrum and suggests the presence of a small amount of hydride as one of the remaining peaks.

Limited work investigated the effect of sulfate reducing bacteria (SRB) on aqueous environment enhanced fatigue. (R.P. Gangloff and R.G. Kelly, "Microbe Enhanced Environmental Fatigue Crack Propagation in HY130 Steel," *Corrosion*, Vol. 50, No. 5, pp. 345-354, 1994).

- oo Sulfate reducing bacteria, *Desulfovibrio vulgaris* in diluted Postgate C, greatly enhance rates of fatigue crack propagation and reduce fatigue crack initiation life in a

martensitic alloy steel (HY130) under cathodic polarization ( $-1000 \text{ mV}_{\text{sce}}$ ). Metabolic sulfide-enhanced atomic hydrogen uptake and crack tip process zone hydrogen embrittlement are implicated.

- oo Transgranular cracking, typical of fatigue in sterile NaCl solution, changes to intergranular cracking due to the presence of SRB.
- oo The severity of the SRB effect on growth rates and intergranular cracking is paramount among those variables which influence environmental fatigue in C-Mn and alloy steels.
- oo The deleterious SRB effects on fatigue crack propagation, and fatigue crack initiation, are not mitigated by cathodic polarization.
- oo Transient environmental FCP in the SRB solution is likely due to time-dependent bacterial growth and enhanced metabolically reduced sulfides. Transient FCP at constant  $\Delta K$  may also be due to diffusion of metabolites from the bulk to the crack tip solution, and hydrogen penetration from boldly exposed specimen surfaces. SRB may not colonize the occluded alkaline crack tip.
- oo Transient fatigue cracking in SRB solutions can compromise life prediction based on stress intensity similitude.

A review on the application and interpretation of laboratory methods to corrosion fatigue cracking was completed. (R.P. Gangloff, "Corrosion Fatigue Cracking," in Manual on Corrosion Tests and Standards: Application and Interpretation, R. Baboian, Ed., ASTM, Philadelphia, PA, in press, 1994.)

#### ABSTRACT

Corrosion fatigue (CF) is an important but complex mode of failure for high performance structural metals operating in aggressive environments. This view is based on the likelihood of cyclically varying loads and chemical environments in service, the need for predictable long-life component performance and life extension, the universal susceptibility of pure metals and alloys to CF damage, and the time-dependent multi-variable character of corrosion fatigue. For example, stress corrosion cracking immune alloys are susceptible to CF. Corrosion fatigue has affected nuclear power systems, steam and gas turbines, aircraft, marine structures, pipelines, and bridges; CF issues are central to the behavior of many aging systems.

The objective of this chapter is to highlight modern laboratory methods for characterizing the corrosion fatigue behavior of metals in aqueous electrolytes. The principles and mechanisms of CF are summarized in Section I, followed by discussions of experimental methods in Section II. Specimen design and loading, environment control, strain and crack size measurement, and computer automation are discussed. The emphasis throughout is on exemplary experimental methods and results, as well as on CF data analysis and interpretation. Section III cites applications of CF data to service, the advantages and limitations of the experimental methods, and directions for research on CF experimentation. Symbols and terms are defined in Section IV. This Chapter, with extensive references, extends previous reviews of corrosion fatigue test techniques.



**APPENDIX A - PUBLICATIONS FROM ONR GRANT**

**NO. N00014-91-J-4164**

**AQUEOUS ENVIRONMENTAL CRACK PROPAGATION  
IN HIGH STRENGTH BETA TITANIUM ALLOYS**

**Lisa M. Young  
George A. Young, Jr.  
John R. Scully  
Richard P. Gangloff**

## AQUEOUS ENVIRONMENTAL CRACK PROPAGATION IN HIGH STRENGTH BETA TITANIUM ALLOYS

Lisa M. Young, George A. Young, Jr., John R. Scully and Richard P. Gangloff<sup>1</sup>

### ABSTRACT

*The aqueous environment assisted cracking (EAC) behavior of two peak aged beta-titanium alloys was characterized with a fracture mechanics method. Beta-21S is susceptible to EAC under rising load in neutral 3.5% NaCl at 25°C and -600 mV<sub>SCE</sub>, as indicated by a reduced threshold for subcritical crack growth ( $K_{TH}$ ), an average crack growth rate of up to 10  $\mu\text{m/sec}$ , and intergranular fracture compared to microvoid-rupture in air. In contrast the initiation fracture toughness ( $K_{IC1}$ ) of Ti-15-3 in moist air is lower than that of Beta-21S at similar high  $\sigma_{YS}$  (1300 MPa), but is not degraded by chloride and cracking is by transgranular microvoid formation. The intergranular EAC susceptibility of Beta-21S correlates with both  $\alpha$ -colonies precipitated at  $\beta$  grain boundaries and intense slip localization, however, the causal factor is not defined. Data suggest that both features, and EAC, are promoted by prolonged solution treatment at high temperature. In a hydrogen environment embrittlement scenario, crack tip H could be transported by planar slip bands to strongly binding trap sites and stress/strain concentrations at  $\alpha$ -colony or  $\beta$  grain boundaries. EAC in Beta-21S is eliminated by cathodic polarization (to -1000 mV<sub>SCE</sub>), as well as by static loading for times which otherwise produce rising-load EAC. These beneficial effects could relate to reduced H production at the occluded crack tip during cathodic polarization, and to increased crack tip passive film stability or reduced dislocation transport during deformation at slow crack tip strain rates. High-strength  $\beta$ -titanium alloys are resistant, but not intrinsically immune to chloride EAC, with processing condition possibly governing fracture.*

---

<sup>1</sup> L.M. Young and G.A. Young, Jr., formerly Graduate Research Associates at the University of Virginia, are currently Metallurgist at the General Electric Corporate Research and Development Center (Schenectady, NY, 12301) and Engineer at the Knolls Atomic Power Laboratory (Schenectady, NY, 12301), respectively. J.R. Scully and R.P. Gangloff are Assistant Professor and Professor, respectively, in the Department of Materials Science and Engineering, School of Engineering and Applied Science, University of Virginia, Charlottesville, VA, 22903.

## INTRODUCTION

Metastable beta titanium alloys are being developed for structural applications that require formability, hardenability, fracture toughness, and aqueous corrosion resistance<sup>[1-4]</sup>. The environment-assisted cracking (EAC) behavior of these alloys is important for long-life components stressed in aggressive marine, oil or gas well, aerospace, and medical implant environments<sup>[5,6]</sup>. While the stress corrosion cracking, hydrogen embrittlement and corrosion fatigue of  $\alpha$  and  $\alpha/\beta$ -titanium alloys have been researched extensively<sup>[7-11]</sup>, EAC in beta and  $\alpha$ -precipitation hardened  $\beta$ -titanium alloys is relatively unexplored.<sup>2</sup>

Solution treated and aged (STA)  $\beta$ -titanium alloys with  $\alpha$  precipitates exhibit excellent yield strength ( $\sigma_{YS}$ ) and fracture toughness ( $K_{IC}$ ), but can be susceptible to brittle cracking in ambient temperature aqueous solutions with halide ions<sup>[10,12]</sup>. Early experiments utilizing cracked specimens and fracture mechanics methods demonstrated that developmental  $\beta$ -titanium alloys (Ti-11.5Mo-6Zr-4.5Sn and Ti-13V-11Cr-3Al; both STA)<sup>3</sup> and model Ti-Mo compositions were prone to EAC in NaCl and KCl solutions at static or quasi-static load threshold stress intensities ( $K_{ISCC}$ ) as low as 15% of  $K_{IC}$ <sup>[8,13-15]</sup>. EAC in these high strength  $\beta$ -titanium alloys progressed by intergranular separation and transgranular cleavage or "quasi-cleavage", depending on alloy composition and microstructure<sup>[7,11,13]</sup>. EAC was exacerbated at intermediate loading rates, at intermediate applied electrode potentials (near -600 mV<sub>SCE</sub>), and by increased  $\sigma_{YS}$ <sup>[8,14-16]</sup>, however, data were limited.

Studies of EAC in modern  $\beta$ -titanium alloys, employing the slow strain rate technique with smooth uniaxially loaded tensile specimens, demonstrated resistance to brittle cracking in aqueous NaCl at 25°C and near free corrosion potentials<sup>[12,17-22]</sup>. For example, high strength STA Ti-3Al-8V-6Cr-4Mo-4Zr (Beta-C<sup>TM</sup>) was not susceptible to EAC in neutral chloride, with or without cathodic polarization; such conditions promoted cracking of  $\alpha/\beta$  Ti-6Al-4V<sup>[20,21]</sup>. Similar good EAC resistance was reported for STA Ti-15Mo-3Nb-3Al (Beta-21S or TIMETAL-21S<sup>TM</sup>)<sup>[22]</sup>, however, Ti-15V-3Cr-3Al-3Sn (Ti-15-3) was susceptible to brittle cracking in neutral aqueous

---

<sup>2</sup>  $\alpha$  is the hexagonal-close-packed phase, while  $\beta$  is body-centered-cubic.

<sup>3</sup> All compositions are in weight percent.

chloride, but only at intermediate loading rates and electrode potentials<sup>[17]</sup>.<sup>4</sup> While immune to cracking in neutral chloride at 25°C, EAC was produced in Beta-C due to H<sub>2</sub>S addition with cathodic polarization<sup>[23]</sup>, with increased temperature to above 150°C<sup>[18]</sup>, in anhydrous methanol-chloride<sup>[19]</sup>, and after STA<sup>[23]</sup>. Precracked specimen experiments with modern  $\beta$ -titanium alloys are limited. Results suggest that STA Ti-15-3 and Beta-C resist EAC in chloride for mechanical and electrochemical conditions that embrittle Ti-6Al-4V<sup>[24,25]</sup>.

The objective of this research is to characterize the environment assisted crack propagation behavior of two high strength  $\beta$ -titanium alloys in aqueous chloride. Experiments are designed to control the variables that may exacerbate EAC based on studies of high strength steels and  $\alpha/\beta$ -titanium alloys. Specific factors include: (a) a fatigue precrack and triaxial constraint<sup>[26]</sup>, (b) active crack tip straining<sup>[27]</sup>, (c) high yield strength from STA<sup>[28]</sup>, (d) controlled electrode potential<sup>[14,15]</sup>, and (e) heterogeneous  $\alpha/\beta$  microstructures<sup>[15,29]</sup>. These results provide a basis to understand the contributions of crack tip depassivation, transient dissolution and hydrogen uptake in the EAC mechanism of  $\beta$ -titanium alloys.

## EXPERIMENTAL PROCEDURE

### Materials

Two alloys, Beta-21S (Ti-15.4Mo-3.0Nb-2.9Al-0.13 O; measured wt%) and Ti-15-3 (Ti-14.9V-3.0Cr-3.2Al-3.6Sn-0.12 O; measured wt%), were obtained as 10.2 and 9.5 mm thick hot cross-rolled plates, respectively, in a solution treated (ST) condition (871°C for 8 hr and 816°C for 30 minutes, respectively). Oversized blanks of each alloy were peak aged at 538°C for 8 hr before specimen machining. (This condition is referred to as STA.) The resulting microstructures are similar, consisting of a large volume fraction of fine intragranular and grain boundary  $\alpha$ -plate precipitates in a  $\beta$  matrix of 100  $\mu$ m diameter grains (Fig. 1). Figures 1b and 1c suggest that  $\alpha$  plates are coarser in Ti-15-3 compared to Beta-21S. While not evident in Fig. 1, these two alloys exhibit dramatically different grain boundary  $\alpha$  precipitation, as detailed in an ensuing section. X-ray diffraction and transmission electron microscopy (TEM) did not resolve the  $\omega$ -phase in ST or STA Ti-15-3 or Beta-21S<sup>[30,31]</sup>. Athermal  $\omega$ -phase is not expected to form in highly  $\beta$ -

---

<sup>4</sup> The smooth specimen gauge strain rate for maximum susceptibility to EAC was about  $5 \times 10^{-6} \text{ sec}^{-1}$  and the most deleterious electrode potential was -500 mV<sub>SCE</sub><sup>[17]</sup>.

stabilized Ti-15-3 or Beta-21S, during cooling from solution treatment temperatures, and isothermal  $\omega$  should not precipitate prior to  $\alpha$  nucleation during subsequent peak aging of either alloy at 538°C<sup>[32-35]</sup>.

Uniaxial tensile data listed in Table I show that the strength of STA Ti-15-3 is less than that of Beta-21S, with the results exhibiting substantial variability, particularly for the former alloy. (Tensile specimens were machined from the ends of broken EAC and fracture toughness specimens that were also characterized in terms of hardness. Tests 1 and 2 in Table I refer to replicate tensile specimens from one-half of a broken EAC or toughness specimen.) The reproducible hardnesses (Rockwell C scale;  $R_c$ ) and tensile yield strengths ( $\sigma_{ys}$ ) in Table I for each fracture specimen demonstrate that the strength variability is between fracture specimens. The cause of this variability is not known, but may be due to temperature differences during the aging of blanks.

The important point for the current study is to account for strength variations in comparisons of EAC susceptibility. Based on the data in Table I, and additional results<sup>[36]</sup>, yield strength and hardness are related according to:

$$\sigma_{ys} \text{ (MPa)} = -97.93 + 33.67 (R_c) \quad (1)$$

for both Beta-21S and Ti-15-3. Equation 1 agrees with a correlation for tempered martensitic

Table I: *Tensile Properties of STA  $\beta$ -Titanium Alloys*

| Alloy    | Test | $R_c$ | $\sigma_{ys}$<br>(MPa) | E<br>(GPa) | $n^*$ | RA**<br>(%) |
|----------|------|-------|------------------------|------------|-------|-------------|
| Ti-15-3  | 1    | 35.7  | 1030                   | 94.2       | 0.036 | 21          |
|          | 2    |       | 1050                   | 93.3       | 0.037 | 28          |
| Ti-15-3  | 1    | 39.2  | 1315                   | 96.6       | 0.032 | 13          |
|          | 2    |       | 1315                   | 97.7       | 0.031 | 14          |
| Beta-21S | 1    | 44.7  | 1420                   | 102.2      | 0.016 | 6           |
|          | 2    |       | 1430                   | 98.2       | 0.015 | 0           |
| Beta-21S | 1    | 43.8  | 1335                   | 103.2      | 0.018 | 2           |
|          | 2    |       | 1325                   | 101.8      | 0.018 | 1           |

\*  $n$  is the exponent in the power-law relationship between true stress and true plastic strain.

\*\* RA = (Initial Diameter - Diameter at Fracture)/ Initial Diameter.

steels<sup>[28]</sup>. Each fracture toughness and EAC specimen was characterized by either measured  $\sigma_{YS}$  or measured  $R_C$  and calculated  $\sigma_{YS}$  from Eq. 1.

## Environmental Cracking

EAC resistance was characterized with a slow-rising load fracture mechanics method<sup>[37-40]</sup> applied to a fully rotating single edge cracked specimen (initial crack length = 17.8 mm, thickness = 5.08 mm, width = 38.1 mm). A servohydraulic machine was employed for fatigue cracking (load control) and increasing load EAC experiments (actuator displacement control). Specimens were fatigue precracked in the aqueous environment, involving a three day exposure, and then were subjected to rising load at a programmed constant actuator displacement rate. Crack mouth opening displacement rate is not constant after the onset of crack growth due to load-train compliance.

Crack length was determined by the computer-automated direct current electric potential difference (dcEPD) method. Applied current was typically maintained at  $8.000 \pm 0.005$  amperes by a constant current power supply. Current polarity switching eliminated thermal voltages, and reference probes were used to account for the effects of temperature and small current variations during long term experiments<sup>[36,41]</sup>. Potential differences, local to the crack tip and between 200 and 500  $\mu V$ , were amplified by 10,000 times and input to the data acquisition system. Crack length ( $a$ ) was calculated from averaged measured voltages through a closed-form solution for the edge-cracked geometry<sup>[36,41]</sup>. Voltage resolution was  $\pm 0.3 \mu V$ , corresponding to a crack length resolution of  $\pm 5 \mu m$ , assuming uniform advance of the crack front. Applied stress intensity ( $K$ ) was calculated from measured load and crack length with an elastic solution for the single edge crack geometry<sup>[42]</sup>. J-integral calculations indicated that the plastic contribution to  $J_{Total}$  is small compared to  $J_{Elastic}$ <sup>[42]</sup>; thus small scale yielding is maintained and the elastic  $K$  analysis is sufficient.

A schematic of the EAC procedure is presented in Fig. 2. The critical  $K$  for the onset (initiation) of crack growth in air or in the solution was defined by the first resolved nonlinearity in the load versus actuator displacement record, which was generally coincident with the first change in the slope of the initially linear (but more variable) electrical potential versus load record<sup>[36,43]</sup>. This critical  $K$  is a lower bound ( $K_{IC1}$ ) of the standardized plane strain fracture

toughness ( $K_{IC}$ ) for loading in moist air<sup>[44]</sup>, and a threshold ( $K_{TH}$ ) for cracking in aggressive environments<sup>[37-40]</sup>. At initiation, the crack growth increment ( $\Delta a$ ) was assumed to equal zero; subsequent crack lengths and  $\Delta a$  were calculated utilizing dcEPD values normalized with the potential at the known fatigue precrack length<sup>[36,41]</sup>. Environmental effects on crack propagation are indicated by the slope of  $K$ - $\Delta a$  data, and by subcritical crack growth rates ( $da/dt$ ) calculated from measured crack length vs time.

Experiments were conducted in either moist air or neutral (pH 8) 0.6M (3.5 wt%) aqueous NaCl at fixed electrode potential and 25°C. The central portion of the edge cracked specimen was immersed continuously in a sealed 1 liter plexiglass cell, and exposed to flowing (60 ml/min) chloride from a 23 liter reservoir. Environment control was complete; no dissimilar metal contacted the specimen, all tubing was teflon, and the electrolyte was argon deaerated. The grounded specimen was maintained at constant electrode potential by a Wenking potentiostat in conjunction with a Ag/AgCl reference electrode and two platinum counter electrodes located adjacent to each side of the specimen and about 30 mm from the propagating crack. Reference and counter electrodes were isolated to minimize solution contamination. Electrode potentials are reported with respect to the saturated calomel electrode ( $mV_{SCE}$ ).

## RESULTS

### Moist Air Fracture Toughness ( $K_{ICi}$ )

Slow rising load experiments were generally performed at a constant actuator displacement rate of 25.4  $\mu m/min$  to obtain the moist air fracture toughnesses of STA Ti-15-3 and STA Beta-21S.  $K_{ICi}$  values in Table II are for plane strain constraint, based on ASTM Standard E813<sup>[45]</sup>, and are slightly less than or equal to  $K_{IC}$  from ASTM Standard E399<sup>[44,46]</sup>. Fracture toughness is variable for each alloy, but correlates reasonably with varying yield strength.  $K_{ICi}$  generally decreases with increasing strength, and Beta-21S is tougher than Ti-15-3 at fixed  $\sigma_{YS}$ .<sup>5</sup> Fracture toughness variability may also be due to subtle uncertainties in defining the electrical potential corresponding to crack initiation<sup>[36,43]</sup>. Crack tip plastic deformation, microvoid damage and macrocrack growth can contribute to voltage increases.

---

<sup>5</sup> Linear regression analysis of the limited data in Table II support this conclusion.  $K_{ICi}$  equals  $(131.3 - 0.046 \sigma_{YS})$  for Beta-21S and  $(166.0 - 0.085 \sigma_{YS})$  for Ti-15-3, with  $K_{ICi}$  in units of  $MPa/m$  and  $\sigma_{YS}$  in  $MPa$ <sup>[36]</sup>.



Table II: *Moist Air Fracture Toughness of STA  $\beta$ -Titanium Alloys*

| Alloy    | $\sigma_{YS}$ (MPa) | $K_{ICl}$ (MPa/m) |
|----------|---------------------|-------------------|
| Ti-15-3  | 1040                | 79                |
| Ti-15-3  | 1230**              | 59                |
| Ti-15-3  | 1315                | 57                |
| Beta-21S | 1285**              | 77                |
| Beta-21S | 1330                | 66                |
| Beta-21S | 1425                | 68                |

\*\* These values were calculated from measured hardnesses and Eq. 1, while all other  $\sigma_{YS}$  values were measured with tensile specimens from broken fracture test-pieces, as summarized in Table I.

Fracture in moist air was predominantly transgranular for both STA Ti-15-3 and STA Beta-21S, as shown by the scanning electron microscope (SEM) fractographs in Fig. 3. The fatigue crack is at the top of each fractograph and the crack growth direction is from top to bottom. (All ensuing fractographs are in this orientation.) The fracture process zone, estimated by four to eight blunted crack tip opening displacements at the crack initiation toughness (or  $2$  to  $4K_{ICl}^2/\sigma_{YS}E$ ), is on the order of 60 to 120  $\mu\text{m}$ . Higher magnification microscopy revealed microvoided crack surfaces, with a small areal fraction of intergranular cracking and possible cleavage facets for each alloy, particularly Beta-21S<sup>[36]</sup>.

### Aqueous Chloride Environmental Cracking Resistance ( $K_{TH}$ )

*Constant Displacement Rate Experiments* STA Ti-15-3 is resistant to EAC during rising load, as shown by the  $K-\Delta a$  results in Fig. 4. For exposure to aqueous chloride at a fixed potential of  $-600 \text{ mV}_{SCE}$ ,  $K_{TH}$  (at  $\Delta a = 0$ ) ranges from 61 to 64  $\text{MPa}/\text{m}$ , independent of actuator displacement rates of 1.3 and 25.4  $\mu\text{m}/\text{min}$ , for specimen hardnesses of  $R_C$  37.5 and 37.9. NaCl exposure does not decrease the crack initiation toughness from the measured moist air  $K_{ICl}$  value of 59  $\text{MPa}/\text{m}$  for a Ti-15-3 hardness of  $R_C$  39.4 (upper  $\circ$ -set in Fig. 4 and  $\sigma_{YS}$  of 1230

MPa in Table II), or from  $K_{ICl}$  of 66 MPa/m estimated through Eq. 1 and Footnote 3 for a hardness of  $R_C$  37.7 (the average  $R_C$  for • and ■ in Fig. 4)<sup>[36]</sup>. Resistance to stable crack extension under plane strain constraint, given by a small but finite slope ( $dK/d\Delta a$ ), is not influenced by chloride. The difference in the average slope of  $K$  versus  $\Delta a$  is larger for the replicate air experiments compared to the aqueous chloride environmental effect.

Loading in NaCl did not alter the microscopic fracture morphology for Ti-15-3 compared to cracking in moist air. A typical scanning electron fractograph of the crack initiation region, adjacent to the fatigue precrack, is presented in Fig. 5 for Ti-15-3 in NaCl. Equivalent to the moist air fracture, the crack surface is mainly populated by transgranular features indicative of microvoid-based cracking, as confirmed by high magnification SEM observations (Fig. 5b).

In contrast to Ti-15-3, peak aged Beta-21S is embrittled by rising load in NaCl at -600 mV<sub>SCE</sub>, as shown by the  $K$ - $\Delta a$  data in Fig. 6. While  $K_{ICl}$  is high for moist air (66 and 68 MPa/m, Table II, and ○ in Fig. 6),  $K_{TH}$  ranges from 39 to 46 MPa/m for STA Beta-21S in NaCl at two constant actuator displacement rates. The macroscopic crack growth resistances (average  $dK/d\Delta a$ ) are similar for each loading rate in NaCl and for each environment. The variability in  $K_{TH}$  for the faster rate does not correlate with strength, since the lower threshold of 39 MPa/m was observed for the lower hardness specimen<sup>[28]</sup>. The two values of  $K_{TH}$ , 39 and 46 MPa/m, may represent the distribution resulting from multiple environmental cracking experiments with an STA  $\beta$ -titanium alloy. Factors such as experimental definition of crack growth initiation, as well as differences in crack tip process zone microstructure, are likely to govern the distribution of  $K_{TH}$  values, as suggested by more extensive data for Beta-21S<sup>[36]</sup>. Variability does not cloud the conclusion that Beta-21S is susceptible to environmental cracking, compared to the moist air case. The data in Fig. 6 show that the two displacement rates were sufficiently high to offset stress intensity reductions due to increasing specimen compliance and declining load during environmental crack growth. The constant actuator displacement rate EAC experiments were generally of the increasing- $K$  type, at least during the first 2 mm of crack extension.

Aqueous NaCl caused a dramatic fracture mode transition in STA Beta-21S. Compared to transgranular microvoid-based fracture for Beta-21S in moist air (Fig. 3b), Fig. 7 shows that EAC in chloride is essentially intergranular, with limited evidence of transgranular ductile fracture. The initial stage of EAC, within 25  $\mu$ m of the fatigue crack (top of Fig. 7), involved some transgranular cracking, similar to that observed for moist air, while boundary cracking

initiated immediately adjacent to the fatigue crack tip in other grains. Presumably, this distribution of modes is related to the location of the fatigue crack within the 30 to 100 grains along the crack front. Fatigue precracking at a loading frequency of 5 Hz and in aqueous NaCl did not produce intergranular cracking, as shown in Fig. 7<sup>[36]</sup>. The transition from transgranular ductile fracture for air to intergranular cracking was observed for each specimen fractured in NaCl and is consistent with the environmental effect on crack initiation resistance (Fig. 6).

The macroscopic crack paths and causal fracture mechanisms are markedly different for STA Beta-21S in moist air and NaCl, however,  $dK/d\Delta a$  are similar. The resistance to stable tearing in benign environments ( $dK/d\Delta a$ ) is determined by rate independent intrinsic material properties, including the process zone fracture strain and plastic flow properties<sup>[47]</sup>. In contrast  $dK/d\Delta a$  during EAC is governed by the rate of environmental crack advance, which depends on alloy cracking resistance and environment chemistry, coupled with the applied crack mouth opening displacement rate and specimen compliance. Intuitively, the crack growth resistance slope should be less, or even negative, for EAC compared to the typical moist air R-curve, and could approach this latter value at rapid loading rates. This difference may be negligible for Beta-21S (Fig. 6) because the crack growth resistance is small for the plane strain moist air case.

This study emphasized  $K_{TH}$  at the onset of environmental cracking, however, average rates of intergranular EAC ( $da/dt$ ) were estimated. As indicated by the  $K-\Delta a$  data in Fig. 6, subcritical crack growth occurred in STA Beta-21S due to NaCl exposure and at  $K$  levels well below  $K_{IC}$ . For an experiment at an actuator displacement rate of 25.4  $\mu\text{m}/\text{min}$ , intergranular EAC initiated at a  $K_{TH}$  of 39  $\text{MPa}/\text{m}$  and after 1220 seconds of steadily rising load; 2.0 mm of stable crack growth then occurred in 180 seconds, for an average crack growth rate of about 10  $\mu\text{m}/\text{sec}$ . ( $K$  increased from 39 to 50  $\text{MPa}/\text{m}$  during this amount of EAC at increasing load line displacement.) For the slower loading rate experiment in Fig. 6, intergranular EAC initiated at a  $K_{TH}$  of 46  $\text{MPa}/\text{m}$ , after 4.8 hours of loading; subsequently, 2.0 mm of stable crack growth occurred in 1800 seconds, for an average  $da/dt$  of 1  $\mu\text{m}/\text{sec}$ . ( $K$  increased from 46 to 57  $\text{MPa}/\text{m}$  during this amount of EAC.) Cracking at this slower loading rate involved two periods of substantially faster crack extension, each 300  $\mu\text{m}$  long, at  $K$  levels between  $K_{TH}$  and  $K_{IC}$ , as suggested by the groupings of data points in Fig. 6. Presumably, the 1  $\mu\text{m}/\text{sec}$  average growth rate is constituted by alternating periods of substantially slower and faster environmental cracking. The fast and slow rates were not measured. Work is required to better resolve the relationship between  $da/dt$ ,

K,  $\Delta a$  and loading compliance during a rising displacement experiment with  $\beta$ -titanium alloys in chloride.<sup>6</sup>

**Static Load Results** Fatigue precracked specimens of STA Ti-15-3 and STA Beta-21S were loaded statically during immersion in NaCl at  $-600 \text{ mV}_{\text{SCE}}$ . These experiments were performed at several constant K levels (35, 45, 55 and  $60 \text{ MPa}\sqrt{\text{m}}$ ) for 24 hour intervals, while crack length was monitored continuously by dcEPD. Crack growth rate resolution over a 24 hour period was  $3 \times 10^{-4} \text{ }\mu\text{m}/\text{sec}$ . This exposure, while short compared to classic stress corrosion cracking experiments, is longer than the durations of the slow displacement rate experiments represented in Figs. 4 and 6 which required 0.5 or 10 hours for the two loading rates. Additionally, a 24 hour hold-time was reported to produce 17 meters of crack advance in EAC-sensitive STA Ti-12Mo-6Zr-3Sn in aqueous NaCl at about  $-600 \text{ mV}_{\text{SCE}}$  [48].

Static loading for 24 hours did not cause resolvable environmental crack growth for either STA Ti-15-3 or Beta-21S in NaCl. In one instance NaCl-enhanced subcritical crack growth was produced in Beta-21S, but only after 94 hours at a K level of  $60 \text{ MPa}\sqrt{\text{m}}$ . The average crack growth rate increased from about  $10^{-2} \text{ }\mu\text{m}/\text{sec}$  to  $20 \text{ }\mu\text{m}/\text{sec}$  with time and crack length (from 20.2 mm to 22.2 mm) at this constant applied K.

**Effect of Applied Electrode Potential** The effect of applied electrode potential on EAC in the STA Ti-15-3 and Beta-21S/NaCl systems was investigated. In addition to  $-600 \text{ mV}_{\text{SCE}}$ , applied potentials of  $-150 \text{ mV}_{\text{SCE}}$  and  $-1000 \text{ mV}_{\text{SCE}}$  were employed in conjunction with the rising load method. The free corrosion potential of these two  $\beta$ -titanium alloys in the deaerated neutral 0.6M NaCl was measured to equal between  $-400$  and  $-600 \text{ mV}_{\text{SCE}}$ .<sup>7</sup>

Peak aged Ti-15-3 was not susceptible to EAC in aqueous 3.5% NaCl at any of the applied electrode potentials and a constant actuator displacement rate of  $1.3 \text{ }\mu\text{m}/\text{min}$ .  $K_{\text{TH}}$  values were as follows:  $66 \text{ MPa}\sqrt{\text{m}}$  for  $-150 \text{ mV}_{\text{SCE}}$  ( $R_C$  37.0),  $61 \text{ MPa}\sqrt{\text{m}}$  for  $-600 \text{ mV}_{\text{SCE}}$  ( $R_C$  37.9), and

<sup>6</sup> The distances of fast crack growth and average  $da/dt$  values are based on the assumption of uniform crack advance along the crack front, as required to analyze the dcEPD voltages [36].

<sup>7</sup> Immersed in aerated neutral 0.6 M NaCl, Ti-15-3 exhibited a free corrosion potential of  $-400 \text{ mV}_{\text{SCE}}$  and a passive current density of  $0.5 \text{ }\mu\text{A}/\text{cm}^2$ . These values were  $-300 \text{ mV}_{\text{SCE}}$  and  $0.5 \text{ }\mu\text{A}/\text{cm}^2$  for Beta-21S. No active-passive transitions were observed because each alloy was spontaneously passive in near-neutral chloride solution at  $25^\circ\text{C}$ . The pitting potential for each alloy in this chloride solution was well above  $+1000 \text{ mV}_{\text{SCE}}$  [49,50].

greater than 65 MPa√m for -1000 mV<sub>SCE</sub> ( $R_C$  36.8).<sup>8</sup> Measured  $K_{ICl}$  equals between 57 and 59 MPa√m for the  $R_C$  39 to 40 hardness of Ti-15-3 in moist air, Fig. 4. Estimated  $K_{ICl}$  equals 65 MPa√m for the  $R_C$  37.9 hardness of Ti-15-3 and 69 MPa√m for the  $R_C$  36.8 case. For each electrode potential, the crack surface was transgranular, typical of that shown in Fig. 5 and indicative of ductile fracture without a chloride environmental effect.

Peak aged Beta-21S exhibited EAC at -150 mV<sub>SCE</sub> (and -600 mV<sub>SCE</sub>), but not at -1000 mV<sub>SCE</sub>, as shown by the constant displacement rate (25.4 μm/min) K-Δa data in Fig. 8. Although  $K_{TH}$  was reduced significantly at -150 mV<sub>SCE</sub>, crack growth resistance (given by dK/dΔa) was relatively high, perhaps indicating that average da/dt was low compared cracking at the more active potential. The microscopic fracture mode for the -150 mV<sub>SCE</sub> case supports environmental embrittlement; as shown in Fig. 9a, this chloride mode consisted of intergranular cracking joined by limited ductile tearing and with some transgranular cracking adjacent to segments of the initial fatigue crack. These features are similar to those observed for the Beta-21S crack surface produced in NaCl at -600 mV<sub>SCE</sub> (Fig. 6), a condition that also promoted EAC. In contrast NaCl with an applied electrode potential of -1000 mV<sub>SCE</sub> did not degrade fracture resistance relative to the behavior of Beta-21S in moist air.  $K_{TH}$  for this case equals  $K_{ICl}$  for Beta-21S, and the NaCl/cathodic polarization cracking mechanism is transgranular microvoid coalescence (Fig. 9b) similar to that observed for moist air (Fig. 3b).

## DISCUSSION

### Moist Air Fracture Toughness of STA β-Titanium Alloys

The moist air fracture toughnesses of STA Ti-15-3 ( $K_{ICl}$  = 57 to 59 MPa√m for  $\sigma_{YS}$  = 1230 to 1315 MPa; Table II and Footnote 3) and STA Beta-21S ( $K_{ICl}$  = 66 to 68 MPa√m for  $\sigma_{YS}$  = 1330 to 1425 MPa) are comparable to values reported for β-titanium alloys at similar high yield strengths<sup>[29,51-54]</sup>. This result validates the accuracy of the rising load experiment. Both Ti-15-3 and Beta-21S cracked by microvoid-based processes for the moist air case, however, each fracture morphology is complex because of the underlying two phase microstructure.

STA Beta-21S is tougher than Ti-15-3 at constant  $\sigma_{YS}$ , in spite of some grain boundary

---

<sup>8</sup> A data acquisition system failure preempted the conclusion of the experiment at -1000 mV<sub>SCE</sub>, however, stable crack growth had not initiated at an applied K of 65 MPa√m.

participation in ductile fracture. The microstructural origins of improved  $K_{IC}$  are not fully understood. For example, grain boundaries in the Beta-21S under study were preferred nucleation sites for large colonies of  $\alpha$  plates, as discussed in an ensuing section. A similar surprising result was reported for Ti-15-3, where large heterogeneous grain boundary  $\alpha$  precipitates correlated with increased fracture toughness compared to a more homogeneous  $\alpha$ -microstructure<sup>[54]</sup>. Other factors can affect the fracture toughness of these STA  $\beta$ -Ti alloys. Locally intense planar slip and a 1 to 10  $\mu\text{m}$  thick grain boundary  $\alpha$  "film" degrade  $K_{IC}$  due to strain localization in the  $\alpha$  phase, or in the softer precipitate-free  $\beta$  phase, relative to adjacent  $\alpha$ -precipitation hardened  $\beta$ , as well as due to preferred microvoid nucleation at  $\alpha/\beta$  interfaces<sup>[4,51-53]</sup>. Since STA Beta-21S may be more prone to locally intense slip compared to Ti-15-3 (see an ensuing section)<sup>[30]</sup>, decreased  $K_{IC}$  is expected; therefore, the observed toughness increase for Beta-21S does not correlate with a deleterious effect of slip localization. A 0.1 to 0.4  $\mu\text{m}$  thick layer of grain boundary  $\alpha$  was observed for both STA Beta-21S and Ti-15-3. Additional factors such as the size, distribution, and strength of  $\alpha$  and  $\beta$ ; solute (e.g., aluminum and oxygen) partitioning to each phase; and inclusion content may affect initiation fracture toughness.

## Environmental Cracking of STA $\beta$ -Titanium Alloys

*EAC Behavior Compared to Other Alloys*      The results in Figs. 4 and 6 through 8 show that STA Ti-15-3 resists environmental cracking in aqueous NaCl, however, peak aged Beta-21S is susceptible to severe intergranular EAC at electrode potentials near the free corrosion level. There are no precracked specimen fracture mechanics data in the literature for modern  $\beta$ -titanium alloys exposed to chloride, particularly under actively rising load<sup>[8,13-15,25,48]</sup>. Recent data indicate that  $K_{TH}$  for Ti-15-3 in aqueous chloride equals  $K_{IC}$ ,<sup>[24]</sup> analogous to the results in Fig. 4. In contrast Gagg and Toloui reported that smooth specimens of STA Ti-15-3 suffered chloride cracking, and Bavarian et al. reported that STA Beta-21S was immune to EAC under similar conditions (limited intergranular corrosion fatigue crack initiation was observed)<sup>[17,22]</sup>. These results demonstrate that EAC in STA  $\beta$ -titanium alloys occurs only within windows of many variables including electrode potential, an occluded crack tip, crack tip strain rate, yield strength, and alloy composition or processing-based microstructure. That smooth specimens of Beta-21S are immune, but precracked and dynamically loaded specimens are prone

to EAC, is consistent with the well-known behavior of  $\alpha/\beta$  alloys such as Ti-6Al-4V in chloride<sup>[26,57]</sup>. The EAC susceptibility of STA Ti-15-3, without an existing crack, could be due to a microstructural effect, as discussed in an ensuing section.

Table III compares the severity of EAC in  $\beta$  and  $\alpha/\beta$  titanium alloys to that in quenched and tempered martensitic alloy steels, for similar strength levels and aqueous NaCl at  $-600 \text{ mV}_{\text{SCE}}$ . For high  $\sigma_{\text{YS}}$  (1300 MPa), the EAC resistance of  $\beta$  Ti-15-3 is superior to that of a typical martensitic steel such as AISI 4340. Intergranular EAC in STA Beta-21S occurs at  $K_{\text{TH}}$  levels somewhat above typical values for high strength steels such as 4340 at similar high strengths. The  $\sigma_{\text{YS}}\text{-}K_{\text{TH}}$  properties of STA Ti-15-3 exceed the performance of mill annealed Ti-8-1-1; thermomechanical processing of this and other  $\alpha/\beta$  alloys will not generally produce the high strengths achievable with STA  $\beta$ -titanium alloys, but can improve  $K_{\text{ISCC}}$ <sup>[56]</sup>. HY130 steel is resistant to chloride EAC, by virtue of relatively low yield strength compared to 4340<sup>[28]</sup>, and intrinsically compared to the  $\alpha/\beta$  Ti alloy at a similar modest  $\sigma_{\text{YS}}$  of 850 to 1000 MPa.  $K_{\text{TH}}$  results have not been reported for solution treated, single phase  $\beta$ -titanium alloys in aqueous chloride; since such alloys exhibit strengths similar to HY130 steel, high EAC resistance is expected unless slip localization<sup>[30,57]</sup> or active crack tip plastic strain<sup>[28]</sup> prove to be detrimental.

Table III: *Fracture Resistance of High Strength Titanium Alloys and Martensitic Steels*

|  | Ti-15-3<br>(STA) | Beta-21S<br>(STA) | Ti-8Al-1Mo-1V<br>(Mill Anneal) <sup>[56]</sup> | HY130 Steel<br>(Quench/Temper) | AISI 4340 Steel <sup>[28]</sup><br>(Quench/Temper) |
|--|------------------|-------------------|--|--------------------------------|--|
| $\sigma_{\text{YS}}$ (MPa)                                       | 1300             | 1330              | 850  | 1025                           | 1350   |
| $K_{\text{IC}}$ or $K_{\text{ICl}}$<br>(MPa $\sqrt{\text{m}}$ )  | 59               | 66                | 120  | 110*                           | 90 to 100  |
| $K_{\text{TH}}$ or $K_{\text{ISCC}}$<br>(MPa $\sqrt{\text{m}}$ ) | 61 to 64         | 39 to 46          | 35   | 70*                            | 25<br>(12 to 38)                                   |

\* Measured by the methods employed in this study, but for either moist air or 3.5% NaCl at  $-1000 \text{ mV}_{\text{SCE}}$ .  $K_{\text{TH}}$  is between 70 and 120 MPa $\sqrt{\text{m}}$  for HY130 steel in chloride at  $-600 \text{ mV}_{\text{SCE}}$ <sup>[28]</sup>.

**Hydrogen Environment Embrittlement Mechanism** Our working hypothesis is that EAC in the  $\beta$ -titanium/25°C aqueous chloride system is caused by crack tip hydrogen production, uptake, and process zone embrittlement; the so-called hydrogen environment embrittlement (HEE) mechanism<sup>[30,31,36,57-61]</sup>. For Ti alloys, the elements of HEE include: (1)

anodic dissolution of Ti and alloying elements to produce hydrolyzable cations which lower the crack tip solution pH, (2) dissolution-coupled hydrogen ion and water reduction on strain-bared Ti, (3) transient crack tip repassivation to reduce cathodic hydrogen production and to form a barrier film to atomic hydrogen (H) uptake, (4) film rupture by crack tip strain, (5) H transport within the crack tip process zone, by bulk diffusion and possibly grain boundary/dislocation pipe diffusion or mobile dislocation transport, (6) H partitioning to microstructural trap sites, and (7) process zone embrittlement, possibly involving titanium hydride formation in either the  $\alpha$  or  $\beta$  phases, interface or lattice plane decohesion, as well as H-enhanced localized plasticity. The observation that cathodic polarization eliminated EAC (Fig. 8) does not preclude HEE because of the complex effect of applied potential on occluded crack chemistry, and the dependence of crack tip H production and uptake on this chemistry. It is not possible to rule-out (or prove) HEE, based on the effect of applied electrode potential, without considering the crack electrochemistry issues amplified in an ensuing section<sup>[59]</sup>.

*Effect of  $\beta$ -titanium Microstructure on EAC* It is important to determine the conditions which promote intergranular environmental cracking in peak aged Beta-21S, particularly the effects of yield strength and  $\alpha$ -phase distribution in the  $\beta$  matrix.

*Effect of Yield Strength on EAC:* STA Beta-21S is stronger than STA Ti-15-3, with  $R_C$  varying between 41 and 45 for edge cracked specimens of the former (Figs. 6 and 8) compared to between 36 and 38 for Ti-15-3 (Fig. 4). While  $K_{TH}$  decreases strongly with increasing  $\sigma_{YS}$  for martensitic steels in NaCl<sup>[28]</sup>, the data in Fig. 6 suggest similar  $K_{TH}$  for Beta-21S at hardness levels of  $R_C$  41 and 45 ( $\sigma_{YS}$  of 1283 and 1417 MPa from Eq. 1). Solution treated (816°C for 30 minutes) specimens of Ti-15-3 were aged at 510°C for 14 hours to produce higher hardness ( $R_C$  41 to 42) compared to the standard (538°C, 8 hr) age. The moist air  $K_{ICi}$  for higher strength Ti-15-3 was 57.1 MPa/m, while  $K_{TH}$  for slow displacement rate (25.4  $\mu\text{m}/\text{min}$ ) loading in NaCl (-600 mV<sub>SCE</sub>) equalled 50.7 MPa/m. The corresponding fracture modes were transgranular-dimpled for both air and NaCl exposures, with a small amount of intergranular cracking for the latter. These results indicate that the EAC resistance of Ti-15-3 may decrease with increasing  $\sigma_{YS}$ ; this trend should be defined systematically for a wider range of strengths. This modest decline in  $K_{TH}$  with increasing  $\sigma_{YS}$  is not, however, sufficient to explain the intergranular EAC sensitivity of Beta-21S.



Effect of Solution Treatment Conditions on Microstructure: Optical microscopy, SEM and TEM of each alloy in the under<sup>9</sup> and peak aged conditions revealed extensive  $\alpha$  precipitation at most  $\beta$  grain boundaries in Beta-21S, but not in Ti-15-3. This behavior is detailed by the under aged microstructures presented in parts a and c of Figs. 10 (optical) and 11 (SEM). For Ti-15-3 (Figs. 10a and 11a), relatively homogeneous  $\alpha$  precipitation occurred within  $\beta$  grains after the short under aging time; large  $\alpha$  plates only infrequently nucleated on or adjacent to  $\beta$  grain boundaries. For under aged Beta-21S, a large amount of  $\alpha$  initially nucleated on or very near to  $\beta$  grain boundaries, and grew in a colony morphology toward grain interiors (Figs. 10c and 11c). Intragranular  $\alpha$  precipitation was limited for under aged Beta-21S. While considerably more difficult to discern, peak aged Ti-15-3 exhibits homogeneously distributed  $\alpha$  plates within  $\beta$  grains, Fig. 1b, with only occasional grain boundary  $\alpha$  colonies (Fig. 1b). In contrast STA Beta-21S exhibits intragranular  $\alpha$  plates and extensive coarse grain boundary  $\alpha$  colonies<sup>[36]</sup>. These peak aged microstructures are consistent with the likely further evolution of the structures shown in Figs. 10 and 11. Extensive grain boundary  $\alpha$  colonies should not form in Ti-15-3, during longer time aging, given the extensive intragranular precipitation at short aging times.

Beta grain boundary microstructures are amplified by the TEM results in Fig. 12. Boundaries in under aged Ti-15-3 contain a 0.1  $\mu\text{m}$  thick layer of  $\alpha$  (Fig. 12a). This  $\alpha$  does not grow substantially during additional aging to peak strength (Fig. 12b). The micrograph in Fig. 12c for STA Beta-21S shows that an  $\alpha$  layer is present at  $\beta$  grain boundaries, analogous to Ti-15-3, and further suggests that colony  $\alpha$  nucleates from this boundary  $\alpha$  layer.  $\alpha$  plates near grain boundaries in Ti-15-3 appear at angles typical of a crystallographic relationship with the  $\beta$  matrix (Fig. 12b). Colony  $\alpha$  in Beta-21S does not have this appearance, as shown in Fig. 12c; rather traces of  $\alpha$ -plates appear approximately normal to the grain boundary and extend into each grain as shown in Fig. 10c. Colony- $\alpha$  has not been reported widely, however, there is precedent for this microstructure<sup>[54]</sup>.

Homogeneous intragranular  $\alpha$  precipitation in  $\beta$ -titanium alloys should be promoted by several factors, including dislocation sites typical of partial recovery and recrystallization during hot working and solution treatment, post-solution treatment cold work, a supersaturation of

---

<sup>9</sup> Specimens of solution treated Ti-15-3 and Beta-21S were under aged at 538°C for 1 hour to clarify the initial stage of  $\alpha$  precipitation.

vacancies quenched from solution temperatures, lower aging temperatures, as well as by precursor  $\omega$  or  $\beta'$  precipitates<sup>[29,32,34,35,54,62,63]</sup>. Athermal or "isothermal"  $\omega$ , from cooling after solution treatment<sup>[32,34,35]</sup>, were not observed by X-ray diffraction and TEM of either solution treated or STA Beta-21S and Ti-15-3. Since a higher concentration of quenched vacancies is expected for ST Beta-21S, due to the higher solution treatment temperature compared to Ti-15-3, the vacancy explanation does not explain the occurrence of boundary  $\alpha$ -colonies in Beta-21S. Moreover, vacancies promoted intragranular  $\alpha$  precipitation at low aging temperatures, but were not influential at the higher level (538°C) employed in the current work<sup>[63]</sup>.

It is reasonable to hypothesize that the difference in solution treatment conditions, 8 hours at 871°C for Beta-21S compared to 30 minutes at 816°C for Ti-15-3, causes grain boundary  $\alpha$ -colony precipitation for the former alloy by a mechanism other than vacancies. As-received Ti-15-3 was resolutionized at either 1038°C for 2 hr<sup>[36]</sup> or 950°C for 12 hr<sup>[30]</sup>. Metallographic analyses summarized in Figs. 10b and 11b reveal  $\alpha$ -colony precipitation at Ti-15-3 grain boundaries, for both solution treatments followed by under aging, similar to Beta-21S. These experiments confirm the importance of high solution treatment temperatures and longer times in promoting grain boundary  $\alpha$ -colony precipitation. This effect may be explained by heterogeneous  $\alpha$  nucleation at dislocation substructure in preference to grain boundary sites. Higher solution treatment temperatures and longer times could favor recovery and recrystallization of intragranular dislocation sites, and thus promote heterogeneous  $\alpha$  nucleation to grain boundaries. Substructure that survives at lower solution treatment temperatures could cause  $\alpha$  precipitation within grains.

Effect of Solution Treatment and Microstructure on EAC: The current results suggest the hypothesis that the contrasting chloride EAC resistance of STA Ti-15-3 vs the susceptibility of STA Beta-21S may be traced to either microstructural or slip mode differences derived from variations in thermomechanical processing and solution heat treatment. This idea is supported by the experimental observation that resolution treated and peak aged Ti-15-3 (RSTA: 1038°C for 2 hr plus 538°C for 8 hr) is susceptible to EAC in NaCl, as demonstrated in Figs. 13 and 14. The moist air  $K_{ICl}$  for the RSTA case is higher (74 MPa/m in Fig. 13) than that for short-time low temperature STA Ti-15-3 (57 to 59 MPa/m in Fig. 4) at constant yield strength ( $R_C 39 \pm 1$ ). This result parallels the higher moist air fracture toughness of STA Beta-21S, including the point that fracture involved some grain boundary cracking.  $K_{TH}$  for RSTA Ti-15-3 in NaCl (64 MPa/m) is less than  $K_{ICl}$  (74 MPa/m), in contrast to essentially equal  $K_{TH}$  and  $K_{ICl}$

for low temperature STA Ti-15-3 (Fig. 4). As shown in Fig. 14, EAC of RSTA Ti-15-3 is more intergranular compared to both transgranular cracking of the lower temperature solution treatment condition in NaCl (Fig. 5), and transgranular/intergranular cracking of RSTA Ti-15-3 in air. STA Beta-21S is more severely embrittled by NaCl compared to RSTA Ti-15-3.

It is reasonable to speculate that intergranular EAC in Beta-21S and RSTA Ti-15-3 correlates with grain boundary  $\alpha$  colonies, given the metallographic results in Figs. 10 through 12. Since both Beta-21S and Ti-15-3 exhibit a similar 0.1  $\mu\text{m}$  thick layer of boundary  $\alpha$  (which could hydride due to the low solubility of H in this phase relative to  $\beta$ <sup>[4,8,64]</sup>), this feature does not explain the observed difference in EAC resistance. There is no evidence that a hydride phase formed throughout the  $\alpha$  colonies, present on most grain boundaries in STA Beta-21S and RSTA Ti-15-3<sup>[31]</sup>. The intergranular facets shown in Fig. 7 seem to be free of the microscopic detail which would be expected if EAC progressed through hydrided  $\alpha$  colonies. An explanation for the lack of hydrided grain boundary  $\alpha$  is that this phase contains high Al, partitioned from the  $\beta$  phase. Hydriding is suppressed in Ti-Al binary alloys<sup>[65]</sup>.

Pound employed an electrochemical potentiostatic pulsing technique to conclude that the apparent irreversible hydrogen trapping constant, and hence the capability (trap density plus size) of irreversible H trap sites, are higher in STA Beta-21S compared to equal levels for both ST and STA Ti-15-3<sup>[66,67]</sup>.<sup>10</sup> He speculated that hydrogen was trapped irreversibly at  $\alpha/\beta$  interfaces associated with the  $\alpha$ -colony microstructure, and that H localization by trapping explains severe intergranular EAC in STA Beta-21S. It is plausible that an increased hydrogen concentration at interfaces which are demonstrated brittle crack paths (Fig. 7) can lead to increased EAC susceptibility through the HEE mechanism. Hydrogen trapping at  $\alpha/\beta$  interfaces in STA  $\beta$ -titanium alloys could result from misfit strain, and depend on the compositions of the  $\alpha$  and  $\beta$  phases through changes in the lattice parameter of each<sup>[68]</sup>. Alternately,  $\alpha$ -colony interfaces could be incoherent and disordered, particularly if not crystallographically related to the  $\beta$  matrix such as at  $\alpha$  plate ends, and hence form irreversible H trap sites<sup>[68]</sup>.

The correlation between grain boundary  $\alpha$ -colonies, H trapping and intergranular EAC susceptibility in STA Beta-21S, RSTA Ti-15-3, and other  $\beta$ -titanium alloys is useful, but

---

<sup>10</sup> Pound studied as-heat treated specimens of Beta-21S and Ti-15-3 that were provided from the current research.

speculative and premature<sup>[66,67]</sup>. H trapping is but one element in a complex cracking sequence that depends on hydrogen production and entry, microstructural, and micromechanical factors.<sup>11</sup> The detailed elements of the HEE sequence are uncertain for  $\beta$ -titanium alloys, and it is necessary to define the precise crack path through  $\beta$  grain boundaries with adjacent  $\alpha$  colonies. For example, colony  $\alpha$  may be hard and prone to HEE due to partitioned aluminum in ordered solid solution or causing  $\text{Ti}_3\text{Al}$  precipitation analogous to  $\alpha/\beta$  titanium alloys<sup>[11,48]</sup>. Both the trapped hydrogen content and normal stresses ( $\sigma_N$ ) local to connected interfaces are important in governing H-failure<sup>[28,36]</sup>. The level of localized hydrogen necessary for interface cracking should decrease with increasing  $\sigma_N$ , suggesting that a trapping-only explanation is inadequate. Plastic deformation could localize in softer adjacent  $\beta$ <sup>[51-53]</sup>, but aluminum hardened  $\alpha$ -colonies could constrain this deformation and promote high stresses normal to the  $\alpha/\beta$  boundary. It is equally reasonable to speculate that EAC is affected by locally intense planar slip, interacting with trapped H, and governed by heat treatment and microstructure. Since plastically deformed microstructures were not examined in the H trapping study (see footnote 10)<sup>[66,67]</sup>, there is no information on the characteristics and importance of traps associated with dislocation structures, including locally planar slip and microvoids at slip-band intersections.

An important role of slip mode in EAC is suggested by the observation that solution treated Beta-21S was more susceptible to embrittlement by internally predissolved H compared to ST Ti-15-3, in the absence of  $\alpha$  and associated hydrogen trap sites<sup>[30,31]</sup>. High temperature-resolution treated Ti-15-3 (without aging) was similarly susceptible to embrittlement by predissolved hydrogen without  $\alpha$  precipitates. High temperature-long time solution treated, single phase Beta-21S (871°C for 8 hr) and Ti-15-3 (950°C for 12 hr) each deform by localized planar slip<sup>[30, 31,57]</sup>. In contrast low temperature-short time ST Ti-15-3 deforms by both localized-planar and localized but irregular (wavy) slip, and was not susceptible to internal hydrogen embrittlement.<sup>12</sup>

While the solution treatment time-temperature effect on slip mode in single phase  $\beta$  is

---

<sup>11</sup> For example, the correlation between H-trapping capacity and EAC was claimed for an alloy steel where the irreversible hydrogen trap site was identified as widely spaced MnS inclusions<sup>[69]</sup>. For this case, the environmental crack path was along prior austenite grain boundaries and did not generally intersect the MnS trap sites, suggesting that the correlation is fortuitous and indicating the need for a broader view that couples trapping with the micromechanics of H cracking.

<sup>12</sup> It is also possible that these solution treatment conditions produced varying sites for irreversible H trapping, and hence varying susceptibilities to hydrogen embrittlement, unrelated to deformation mode<sup>[69]</sup>.

clear, the causal mechanism and the effect of  $\alpha$  precipitation on this deformation mode in STA alloys were not determined<sup>[30, 31, 57]</sup>. Slip may be even more intensely planar in STA Beta-21S compared to standard STA Ti-15-3. Okada et al. report that slip localization in the  $\beta$  matrix of Ti-15-3 is enhanced by colonies of shearable fine  $\alpha$  plates compared to slip homogenization from large intragranular  $\alpha$  plates in multiple orientations<sup>[70]</sup>. TEM showed that intragranular  $\alpha$  in low temperature-short time solution treated then peak aged Ti-15-3 and Beta-21S was similarly of the Burger's orientation (viz.,  $(110)_\beta // (0001)_\alpha$  and  $[111]_\beta // [11-20]_\alpha$ ). This phase was somewhat larger in STA Ti-15-3, due to earlier nucleation during peak aging, and could further homogenize slip. In contrast grain boundary  $\alpha$  colonies could intensify localized slip for STA Beta-21S (and in high temperature long-time ST Ti-15-3) if colony  $\alpha$  plates are aligned crystallographically to favor easy passage of slip<sup>[70]</sup>.

The microstructural factor which affects EAC in STA  $\beta$ -titanium alloys could, therefore, be locally intense planar slip as reported for a variety of aluminum<sup>[71]</sup> and  $\alpha/\beta$  titanium<sup>[7, 8, 11]</sup> alloys. Beta composition, the  $\alpha$ -colony structure, and perhaps high aluminum in this  $\alpha$  could favor localized slip which would intersect  $\beta$  grain boundaries. Such slip could promote H transport from the crack tip surface, H trapping at deformation induced interfacial defects (e.g., microvoids at grain boundaries or slip band intersections), and local stress/strain concentration; all of which could contribute to increased HEE. These factors must be considered in concert with irreversible trapping at colony- $\alpha/\beta$  interfaces, as well as with the micromechanics of process zone H-damage, in order to fully understand intergranular EAC in  $\beta$ -titanium alloys.

If colony- $\alpha$  is proven to be an important factor in the intergranular EAC of  $\beta$ -titanium alloys such as Beta-21S, then processing could mitigate such cracking by homogenizing the distribution of  $\alpha$  precipitates. Either cold deformation of high temperature-long time solution treated Beta-21S prior to aging, or lower temperature-short time solution treatment, should provide intragranular nucleation sites for  $\alpha$  precipitates and perhaps alter slip localization. Alternately, duplex temperature aging may nucleate  $\alpha$  uniformly on precursor  $\omega$  or  $\beta'$  sites and reduce the likelihood of grain boundary  $\alpha$  colonies<sup>[29]</sup>. Other factors not considered here, including grain boundary segregation of an alloying element or unknown impurity, could promote intergranular EAC in  $\beta$ -titanium alloys.

*Effect of Loading Rate on EAC*      At issue is why NaCl EAC in STA Beta-21S was

not produced during constant load exposures for times that were an order of magnitude longer than those which produced intergranular embrittlement during rising load. As reported for several  $\alpha/\beta$  and  $\beta$  alloys including Ti-15-3, aqueous EAC is maximized at intermediate loading rates for both smooth uniaxial tensile specimens<sup>[17]</sup> and precracked fracture mechanics specimens<sup>[8,27]</sup>.<sup>13</sup> The lack of resolvable EAC during constant load exposures of STA Beta-21S and Ti-15-3 is consistent with this trend. For a stationary crack, the near-tip strain rate at constant load is determined by the process zone creep rate and is orders of magnitude slower than the crack tip strain rates typical of the rising load experiments which produced intergranular EAC, Figs. 6 and 8<sup>[36]</sup>.

Average crack growth rates for peak aged Beta-21S in NaCl appear to increase with increasing loading rate at stress intensities below  $K_{IC}$ . Since absolute  $K_{TH}$  levels were similar for the two loading rates represented in Fig. 6, a 20-fold increase in the initial crack tip strain rate (at  $K_{TH}$  and any location within the crack tip process zone) resulted in a 10-fold increase in average  $da/dt$  estimated from electrical potential measurements of crack length. This strain rate difference is amplified by the faster crack growth rate which can affect crack tip strain rate in addition to the effect of loading rate<sup>[39,72]</sup>. Based on the data in Fig. 6, stress intensities are similar and did not decline significantly during EAC extension at either rate; there is no simple  $K$ -driving force or compliance-based explanation for the reduction in  $da/dt$  with decreasing loading rate. The stress intensity and crack tip strain rate dependencies of  $da/dt$  were not characterized systematically, and the present results only provide an indication of subcritical crack growth kinetics. It is particularly important to accurately resolve the magnitudes of  $da/dt$  for the alternating slow-fast regimes of subcritical EAC in  $\beta$ -titanium alloys, and to explain this possibly unique behavior.

Reduced  $da/dt$  and increased  $K_{TH}$  with decreasing strain rate are predicted qualitatively by crack tip film rupture-transient dissolution modeling of EAC<sup>[72]</sup>. The amount of anodic dissolution-charge passed per unit time, and hence  $da/dt$ , decrease as the frequency of rupture events is reduced due to decreased crack tip strain rate. This strain rate effect can be considered based on HEE. Hydrogen production, uptake and embrittlement could be severe at intermediate

---

<sup>13</sup> Analogous behavior is not observed for all  $\alpha/\beta$  titanium alloys. Aqueous chloride EAC, with  $K_{ISCC}$  well below  $K_{IC}$ , was produced by static loading<sup>[25,26,56]</sup>.  $K_{TH}$  was claimed to be minimized at intermediate loading rates, however, only a modest range of strain rates was investigated and constant load experiments were not conducted<sup>[27]</sup>.

crack tip strain rates which balance three factors: (1) surface passive film destabilization by rupture (promoted by increased loading rate), (2) the time necessary for H diffusion into the crack tip process zone (promoted by decreased loading rate), and (3) dislocation transport of H (promoted by increased loading rate up to a critical dislocation velocity). Static loading may not provide the strain rate and accumulated strain necessary to mechanically destabilize the crack tip passive film; this film could hinder H production and/or uptake<sup>[60]</sup>. Alternately, creep strain rates from static loading may hinder dislocation motion to transport H from the crack tip surface to trap sites within the process zone, for example at  $\beta$  grain boundaries and  $\alpha$  colonies. The contributions of each factor must be established, as does the extent of EAC at higher loading rates where H transport and electrochemical reactions are minimized.

*Effect of Electrode Potential on EAC* That intergranular chloride EAC in STA Beta-21S is mitigated by cathodic polarization (Fig. 9) is explainable based on HEE, provided that local electrochemical conditions near the crack tip are considered. It is well established that HEE in the ferritic steel/NaCl system is promoted at anodic potentials, where enhanced dissolution favors hydrolytic acidification and H production/uptake at the occluded crack tip, as well as at cathodic potentials where H production increases due to increasing overpotential for increasingly rapid water reduction kinetics<sup>[59,60]</sup>.

The situation is different for  $\beta$ -titanium alloys in aqueous chloride. We assume that a crack tip passive film forms at all potentials investigated, but is ruptured by crack tip strain above a critical rate; the potential of the bared metal is very active (e.g., -1600 mV<sub>SCE</sub>)<sup>[73]</sup>. At free corrosion and more anodic applied potentials, cation hydrolysis to promote lowered pH, as well as an IR-based crack tip potential difference, enhance the rate of H production from H<sup>+</sup> reduction to support HEE. With increasing cathodic polarization, hydrolytic acidification is reduced and the crack tip solution becomes alkaline due to OH<sup>-</sup> production from water reduction. Recent experiments with scratched electrodes of  $\beta$ -titanium alloys in simulated crack solutions show that repassivation rates are similar for pH 1 conditions (approximating solution at the crack tip at free corrosion), pH 8 (a lower bound simulating the crack tip during cathodic polarization at -1000 mV<sub>SCE</sub>), and pH 10 solution<sup>[73]</sup>. Critically, however, the open circuit potential of bare titanium becomes increasingly active with increasing alkalinity, but at a slope that is less than the pH-dependence of the hydrogen reversible potential. Accordingly, the overpotential for H production



*at the bare crack tip* decreases with increasingly cathodic potentials applied to the specimen surface. Additionally, the exchange current density for hydrogen production on bare titanium decreases with increasing pH. These two factors result in a large decrease in the H production rate, and hence decreasing H surface coverage, with cathodic polarization.

We speculate that  $K_{TH}$  for NaCl EAC in STA Beta-21S is low at  $-600 \text{ mV}_{SCE}$ , because of H production and uptake from acid solution at the crack tip, analogous to the steel case.  $K_{TH}$  increases to equal  $K_{ICl}$  with increasing cathodic polarization because H production is reduced at the bared titanium crack tip in alkaline crack solution, in contrast to the steel case.

Since electrochemical experiments reveal similar transient repassivation characteristics<sup>[73]</sup>, it is likely that similar concentrations of crack tip-surface adsorbed H are produced for bared surfaces of both Beta-21S and Ti-15-3 in (simulated) crack solution. The dramatically different chloride EAC susceptibilities of these alloys is therefore traceable to processing-related changes in deformation mode and microstructure; factors that influence the effect of a given level of H on process zone embrittlement.

## CONCLUSIONS

1. Peak aged (STA) Beta-21S is susceptible to environment assisted cracking (EAC) in aqueous NaCl at  $-600 \text{ mV}_{SCE}$  when subjected to rising stress intensity. The threshold for subcritical crack propagation ( $K_{TH} = 39 \text{ to } 46 \text{ MPa}/\text{m}$ ) is significantly reduced compared to the plane strain fracture toughness ( $K_{ICl}$ ) of  $66 \text{ MPa}/\text{m}$ , average subcritical crack growth rates are on the order of  $10 \text{ }\mu\text{m}/\text{sec}$ , and EAC is intergranular for Beta-21S in chloride compared to microvoid-based for moist air.
2. For STA Ti-15-3,  $K_{ICl}$  ( $57 \text{ to } 64 \text{ MPa}/\text{m}$ ) and transgranular microvoid fracture processes are unaffected by aqueous chloride exposure for several slow loading rates and applied electrode potentials. Intergranular EAC in peak aged Ti-15-3 is promoted by increased solution treatment temperature and/or time.
3. Intergranular EAC in STA Beta-21S (as well as in resolution treated and aged Ti-15-3) correlates with  $\alpha$ -colonies precipitated at  $\beta$  grain boundaries and with localized planar slip; the governing causal factor is not defined. Both features are promoted by high temperature-long time solution treatment. The relative importance of these features and other alloy-dependent factors is not established, however, hydrogen trapping at  $\alpha/\beta$  interfaces coupled with stress and strain localization near  $\beta$  grain boundaries may be important.



4. EAC in peak aged Beta-21S is not produced during static loading, for times similar to the deleterious rising load case, and average subcritical EAC growth rates decrease with decreasing crack tip strain rate.
5. EAC in STA Beta-21S is eliminated by applied cathodic polarization at  $-1000 \text{ mV}_{\text{SCE}}$ , and occurs, but is not exacerbated during anodic polarization at  $-150 \text{ mV}_{\text{SCE}}$ .
6. EAC in STA Beta-21S may proceed by hydrogen environment embrittlement. The beneficial effects of cathodic polarization and stagnant crack tip strain rate are speculatively traced to reduced hydrogen production at the occluded crack tip for the former, and to increased crack tip passive film stability or reduced dislocation transport of process zone hydrogen for the latter.
7. The  $25^\circ\text{C}$  chloride EAC resistance of STA  $\beta$ -titanium alloys can be superior to that of quenched and tempered martensitic steels at similar high strengths, certainly for cathodic polarization and short term static loading. Beta titanium alloys are not, however, immune to chloride EAC; thermomechanical processing must be controlled for cracking resistance.

## ACKNOWLEDGEMENTS

This research was supported by the Office of Naval Research (Grant N00014-91-J-4164), with Dr. A. John Sedriks as Scientific Monitor, and by the Virginia CIT Center for Electrochemical Science and Engineering at the University of Virginia. Material was donated by the Titanium Metals Corporation. Transmission electron microscopy was conducted by Professor K.R. Lawless. These contributions are gratefully acknowledged.

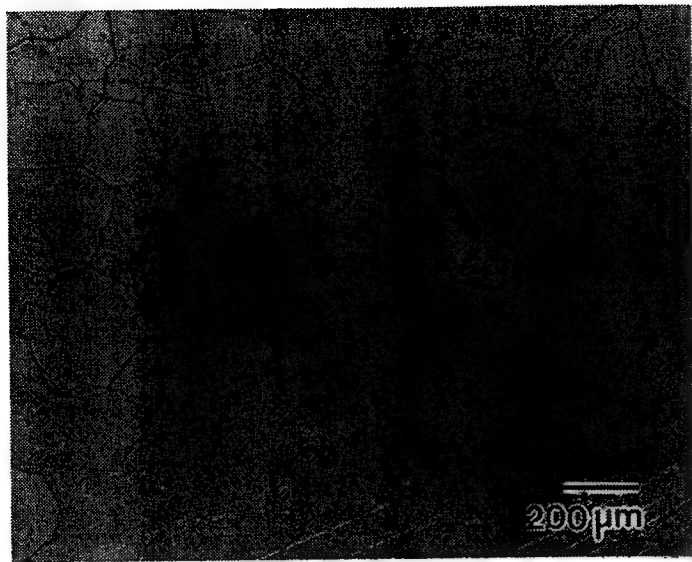
## REFERENCES

1. Beta Titanium Alloys in the 80's, R.R. Boyer and H.W. Rosenberg, eds., TMS-AIME, Warrendale, PA, pp. 209-229, 1983.
2. Seventh World Conference on Titanium, F.H. Froes, ed., TMS-AIME, Warrendale, PA, in press, 1993.
3. Beta Titanium Alloys in the 1990's, D. Eylon, R.R. Boyer and D.A. Koss, eds., TMS-AIME, Warrendale, PA, 1993.
4. T.W. Duerig and J.C. Williams, in Beta Titanium Alloys in the 80's, R.R. Boyer and H.W. Rosenberg, eds., TMS-AIME, Warrendale, PA, pp. 19-67, 1983.
5. R.W. Schutz, "Effective Utilization of Titanium Alloys in Offshore Systems", Paper No. 6909, 24th Annual Offshore Technology Conference, Houston, TX, 1992.
6. W.W. Love, C.J. Cron and D. Holligan, in Sixth World Conference on Titanium, P. Lacombe, R. Tricot and G. Beranger, eds., Societe Francaise de Metallurgie, Les Ulis Cedex, France, pp. 443-448, 1988.

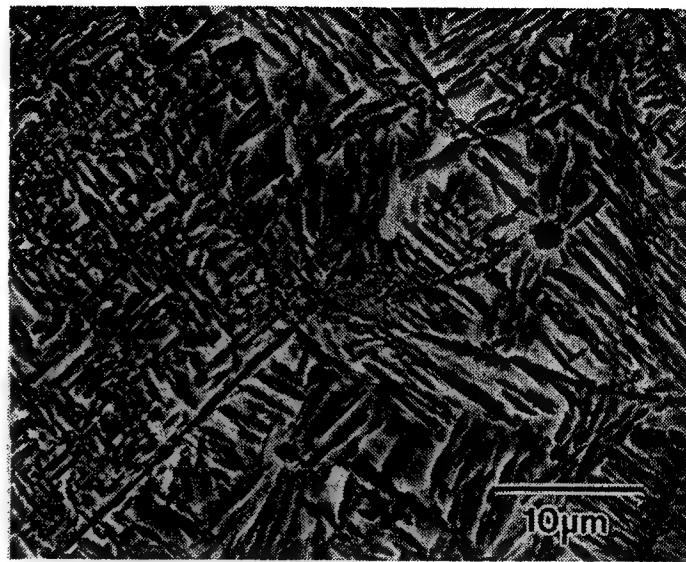
7. R.J.H. Wanhill, British Corrosion Journal, Vol. 10, No. 2, pp. 69-78, 1975.
8. M.J. Blackburn, J.A. Feeney, and T.R. Beck, in Advances in Corrosion Science and Technology, M.G. Fontana and R.W. Staehle, eds., Vol. 3, Plenum Publishing, NY, NY, pp. 67-292, 1972.
9. R.W. Schutz and D.E. Thomas, in Corrosion; Metals Handbook, Vol. 13, Ed. 9, ASM International, Metals Park, OH, pp. 669-706, 1987.
10. R.W. Schutz, in Stress Corrosion Cracking, R.H. Jones, ed., ASM International, Metals Park, OH, pp. 265-297, 1992.
11. M.J. Blackburn, W.H. Smyrl, and J.A. Feeney, Chapter 5 in Stress Corrosion Cracking High Strength Steel and in Titanium and Aluminum Alloys, B.F. Brown, ed., Naval Research Laboratory, Washington, D.C., pp. 245-363, 1972.
12. R.W. Schutz in Beta Titanium Alloys in the 1990s, D. Eylon, R.R. Boyer and D.A. Koss, eds., TMS-AIME, Warrendale, PA, pp. 75-91.
13. D.N. Fager and W.F. Spurr, Trans. ASM, Vol. 61, pp. 283-292, 1968.
14. J.A. Feeney and M.J. Blackburn, Met. Trans., Vol. 1, pp. 3309-3323, 1970.
15. M.J. Blackburn, J.A. Feeney and T.R. Beck, "State-of-the-Art of Stress Corrosion Cracking of Titanium Alloys", Monograph Review, Part 4, Advanced Research Projects Agency, ARPA Order No. 878 (or NAS7-489) 1970.
16. Corrosion; Metals Handbook, Vol. 13, Ed. 9, ASM International, Metals Park, OH, pp. 483-485, 1987.
17. C. Gagg and B. Toloui, in Sixth World Conference on Titanium, P. Lacombe, R. Tricot and G. Beranger, eds., Societe Francaise de Metallurgie, Les Ulis Cedex, France, pp. 545-550, 1988.
18. R.W. Schutz, M. Xiao and T.A. Bednarowicz, "Stress Corrosion Behavior of Ti-3Al-8V-6Cr-4Mo Under Deep Sour Gas Well Conditions", Paper No. 51, Corrosion 92, NACE, Houston, TX, 1992.
19. R.W. Schutz and M. Xiao, "Stress Corrosion Behavior of Ti-38644 Titanium Alloys Products in Methanol Solutions", Paper No. 148, Corrosion 93, NACE, Houston, TX, 1993.
20. I. Azkarate and A. Pelayo, "Hydrogen Assisted Stress Cracking of Titanium Alloys in Aqueous Chloride Environments", presented at INASMET Conference, San Sebastian, Spain, 1992.
21. L.H. Wolfe, C.C. Burnette and M.W. Jossten, Materials and Protection, pp. 14-21, July, 1993.
22. B. Bavarian, V. Wahi and M. Zamanzadeh, "Corrosion Behavior of Beta-21S Titanium Alloy in Chloride-Containing Environments", Paper No. 284, Corrosion 93, NACE, Houston, TX, 1993.
23. D.E. Thomas and S.R. Seagle in Titanium Science and Technology, G. Lutjering, U. Zwicker and W. Bunk, eds., pp. 2533-2540, 1984.
24. D.A. Meyn and P.S. Pao, in Slow Strain Rate Testing for the Evaluation of Environmentally Induced Cracking: Research and Engineering Applications, ASTM STP 1210, R.D. Kane, ed., ASTM, Philadelphia, PA, pp. 158-169, 1993.
25. W.F. Czyrkliis and M. Levy, Corrosion, Vol. 32, pp. 99-102, 1976.
26. B.F. Brown, Mater. Res. Std., Vol. 6, pp. 129-136, 1966.
27. J.A. Muskovitz and R.M. Pelloux, Corrosion, Vol. 35, pp. 509-514, 1979.
28. R.P. Gangloff, in Corrosion Prevention and Control, M. Levy and S. Isserow, eds., US Army Laboratory Command, Watertown, MA, pp. 64-111, 1986.

29. L. Wagner and J.K. Gregory, in Beta Titanium Alloys in the 1990's, D. Eylon, R.R. Boyer and D.A. Koss, eds., TMS-AIME, Warrendale, PA, pp. 199-209, 1993.
30. G.A. Young, Jr., "Hydrogen Effects in Metastable  $\beta$ -Titanium Alloys", M.S. Thesis, University of Virginia, Charlottesville, VA, 1993.
31. G.A. Young, Jr. and J.R. Scully, "Internal Hydrogen Embrittlement of Solution Heat Treated and Aged Ti-15V-3Cr-3Al-3Sn and Ti-15Mo-3Nb-3Al", Corrosion, in press, 1994.
32. T.W. Duerig, G.T. Terlinde and J.C. Williams, Metall. Trans. A, Vol. 11A, pp. 1987-1998, 1980.
33. G. Hari Narayanan and T.F. Archbold, Met. Trans. Vol. 1, pp. 2281-2290, 1990.
34. T.J. Headley and H.J. Rack, Metall. Trans. A, Vol. 10A, pp. 909-920, 1979.
35. J.C. Williams, in Titanium Science and Technology, R.I. Jaffee and H.M. Burte, eds., TMS-AIME, New York, pp. 1433-1494, 1973.
36. L.M. Young, "Environment Assisted Cracking in  $\beta$ -Titanium Alloys", M.S. Thesis, University of Virginia, Charlottesville, VA, 1993.
37. D.R. Anderson and J.P. Gudas, in Environment Sensitive Fracture: Evaluation and Comparison of Test Methods, ASTM STP 821, S.W. Dean, E.N. Pugh and G.M. Ugiansky, eds., ASTM, Philadelphia, PA, pp. 98-113, 1984.
38. E.M. Hackett, P.J. Moran and J.P. Gudas, in Fracture Mechanics: Seventeenth Volume, ASTM STP 905, J.H. Underwood, et al., eds., ASTM, Philadelphia, PA, pp. 512-541, 1986.
39. R.A. Mayville, T.J. Warren and P.D. Hilton, Trans. ASME, Vol. 109, pp. 188-193, 1987.
40. W. Dietzel, K.-H. Schwalbe and D. Wu, Fatigue and Fracture of Engineering Materials and Structures, Vol. 12, pp. 495-510, 1989.
41. J.K. Donald and J. Ruschau, in Fatigue Crack Measurement: Techniques and Applications, K.J. Marsh, R.A. Smith and R.O. Ritchie, eds., EMAS, Ltd, West Midlands, UK, pp. 11-37, 1991.
42. V. Kumar, M.D. German and C.F. Shih, An Engineering Approach for Elastic-Plastic Fracture Analysis, Electric Power Research Institute, Report NP-1931, Palo Alto, CA (1981).
43. P. Doig and K.R. Abbott, J. Test. Eval., Vol. 12, pp. 297-304, 1984.
44. W.C. Porr, Jr. and R.P. Gangloff, Metall. and Matls. Trans. A, Vol. 25A, pp. 365-379 (1994).
45. "Standard Test Method for  $J_{IC}$ , A Measure of Fracture Toughness", Designation E 813-89, Annual Book of ASTM Standards, 3.01, ASTM, Philadelphia, PA, pp. 732-746, 1992.
46. "Standard Test Method for Determining Plane-Strain Fracture Toughness of Metallic Materials", Designation E 399-83, Annual Book of ASTM Standards, 3.01, ASTM, Philadelphia, PA, pp. 506-536, 1992.
47. K.S. Chan, Acta Metall., Vol. 37, pp. 1217-1226, 1989.
48. M.J. Blackburn and W.H. Smyrl, in Titanium Science and Technology, R.I. Jaffee and H.M. Burte, eds., Plenum Press, NY, NY, pp. 2577-2609, 1973.
49. D.G. Kolman and J.R. Scully, J. Electrochem. Soc., Vol. 140, pp. 2771-2779, 1993.
50. D.G. Kolman and J.R. Scully, "Electrochemistry and Passivity of a Ti-15V-3Cr-3Al-3Sn  $\beta$ -Titanium Alloy in Ambient Temperature Aqueous Chloride Solutions", J. Electrochem. Soc., in press, 1994.
51. F.H. Froes, J.C. Chesnutt, C.G. Rhodes and J.C. Williams, in Toughness and Fracture Behavior of Titanium, ASTM STP 651, ASTM, Philadelphia, PA, pp. 115-153, 1978.

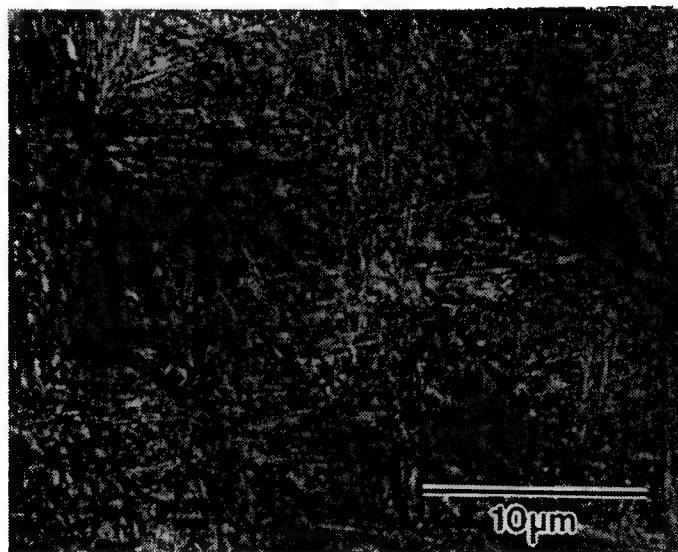
52. E. Breslauer and A. Rosen, Matls. Sci. and Tech., Vol. 7, pp. 441-446, 1991.
53. G. Terlinde and K.-H. Schwalbe, in Microstructure, Fracture Toughness and Fatigue Crack Growth in Titanium Alloys, A.K. Chakrabarti and J.C. Chesnutt, eds., TMS-AIME, Warrendale, PA, pp. 97-109, 1987.
54. N. Niwa and H. Takatori, in Beta Titanium Alloys in the 1990s, D. Eylon, R.R. Boyer and D.A. Koss, eds., TMS-AIME, Warrendale, PA, pp. 237-247, 1993.
55. H. Buhl, in Stress Corrosion Cracking-The Slow Strain Rate Technique, ASTM STP 665, G.M. Ugiansky and J.H. Payer, eds., ASTM, Philadelphia, PA, pp. 333-346, 1979.
56. W.F. Czyrkis and M. Levy, in Environment Sensitive Fracture of Engineering Materials, Z.A. Foroulis, ed., TMS-AIME, Warrendale, PA, pp. 303-313, 1979.
57. G.A. Young, Jr. and J.R. Scully, in Beta Titanium Alloys in the 1990s, D. Eylon, R.R. Boyer and D.A. Koss, eds., TMS-AIME, Warrendale, PA, pp. 147-158, 1993.
58. R.P. Gangloff, Matls. Sci. Engr., Vol. A103, pp. 157-166, 1988.
59. R.P. Gangloff and A. Turnbull, in Modeling Environmental Effects on Crack Initiation and Propagation, R.H. Jones and W.W. Gerberich, eds., TMS-AIME, Warrendale, Pa., pp. 55-81, 1986.
60. J.R. Scully and P.J. Moran, J. Electrochem. Soc., Vol. 135, pp. 1337-1348, 1988.
61. H.G. Nelson, in Hydrogen in Metals, I.M. Bernstein and A.W. Thompson, eds., TMS-AIME, Warrendale, PA, pp. 445-464, 1973.
62. M.A. Imam, P.K. Poulouse and B.B. Rath, in Beta Titanium Alloys in the 1990s, D. Eylon, R.R. Boyer and D.A. Koss, eds., TMS-AIME, Warrendale, PA, pp. 261-271, 1993.
63. H. Fujii and H.G. Suzuki, in Beta Titanium Alloys in the 1990s, D. Eylon, R.R. Boyer and D.A. Koss, eds., TMS-AIME, Warrendale, PA, pp. 249-259, 1993.
64. J.E. Costa, D. Banerjee and J.C. Williams, in Beta Titanium Alloys in the 80's, R.R. Boyer and H.W. Rosenberg, eds., TMS-AIME, Warrendale, PA, pp. 69-84, 1983.
65. J.D. Boyd, Trans. ASM, Vol. 62, pp. 977-988, 1969.
66. B.G. Pound, Acta Metall. et Mater., Vol. 42, pp. 1551-1559, 1993.
67. B.G. Pound, "Hydrogen Trapping in  $\beta$ -Titanium Alloys-The Link Between Microstructure and Hydrogen Embrittlement", Acta Metall. et Mater., in review, 1994.
68. G.M. Pressouyre, Metall. Trans. A, Vol. 10A, pp. 1571-1592, 1979.
69. B.G. Pound, "Predicting the Susceptibility to Hydrogen Embrittlement", in Proceedings, 12th International Corrosion Congress, NACE, Houston, TX, in press, 1994.
70. M. Okada, D. Banerjee, and J.C. Williams, in Titanium Science and Technology, Vol. 3, G. L. tjerling, U. Zwicker, and W. Bunk, eds., Oberursel, Deutsche Gesellschaft f. r Metallkunde, pp. 1835-1842, 1984.
71. J. Albrecht, A.W. Thompson and I.M. Bernstein, Metall. Trans. A, Vol. 10A, pp. 1759-1766, 1979.
72. F.P. Ford in Environment Induced Cracking of Metals, R.P. Gangloff and M.B. Ives, eds., NACE, Houston, TX, pp. 139-166, 1990.
73. D.G. Kolman and J.R. Scully, unpublished research, University of Virginia, Charlottesville, VA, 1993.



(a)



(b)



(c)

Figure 1 (a) Optical micrograph of as-received solution treated Beta-21S, and scanning electron micrographs of solution treated and peak aged: (b) Ti-15-3 and (c) Beta-21S.

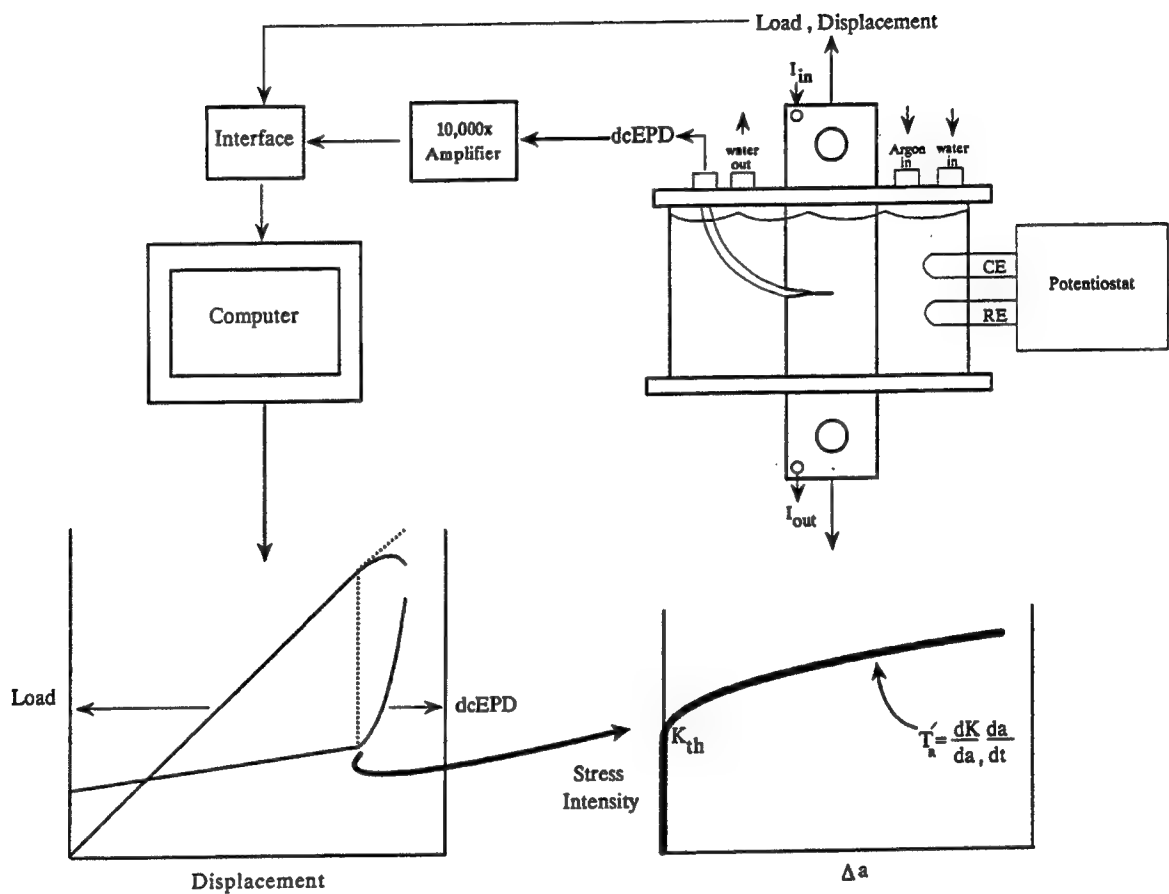
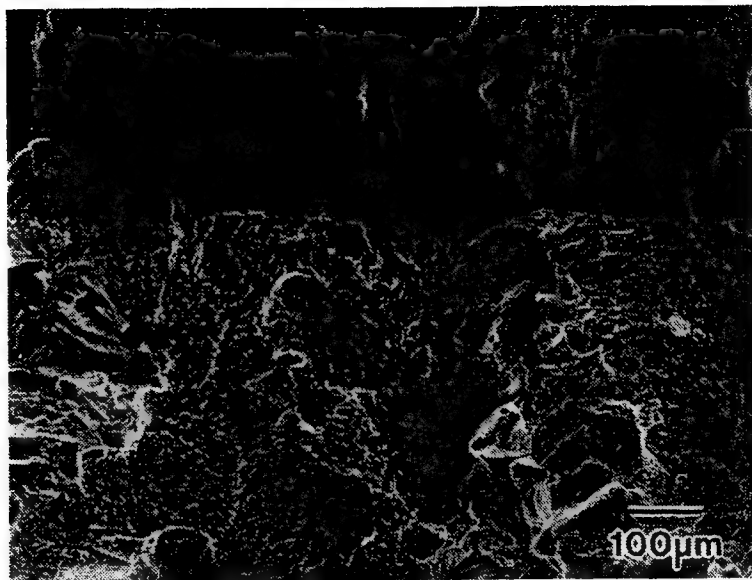
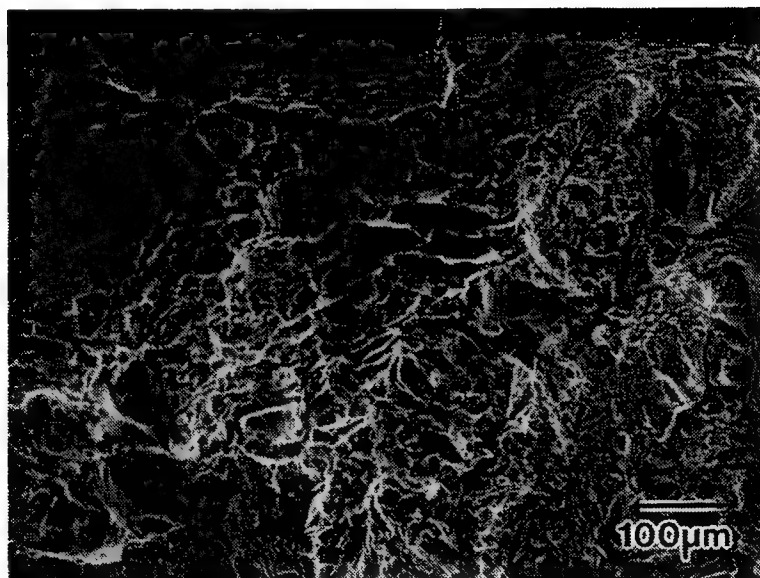


Figure 2 The rising load EAC experimental method. ( $K_{TH}$  is defined at the first resolved increment of crack extension, while stable crack growth is characterized by  $dK/d\Delta a$  and by  $da/dt$ .)



(a)



(b)

Figure 3 Scanning electron fractographs for: (a) STA Ti-15-3 in moist air and (b) STA Beta-21S in moist air. The fatigue crack is at the top of each image and the crack grew from top to bottom.

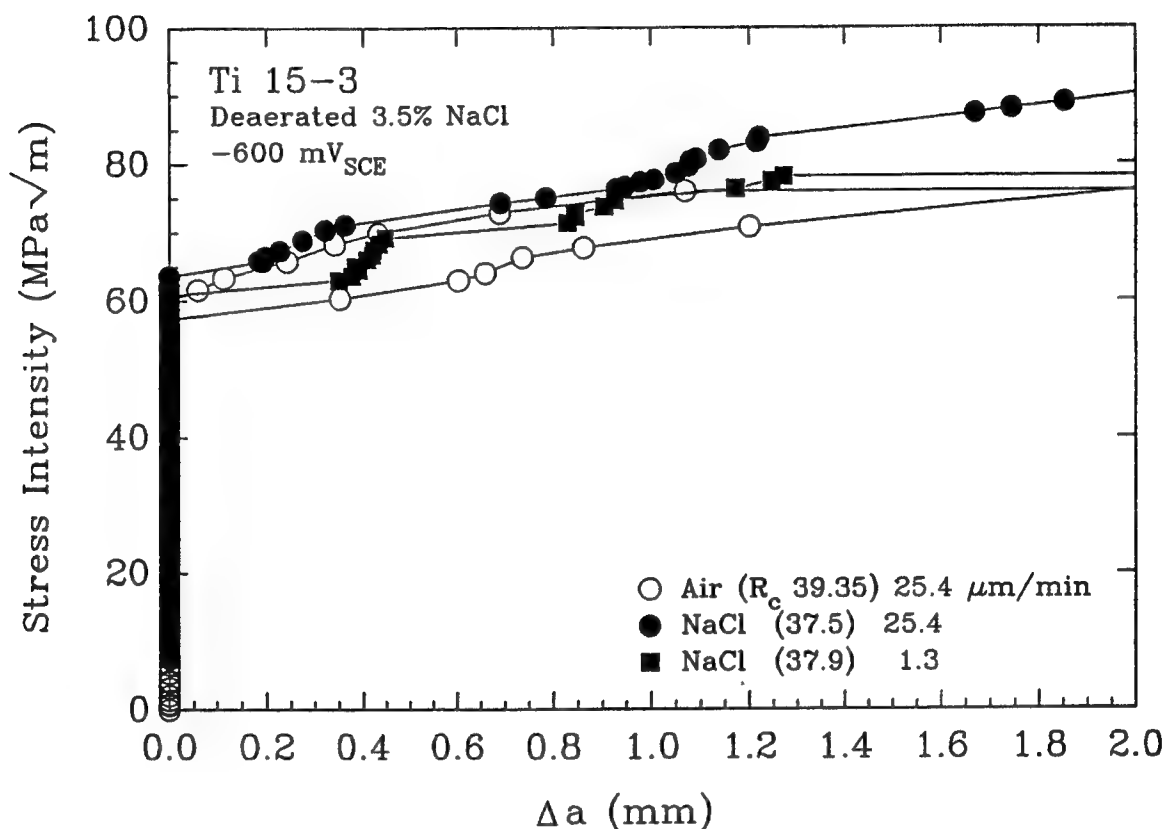
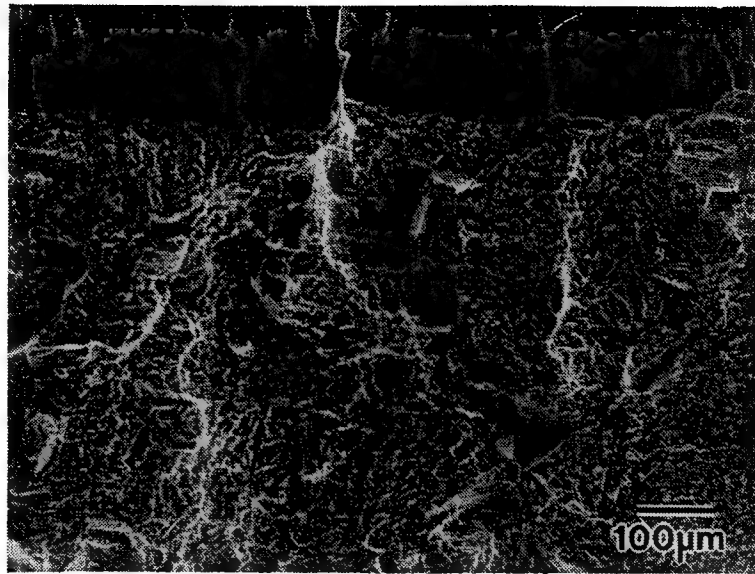
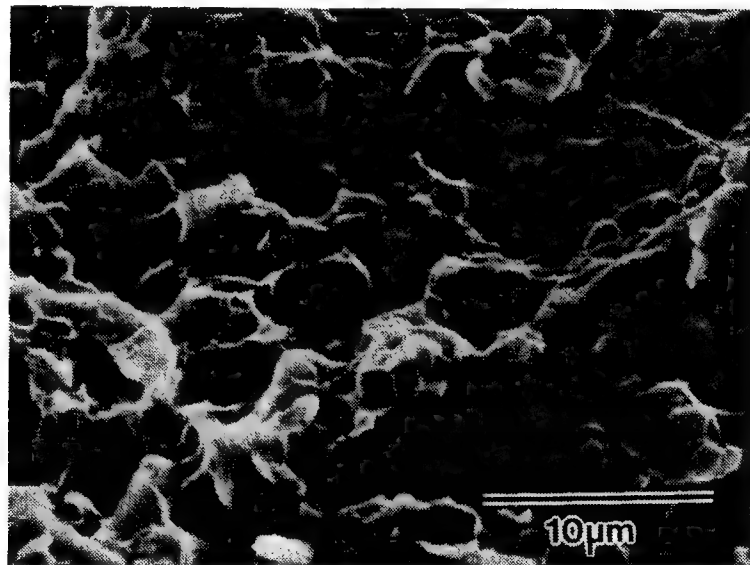


Figure 4 K- $\Delta a$  data for STA Ti-15-3 in air and 3.5% NaCl ( $-600 \text{ mV}_{\text{SCE}}$ ) at two fixed actuator displacement rates. Hardness values ( $R_c$ ) for each specimen are given in the legend. (Replicate air experiments are represented by two trend lines with open circles, and are summarized in Table II. The lower toughness case is for a displacement rate of  $25.4 \text{ } \mu\text{m}/\text{min}$ , while the higher toughness case is for a rate of  $1.3 \text{ } \mu\text{m}/\text{min}$ ; specimen hardness was  $R_c 39.4$  for each experiment.)





(a)



(b)

Figure 5 Scanning electron fractographs for STA Ti-15-3 in 3.5% NaCl ( $-600 \text{ mV}_{\text{SCE}}$  and  $25.4 \text{ } \mu\text{m}/\text{min}$ ) at: (a) low magnification showing the fatigue precrack (top) and initial transgranular cracking in the aqueous solution and (b) high magnification showing microvoids.

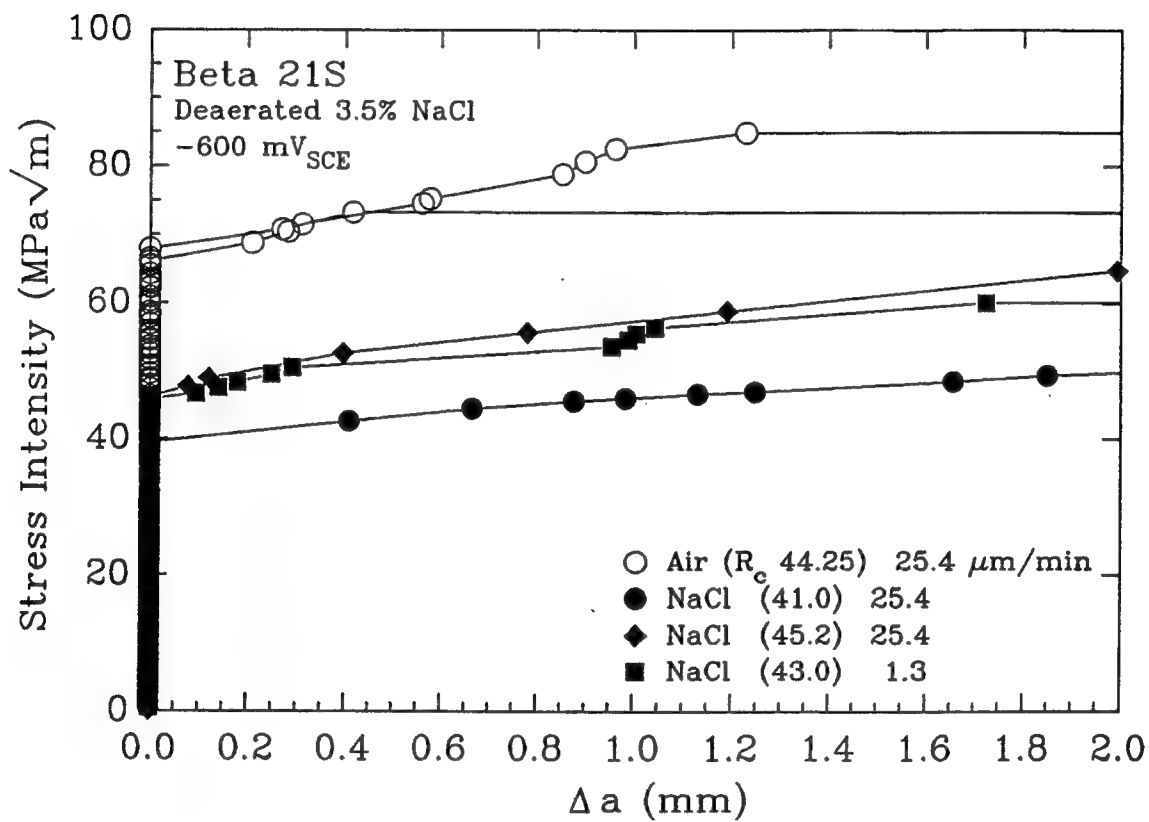


Figure 6 K-Δa for STA Beta-21S in air and 3.5% NaCl ( $-600 \text{ mV}_{\text{SCE}}$ ) at two loading rates. Hardness values ( $R_c$ ) for each specimen are in the legend.

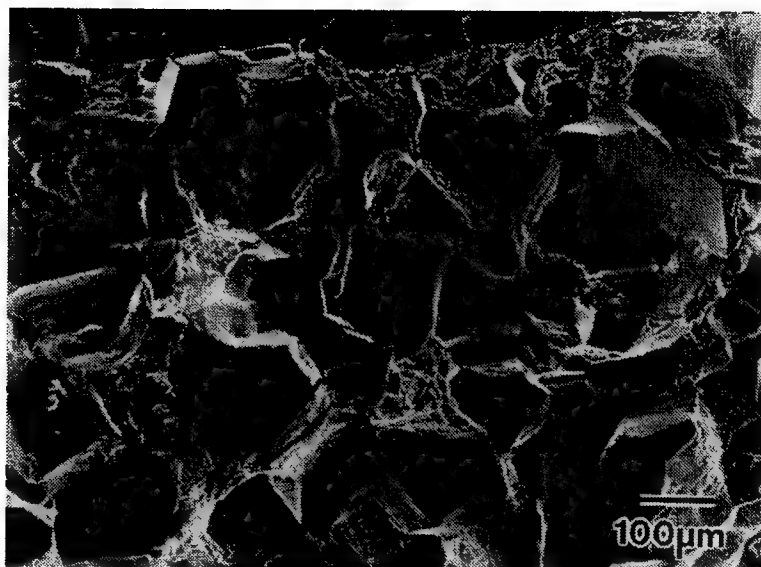


Figure 7 Scanning electron fractograph showing intergranular cracking in STA Beta-21S exposed to 3.5% NaCl at  $-600 \text{ mV}_{\text{SCE}}$  and an actuator displacement rate of  $25.4 \text{ } \mu\text{m}/\text{min}$ .

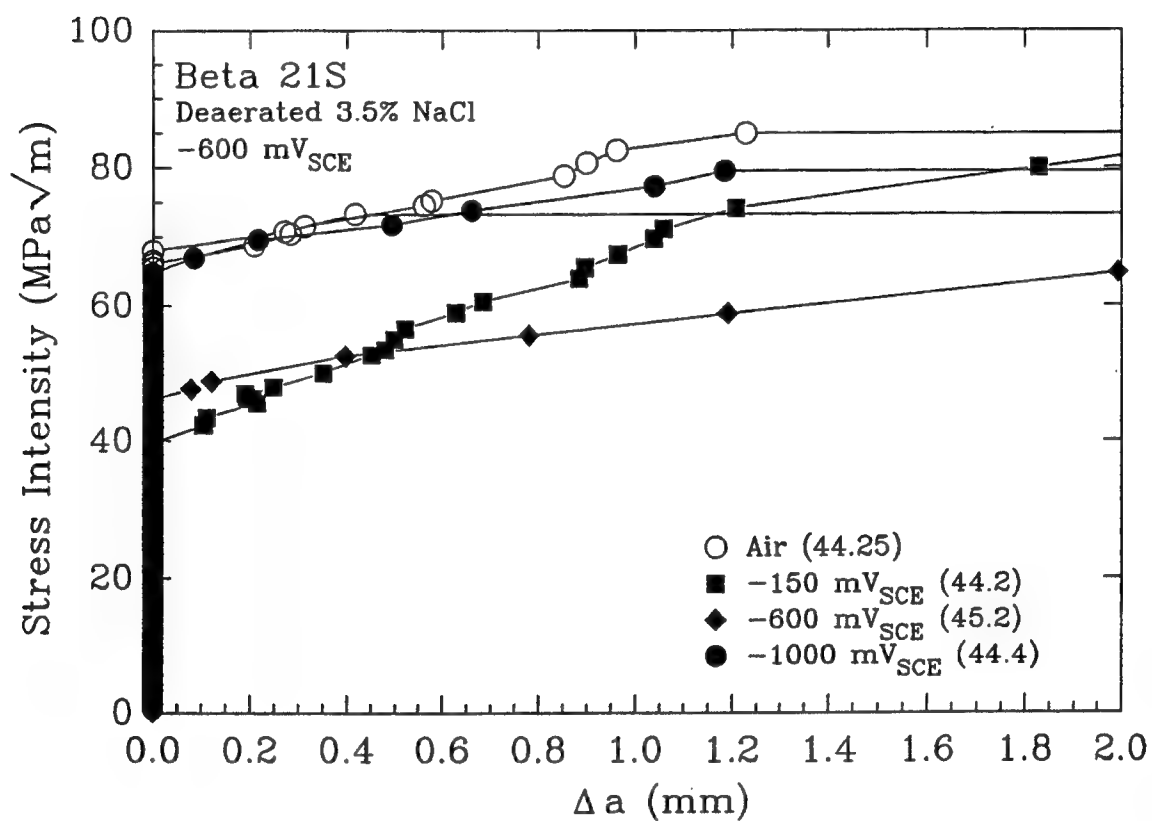
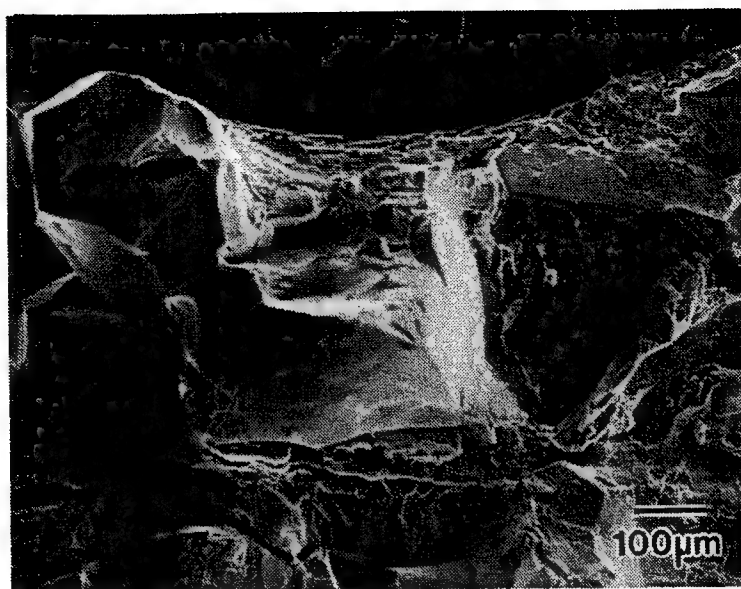
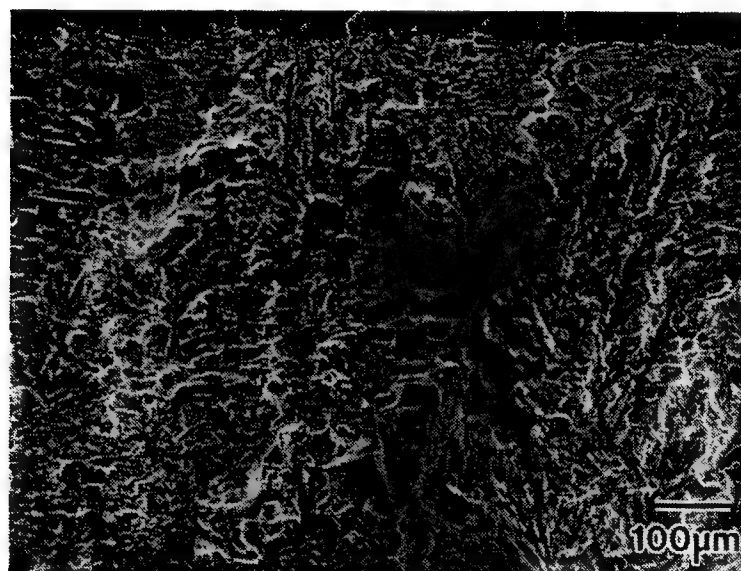


Figure 8 Effect of applied electrode potential on K-Δa for STA Beta-21S in 3.5% NaCl at a constant displacement rate of 25.4 μm/min. Hardness values (R<sub>c</sub>) for each specimen are provided in the legend.



(a)

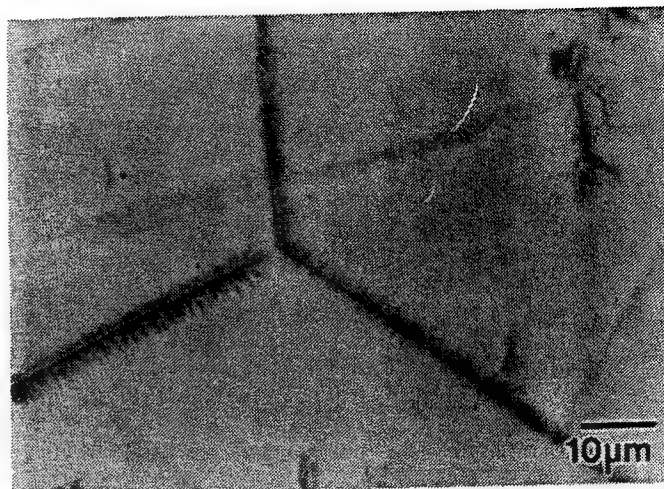


(b)

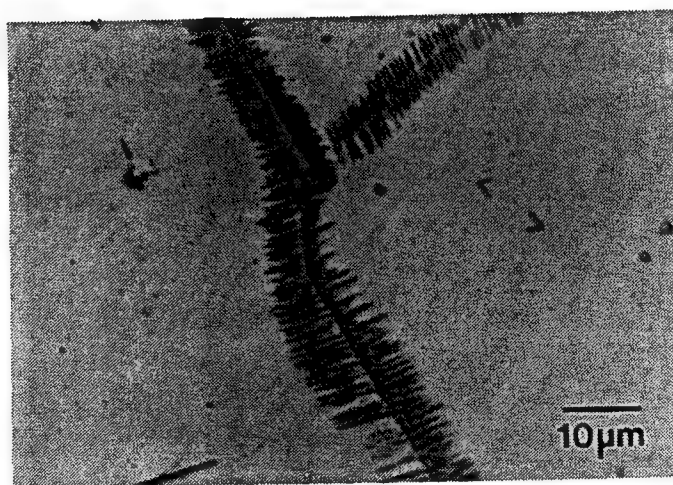
Figure 9 SEM fractographs of STA Beta-21S in NaCl at: (a)  $-150 \text{ mV}_{\text{SCE}}$  and (b)  $-1000 \text{ mV}_{\text{SCE}}$ .



(a)



(b)

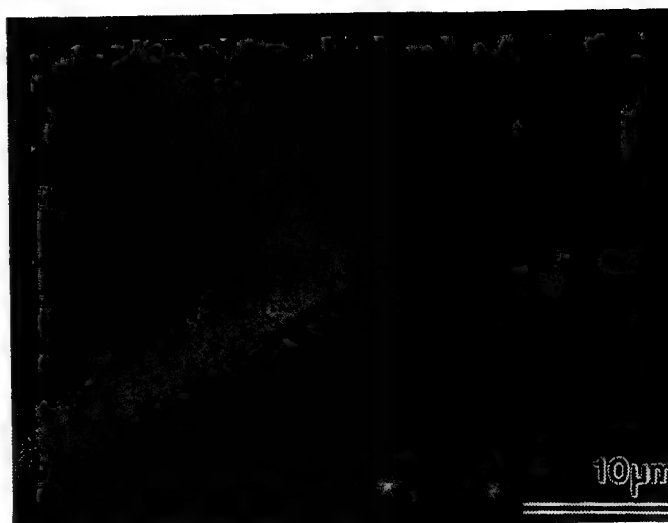


(c)

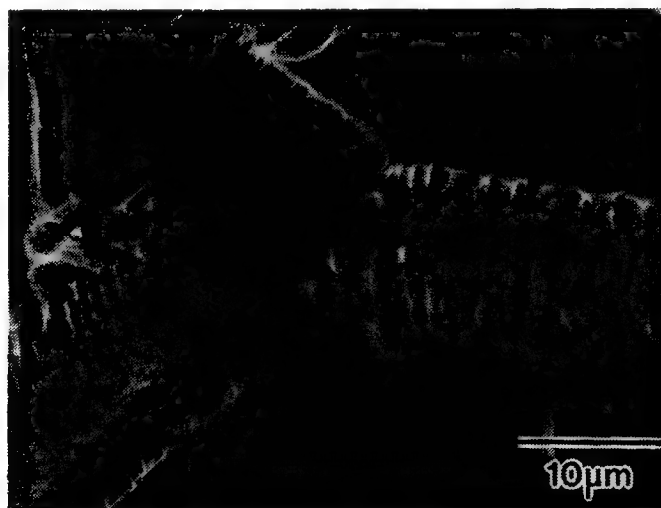
Figure 10 Optical micrographs of under aged (1 hr at 538°C): (a) as received ST (816°C for 0.5 hr) Ti-15-3, (b) resolution treated (950°C for 12 hr) Ti-15-3, and (c) as received ST (871°C for 8 hr) Beta-21S.



(a)



(b)



(c)

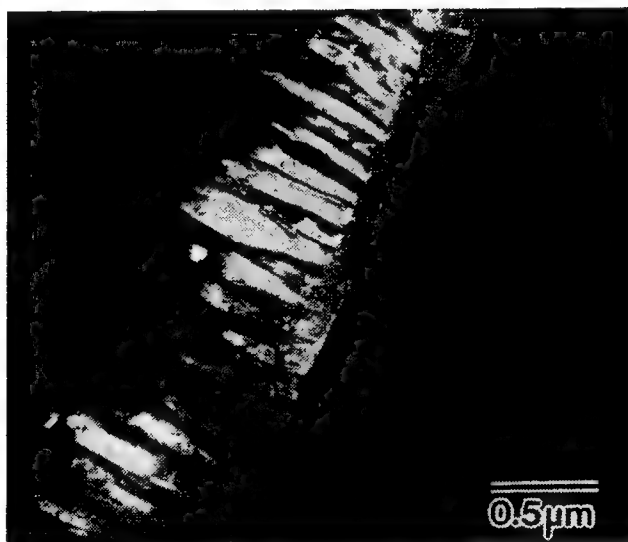
Figure 11 Scanning electron micrographs of under aged (1 hr at 538°C): (a) as received ST (816°C for 0.5 hr) Ti-15-3, (b) resolution treated (1038°C for 2 hr) Ti-15-3, and (c) as received ST (871°C for 8 hr) Beta-21S.



(a)



(b)



(c)

Figure 12 Transmission electron micrographs of: (a) under aged (1 hr at 538°C) Ti-15-3, (b) peak aged (8 hr at 538°C) Ti-15-3, and (c) peak aged (8 hr at 538°C) Beta-21S; all beginning with the as received solution treatments.



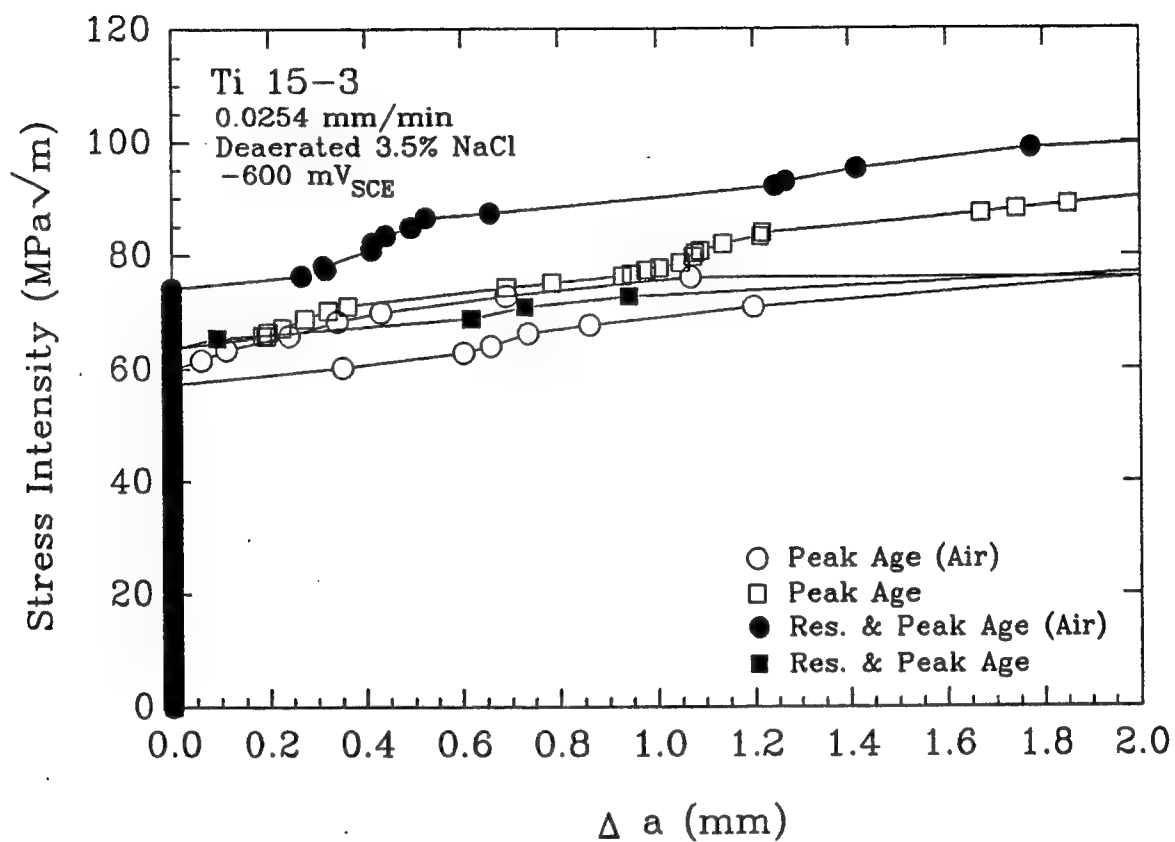


Figure 13 K-Δa for resolution treated (1038°C for 2 hr) and peak aged (8 hr at 538°C) RSTA Ti-15-3 in moist air and NaCl (-600 mV<sub>SCE</sub>), for a single displacement rate of 25.4 μm/min.

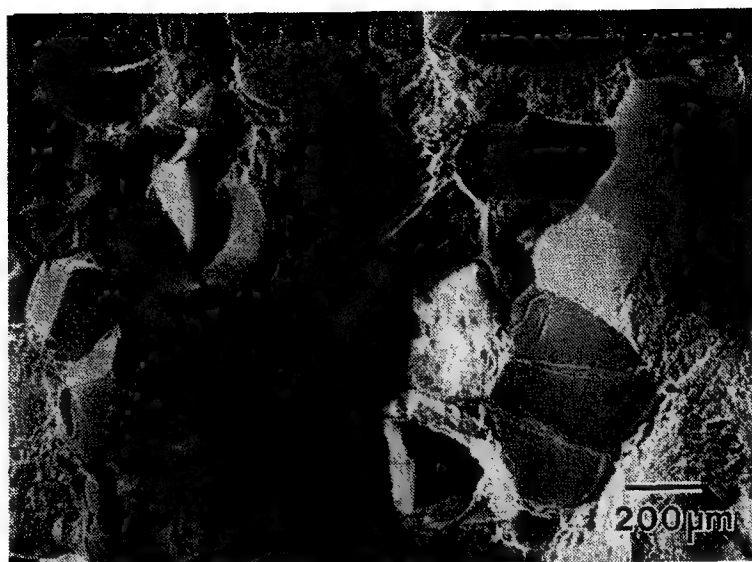


Figure 14 SEM fractograph of RSTA Ti-15-3 in NaCl at  $-600 \text{ mV}_{\text{SCE}}$  and a displacement rate of  $25.4 \text{ } \mu\text{m}/\text{min}$ .

**HYDROGEN ENVIRONMENT EMBRITTLEMENT OF BETA  
TITANIUM ALLOYS**

**Lisa M. Young  
Richard P. Gangloff**

## HYDROGEN ENVIRONMENT EMBRITTLEMENT OF BETA TITANIUM ALLOYS

Lisa M. Young and Richard P. Gangloff

Department of Materials Science and Engineering  
University of Virginia  
Charlottesville, VA 22903-2442

### ABSTRACT

The environment assisted cracking (EAC) resistance of two peak aged metastable  $\beta$ -titanium alloys, Beta 21S and Ti-15-3, is characterized by a fracture mechanics resistance-curve method. Rising load experiments in aqueous 3.5% NaCl at -600 mV<sub>sce</sub> show that Beta 21S is susceptible to environmental cracking. Relative to a moist air crack initiation toughness (plane strain  $K_{IC}$ ) of 67 MPa/m with transgranular fracture, the threshold for stable crack growth ( $K_{TH}$ ) in chloride is as low as 38 MPa/m and fracture occurs by intergranular separation. The reduction from  $K_{IC}$  to  $K_{TH}$  mildly depends on loading rate;  $K_{TH}$  for Beta 21S appears to be minimized at crack tip strain rates between  $10^{-5}$  sec<sup>-1</sup> and  $10^{-4}$  sec<sup>-1</sup>; cracking in chloride is discontinuous in this regime. In contrast the moist air initiation toughness of Ti-15-3 is lower (58 MPa/m) than that of Beta 21S, but is unaffected by exposure to NaCl at several loading rates where  $K_{TH}$  equals  $K_{IC}$ . The reduced EAC resistance of Beta 21S, compared to Ti-15-3, is attributed to abundant  $\alpha$  precipitation at  $\beta$  grain boundaries, and perhaps to higher yield strength for the former alloy. The mechanistic contributions of localized dissolution, film rupture and hydrogen embrittlement are not determined, however, the latter is suspected for EAC of Beta 21S.

### INTRODUCTION

High strength  $\beta$ -titanium alloys are susceptible to brittle environment assisted cracking (EAC) in ambient temperature halide ion solutions. Fracture mechanics experiments demonstrate that early developmental alloys (Ti-11.5Mo-6Zr-4.5Sn and Ti-13V-11Cr-3Al; wt%) and binary model compositions (Ti-Mo), stressed in NaCl and KCl solutions, exhibit stable crack growth at stress intensities ( $K$ ) well below the plane strain fracture toughness,  $K_{IC}$  [1-3]. Environmental fracture progresses by intergranular separation and transgranular "cleavage" or "quasi-cleavage"; the cleavage plane is {100} [2]. Cracking in neutral NaCl is exacerbated at intermediate loading rates (crack tip strain rates) and applied electrode potentials (near -600 mV<sub>sce</sub>), by increased yield strength ( $\sigma_{ys}$ ), and by cathodic polarization with H<sub>2</sub>S addition [1,3-6]. Relative to steels and  $\alpha/\beta$ -titanium alloys, environmental cracking in  $\beta$ -titanium alloys is poorly characterized and understood.

It is reasonable to attribute cracking of  $\beta$ -titanium alloys in aqueous electrolytes to hydrogen embrittlement (hydrogen environment assisted cracking, HEAC) because of the extreme hydrogen susceptibility of high strength body-centered cubic steels [7], because both gaseous hydrogen and cathodically precharged hydrogen embrittle  $\beta$ -titanium alloys [8,9], and by analogy with HEAC in  $\alpha/\beta$ -titanium alloys [10]. The HEAC mechanism for  $\beta$ -titanium alloys in neutral chloride involves: (a) development of an occluded crack electrochemistry, (b) coupled crack surface dissolution, passive film formation and cathodic H production, (c) film rupture, (d) hydrogen absorption and diffusion into the crack tip process zone, (e) segregation at microstructural trap sites, and (f) hydrogen assisted microcracking, probably

by decohesion, localized plasticity or hydride mechanisms. The crack surface passive film should play a central role in HEAC, with a sound film blocking hydrogen production and/or uptake. Many factors; including alloy composition, microstructure, applied electrode potential, bulk electrolyte composition, slip deformation mode, and dynamic cyclic strain; could compromise the passive film and enhance the uptake of embrittling hydrogen.

Research was initiated to investigate surface passivity and localized dissolution in addition to hydrogen production, uptake, trapping and embrittlement in the crack tip region of high strength  $\beta$ -titanium alloys in aqueous marine environments [11]. The objective of the work reported here is to characterize the EAC behavior of two modern  $\beta$ -titanium alloys, subjected to dynamic straining to destabilize crack tip passivity, and employing advanced fracture mechanics methods.

## EXPERIMENTAL PROCEDURE

Two alloys, Beta 21S (Ti-15Mo-2.7Nb-3Al-0.2Si-0.15 O; wt%) and Ti-15-3 (Ti-15V-3Cr-3Al-3Sn; wt%), were obtained as 10.2 and 9.5 mm thick hot rolled plate, respectively, in the solution treated conditions (871°C for 8 hours and 816°C for 30 minutes, respectively). Oversized blanks of each alloy were peak aged at 538°C for 8 hours. The resultant microstructures are homogeneous and isotropic in all directions, and consist of fine  $\alpha$  platelets in a  $\beta$  matrix of 100  $\mu$ m diameter grains, as illustrated for Beta 21S in Fig. 1. The optical microstructure of Ti-15-3 is identical to that shown in Fig. 1, with the exception of differences in grain or near-grain boundary  $\alpha$  precipitation (see Discussion). Each alloy is presumed to be stable with regard to  $\omega$  and  $\beta'$  precipitation. Measured yield strengths from replicate specimens of this aging condition are 1380 MPa ( $R_e 42.5 \pm 1.3$ ) for Beta 21S and 1315 MPa ( $R_e 36.9 \pm 1.3$ ) for Ti-15-3.

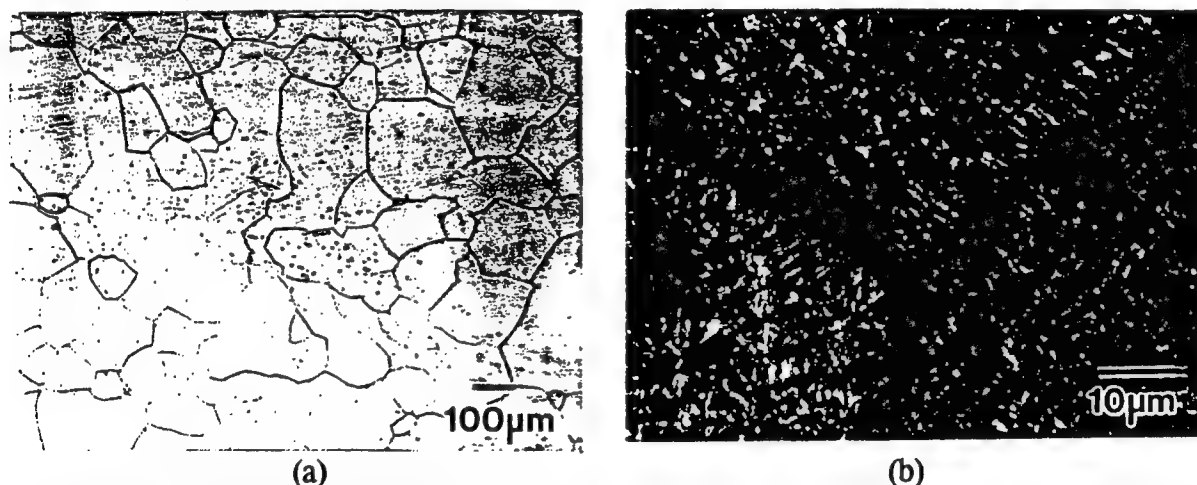


Figure 1: Optical micrographs of Beta 21S in the: (a) as-received solution annealed and (b) peak aged conditions.

EAC resistance was characterized with a slowly rising load fracture mechanics method applied to the fully rotating single edge precracked specimen (SEN; nominal crack length = 17.8 mm, thickness = 5.08 mm, width = 38.1 mm) [12-14]. A servohydraulic machine was employed for fatigue precracking (load control with  $K_{max}$  less than 30 MPa/m) and rising load cracking (actuator displacement control). Specimens were precracked in the aqueous environment, then fractured under rising load. Crack length was monitored using a computer-automated direct current (applied current = 2 to 4 amperes) potential difference (DCPD) method, including current polarity switching to eliminate thermal voltages and a reference probe pair to account for temperature and current variations during prolonged

experiments [15]. Measured voltages were related to crack length through Johnson's analytical equation for the SEN specimen. Applied stress intensity was calculated from load and crack length with a standard elastic solution [16], and plotted as a function of crack extension increment ( $\Delta a$ ). The threshold  $K$  for crack growth initiation ( $K_{IC}$  in air and  $K_{TH}$  for aggressive environments) was calculated from the applied load at the first change in the slope of the initially linear electrical potential versus load record;  $\Delta a$  is assumed to equal zero prior to this point [17]. While ASTM Standard E399 was not adhered to for  $K_{IC}$  [18], crack initiation occurred under plane strain constraint based on the J-integral approach (thickness and ligament  $> 25 J_{initiation}/\sigma_{ys}$ ) [12,13,19]. Since small scale yielding was maintained for all cases, the contribution of  $J_{plastic}$  to  $K$  was negligible and assumed to equal zero. Environmental effects on crack propagation under increasing  $K$  are indicated by the slope of the  $K$ - $\Delta a$  data. Shear walls, present after initiation, indicate that the crack propagated under mixed plane strain and plane stress.

Fracture experiments were conducted in either moist air or 0.6M (3.5 wt%) NaCl at fixed electrode potential, near-neutral pH of 7, and 25°C. The central portion of the edge cracked specimen was immersed in flowing (60 ml/min) chloride (pH 8, 23°C) in a sealed plexiglass chamber. The specimen was maintained at constant potential by a Wenking potentiostat in conjunction with a Ag/AgCl reference electrode and two platinum counter electrodes, each isolated to minimize solution contamination.

## RESULTS

Ti-15-3 is resistant to EAC during rising load at various slow displacement rates; these conditions promote HEAC in ferritic and martensitic steels exposed to NaCl [7].  $K$ - $\Delta a$  results are presented in Fig. 2. For benign moist air, the initiation toughness ( $K_{IC}$ ) of Ti-15-3 is 57 and 59 MPa $\sqrt{m}$  based on replicate experiments. For aqueous chloride at a fixed potential of -600 mV<sub>sce</sub>,  $K_{TH}$  ranges from 61 to 65 MPa $\sqrt{m}$ , independent of actuator displacement rate varying between 25 and 0.25  $\mu m/min$ . The chloride environment does not degrade the crack initiation toughness. For each environment, some stable crack extension is observed ( $dK/d\Delta a > 0$ ), however, this tearing resistance is not environmentally influenced. The difference in  $dK/d\Delta a$  is larger for the replicate air tests compared to the aqueous environmental effect; actuator displacement rate does not affect the EAC propagation resistance of Ti-15-3.

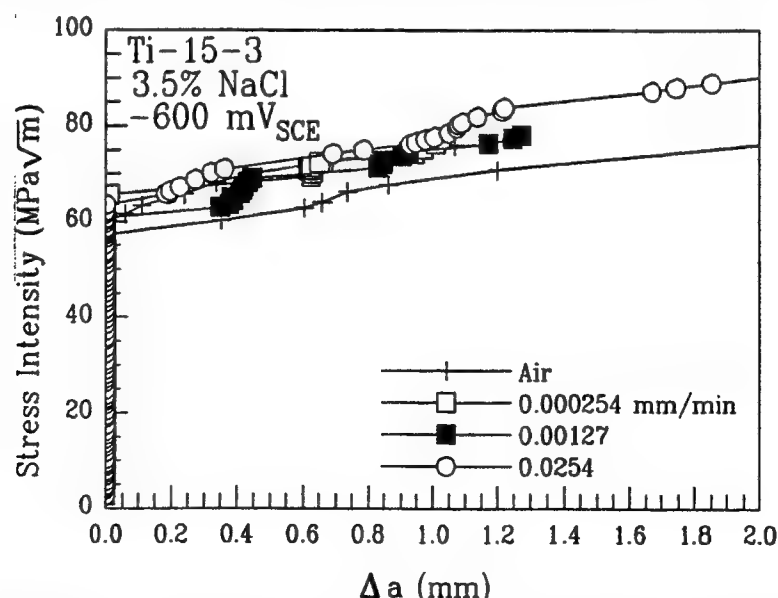


Figure 2: Rising load stress intensity versus crack extension data for Ti-15-3 in moist air and deaerated 3.5% NaCl (-600 mV<sub>sce</sub>) as a function of loading rate.

The variability of the crack propagation results for moist air may be related to subtle inaccuracies in defining the electrical potential corresponding to crack initiation. The problem is that crack tip plastic deformation, microvoid damage and macrocrack growth can contribute to voltage increases. Discontinuous crack bursts were indicated by measured DCPD, but only for the aqueous environment and not moist air.

Environment did not influence the microscopic fracture morphology for Ti-15-3. Typical scanning electron fractographs of the crack initiation region, adjacent to the fatigue precrack, are presented in Fig. 3 for air and aqueous NaCl. For each case, the crack surface is mainly populated by transgranular features indicative of microvoid-based cracking, as confirmed by high magnification observation. Scattered facets are present, indicating limited intergranular microvoid rupture; intergranular EAC is not likely for Ti-15-3 because similar facets are observed for cracking in NaCl, moist air and ultra-high vacuum.

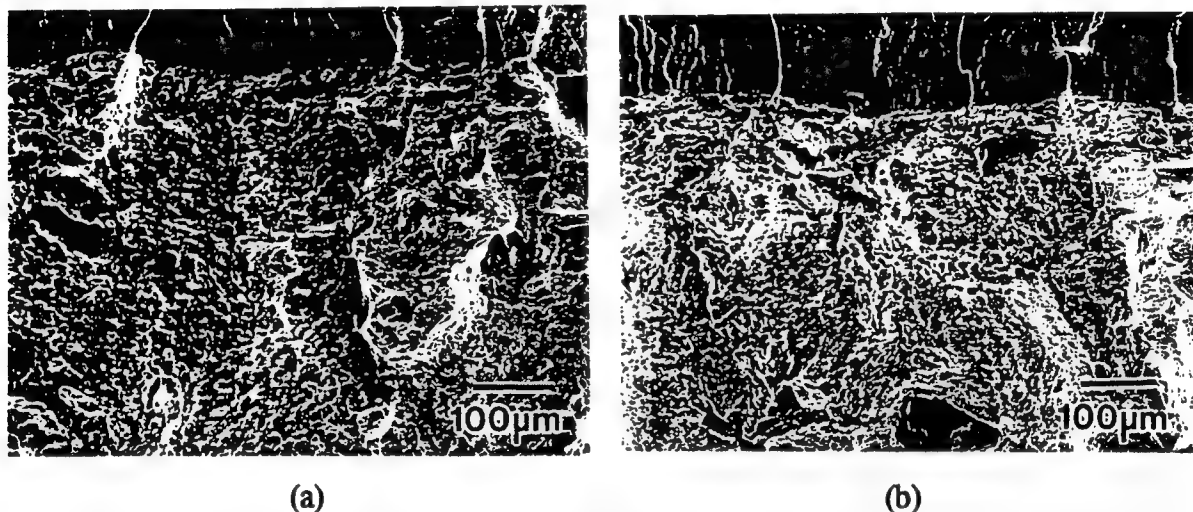


Figure 3: SEM fractographs of the fatigue precrack (top) and rising load fracture toughness crack surfaces in Ti-15-3: (a) air; (b) deaerated 3.5% NaCl.

In contrast to Ti-15-3, Beta 21S is embrittled by aqueous chloride at  $-600 \text{ mV}_{\text{sce}}$ , as shown by the  $K_{\Delta a}$  data in Fig. 4. While  $K_{\text{IC}}$  is high (66 and 68  $\text{MPa}/\text{m}$ ) for moist air,  $K_{\text{TH}}$  values range from 38 to 51  $\text{MPa}/\text{m}$  for Beta 21S in NaCl at  $-600 \text{ mV}_{\text{sce}}$ . The macroscopic

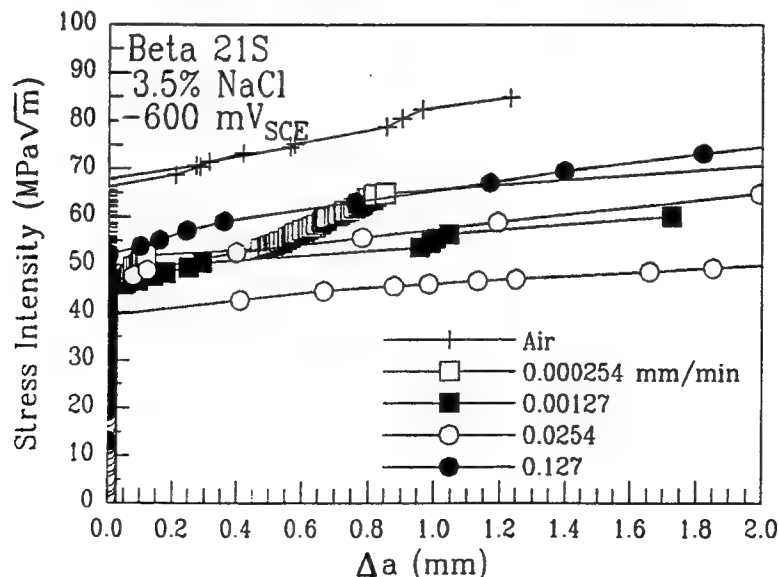


Figure 4: Rising load stress intensity versus crack extension data for Beta 21S in moist air and deaerated 3.5% NaCl ( $-600 \text{ mV}_{\text{sce}}$ ) as a function of loading rate.

crack growth resistances (average  $dK/d\Delta a$ ) are similar for each environment. Aqueous NaCl caused a dramatic fracture mode transition. The fractographs in Fig. 5 show that, while the air crack appears to involve intergranular microvoid fracture (with limited tear-free facets), the chloride case is almost entirely intergranular with little evidence of resolvable localized plasticity.

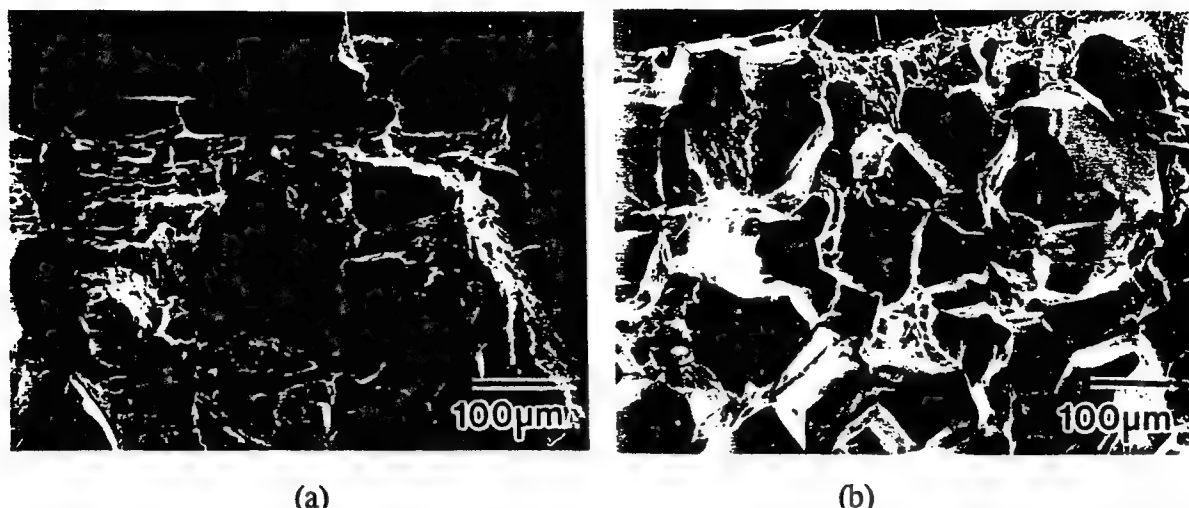


Figure 5: SEM fractographs of the fatigue precrack (top) and rising load fracture toughness crack surfaces in Beta 21S: (a) air; (b) deaerated 3.5% NaCl.

Actuator displacement rate mildly affects  $K_{TH}$  for EAC of Beta 21S in NaCl. While obscured by variability for replicate experiments at  $25.4 \mu\text{m}/\text{min}$  and a recently measured high value ( $K_{TH} = 52 \text{ MPa}/\text{m}$ ) at  $12.7 \mu\text{m}/\text{min}$ ,  $K_{TH}$  appears to be broadly minimized at displacement rates between  $0.6$  and  $6 \mu\text{m}/\text{min}$ . Additional experiments are in progress to define the strain rate dependence of HEAC. Recent results suggest that  $K_{TH}$  equals  $K_{IC}$  at high loading rates and that crack growth is not observed for static loading (24 hours) at  $K$  levels up to  $60 \text{ MPa}/\text{m}$ . Crack bursts were observed for Beta 21S in NaCl, but only for the two slowest loading rates. Bursts were large ( $50$  to  $300 \mu\text{m}$ ) and occurred at about five hour intervals. Discontinuous cracking, below  $20 \mu\text{m}$  bursts, would not be resolved by DCPD.

## DISCUSSION

**Fracture Toughness: Moist Air** The moist air fracture toughnesses of Ti-15-3 ( $K_{IC} = 57$  to  $59 \text{ MPa}/\text{m}$ ) and Beta 21S ( $K_{IC} = 66$  to  $68 \text{ MPa}/\text{m}$ ) are comparable to values reported for  $\beta$ -titanium alloys at similar yield strengths [20-22]. This agreement suggests that the DCPD-based  $K-\Delta a$  approach accurately characterizes plane strain fracture toughness in spite of small specimen thickness compared to the requirement of Standard E399 [18].

The fracture toughness of Beta 21S is superior to that of Ti-15-3, particularly considering the higher yield strength of the former. This is curious because cracking of Beta 21S in air appears to involve grain boundary microvoiding. Beta 21S contains substantial  $\alpha$  precipitates at or near  $\beta$  grain boundaries, a microstructure that is not observed for Ti-15-3. Lee et al. and Froes et al. report that  $K_{IC}$  is degraded by grain boundary  $\alpha$  [21,22]. Localized plastic deformation in low strength  $\alpha$  results in strain concentration and microvoid nucleation at  $\alpha/\beta$  interfaces near  $\beta$  grain boundaries. The fracture toughness of Beta 21S may be further improved by processing to eliminate  $\alpha$  precipitates at  $\beta$  grain boundaries.

**Environmental Cracking Resistance**  $K_{TH}$  for HEAC of the  $1350 \text{ MPa}$  yield strength level of tempered martensitic steels in aqueous chloride varies between  $12 \text{ MPa}/\text{m}$  and  $38 \text{ MPa}/\text{m}$ , but typically equals  $25 \text{ MPa}/\text{m}$ , depending on metallurgical and mechanical variables [7].



The EAC resistances of high strength Beta 21S and particularly Ti-15-3 are good compared to such steels, consistent with previous results [23]. Ti-15-3 may be embrittled by more aggressive hydrogen producing environments, for example acidified NaCl with sulfide addition and cathodic polarization [1,5-7]. Additional experiments are in progress and include longer exposure times, a range of loading rates and applied electrode potentials, in addition to low amplitude ripple loading [24].

The rising load EAC results do not, in isolation, define the embrittlement mechanism for the  $\beta$ -titanium alloys; this is being examined in parallel studies [8,24,25]. Two points are notable. Intermittent crack bursts, over distances greatly in excess of the crack tip process zone and on the order of one to five grain diameters, suggests HEAC with a strong role of grain boundary traps. Intergranular cracking is a classic damage mechanism for hydrogen embrittled steels [7]. The extent to which predissolved hydrogen degrades  $K_{IC}$  during rising loading and produces intergranular cracking is being determined for comparison with the EAC behavior of Beta 21S and Ti-15-3 in NaCl [25].

It is important to understand the different EAC sensitivities of Ti-15-3 and Beta 21S. Assuming HEAC, the resistance of Ti-15-3 may be explained by yield strength. Modeling and experiment show that lower strength steels are less susceptible to HEAC, particularly for NaCl and strengths below 1500 MPa [7]. The expected yield strengths of Beta 21S and Ti-15-3 are 1210 MPa and 1010 MPa, respectively, for the eight hour age at 538°C [23,26], suggesting better HEAC resistance for Ti-15-3. Gagg and Toloui report that Ti-15-3, aged at 510°C for six hours (ultimate tensile strength = 1260 MPa and  $\sigma_{ys} \approx 1200$  MPa), is embrittled during slow strain rate loading of smooth tensile specimens in several chloride solutions [5]. These  $\sigma_{ys}$  values are substantially less than the measured strengths of the two alloys studied here; the reason is undetermined. A strong yield strength effect on  $K_{TH}$  is not likely because of the small measured strength difference between Beta 21S and Ti-15-3. Additional work is, however, required because of the unexpectedly high values of  $\sigma_{ys}$ .

The relative HEAC behaviors of Ti-15-3 and Beta 21S are not explained by occluded crack solution hydrogen production and uptake [11]. Cr and V solute in the  $\beta$  phase of Ti-15-3 should dissolve and hydrolyze at -600 mV<sub>sce</sub> to produce a more acid crack tip pH compared to Beta 21S which contains Mo and Nb. Mo should promote crack tip passivity and hinder hydrogen uptake. These hypothesis are not consistent with the measured HEAC resistances of the two alloys.

It is reasonable to speculate that Beta 21S is sensitive to intergranular EAC in NaCl because of extensive  $\alpha$  precipitation at or near beta grain boundaries. This microstructure was not observed for Ti-15-3, as demonstrated by interrupted aging (2 hours at 538°C); Fig. 6. Whether very fine  $\alpha$  is present at Ti-15-3 boundaries must be determined by electron microscopy. Gagg and Toloui did not report the microstructure or the solution treatment conditions of Ti-15-3 that was embrittled by NaCl [5]. The Beta 21S microstructure may be environment sensitive because a brittle continuous hydride film forms in hcp  $\alpha$ -titanium and at  $\alpha/\beta$  interfaces [1,27,28]. Intergranular cracking may also be traced to hydrogen trapping at  $\alpha/\beta$  interfaces, to localized plastic deformation in the soft  $\alpha$  that produces stress/strain concentrations that interact with embrittling hydrogen, or to local dissolution of  $\alpha$ . Either cold rolling of Beta 21S prior to aging, or restricted recovery and recrystallization during hot rolling and solution treatment, should provide distributed intragranular nucleation sites for  $\alpha$  precipitates, apart from  $\beta$  grain boundaries [29]. The more homogeneous microstructure should be resistant to HEAC [1].

EAC and HEAC depend on strain rate. For NaCl, embrittlement is maximum at an intermediate strain rate of order  $6 \times 10^{-6} \text{ sec}^{-1}$  for  $\beta$  Ti-15-3 and  $2 \times 10^{-3} \text{ sec}^{-1}$  for  $\alpha/\beta$  Ti-6Al-4V [1,5,10,30]. For Beta 21S in NaCl, the mild minimum in  $K_{TH}$  (Fig. 3) occurs at an

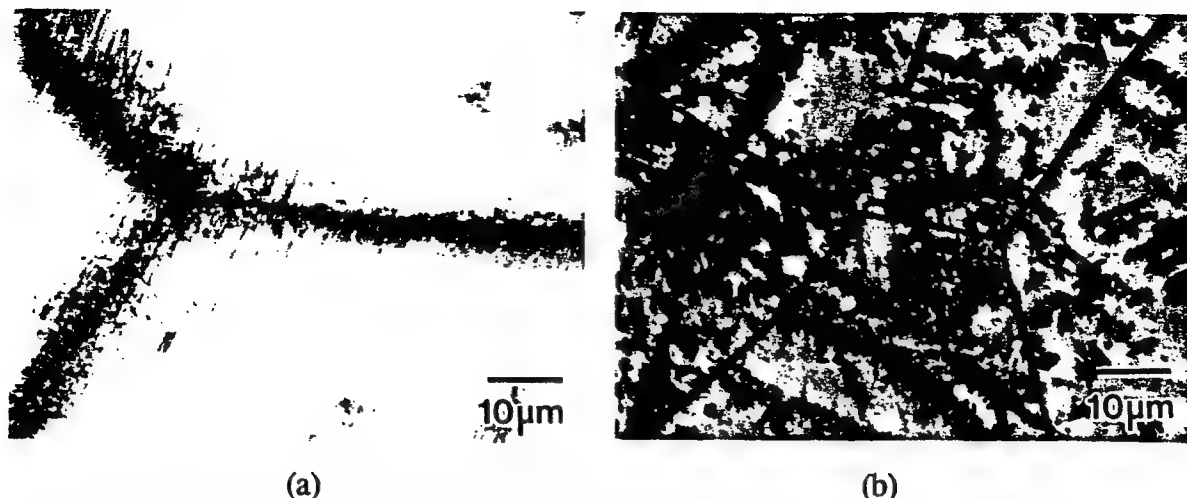


Figure 6: Optical micrographs of underaged (a) Beta 21S and (b) Ti-15-3.

estimated crack tip strain rate of between  $10^{-5}$  and  $10^{-4} \text{ sec}^{-1}$ , corresponding to actuator displacement rates of 0.6 and  $6 \mu\text{m}/\text{min}$  and constant loading rates of 15 and  $150 \text{ N}/\text{min}$ . It is not possible to quantitatively compare smooth specimen and crack tip strain rates because the former is typically not measured or maintained constant [5]. Crack tip strain rate varies with distance into the process zone and is not accurately known [31]. (The above strain rates were calculated at a distance of one blunted crack tip opening displacement ahead of the crack tip.) From the HEAC perspective, embrittlement may be most severe at the strain rate that balances surface film destabilization and hydrogen uptake (promoted by increased rate) with the time necessary for hydrogen diffusion into the crack tip process zone (promoted by decreased rate). The kinetics of each process are not defined.

## CONCLUSIONS

1. The threshold stress intensity for stable crack propagation in Beta 21S is significantly reduced by simultaneous slow loading and exposure to aqueous NaCl at  $-600 \text{ mV}_{\text{sc}}$ . Cracking in chloride is intergranular compared to grain boundary and transgranular microvoid processes for moist air, and is possibly by hydrogen embrittlement.
2. The crack initiation fracture toughness and microscopic fracture processes of Ti-15-3 are unaffected by chloride environment exposure for several slow constant actuator displacement rates.
3. The EAC susceptibility of Beta 21S and the resistance of Ti-15-3 are explained by copious  $\alpha$  precipitation at  $\beta$  grain boundaries and the high yield strength of the former alloy.
4. The chloride environmental cracking thresholds of Ti-15-3 and Beta 21S are superior to the behavior of tempered martensitic steels at equal yield strength.
5. Dynamic loading rate affects EAC in Beta 21S;  $K_{\text{TH}}$  for crack growth in NaCl may be minimized at a crack tip strain rate between  $10^{-5}$  and  $10^{-4} \text{ sec}^{-1}$ .

## ACKNOWLEDGEMENTS

This research was supported by the Office of Naval Research (Grant N00014-91-J-4164) with Dr. A. John Sedriks as Scientific Officer, and by the Virginia CIT Center for Electrochemical Science and Engineering at the University of Virginia. Material was donated by the Titanium Metals Corporation. This support is gratefully acknowledged, as are informative discussions with Dr. J.R. Scully and Messrs G.A. Young and D.G. Kolman.

## REFERENCES

1. M.J. Blackburn, J.A. Feeney, and T.R. Beck, in Advances in Corrosion Science and Technology, M.G. Fontana and R.W. Staehle, eds., Vol. 3, Plenum Publishing, NY, NY, pp. 67-292, 1972.
2. D.N. Fager and W.F. Spurr, Trans. ASM, Vol. 61, pp. 283-292, 1968.
3. J.A. Feeney and M.J. Blackburn, Met. Trans., Vol. 1, pp. 3309-3323, 1970.
4. Corrosion; Metals Handbook, Vol. 13, Edition 9, ASM International, Metals Park, OH, pp. 483-485, 1987.
5. C. Gagg and B. Toloui, in Sixth World Conference on Titanium, pp. 545-550, 1988.
6. D.E. Thomas and S.R. Seagle, in Titanium Science and Technology, Vol. 4, G. Lutjering, U. Zwicker and W. Bunk, eds., pp. 2533-2540, 1984.
7. R.P. Gangloff, in Corrosion Prevention and Control, M. Levy and S. Isserow, eds., US Army Laboratory Command, Watertown, MA, pp. 64-111, 1986.
8. N.E. Paton, R.A. Spurling and C.G. Rhodes, in Hydrogen Effects in Metals, I.M. Bernstein and A.W. Thompson, eds., TMS-AIME, Warrendale, PA, pp. 269-279, 1981.
9. W.W. Gerberich, N.R. Moody and C.L. Jensen, in Hydrogen Effects in Metals, I.M. Bernstein and A.W. Thompson, eds., TMS-AIME, Warrendale, PA, pp. 731-745, 1981.
10. H.B. Nelson, in Hydrogen in Metals, I.M. Bernstein and A.W. Thompson, eds., ASM International, Metals Park, OH, pp. 445-464, 1974.
11. R.P. Gangloff and J.R. Scully, "Mechanisms for the Environmental Cracking Resistance of High Strength Titanium Alloys", Proposal MS-DOD/ONR-4956-91, University of Virginia, Charlottesville, VA, 1991.
12. D.R. Anderson and J.P. Gudas, in Environment Sensitive Fracture: Evaluation and Comparison of Test Methods, ASTM STP 821, S.W. Dean, E.N. Pugh and G.M. Ugiansky, eds., ASTM, Philadelphia, PA, pp. 98-113, 1984.
13. E.M. Hackett, P.J. Moran and J.P. Gudas, in Fracture Mechanics: Seventeenth Volume, ASTM STP 905, J.H. Underwood, et al., eds., ASTM, Philadelphia, PA, pp. 512-541, 1986.
14. R.A. Mayville, T.J. Warren and P.D. Hilton, Trans. ASME, Vol. 109, pp. 188-193, 1987.
15. J.K. Donald and J. Ruschau, in Fatigue Crack Measurement: Techniques and Applications, K.J. Marsh, R.A. Smith and R.O. Ritchie, eds., EMAS, Ltd., West Midlands, UK, pp. 11-37, 1991.
16. H. Tada, P.C. Paris and G.R. Irwin, The Handbook, Del Research Corp., St. Louis, MO, p. 2.11, 1985.
17. P. Doig and K.R. Abbott, J. Test. Eval., Vol. 12, pp. 297-304, 1984.
18. "Standard Test Method for Plane Strain Fracture Toughness of Metallic Materials", ASTM Standard E399-90, Annual Book of ASTM Standards, Vol. 03.01, ASTM, Philadelphia, PA, pp. 506-536, 1992.
19. "Standard Test Method for  $J_{IC}$ , A Measure of Fracture Toughness", ASTM Standard E813-89, Annual Book of ASTM Standards, Vol. 03.01, ASTM, Philadelphia, PA, pp. 732-746, 1992.
20. R.R. Boyer, J. Metals, March, pp. 61-65, 1980.
21. C.S. Lee, S.J. Kim, C.G. Park and Y.W. Chang, "Effect of Microstructural Variation on the Mechanical Properties of Ti-10V-2Fe-3Al", Unpublished Research, 1992.
22. F.H. Froes, J.C. Chesnutt, C.G. Rhodes and J.C. Williams, in Toughness and Fracture Behavior of Titanium, ASTM STP 651, ASTM, Philadelphia, PA, pp. 115-153, 1978.
23. P.J. Bania, G.A. Lenning, and J.A. Hall, in Beta Titanium Alloys in the 80's, R.R. Boyer and H.W. Rosenberg, eds., TMS-AIME, Warrendale, PA, pp. 209-229, 1983.
24. L.M. Young, "Marine Environmental Cracking of High Strength Beta Titanium Alloys", MS Thesis, University of Virginia, Charlottesville, VA, in preparation, 1992.
25. G.R. Young and J.R. Scully, Unpublished Research, University of Virginia, Charlottesville, VA, 1992.
26. P.J. Bania and W.M. Parris, "Beta-21S: A High Temperature Metastable Beta Titanium Alloy", presented at the 1990 TDA International Conference, Orlando, FL, 1990.
27. T.W. Duerig and J.C. Williams, in Beta Titanium Alloys in the 80's, R.R. Boyer and H.W. Rosenberg, eds., TMS-AIME, Warrendale, PA, pp. 19-67, 1983.
28. J.E. Costa, D. Banerjee and J.C. Williams, in Beta Titanium Alloys in the 80's, R.R. Boyer and H.W. Rosenberg, eds., TMS-AIME, Warrendale, PA, pp. 69-84, 1983.
29. J.C. Williams, in Titanium Science and Technology, R.I. Jaffee and H.M. Burte, eds., TMS-AIME, New York, pp. 1433-1494, 1973.
30. J.A. Muskovitz and R.M. Pelloux, Corrosion, Vol. 35, pp. 509-514, 1979.
31. W.W. Gerberich and S. Chen, in Environment Induced Cracking of Metals, R.P. Gangloff and M.B. Ives, eds., NACE, Houston, TX, pp. 167-187, 1990.

**YIELD STRENGTH AND SOLUTION COMPOSITION EFFECTS  
ON AQUEOUS ENVIRONMENTAL CRACKING OF**

**Ti-8V-6Cr-4Zr-4Mo-3Al (BETA C)**

**Brian P. Somerday  
Jennifer A. Grandle  
Richard P. Gangloff**

B.P. Somerday, J.A. Grandle and R.P. Gangloff, "Yield Strength and Solution Composition Effects on Aqueous Environmental Cracking of Ti-8V-6Cr-4Zr-4Mo-3Al (Beta C)," in Proc. of the Tri-Service Conference on Corrosion, Materials Laboratory, Wright Patterson Air Force Base, OH, in review, (1994).

---

## **Yield Strength and Solution Composition Effects on Aqueous Environmental Cracking of Ti-8V-6Cr-4Zr-4Mo-3Al (Beta C)**

Brian P. Somerday, Jennifer A. Grandle,  
and Richard P. Gangloff

Department of Materials Science and Engineering  
University of Virginia  
Charlottesville, VA 22903-2442

### **ABSTRACT**

A high-strength,  $\alpha$ -precipitation hardened  $\beta$  titanium alloy (Ti-8V-6Cr-4Zr-4Mo-3Al, STA Beta C) is prone to intergranular environmentally assisted cracking (EAC) in neutral aqueous NaCl given an occluded crack, active crack tip strain rate and electrode potential near free corrosion. The threshold stress intensity for EAC is reduced to about one-third of the plane strain fracture toughness and subcritical crack growth rates are 30 to 100  $\mu\text{m}/\text{sec}$ . STA Beta C is immune to EAC with static loading or sufficiently cathodic polarization. Lower strength solution treated Beta C resists EAC in both pure NaCl and acidic sulfur-species-bearing chloride solutions, where fracture is by transgranular microvoid formation. These results are consistent with findings for STA Beta 21S and are qualitatively understood based on hydrogen environment embrittlement. EAC propagation in STA Beta C exhibits slow-rapid oscillation under rising crack mouth opening displacement but not during constant rate loading. This result implies that stress intensity factor and crack tip strain rate interactively govern  $da/dt$ .

### **INTRODUCTION**

High-performance applications of  $\beta$  titanium alloys in aggressive stress-chemical environments (e.g., geothermal brine and deep sour gas well tubulars, offshore production elements, marine fasteners, biomedical devices, and aerospace components<sup>(1)</sup>) require definition of the windows of variables that promote the aqueous environment-assisted cracking (EAC)

susceptibility of these alloys. While such investigations are extensive for  $\alpha$  and  $\alpha/\beta$  titanium alloys,<sup>[2-5]</sup> insufficient data exist to predict EAC for body-centered cubic  $\beta$ -based alloys. For titanium alloys, the challenge is complicated because EAC susceptibility is a function of test method; particularly, smooth versus cracked specimens.<sup>[3]</sup>

The objective of this research is to characterize the ambient temperature, aqueous chloride EAC behavior of a modern  $\beta$  titanium alloy, Ti-3Al-8V-6Cr-4Zr-4Mo (Beta C), as a function of microstructure and/or yield strength, electrode potential, and solution composition for a single active loading rate. Precracked specimens and a fracture mechanics approach are employed. EAC susceptibility is characterized by the threshold for the onset of crack growth ( $K_{TH}$ ), subcritical crack growth rate ( $da/dt$ ), and the fracture mode in the aqueous environment versus the behavior in air. In addition to determining windows of variables for EAC susceptibility, these data are necessary input for damage-tolerant life prediction and fundamental studies of the crack tip damage mechanisms that govern EAC.

## LITERATURE BACKGROUND

EAC of titanium alloys in aqueous halogen-bearing electrolytes is affected by several critical variables; including loading rate (crack tip strain rate), electrode potential, alloy composition, microstructure, and yield strength.

Titanium alloys, including  $\alpha/\beta$  Ti-6Al-6V-2Sn, exhibit a minimum in  $K_{TH}$  for intermediate loading rates.<sup>[6]</sup> Similar results were reported for the solution treated (ST)  $\beta$  alloy Ti-13V-11Cr-3Al (VCA 120),<sup>[3]</sup> solution treated + aged (STA)  $\beta/\alpha$  Ti-11.5Mo-6Zr-4.5Sn (Beta III),<sup>[7]</sup> and modern STA  $\beta/\alpha$  Ti-15Mo-3Nb-3Al (Beta 21S).<sup>[8]</sup> STA  $\beta/\alpha$  Beta 21S and a specific age-condition of  $\beta/\alpha$  Beta III were immune to EAC under static load but susceptible under constant displacement rate deformation.<sup>[7,8]</sup> This complex loading rate dependence of EAC is unique to titanium alloys; however, some titanium alloys, including an alternate age-condition of  $\beta/\alpha$  Beta III, are susceptible to EAC under static load.<sup>[7,9]</sup>

The threshold for EAC of titanium alloys in halogenated electrolytes is generally a minimum at electrode potentials near  $-500 \text{ mV}_{SCE}$ . This behavior was reported for  $\alpha/\beta$  Ti-8Al-1Mo-1V and for the  $\beta$  or  $\beta/\alpha$  alloys Ti-8Mn, Beta III (STA), VCA 120 (ST), and Beta 21S (STA).<sup>[2-5,8]</sup> Immunity to EAC was achieved at cathodic potentials greater than  $-1000 \text{ mV}_{SCE}$ .

The chloride EAC susceptibility of titanium alloys depends on alloy composition, microstructure, and/or yield strength ( $\sigma_{YS}$ ). ST  $\beta$  VCA 120 exhibits EAC under static loading,<sup>[10]</sup> while the ST  $\beta$  alloys Beta III and Ti-

8Mo-8V-3Al-2Fe are immune. These latter two alloys become EAC-susceptible upon aging to precipitate the  $\alpha$  phase.<sup>[3]</sup> STA  $\beta/\alpha$  Beta III is susceptible to EAC under static loading for the aging condition 480°C/100 hr ( $\sigma_{ys} = 1000$  MPa), but not for 620°C/16 hr ( $\sigma_{ys} = 800$  MPa).<sup>[7]</sup> EAC was produced in STA  $\beta/\alpha$  Beta 21S under rising displacement but not in STA  $\beta/\alpha$  Ti-15V-3Cr-3Al-3Sn (Ti-15-3) for similar  $\sigma_{ys}$  (1300 MPa).<sup>[8]</sup> The dependence of the EAC threshold on  $\sigma_{ys}$  for  $\beta$  and  $\beta/\alpha$  titanium alloys is not clear; however, limited data suggest a trend similar to that for high-strength steels.<sup>[3,5,11,12]</sup>

Sulfide additions to chloride solutions exacerbate EAC of ferritic and martensitic steels, particularly for lower strength levels.<sup>[11]</sup> Sulfide-EAC of  $\beta$  and  $\beta/\alpha$  titanium alloys has not been investigated broadly.<sup>[13]</sup>

Considering Beta C, several studies show that this alloy is immune to chloride EAC, for the ST and STA conditions.<sup>[13-18]</sup> While smooth, notched and precracked specimens were employed, it is possible that these experiments did not sufficiently probe the intersections of the variables that cause EAC in titanium alloys.

## EXPERIMENTAL PROCEDURES

### Material

Beta C, of composition Ti-3.4Al-8.3V-5.9Cr-4.4Zr-4.1Mo (wt.%; with trace amounts of Nb, Fe, C, N and O as reported by the manufacturer, RMI Titanium Company) was studied. This material was provided as hot-rolled 4.1-cm diameter round bar that was solution treated above the  $\beta$  transus at 815°C for 1 hour followed by air cooling. EAC specimens were tested in the ST and STA conditions. The aging treatment consisted of heating ST blanks at 500°C for 24 hours followed by air cooling. This treatment precipitated  $\alpha$  as 1 to 5  $\mu\text{m}$  long platelets within 120  $\mu\text{m}$  grains and infrequently in a colony structure at  $\beta$  grain boundaries. Transmission electron microscopy was not conducted; particularly, the occurrence of a submicron  $\alpha$  film on  $\beta$  grain boundaries was not determined. Rockwell C hardnesses were  $R_c$  28 and  $R_c$  41 for the ST and STA conditions, respectively, which correspond to yield strengths of 830 and 1280 MPa from a hardness- $\sigma_{ys}$  correlation given for two  $\beta$  titanium alloys.<sup>[8]</sup>

### Environment

Experiments were conducted at 25°C in either moist air or neutral (pH 6) 0.6M (3.5 wt.%) aqueous NaCl at free corrosion or fixed electrode potentials of -150, -600, and -1000 mV<sub>SCE</sub>. Experiments were also conducted in the acidified sulfur-species-bearing solutions indicated in Table I. A plexiglass cell was secured to the specimen in order to flow solution



at 25 ml/min from a two-liter reservoir through the machined notch tip and fatigue precrack. A schematic of the cell is shown in Fig. 1. Dissimilar metals did not contact the specimen and all tubing was PTFE. The grounded specimen (working electrode) was maintained at a constant potential by a Wenking potentiostat in conjunction with a chloridized silver wire reference electrode and a platinized niobium counter electrode. The reference electrode for polarization was located on one side of the specimen, near the notch (Fig. 1). A second reference electrode indicated that the potential of the opposite face was 0 to 200 mV more noble than the polarized side, depending on the magnitude of the current.

**Table 1.** Sulfur-Species Additions to the Aqueous NaCl Environment

| Solution               | Salt       | Acid / pH                          | Sulfur Compound   | Sulfur Species  |
|------------------------|------------|------------------------------------|---|---|
| Sulfide + acetic       | 0.6 M NaCl | 1.5M acetic, 0.1M acetate / pH 3.3 | 10 ppm S as Na <sub>2</sub> S                             | CH <sub>3</sub> COSH (?)  |
| Sulfide + hydrochloric | 0.6 M NaCl | 0.1 M HCl pH 1.3                   | 4 ppm S as Na <sub>2</sub> S                              | H <sub>2</sub> S  |
| Thiosulfate + acetic   | 0.9 M NaCl | 0.15 M acetic pH 2.6               | 60 ppm S as Na <sub>2</sub> S <sub>2</sub> O <sub>3</sub> | S <sub>2</sub> O <sub>3</sub> <sup>2-</sup> - S → H <sub>2</sub> S(?) |

### EAC-Fracture Mechanics

Sidegrooved compact tension (CT) specimens were machined with the longitudinal axis of the round bar perpendicular to the crack plane and crack growth in the radial direction. CT specimen gross thickness was 6.3 mm, net thickness was 5.1 mm, and width was 30.5 mm. Specimens were fatigue precracked in room temperature moist air, terminating with a  $K_{MAX}$  of 25 MPa $\sqrt{m}$ ,  $R$  of 0.4 ( $R = K_{MIN}/K_{MAX}$ ), and a crack length-to-width ratio ( $a/W$ ) of approximately 0.52.

Precracked specimens were loaded under monotonically rising crack mouth opening displacement (CMOD) at a constant rate ( $\dot{\delta}_m$ ) of 1.8  $\mu\text{m}/\text{min}$  using a servohydraulic mechanical test system. CT specimens were instrumented to measure applied load, CMOD and crack extension. CMOD was measured and controlled using a clip gauge mounted across the mouth of the machined notch, as shown in Fig. 1. The direct current potential difference (DCPD) method was used to resolve crack tip process zone damage initiation and subsequent crack growth. The expression used to calculate  $a/W$  from measured voltage, and other details of the technique,



are given in References 8, 19 and 22. Applied load, DCPD, CMOD and time were recorded using a PC-based data acquisition system.

The fracture mechanics were characterized using the elastic-plastic J-integral, as detailed elsewhere.<sup>[19]</sup> For STA specimens  $J_{\text{plastic}}$  was small compared to the applied total J; thus small-scale yielding was maintained and elastic K analysis was sufficient. All experiments satisfied the criterion for plane strain defined in an ASTM Standard.<sup>[20]</sup>

The plot of load and DCPD versus CMOD in Fig. 2 is typical of the experiments with high-strength STA specimens in NaCl. Two measures of the threshold K for the initiation of crack growth were determined. A lower-bound value is defined by the first deviation from the initial baseline DCPD versus CMOD trend when coincident with the onset of nonlinearity in the load versus CMOD plot.<sup>[8,19]</sup> For loading in moist air, this value ( $K_{\text{IC}}$ ) is a lower bound of the standardized plane strain fracture initiation toughness ( $K_{\text{IC}}$ ),<sup>[19]</sup> and in aggressive environments this value ( $K_{\text{THI}}$ ) represents a lower bound of the threshold ( $K_{\text{TH}}$ ) for subcritical crack growth initiation.<sup>[21]</sup>  $K_{\text{TH}}$  is

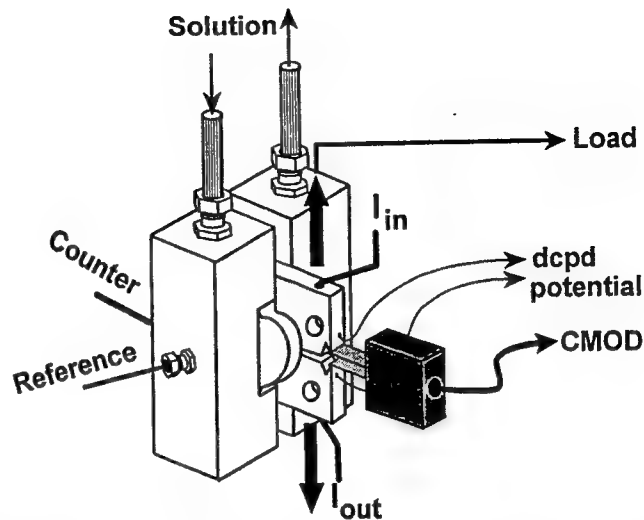


**Figure 1.** Cell and CT specimen for rising CMOD EAC experiments. ("dcpd" indicates the measurement probes for electrical potential difference due to a direct current,  $I$ , through the uncracked portion of the specimen.)

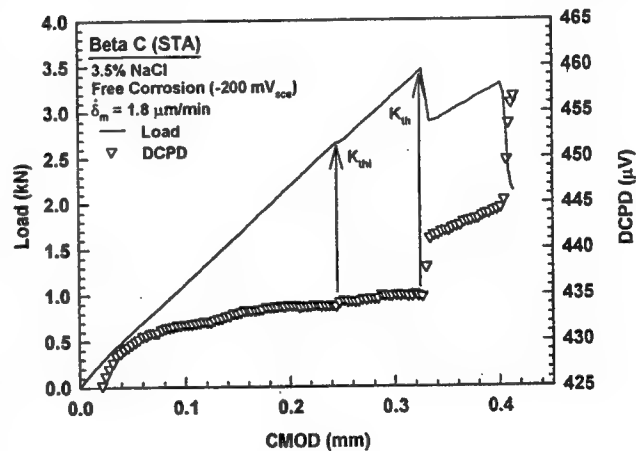


**Figure 2.** Load and DCPD versus CMOD data for STA Beta C in 3.5% NaCl. (Note the definition of threshold stress intensity ( $K_{\text{TH}}$ ) and initiation threshold stress intensity ( $K_{\text{THI}}$ ).)

defined at the first major load drop. At  $K_{TH}$ , the crack growth increment ( $\Delta a$ ) is assumed to equal zero; subsequent crack lengths are calculated using DCPD values normalized with the potential at the known fatigue precrack length.<sup>[19,22]</sup> Average subcritical crack growth rate ( $da/dt$ ) was calculated using linear regression over a small time interval.

A single critical J for the initiation of crack growth was calculated for each ST experiment since DCPD versus CMOD data did not indicate crack initiation. The initiation point was determined from DCPD measurements with the measured final crack length as a reference, then selecting the P-CMOD data point corresponding to the measured fatigue precrack length.

## RESULTS

### ST Beta C in Air and Chloride

Static Crack / Threshold Behavior Results for ST Beta C tested in moist air and four different aqueous environments, each at the free corrosion potential, are shown in Fig. 3. These experiments establish that Beta C in the moderate strength, single phase condition is not embrittled by severe mechanical and environmental conditions. The CMOD rate used for these experiments produced maximum EAC susceptibility (minimum  $K_{TH}$ ) for STA  $\beta/\alpha$  Beta 21S in aqueous NaCl near free corrosion.<sup>[8]</sup> The moist air fracture toughness ( $K_{IC}$ ) of ST Beta C is 115 MPa $\sqrt{m}$ , which compares favorably with a reported value of 96 MPa $\sqrt{m}$ .<sup>[23]</sup> The higher value may reflect the use of elastic-plastic fracture mechanics for small specimens of a moderate strength-high toughness alloy, compared to the less rigorous elastic analysis employed in Ref. 23.  $K_{TH}$  (114 MPa $\sqrt{m}$ ) in neutral NaCl ( $E_{corr} = -200$  to  $-150$  mV<sub>SCE</sub>) was not reduced compared to  $K_{IC}$ .

The addition of sulfur species to NaCl solutions, particularly those that form hydrogen sulfide ( $H_2S$ ), exacerbates EAC in steel.<sup>[24-27]</sup> In contrast Fig. 3 shows that  $K_{TH}$  (113 to 120 MPa $\sqrt{m}$ ) for ST Beta C in three different sulfur-species-containing aqueous media ( $E_{corr} \sim -250$  mV<sub>SCE</sub>) is not reduced compared to either  $K_{IC}$

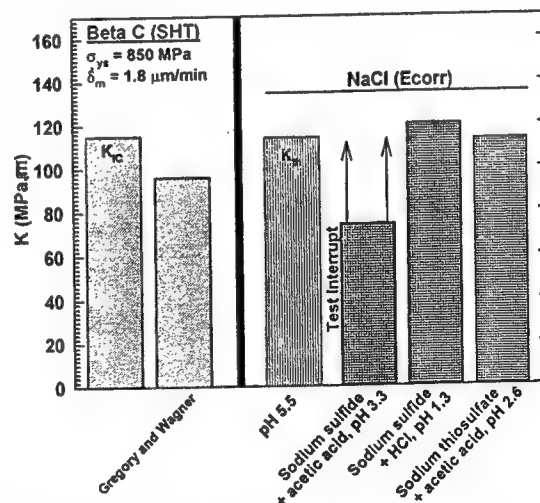
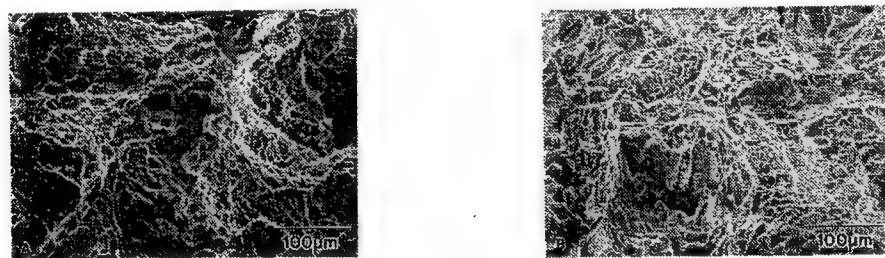


Figure 3.  $K_{IC}$  and  $K_{TH}$  data for ST Beta C.  $K_{IC}$  is for moist air, compared to the value from Ref. 23, while  $K_{TH}$  data are for the NaCl/sulfur-species solutions listed in Table I.

or  $K_{TH}$  for pure NaCl. In the  $Na_2S$ /acetic acid solution,  $Na_2S$  reacts to form thioacetic acid;<sup>[24]</sup>  $H_2S$  gas was not detected by smell. (Crack growth was not detected at the point where this experiment was terminated due to cell leakage.  $K_{TH}$  therefore exceeded the  $K$  value calculated at the test-interrupt load.)  $H_2S$  formed in the  $Na_2S$ /HCl acid solution.<sup>[25]</sup> The sodium thiosulfate/acetic acid solution forms elemental sulfur and  $H_2S$  in the presence of steel.<sup>[26]</sup>

Figure 4 shows typical scanning electron microscope (SEM) fractographs of the  $K_{IC}$  or  $K_{TH}$  regions of CT specimens of ST Beta C, fractured in moist air or acidified NaCl/ $Na_2S$ . The fracture mode is identical for moist air and all aqueous environments in Table I, and consists predominately of fine (of order 2  $\mu m$ ) transgranular microvoids.



**Figure 4.** SEM fractographs for ST Beta C in (a) moist air and (b) acidic NaCl/ $Na_2S$ . The crack grew from top to bottom, and the fractographs are located in the central crack initiation region.

Equal  $K_{IC}$  and  $K_{TH}$ , as well as identical fracture modes in moist air and the solutions, indicates that ST Beta C is immune to EAC, at least for the loading rate and electrode potential conditions that were examined.

#### **STA Beta C in Air and Chloride**

Static Crack/Threshold Behavior Results for high-strength STA Beta C, tested in moist air and neutral aqueous NaCl at  $-600 \text{ mV}_{SCE}$  and fixed  $\delta_M$ , are shown in Fig. 5. Filled circles represent the results of individual experiments, while averages are given by the bars.  $K_{IC}$  is 50% lower (56  $\text{MPa}\sqrt{m}$ ) than for the ST condition, consistent with the substantially higher strength from aging.  $K_{TH}$  for chloride (35  $\text{MPa}\sqrt{m}$ ) is reduced by about one-third compared to  $K_{IC}$ . Data for STA Beta 21S and STA Ti-15-3,<sup>[8]</sup> obtained with single-edge-cracked specimens fractured in air and neutral aqueous NaCl at  $-600 \text{ mV}_{SCE}$  by the same procedure as Beta C, are included in Fig. 5. The plane strain fracture toughness of STA Beta C is lower than that of the other two high-strength alloys. Similar to the behavior of Beta C,  $K_{TH}$  for

Beta 21S is reduced compared to  $K_{IC}$ . In contrast  $K_{TH}$  equals  $K_{IC}$  for Ti-15-3.

Figure 6 shows SEM fractographs from CT specimens of STA Beta C tested in moist air and aqueous NaCl. Fracture in air occurs predominately *via* transgranular microvoid coalescence. Both small (of order 2 to 5  $\mu\text{m}$ ) equiaxed and larger elongated microvoids are observed. Some facets are also present and may consist of fine (of order 1  $\mu\text{m}$ ) microvoids.

Fracture occurs by intergranular separation in the chloride environment. No transition region is evident between the fatigue crack front and EAC intergranular facets. Fine void-like features are present on grain facets. The moist air fracture modes for STA Beta 21S and STA Ti-15-3<sup>[8,28]</sup> resemble that for Beta C in air. The air fracture mode was not altered for Ti-15-3 tested in aqueous NaCl, whereas Beta 21S failed by intergranular separation.<sup>[8]</sup>

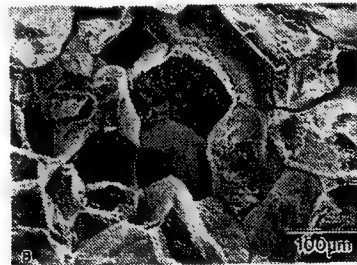
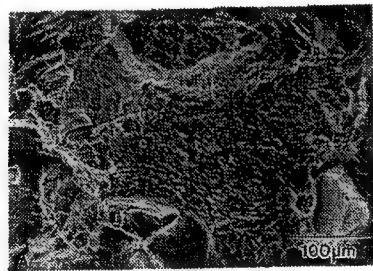


**Figure 6.** SEM fractographs for STA Beta C in (a) moist air and (b) 3.5% NaCl. The crack grew from top to bottom.

$K_{TH}$  less than  $K_{IC}$ , as well as the change in fracture mode from transgranular microvoid rupture to grain boundary separation, indicates that STA Beta C is susceptible to EAC in neutral aqueous NaCl at electrode potentials near  $-600 \text{ mV}_{SCE}$  and under rising CMOD.

Figure 7 shows the effect of maintaining a CT specimen of Beta C at constant CMOD in aqueous NaCl after interrupting the rising CMOD at a

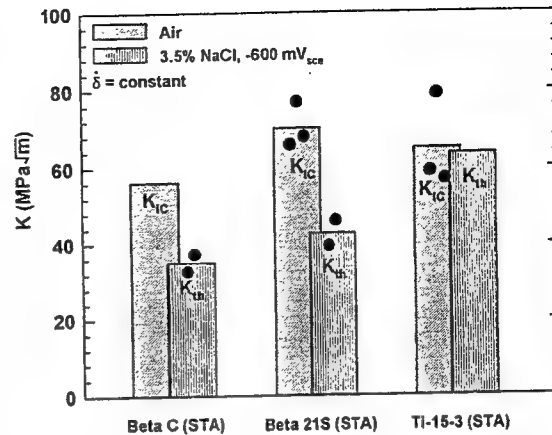


**Figure 5.** Rising CMOD  $K_{IC}$  and  $K_{TH}$  data for Beta C, Beta 21S<sup>[8]</sup>, and Ti-15-3<sup>[8]</sup> (all STA) in air and aqueous NaCl. The bars are average values and filled circles represent individual results.

K level (47 MPa√m) greater than  $K_{TH}$ . (For this experiment, the rising CMOD was interrupted during decreasing load and rapid subcritical crack propagation.) Crack propagation continued for less than one minute after CMOD was fixed. At this point, DCPD data indicate no crack growth, or at most a limiting  $da/dt$  of 0.001  $\mu\text{m/s}$  over 90 hours. Crack growth-induced compliance changes were not detected ( $dP/dt$  was essentially zero over this time period), suggesting that  $da/dt$  was zero.

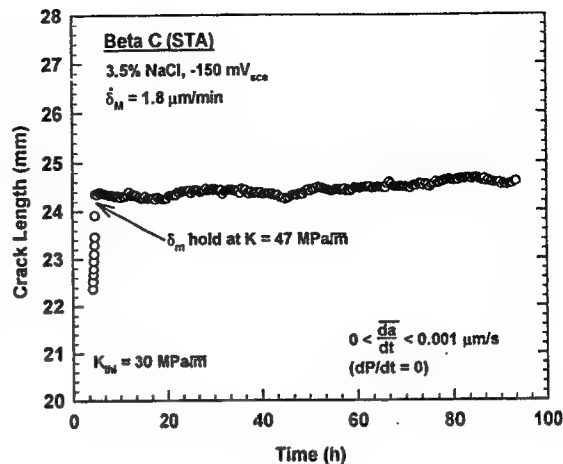


Figure 7. Crack length versus time for an experiment with STA Beta C in NaCl which was interrupted and maintained at constant CMOD ( $\delta_m$ ) for a K level above  $K_{TH}$ .

**Potentiostatic Polarization** The severity of EAC for STA Beta C in pure NaCl depends on applied electrode potential, as shown in Fig. 8. Both  $K_{TH}$  and  $K_{TH}$  are compared to  $K_{TH}$  data for Beta 21S.<sup>[8,28]</sup> EAC is observed ( $K_{TH}$  and  $K_{TH}$  are less than  $K_{IC}$ , coupled with intergranular cracking) for applied potentials between -150 and -600 mV<sub>SCE</sub>, and threshold is a minimum for a potential of -600 mV<sub>SCE</sub>. At a potential of -1000 mV<sub>SCE</sub>, STA Beta C is immune to EAC ( $K_{TH}$  equals  $K_{IC}$  and fracture is by microvoid rupture for chloride and moist air). The effect of potential is similar for STA Beta 21S.

**Subcritical Crack Propagation** Two distinct subcritical crack propagation rate responses were observed for STA Beta C in NaCl. Figure 9 shows results for an experiment at -150 mV<sub>SCE</sub>. Subcritical crack propagation was slow (on the order of 0.1  $\mu\text{m/s}$ ) for rising K levels just above  $K_{TH}$  (30 MPa√m). At K equal to  $K_{TH}$  (41 MPa√m), the  $da/dt$  accelerated by two orders of magnitude under decreasing K from 41 to 35 MPa√m (applied K values are indicated at several points in Fig. 9). After a crack growth increment of 2 mm,  $da/dt$  decreased abruptly to near the initial rate. This slow-fast sequence was repeated several times as the

chloride crack propagated subcritically in several EAC experiments.<sup>1</sup>

In contrast to the behavior in Fig. 9, alternating slow-fast  $da/dt$  was not observed for EAC experiments with STA Beta C/NaCl under rising load control. Figure 10 shows that rapid crack propagation is not arrested and continues until specimen fracture. The fast crack growth rates indicated in Figs. 9 and 10 are consistent with limited values reported for other  $\beta$ -titanium alloys.<sup>[3,5,7,28]</sup> It is difficult to quantify the slower EAC rates in Fig. 10, at  $K$  just above  $K_{TH}$ . This behavior appears akin to the so-called Stage IIA behavior reported for  $\alpha/\beta$  titanium alloys in aqueous chloride.<sup>[29]</sup>

## DISCUSSION

### Comparison to Literature Results for EAC of Beta C

Literature results indicate that Beta C is immune to aqueous chloride EAC.<sup>[13-18]</sup> Aylor studied ST Beta C ( $\sigma_{YS} = 850$  MPa) with blunt-notched tensile specimens under rising displacement in aqueous NaCl at free corrosion and applied electrode potentials between

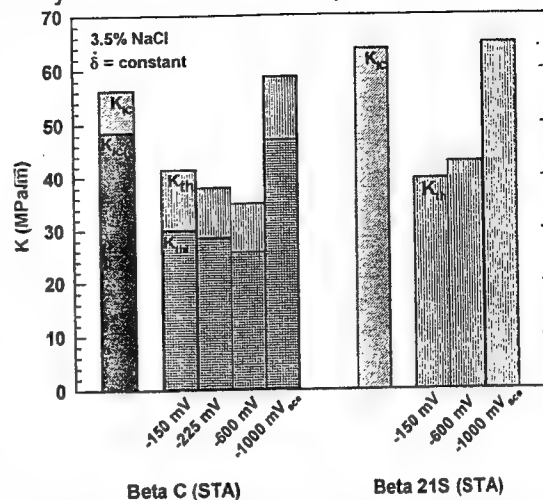


Figure 8.  $K_{TH}$  and  $K_{TII}$  as a function of applied electrode potential for STA Beta C and STA Beta 21S<sup>[8]</sup> in aqueous chloride solution. Moist air  $K_{IC}$  is also shown.

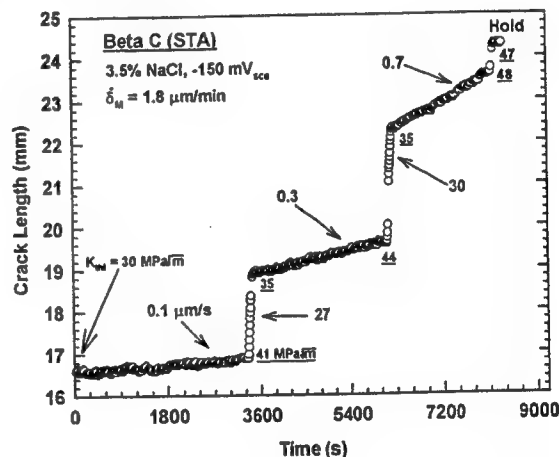


Figure 9. Crack length versus time for STA Beta C in 3.5% NaCl at  $-150$  mV<sub>SCE</sub> and constant  $\delta_M$ . Average crack growth rates at various  $K$  levels (underlined) are shown.

<sup>1</sup>The point marked "Hold" in Fig. 9 shows the onset of the fixed CMOD experiment shown in Fig. 7, which did not produce EAC propagation in Beta C/NaCl. Here, CMOD was fixed during a rapid  $da/dt$  event under decreasing  $K$ . A similar result (viz., no subcritical EAC propagation for 50 hours at constant CMOD and applied  $K$  greater than  $K_{TH}$ ) was observed for an experiment interrupted during slow  $da/dt$  and rising  $K$ .

-850 and -1250 mV<sub>SCE</sub>.<sup>[14]</sup> These conditions did not produce EAC in Beta C. This procedure indicated that  $\alpha/\beta$  Ti-6Al-4V (Ti-6-4) at this same yield strength is chloride-cracking resistant,<sup>[14]</sup> but such is not the case.<sup>[9,30]</sup> Azkarate and Pelayo tested smooth tensile specimens of STA Beta C ( $\sigma_{YS} = 1250$  MPa) under rising displacement in neutral NaCl at free corrosion, -1000 and -1500 mV<sub>SCE</sub>.<sup>[16]</sup> STA Beta C was immune to EAC for the conditions examined, but Ti-6-4 ( $\sigma_{YS} = 1000$  MPa) exhibited EAC at -1500 mV<sub>SCE</sub>. Wolfe *et al.* reported that smooth tensile specimens of STA Beta C ( $\sigma_{YS} = 1100$  MPa) were immune to EAC in seawater with cathodic protection.<sup>[15]</sup> Comparison of these results to the data in Figs. 5 and 6 attests to the importance of an occluded crack to promote EAC.

Limited studies with statically loaded precracked specimens showed that STA Beta C is immune to EAC. Thomas and Seagle did not produce brittle cracking in precracked C-rings in NaCl at several electrode potentials.<sup>[13]</sup> (EAC was produced by this method when H<sub>2</sub>S was added to the environment and specimens were polarized cathodically.) Early studies with statically loaded precracked cantilever beam specimens of Beta C in aqueous chloride demonstrated similar immunity to EAC, however, low plane strain fracture toughness clouded the results.<sup>[17,18]</sup> Comparison of these findings to the data in Figs. 5, 6 and 7 attests to the importance of active loading to promote EAC of Beta C.

The experimental results for intergranular EAC of STA Beta C, showing the deleterious effects of the fatigue crack plus active loading and electrode potentials near free corrosion levels, are identical to data obtained for STA Beta 21S.<sup>[8,28]</sup>

### Comparison of EAC in $\beta$ Titanium Alloys and Ferritic Steels

Figure 11 summarizes  $K_{TH}$  and  $K_{IC}$  versus  $\sigma_{YS}$  results for Beta C in chloride solutions, compared to data for STA Beta 21S and STA Ti-15-3,<sup>[8]</sup> and superimposed with EAC  $K_{TH}$  for ferritic and martensitic steels in a variety

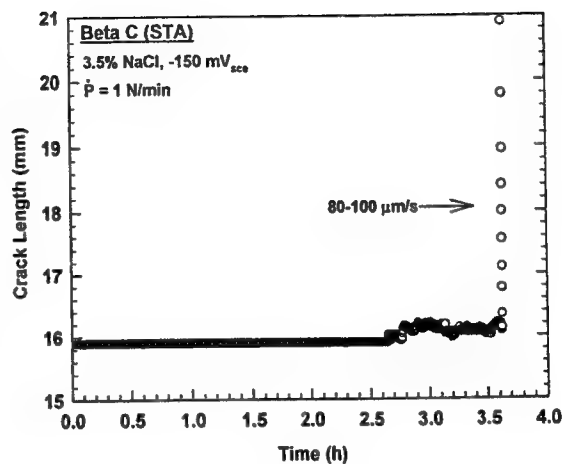


Figure 10. Crack length versus time for a constant loading rate of 1 N/min. (STA Beta C in 3.5% NaCl at -150 mV<sub>SCE</sub>,  $K_{TH} = 44$  MPa $\sqrt{m}$ ,  $da/dt = 80$  to  $100$   $\mu\text{m/s}$ .)

of hydrogen-producing gases and electrolytes.<sup>[11]2</sup> The large shaded band shows the range of  $K_{TH}$  results, with upper (UB) and lower (LB) bounds on extensive threshold data for many steels in neutral chloride at free corrosion. (The open diamond shows a single  $K_{TH}$  result for moderate strength HY130 steel in NaCl, obtained with a single-edge-crack specimen and the fracture mechanics method used in the current study.)

For steels, it is well established that  $K_{TH}$  for hydrogen environment embrittlement decreases with increasing  $\sigma_{YS}$ .<sup>[11,31]</sup> For the  $\beta$ -titanium alloys, plane strain fracture toughness decreases with increasing  $\sigma_{YS}$  (small filled circles), with a single trend observed for Beta C and Ti-15-3 and a higher strength-toughness trend seen for Beta 21S.  $K_{TH}$  values for STA Ti-15-3 (large open circles) and ST Beta C (large filled circles at  $\sigma_{YS}$  of 850 MPa) in NaCl essentially equal the  $K_{IC}$ - $\sigma_{YS}$  trend line, indicating immunity to EAC. The results for ST Beta C (large filled circles) and STA Beta C (open squares) suggest a strength effect on  $K_{TH}$  that is similar to the trend for steels in neutral chloride. Alloy microstructure may play a critical role in determining the EAC resistance of  $\beta$ -titanium alloys. The relative contributions of microstructure and yield strength in governing the EAC resistance of ST Beta C and the susceptibility of STA Beta C are not defined.

### Intergranular EAC and Microstructure of $\beta$ -Titanium Alloys

An analysis of STA Beta 21S and Ti-15-3 correlated intergranular chloride EAC with microstructure, particularly  $\alpha$  colonies precipitated at  $\beta$  grain boundaries and/or intense slip localization.<sup>[8,28,32]</sup>

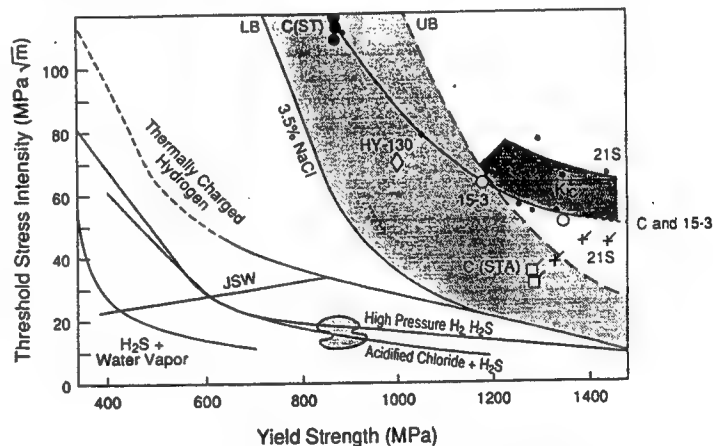


Figure 11.  $K_{TH}$  versus  $\sigma_{YS}$  for steels<sup>[11]</sup> and selected  $\beta$ -Ti alloys in chloride and other hydrogen-producing environments including sulfur-species additions.

<sup>2</sup>Hydrogen-producing environments are capable of generating atomic hydrogen on strain-cleaned crack tip surfaces by cathodic proton or water reduction for aqueous electrolytes, by dissociative chemical adsorption for  $H_2$ , or by chemical reaction for  $H_2S$  or  $H_2O$  gases. This hydrogen is available to embrittle metal within the crack tip process zone.<sup>[31]</sup>



EAC-prone Beta 21S exhibited both microstructural features, but EAC-resistant Ti-15-3 did not. Both microstructural features, as well as EAC and internal hydrogen embrittlement, appear to be promoted by prolonged solution treatment (in excess of 1 hour) at high temperature (above 950°C).

Beta C, solution treated in the EAC-resistant regime of relatively shorter time and lower temperature, exhibited an  $\alpha$ -precipitate distribution and slip morphology between that of Beta 21S and Ti-15-3. While STA microstructures are complex, heat treatment experiments indicated that grain boundary  $\alpha$ -colonies are less frequent in STA Beta C,<sup>[33]</sup> compared to both the microstructure of STA Beta 21S<sup>[8]</sup> and the amount of intergranular EAC shown in Fig. 6. These preliminary microstructural results, and the low solution treatment time and temperature, are inconsistent with a correlation between large  $\alpha$ -colonies at  $\beta$  grain boundaries and intergranular EAC in Beta C. Work is in progress to better address this issue.

Considering slip morphology, compression experiments showed that plastic deformation in ST Beta C is qualitatively homogeneous, with some grains deforming by locally intense slip bands.<sup>[33]</sup> Upon aging to the STA condition, slip band spacing decreases, and bands appear more planar and likely to cross entire grains. Similar locally planar deformation modes are observed for STA Beta C and Beta 21S, compared to homogeneous deformation in STA Ti-15-3.<sup>[8,32-35]</sup> This comparison suggests that slip localization plays a role in the intergranular chloride EAC of ST and STA  $\beta$  titanium alloys, however, additional research is required.

The present results for Beta C show that high solution treatment temperature and/or prolonged time are not the sole requisite for intergranular EAC in  $\beta$  titanium alloys. Interactions between yield strength and microstructure, or additional microstructural effects such as grain boundary impurity segregation,<sup>[36]</sup> must be considered.

### Sulfur-Species Additions

Figure 11 shows that acidified chloride/H<sub>2</sub>S solution at 25°C severely decreases the threshold for EAC of ferritic steels from that of aqueous chloride alone. Also shown in Fig. 11 are the data for ST Beta C in neutral NaCl and the acidified chloride/sulfur compound solutions summarized in Table I (large filled circle symbols plotted from Fig. 3). Notably for Beta C,  $K_{TH}$  did not decrease for any of the sulfur-bearing solutions, even acidified (pH 1.3) NaCl with Na<sub>2</sub>S which formed H<sub>2</sub>S. This sulfide-EAC resistance of ST Beta C is striking. For steels at a similar yield strength, acidified chloride and H<sub>2</sub>S decrease  $K_{TH}$  to values as low as 15 MPa $\sqrt{m}$ .  $K_{TH}$  for ST Beta C in the various sulfur-species-bearing electrolytes is about 5-fold higher than this lower limit and equals  $K_{IC}$ .

The sulfide EAC resistance of ST Beta C may be reduced by long term exposure that allows bulk specimen hydrogen uptake from boldly exposed surfaces. The short term-rising displacement experiments employed to obtain the data in Fig. 3 involved 24 hour exposures to the solution and were designed to emphasize crack dissolution and hydrogen production. Given a typical hydrogen diffusivity ( $D_H$ ) in single phase  $\beta$  titanium alloys of  $4 \times 10^{-7} \text{ cm}^2/\text{sec}$  or faster,<sup>[32]</sup> about 12 hours are required for substantial hydrogen penetration from the root of the side-groove to the center line of the CT specimen, parallel to the crack front. If  $D_H$  is slower for ST Beta C or if reactions involving sulfide are relatively slow-building then longer exposure times could result in lower  $K_{TH}$  based on a hydrogen embrittlement scenario.<sup>[11,13,28]</sup> This issue must be investigated for cases where ST  $\beta$ -titanium alloys encounter sulfide in an electrolyte, for example, as produced by sulfate-reducing bacteria in marine environments.<sup>[37]</sup>

#### **Potentiostatic Polarization and $K_{TH}$ for EAC**

The threshold for chloride EAC in STA Beta C depends on applied electrode potential. This alloy was immune to EAC under cathodic polarization to  $-1000 \text{ mV}_{SCE}$ , showed a minimum resistance ( $K_{TH}$ ) at  $-600 \text{ mV}_{SCE}$ , and was somewhat less cracking-prone with increasing potential at  $-150 \text{ mV}_{SCE}$  (Fig. 8). The beneficial effect of cathodic polarization was reported by others for  $\alpha/\beta$  and  $\beta/\alpha$  titanium alloys in halogenated electrolytes.<sup>[2-5,38]</sup> In particular Young *et. al.*<sup>[8]</sup> reported that the neutral chloride  $K_{TH}$  for STA Beta 21S increased to equal  $K_{IC}$  when the specimen was polarized cathodically to  $-1000 \text{ mV}_{SCE}$ , Fig. 8. Similar low  $K_{TH}$  values were observed at  $-600$  and  $-150 \text{ mV}_{SCE}$ , without evidence of a minimum EAC resistance. A speculative hydrogen environment embrittlement mechanism, focusing on atomic hydrogen production and uptake at the occluded and strain-bared crack tip, was proposed to explain the electrode potential dependence shown in Fig. 8.<sup>[8]</sup>

The chloride EAC resistance of STA Beta C, under cathodic polarization, may be reduced by long term exposures that allow bulk specimen hydrogen uptake from boldly exposed specimen surfaces. That is, hydrogen may be produced on such surfaces, even if crack tip production and uptake are minimized by cathodic polarization.<sup>[39]</sup>

#### **Implications of Slow-Rapid EAC Growth Rates**

Alternating slow-rapid subcritical crack propagation could be explained mechanistically; hydrogen from cathodic reaction diffuses ahead of the crack tip, embrittles the process zone, and the crack rapidly propagates until arrest by surrounding non-embrittled material.<sup>[28]</sup> For STA

Beta C in NaCl, rapid EAC propagation occurs over distances that are much larger than the crack tip process or plastic zone (Fig. 9), transitions in the fracture surface morphology are not observed by SEM, and oscillating crack growth kinetics are not evident under rising load control. Thus, the slow-rapid  $da/dt$  phenomenon is not ascribed to time-dependent hydrogen diffusion.

Meyn and Pao observed oscillating subcritical crack growth kinetics for  $\alpha/\beta$  Ti-6-4 and perhaps  $\beta/\alpha$  STA Ti-15-3 in neutral aqueous NaCl during slow constant extension rate experiments.<sup>[40]</sup> At higher extension rates, continuous Stage II EAC occurred. It was proposed that a critical crack tip strain rate was necessary to maintain conditions conducive to Stage II crack growth. Webb and Meyn recently developed a crack driving force vs resistance model of oscillating EAC  $da/dt$ , based on assumed  $da/dt$  vs strain energy release rate ( $G$ ) dependencies, and including test system compliance.<sup>[41]</sup> While they do not provide a mechanistic explanation for the form of  $da/dt$  vs  $G$  necessary to produce slow-rapid  $da/dt$  during rising displacement loading, they suggest that titanium alloy/environment systems exhibiting Stage IIA-Stage II subcritical crack growth kinetics are unique candidates for oscillations. Oscillating crack growth kinetics are expected to yield a sawtooth  $K$ - $\Delta a$  curve, where the minimum and maximum  $K$  levels are constant. Measured minimum and maximum  $K$  levels for STA Beta C/NaCl in Fig. 9 are not constant.

Classically, subcritical EAC  $da/dt$  is measured and modeled based on either  $K$ -control or crack tip strain rate ( $\dot{\epsilon}_{CT}$ )-control.<sup>[11,42]</sup> Rather, for titanium alloys in chloride, we propose that  $da/dt$  depends interactively on both  $K$  and  $\dot{\epsilon}_{CT}$ , with steep near-threshold regimes for both variables. This hypothesis is based on the notion that  $K$  governs the crack tip process zone, relevant to hydrogen embrittlement, while  $\dot{\epsilon}_{CT}$  governs the extent of crack surface electrochemical reactions, pertinent to hydrogen production, or process zone dislocation transport. The slow-rapid crack growth behavior shown in Fig. 9 is then controlled by specimen compliance-based changes in  $K$  and  $\dot{\epsilon}_{CT}$  for the experiments conducted in rising-CMOD control. Note that  $da/dt$  is not a unique function of  $K$  for STA Beta C. For example, both slow and rapid  $da/dt$  are observed at a  $K$  level of 40 MPa $\sqrt{m}$ .

Determination of the three-dimensional relationship between  $da/dt$ ,  $K$  and  $\dot{\epsilon}_{CT}$  is complicated by uncertainties in the calculation of crack tip strain rate. For a propagating crack, this quantity depends on  $K$ ,  $dK/dt$  and  $da/dt$ , however, the precise function is clouded by uncertain parameters in the continuum mechanics formulation,<sup>[43,44]</sup> and by the role of localized dislocation processes. None-the-less, a continuum estimate of the crack tip opening displacement rate ( $\delta_+$ ),<sup>[43,44]</sup> which may be proportional to  $\dot{\epsilon}_{CT}$ , shows

that  $\delta_T$  at the onset of rapid crack propagation is at least an order of magnitude less than that at the point where rapid  $da/dt$  begins to arrest. This estimate indicates that  $da/dt$  must be controlled by the interaction of  $K$  and  $\dot{\epsilon}_{CT}$ . Experiments and additional analyses are required to test the relative contributions of stress intensity and crack tip strain rate, and to determine the extent to which slow-fast  $da/dt$  behavior is unique to titanium alloys in environments that form a passive film at the crack tip.

### CONCLUSIONS

1. The high-strength  $\beta/\alpha$  titanium alloy, STA Beta C, is embrittled by loading in neutral aqueous NaCl solution at 25°C, given an occluded crack, active strain rate and electrode potentials near free corrosion. This behavior is analogous to that of STA Beta 21S.
2. STA Beta C resists crack propagation in NaCl under static load/displacement or cathodic polarization, at least for short-term experiments. This behavior is analogous to that of STA Beta 21S.
3. Moderate strength, single phase ( $\beta$ ) ST Beta C is immune to chloride EAC at the free corrosion potential and under short-term rising displacement. Sulfur-species and acid additions to NaCl that embrittle ferritic steels do not promote intergranular EAC in ST Beta C.
4. EAC in STA Beta C is intergranular; the contributions of grain boundary  $\alpha$  precipitation, locally intense planar slip and impurity segregation are not defined. Moist air fracture of the STA and ST conditions, as well as ST fracture in chloride-sulfur-species solutions, are by transgranular microvoid rupture.
5. The rising CMOD method is effective, but requires instrumentation and analysis of  $da/dt$  as a function of  $K$  and crack tip strain rate.
6. Alternating slow-rapid EAC propagation rate is speculatively attributed to coupled  $K$ - and crack tip strain rate-control, and specimen compliance-induced changes in these driving force parameters.

## ACKNOWLEDGEMENTS

This research was supported by the Office of Naval Research (Grant N00014-91-J-4164), with A. John Sedriks as Scientific Monitor and a National Science Foundation Graduate Research Fellowship (for JAG). Material was donated by RMI Titanium Company and R.W. Schutz. These contributions are gratefully acknowledged, as are informative discussions with J.R. Scully, R.G. Kelly, M.A. Gaudett, and D.G. Kolman.

## REFERENCES

1. R.W. Schutz, JOM, vol. 46, no. 7, 1994, pp. 24-29.
2. R.W. Schutz and D.E. Thomas, in Metals Handbook: Corrosion, vol. 13, 9th ed., ASM Int'l, Materials Park, OH, 1987, pp. 669-706.
3. M.J. Blackburn, J.A. Feeney, and T.R. Beck, in Advances in Corrosion Science and Technology, M.G. Fontana and R.W. Staehle, eds., vol. 3, Plenum Publishing, NY, NY, 1972, pp. 67-292.
4. R.W. Schutz, in Stress Corrosion Cracking, R.H. Jones, ed., ASM Int'l, Materials Park, OH, 1992, pp. 265-297.
5. M.J. Blackburn, W.H. Smyrl, and J.A. Feeney, in Stress Corrosion Cracking in High Strength Steel and in Titanium and Aluminum Alloys, B.F. Brown, ed., Naval Research Laboratory, Washington, DC, 1972, pp. 245-363.
6. J.A. Moskovitz and R.M. Pelloux, Corrosion, vol. 35, 1979, pp. 509-514.
7. J.A. Feeney and M.J. Blackburn, Met. Trans., vol. 1, 1970, pp. 3309-3323.
8. L.M. Young, G.A. Young, Jr., J.R. Scully, and R.P. Gangloff, Metall. Mater. Trans. A, in review, 1994.
9. B.F. Brown, Mater. Res. Std., 1966, vol. 6, pp. 129-136.
10. D.N. Fager and W.F. Spurr, Trans. ASM, vol. 61, 1968, pp. 283-292.
11. R.P. Gangloff, in Corrosion Prevention and Control, M. Levy and S. Isserow, eds., US Army Laboratory Command, Watertown, MA, 1986, pp. 64-111.
12. Atlas of Stress-Corrosion and Corrosion Fatigue Curves, A.J. McEvily, Jr., ed., ASM Int'l, Materials Park, OH, 1990, pp. 457, 484.
13. D.E. Thomas and S.R. Seagle in Titanium Science and Technology, G. Lutjering, U. Zwicker and W. Bunk, eds., 1984, pp. 2533-2540.
14. D.M. Aylor, "An Environmental Cracking Evaluation of Fastener Materials for Seawater Applications" (paper No. 484 presented at NACE Corrosion '94, Houston, TX, 1994).
15. L.H. Wolfe, *et al.*, Materials Performance, vol. 32, no.7, 1993, pp. 14-21.
16. I. Azkarate and A. Pelayo, "Hydrogen Assisted Stress Cracking of Titanium Alloys in Aqueous Chloride Environments" (paper presented at INASMET, San Sebastian, Spain, 1992).
17. W.F. Czyrklis and M. Levy, Corrosion, vol. 32, 1976, pp. 99-102.
18. J.W. Hagemeyer and D.E. Gordon, in Titanium Science and Technology, Plenum Press, New York, NY, 1973, pp. 1957-1968.
19. B.P. Somerday, Y. Leng, and R.P. Gangloff, Fatigue and Fracture of Engineering Materials and Structures, in review, 1994.

20. Annual Book of ASTM Standards, Designation E1152-87, vol. 3.01, ASTM, Philadelphia, PA, 1989, pp. 814-824.
21. R.A. Mayville, T.J. Warren, and P.D. Hilton, Trans. ASME, vol. 109, 1987, pp. 188-193.
22. J.K. Donald and J. Ruschau, in Fatigue Crack Measurement: Techniques and Applications, K.J. Marsh *et al.*, eds., EMAS, West Midlands, UK, 1991, pp. 11-37.
23. J.K. Gregory and L. Wagner, "Heat Treatment and Mechanical Behavior in Beta C" (paper presented at GTT, Torino, Italy, 1991).
24. S. Mat and R.C. Newman, "Local Chemistry Aspects of Hydrogen Sulfide-Assisted Stress Corrosion Cracking of Stainless Steels" (paper No. 228 presented at NACE Corrosion '94, Houston, TX, 1994).
25. J.R. Scully and P.J. Moran, Corrosion, vol. 44, 1988, pp. 176-185.
26. S. Tsujikawa *et al.*, Corrosion, vol. 49, 1993, pp. 409-419.
27. H.H. Uhlig, Materials Performance, vol. 16, no. 1, 1977, pp. 22-25.
28. L.M. Young, Environment-Assisted Cracking in Beta Titanium Alloys, MS Thesis, University of Virginia, Charlottesville, VA, 1993.
29. H.B. Bomberger, D.A. Meyn and A.C. Fraker, in Titanium Science and Technology, G. Lütjering, U. Zwicker and W. Bunk, eds., Deutsche Gesellschaft für Metallkunde e.V., Obserusel, West Germany, 1985, pp. 2435-2454.
30. H. Buhl, in Stress Corrosion Cracking-The Slow Strain Rate Technique, ASTM STP 665, G.M. Ugiansky and J.H. Payer, eds., ASTM, Philadelphia, PA, 1979, pp. 333-346.
31. R.P. Gangloff, Mats. Sci. Engr. A, vol. 103, 1988, pp. 157-166.
32. G.A. Young, Jr., Hydrogen Effects in Metastable  $\beta$ -Titanium Alloys, M.S. Thesis, University of Virginia, Charlottesville, VA, 1993.
33. M.A. Gaudett and J.R. Scully, unpublished research, University of Virginia, Charlottesville, VA, 1994.
34. G.A. Young, Jr. and J.R. Scully, Scripta Metall., vol. 28, 1993, pp. 507-512.
35. G.A. Young, Jr. and J.R. Scully, in Beta Titanium Alloys in the 1990s, D. Eylon, R.R. Boyer and D.A. Koss, eds., TMS-AIME, Warrendale, PA, 1993, pp. 147-158.
36. H.J. Rack, Metall. Trans. A, vol. 6A, 1975, pp. 947-949.
37. R.P. Gangloff and R.G. Kelly, Corrosion, vol. 50, 1994, pp. 345-354.
38. T.R. Beck, J. Electrochem. Soc., vol. 114, 1967, pp. 551-556.
39. A. Turnbull, Scripta Metall., vol. 20, 1986, pp. 365-369.
40. D.A. Meyn and P.S. Pao, in Slow Stain Rate Testing for the Evaluation of Environmentally Induced Cracking: Research and Engineering Applications, ASTM STP 1210, R.D. Kane, ed., ASTM, Philadelphia, PA, 1993, pp. 158-169.
41. T.W. Webb and D.A. Meyn, Fracture Mechanics 26th Volume, ASTM STP 1256, W.G. Reuter, J.H. Underwood and J.C. Newman, Jr., eds., ASTM, Philadelphia, PA, in review, 1994.
42. F.P. Ford, in Environment Induced Cracking of Metals, R.P. Gangloff and M.B. Ives, eds., NACE, Houston, TX, 1990, pp. 139-166.
43. J.R. Rice, W.J. Drugan and T-L. Sham, in Fracture Mechanics: 12th Conference, ASTM STP 700, ASTM, Philadelphia, PA, 1980, pp. 189-221.
44. J.R. Rice and E.P. Sorensen, J. Mech. Phys. Solids, vol. 26, 1978, pp. 163-186.

**ELECTROCHEMISTRY AND PASSIVITY OF A Ti-15Mo-3Nb-3Al  
BETA TITANIUM ALLOY IN AMBIENT TEMPERATURE  
AQUEOUS CHLORIDE SOLUTIONS**

**David G. Kolman  
John R. Scully**

# Electrochemistry and Passivity of a Ti-15Mo-3Nb-3Al Beta-Titanium Alloy in Ambient Temperature Aqueous Chloride Solutions

D. G. Kolman\* and J. R. Scully\*\*

Center for Electrochemical Science and Engineering, Department of Materials Science, University of Virginia,  
Charlottesville, Virginia 22903.

## ABSTRACT

To understand the effect of Mo-Nb additions on the electrochemical behavior of  $\beta$ -titanium alloys in ambient temperature chloride solutions, characterization of the electrochemistry and passivity of a Ti-15Mo-3Nb-3Al alloy ( $\beta$ -21S) was undertaken. Both solution heat-treated (SHT) and peak-aged (PA) alloys exhibited passive anodic behavior in aerated and deaerated 0.6M NaCl, aerated and deaerated 0.6M NaCl adjusted to pH 1 with HCl, as well as aerated 5M HCl. X-ray photoelectron spectroscopy (XPS) performed after exposure to neutral 0.6M NaCl indicated that both PA and SHT  $\beta$ -21S formed a predominantly  $\text{TiO}_2$  film. Auger electron spectroscopy (AES) and cathodic kinetics suggest that the Mo and Nb alloying additions are incorporated into the oxide in amounts less than that found in the alloy. The predominance of the passivating  $\text{TiO}_2$  may explain the similarity of the electrochemical behavior observed. However, in deaerated 5M HCl, all materials displayed active-passive behavior except for SHT  $\beta$ -21S which was spontaneously passive. This result suggests that the presence of the  $\alpha$ -phase is deleterious to the formation of a protective passive film on PA  $\beta$ -21S in deaerated 5M HCl.

Metastable  $\beta$ -titanium alloys incorporating Mo and Nb, such as  $\beta$ -21S, were designed initially for improved high temperature properties such as oxidation resistance, elevated temperature strength, and creep resistance.<sup>1</sup> However, interest in these materials for high strength applications in room temperature marine environments is increasing. One question regarding their seawater performance is their resistance to environmentally assisted cracking (EAC). The EAC resistance of  $\alpha$ -titanium alloys in seawater is controlled by the tendency of the  $\alpha$ -phase to hydride.<sup>2,3</sup> In  $\alpha + \beta$  alloys, a discontinuous  $\beta$ -phase has a positive effect on the EAC resistance, plastically blunting cleavage cracks propagating through the hydrided  $\alpha$ -phase.<sup>4</sup> Little is known about the effects of  $\alpha$ -phase in a  $\beta$ -titanium matrix, however a continuous  $\beta$ -phase is detrimental to hydrogen embrittlement resistance.<sup>5</sup> In contrast to  $\alpha$ -titanium, a large hydrogen concentration ( $>40$  a/o) is required to hydride  $\beta$ -titanium in Ti-H binary compounds.<sup>6</sup> It is unclear whether such levels can be obtained in  $\beta$ -titanium alloys following film rupture in a marine environment. Thus, it is unknown whether a hydrogen mechanism is involved in the EAC behavior of these alloys because of a sequence of events involving (i) crack tip passive film destabilization, (ii) dissolution, (iii) hydrogen production, and (iv) hydrogen absorption, or whether EAC is controlled by an entirely different mechanism such as slip-film rupture-dissolution, pre-existing active path dissolution, or film-induced cleavage.<sup>7</sup>

EAC has been observed in PA  $\beta$ -21S in monotonic loading experiments on precracked specimens exposed to 0.6M NaCl at  $-0.6$  and  $-0.15$  V vs. SCE.<sup>8</sup> Cracking was maximized at intermediate strain rates, suggesting that a balance exists between a combination of film rupture frequency and repassivation rate, and the need for sufficient time to accommodate a time-dependent transport process. Intergranular cracking was observed only when preferential  $\alpha$ -precipitation on  $\beta$ -grain boundaries occurred.<sup>9</sup> Coincidentally, coplanar slip was favored in the  $\beta$ -Ti which was prone to preferential grain boundary  $\alpha$ -precipitation as opposed to wavy slip.<sup>9</sup> Therefore, it is useful to ascertain whether a preferential dissolution path may have developed. However, little is known about the passivity and repassivation kinetics of  $\beta$ -titanium alloys stabilized with molybdenum and niobium in marine environments over this range of potentials. Tomashov *et al.* reported for Ti-15Mo in 40%  $\text{H}_2\text{SO}_4$  at  $90^\circ\text{C}$  that dissolution is lowest for 100%  $\beta$ -alloys and increases for  $\beta + \alpha$  and  $\beta + \omega$  alloys.<sup>10</sup>

Additionally, passive dissolution of hcp  $\alpha$  was higher when alloyed with small additions of Al, V, Mo, Zr, or Nb.<sup>10</sup> All these elements increased the passive dissolution rate of  $\alpha$ -Ti in  $\text{H}_2\text{SO}_4$  at  $80^\circ\text{C}$  polarized to  $+1$  V. Tomashov *et al.* attributed this effect to a change in ionic conductivity of the predominantly  $\text{TiO}_2$  oxide and did not attribute this behavior to any change in the chemical stability of the protective oxide.<sup>10</sup> Initial corrosion research on  $\beta$ -21S alloy has extended only to weight loss measurements.<sup>11</sup> In that study  $\beta$ -21S had a lower dissolution rate and hydrogen uptake efficiency compared to commercially pure Ti and Ti-15Mo. Previous research on molybdenum-containing titanium alloys generally has focused on materials including Zr.<sup>12-18</sup> Others have studied Nb additions<sup>16</sup> and found that there was little effect on the high temperature oxidation resistance of titanium. Therefore, as an initial step in elucidating the role of electrochemical processes on the EAC mechanism of a Mo and Nb stabilized alloy, characterization of the dissolution and passivity of  $\beta$ -21S has been undertaken in room temperature chloride solutions. A subsequent study addresses repassivation kinetics.<sup>17</sup>

To obtain the required strength levels, these alloys are precipitation hardened through growth of an  $\alpha$ -precipitate with a needlelike morphology.<sup>8</sup> Hence, a goal of this study is to examine the effect of both composition and microstructure on the electrochemical behavior of these alloys. Both SHT and PA materials were investigated.

## Experimental Procedure

The composition of  $\beta$ -21S is reported in Table I.  $\beta$ -21S was SHT for 8 h at  $871^\circ\text{C}$  ( $1600^\circ\text{F}$ ) followed by an air cool. Peak-aging comprised a subsequent single-step heat-treatment at  $538^\circ\text{C}$  ( $1000^\circ\text{F}$ ) for 8 h followed by an air cool. The presence of an  $\alpha/\beta$ -microstructure, and the absence of other phases, was confirmed by both x-ray diffraction experiments and optical microscopy.<sup>18</sup>  $\alpha$ -platelets preferentially nucleate and grow along  $\beta$ -grain boundaries with a Burger's orientation of  $(110)_\beta \parallel (0001)_\alpha$ ,  $[111]_\beta \parallel [1120]_\alpha$ .<sup>19</sup> This orientation relationship is observed throughout the matrix.<sup>19</sup> Mo and Nb are  $\beta$ -phase stabilizers, while Al is an  $\alpha$ -stabilizer.<sup>20</sup>  $\alpha$ -Precipitates are Al rich and Mo poor, whereas the  $\beta$ -matrix is the opposite.<sup>21</sup> Therefore, grade 6

Table I. Vendor reported average chemical composition of  $\beta$ -21S.

|                     | Ti   | Mo   | Al   | Nb   | Si    | O    | Fe    | N |
|---------------------|------|------|------|------|-------|------|-------|---|
| Weight percent rem. | 14.9 | 3.15 | 2.64 | 0.22 | 0.198 | 0.15 | 0.014 |   |
| Atomic percent rem. | 7.89 | 5.99 | 1.44 | 0.40 | 0.629 | 0.14 | 0.051 |   |

\* Electrochemical Society Student Member.

\*\* Electrochemical Society Active Member.



Table II. Vendor reported chemical compositions of grades 2 and 6 Ti in weight percent.

|            | Ti   | Al   | Sn   | Fe   | O    | N     | H      |
|------------|------|------|------|------|------|-------|--------|
| Grade 2 Ti | rem. | —    | —    | 0.16 | 0.13 | 0.005 | 0.0036 |
| Grade 6 Ti | rem. | 5.20 | 2.30 | 0.46 | 0.13 | 0.010 | 82 ppm |

Ti (Ti-5 Al-2.5 Sn) was utilized to simulate the approximate composition of the  $\alpha$ -precipitates found in the  $\beta$ -titanium alloys. The compositions of grades 2 and 6 Ti are listed in Table II. Commercially pure grade 2 Ti ( $\alpha$ -phase) also was examined for a baseline comparison.

Samples were polished to a 600 grit finish followed by degreasing in acetone. The testing apparatus comprised 1 cm<sup>2</sup> working electrode area exposed in a flat cell containing a platinized niobium mesh counterelectrode. A saturated calomel reference electrode (SCE) was situated in a well possessing a Luggin capillary.

Rotating disk electrode (RDE) experiments comprised identical counter and reference electrodes as above. The working electrode (0.635 cm diam) surface preparation was the same as stated above. The disk was imbedded in a Kel-F mandrel attached to an analytical rotator and ASR speed controller from Pine Instrument Co. A standard RDE cell was utilized for these experiments.

Polarization measurements were performed with either a Princeton Applied Research (PAR) 173 or PAR 273 potentiostat at a scan rate of 0.05 mV/s. All polarization experiments were performed following exposure to solution for 2 h at open circuit.

Each electrochemical impedance spectroscopy (EIS) experiment comprised ten individual impedance scans. An initial scan was conducted at the open-circuit potential followed by nine scans at 300 mV intervals from -0.3 to 2.1 V vs. SCE. Each scan was preceded by a 2 h potentiostatic hold at the given potential, except the open-circuit potential scan which was preceded by 2 h at open circuit. EIS measurements were performed with a Solartron 1286 electrochemical interface and a Model 1255 frequency response analyzer. A 10 mV rms ac voltage signal was applied at frequencies between 10 kHz and 5 mHz using potentiostatic control. Impedance data fitting was performed with CNLS circuit fitting software.<sup>22</sup>

Electrochemical tests were performed on the materials utilizing six different room temperature solutions. These were 0.6M NaCl, 0.6M NaCl adjusted to pH 1 with HCl, and 5M HCl, each in both the aerated and deaerated condition. NaCl solutions (0.6M) comprised reagent grade NaCl added to distilled deionized water. Solutions were adjusted to pH 1 with reagent grade HCl. HCl solutions (5M) comprised reagent grade HCl and distilled deionized water. The pH of these solutions is -1.64 when the effect of Cl<sup>-</sup> on the activity of H<sup>+</sup> is incorporated into the calculation.<sup>23</sup> Deaeration was performed with commercially pure Ar gas. 0.6M NaCl solution was utilized to model alloy behavior when exposed to the bulk solution in a marine environment. The pH 1, 0.6M NaCl was utilized to discern the behavior of the alloys in a simulated crack tip environment. Although a crack tip solution and its pH has yet to be isolated, a pH 1, 0.6M NaCl is considered to be a rough estimate of that solution. Beck<sup>24</sup> has reported that a pH < 1.3 was found next to a corroding pit exposed to neutral chloride solution.<sup>25</sup> Others have reported a pH of 1.7 at a crack tip in Ti-8 Al-1 Mo-1 V.<sup>26</sup> HCl (5M) was utilized to analyze material behavior under extremely acidic conditions that are perhaps more severe than a crack tip environment.

Sample surfaces were prepared for Auger electron spectroscopy (AES) in the manner stated above. EIS was then performed on each sample in pH 1, 0.6M NaCl as described above, with the final potential at 1.5 V vs. SCE. Samples were removed from the cell and rinsed in distilled deionized water. AES was performed on a Perkin Elmer PHI 600 system utilizing a 5 keV beam operated at 0.54  $\mu$ A. Sputter depth profiling was performed with a 3 keV Ar<sup>+</sup> ion beam. The particular Auger electron transition energies utilized

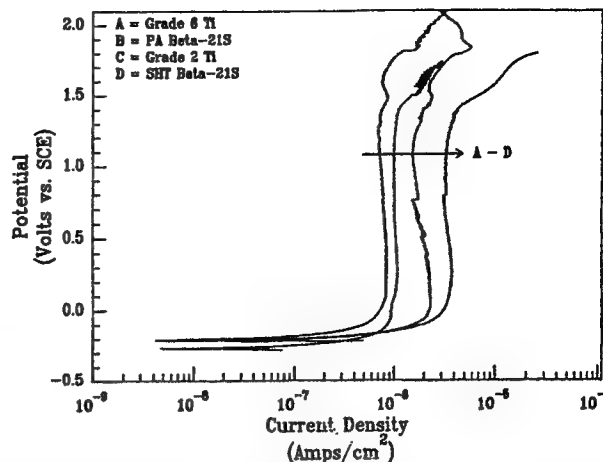


Fig. 1. Representative anodic polarization scans for the four titanium alloys examined in one particular solution (aerated pH 1, 0.6M NaCl).

for analysis for each element were selected at Auger energies as close as possible to each other for different elements to obtain comparable escape depths. The transition energies used were Ti<sub>LMM</sub>-418 eV, O<sub>KLL</sub>-503 eV, Mo<sub>MNN</sub>-186 eV, and Al<sub>KLL</sub>-1396 eV.

X-ray photoelectron spectroscopy (XPS) was performed on a Kratos XSAM800 utilizing a Mg x-ray source operated at 13 kV and 20 mA, perpendicular to the sample surface. Samples were potentiostatically held at -0.6 V vs. SCE in pH 1 0.6M NaCl and the surfaces mechanically abraded with SiC paper, thereby allowing the oxides to reform at -0.6V. Samples were rinsed in distilled water upon removal from the cell. The following peaks were used for analysis: Ti-2p<sub>3/2</sub>, O-1s, Mo-3d<sub>3/2</sub> and 3d<sub>5/2</sub>, Nb-3d<sub>3/2</sub> and 3d<sub>5/2</sub>, and Al-2p. Reference to C 1s was used in order to account for specimen charging.

## Results and Discussion

**Electrochemistry and passivity in pH 1, 0.6M NaCl solutions.—Electrochemistry.**—Representative anodic polarization data are reported in Fig. 1 and 2. Figure 1 shows the anodic polarization behavior of the four different materials (SHT and PA  $\beta$ -21S, grade 2, and grade 6) in a particular solution (aerated pH 1, 0.6M NaCl). Figure 2 reveals the behavior of one particular material (SHT  $\beta$ -21S) in the six solutions (0.6M NaCl, pH 1, 0.6M NaCl, and 5M HCl, each in the aerated and deaerated conditions). It may be seen in Fig. 1 that a significant increase in anodic current density is observed for each material at approximately 1.4 V. This increase in anodic current density corresponds to the onset

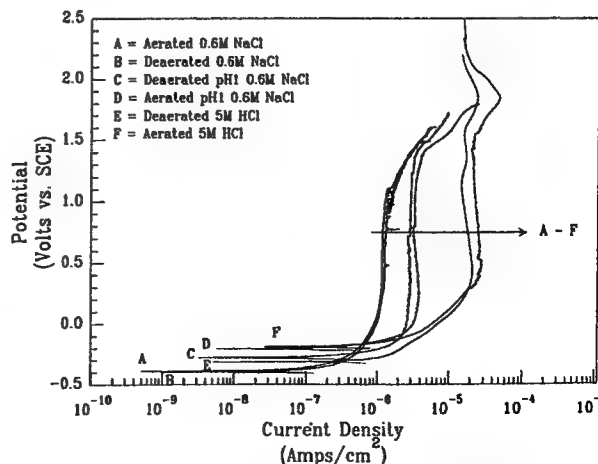


Fig. 2. Representative anodic polarization scans for SHT  $\beta$ -21S in the six chloride-containing solutions.

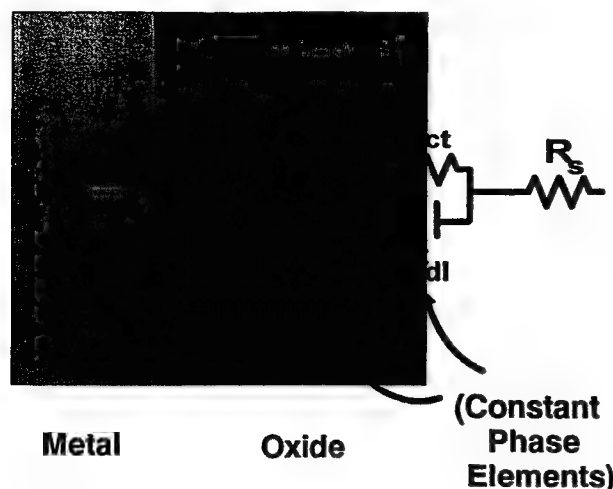


Fig. 3. Proposed circuit model for a passive titanium surface exposed to an aqueous solution.

of oxygen evolution and is not due to pitting. This result has been confirmed by optical microscopy which did not show evidence of pitting. This has also been confirmed by others, who have stated that pitting is not observed on titanium in room temperature chloride solutions until +9 V is reached.<sup>24</sup> Additionally, Fig. 1 reveals that SHT  $\beta$ -21S has the highest passive current density of all of the materials. This was true in all the NaCl solutions examined. In contrast, the magnitudes of the passive current densities of the other materials varied between solutions and were probably within experimental error.

Figure 1 additionally reveals that the open-circuit potentials for all of the materials are within experimental variability for one material. Grade 6 Ti, which approximates the composition of the  $\alpha$ -precipitates in the PA  $\beta$ -21S, has a similar open-circuit potential to that of the SHT materials. This similarity indicates that galvanic cells are unlikely between the  $\beta$ -titanium matrix and the  $\alpha$ -precipitates in the PA materials in this solution. Further, no distinct increases in anodic current density are observed at applied potential corresponding to the thermodynamic oxidation potentials of the alloying additions.

Figure 2 displays the polarization curves for SHT  $\beta$ -21S in the six solutions. As the pH decreases, the passive current density increases. Additionally, all of the materials are passive with no pitting observed at potentials as high as 1.7 V vs. SCE. Moreover, no significant differences are observed between the aerated and deaerated conditions, except for a slightly higher passive current density observed in deaerated 5M HCl. The lack of effect of deaeration has been observed previously by others in abrasion experiments.<sup>27</sup>

From Figure 2, we see that the oxygen evolution reaction rate becomes small relative to the passive current density at 2.0 V in 5M HCl. This may be due to increased difficulty for electron-tunneling through the semiconducting passive film which thickens with increasing potential. This phenomenon was observed in all solutions and on all materials, albeit at different potentials.

**In situ characterization of passivity.**—EIS was used for *in situ* characterization of the passive layer. A proposed circuit model for the electrochemical interface may be seen in Fig. 3. This model includes  $C_{ox}$  which represents the space charge capacitance of a compact nonporous oxide. The model also comprises a double-layer capacitance ( $C_{dl}$ ) at the oxide/solution interface. Constant-phase elements are used to better represent the nonidealities of such capacitances. EIS data is interpreted in the context of this model.

The impedance response of SHT  $\beta$ -21S exposed to aerated pH 1, 0.6M NaCl is seen in Fig. 4a and b. As the potential is increased, the low frequency impedance decreases. Further, as the potential is made more positive with respect

to the open circuit, the emergence of two time constants is seen. This occurs until 1.8 V is reached, wherein the two time constants merge again. At these potentials, deconvolution of the data becomes increasingly difficult. However, good correlation was obtained between the model and the experimental data, as seen in Fig. 5.

It was hypothesized here that the high frequency time constant was attributable to the oxide and that the low frequency time constant was attributable to the parallel  $R_{ct}/C_{dl}$  combination. To confirm this hypothesis, comparison was undertaken between impedance derived oxide thickness and ellipsometric titanium oxide thickness at various potentials in 0.1M HCl.<sup>28</sup> Impedance spectra for grade 2 Ti were obtained at 0, 2, 4, 6, and 8 V vs. NHE (normal hydrogen electrode), with the specimen prepared in identical fashion to those of the ellipsometric study.<sup>28</sup> Utilizing a dielectric constant of 100 for  $TiO_2$  in conjunction with the obtained value for  $C_{ox}$ , a good correspondence was obtained for the oxide thickness (Fig. 6). This result confirms the hypothesis that the high frequency time constant was indeed attributable to the oxide.

The charge transfer resistance,  $R_{ct}$ , is approximately one order of magnitude larger than the oxide resistance,  $R_{ox}$ , at the lower potentials. Therefore, we conclude that the charge-transfer reaction is the rate-determining step and dominates the passive dissolution of the alloys. Also,  $R_{ct}$  for grade 2 Ti in aerated pH 1, 0.6M NaCl increases with potential until approximately 1.2 V whereupon the charge-transfer resistance begins to decrease. The decrease in the charge-transfer resistance coincides with the onset of oxygen evolution, as discussed earlier.

Oxide thickness and apparent resistivity were calculated from the parameters obtained by circuit fitting. The oxide thickness may be calculated by utilizing the equation

$$d_{ox} = \frac{\epsilon \epsilon_0 A}{C_{ox}} \quad [1]$$

where  $d_{ox}$  is the oxide thickness,  $C_{ox}$  is the oxide capacitance,  $\epsilon$  is the dielectric constant of the oxide,  $\epsilon_0$  is the permittivity of free space, and  $A$  is the surface area. The apparent oxide resistivity may be calculated as follows, assuming that it varies linearly with thickness. From Eq. 1

$$\frac{A}{d_{ox}} = \frac{C_{ox}}{\epsilon \epsilon_0} \quad [2]$$

Assuming that

$$\rho_{ox} = R_{ox} \left( \frac{A}{d_{ox}} \right) \quad [3]$$

and, substituting Eq. 2 into Eq. 3, the following equation is obtained

$$\rho_{ox} = \frac{R_{ox} C_{ox}}{\epsilon \epsilon_0} \quad [4]$$

Equation 4 provides an indication of apparent oxide resistivity that is independent of geometric thickness.

Figures 7 and 8 show plots of the oxide thicknesses and apparent resistivities, respectively, vs. potential for the materials in aerated pH 1 solution, utilizing a dielectric constant of 100 for all materials. The oxide thicknesses increase linearly with increasing potential and the growth rate of the  $\beta$ -21S alloys is less than that of either grade 2 or grade 6 Ti. The oxide growth rate for grade 2 Ti (approximately 23 Å/V) corresponds with earlier observations for commercially pure titanium in 0.1M HCl.<sup>28</sup> Additionally, the apparent oxide resistivity decreases with potential, implying that the oxide is becoming increasingly defective. Handbook values for bulk  $TiO_2$  resistivity are in the range of  $10^{13}$ – $10^{18}$   $\Omega$  cm,<sup>29</sup> while calculated values from the experiments here yield values in the  $10^7$  to  $10^{10}$  range, depending on potential. This discrepancy may be because a 10–50 Å oxide grown in solution is more electronically and/or ionically defective than a bulk three-dimensional oxide, the oxide incorporates alloying additions, oxide hydration, or chloride ion incorporation. Tomashov *et al.* have expressed a similar viewpoint in their review of the passivity of a broad range of Ti base alloys.<sup>10</sup> The relative rankings of the

Fig. 4 (a) Electrochemical impedance response of SHT $\beta$ -21S exposed to aerated pH 1, 0.6M NaCl at potentials ranging from open circuit to 0.6 V vs. SCE.

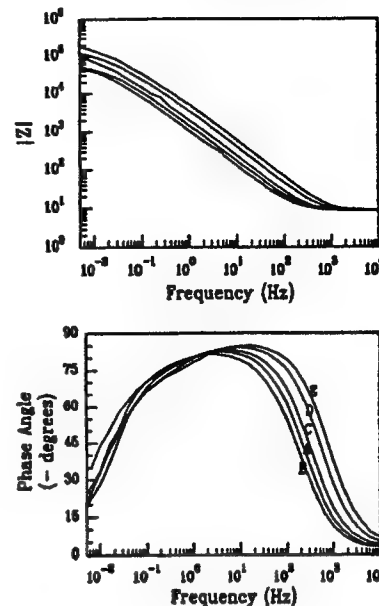
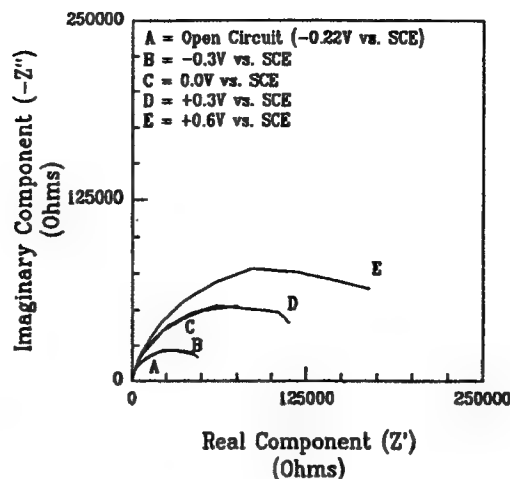
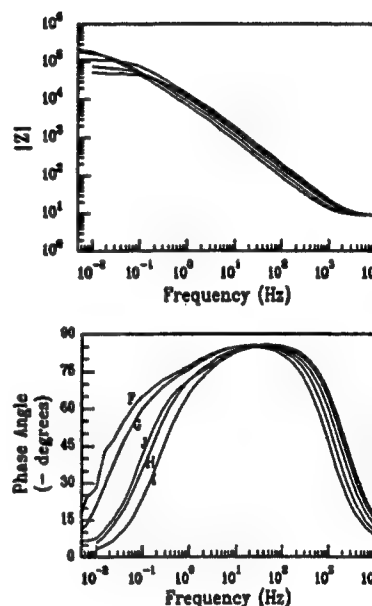
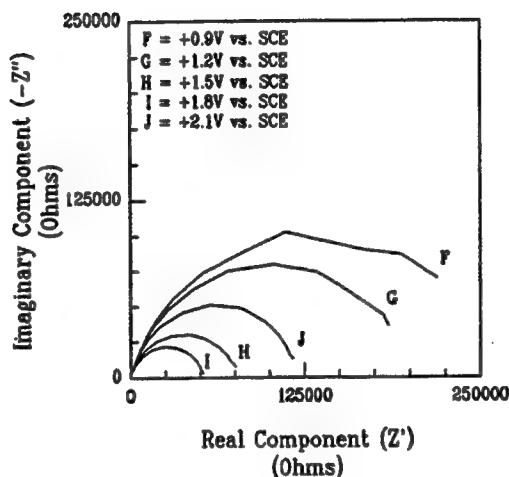


Fig. 4 (b) Electrochemical impedance response of SHT $\beta$ -21S exposed to aerated pH 1, 0.6M NaCl at potentials ranging from 0.9 to 2.1 V vs. SCE.



oxide thickness and apparent resistivity, from the material with the highest property to that with the lowest, varied nonsystematically from solution to solution.

**Ex situ characterization of passivity.**—AES was conducted on SHT  $\beta$ -21S previously exposed to aerated pH 1, 0.6M NaCl at 1.5 V vs. SCE. A sputter depth profile is shown in Fig. 9. The pH 1, 0.6M NaCl solution was chosen for *ex situ* characterization experiments because its aggressiveness is between that of 5M HCl and 0.6M NaCl. EIS experiments were performed every 300 mV from open circuit up to 1.5 V vs. SCE, so that the oxide examined by AES after sample removal from the electrochemical cell experienced the same history as in the dc and ac experiments discussed earlier. Due to the small amount of Nb (atomic number 41) in the bulk alloy and significant peak overlap with Mo (atomic number 42), the Nb concentration cannot be accurately determined and is not shown. Na or Cl peaks were not detected. Figure 9 shows that the passive film is rich in O and Ti at an approximate composition of TiO<sub>2</sub>. The concentration of Al throughout the passive film appears constant at the concentration observed within the bulk alloy. The increase in Mo concentration as the base metal is approached has been seen elsewhere in  $\beta$ -titanium alloys.<sup>14</sup>

This increase has been attributed to a lower mobility of Mo ions through the passive film relative to Ti cations.<sup>14</sup> The low concentration of alloying additions within the passive film may explain the similar passive electrochemical behavior observed between  $\beta$ -21S and grades 2 and 6 Ti.

To determine an oxide thickness, a grade 2 Ti standard was used. EIS experiments were performed in the manner discussed above, with the thickness determined after a final potential of 1.5 V vs. SCE was reached. The oxide thickness was computed utilizing a dielectric constant of 100. The oxide was sputter depth profiled to determine the beam sputter rate. This rate was utilized to determine the thickness of the  $\beta$ -21S sample, assuming a uniform sputter rate. The oxide thickness was chosen to be the thickness at which the concentration of oxygen is one-half its maximum. The oxide thickness for SHT  $\beta$ -21S was 24 Å at 1.5 V vs. SCE. This value is in agreement with the value determined by EIS (Fig. 7).

From AES, we see that there is little incorporation of alloying additions into the outer layers of the passive film. The minimization of alloying additions in the passive film may account for the similar passive electrochemical behaviors of SHT and PA  $\beta$ -21S, grade 2 and grade 6 titanium as observed here by both the dc and ac methods.

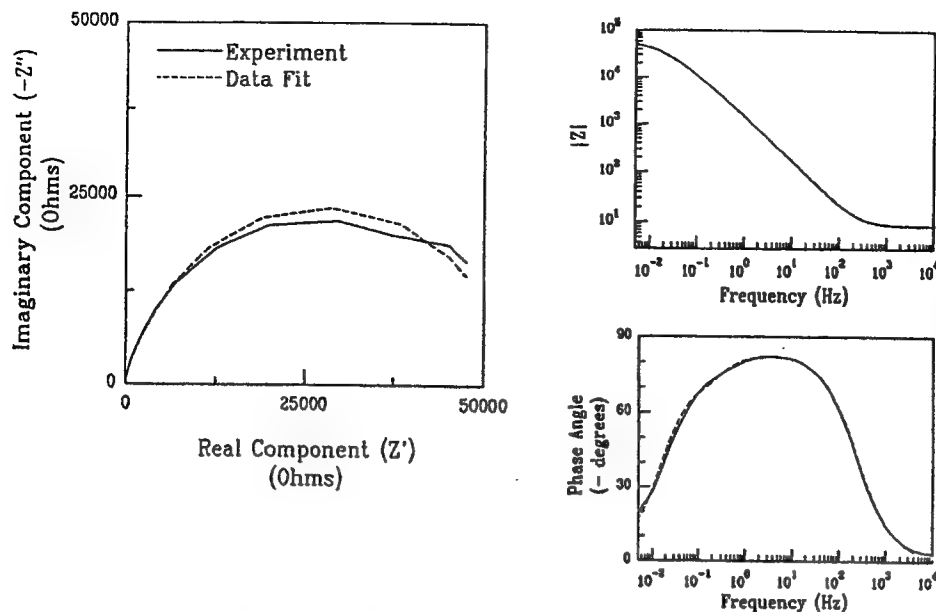


Fig. 5. Comparison of experimental data (SHT  $\beta$ -21S, aerated pH 1, 0.6M NaCl, open circuit) to that obtained by data fitting with CNLS fitting software<sup>22</sup> using the circuit model shown in Fig. 3.

To examine an oxide formed in solution, XPS experiments were performed on oxide films of SHT  $\beta$ -21S, PA  $\beta$ -21S, and grade 2 Ti formed at  $-0.6$  V vs. SCE following mechanical abrasion with SiC paper in aerated pH 1, 0.6M NaCl. XPS revealed that the compositions of the oxides on both PA and SHT  $\beta$ -21S were similar. All oxides were predominantly  $\text{TiO}_2$ , with small amounts of  $\text{MoO}_2$ ,  $\text{MoO}_3$ ,  $\text{Nb}_2\text{O}_5$ , and  $\text{Al}_2\text{O}_3$  also detected within the oxides on  $\beta$ -21S (Table III). The particular oxidation states seen here are in agreement with observations on other  $\beta$ -titanium alloys.<sup>12</sup> The smaller peaks associated with all alloying additions occurred at binding energies which were consistent with their being oxidized. Table III contains the energies of the obtained photoelectron peaks, the corresponding handbook values for the compounds attributed to these peaks,<sup>30</sup> and the formation potentials for such oxides over a range of potentials,<sup>31,32</sup> since the surface pH upon mechanical destabilization of the oxide film is not known. For Mo, the observation of  $\text{MoO}_3$  is consistent with the participation of hydrated  $\text{MoO}_3$  ( $\text{H}_2\text{MoO}_4$ ).<sup>31</sup> Because most hexavalent Mo compounds have nearly identical binding energies,<sup>33</sup> the binding energy of  $\text{H}_2\text{MoO}_4$  is assumed to be equal to that of  $\text{MoO}_3$ . The similar oxide compositions may explain the similar electrochemical behaviors of the PA and SHT materials. Moreover, there is no evidence suggesting that the oxidation mechanism of  $\beta$ -21S is different from that of grade 2 Ti in pH 1, 0.6M NaCl.

*Electrochemistry and passivity in 0.6M NaCl solutions.—Electrochemistry and in situ characterization of passiv-*

*ity.*—The behavior of the titanium alloys in neutral 0.6M NaCl (Fig. 10) was similar to that observed in pH 1 adjusted solutions. The passive current densities for all the materials were lower in the neutral solution than in pH 1. These current densities were confirmed by impedance measurements wherein the charge-transfer resistances which dominate the polarization resistance and, hence, the passive current densities were higher. Additionally, the oxide resistances appeared to be higher for the neutral solutions due to both increased apparent oxide resistivity and increased oxide thickness.

As in the pH 1 solutions, there appeared to be no discernible difference between aerated and deaerated conditions. Additionally, as in previous experiments, SHT  $\beta$ -21S displayed the highest passive current density of all the materials examined. The open-circuit potentials, including grade 6 Ti, were within experimental variability, again indicating that no significant galvanic couples are present in the PA material.

Cathodic polarization scans (Fig. 11) performed in deaerated 0.6M NaCl indicated similar exchange current densities for the hydrogen evolution reaction (HER) on the  $\beta$ -titanium materials, ranging from  $2.0 \times 10^{-11}$  to  $4.6 \times 10^{-11}$  A/cm<sup>2</sup>. Although these are higher than that found for grade 2 Ti ( $1 \times 10^{-12}$  A/cm<sup>2</sup>), the exchange current densities are far below those found for the HER on pure Mo and Nb,<sup>34</sup> which are the major alloying additions. This result again suggests that there is a low concentration of alloying addi-

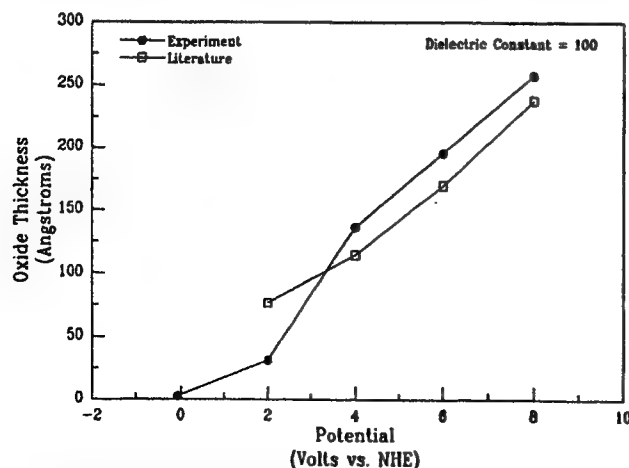


Fig. 6. Comparison of oxide thicknesses on grade 2 Ti as a function of applied potential to that found in the literature.<sup>28</sup>

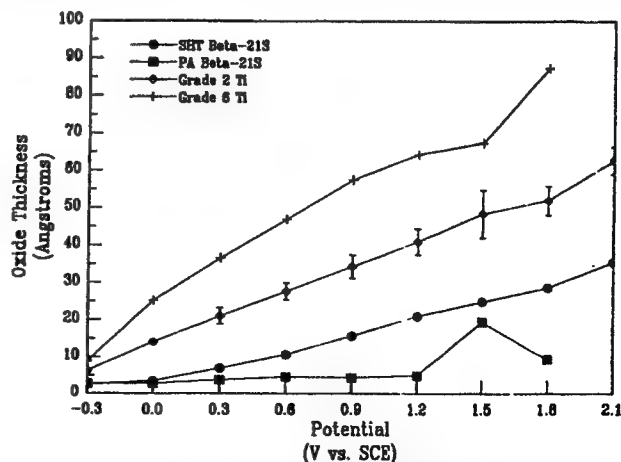


Fig. 7. Relationship between oxide thicknesses and potential for SHT and PA  $\beta$ -21S, grade 2 Ti and grade 6 Ti exposed to aerated pH 1, 0.6M NaCl. A dielectric constant of 100 was assumed.

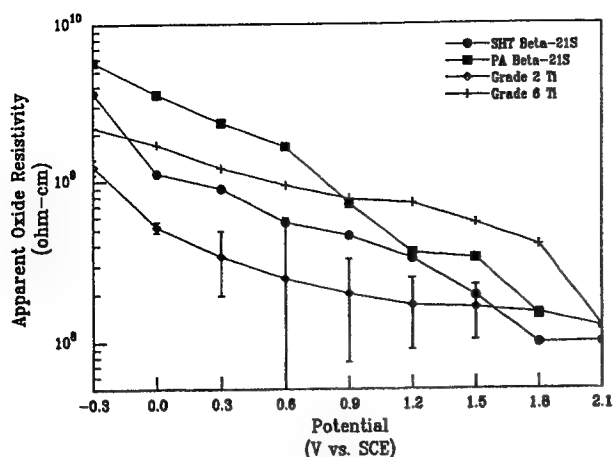


Fig. 8. Relationship between apparent oxide resistivities and potential for SHT and PA  $\beta$ -21S, grade 2 Ti and grade 6 Ti exposed to aerated pH1, 0.6M NaCl. A dielectric constant of 100 was assumed.

tions incorporated into the outer layers of the passive films of SHT and PA  $\beta$ -21S and that the  $\text{TiO}_2$ -dominated oxide may account for the similar passive electrochemical behavior observed for all the materials examined in neutral 0.6M NaCl.

**Electrochemistry and passivity in 5M HCl solutions.—Electrochemistry.**—All the materials examined were passive in aerated 5M HCl except for grade 2 Ti which displayed an active/passive transition (Fig. 12). Others have observed that for commercially pure Ti, an active/passive transition is present in 5M HCl<sup>35</sup> but not in 0.1M HCl<sup>28</sup> (approximately pH 1). The more active open-circuit potential of grade 2 Ti enables the observation of the active/passive transition. To verify the existence of such a transition on the other materials, similar experiments were performed in deaerated 5M HCl (Fig. 13). An active/passive transition occurred on all the alloys in deaerated 5M HCl, except for SHT  $\beta$ -21S, which had a significantly higher open-circuit potential. A similar result was observed by Laser and Marcus<sup>14</sup> for beta III (Ti, 11.5% Mo, 4.5% Sn, 6% Zr) which exhibited spontaneous passivity when pure Ti showed an active/passive transition in a pH 2.3 electrolyte. Previous research has observed an active/passive transition on other  $\beta$ -titanium alloys (Ti-13V-11Cr-3 Al) in 20% HCl (6.5M), albeit at 35°C.<sup>36</sup> A transition was observed in 5% HCl (1.6M) at 65°C.<sup>36</sup> In general, increasing temperatures tend to promote the development of an active/passive transition at fixed HCl concentration.<sup>36</sup> The open-circuit potential of SHT  $\beta$ -21S is more noble than that of both PA  $\beta$ -21S and grade 6 Ti, indicating that the  $\alpha$ -phase lowers the open-circuit potential of PA  $\beta$ -21S. An active/passive tran-

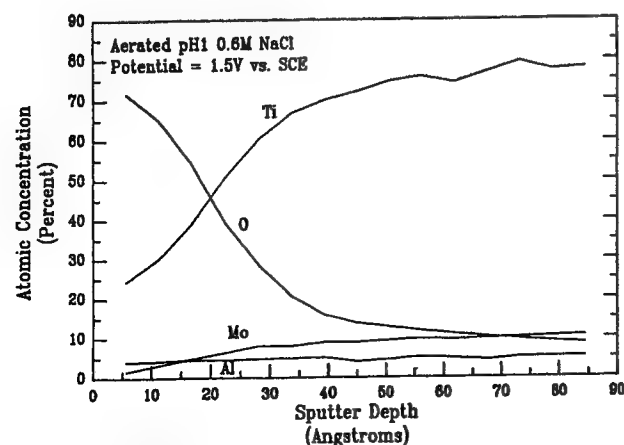


Fig. 9. AES sputter depth profile of SHT  $\beta$ -21S exposed to aerated pH1, 0.6M NaCl.

Table III. Binding energies obtained from XPS experiments after abrasion (pH 1, 0.6M NaCl, -0.6 V vs. SCE), handbook values for the binding energies of the metal oxides,<sup>30</sup> and the corresponding formation potential of the oxides at two different pH.<sup>31,32</sup>

|   | Ti 2p <sub>3/2</sub><br>TiO <sub>2</sub> | Mo 3d <sub>5/2</sub><br>MoO <sub>2</sub> | Mo 3d <sub>5/2</sub><br>MoO <sub>3</sub> | Nb 3d <sub>5/2</sub><br>Nb <sub>2</sub> O <sub>5</sub> | Al 2p<br>Al <sub>2</sub> O <sub>3</sub> |
|---|--|--|--|--|---|
| Grade 2 Ti                              | 458.5                                    | n/a                                      | n/a                                      | n/a  | n/a                                     |
| SHT $\beta$ -21S                        | 458.9                                    | 229.7                                    | 232.0                                    | 207.2  | 74.4                                    |
| PA $\beta$ -21S                         | 458.3                                    | 229.6                                    | 232.2                                    | 207.2  | 74.3                                    |
| Handbook <sup>30</sup>                  | 458.5                                    | 229.2                                    | 232.7                                    | 207.3  | 74.7                                    |
| Minimum formation potential (V vs. SCE) | -0.889                                   | -0.15 <sup>a</sup>                       | -1.391                                   | -0.589   | -2.022 <sup>b</sup>                     |
| pH 1                                    |  |  |  |  |   |
| pH = 8                                  | -1.303                                   | -0.786                                   | -1.805                                   | -1.003   | -2.264                                  |

<sup>a</sup>— $\text{Mo}^{3+} + 2 \text{H}_2\text{O} \rightarrow \text{MoO}_2 + 4 \text{H}^+ + 4 \text{e}^-$  reaction, assuming  $[\text{Mo}^{3+}] = 10^{-6} \text{ M}$ ; from Yang *et al.*<sup>32</sup>

<sup>b</sup>— $\text{Al} \rightarrow \text{Al}^{3+} + 3 \text{e}^-$  reaction, assuming  $[\text{Al}^{3+}] = 10^{-6} \text{ M}$ .

sition is observed in addition to an increased passive current density. Moreover, a galvanic couple between the  $\alpha$  and  $\beta$ -phases may be present under these conditions.

The Mo/Nb alloying addition promotes spontaneous passivity on SHT  $\beta$ -21S in deaerated 5M HCl. However, it was unclear if the lack of an active/passive transition is due to an actual effect upon the anodic oxidation process or whether increased cathodic kinetics (exchange current density, or lower Tafel slope) raised the open-circuit potential above such a transition. Therefore, cathodic scans on SHT  $\beta$ -21S in deaerated 5M HCl were performed. Although the exchange current density for the HER on SHT  $\beta$ -21S is higher than that on the  $\alpha$ -alloys (Table IV), it is not high enough to account for a 300 mV increase in the open-circuit potential. PA  $\beta$ -21S supports a higher exchange current density for hydrogen evolution than SHT  $\beta$ -21S, even though its open-circuit potential is lower. Therefore, we conclude that the presence of Mo and Nb affects the anodic process, rendering titanium spontaneously passive in deaerated 5M HCl. The exact process by which the material is rendered passive is unknown. One hypothesis is that incorporation of  $\text{Mo}^{3+}$  into a normally nonprotective  $\text{Ti}_2\text{O}_3$  film renders it more protective. Another hypothesis is that Mo in the solid state lowers the oxidation rate of the metal substrate beneath the nonprotective film. A nonprotective  $\text{Ti}_2\text{O}_3$  film exists in the potential region associated with the active/passive transition on Ti.<sup>37</sup> It is possible that elemental Mo occupies kink sites to impede metal dissolution. Additionally, others have put forth models explaining beneficial effects of Mo on passive films that may be applicable

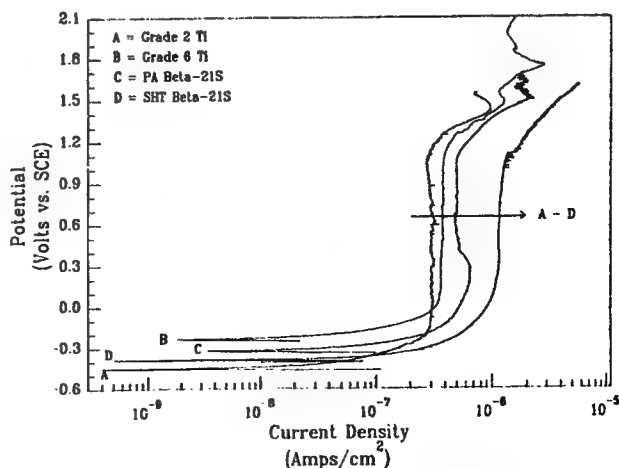


Fig. 10. Anodic polarization scans for SHT  $\beta$ -21S, PA  $\beta$ -21S, grade 2 Ti, and grade 6 Ti aerated 0.6M NaCl.



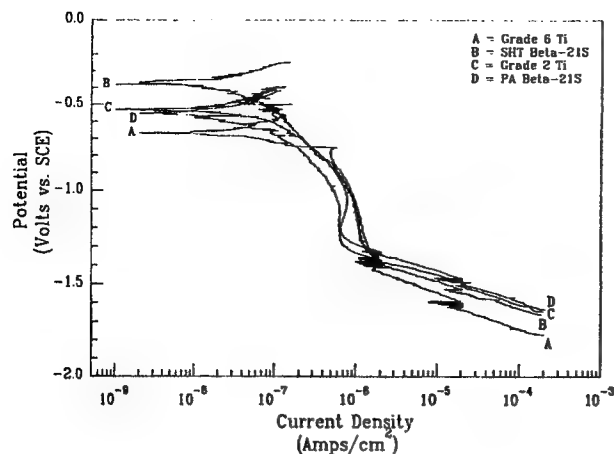


Fig. 11. Cathodic polarization scans for SHT  $\beta$ -21S, PA  $\beta$ -21S, grade 2 Ti, and grade 6 Ti exposed to 0.6M NaCl.

here,<sup>38</sup> however these theories require the presence of  $\text{Mo}^{+6}$  which is not thermodynamically stable over a portion of the potential range we have examined.

A pitting potential was not observed for any alloy in 5M HCl up to 2.0 V vs. SCE. Furthermore, the passive current densities for all the materials were highest in 5M HCl. As in NaCl solutions, SHT  $\beta$ -21S displayed the highest passive current density of all of the materials in aerated 5M HCl, but PA  $\beta$ -21S displayed a higher passive current density in deaerated 5M HCl.

The peak current density for PA  $\beta$ -21S in 5M HCl ( $4.5 \times 10^{-5} \text{ A/cm}^2$ ), the most aggressive solution examined, is two orders of magnitude too low to account solely for the slowest crack growth rates observed ( $10^{-6} \text{ mm/s}$ ,  $2.54 \times 10^{-4} \text{ mm/min}$  displacement rate).<sup>5</sup> Therefore, we conclude that highly localized mechanical destabilization of the passive film is required for EAC of these alloys even after crack tip cation hydrolysis and acidification, regardless of the exact mechanism of EAC.

*In situ characterization of passivity.*—Impedance spectra for grade 2 Ti exposed to aerated 5M HCl in the active range display distinct two time constant behavior although the polarization curve indicates that the material is active upon anodic polarization over a wide potential range. However, active behavior does not imply that no oxide is present. Other researchers have stated that even in the active region, dissolution is strongly inhibited by an oxide which apparently can exist metastably even in strong acid solution.<sup>39</sup> It was hypothesized that steady-state dissolution may proceed through oxide formation and dissolution steps.<sup>39</sup> Others have noted that in the active region, a porous film of  $\text{Ti}_2\text{O}_3$  is present.<sup>37</sup>

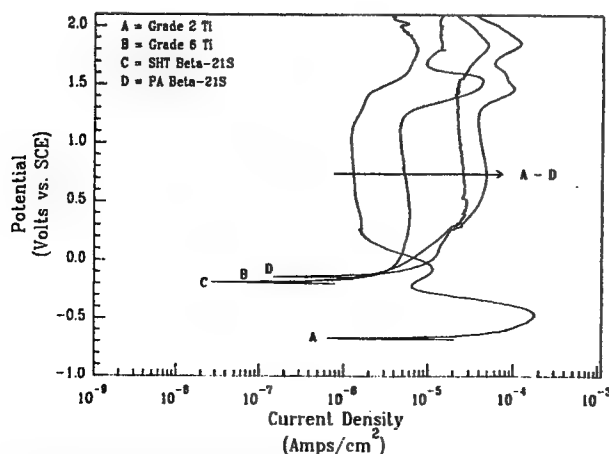


Fig. 12. Anodic polarization scans for SHT  $\beta$ -21S, PA  $\beta$ -21S, grade 2 Ti, and grade 6 Ti in aerated 5M HCl.

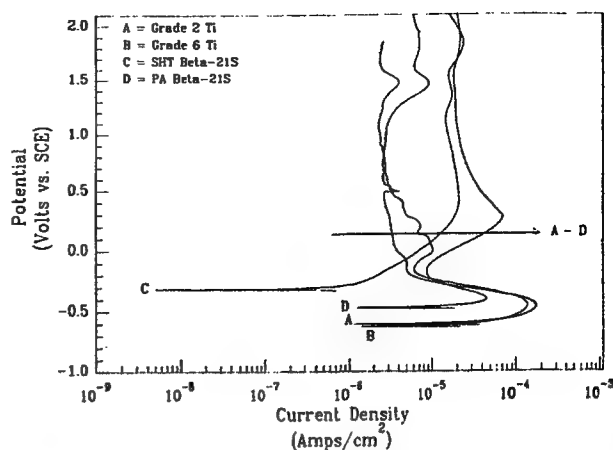


Fig. 13. Anodic polarization scans for SHT  $\beta$ -21S, PA  $\beta$ -21S, grade 2 Ti, and grade 6 Ti in deaerated 5M HCl.

Good correlation between the proposed impedance circuit model and data was observed for all the materials in all the examined solutions except 5M HCl. Figure 14 displays the impedance response of PA  $\beta$ -21S in aerated 5M HCl at five different potentials. Additional time constants (*i.e.*, low frequency inductive looping) are present in the spectra that are not seen in any spectra from other solutions. The origin of this looping is unclear but it may indicate a change in the properties of the electrochemical interface.

Impedance spectra similar to that seen for  $\beta$ -21S exposed to aerated 5M HCl have been observed by others. Impedance behavior of Al exposed to 0.5M NaCl below its pitting potential displayed low frequency looping.<sup>40</sup> This looping was attributed to a diffusion-controlled process within the oxide. Others have suggested that a buildup of surface charge at the metal-oxide interface may yield similar behavior.<sup>41</sup>

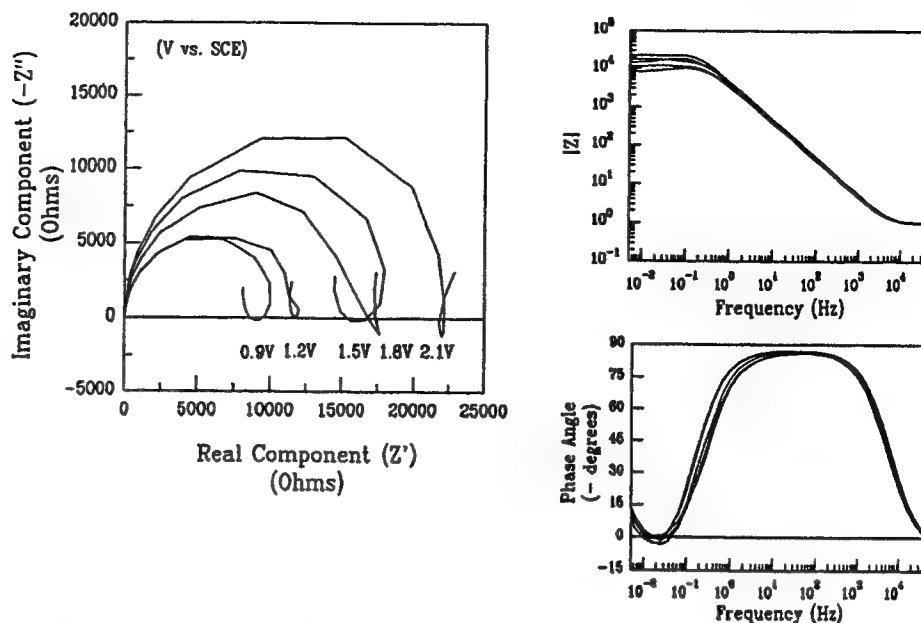
Although the polarization curves in aerated 5M HCl displayed a potential independent region indicative of passivity, it was of interest to confirm this, as the impedance spectra did not yield good agreement with the proposed circuit model for passivated titanium. Therefore, rotating disk electrode experiments were undertaken to distinguish possible anodic mass-transport control from passivity. If the system was passive, the behavior of the system within the passive region should be fluid velocity and, hence, rotation rate independent. However, if the system was anodically mass-transport limited, a change in anodic current density would be observed as a function of rotation rate. Anodic polarization experiments conducted with PA  $\beta$ -21S at 0, 250, 1000, and 5000 rpm in aerated 5M HCl are illustrated in Fig. 15. There is no discernible effect of rotation on the anodic current density of PA  $\beta$ -21S in its region of potential independent behavior. Therefore, we conclude that  $\beta$ -21S is passive in aerated 5M HCl.

Experiments in 5M HCl proved to be beneficial in elucidating the effect of Mo/Nb additions on the passivity of  $\beta$ -21S. The alloying additions promote formation of a passive film on SHT  $\beta$ -21S in deaerated 5M HCl by not only increasing cathodic kinetics, thereby raising the open-circuit potential, but by affecting the anodic process as well. PA  $\beta$ -21S undergoes an active/passive transition, indicat-

Table IV. Exchange current densities and Tafel slopes for the hydrogen evolution reaction on alloys exposed to deaerated 5M HCl.

|                  | Exchange current density<br>( $\text{A/cm}^2$ ) | Tafel slope<br>(mV/decade) |
|------------------|---|----------------------------|
| SHT $\beta$ -21S | $6.7 \times 10^{-10}$                           | 84                         |
| PA $\beta$ -21S  | $3.9 \times 10^{-9}$                            | 87                         |
| Grade 2 Ti       | $2.0 \times 10^{-10}$                           | 91                         |
| Grade 6 Ti       | $2.9 \times 10^{-10}$                           | 84                         |

Fig. 14. Electrochemical impedance response of PA  $\beta$ -21S exposed to aerated 5M HCl.



ing that the  $\alpha$ -precipitates within the  $\beta$ -matrix are deleterious to the formation of a passive layer. This condition is confirmed since grade 6 Ti, which roughly models the  $\alpha$ -precipitates, was active in deaerated 5M HCl up to approximately  $-0.15$  V vs. SCE.

### Conclusion

Analysis of the passive film on Mo and Nb stabilized  $\beta$ -titanium alloy ( $\beta$ -21S) in room temperature solutions simulating crack tip chemistries possible in marine environments has been performed utilizing both dc and ac methods. There are no major electrochemical differences between  $\beta$ -21S exposed to 0.6M NaCl and pH 1, 0.6M NaCl in its PA and SHT forms, although SHT  $\beta$ -21S almost always yielded the largest passive current density. Moreover, significant differences do not exist between either the model precipitate (grade 6 Ti) or commercially pure Ti (grade 2 Ti) and  $\beta$ -21S in the NaCl solutions. This finding suggests that there is minimal galvanic interaction between the matrix and precipitates in PA  $\beta$ -21S in the NaCl environments. All the alloys were spontaneously passive in the NaCl solutions examined and no pitting potentials were observed up to 2.1 V vs. SCE. However, experiments in deaerated 5M HCl reveal an active/passive transition for all alloys except SHT  $\beta$ -21S, indicating that the  $\alpha$ -precipitates in PA  $\beta$ -21S have a deleterious effect upon passivity and that local galvanic coupling between the  $\alpha$ - and  $\beta$ -phases may occur. Both the anodic and cathodic kinetics

were affected by the Mo/Nb additions in  $\beta$ -21S. Rotating disk electrode experiments confirmed that  $\beta$ -21S is passive in a 5M HCl environment. Similarity of hydrogen evolution kinetics, the lack of observed alloying addition oxidation, and AES and XPS studies indicate limited incorporation of alloying additions into the passive film in the NaCl solutions. The passive film on all Ti alloys was predominantly  $\text{TiO}_2$  with lesser amounts of oxidized Mo, Nb, and Al contained in the oxides on  $\beta$ -21S. The small quantity of alloying additions within the passive film may account for the similar passive electrochemical behaviors observed among the studied alloys. All the alloys in this study yielded peak current densities that were too low to account solely for crack growth rates observed in separate studies, even after crack tip acidification. The passive film, therefore, must be mechanically destabilized to account for these crack growth rates, regardless of the exact mechanism.

### Acknowledgments

The authors acknowledge the Office of Naval Research (Grant No. N00014-91-J-4164) and the Virginia Center for Innovative Technology for their support of this work. The authors also thank Titanium Metals Corporation for their generous donation of alloys. The authors acknowledge Dr. R. Bayles and the Naval Research Laboratory for help with AES experiments, S. McCartney and Virginia Polytechnic Institute for help with XPS experiments, and L. Young, G. Young, and R. P. Gangloff for helpful discussions.

Manuscript submitted April 2, 1993; revised manuscript received June 18, 1993. This was Paper 144 presented at the Toronto, ON, Canada, Meeting of the Society, Oct. 11-16, 1992.

The University of Virginia assisted in meeting the publication costs of this article.

### REFERENCES

1. *Titanium and Its Alloys*, Titanium Development Association, Boulder, CO (1992).
2. D. N. Williams, *J. Inst. Met.*, **91**, 147 (1962-1963).
3. H. G. Nelson, in *First Thermal Structures Conference*, E. Thornton, Editor, p. 301, University of Virginia, Charlottesville, VA (1990).
4. D. N. Fager and W. F. Spurr, *Trans. ASM*, **61**, 283 (1968).
5. H. G. Nelson, D. P. Williams, and J. E. Stein, *Metall. Trans. A*, **33**, 469 (1972).
6. A. D. McQuillan, *Proc. R. Soc. London, Ser. A*, **204**, 309 (1950).
7. T. R. Beck, *Corrosion*, **30**, 408 (1974).
8. L. M. Hartman and R. P. Gangloff, *Proceedings, Seventh World Conference on Titanium*, S. H. Froes, Editor, TMS-AIME, Warrendale, PA in press.

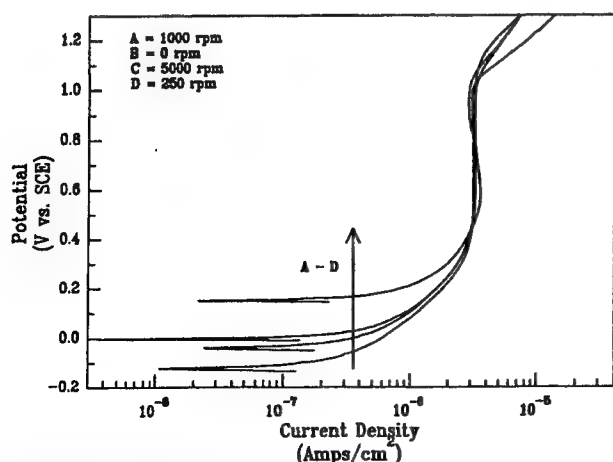


Fig. 15. Anodic polarization response of a PA  $\beta$ -21S rotating disk electrode exposed to aerated 5M HCl.

9. G. A. Young, Jr., and J. R. Scully, *Proceedings of the  $\beta$ -titanium Symposium*, TMS Annual Meeting, Denver, CO, D. Eylon, Editor, Feb. 21-25, 1993.
10. N. D. Tomashov, G. P. Chernova, Y. S. Ruscol, and G. A. Ayuyan, *Electrochim. Acta.*, **19**, 159 (1974).
11. J. S. Grauman, *Proceedings, Seventh World Conference on Titanium*, S. H. Froes, Editor, TMS-AIME, Warrendale, PA, in press.
12. P. A. Mäusli, S. G. Steinemann, and J. P. Simpson, in *Proceedings of the Sixth World Conference on Titanium*, P. Lacombe, R. H. Tricot, and G. Béranger, Editors, p. 1759 (1988).
13. R. W. Schutz and J. S. Grauman, in *Industrial Applications of Titanium and Zirconium: Fourth Volume*, ASTM STP 917, C. S. Young and J. C. Durham, Editors, p. 130, American Society for Testing and Materials, Philadelphia (1986).
14. D. Laser and H. L. Marcus, *This Journal*, **127**, 763 (1980).
15. J. A. Petit, D. Delaunay, D. Leroy, and G. Chatainier, *Proceedings, Fourth World Conference on Titanium*, H. Kimura and O. Izumi, Editors, p. 1363, TMS-AIME, Warrendale, PA.
16. P. Kofstad, K. Haufler, and H. Kjølesdal, *Acta Chem. Scand.*, **12**, 239 (1958).
17. D. G. Kolman and J. R. Scully, Unpublished research.
18. G. A. Young, Jr., and J. R. Scully, UVA Report No. UVA/525464/MSE93/101, October 1992.
19. G. A. Young, Jr., Master's Thesis, University of Virginia, Charlottesville, VA (1993).
20. *Metals Handbook*, 8th ed., Vol. 8, American Society for Metals, Metals Park, OH (1973).
21. E. W. Collings, *Physical Metallurgy of Ti Alloys*, p. 70, ASM International, Metals Park, OH (1984).
22. J. R. MacDonald, *Complex Nonlinear Least Squares Immitance Fitting Program*, University of North Carolina, Chapel Hill, NC, Version 3.02.
23. P. O. Garland, SINTEF publication STF16-A88085, Trondheim, Norway (1988).
24. T. R. Beck, *Localized Corrosion*, B. F. Brown et al., Editors, p. 644, NACE, Houston, TX (1974).
25. R. W. Powers and J. F. Wilfore, in *Fundamentals of Electrochemical Machining*, C. L. Faust, Editor, p. 135, The Electrochemical Society, Inc., Princeton, NJ (1971).
26. B. F. Brown, C. T. Fujii, and E. P. Dahlberg, *This Journal*, **116**, 218 (1969).
27. N. D. Tomashov and L. P. Vershinina, *Electrochim. Acta.*, **15**, 501 (1970).
28. T. Ohtsuka, M. Masuda, and N. Sato, *This Journal*, **132**, 787 (1985).
29. *Handbook of Chemistry and Physics*, 64th ed., R. C. Weast, Editor, p. E-55, Chemical Rubber Publishing Co., Boca Raton, FL (1983-1984).
30. *Handbook of X-ray Photoelectron Spectroscopy*, C. D. Wagner et al., Editors, Perkin Elmer Corp., Norwalk, CT (1979).
31. *Atlas of Electrochemical Equilibria in Aqueous Solutions*, M. Pourbaix, 2nd ed, NACE, Houston, TX (1974).
32. W. Yang, R. Ni, H. Hua, and A. Pourbaix, *Corros. Sci.*, **24**, 691 (1984).
33. W. E. Swartz and D. M. Hercules, *Anal. Chem.*, **43**, 1774 (1971).
34. B. E. Conway, *Electrochemical Data*, Elsevier, New York (1952).
35. A. Caprani and J. P. Frayret, *Electrochim. Acta.*, **24**, 835 (1979).
36. M. Levy and G. N. Sklover, *This Journal*, **116**, 323 (1969).
37. H. Kaesche, *Metallic Corrosion*, p. 265, NACE, Houston, TX (1985).
38. D. D. Macdonald, in *Critical Factors in Localized Corrosion*, G. S. Frankel and R. C. Newman, Editors, PV 92-9, p. 1, The Electrochemical Society Proceedings Series, Pennington, NJ (1992).
39. T. R. Beck, *Electrochim. Acta.*, **18**, 815 (1973).
40. J. B. Bessone, D. R. Salinas, C. E. Mayer, M. Ebert, and W. J. Lorenz, *ibid.*, **37**, 2283 (1992).
41. H. J. de Wit, C. Wijenberg, and C. Crevecoeur, *This Journal*, **126**, 779 (1979).





**ELECTROCHEMISTRY AND PASSIVITY OF Ti-15V-3Cr-3Al-3Sn  
BETA TITANIUM ALLOY IN AMBIENT TEMPERATURE  
AQUEOUS CHLORIDE SOLUTIONS**

**David G. Kolman  
John R. Scully**

# Electrochemistry and Passivity of Ti-15 V-3 Cr-3 Al-3 Sn $\beta$ -Titanium Alloy in Ambient Temperature Aqueous Chloride Solutions

D. G. Kolman\* and J. R. Scully\*\*

Center for Electrochemical Science and Engineering, Department of Materials Science and Engineering,  
University of Virginia, Charlottesville, Virginia 22903

## ABSTRACT

Examination of the electrochemical behavior of Ti-15 V-3 Cr-3 Al-3 Sn (Ti-15-3) alloy was performed as an initial step in understanding mechanisms for environmentally assisted cracking of  $\beta$ -titanium alloys in room temperature aqueous chloride solutions. Both solution heat-treated (SHT) and peak-aged (PA) Ti-15-3 were studied, in addition to SHT commercially pure Ti (grade 2 Ti) and Ti-5 Al-2.5 Sn (grade 6 Ti). The latter roughly models  $\alpha$  precipitates within the  $\beta$ -titanium matrix in PA Ti-15-3. Anodic polarization studies in 0.6M NaCl and 0.6M NaCl adjusted to pH 1 with HCl revealed that Ti-15-3 was spontaneously passive in each solution, with no observed pitting potential at potentials as positive as 2.1 V vs. SCE. However, an active/passive transition was observed on all alloys in both aerated and deaerated 5M HCl. *In situ* characterization of passivity by electrochemical impedance spectroscopy confirmed that passive film growth was linear with potential above primary passivation potentials in all solutions, and that the passive dissolution rate is limited by the charge-transfer reaction, especially at lower potentials. Similar passive current densities, active/passive transition potentials, and apparent oxide resistivities on SHT and PA Ti-15-3 suggest little effect of the  $\alpha$  precipitate on the passive behavior of PA Ti-15-3. Auger electron spectroscopy and hydrogen evolution kinetics suggested less than stoichiometric incorporation of alloying additions into the passive film of Ti-15-3. X-ray photoelectron spectroscopy indicated that, to the limited extent that alloying additions are found in the passive film, they are oxidized. The valence states present are discussed. Predominantly TiO<sub>2</sub> passive films may explain the similar passive electrochemical behaviors observed on the materials examined.

Metastable  $\beta$ -titanium alloys have received much attention recently for use in petrochemical, aerospace, and marine environments. These alloys are attractive because of their high strength, formability, and general resistance to corrosion.<sup>1-3</sup> However, the susceptibility of  $\beta$ -titanium alloys to environmentally assisted cracking (EAC) in room temperature aqueous chloride-containing solutions at intermediate strain rates has been documented.<sup>4</sup> While the EAC of  $\alpha$ -titanium alloys is known to be controlled by the tendency of the  $\alpha$  phase to hydride,<sup>5,6</sup> the mechanism for EAC in  $\beta$ -titanium is unknown. Unlike  $\alpha$ -titanium, a large concentration of hydrogen (>40 atomic percent (a/o)) is required to hydride the  $\beta$  phase in the Ti-H system.<sup>7</sup> It is unclear whether such a hydrogen concentration may be obtained in  $\beta$ -titanium alloys following a sequence of events involving (i) crack tip passive film destabilization, (ii) dissolution, (iii) hydrogen production, and (iv) hydrogen absorption. Further, it is possible that the EAC of these alloys does not originate from a hydrogen mechanism but from some other phenomenon such as slip-film rupture-dissolution, preexisting active path dissolution, or film-induced cleavage.<sup>8</sup> EAC at intermediate strain rates suggests that a balance exists between a requirement for mechanical destabilization of protective oxides and the need for sufficient time to support some time independent transport process in the fracture process zone or crack tip solution.

EAC has been observed on long time, high temperature, resolutionized, and subsequently peak-aged Ti-15-3 in monotonic loading experiments on precracked samples exposed to 0.6M NaCl at -0.6 V vs. saturated calomel electrode (SCE).<sup>9</sup> In this condition, preferential precipitation of  $\alpha$  precipitates perpendicular to  $\beta$  grain boundaries and coplanar slip were noted.<sup>10</sup> However, little is known about the passive film on this alloy, including the effects of V and Cr alloying additions, and the partitioning of these elements on aging. Early work in high temperature oxidation,<sup>11</sup> as cited by Kubaschewski and Hopkins,<sup>12</sup> found that V had virtually no effect on the oxidation of Ti and that several percent of Cr actually increased the oxidation rate. Tomashov *et al.* reported for Ti-15 Mo in 40% H<sub>2</sub>SO<sub>4</sub> at 90°C that dissolution is lowest for 100%  $\beta$  alloys and increases for  $\beta + \alpha$  and  $\beta + \omega$  alloys.<sup>13</sup> Additionally, passive dissolution

of HCP  $\alpha$  was increased when alloyed with small additions of Al, V, Mo, Zr, or Nb.<sup>13</sup> All these elements increased the passive dissolution rate of  $\alpha$ -titanium in H<sub>2</sub>SO<sub>4</sub> at 80°C polarized to +1 V. Tomashov *et al.* attributed this effect to a change in ionic conductivity of the predominantly TiO<sub>2</sub> oxide and did not attribute this behavior to any change in the chemical stability of the protective oxide.<sup>13</sup> Levy and Sklover examined the effects of HCl concentration and temperature on the anodic polarization behavior of mill-annealed Ti-13 V-11 Cr-3 Al exposed to elevated temperature HCl solutions, observing an active/passive transition on this alloy.<sup>14</sup> Other previous work has focused on the stress corrosion cracking susceptibility of  $\beta$ -titanium alloys, such as Ti-3 Al-8 V-6 Cr-4 Mo-4 Zr (Ti 38644),<sup>15</sup> but little examination of its passivity has been undertaken. Others have examined the corrosion behavior of Ti 38644, Ti-13 V-11 Cr, and Ti-15-3 in various chloride-containing media by gravimetric analysis.<sup>16</sup> From this latter study it was noted that Ti-15-3 had a higher corrosion rate in boiling HCl than other  $\alpha$ ,  $\beta$ , and  $\alpha/\beta$  alloys studied, including commercially pure Ti.<sup>16</sup> Hence, as an initial step in elucidating the role of electrochemical processes on the EAC mechanism of a V and Cr stabilized  $\beta$ -titanium alloy, characterization of the dissolution and passivity of Ti-15-3 has been undertaken. Additionally, the effect of the  $\alpha$  precipitate within the  $\beta$  matrix on the electrochemical behavior of PA Ti-15-3 is unknown. Therefore, a goal of this study is to

Table I. Vendor reported average chemical composition of Ti-15-3.

|               | Ti   | V    | Al   | Cr   | Sn   | Fe   | C     | N |
|---------------|------|------|------|------|------|------|-------|---|
| w/o remainder | 15.0 | 3.14 | 2.99 | 2.81 | 0.19 | 0.03 | 0.018 |   |
| a/o remainder | 14.1 | 5.59 | 2.76 | 1.14 | 0.16 | 0.12 | 0.062 |   |

Table II. Vendor reported chemical compositions of grades 2 and 6 Ti in weight percent.

|                      | Ti   | Al   | Sn   | Fe   | O     | N      | H |
|----------------------|------|------|------|------|-------|--------|---|
| Grade 2 Ti remainder | —    | —    | 0.16 | 0.13 | 0.005 | 0.0036 |   |
| Grade 6 Ti remainder | 5.20 | 2.30 | 0.46 | 0.13 | 0.010 | 82 ppm |   |

\* Electrochemical Society Student Member.

\*\* Electrochemical Society Active Member.

Table III. Weight percentages of elements present in  $\alpha$  precipitates and the  $\beta$  matrix in PA Ti-15-3, calculated from energy dispersive spectroscopy analysis.

|          | Ti | V   | Al  | Cr   | Sn  |
|----------|----|-----|-----|------|-----|
| $\alpha$ | 87 | 5.4 | 5.0 | 0.60 | 2.0 |
| $\beta$  | 70 | 20  | 2.7 | 4.9  | 2.2 |

examine the effect of microstructure on the electrochemical behavior of this alloy, by comparing SHT and PA Ti-15-3.

### Experimental Procedure

The composition of Ti-15-3 may be seen in Table I. Ti-15-3 was SHT for 30 min at 816°C (1500°F) followed by an air cool. Peak-aging comprised a subsequent single-step heat-treatment at 538°C (1000°F) for 8 h followed by an air cool. The presence of an  $\alpha/\beta$  microstructure, and the absence of other phases, was confirmed by both x-ray diffraction experiments, TEM/selected area diffraction, and optical microscopy on PA Ti-15-3.<sup>10</sup>  $\alpha$  platelets nucleate and grow with a Burger's orientation of  $(110)_\beta \parallel (0001)_\alpha$ ,  $[111]_\beta \parallel [1120]_\alpha$ .<sup>10</sup> Further, V and Cr are known to be  $\beta$  phase stabilizers, while Al is known to be an  $\alpha$  stabilizer.<sup>17</sup> Because Al is known to segregate to the  $\alpha$  phase within an  $\alpha/\beta$  structure,<sup>18</sup> grade 6 Ti (Ti-5 Al-2.5 Sn) was used to simulate the approximate composition of the  $\alpha$  precipitates found in the  $\beta$ -titanium alloys. Commercially pure grade 2 Ti ( $\alpha$  phase) was examined for base line comparison. The compositions of Grades 2 and 6 Ti are listed in Table II.

Energy dispersive spectroscopy (EDS) experiments were performed on PA Ti-15-3 to discern the extent that  $\beta$  stabilizing elements partition to the  $\beta$  phase. Experiments were conducted on a Phillips 400T transmission electron microscope (TEM). To reduce the interaction volume of the electron beam so that only a single phase was sampled, experiments were performed near the edge of a TEM foil prepared by ion milling. Because the  $\alpha$  precipitates have a needlelike morphology, the electron beam was astigmatized to an ellipsoidal shape during  $\alpha$  phase analysis to minimize sampling of the surrounding  $\beta$  matrix. It is likely, however, that some corruption of the signal occurred and that the  $\beta$  matrix results are more accurate than those for the  $\alpha$  phase. The results (Table III), which are averages of multiple spectra, indicate that the  $\alpha$  precipitate in PA Ti-15-3 is depleted of  $\beta$  stabilizing elements and enriched with Al while the  $\beta$  phase is enriched with V and Cr and depleted of Al. Thus, grade 6 Ti is an approximate model of the  $\alpha$  precipitates within PA Ti-15-3.

Electrochemistry samples were polished to a 600 grit finish followed by degreasing in acetone. The testing apparatus comprised 1 cm<sup>2</sup> area of the working electrode exposed in a flat cell containing a platinized niobium mesh counterelectrode and an SCE situated in a separate well possessing a Luggin capillary.

Polarization measurements were performed with either a Princeton Applied Research (PAR) 173 or PAR 273 potentiostat at a scan rate of 0.05 mV/s. All polarization experiments were performed following exposure to solution for 2 h at open circuit.

Each electrochemical impedance spectroscopy (EIS) experiment comprised ten individual impedance scans. An initial scan was conducted at the open-circuit potential followed by nine scans at 300 mV intervals from -0.3 to 2.1 V vs. SCE. Each scan was preceded by a 2 h potentiostatic hold at the given potential, except the open-circuit potential scan which was preceded by 2 h at open circuit. EIS measurements were performed with a Solartron 1286 electrochemical interface and a Model 1255 frequency response analyzer. A 10 mV rms ac voltage signal was applied at frequencies between 100 kHz and 5 mHz using potentiostatic control. Impedance data fitting was performed with complex nonlinear least squares (CNLS) circuit fitting software.<sup>19</sup>

Electrochemical tests were performed on the materials using six different room temperature solutions. These were

0.6M NaCl, 0.6M NaCl adjusted to pH 1 with HCl, and 5M HCl, each in the aerated and deaerated condition. 0.6M NaCl solutions comprised reagent grade NaCl added to distilled deionized water. Solutions were adjusted to pH 1 with reagent grade HCl. 5M HCl comprised reagent grade HCl and distilled deionized water. The pH of 5M HCl is calculated to be -1.64 when the effect of Cl<sup>-</sup> on the activity of H<sup>+</sup> is incorporated into the calculation.<sup>20</sup> Deaeration was performed with commercially pure Ar gas. 0.6M NaCl solution was utilized to model alloy behavior when exposed to the bulk solution in a marine environment. The 0.6M NaCl pH 1 was utilized to discern the behavior of the alloys in a simulated crack tip environment. Although a crack tip solution and its pH has yet to be isolated, 0.6M NaCl pH 1 is considered to be a rough estimate of that solution. Beck<sup>21</sup> has reported that a pH < 1.3 was found next to a corroding Ti pit exposed to neutral chloride solution.<sup>22</sup> Others have reported pH 1.7 at a crack tip for a Ti-8 Al-1 Mo-1 V alloy.<sup>23</sup> 5M HCl was used to analyze material behavior under extremely acidic conditions that perhaps are more severe than a crack tip environment.

Sample surfaces were prepared for Auger electron spectroscopy (AES) in the manner stated above. EIS was then performed on each sample in 0.6M NaCl pH 1 as described above, with the final potential at 1.5 V vs. SCE. Samples were removed from the cell and rinsed in distilled deionized water. AES was performed on a Perkin Elmer PHI 600 system using a 5 keV beam operated at 0.54  $\mu$ A. Sputter depth profiling was performed with a 3 keV Ar<sup>+</sup> ion beam. The particular Auger electron transition energies used for analysis for each element were selected at Auger energies as close as possible to each other for different elements to obtain comparable escape depths. The Auger transition energies used were Ti<sub>LMM</sub>-418 eV, O<sub>KLL</sub>-503 eV, V<sub>LMM</sub>-473 eV, Cr<sub>LMM</sub>-529 eV, and Al<sub>KLL</sub>-1396 eV.

X-ray photoelectron spectroscopy (XPS) was performed on a Kratos XSAM800 using an Mg x-ray source operated at 13 kV and 20 mA, perpendicular to the sample surface. Samples were potentiostatically held at -0.6 V vs. SCE in 0.6M NaCl pH 1 and the surfaces mechanically abraded with SiC paper, thereby allowing the oxides to reform at -0.6 V. Samples were rinsed in distilled water on removal from the cell. Peaks used for analysis were as follows: Ti-2p<sup>3/2</sup>, O-1s, V-2p<sup>3/2</sup>, Cr-2p<sup>3/2</sup>, Sn-3d<sup>5/2</sup>, and Al-2p. Reference to the C 1s signal was used to account for specimen charging.

### Results and Discussion

**Electrochemistry and passivity in 0.6M NaCl pH 1.—Electrochemistry.**—The anodic polarization behaviors of all alloys in aerated 0.6M NaCl pH 1 are displayed in Fig. 1. All the alloys display a large potential independent region,

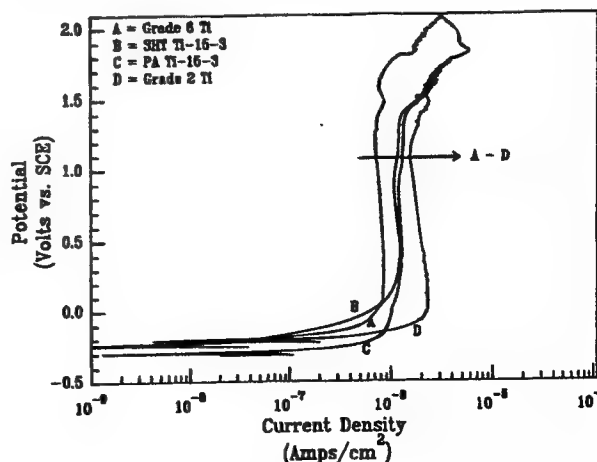


Fig. 1. Representative anodic polarization scans for the four titanium alloys examined in one particular solution (aerated 0.6M NaCl pH 1).

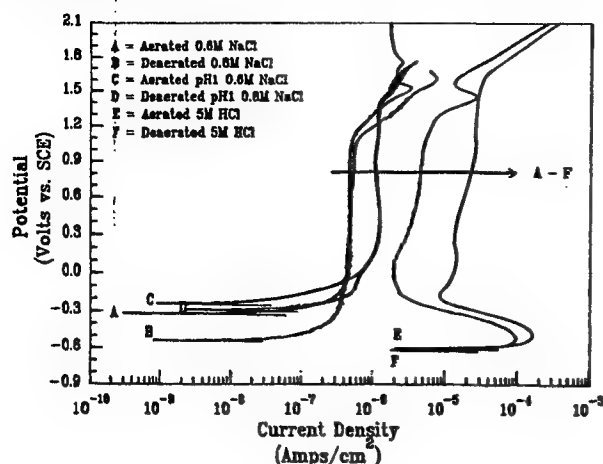


Fig. 2. Representative anodic polarization scans for SHT Ti-15-3 in the six chloride-containing solutions.

indicative of passivity, terminated by a region comprising a significant increase in current density. This increase is not due to the onset of pitting, but rather due to the commencement of oxygen evolution. This has been confirmed by optical microscopy, as well as by others, who have stated that pitting is not observed in room temperature chloride solutions until +9 V is reached.<sup>21</sup> Moreover, the decrease in current density observed above 1.9 V vs. SCE for grade 2 Ti (Fig. 1) may be attributed to a decreasing rate of the oxygen evolution reaction due to increased difficulty in electron tunneling through the thickening passive film. This phenomenon has been observed for all the alloys, albeit at different potentials. No distinct increases in anodic current density are observed at potentials corresponding to the thermodynamic oxidation potentials of alloying additions. Moreover, the passive current densities of the four alloys are all small, with the largest approaching  $2 \times 10^{-6}$  A/cm<sup>2</sup>. Additionally, the open-circuit potentials of the alloys are all similar, although they were somewhat variable ( $\pm 200$  mV), as observed by others.<sup>24,25</sup> This indicates that there is little galvanic coupling between  $\alpha$  precipitates and the  $\beta$  matrix in PA Ti-15-3, assuming that grade 6 Ti approximates the composition of  $\alpha$  precipitates found in the  $\beta$  matrix. Further, there is no discernible difference between the passive electrochemical behaviors of SHT and PA Ti-15-3, implying that the  $\alpha$  precipitates have little effect on the anodic behavior of Ti-15-3. Therefore, the overall steady-state passive behavior of the V and Cr-stabilized  $\beta$ -titanium alloys appears to be identical to both commercially pure grade 2 and grade 6  $\alpha$ -titanium alloys. This suggests that the passive films on these alloys may be similar.

The anodic polarization behavior of SHT Ti-15-3 in 0.6M NaCl, 0.6M NaCl adjusted to pH 1 with HCl, and 5M HCl is seen in Fig. 2. The alloy is spontaneously passive and passivity is suggested at the open-circuit potential. The passive current density increases with decreasing pH, as is expected due to increased aggressiveness. Little effect of aeration on the anodic passive electrochemical behavior is observed in the NaCl experiments. This has been observed previously by others in abrasion experiments.<sup>24</sup> Anodic polarization in 5M HCl revealed an active/passive transition and that Ti-15-3 had a lower passive current density in aerated than in deaerated solution. Polarization results were reproducible in 5M HCl as seen in Fig. 3. The peak current density for PA Ti-15-3 in 5M HCl ( $3 \times 10^{-4}$  A/cm<sup>2</sup>), the most aggressive solution examined, is approximately 1 to 5 orders of magnitude too low to account solely for observed crack growth rates ( $1.5 \times 10^{-6}$  to  $4 \times 10^{-2}$  mm/s) through a dissolution-based mechanism.<sup>9</sup> It may be possible that the presence of other species (e.g., TiCl<sub>3</sub>) may promote increased dissolution, however, it is unlikely that additional species increase the dissolution rate above that in

5M HCl by enough to account for the observed crack growth rates. A current density of greater than 35 A/cm<sup>2</sup> is required to support the highest observed crack growth rates.<sup>9</sup> Therefore, we conclude that highly localized mechanical destabilization of the passive film is required for EAC of these alloys even after crack tip cation hydrolysis and acidification, regardless of the exact mechanism of EAC.

**In situ characterization of passivity.**—To characterize the passive layers of the alloys further, EIS experiments were performed. Figures 4a and b include impedance spectra of PA Ti-15-3 exposed to aerated 0.6M NaCl pH 1 at different potentials ranging from open circuit to 2.1 V vs. SCE. The electrochemical impedance responses of the alloys displayed two time constant behavior, as seen in Fig. 4 and 5. The impedance behavior of a passive titanium electrochemical interface exposed to aqueous solution may be modeled by the circuit model seen in Fig. 6. The proposed circuit model features a solution resistance and two parallel RC combinations, each in series. One time constant is attributed to the oxide resistance ( $R_{ox}$ )/capacitance ( $C_{ox}$ ) parallel combination across the oxide and the second is attributed to the charge-transfer resistance ( $R_{ct}$ )/double-layer capacitance ( $C_{dl}$ ) parallel combination. Constant phase elements were used to account for the nonidealities of the capacitive elements. The higher frequency time constant was assumed to originate from the  $R_{ox}/C_{ox}$  combination while the low frequency time constant was assumed to arise from the  $R_{ct}/C_{dl}$  combination. Two distinct time constants are observed in Fig. 5a, as opposed to Fig. 5b wherein the time constants are overlapping. Utilizing commercial software,<sup>19</sup> excellent correspondence between the model and the data is obtained, as seen in Fig. 5. To confirm that the high frequency time constant was attributable to the oxide, comparison with an ellipsometric study of titanium exposed to 0.1M HCl<sup>27</sup> was undertaken. A grade 2 Ti sample was prepared in the identical manner<sup>27</sup> to that in the previous study. An impedance spectrum was then acquired at 0, 2, 4, 6, and 8 V vs. NHE to facilitate comparison with the literature. Utilizing the computer fit value for  $C_{ox}$  and a dielectric constant of 100, we see that good correspondence was obtained for the oxide thickness (Fig. 7). Each oxide thickness represents an average of three separate experiments. The slight offset between the oxide thicknesses may be attributed to the value used for the dielectric constant, over which there is some controversy. This confirmed that the high frequency time constant was attributable to the oxide. Further, Fig. 4 and 5 reveal that  $R_{ct}$  is much larger than  $R_{ox}$ , especially at lower potentials. Hence, the rate-determining step in the passive electrochemical dissolution of Ti-15-3 is the charge-transfer reaction. However, the details of this process (e.g., controlling interface, anion or cation transport, etc.) are unclear. Further, it is observed that  $R_{ct}$  increases with increasing potential until 1.2 V is

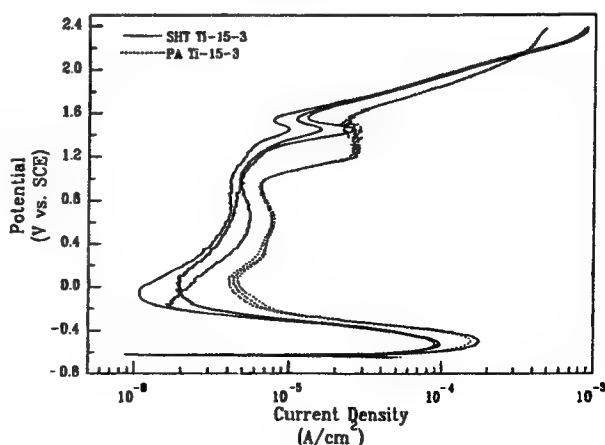


Fig. 3. Replicate anodic polarization scans in aerated 5M HCl displaying the reproducibility of anodic polarization experiments.

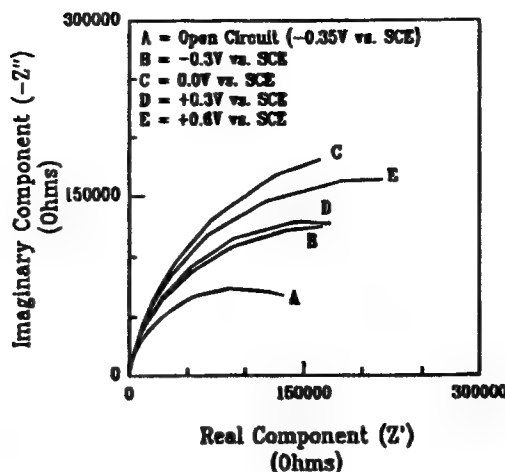
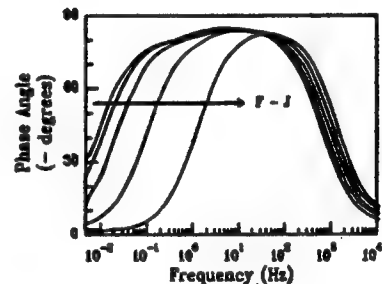
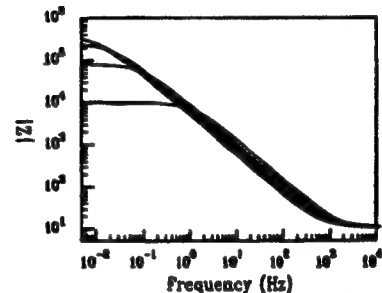
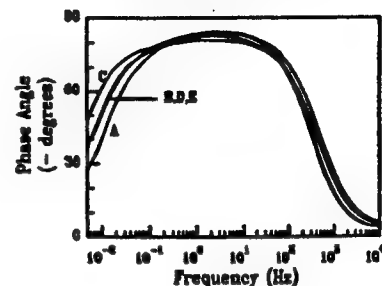
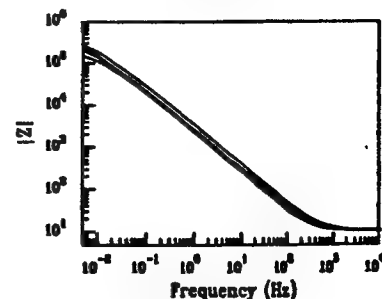
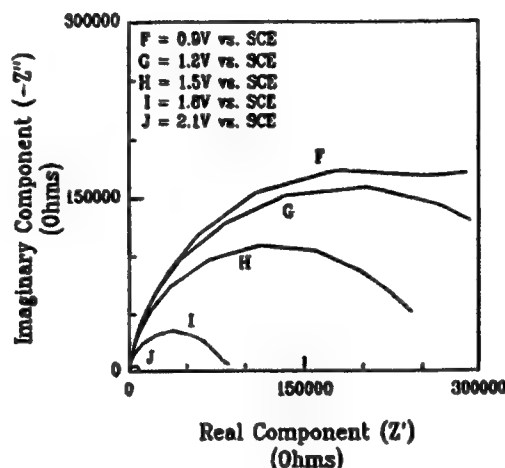


Fig. 4. (a, top) Electrochemical impedance response of PA Ti-15-3 exposed to aerated 0.6M NaCl pH 1 at potentials ranging from open circuit to 0.6 V vs. SCE. (b, bottom) Electrochemical impedance response of PA Ti-15-3 exposed to aerated 0.6M NaCl pH 1 at potentials ranging from 0.9 to 2.1 V vs. SCE.



reached (Fig. 4), followed by a marked decrease above 1.2 V. This decrease corresponds to the onset of the oxygen evolution reaction, as discussed earlier, and is in agreement with polarization data.

Apparent oxide thickness and resistivity were calculated from the parameters obtained by circuit fitting. The oxide thickness may be calculated by using the equation

$$d_{ox} = \frac{\epsilon \epsilon_0 A}{C_{ox}} \quad [1]$$

where  $d_{ox}$  is the oxide thickness,  $C_{ox}$  is the oxide capacitance,  $\epsilon$  is the dielectric constant of the oxide,  $\epsilon_0$  is the permittivity of free space, and  $A$  is the surface area. The apparent oxide resistivity may be calculated as follows, assuming that oxide resistance varies linearly with thickness. From Eq. 1

$$\frac{A}{d_{ox}} = \frac{C_{ox}}{\epsilon \epsilon_0} \quad [2]$$

Assuming that

$$\rho_{ox} = R_{ox} \left( \frac{A}{d_{ox}} \right) \quad [3]$$

and, substituting Eq. 2 into Eq. 3, the following equation is obtained

$$\rho_{ox} = \frac{R_{ox} C_{ox}}{\epsilon \epsilon_0} \quad [4]$$

Equation 4 provides an indication of apparent oxide resistivity without explicit determination of oxide thickness.

Figures 8 and 9 show plots of the oxide thicknesses and apparent resistivities, respectively, in aerated 0.6M NaCl pH 1. The error bars show the standard deviation from six replicate tests. All calculations assume a dielectric constant of 100 for all four alloys. The oxide thicknesses increased linearly with potential for all the materials in all the solutions. The oxide thicknesses and oxide growth rates (vs. potential) of the Ti-15-3 alloys are lower than those of the  $\alpha$  alloys in 0.6M NaCl pH 1. The oxide growth rate found for grade 2 Ti exposed to 0.6M NaCl pH 1 is the same (23 Å/V) as found for commercially pure titanium exposed to 0.1M HCl.<sup>27</sup> The apparent oxide resistivity on all the alloys decreases with increasing potential, indicating that an increasingly defective oxide exists at higher potentials. The resistivities of the four alloys were generally within experimental variability. Handbook values<sup>28</sup> for bulk TiO<sub>2</sub> resistivity are in the range of 10<sup>11</sup> to 10<sup>16</sup> Ω-m, while calculated values from the experiments here yield values in the 10<sup>7</sup> to 10<sup>10</sup> range, depending on potential. This discrepancy may be because a 10 to 50 Å oxide grown in solution is more defective than a bulk three-dimensional oxide, the oxide incorporates alloying additions, the oxide is hydrated, or

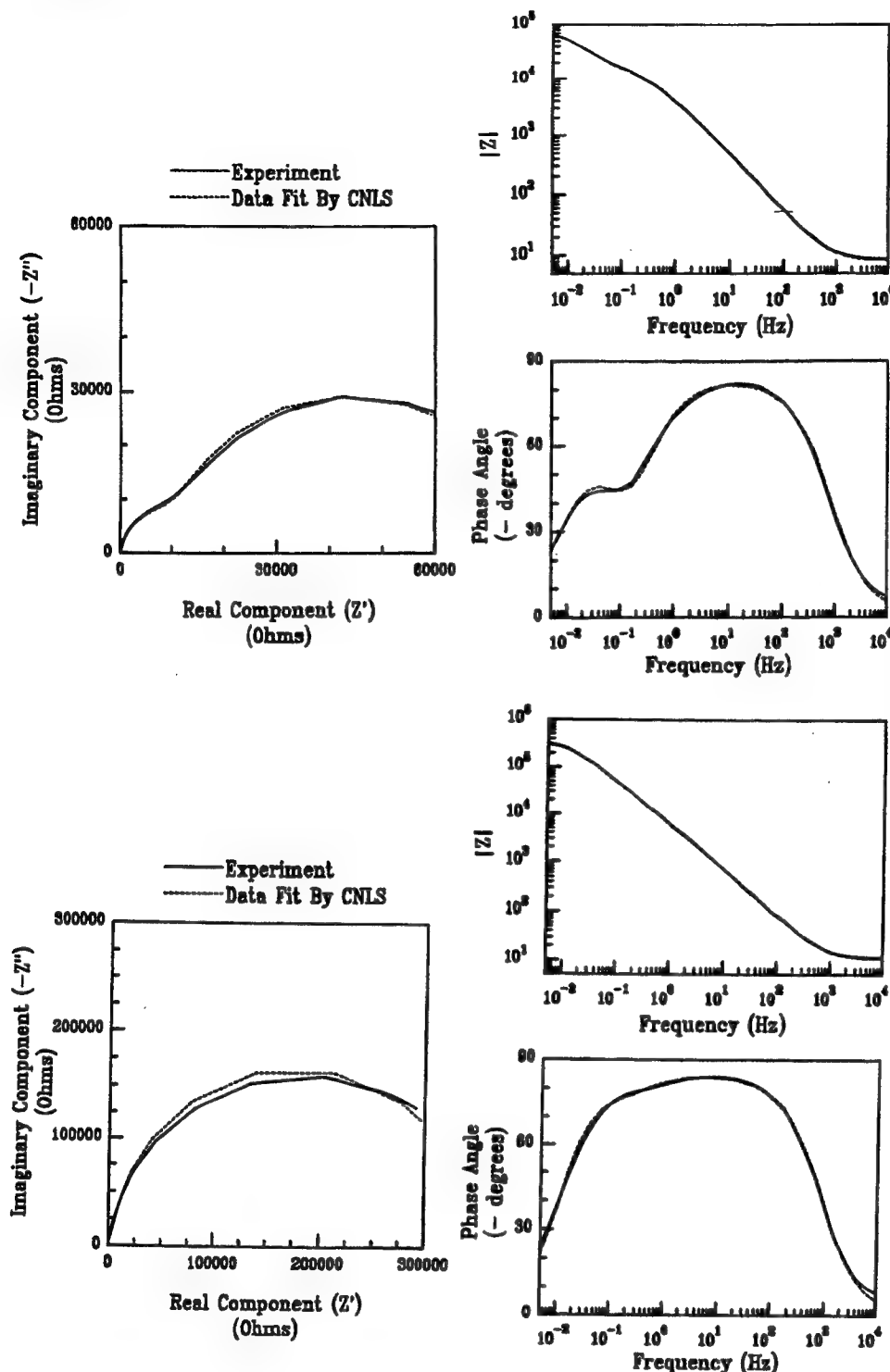


Fig. 5 (a, top) Comparison of experimental data (SHT Ti-15-3, 0.6M NaCl pH 1,  $E = 1.2 V_{SCE}$ ) to that obtained by data fitting with CNLS fitting software<sup>19</sup> using the circuit model shown in Fig. 6. (b, bottom) Comparison of experimental data from Fig. 4b (PA Ti-15-3, 0.6M NaCl pH 1,  $E = 1.2 V_{SCE}$ ) to that obtained by data fitting with CNLS fitting software<sup>19</sup> using the circuit model shown in Fig. 6.

the oxide has incorporated chloride ions from solution. Tomashov *et al.* have expressed a similar viewpoint in their review of the passivity of a broad range of Ti based alloys.<sup>13</sup> The relative ranking of magnitudes of oxide thickness, growth rate, and apparent resistivity varied between solutions. As before, the passive electrochemical behaviors of the V/Cr  $\beta$ -stabilized alloy is similar to that of both of the  $\alpha$ -titanium alloys, indicating that the oxide formation and growth mechanism may be similar.

The current density arising from oxygen evolution on the passive film is dependent on the oxide resistance. The resistance is proportional to its thickness, which increases with increasing potential, and its resistivity, which decreases with potential. Therefore, as the potential is increased, the oxygen evolution reaction commences and ceases as the film properties change and offset one another. Small variations in these oxide properties change the magnitude of

oxygen evolution observed on the passive film, as seen in replicate testing of SHT Ti-15-3 (Fig. 3).

**Ex situ characterization of passivity.**—Both dc and ac experiments reveal similar passive electrochemical behaviors of SHT and PA Ti-15-3, grade 2 Ti, and grade 6 Ti. Because the compositions and microstructures of the four alloys are dissimilar, we hypothesized that the oxides on these alloys were comparable. To investigate the oxide compositions, AES was employed. Both SHT Ti-15-3 and grade 2 Ti samples were polarized to 1.5 V vs. SCE with impedance spectra acquired at 300 mV intervals so that the oxide examined by AES after sample removal from the electrochemical cell experienced the same history as in the dc and ac experiments discussed earlier. The experiments were performed in 0.6M NaCl pH 1, which is less aggressive than the 5M HCl but more aggressive than the 0.6M NaCl. Using a dielectric constant of 100, the thickness of the oxide on the grade 2 sample was determined from impedance



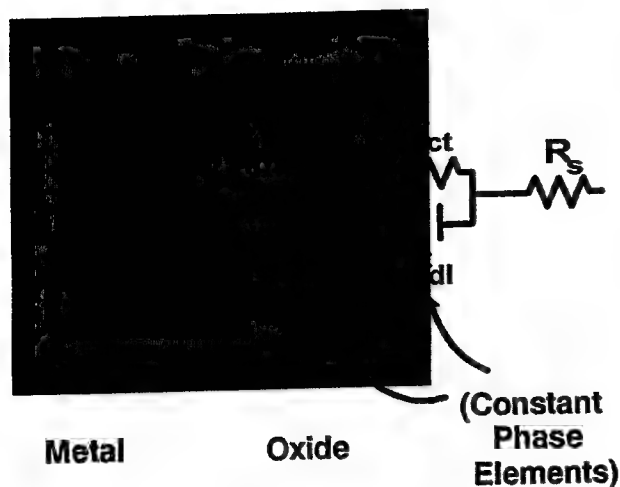


Fig. 6. Proposed circuit model for a passive titanium surface exposed to an aqueous solution.

spectra. This oxide was used as a standard to determine the sputter rate of the  $\text{Ar}^+$  beam, assuming a constant sputter rate, with the oxide thickness being taken as the thickness at which the concentration of oxygen is one half its maximum achieved at the surface.

The sputter depth profile of the oxide on SHT Ti-15-3 is displayed in Fig. 10. No Na or Cl was discerned in the oxide and an Sn spectrum was not acquired due to significant peak overlap with other elements. The passive film is rich in Ti and O at an approximate composition of  $\text{TiO}_2$ . The concentration of Al is low but close to its concentration in the bulk alloy. The oxide is V poor and Cr rich, with Cr segregating to the oxide/solution interface. V-depleted oxides on  $\alpha/\beta$  alloys have been observed by others.<sup>29,30</sup> However, the overall concentration of alloying additions within the passive film is less than that in the bulk alloy, and the outer layer of oxide is primarily  $\text{TiO}_2$ . This finding suggests that the comparable passive electrochemical behaviors of the alloys may be due to the similarities of the oxides on these alloys. Additionally, a good correlation of oxide thickness was obtained between calculations from EIS measurements and AES sputter depth profiling.

The oxide film at a crack tip may be destabilized and reformed in solution. Therefore, an oxide that had been formed in solution instead of in air was examined. Additionally, the oxides on SHT and PA Ti-15-3 were compared with that of grade 2 Ti. Samples were potentiostatically held at  $-0.6$  V vs. SCE and abraded with SiC paper, allowing the oxide to reform in solution. *Ex situ* XPS was then performed. Table IV contains the energies of the photoelectron peaks obtained, the corresponding handbook values

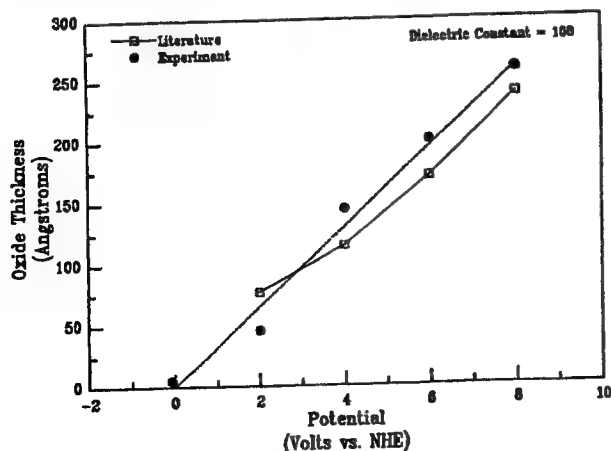


Fig. 7. Comparison of oxide thicknesses on grade 2 Ti as a function of applied potential to that found in the literature.<sup>27</sup> Each thickness is an average of three individual experiments.

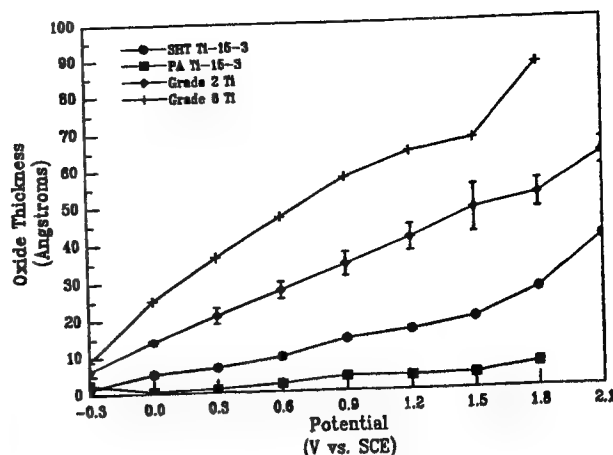


Fig. 8. Relationship between oxide thicknesses and potential for SHT and PA Ti-15-3, grade 2 Ti and grade 6 Ti exposed to aerated 0.6M NaCl pH 1. A dielectric constant of 100 was assumed.

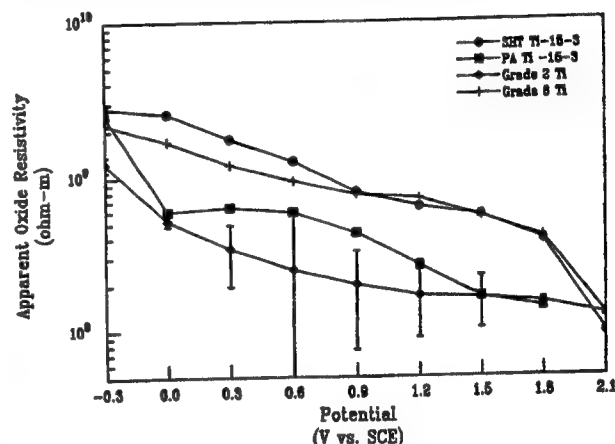


Fig. 9. Relationship between apparent oxide resistivities and potential for SHT and PA Ti-15-3, grade 2 Ti and grade 6 Ti exposed to aerated 0.6M NaCl pH 1. A dielectric constant of 100 was assumed.

for the oxides assigned to these peaks,<sup>31</sup> and the formation potentials for the oxides over a range of potentials,<sup>32</sup> since the surface pH on mechanical destabilization of the oxide film is not known.

The oxides on SHT and PA Ti-15-3 were nearly identical. All the oxides were predominantly  $\text{TiO}_2$ , with small amounts of  $\text{Al}_2\text{O}_3$  and oxidized V. Trace amounts of  $\text{SnO}_2$  or  $\text{SnO}$  were detected, but similarities in binding energies and a low signal-to-noise ratio make differentiation difficult. No binding energy is listed for Sn within the SHT Ti-15-3 oxide because the peak was too small and broad to obtain

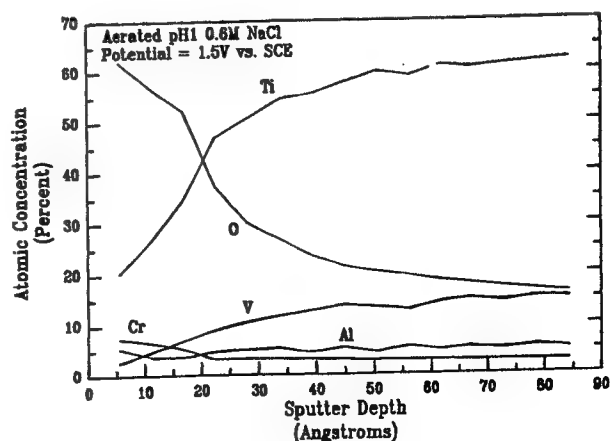


Fig. 10. AES sputter depth profile of SHT Ti-15-3 exposed to aerated 0.6M NaCl pH 1.

Table IV. Binding energies obtained from XPS experiments after abrasion (0.6M NaCl pH 1, -0.6 V vs. SCE), handbook values for the binding energies of the metal oxides,<sup>31</sup> and the corresponding formation potential of the oxides at two different pH.<sup>32</sup>

|  | Ti 2p <sup>3/2</sup><br>TiO <sub>2</sub> | V 2p <sup>3/2</sup> | Al 2p<br>Al <sub>2</sub> O <sub>3</sub> | Sn 3d <sup>5/2</sup> |
|--|--|---------------------|---|----------------------|
| Grade 2 Ti                                   | 458.5                                    | n/a                 | n/a                                     | n/a                  |
| SHT Ti-15-3                                  | 458.8                                    | 516.1               | 74.3                                    | —                    |
| PA Ti-15-3                                   | 459.0                                    | 515.9               | 74.3                                    | 486.1                |
| Handbook <sup>31</sup>                       | 458.5                                    | —                   | 74.7                                    | —                    |
| Minimum formation potential (V vs. SCE) pH 1 | -0.889                                   | —                   | -2.022 <sup>a</sup>                     | —                    |
| pH 8   | -1.303                                   | —                   | -2.264                                  | —                    |

<sup>a</sup>-Al → Al<sup>3+</sup> + 3e<sup>-</sup> reaction, assuming [Al<sup>3+</sup>] = 10<sup>-6</sup>M.

a binding energy with a high degree of accuracy. A broad binding energy peak for V appears to indicate the presence of multiple oxidation states of V within the oxide, as seen by others on  $\alpha/\beta$  alloys.<sup>30,33</sup> Because of the uncertainty of the valence state of both Sn and V within the oxide, the handbook values for these oxides are not given. No Cr peak was detected, indicating that <0.1 a/o is present. This is in contrast to the +1.5 V vs. SCE air formed oxide which contained elevated concentrations of Cr. Although exact concentrations could not be computed, the relative concentrations of alloying additions within the passive films on both SHT and PA Ti-15-3 were nearly identical. This again indicates that the similar passive behaviors of the materials observed during both dc and ac experiments may be attributable to the analogous oxide compositions on the alloys.

**Electrochemistry and passivity in 0.6M NaCl solutions.—***Electrochemistry and in situ characterization passivity.*—To examine the performance of metastable  $\beta$ -titanium alloys exposed to bulk seawater, 0.6M NaCl solutions were used. Polarization curves for grade 2 Ti, grade 6 Ti, and SHT and PA Ti-15-3 exposed to aerated 0.6M NaCl (Fig. 11) reveal that the passive current densities for the four materials are lower than in the solution adjusted to pH 1, ranging from  $3 \times 10^{-7}$  to  $5 \times 10^{-7}$  A/cm<sup>2</sup>. This was confirmed by impedance measurements wherein the charge-transfer resistances which dominate the polarization resistance and, hence, the passive current density, were higher. Good correlation between the proposed circuit model and the impedance spectra was obtained. As in the pH 1 solutions, there was little difference between the behavior of the alloys, and no difference between aerated and deaerated solutions was discerned. The open-circuit potentials of all

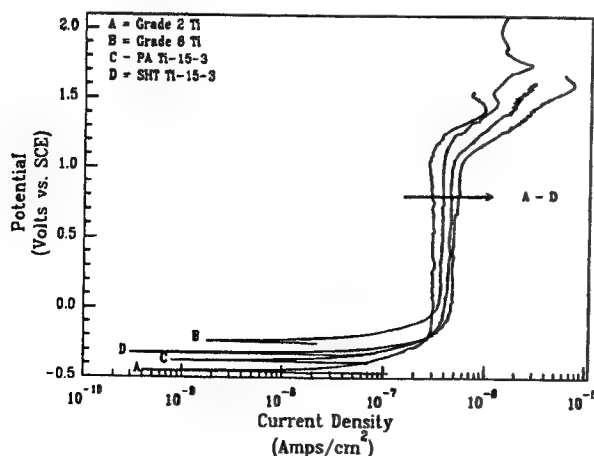


Fig. 11. Anodic polarization scans for SHT and PA Ti-15-3, grade 2 Ti, and grade 6 Ti in aerated 0.6M NaCl.

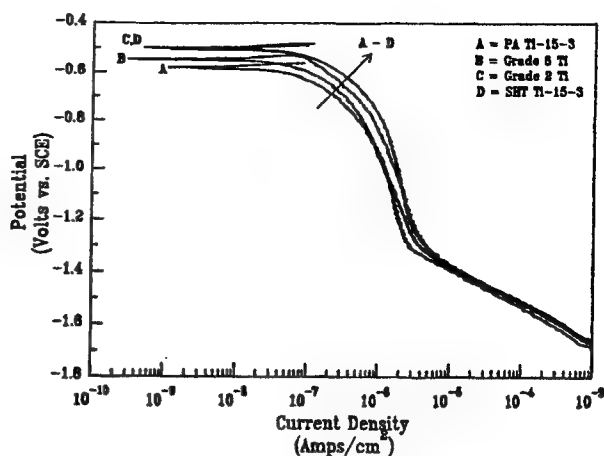


Fig. 12. Cathodic polarization scans for SHT and PA Ti-15-3, grade 2 Ti, and grade 6 Ti exposed to 0.6M NaCl.

four alloys are close, again indicating that there is little galvanic interaction between the  $\alpha$  precipitates and the  $\beta$  matrix in the PA material. No pitting was observed on the titanium alloys up to 1.7 V vs. SCE, the increase in anodic current density above 1.0 V being attributed to oxygen evolution. As before, this was confirmed by both optical microscopy and EIS measurements. Oxide thicknesses increased linearly with potential and apparent oxide resistivities decreased with potential, as observed in pH 1 adjusted solutions.

Little difference between the passive electrochemical behaviors of the metastable  $\beta$ -titanium alloys and the  $\alpha$ -titanium alloys was observed. To confirm further that the comparable behaviors were attributable to similarity of oxides, the exchange current densities for the hydrogen evolution reaction on the oxides were examined. If large percentages of alloying additions were present in the passive film, changes in exchange current density may be expected. Exchange current densities were obtained from cathodic polarization experiments (Fig. 12) by extrapolation of the Tafel plot to the reversible potential for hydrogen evolution. The exchange current densities for all the materials were low ( $2.0 \times 10^{-10}$  to  $5.7 \times 10^{-10}$  A/cm<sup>2</sup>) and within experimental error in replicate testing. Exchange current densities for grade 2 titanium and grade 6 titanium are higher than reported earlier<sup>34</sup> and represent increased precision as a result of replicate testing. The exchange current densities for V and Cr are known to be approximately 2 orders of magnitude greater<sup>35</sup> than those observed here. This indicates that the oxides are dominated by TiO<sub>2</sub>, and may account for the similar behaviors observed from dc and ac experiments.

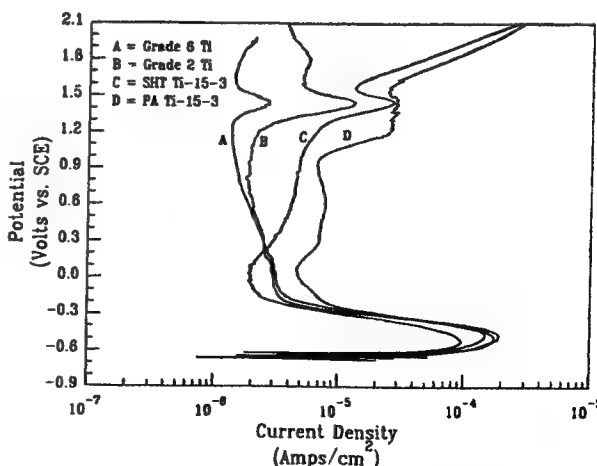


Fig. 13. Anodic polarization scans for SHT and PA Ti-15-3, grade 2 Ti, and grade 6 Ti in aerated 5M HCl.



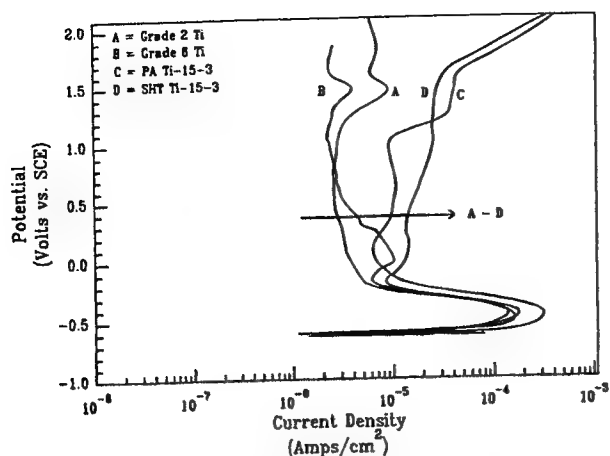


Fig. 14. Anodic polarization scans for SHT and PA Ti-15-3, grade 2 Ti, and grade 6 Ti in deaerated 5M HCl.

*Electrochemistry and passivity in 5M HCl solutions.—Electrochemistry and in situ characterization of passivity.—Anodic polarization tests for the titanium alloys ex-*

posed to aerated 5M HCl may be seen in Fig. 13. All the materials examined were active/passive in aerated 5M HCl. This was confirmed by replicate tests (Fig. 3). Others have observed an active/passive transition for commercially pure Ti in 5M HCl<sup>36</sup> but not in 0.1M HCl.<sup>27</sup> The more active open-circuit potentials enable the observation of the active/passive transition. Ti-15-3 showed the greatest passive current density, consistent with pH 1 NaCl (Fig. 1) and neutral NaCl (Fig. 11) experiments. Similar experiments performed in deaerated 5M HCl (Fig. 14) reveal that an active/passive transition occurs on all the alloys. Previous research has observed an active/passive transition on other  $\beta$ -titanium alloys (Ti-13 V-11 Cr-3 Al) in 20% HCl (6.5M), albeit at 35°C.<sup>14</sup> A transition also was observed in 5% HCl (1.6M) at 65°C.<sup>14</sup> As seen previously, the open-circuit potentials of all the materials are nearly identical, indicating little thermodynamic driving force for galvanic coupling between the matrix and precipitates in the PA material. Unlike that seen for Mo and Nb-stabilized  $\beta$ -titanium alloys,<sup>34</sup> the impedance spectra reveal distinct two time constant behavior (Fig. 15a and b) and correlate well with the proposed circuit model, indicating that an oxide is present in 5M HCl. Although the materials are active on

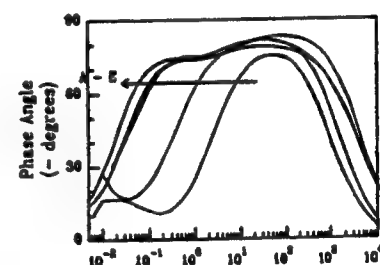
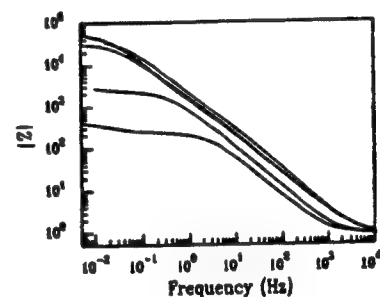
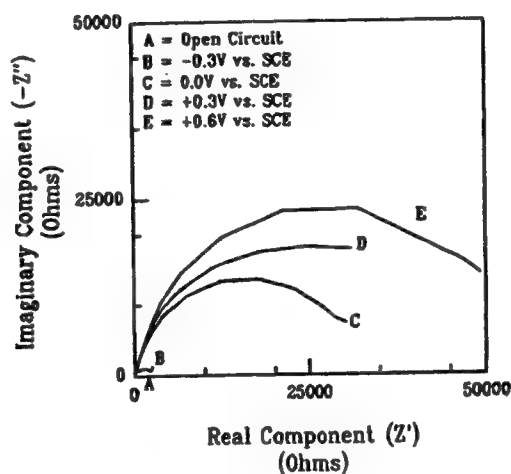
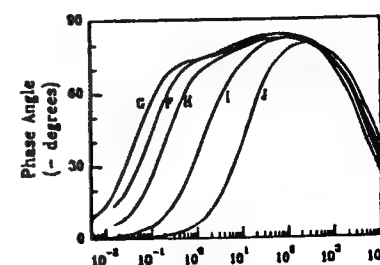
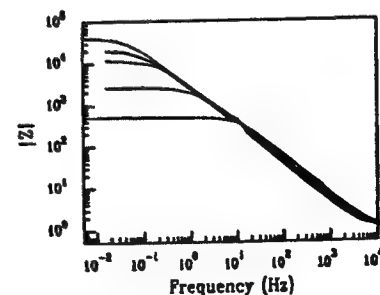
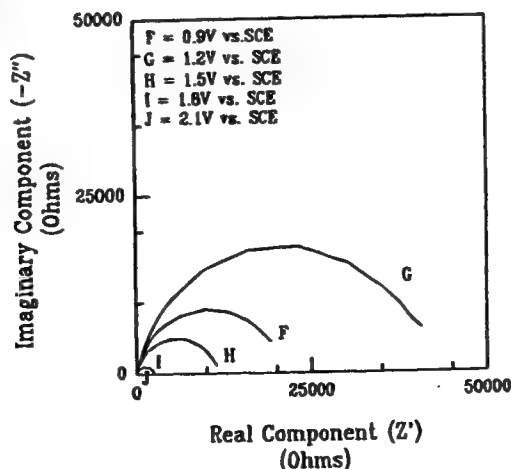


Fig. 15. (a, top) Electrochemical impedance response of SHT Ti-15-3 exposed to aerated 5M HCl at potentials ranging from open circuit to 0.6 V vs. SCE. (b, bottom) Electrochemical impedance response of SHT Ti-15-3 exposed to aerated 5M HCl at potentials ranging from 0.9 to 2.1 V vs. SCE.



anodic polarization over a wide potential range (hundreds of millivolts), this does not imply that an oxide is not present. Other researchers have stated that even in the active region, dissolution is strongly inhibited by an oxide which apparently can exist metastably even in strong acid solution.<sup>37</sup> Beck hypothesized that steady-state dissolution may proceed through oxide formation and dissolution steps.<sup>37</sup> Others have noted that in the active region, a porous film of  $\text{Ti}_2\text{O}_3$  is present.<sup>38</sup>

Both the  $\beta$  matrix and the  $\alpha$  precipitates in PA Ti-15-3 were active in deaerated 5M HCl, unlike that observed for Mo/Nb stabilized  $\beta$ -titanium alloys wherein the  $\beta$  matrix was passive.<sup>34</sup> Although the preferential precipitation of  $\alpha$  phase along the  $\beta$  grain boundaries in Ti-15-3 may provide a low resistance path for dissolution-controlled crack growth,<sup>9</sup> galvanic coupling of the  $\alpha$  precipitates to the  $\beta$  matrix appears to be an unlikely mechanism. Moreover, as stated earlier, the measured peak current densities for the materials in 5M HCl, the most aggressive solution examined, are too low to account solely for crack growth rates observed.<sup>9</sup> Therefore, we conclude that highly localized mechanical destabilization of the passive film is required for EAC of these alloys, regardless of the exact mechanism of EAC.

### Conclusion

Examination of the passivity of Ti-15-3 exposed to a range of room temperature solutions bracketing crack tip chemistries possible in marine environments was undertaken as an initial step in elucidating the EAC mechanism of a V/Cr containing metastable  $\beta$ -titanium alloy in seawater. No major electrochemical differences were observed between SHT Ti-15-3, PA Ti-15-3, commercially pure (grade 2) Ti, and grade 6 Ti, which approximate the composition of the  $\alpha$  precipitates present in PA Ti-15-3. Similar open-circuit potentials between grade 6 Ti and the  $\beta$ -titanium alloys indicate that little galvanic coupling occurs between the  $\alpha$  precipitates and the  $\beta$  matrix in the PA alloy. All the alloys were spontaneously passive in all the NaCl solutions examined, as confirmed by EIS, and no pitting was observed on these alloys up to 1.7 V vs. SCE. However, active/passive transitions were observed on all four materials in 5M HCl. Ti-15-3 and grade 6 Ti oxide thicknesses increased linearly with potential, as found with commercially pure grade 2 Ti, suggesting comparable oxide growth mechanisms. Similar passive electrochemical behaviors among the four alloys are explained by the fact that the oxides on these materials are quite close in composition. *Ex situ* AES sputter depth profiles show that the oxide on SHT Ti-15-3 is predominantly  $\text{TiO}_2$  and contains less than stoichiometric concentrations of alloying additions. *Ex situ* XPS tests indicate little difference between the oxides on SHT and PA Ti-15-3. Oxide similarity was confirmed by comparable hydrogen evolution kinetics. The peak dissolution rates of the  $\beta$ -titanium alloys were too low to account solely for EAC. Therefore, mechanical destabilization of the passive film is required to obtain observed crack growth rates, even after crack tip cation hydrolysis and acidification, regardless of the exact mechanism of EAC.

### Acknowledgments

The authors acknowledge the Office of Naval Research and the Virginia Center for Innovative Technology for their support of this work. The authors also thank Titanium Metals Corporation for their generous donation of alloys. The authors recognize R. Bayles and the Naval Research Laboratory for help with AES experiments, S. McCartney and Virginia Polytechnic Institute for help with XPS experiments, K. Lawless for his TEM work, and L. Young, G. Young, and R. P. Gangloff for helpful discussions.

Manuscript submitted Jan. 24, 1994; revised manuscript received May 25, 1994. This was Paper 144 presented at the Toronto, ON, Canada, Meeting of the Society, Oct. 11-16, 1992.

University of Virginia assisted in meeting the publication costs of this article.

### REFERENCES

1. *Titanium and Its Alloys*, Titanium Development Association, Boulder, CO (1992).
2. J. S. Grauman, in *Proceedings, Seventh World Conference on Titanium*, S. H. Froes, Editor, Vol. 3, p. 2209, TMS-AIME, Warrendale, PA (1993).
3. P. J. Bania, G. A. Lenning, and J. A. Hall, *Beta Titanium Alloys in the 80's*, R. R. Boyer and H. W. Rosenberg, Editors, TMS-AIME, Warrendale, PA p. 209 (1984).
4. L. M. Hartman and R. P. Gangloff, in *Proceedings, Seventh World Conference on Titanium*, S. H. Froes, Editor, Vol. 3, p. 2737, TMS-AIME, Warrendale, PA (1993).
5. D. N. Williams, *J. Inst. Met.*, **91**, 147 (1962-63).
6. H. G. Nelson, in *First Thermal Structures Conference*, E. Thornton, Editor, p. 301, University of Virginia, Charlottesville, VA (1990).
7. A. D. McQuillan, *Proc. R. Soc. London, Ser. A*, **204**, 309 (1950).
8. T. R. Beck, *Corrosion*, **30**, 408 (1974).
9. L. M. Young, Master's Thesis, University of Virginia, Charlottesville, VA (1993).
10. G. A. Young, Jr., Master's Thesis, University of Virginia, Charlottesville, VA (1993).
11. W. Kinna and W. Knorr, *Z. Metallk.*, **47**, 594 (1956).
12. O. Kubaschewski and B. E. Hopkins, *Oxidation of Metals and Alloys*, p. 215, Butterworth and Co., Ltd., London (1962).
13. N. D. Tomashov, G. P. Chernova, Y. S. Ruscol, and G. A. Ayuyan, *Electrochim. Acta*, **19**, 159 (1974).
14. M. Levy and G. N. Sklover, *This Journal*, **116**, 323 (1969).
15. W. F. Czyszkli and M. Levy, *Corrosion*, **32**, 99 (1974).
16. R. W. Schutz and J. S. Grauman, in *Industrial Applications of Titanium and Zirconium: Fourth Volume, ASTM STP 917*, C. S. Young and J. C. Durham, Editors, p. 130, American Society for Testing and Materials, Philadelphia (1986).
17. *Metals Handbook*, 8th ed., Vol. 8, American Society for Metals, Metals Park, OH (1973).
18. E. W. Collings, *Physical Metallurgy of Ti Alloys*, p. 70, ASM International, Metals Park, OH (1984).
19. J. R. MacDonald, Complex Nonlinear Least Squares Imittance Fitting Program, University of North Carolina, Chapel Hill, NC, Version 3.02.
20. P. O. Gartland, SINTEF publication STF16-A88085, Trondheim, Norway (1988).
21. T. R. Beck, in *Localized Corrosion*, V. R. Evans and R. W. Staehle, Editors, p. 644, NACE, Houston, TX (1974).
22. R. W. Powers and J. F. Wilfore, in *Fundamentals of Electrochemical Machining*, C. L. Faust, Editor, p. 135, The Electrochemical Society, Inc., Princeton, NJ (1971).
23. B. F. Brown, C. T. Fujii, and E. P. Dahlberg, *This Journal*, **116**, 218 (1969).
24. J. R. Ambrose and J. Kruger, *ibid.*, **121**, 599 (1974).
25. T. R. Beck, *ibid.*, **114**, 551 (1967).
26. N. D. Tomashov and L. P. Vershinina, *Electrochim. Acta*, **15**, 501 (1970).
27. T. Ohtsuka, M. Masuda, and N. Sato, *This Journal*, **132**, 787 (1985).
28. *Handbook of Chemistry and Physics*, 64th ed., R. C. Weast, p. E-55, Chemical Rubber Publishing Co., Boca Raton, FL (1983-4).
29. P. A. Mäusli, S. G. Steinemann, and J. P. Simpson, in *Proceedings of the Sixth World Conference on Titanium*, P. Lacombe, R. Tricot, and G. Béranger, Editors, p. 1759, TMS-AIME, Warrendale, PA (1988).
30. R. Sodhi, A. Weninger, J. E. Davies, and K. Sreenivas, *J. Vac. Sci. Technol.*, **A9**, 1329 (1991).
31. J. F. Moulder, W. F. Stickle, P. E. Sobol, and K. D. Bomben, *Handbook of X-Ray Photoelectron Spectroscopy*, Elmer Corp., Eden Prairie, MN (1992).
32. M. Pourbaix, *Atlas of Electrochemical Equilibria in Aqueous Solutions*, 2nd ed., NACE, Houston, TX (1974).
33. M. Ask, J. Lausmaa, and B. Kasemo, *Appl. Surf. Sci.*, **35**, 283 (1989).
34. D. G. Kolman and J. R. Scully, *This Journal*, **140**, 2771 (1993).
35. A. Bélanger and A. K. Vijh, *ibid.*, **121**, 225 (1974).
36. A. Caprani and J. P. Frayret, *Electrochim. Acta*, **24**, 835 (1979).
37. T. R. Beck, *ibid.*, **18**, 815 (1973).
38. H. Kaesche, *Metallic Corrosion*, p. 265, NACE, Houston, TX (1985).

**LIMITATIONS OF POTENTIOSTATIC REPASSIVATION TECHNIQUES  
AND THEIR RELATIONSHIP TO THE APPLICABILITY OF  
THE HIGH FIELD APPROXIMATION TO THE REPASSIVATION  
OF TITANIUM**

**David G. Kolman  
John R. Scully**

Submitted to *Journal of the Electrochemical Society*, October 1994.

Limitations of Potentiostatic Repassivation Techniques and  
Their Relationship to the Applicability of the  
High Field Approximation to the Repassivation of Titanium

D.G. Kolman and J.R. Scully

Center for Electrochemical Science and Engineering  
Department of Materials Science  
University of Virginia  
Charlottesville, VA 22903

Abstract

Bare surface and repassivation kinetics are critical to the understanding of environmental cracking of titanium. A variety of potentiostatic repassivation techniques have been utilized by previous researchers to obtain this information. However, the apparent repassivation kinetics are a function of depassivation speed, solution resistance, potentiostat response, etc. The effect of each of these limitations on repassivation behavior is examined. The applicability of the high field approximation to potentiostatic repassivation tests in chloride solutions is also discussed. It was found that the above experimental limitations, as well as a significant difference between the total measured current and the oxide formation current (due to anodic dissolution), render the high field approximation to oxide growth an ineffective model of the current decay observed on titanium and explains the wide range of high field parameters that have been reported in the literature for this material.

## Introduction

The kinetics of repassivation is critical to understanding the mechanisms of environmentally assisted cracking (EAC)<sup>1-3</sup>. Unfortunately, the high rate of repassivation<sup>4-6</sup> of many metals makes the acquisition of the rapid current decay due to film growth difficult. A variety of methods<sup>7</sup> have been employed in order to obtain the kinetic information required for the evaluation of EAC models, often with limited results. Potentiostatic methods are desirable in order to predict material behavior at different potentials. These methods are also attractive because the current decay with time can be modelled through use of the high field approximation<sup>8</sup>. Unfortunately, the rate of oxide removal, potentiostat and reference electrode response time, inaccuracy in solution resistance ( $R_s$ ) and bared area determination<sup>9</sup>, and capacitive current from the adjacent electrode surface exposed to solution<sup>10</sup> are just some of the many errors that may influence and/or invalidate potentiostatic repassivation results. It is the object of this work to delineate the requirements for valid repassivation data acquisition, through comparison of thin film fracture experiments and manual scratch testing techniques on titanium exposed to 0.6M NaCl, and to evaluate the effectiveness of the high field approximation as a model for repassivation kinetics. While this is not the first attempt to explain artifacts in repassivation data<sup>6,10,11</sup>, it is the only attempt that comprehensively examines these issues for the case of titanium repassivation.

## Experimental Procedure

The experimental procedure for manual scratch testing was similar to that of others<sup>10</sup>. Manual scratch testing comprised commercially pure grade 2 Ti mounted flush in epoxy so that a 0.09 cm x 0.6 cm rectangular area was exposed to solution. Electrical connection was made through the back of the sample, opposite to the side exposed in solution. The sample was coated with a thin layer of vacuum grease to minimize capacitive current arising from the oxide adjacent the scratch<sup>10</sup>. Capacitive charging/discharging current from the surrounding oxide has been shown to alter the current response during potentiostatic testing<sup>10</sup>. A diamond tipped glass marker was utilized to scratch through both the vacuum grease and underlying titanium. Samples were examined with an optical microscope to ensure that no vacuum grease contaminated the scratched region. A Mitutoyo SurfTest 401

surface profilometer was utilized to determine the scratch area. The amount of area bared in a typical experiment was obtained by the averaging of many separate scratch tests.

Thin film fracture samples comprised a 500 nm thick titanium layer evaporated onto a glass substrate. A 200 nm thick layer of insulating  $\text{SiO}_2$  was sputter deposited on top of the titanium to prevent capacitive current<sup>6,10</sup> flowing to the freshly bared titanium surface from its surrounding oxide. The samples were 1 cm in width, yielding an exposed area of  $5 \times 10^{-5} \text{ cm}^2$  upon fracture. The samples were scored on the glass side of the sample and mounted in the cell (Figure 1). The samples were fractured by impressing a rotary acrylic breaker onto the bottom of the sample. This method was found to be more satisfactory than guillotining the sample, resulting in far less cell vibration and solution mixing.

Both scratch testing and thin film experiments incorporated a saturated calomel reference electrode (SCE) and a platinized niobium mesh counter electrode. The reference electrode was placed away from the newly exposed metal to allow calculation of the solution resistance, using an approach which assumes that the reference electrode is placed infinitely far from the exposed area<sup>9</sup>. It is not practical to place the reference electrode (or a Luggin capillary) close to the narrow scratch (approximately 50  $\mu\text{m}$  wide) to reduce the solution resistance and associated ohmic drop, because this would likely lead to screening of the working electrode.

Samples were held potentiostatically with a Princeton Applied Research (PAR) 273 potentiostat. Surface potential and repassivation current were measured with either an Hewlett Packard 54600A oscilloscope (thin film experiments, 500 ns/data pt.) and/or 7090A measurement plotting system (thin film and scratch tests, 100 $\mu\text{s}$ /data pt). The potential and current signals were sampled through their respective analog outputs on the potentiostat.

Solution resistance calculations were confirmed both through a) current interrupt measurements using a PAR 273 potentiostat and b) through electrochemical impedance spectroscopy (EIS) measurements performed with a Solartron 1286 electrochemical interface and 1255 frequency response analyzer.

0.6M NaCl solutions ( $\kappa = 0.052 (\Omega\text{-cm})^{-1}$ ) incorporating reagent grade NaCl added to distilled, deionized, 18 M $\Omega$  water were utilized in the experiments reported here.

## Results

### *Ohmic Loss in Solution*

A comparison of current transients ( $E_{\text{applied}} = 0V_{\text{SCE}}$ , 0.6M NaCl) observed during potentiostatic scratch and fractured thin film repassivation experiments are seen in Figure 2. The peak current density observed for the fractured thin film test is seen to be approximately 50 times that for the scratch test. The peak current density was assumed to occur at 0.25  $\mu$ s for plotting purposes. The observed current densities fall below those required for salt film production<sup>12</sup> at any time and thus do not appear to be limited by mass transport.

The true surface potential of each sample can be calculated by correcting for ohmic drop in solution. Assuming the bared area is of rectangular cross-section and the reference electrode is positioned an infinite distance from the bared area, solution resistance may be calculated by<sup>9</sup>

$$R_s = \left( \frac{1}{2 \pi \kappa b} \right) \ln \left( \frac{4b}{a} \right) \quad (1)$$

where  $R_s$  is the solution resistance (ohms),  $\kappa$  is the solution conductivity (ohm-cm)<sup>-1</sup>,  $a$  is half the bare electrode width (cm), and  $b$  is half the bare electrode length (cm). In order to utilize this equation for scratch testing, two issues must first be addressed - 1) acquisition of the true bare surface area and 2) its relation to a rectangular cross-section geometry. For scratch tests, the scratch width was found by averaging many surface profilometry measurements. The scratch did not have a rectangular cross-section but rather a triangular cross-section (Figure 3a), with mounding along the scratch edges resulting from plastic flow of the material. The scratch width was assumed to be the path length between the mound tops. In order to utilize equation 1, the scratch cross-section was assumed to be rectangular with the bared path length across the scratch equal to the width of the assumed rectangular geometry (Figure 3b). The bared area for fracture experiments was assumed to be the cross-sectional area of titanium on the substrate (i.e., a perfectly brittle fracture straight across the sample was assumed). Both EIS and current interrupt methods were used to confirm solution resistance calculations (Table 1). Excellent agreement was observed between the calculated values and those determined experimentally. The surface potentials

for the experiments in Figure 2, corrected for  $IR_s$ , are shown in Figure 4.

### *Potentiostat Response*

Potentiostat response time may further alter the surface potential. Figure 5 shows the current and potential response resulting from a fracture test ( $E_{\text{applied}} = 0V_{\text{SCE}}$ ). Upon fracture, there is a loss of potentiostatic control for roughly the first 5  $\mu\text{s}$  (utilizing either 10 mA, 1 mA, or 100  $\mu\text{A}$  current measuring resistors) with the PAR 273 potentiostat. This occurs because there is a change in the current required to maintain a constant applied potential when the bare electrode is created. The potentiostat is unable to supply current fast enough to maintain the applied potential. Thus, the surface potential for the fracture test can be further corrected for loss of potentiostatic control, as seen in Figure 4. Identical potentiostat response time was observed during tests utilizing resistors as dummy cells. (The capacitances of the 100  $\Omega$  - 10 k $\Omega$  resistors was approximately 10 pF and thus did not significantly affect the tests.) In these tests, a voltage step was applied to a test resistor. Current could not be supplied fast enough to result in an instantaneous shift in potential to the applied voltage, similar to that seen in electrochemical testing. It is unclear whether the peak current density is affected by the lack of instantaneous potentiostat response. It is likely, however, that the early portion of a current transient (i.e., the initial decay behavior) is affected by both the finite rise time of the potentiostat and the changing  $IR_s$  drop in solution. Numerous investigators have attached significance to the length of the plateau, as well as the magnitude of the peak current. Models have been developed<sup>13</sup> and used<sup>14-16</sup> which attribute the plateau length to the time required for the formation of the initial monolayer of oxide. Clearly, experimental artifacts may affect the length and magnitude (current) of the plateau and any resulting attempts at modelling repassivation and, hence, EAC.

### *Reference Electrode Response*

It was not initially understood whether the SCE reference electrode, which has a high impedance, affected the potentiostat response as well. Previous researchers<sup>17-21</sup> have discussed the applicability of SCEs to transient methods and have found that the reference electrode may be a source of error during potentiodynamic (voltage step and EIS) testing. Low solution resistance ( $\leq 330\Omega$ ) and the absence of a Luggin capillary have been correlated



with reduced corruption by artifacts<sup>17,20</sup>. (The present work does not incorporate a large  $R_s$  or a Luggin capillary for this reason.) However, the effect of the SCE on a resulting current transient during potentiostatic testing is unclear. It was found in this study that the response time of the SCE added no additional limitations to potentiostatic testing. That is, the response time of the electrode in electrochemical testing was within the response time of the potentiostat observed with the dummy cell. Tests utilizing a bare chloridized silver wire (Ag/AgCl) reference electrode revealed similar potential and current response but with greater instability with respect to cell vibration resulting from fracture.

While many limitations of reference electrode response have been delineated for AC work<sup>17,20</sup>, it was initially unclear how this related to potentiostatic repassivation experiments because the amplitudes of the AC currents at specific frequencies which sum to produce the thin film transient were unknown. Thus, a fourier transform of the thin film transient seen in Figure 2 was undertaken. It was found that greater than 80% of the signal energy arises from the 0-100 kHz regime and greater than 50% arises from the 0-16 kHz regime. Therefore, it appears that higher frequency components (100 kHz - 1 MHz), which would be most susceptible to artifactual corruption from the potentiostat or reference electrode, play little role in determining the transient morphology. It may be argued, however, that this reasoning is circular because it is possible that high frequency components that might be present without corruption are not present in the data due to signal corruption. An intuitive argument can be made in favor of the hypothesis that the majority of the signal energy originates from lower frequencies. Because the majority of the signal is a large positive peak over approximately 100  $\mu$ s (Figure 5), it is apparent that a series of low frequency AC signals (1-10 kHz) could roughly approximate the peak. In combination with the reference electrode response discussed above, this argument (although not definitive) suggests that the reference electrode is not severely affecting thin film fracture tests.

#### *Lead Wire Inductance*

Corruption of the transient due to changing applied potential arising from lead wire inductance was also considered. Using an estimate of 1  $\mu$ H for the lead inductance and a rate of change of current of 1000 A/s, the lead inductance contribution is 1 mV. Thus, inductance in the lead wires appears to have little affect on the potential during thin film fracture tests.

### *Depassivation Rate*

Recently, repassivation experiments have been performed on fractured thin films in order to produce bare metal as quickly as possible<sup>4-6</sup>. Rapid depassivation is favorable because a slow rate of depassivation (such as by scratching) dramatically influences repassivation experiments. This is illustrated in scratch testing experiments wherein depassivation rate is relatively slow. The stylus is scratched across the titanium sample at roughly 1 m/s. Thus, across a 0.09 cm sample, significant repassivation has occurred at the start of the scratch by the time the end of the scratch length is reached, 0.9 ms later. The current that is measured will be an average along the scratch, which is far lower than if the entire scratch was bared at one time (Figure 6). This ignores the additional galvanic and capacitive current effects between the more noble oxide covered regions at the scratch start and the active bare metal at the scratch end. This effect has not been accounted for even in previous studies of coupled oxide effects<sup>10</sup>. The current in Figure 6 was calculated by assuming logarithmic current decay (slope of -1 on  $\log i$  vs.  $\log t$ ) in each of 1000 independent sections along the scratch. The bare surface current density was taken to be the average maximum current density observed from thin film fracture experiments (at  $0V_{SCE}$ ) with the current density decay originating from this maximum at  $5 \times 10^{-6}s$ .

### *Factors Limiting the Bare Surface Polarization Curve*

Figure 7 compares bare polarization curves generated by potentiostatic repassivation tests at various potentials<sup>22</sup> to those calculated assuming the tests are ohmically limited. Thin film data represent the average of the peak current density from at least two tests at a given applied potential. Scratch data represent the maximum current density observed from multiple tests at a given applied potential. The bare surface open circuit potentials were found to be slightly different for the thin film and scratch tests<sup>22</sup> and were taken to be  $-1.3V_{SCE}$  for the scratch tests and  $-1.6V_{SCE}$  for the thin film experiments.

The observed peak currents fall below the respective ohmic limits for both the scratch tests and the fracture tests (Figure 7). However, scratch tests have the additional limitation of an approximately 0.9 ms depassivation speed. If it is assumed that the peak bare surface current density from scratch tests is equal to the peak current density obtained from fracture tests and that the measured current is limited by scratch speed as in Figure

6, the scratch speed limited polarization curve can be calculated for a variety of corresponding applied potentials. Some error is introduced because the true surface potential of the thin film and scratch are actually different following depassivation (Figure 4), even though the applied potentials are the same. However, good correspondence between the calculated scratch speed limited curve and the data is observed. Thus, peak current densities from scratch tests are indicative of the material behavior only under the particular ohmic and depassivation limitations of the test. They may not be indicative of material behavior at a crack tip, for instance, where the depassivation rate, solution resistance, and area depassivated are likely far different.

As discussed above, the region of steep slope in the fractured thin film bare surface polarization curve is neither ohmically limited nor depassivation speed limited. It is possible that this region is not influenced by experimental limitations and thus is indicative of the true bare surface response. Such a steep slope may be explained by an activationless reaction<sup>23</sup>. This will be a topic of discussion in future work<sup>22</sup>.

### *Charge Density*

The high field approximation of measured current density - time transients pertains to oxide thickening only. All current passed that does not go towards oxide thickening will produce error when applying the high field model. Previous research<sup>24,25</sup> has indicated that a large majority of the charge passed following depassivation of titanium exposed to chloride environments goes towards dissolution. Research in this laboratory indicates that at least 90% of the charge passed goes into solution ( $\text{Ti} \rightarrow \text{Ti}^{3+} + 3\text{e}^-$ ) and not into oxide formation ( $\text{Ti} + 2 \text{H}_2\text{O} \rightarrow \text{TiO}_2 + 4\text{H}^+ + 4\text{e}^-$ ). This was determined by integration of the current - time transient (such as that of Figure 2) followed by comparison to the charge required to reform an oxide layer consisting of  $\text{TiO}_2$  of a certain thickness. This thickness was determined by EIS which has been shown to correspond well to other thickness determination methods<sup>26,27</sup>. For example, the total charge density passed following thin film fracture in Figure 2 (measured up to 0.03s) was found to be  $27.5 \text{ mC/cm}^2$ . The total charge density required for oxide formation is  $1.7 \text{ mC/cm}^2$ , assuming a  $10 \text{ \AA}$  oxide thickness<sup>26,27</sup>,  $5.2 \text{ \AA}$  monolayer thickness<sup>28</sup>, and  $3.4 \text{ g/cm}^3$  oxide density<sup>28</sup>. Therefore, the large majority of charge goes toward dissolution of titanium and not into barrier oxide formation. The calculated total charge density is actually an underestimate of the true total charge density

because it neither incorporates unaccounted charge from cathodic current supplied by the bare surface nor data after 30 ms. Thus, the true charge density passed following depassivation is actually greater. The significance of the large percentage of charge going towards dissolution and not oxide thickening is discussed below.

## Discussion

### *High Field Approximation*

Knowledge of the repassivation behavior of a material is often required in order to fully explain EAC phenomena<sup>1</sup>. Repassivation experiments usually comprise potentiostatic testing, wherein the passive film is removed and the current decay observed. However, fast repassivation rate and initially large current densities present a barrier to data acquisition for numerous reasons. All of the problems arising from the large and rapidly changing current density must be mitigated to obtain valid data. Only then can modelling of the data using the high field model (or any other model) be considered.

Repassivation or, more specifically, oxide thickening of titanium and other valve metals has been assumed to be governed by high field oxide growth<sup>11,14-16,29-31</sup>. Cabrera and Mott modelled high field growth through the relation<sup>8</sup>

$$\frac{dX}{dt} = u \exp\left(\frac{X_1}{X}\right) \quad (2)$$

where  $X$  is the oxide thickness,  $t$  is time,  $u$  is a pre-exponential term incorporating various material parameters, and  $X_1 = B \cdot V$  where  $B$  is the inverse field coefficient (cm/V) and  $V$  is the voltage drop across the film. This equation is an approximation that is only valid for  $X \ll X_1$ , i.e. when the field is so strong that ionic motion is overwhelmingly in one direction. Additionally, the equation applies to oxide thickening such that it is only valid after the first monolayer has formed. The high field approximation offers no explanation for the current density plateau discussed above. Assuming that all charge passed goes towards barrier oxide formation,

$$X = \left( \frac{M}{n F \rho} \right) q = A q \quad \therefore \quad \frac{dX}{dt} = A \frac{dq}{dt} = A i \quad (3)$$

where  $q$  is charge density ( $\text{C}/\text{cm}^2$ ),  $n$  is the number of electrons transferred,  $F$  is Faraday's constant,  $\rho$  is density ( $\text{g}/\text{cm}^3$ ),  $M$  is atomic weight ( $\text{g}/\text{mol}$ ),  $A$  is a constant equal to  $M/nF\rho$  ( $\text{cm}^3/\text{C}$ ), and  $i$  is current density ( $\text{A}/\text{cm}^2$ ). Thus, the relation

$$i = \frac{u}{A} \exp\left(\frac{BV}{X}\right) = i_0 \exp\left(\frac{BV}{X}\right) \quad (4)$$

is obtained, where  $i_0$  represents a pre-exponential constant ( $\text{A}/\text{cm}^2$ ). This the form of the empirically derived equation first proposed by Günterschulze et al.<sup>32</sup>

Equation 4 can be manipulated<sup>14,29</sup> (Appendix A) to produce the differential current density - time relationship

$$dt = - \left( \frac{B V}{i_0 A} \right) \frac{d\left(\frac{i}{i_0}\right)}{\left(\frac{i}{i_0} \cdot \ln\left(\frac{i}{i_0}\right)\right)^2} \quad (5)$$

The solution for the integral has no closed form. Approximations to the solution have been thoroughly discussed in various references<sup>11,14,29,33-35</sup>, although the approximations may, in some cases, incorporate significant error. Equation 5 is easily integrated numerically by computer, assuming that the pre-exponential term  $i_0$  is known *a priori*<sup>11</sup>. If instead it is desirable to fit experimental data in order to obtain parameters such as  $i_0$  and  $B$ , a fit can be obtained through an iterative fitting technique. Iterative fitting is cumbersome, however, even utilizing a computer, requiring numerical integration for each iteration. Therefore, the approximation<sup>11</sup>

$$t = \frac{\left(\frac{BV}{A}\right)}{i \left(\ln\left(\frac{i}{i_0}\right)\right)^2} \quad (6)$$

may be useful, as this may be utilized with commercially available fitting software. Unfortunately, this may incorporate some error into the calculation<sup>11</sup>. A comparison of equation 6 vs. numerical integration of equation 5 is seen in Figure 8.

Although a variety of approximations to the high field approximation have been used to model the repassivation of titanium<sup>11,14,29</sup>, the applicability of the high field model is questionable for several reasons. One reason is the lack of a constant potential drop across the film at a given potential. It has been hypothesized that thickening of the titanium oxide film is controlled by the outward migration of cations, taking advantage of interstitial sites<sup>36</sup>. The voltage drop across the film has been written as<sup>37,38</sup>

$$V = E - E_g \quad (7)$$

where  $E$  is the true surface potential and  $E_g$  is a voltage roughly equal to the reversible potential for oxide formation. The true surface potential changes with time, as shown in Figure 4. Also,  $E_g$  has been shown not to be constant, however, but a function of the film thickening charge and current densities<sup>37</sup>. Thus, for a given applied, the voltage drop across the oxide film will vary. In order to determine  $E_g$  (and thus  $V$ ), the charge and current densities attributable to film thickening must be accurately known. Unfortunately, at early times, these charge and current densities cannot be measured accurately, due to finite depassivation speed (discussed in the ensuing section), potentiostat rise time, a large portion of the charge going towards dissolution instead of oxide formation (discussed below), cathodic current provided by the bare surface which cannot be measured, etc. Therefore, it is difficult to accurately obtain  $E_g$ , especially at early times. The potential drop across the film ( $V$ ) is varying with time due to varying ohmic loss in solution (affecting  $E$ ), potentiostat control (also affecting  $E$ ), and  $E_g$ . Unless  $V$  can be accurately determined, high field modelling of the current response at short times following depassivation may be ineffective.

The high field approximation of measured current density - time transients pertains

to oxide thickening only. Because over 90% of all current passed does not go towards oxide formation, significant error will occur when applying the high field model. Other researchers<sup>14-16</sup> have attempted to model the contributions of initial oxide monolayer current, the dissolution current and the oxide thickening current during titanium repassivation, with the oxide thickening current accounting for the roughly logarithmic current decay. This model is flawed for numerous reasons. Foremost is the fact that the current decay portion of the transient cannot be modelled with only a contribution from oxide thickening, i.e., dissolution current must be incorporated. The modelling also relies on fitting of numerous parameters to the data set without independent confirmation. Additionally, the data is significantly flawed due to very slow depassivation speed (6 cm/s)<sup>14-16</sup>. Thus it is apparent that the high field approximation is invalid for use in the titanium / chloride solution system and that models incorporating the high field approximation to account for measured current decay upon repassivation are erroneous.

Because such a large percentage of the charge goes towards dissolution, the majority of the total current must be dissolution current over the entire length of the transient. A result of the high field approximation is that the slope of the current transient on the  $\log i - \log t$  plot (Figure 2) must be between 0 and -1<sup>11</sup>. However, titanium repassivation transients observed both in the literature<sup>29</sup> and in the current work show slopes steeper than -1. It has been shown that, theoretically, slopes steeper than -1 can be generated in systems that experience  $IR_s$  loss in solution<sup>11</sup>. The diagnostics utilized to examine  $IR_s$  loss rely upon the utilization of the high field approximation<sup>11</sup>, which appears to be invalid for the titanium / chloride system. Moreover, the diagnostics were tested on data<sup>14-16</sup> that were clearly flawed by an extremely slow depassivation speed. This explains why the obtained inverse field coefficient resulted in "a value too small to be accounted for by the conventional interpretation of the parameter"<sup>11</sup>. The current research has shown that there is a slope steeper than -1 over all but the very end of the fracture transient seen in Figure 2. There is no fundamental reason why the slope cannot be steeper than -1 when the majority of the charge goes into dissolution, even though the magnitude of the dissolution current is related to the oxide thickness. Thus, the utility of the high field approximation for modelling titanium exposed to chloride solutions is questionable, unless the total current density can be evaluated to determine the contribution of the current from oxide growth. To the co-authors' knowledge, only a limited number of investigators have attempted to discriminate oxide current from total current in real time<sup>25</sup>.

### *Depassivation Speed*

Depassivation speed affects not only the peak current density, but the subsequent current density decay as well. The current density of the scratch experiment is 50% greater than that of the fractured thin film at  $3 \times 10^{-3}$ s (Figure 2). Other experiments have shown scratch current densities over one order of magnitude greater than that of the fractured thin film at a given time<sup>22</sup>. A similar phenomenon has been observed by others<sup>12</sup>, wherein a fractured titanium wire was observed to have a higher initial current density and current decay originating from an earlier time than that of a larger area fractured titanium rod which was more severely ohmically limited. Because the current density decay commences at an earlier time, the thin film experiment has a lower current density than that of the scratch test at later times. Thus, the sample geometry, solution resistance, method of depassivation, etc. all contribute to the morphology of the current transient. This generates difficulty in data comparison from differing methods. The utility of the high field approximation is thus questioned, because a slow rate of depassivation or a lower ohmic limit delays the onset of repassivation and shifts the current transient out to longer times on the  $\log i - \log t$  plot. This may account for some of the variability in high field constants reported in the literature (Table 2).

### *Data Acquisition Speed*

Data acquisition speed may be critical to evaluation of repassivation data as well. The peak current density is usually a parameter of interest. However, previous researchers have used acquisition rates in the ms regime. It is clear from Figure 2, for example, that this acquisition rate would result in the conclusion that the peak current density of the thin film fracture test was below that of the scratch tests. Therefore, a data acquisition rate should be chosen that ensures that the morphology of the transient is captured. It is important to evaluate not only the repassivation behavior but the depassivation behavior as well so that the effect of depassivation rate may be fully evaluated.

### *Surface Wetting*

The finite rise time for the current transient in Figure 5 appears to result from the finite response time of the potentiostat, as discussed above. It may be possible, however,



that the time for surface wetting influences the rise time or, more likely, the morphology of the current transient. Utilizing a simple estimate, Beck concluded that the time for cavitation bubble collapse was  $5 \times 10^{-5}$  s following fracture of a titanium rod<sup>39</sup>. This could not be confirmed because this time was less than the data acquisition rate used for the fractured rod experiments. A value of  $5 \times 10^{-5}$  s appears unlikely in light of the fractured thin film experiments performed here and elsewhere<sup>4,6</sup>, wherein repassivation is observed in the  $< 10^{-5}$  s regime. The true value is unknown. Calculation of the time required for surface wetting may not be so simple, as the hydrodynamics following fracture are poorly defined. Moreover, the hydrodynamics themselves may influence the observed current transient, as well. Both scratch testing and thin film fracture tests result in a highly disturbed solution at the interface. Whether the enhanced mass transport significantly affects the current transient measurement is unclear. (Recall that dissolution is not shown to be mass transport limited.) Therefore, in addition to the various factors discussed above, both surface wetting speed and solution stirring may possibly influence early time data following depassivation.

In summary, the numerous limitations in repassivation studies discussed above contribute to the wide range of high field parameters obtained for titanium. In addition to these limitations, other variables such as monolayer density and thickness have been widely reported (Table 2). These differences also add to the variability of high field parameters reported in the literature. Thus, it is not surprising that the high field parameters have been reported over a wide range, albeit in different environments. However, differences in aqueous environment have been shown to have little or no effect on repassivation behavior of titanium<sup>22,39</sup>. Therefore, the high field approximation appears to be an ineffective model of the current transient observed upon repassivation of titanium in aqueous chloride environments.

It is clear from the prior discussion that a variety of limitations must be overcome in order to produce reliable data from potentiostatic repassivation experiments. An ideal repassivation experiment should consider the following:

- The speed of depassivation must not influence the measurement. For many metals, including titanium, there is no potential at which bare metal is stable upon exposure to an aqueous environment<sup>43</sup>. Thus, stepping the potential from a region below the reversible potential for oxide formation to a region above the reversible potential in order to observe repassivation behavior<sup>7</sup> is impossible. Therefore, fresh surface must be produced

mechanically. If too low, the rate of mechanical production of fresh surface, i.e. depassivation speed, can result in erroneously low bare current densities, as seen in scratch testing.

- The exposed area must be accurately quantified in order to calculate current density. Knowledge of the exposed area geometry is important for solution resistance calculation as well. The solution resistance should be experimentally verified as well.
- The bare surface current must remain below the ohmic limit (preferably far below the ohmic limit), and the influence of potential drop in solution accounted for in the calculation of the true surface potential. Changes in total exposed area and area geometry are often the most fruitful in reducing solution resistance.
- The effects of potentiostat rise time should be minimized if at all possible. Calculation of the true surface potential can be further modified by accounting for the finite rise time of the applied potential.
- The reference electrode must not influence the measurement.
- A data acquisition rate should be chosen that allows thorough analysis of not only the repassivation current but of the depassivation event as well.
- Capacitive current from areas adjacent the bare surface should be eliminated.
- The effect of surface wetting and solution mixing following fracture on the observed current transient should be understood. To date, these issues have not been examined for repassivation experiments and their effects remains unknown.

### Conclusion

A variety of limitations of potentiostatic repassivation experiments and their effects on high field modelling have been delineated through comparison of scratch testing and thin film fracture methods on titanium exposed to 0.6M NaCl. It was shown that ohmic drop in solution, a finite potentiostat response time, and changing  $E_g$  all contribute to the lack of constant potential across the interface. This results in tests which are not truly potentiostatic. A constant potential drop across the interface is required for high field modelling, unless the potential can be accurately calculated at all points during repassivation. An accurate calculation of the potential is difficult especially at short times following depassivation. Moreover, because the large majority of charge goes into dissolution and the high field approximation models only oxide thickening, the high field model is inappropriate for use with titanium in aqueous chloride solutions. The rate of

oxide removal was also shown to effect the morphology of the current transient during repassivation, an additional argument against using the high field model. The relatively slow depassivation speeds of scratch testing were found to yield erroneously low peak current densities as compared to those resulting from thin film fracture tests. The inaccurate peak current density obtained from scratch testing resulted from significant repassivation at the beginning of the scratch by the time the end of the scratch was reached. Thus, a variety of limitations must be addressed before valid repassivation data may be acquired.

### Acknowledgements

The authors acknowledge the Office of Naval Research (Grant No. N00014-91-J-4164) and the Virginia Center for Innovative Technology for their support of this work. The authors would like to thank Dr. R.G. Kelly, Dr. E. Gileadi and L. Scribner for their helpful input into this work.

### Appendix A

The differential current-time relationship resulting from the high field equation may be found elsewhere<sup>14,29</sup> but the solution is reproduced below with increased clarity.

Equation 4 may be rearranged to produce the form

$$X = \frac{BV}{\ln\left(\frac{i}{i_0}\right)} \quad (8)$$

or the form

$$\ln\left(\frac{i}{i_0}\right) = \frac{BV}{X} \quad (9)$$

From equation 9,  $\ln(i/i_0)$  can be then be differentiated with respect to  $x$ :

$$d\left(\ln\left(\frac{i}{i_0}\right)\right) = -\frac{BV}{X^2} dX \quad (10)$$

Noting that

$$d\left(\ln\left(\frac{i}{i_0}\right)\right) = \left(\frac{d\left(\frac{i}{i_0}\right)}{\frac{i}{i_0}}\right) \quad (11)$$

and that (utilizing equation 8)

$$-\frac{BV}{X^2} dX = -\frac{BV}{X \left( \frac{BV}{\ln\left(\frac{i}{i_0}\right)} \right)} dX \quad (12)$$

equation 10 may be rewritten as

$$\frac{d\left(\frac{i}{i_0}\right)}{\left(\frac{i}{i_0}\right)} = -\frac{BV}{X \left( \frac{BV}{\ln\left(\frac{i}{i_0}\right)} \right)} dX \quad (13)$$

Hence,

$$\frac{d\left(\frac{i}{i_0}\right)}{\left(\frac{i}{i_0}\right) \left( \ln\left(\frac{i}{i_0}\right) \right)} = -\frac{dX}{X} \quad (14)$$

Equation 14 can be converted from a current density -oxide thickness relationship to a current density - time relationship as follows. Equation 3 may be rearranged so that

$$dX = iA dt = (i_0 A dt) \left( \frac{i}{i_0} \right) \quad (15)$$

Substituting equations 8 and 15 into the right hand side of equation 14 yields the desirable current density - time differential

$$dt = - \left( \frac{BV}{i_0 A} \right) \frac{d\left(\frac{i}{i_0}\right)}{\left(\frac{i}{i_0} \cdot \ln\left(\frac{i}{i_0}\right)\right)^2} \quad (4)$$

### References

- 1) F.P. Ford in "Environment-Induced Cracking of Metals", R.P. Gangloff and M.B. Ives eds., NACE, Houston, TX, p. 27 (1990).
- 2) A. Turnbull, "Modelling of Environment Assisted Cracking", National Physical Laboratory Report, Middlesex, United Kingdom (1992).
- 3) J.S. Leach in "Stress Corrosion Cracking and Hydrogen Embrittlement of Iron Base Alloys", R.W. Staehle, J. Hochmann, R.D. McCright and J.E. Slater eds., NACE, Houston, TX, p. 16 (1977).
- 4) G.S. Frankel, B.M. Rush, V.A. Brusic, S.M. Mirzamaani and A.J. Davenport in "Corrosion of Electronic Materials and Devices", J.D. Sinclair ed., The Electrochemical Society, Pennington, NJ p. 263 (1991).
- 5) A.J. Davenport and H.S. Isaacs in "Transient Techniques in Corrosion Science and Engineering", W.H. Smyrl, D.D. Macdonald and W.J. Lorenz eds., The Electrochemical Society, Pennington, NJ p. 357 (1989).
- 6) G.S. Frankel, B.M. Rush, C.V. Jahnes, C.E. Farrell, A.J. Davenport, and H.S. Isaacs, *J. Electrochem. Soc.*, **138**, 643 (1991).
- 7) T.R. Beck in "Electrochemical Techniques for Corrosion", R. Baboian ed., NACE, Houston, TX, p. 27 (1977).
- 8) N.F. Cabrera and N.F. Mott, *Rep. Prog. Phys.*, **12**, 163 (1948/1949).
- 9) R.C. Newman in "Corrosion Chemistry Within Pits, Crevices and Cracks", A. Turnbull ed., Her Majesty's Stationery Office, London, p.317 (1987).
- 10) P.D. Bastek, R.C. Newman and R.G. Kelly, *J. Electrochem. Soc.*, **140**, 1884 (1993).
- 11) G.T. Burstein and A.J. Davenport, *J. Electrochem. Soc.*, **136**, 936 (1989).



- 12) T.R. Beck in "Passivity of Metals", R.P. Frankenthal and J. Kruger eds., The Electrochemical Society, Pennington, NJ p. 1035 (1978).
- 13) M. Fleischmann and H.R. Thirsk in "Advances in Electrochemistry and Electrochemical Engineering, Vol. 3", P. Delahay and C.W. Tobias eds., J. Wiley & Sons, New York, p. 123 (1963).
- 14) H.J. Rätzer-Schibe in "Passivity of Metals and Semiconductors", M. Froment ed., Elsevier Science Publishers, Amsterdam, p.731 (1983).
- 15) H.J. Rätzer-Schibe in "Proceedings of the 8th International Congress on Corrosion", Mainz, FRG, p. 212 (1981).
- 16) H.J. Rätzer-Schibe and H. Buhl in "Titanium Science and Technology - Proceedings of the 5th International Conference on Titanium", G. Lütjering, U. Zwicker and W. Bunk eds., Vol. 4, Deutsche Gessellschaft Für Mettalkunde, FRG, p. 2641 (1984).
- 17) K.C. Stewart, D.G. Kolman and S.R. Taylor in "Electrochemical Impedance: Analysis and Interpretation, ASTM STP 1188", J.R. Scully, D.C. Silverman and M.W. Kendig eds., ASTM, Philadelphia, p.73 (1993).
- 18) S.W. Watson and B.W. Madsen, *Corrosion*, **48**, 727 (1992).
- 19) C.C. Herrmann, G.G. Perrault and A.A. Pilla, *Anal. Chem.*, **40**, 1173 (1968).
- 20) K.C. Stewart, "Analysis and Removal of Artifacts from Electrochemical Impedance Spectra", Master of Science Thesis, University of Virginia, Charlottesville, VA (1993).
- 21) P.J. Moran, *Corrosion*, **42**, 432 (1986).
- 22) D.G. Kolman and J.R. Scully, *J. Electrochem. Soc.*, to be submitted.
- 23) T.R. Beck, *J. Electrochem. Soc.*, **115**, 890 (1968).

- 24) H.A. Johansen, G.B. Adams, Jr. and P. Van Rysselberghe, *J. Electrochem. Soc.*, **104**, 339 (1957).
- 25) G.O.H. Whillock and G.T. Burstein, *J. Electrochem. Soc.*, **136**, 1320 (1989).
- 26) A. Günterschulze and H. Betz, *Z. Physik*, **92**, 367 (1934).
- 27) T.N. Rhodin, Jr., *J. Am. Chem. Soc.*, **72**, 5102 (1950).
- 28) A. Charlesby, *Proc. Phys. Soc.*, **B66**, 317 (1953).
- 29) R. Ghez, *J. Chem. Phys.*, **58**, 1838 (1973).
- 30) U.R. Evans, "The Corrosion and Oxidation of Metals: Scientific Principles and Practical Applications", Edward Arnold Publishers, London (1961).
- 31) A.J. Davenport and G.T. Burstein, *J. Electrochem. Soc.*, **137**, 1496 (1990).
- 32) P.I. Marshall and G.T. Burstein, *Corrosion Science*, **23**, 1219 (1983).
- 33) T.R. Beck, *Electrochim. Acta*, **18**, 807 (1973).
- 34) J.R. Ambrose and J. Kruger, *J. Electrochem. Soc.*, **121**, 599 (1974).
- 35) D.G. Kolman and J.R. Scully, *J. Electrochem. Soc.*, **140**, 2771 (1993).
- 36) D.G. Kolman and J.R. Scully, *J. Electrochem. Soc.*, **141**, 2633 (1994).
- 37) D. Laser, M. Yaniv and S. Gottesfeld, *J. Electrochem. Soc.*, **125**, 358 (1978).
- 38) T.R. Beck, *Electrochim. Acta*, **18**, 815 (1973).
- 39) E.T. Fitzgibbons and W.H. Hartwig, NASA Technical Report No. 86 (1970).

- 40) E.N. Paleolog, A.Z. Fedotova and V.D. Fitulina, *Electrokhimiya*, **4**, 700 (1968).
- 41) I.A. Ammar and I. Kamal, *Electrochim. Acta*, **16**, 1539 (1971).
- 42) M. Pourbaix in "The Theory of Stress Corrosion Cracking", J.C. Scully ed., NATO Scientific Affairs Division, Brussels, p. 16 (1971).
- 43) L.I. Krishtalik in "Comprehensive Treatise of Electrochemistry, Vol. 7, Kinetics and Mechanisms of Electrode Processes", B.E. Conway, J.O'M. Bockris, E. Yeager, S.U.M. Khan, and R.E. White eds., Plenum Press, New York, p.87 (1983).

Table 1

| Depassivation Method | Calculated | EIS  | Current Interrupt |
|----------------------|------------|------|-------------------|
| Fracture             | 69.0       | 66.6 | 68.0              |
| Scratch              | 284        | 300  | -                 |

**Table 1** - Comparison of calculated and experimentally determined solution resistances (ohms) for the different depassivation methods. Experiments were performed in 0.6M NaCl ( $\kappa = 0.0521 \text{ (ohm-cm)}^{-1}$ ).

Table 2

| Reference | $i_0$<br>(A/cm <sup>2</sup> )                  | B<br>(cm/V)                                      | $\rho$<br>(g/cm <sup>3</sup> ) | A<br>(cm <sup>3</sup> /C) | monolayer<br>charge<br>density<br>(C/cm <sup>2</sup> ) | monolayer<br>thickness<br>(Å) |
|-----------|--|--|--------------------------------|---------------------------|--|-------------------------------|
| 29*       | $2 \times 10^{-13}$                            | $6 \times 10^{-6}$                               | 4.2                            | $4.85 \times 10^{-5}$     | $4.25 \times 10^{-4}$                                  | 2.06                          |
| 14-16**   | $2.53 \times 10^{-13}$                         | $6.8 \times 10^{-6}$                             | 3.4                            | $6.09 \times 10^{-5}$     | $4.25 \times 10^{-4}$                                  | 2.59                          |
| 28        | $5 \times 10^{-15}$ -<br>$7 \times 10^{-17}$   | $6.8 \pm 0.2$                                    | $3.4 \pm 0.2$                  |                           |  | $5.2 \pm 0.2$                 |
| 11***     | $3.16 \times 10^{-6}$                          | $1.46 \times 10^{-7}$ ****                       |                                |                           |  |                               |
| 30        | $5 \times 10^{-14}$ -<br>$1 \times 10^{-13}$   | $5.63 \times 10^{-6}$ -<br>$6.75 \times 10^{-6}$ |                                |                           |  |                               |
| 42        | $2.3 \times 10^{-8}$ -<br>$1.1 \times 10^{-7}$ | $6.9 \times 10^{-7}$ -<br>$7.4 \times 10^{-7}$   |                                |                           |  |                               |

- Ref. 40:  $\rho = 2.5-4.0$  g/cm<sup>3</sup>.
- Ref. 41: monolayer thickness =  $5.0 \text{ Å}$ .
- Ref. 31:  $A = 1.2 \times 10^{-3}$  cm<sup>3</sup>/C.

\* -  $i_0$  and B from Ref. 30.

\*\* -  $i_0$ , B and  $\rho$  from Ref. 40.

\*\*\* - Utilizing data from Ref. 14-16.

\*\*\*\* - Calculated by multiplying B' of Ref. 11 by A from Ref. 29.

Table 2 - Comparison of various high field parameters from the literature.

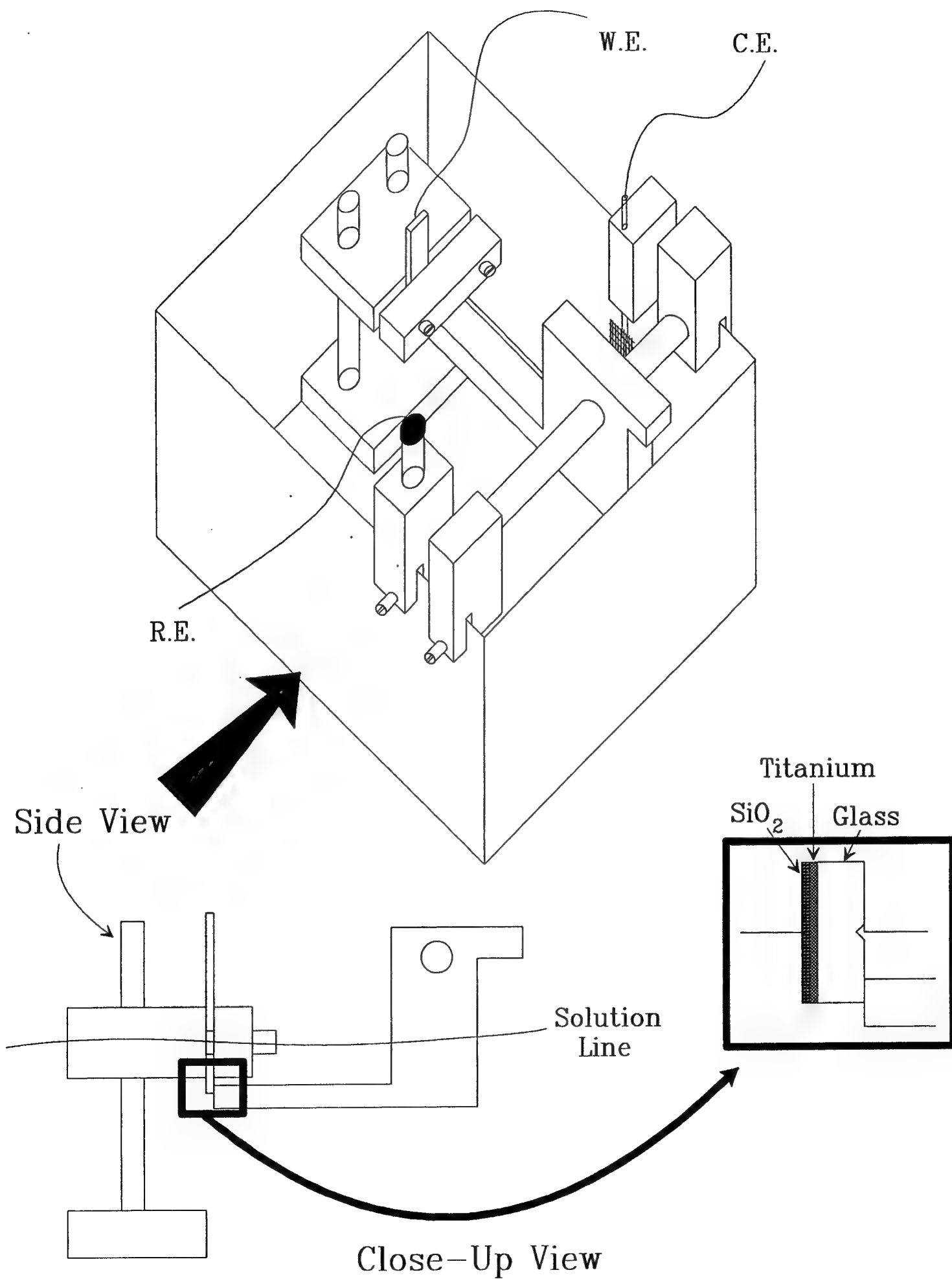


**Figure 1 - Schematic drawing of thin film fracture cell.**

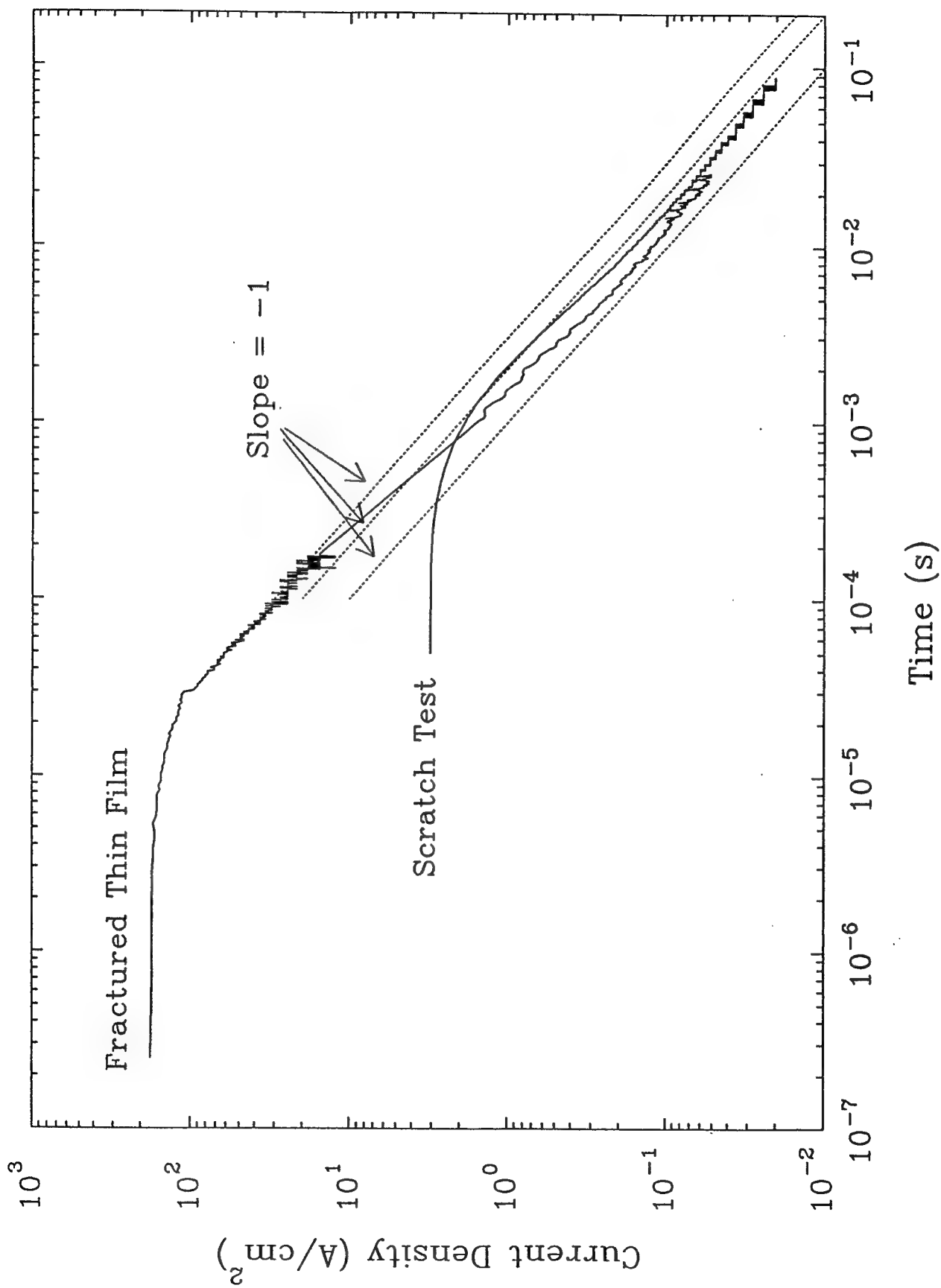


**Figure 2** - Comparison of current transients on titanium arising from scratch testing and thin film fracture testing ( $E_{\text{applied}} = 0V_{\text{SCE}}$ ,  $0.6M \text{ NaCl}$ ).



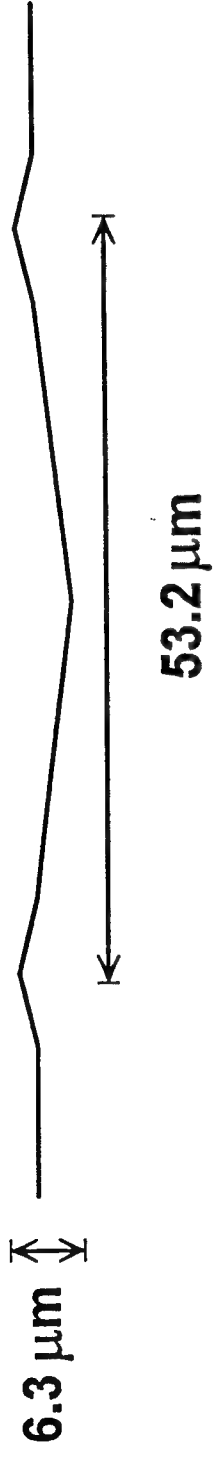


Figure 3a - Schematic drawing of the morphology of a scratch cross-section.

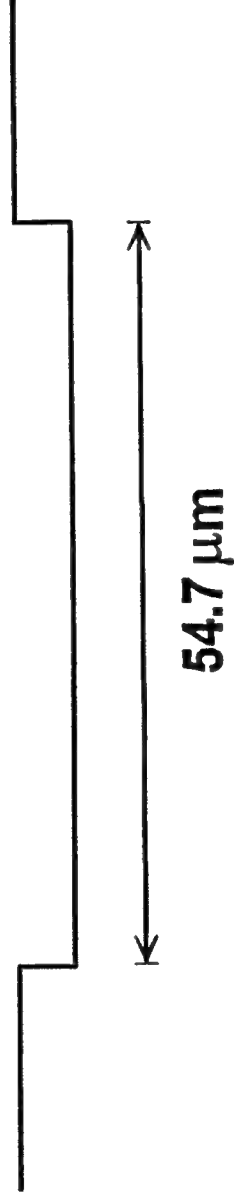


Figure 3b - Assumed cross-section of the scratch for solution resistance calculations.

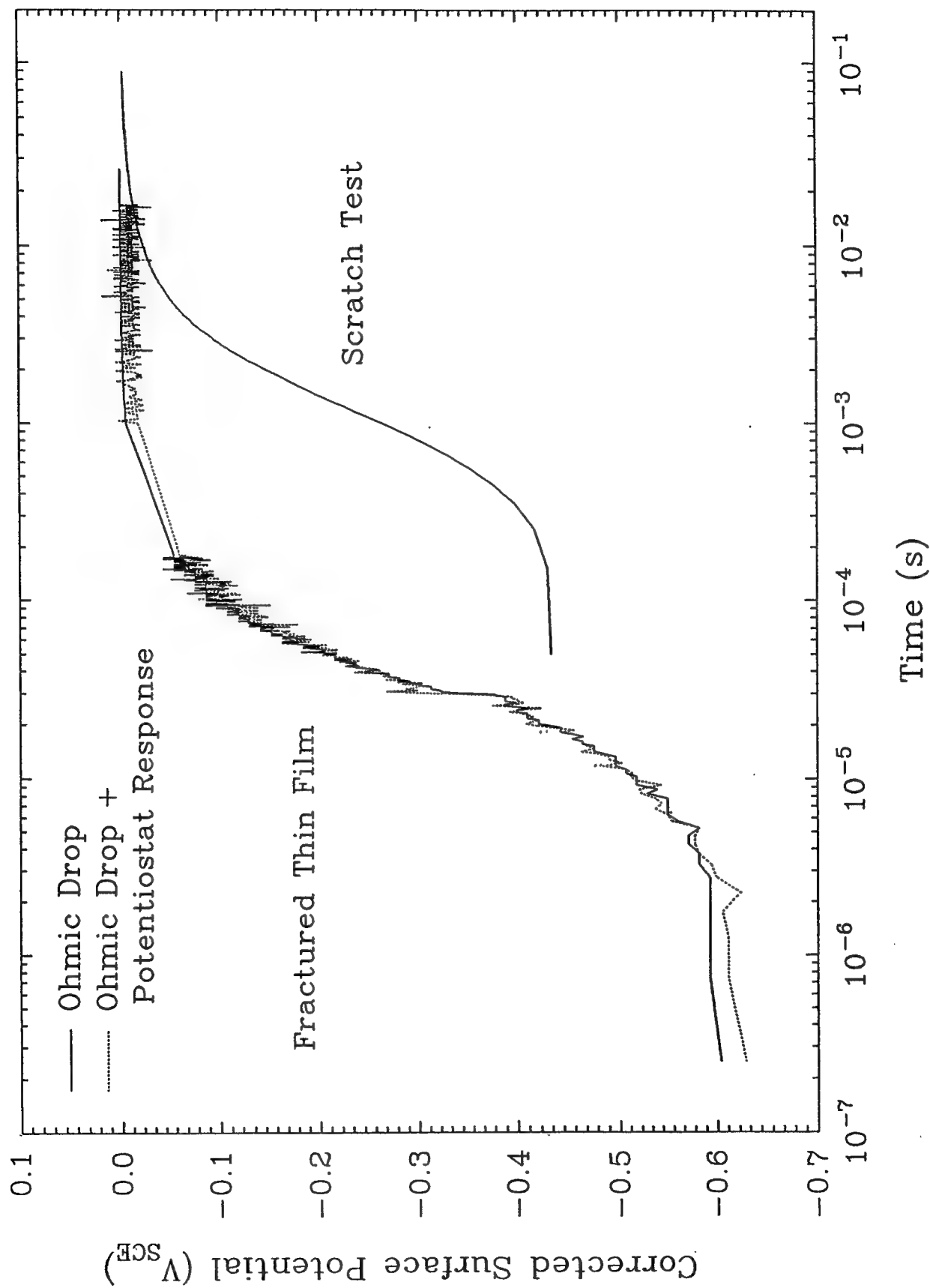


Figure 4 - Comparison of the corrected surface potentials for the current transients of Figure 2.

Thin Film / 0.6M NaCl /  $E_{app} = 0V_{SCE}$

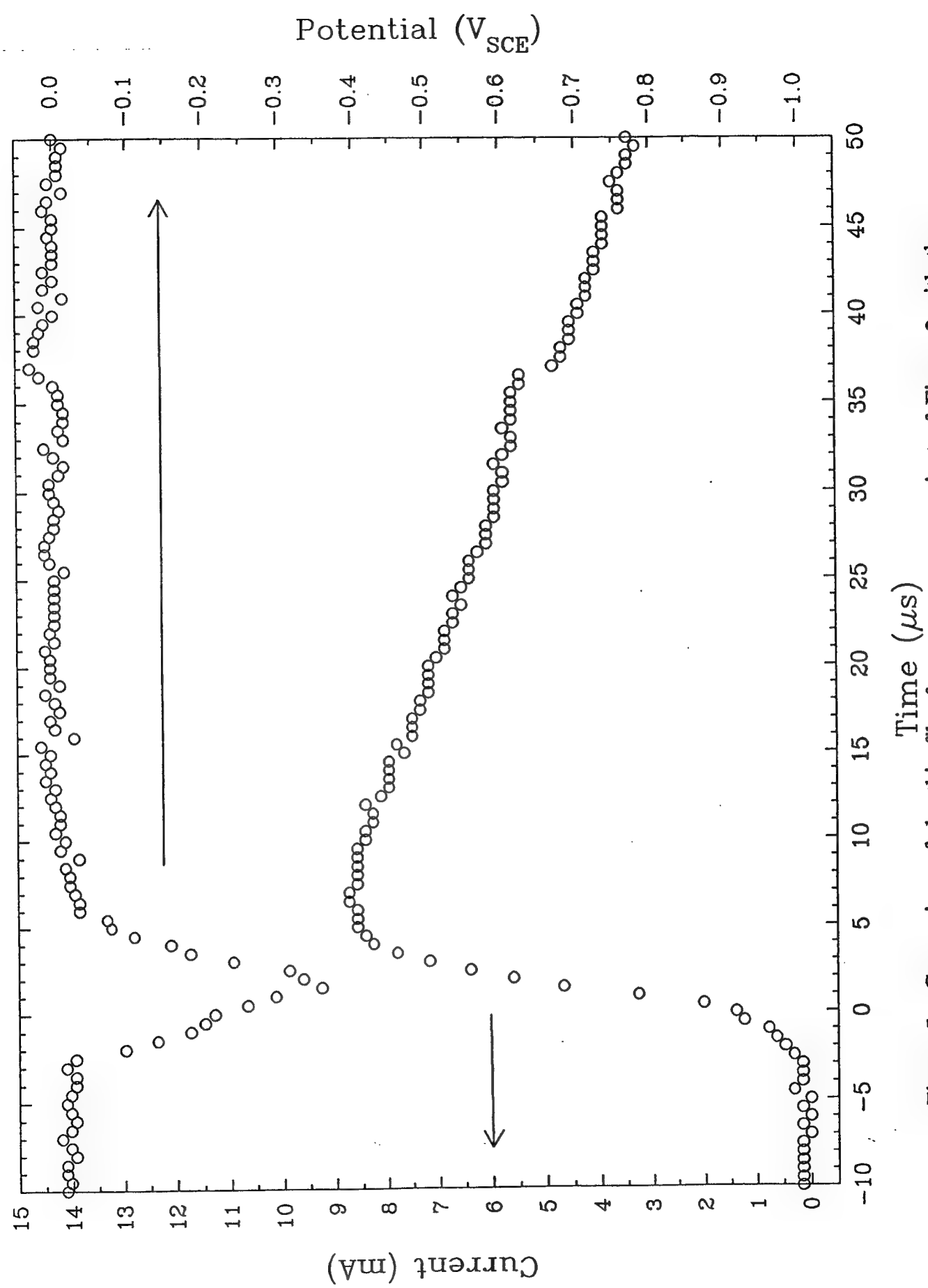
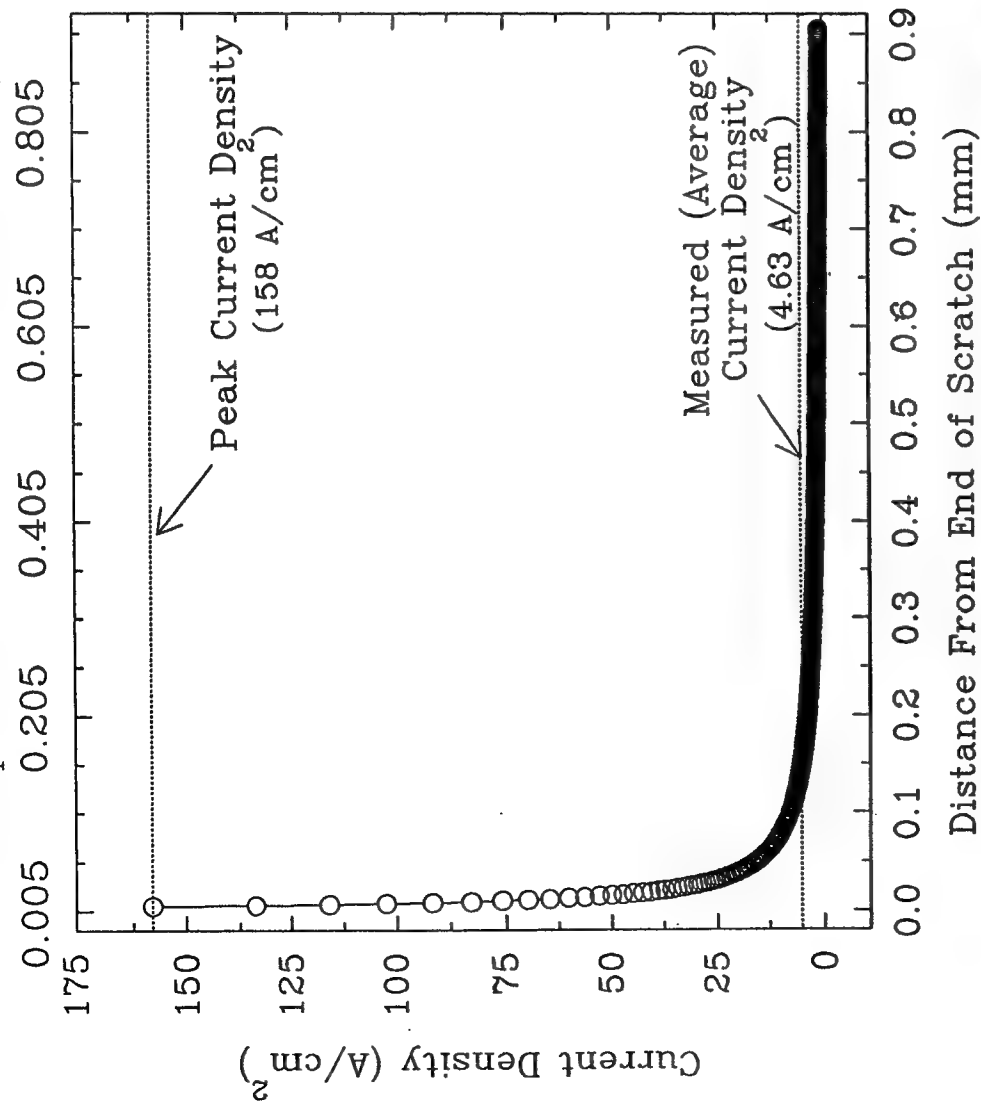
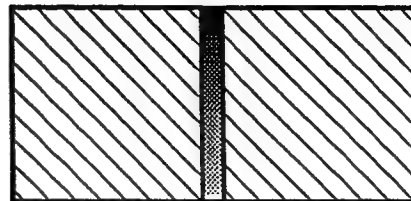


Figure 5 - Comparison of the thin film fracture current transient of Figure 2 with the applied surface potential.

Time Elapsed Before Scratch End Reached (ms)



Scratch Direction



**Figure 6** - Plot of calculated current density along a 0.9mm scratch assuming 1 m/s depassivation rate and logarithmic current decay. The bare surface peak current density was assumed to be equal to the average observed from thin film fracture experiments.

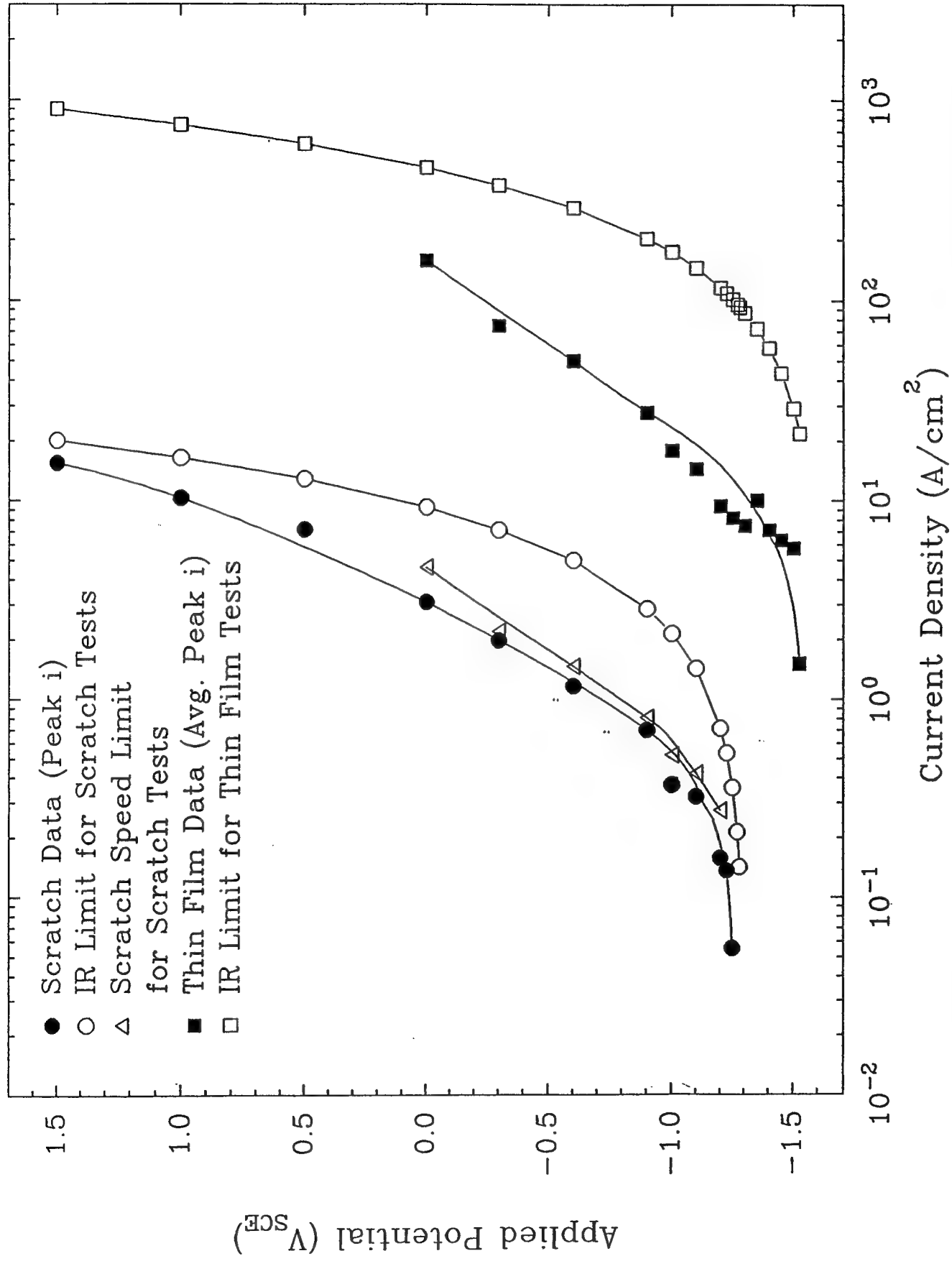
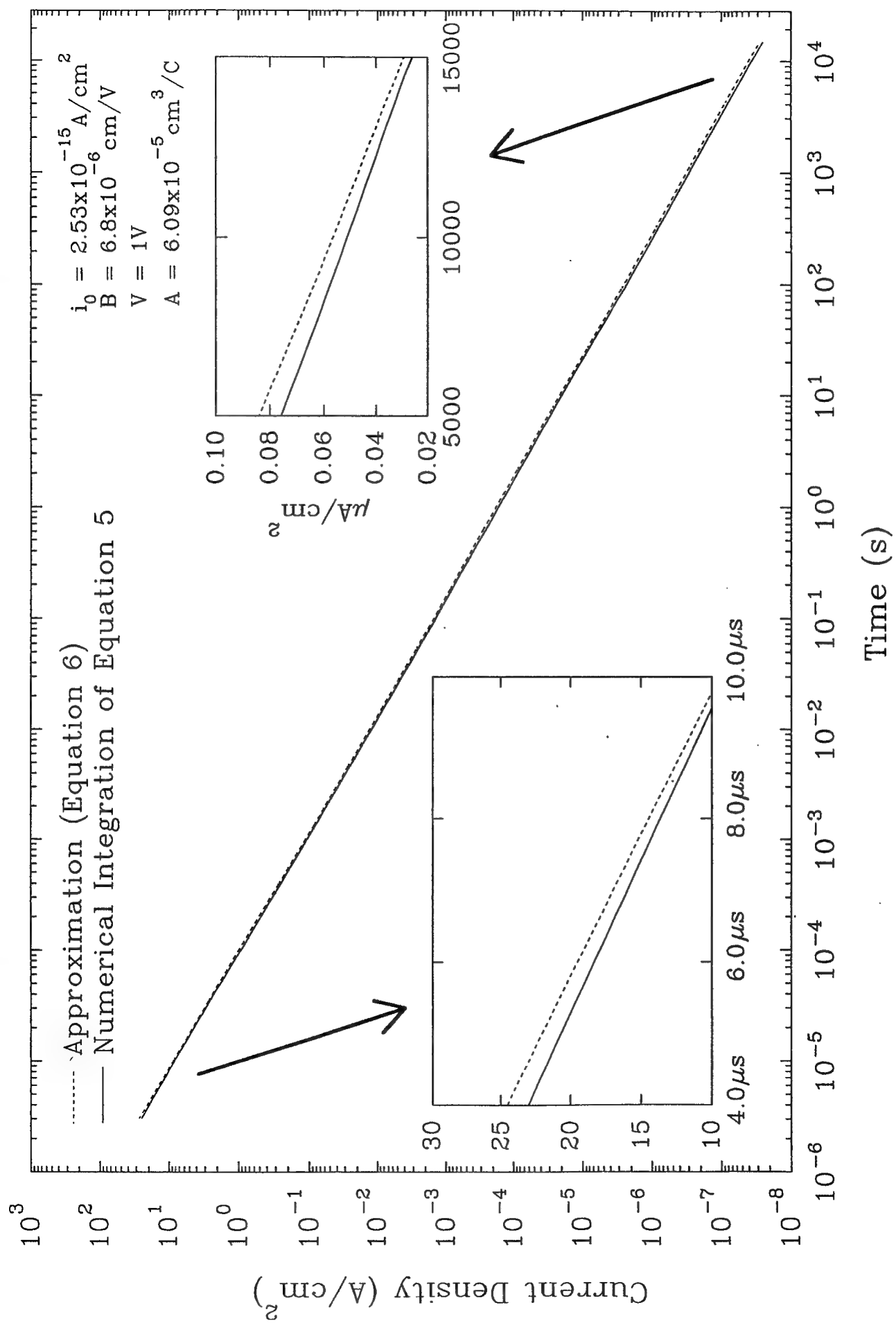


Figure 7 - Comparison of bare surface polarization curves on titanium exposed to 0.6M NaCl. The calculated IR limit for scratch tests is shown for comparison.



**Figure 8** - Comparison of different calculation methods for high field current decay on titanium utilizing identical parameters.

**THE EFFECTS OF HYDROGEN ON THE ROOM TEMPERATURE  
MECHANICAL PROPERTIES OF Ti-15V-3Cr-3Al  
AND Ti-15Mo-3Nb-3Al**

**George A. Young, Jr.  
John R. Scully**

## EFFECTS OF HYDROGEN ON THE MECHANICAL PROPERTIES OF A Ti-Mo-Nb-Al Alloy

George A. Young Jr. and John R. Scully  
Department of Materials Science and Engineering  
The University of Virginia  
Charlottesville, VA 22903

(Received November 10, 1992)  
(Revised December 3, 1992)

### Introduction

Critical aerospace, petrochemical, and marine applications demand high strength, formable materials which are resistant to corrosion, stress corrosion, and hydrogen embrittlement. Modern  $\beta$  titanium alloys are candidates for many such applications due to their excellent strength, toughness, formability, and resistance to general corrosion [1-5]. Furthermore, titanium's compact surface oxide film limits hydrogen entry and the underlying  $\beta$  matrix has a high solubility for hydrogen [6-7]. However, both model binary  $\beta$  titanium alloys as well as early developmental  $\beta$  alloys (Ti-13V-11Cr-3Al) can be susceptible to hydrogen embrittlement [8-15]. Hydrogen has also been implicated as the embrittling species in aqueous environmentally assisted cracking (EAC) of  $\alpha$ - $\beta$  and  $\beta$  alloys [16-20]. Current understanding of the controlling hydrogen embrittlement mechanisms in  $\beta$ -titanium alloys is insufficient to enable critical, damage tolerant applications [21]. The present research seeks to define the effects of a range of internal hydrogen concentrations on the room temperature mechanical properties of the peak aged  $\beta$  titanium alloy, TIMETAL 21S.

### Experimental

Solution annealed and cross-rolled TIMETAL 21S plate (Ti-15Mo-3Nb-3Al, wt%), nominally 10 mm thick, was received from TIMET. The solution annealed condition was 871°C for 8 hours followed by an air cool. Heat treatment of as-received plate consisted of an 8 hour age in air at 538°C, followed by an air cool, as recommended by the vendor. One hour and eight hour aged microstructures are shown in Figure 1. Note that  $\alpha$  precipitates nucleate preferentially on  $\beta$  grain boundaries after the 1 hour age but the  $\alpha$  distribution has homogenized after 8 hours. Hardness for the eight hour, "peak aged" condition was approximately  $R_c 42 \pm 1.2$ . Yield strengths corresponding to this aging condition are approximately 1205-1380 MPa [4,22].

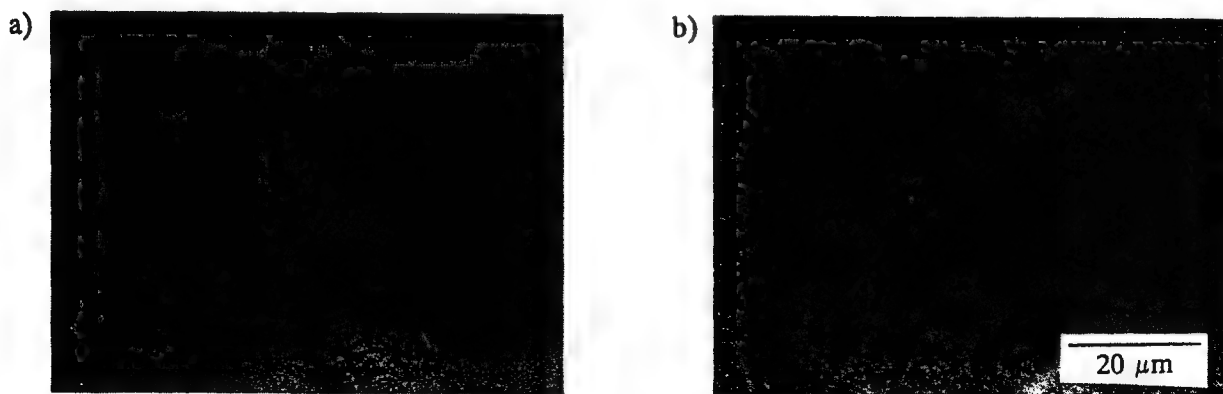


Figure 1. Optical Micrographs of TIMETAL 21S aged at 538°C for a) 1h and b) 8h



Aged plate was machined into circumferentially notched tensile bars. Electrochemical pre-charging of hydrogen was conducted at 90°C, in a solution of 10cc sulfuric acid, 1000cc H<sub>2</sub>O and 0.8g sodium pyrophosphate. Machined specimens were cathodically polarized to 100 A/m<sup>2</sup> to promote hydrogen uptake and to provide cathodic protection [23]. Results of the hydrogen charging operations are summarized in Table I, as analyzed by thermal emission methods (LECO). It is important to note that egress of hydrogen while the specimen is exposed to air is significantly impeded for titanium due to the formation of an oxide film permeation barrier upon removal of specimens from the charging bath.

Table I. Summary of charging times and resulting hydrogen concentrations.

| Charging Time | Total Hydrogen Concentration | Comment           |
|---------------|------------------------------|-------------------|
| As-received   | 50-100 wt. ppm               | "Low Hydrogen"    |
| 24 Hours      | 950-1750 wt. ppm             | "Medium hydrogen" |
| 64 Hours      | 1900-3600 wt. ppm            | "High Hydrogen"   |

The effects of constraint on the failure stress and strain were investigated by employing Bridgman-type, circumferentially notched tensile bars to develop differing levels of net section triaxial constraint [24]. Constraint levels from 0.52 (0.33 = uniaxial tension) to 1.03 (2.5 = sharp notch) were investigated. Degree of embrittlement was quantified by determining the maximum longitudinal stress developed at the centerline of the notched region and the effective plastic strain across the notch diameter at maximum load [24-26]. Following the procedure of Hancock et al. [25], maximum load was used as the comparison point since uncharged bars failed after achieving a maximum load as well as experiencing a load decrease, while hydrogen charged bars consistently failed at maximum load.

### Results/Discussion

#### Mechanical Testing

For each constraint level investigated, hydrogen decreases the longitudinal stress developed at the centerline of the notch at maximum load and the effective plastic strain across the notch diameter. Both stress and strain decrease with increasing hydrogen concentration as shown in Figure 2. The hydrogen concentrations reported here were obtained from a section of each tensile bar near the notch and as such represent an average concentration for the volume of metal tested.

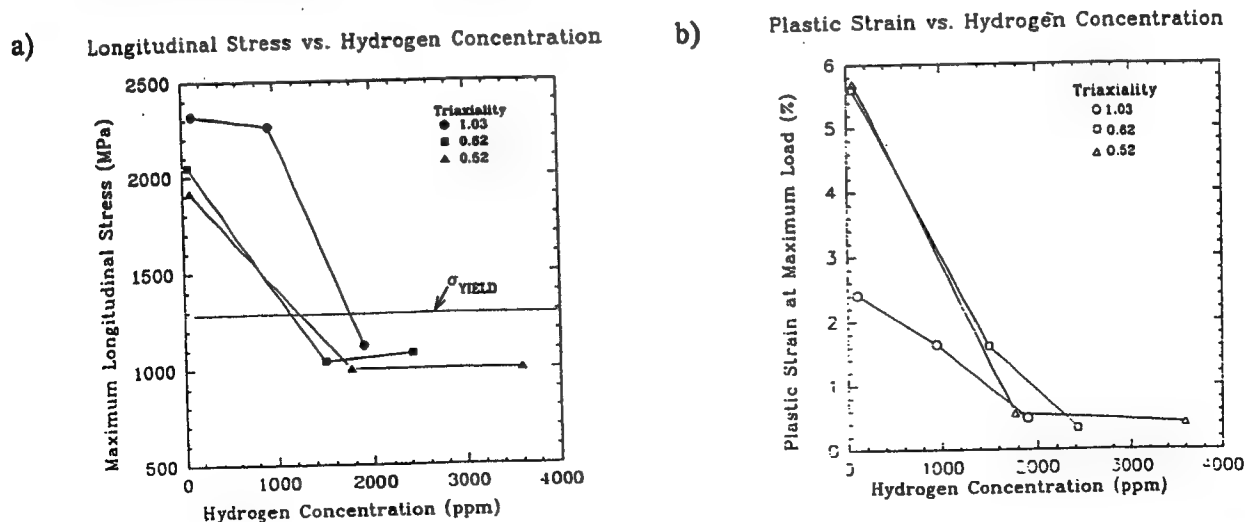


Figure 2. Effect of hydrogen on the a) stress and b) strain developed at maximum load for aged TIMETAL 21S at room temperature.

### Interpretation of Fracture Paths

Four distinct fracture modes were observed as a function of hydrogen concentration and constraint as shown in Figure 3. Ductile fracture of uncharged specimens appears to follow void initiation, growth, and coalescence mechanisms. Large, equiaxed voids are often seen at globular (silicide-phosphide-type) inclusions which are connected by areas of finer voids oriented approximately  $45^\circ$  to the tensile axis. As hydrogen and constraint are increased to the "medium" levels investigated here, a second fracture mode (Transgranular 1) is triggered. This fracture mode, although containing regions which appear microscopically ductile, occurs with significantly less plasticity than uncharged specimens. The tearing features suggest that ductile separation of the  $\alpha/\beta$  interfaces has occurred along with some trans-plate fracture. Hydrogen may segregate to these interfaces as a consequence of coherency strains or it may simply embrittle the surrounding  $\beta$  matrix. At similar constraint levels but higher hydrogen concentrations, the microscopic ductile tearing features disappear and a transgranular fracture mode containing small flat regions joined by ledges results (Transgranular 2). During this fracture process, the increased hydrogen content may embrittle the  $\beta + \alpha$  structure to a degree which precludes ductile tearing of  $\alpha$ - $\beta$  interfaces. Instead, transgranular fracture of the  $\alpha$  and  $\beta$  phases results with very limited plasticity. Both transgranular modes might be expected with sufficient dissolved hydrogen based on the literature which reports a transgranular fracture appearance for both solutionized and aged Ti-15-3 as well as Ti-13-11-3 at room temperature [12,27]. Moreover, for both solutionized and aged Ti-15-3 and "aged and partially resolutionized by dissolved hydrogen" TIMETAL 21S, the ductile to brittle transition temperature inherent to bcc metals is observed to increase above room temperature with dissolved hydrogen [27-28]. Such "lower shelf" behavior has apparently been achieved in the present study at  $25^\circ\text{C}$ .

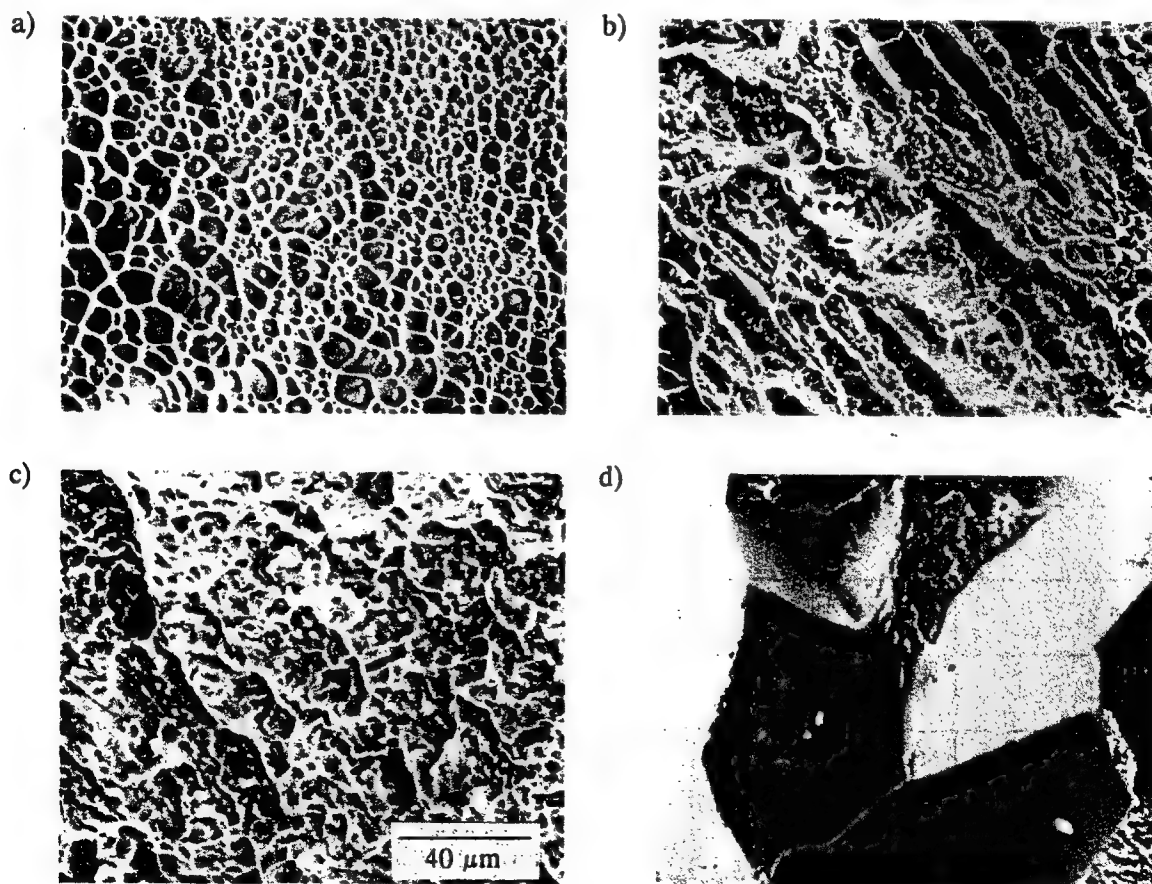


Figure 3. Fracture modes observed in peak aged TIMETAL 21S subjected to differing levels of hydrogen concentration and constraint a) microvoid rupture, b) ductile tearing of  $\alpha$ - $\beta$  interfaces (Transgranular 1), c) transgranular tearing through  $\beta$ - $\alpha$  microstructure (Transgranular 2), and d) intergranular fracture.

Intergranular cracking, seen both with hydrogen in the present study and aqueous chloride testing of aged TIMETAL 21S [19] occurs only at a high degree of triaxiality and hydrogen concentration. Preferential  $\alpha$  precipitation at  $\beta$  grain boundaries (Figure 1) may provide a continuous path for localized hydriding and subsequent fracture. Although bulk hydriding of the  $\alpha$  phase was not detected by x-ray diffraction, it is possible that local hydriding of the  $\alpha$  phase occurred at  $\alpha/\beta$  interfaces [29]. Alpha titanium has a relatively small hydrogen solubility (approximately 80 ppm at 90°C) [30] and stress assisted hydriding in  $\alpha$  and  $\alpha$ - $\beta$  alloys is well established [31,32]. Hydrogen accumulation at  $\alpha/\beta$  interfaces, which serve either as trap sites or sites for local strain induced hydriding, could result in subsequent fracture along  $\alpha$ - $\beta$  interfaces. Alternately, a hydrogen induced strain exhaustion mechanism might apply. Moreover, if the continuous grain boundary  $\alpha$  is removed (as in TIMETAL 15-3 which does not exhibit preferential  $\alpha$  precipitation along  $\beta$  grain boundaries) high hydrogen, high constraint tensile specimens do not fail intergranularly [33] and precracked specimens are resistant to EAC in aqueous chloride environments [19]. While intergranular fracture processes may involve local hydriding of the preferentially nucleated, grain boundary  $\alpha$  phase or trapping at  $\alpha/\beta$  interfaces, it is important to note that overall hydrogen embrittlement of  $\beta$  titanium alloys is not contingent on bulk  $\alpha$  hydriding as shown by the hydrogen embrittlement of solutionized  $\beta$  titanium alloys [8-12].

Inspection of Table II reveals seemingly contradictory information. The intergranular fracture mode occurs near the edge of the specimen where the triaxial stress is lowest according to Bridgman's analysis [24-26]. In contrast, a fracture mode apparently requiring intermediate fracture energy (transgranular) is observed near the specimen centerline. However, these results are consistent with a hydrogen concentration profile which decreases from edge to center. Determinations of the  $\beta$  lattice parameter at various depths from the precharged surface indicate a surface to center concentration profile greater than 10:1. These results imply a hydrogen diffusion coefficient well below  $5.0 \times 10^{-7} \text{ cm}^2/\text{s}$  at 90°C for aged TIMETAL 21S since a diffusion coefficient above this value would ensure completely uniform charging across the notch diameter in 64 hours, assuming diffusion controlled ingress. Holman et al., obtained the following relationship for hydrogen diffusion in solutionized Ti-13V-11Cr-3Al:  $D = 1.58 \times 10^{-3} \text{ EXP}(-21,500 \pm 1250 \text{ J/mole} / \text{RT})$  [34]. This relationship yields a diffusion coefficient of  $8.41\text{-}19.2 \times 10^{-7} \text{ cm}^2/\text{s}$  at 90°C and  $1.62\text{-}4.46 \times 10^{-7}$  at 25°C. Holman's result is in good agreement with Adler's work on the solution annealed  $\beta$ -Ti alloy Ti-8Mo-8V-2Fe-3Al which reported  $D = 8 \pm 2 \times 10^{-7} \text{ cm}^2/\text{s}$  at 25°C [35]. It is clear from the present work that aged TIMETAL 21S has an apparent diffusion coefficient including trapping at  $\alpha$  precipitates, dislocations, and other sites, which is significantly lower than solution annealed  $\beta$ -Ti alloys since uniform charging was not achieved in 64 hours of charging at 90°C.

Table II. Fracture modes of a) near the edge and b) near the center of peak aged, notched, TIMETAL 21S tensile bars at room temperature.

|                   | Degree of Constraint                  |                                       |                                    |
|-------------------|---------------------------------------|---------------------------------------|------------------------------------|
| H Conc. (wt. ppm) | 0.52                                  | 0.62                                  | 1.03                               |
| a) Low (50-100)   | Microvoid Rupture                     | Microvoid Rupture                     | Microvoid Rupture'                 |
| Medium (950-1750) | Transgranular 2/<br>Intergranular     | Transgranular 2/<br>Intergranular     | Transgranular 2<br>/Intergranular  |
| High (1900-3600)  | Transgranular 2                       | Intergranular/<br>Transgranular 2     | Intergranular/<br>Transgranular 2' |
| b) Low (50-100)   | Microvoid Rupture                     | Microvoid Rupture/<br>Transgranular 1 | Microvoid Rupture                  |
| Medium (950-1750) | Microvoid Rupture/<br>Transgranular 1 | Transgranular 1/<br>Microvoid Rupture | Transgranular 1'                   |
| High (1900-3600)  | Transgranular 2'                      | Transgranular 1                       | Transgranular 1                    |

'Denotes case which is shown in Figure 3.

Despite, the non-uniform hydrogen concentration profile, the results shown in Table 2 point to the possibility of a critical stress - hydrogen concentration failure criterion. Although, the stress at the notch surface of the high constraint tensile bar is lower than the stress at the centerline by a factor of 0.59, the hydrogen concentration at the surface is over 10 times greater. Interestingly, rising load fracture mechanics experiments on TIMETAL 21S in 3.5% NaCl at  $-600\text{mV}_{\text{SCE}}$  produced discontinuous crack jumps of distances approximately equal to two  $\beta$  grains ( $\approx 200\text{ }\mu\text{m}$ ) over time periods of several hours suggestive of diffusion controlled hydrogen transport in the fracture process zones [19]. The radial depth of the intergranular zone shown here was approximately  $900\text{ }\mu\text{m}$  after charging for 64 hours. Both results independently imply an apparent diffusion coefficient below  $10^{-8}\text{ cm}^2/\text{s}$ . Together, these results suggest that intergranular cracking is no longer favorable when a high hydrogen concentration does not exist in the fracture process zone over a distance equal to a multiple number of grains.

#### X-ray Diffraction Studies

Analysis of x-ray diffraction (XRD) data from peak aged TIMETAL indicates a  $\beta$  phase lattice parameter of  $0.325\text{ nm}$  for uncharged material ( $\approx 75 \pm 25\text{ ppm}$ ),  $0.328$  for 24 hour charging ( $\approx 1400 \pm 400\text{ ppm}$ ) and  $0.331\text{ nm}$  for 64 hour charging ( $\approx 2600 \pm 800\text{ ppm}$ ). Paton et al. correlated lattice parameter to hydrogen concentration in solution annealed Ti-18 Mo [36]. They obtained  $0.328$  and  $0.331\text{ nm}$  at  $1000$  and  $2100\text{ ppm}$ , respectively, in good agreement with the data presented here. No evidence of hydriding of the  $\beta$  phase was found. Regarding the possibility of hydriding of the  $\alpha$  precipitate, x-ray diffraction analysis was conducted on (a) specimen surfaces, (b) several micrometers beneath the specimen surface, and (c) at a position as near as possible to the centerline of notched region of the high constraint, high hydrogen condition. The latter two conditions were achieved by surface grinding and sectioning, respectively. Neither  $\alpha$  nor  $\beta$  phase hydride formation were detected at (a), (b) or (c). Instead, peaks coinciding with the  $\alpha$  phase are observed, except for immediately at the charged surface where neither the  $\alpha$  phase nor its corresponding hydride are observed. Electron microscopic examination revealed that selective elimination of the  $\alpha$  phase was due to spalling of the near surface  $\alpha$  precipitates. Such spalling would be expected based on the volume change which occurs on hydriding [8,37]. To confirm the notion that surface  $\alpha$  could be hydrided under the electrochemical conditions used here, commercially pure Ti was charged under identical conditions used for TIMETAL 21S. Hydride formation was indeed confirmed by XRD. To summarize, our findings suggest that hydriding of  $\alpha$  precipitates occurs at the free surface but that hydriding of a large volume fraction of the subsurface  $\alpha$  does not occur due to partitioning of hydrogen to the  $\beta$  phase.

#### Conclusions

Peak aged TIMETAL 21S is embrittled by hydrogen concentrations well below those required to hydride the  $\beta$  phase. Fracture path is a function of both level of constraint and hydrogen concentration. Approximate ranking of fracture modes from toughest to most brittle is: microvoid rupture, transgranular tearing of  $\alpha$ - $\beta$  interfaces, transgranular fracture through the  $\alpha$ - $\beta$  microstructure, and intergranular fracture. Intergranular fracture was only produced at the highest constraint and hydrogen concentrations. Preferential  $\alpha$  precipitation on  $\beta$  grain boundaries is suggested to have a detrimental role on HEAC since transgranular cleavage cracking is more typically observed for solutionized  $\beta$  titanium. Alpha precipitates within the  $\beta$  matrix may hydride locally at  $\alpha/\beta$  interfaces although no evidence of this was detected. Alternatively the  $\alpha/\beta$  interface may serve as a trap site whose strength increases with increasing hydrogen concentration due to increased coherency strain. The resulting intergranular fracture morphology in the case of high hydrogen-high constraint, tensile specimens is similar to that observed in 3.5% NaCl at  $-600\text{ mV}_{\text{SCE}}$ , suggesting a hydrogen assisted mechanism for the latter.

#### Acknowledgements

This research was supported by the Office of Naval Research (Grant N00014-91-J-4164) with Dr. A. John Sedriks as Scientific Monitor and by the Virginia Center for Electrochemical Science and Engineering at the University of Virginia. Material was donated by the Titanium Metals Corporation. The authors wish to acknowledge the helpful discussions with L.M. Young, R.P. Gangloff, D.G. Kolman, and B.P. Somerday.

### References

1. H. G. Nelson, First Thermal Structures Conference, E. Thornton, ed., Nov 13-15, The University of Virginia, Charlottesville, VA 22903, p. 301 (1990).
2. P.J. Bania, G.A. Lenning and J. A. Hall, Beta Titanium Alloys in the 80's, R.R. Boyer and H.W. Rosenberg eds., TMS-AIME, Warrendale, PA, p. 209 (1983).
3. A.G. Hicks and H. W. Rosenberg, Beta Titanium Alloys in the 80's, R.R. Boyer and H.W. Rosenberg eds., TMS-AIME, Warrendale, PA, p. 231 (1983).
4. P.J. Bania and W.M. Parris, Titanium Development Association Conference, Orlando, FL (1990).
5. T.W. Duerig and J.C. Williams, Beta Titanium Alloys in the 80's, R.R. Boyer and H.W. Rosenberg, eds., TMS-AIME, Warrendale, PA, p. 19, (1983).
6. R.W. Schutz and D.E. Thomas, Metals Handbook 9th ed. 13, ASM, Metals Park, Ohio, p. 669, (1987).
7. A.D. McQuillan, Proceedings of the Royal Society of London. A204, p. 309 (1950).
8. D.S. Shih, and H.K. Birnbaum, Scripta Met. 20, p. 1261 (1986).
9. J.J. DeLuccia, Report No. NADC-76207-30, Naval Air Development Center, Warminster, PA 1976.
10. J.S. Grauman, Presented at the Titanium Development Association Conference, Orlando, FL (1990).
11. W.W. Gerberich et al., Hydrogen Effects in Metals, I.M. Bernstein and A.W. Thompson eds, TMS-AIME, Warrendale, PA, p. 731 (1981).
12. K. Nakasa and J. Liu, J. Japan Inst. Metals 55, No. 9, p. 922 (1991).
13. N.E. Paton and O. Buck, Effect of Hydrogen Behavior of Materials. I.M. Bernstein and A.W. Thompson eds., TMS-AIME, Warrendale, PA, p. 83 (1975).
14. N.E. Paton, R.A. Spurling and C.G. Rhodes, Hydrogen Effects in Metals, I.M. Bernstein and A.W. Thompson eds., TMS-AIME, Warrendale, PA, p. 269 (1981).
15. J.E. Costa, D. Banerjee, and J.C. Williams, Beta Titanium Alloys in the 80's, R.R. Boyer and H.W. Rosenberg eds., TMS-AIME, Warrendale, PA, p. 69 (1983).
16. D.E. Thomas and S.R. Seagle, Titanium Science and Technology 4, G. Lutjering, U. Zwicker, and W. Bunk eds., p. 2533 (1984).
17. M.J. Blackburn and W.H. Smyrl, Titanium Science and Technology, R.I. Jaffee and H.M. Burte, eds. New York, NY, p. 2577 (1973).
18. H.G. Nelson, Hydrogen in Metals, I.M. Bernstein and A.W. Thompson eds., p. 445 (1973).
19. L.M. Young and R.P. Gangloff, to be published in Proceedings of the Seventh World Conference on Titanium, F.H. Froes, ed., TMS-AIME, Warrendale, PA (1992).
20. D.N. Fager and W.F. Spurr, Trans. ASM 61 (1968).
21. R.P. Gangloff and J.R. Scully, Proposal No. MS-DOD/ONR-4956-91, Univ. of VA, Charlottesville, VA (1991).
22. L.M. Young, Unpublished Research, The University of Virginia (1992).
23. Z.A. Foroulis, Ti'80, Science and Technology, H. Kimura and O. Izumi eds., TMS-AIME, Warrendale, PA, p. 2705 (1980).
24. P.W. Bridgman, Studies in Large Plastic Flow and Fracture, McGraw-Hill Inc., New York, NY (1952).
25. J.W. Hancock and A.C. Mackenzie, J. Mech. Phys. Solids 24, p. 147, Pergamon Press (1976).
26. A.C. Mackenzie, J.W. Hancock, and D.K. Brown, Engineering Fracture Mechanics, 9, p. 167 (1977).
27. K. Nakasa, Personal Communication, 1 September 92.
28. R. Lederich, McDonnell Douglas Corp., Personal Communication, September (1992).
29. D.N. Williams, J. Inst. Met. 91, p. 147 (1962).
30. R.S. Vitt and K. Ono, Met. Trans. 2 (1971).
31. H. Margolin, Met. Trans 7A, p. 1233 (1976).
32. J.D. Boyd, Trans. ASM, p. 977 (1969).
33. G.A. Young and J.R. Scully, Unpublished Research, The University of Virginia, Charlottesville, VA (1992).
34. W.R. Holman, R.W. Crawford, and F. Paredes, Jr., Trans. AIME 22, p. 1836 (1965).
35. P.N. Adler and R.L. Schulte, Scripta Met. 2, p. 669 (1978).
36. N.E. Paton, O. Buck, and J.C. Williams, Scripta Met. 9, p. 687 (1975).
37. J. Liu and K. Nakasa, J. Japan Inst. Metals 54, No. 11, p. 1261 (1990).

**INTERNAL HYDROGEN EMBRITTLEMENT OF SOLUTION HEAT  
TREATED AND AGED Ti-15V-3Cr-3Al-3Sn AND Ti-15Mo-3Nb-3Al**

**George A. Young, Jr.  
John R. Scully**

*To appear in: Corrosion Journal, Vol. 50(12), December 1994.*  
Also this was paper 247 at CORROSION/94 in Baltimore, March 1994.

## INTERNAL HYDROGEN EMBRITTLEMENT OF SOLUTION HEAT TREATED AND AGED

### Ti-15V-3Cr-3Al-3Sn AND Ti-15Mo-3Nb-3Al

George A. Young, Jr.\* and John R. Scully  
Materials Science & Engineering  
The University of Virginia  
Charlottesville, VA 22903-2442

\*Present Address: Knolls Atomic Power Laboratory  
Schenectady, NY 12301-1072

### ABSTRACT

The effects of electrochemically introduced hydrogen on the room temperature mechanical properties of two  $\beta$ -titanium alloys, Ti-15V-3Cr-3Al-3Sn and Ti-15Mo-3Nb-3Al are compared. Solution heat treated (SHT), single step peak aged (PA), and duplex aged (DA) conditions were investigated using notched tensile bars and Bridgman's analysis of longitudinal stress and average effective plastic strain. Ti-15Mo-3Nb-3Al was more susceptible to hydrogen embrittlement than Ti-15V-3Cr-3Al-3Sn based on reductions in longitudinal stress, plastic strain, and fractography at hydrogen concentrations above 1000 wt. ppm. Hydriding of the  $\alpha$  or  $\beta$  phase was not observed over the range of hydrogen concentrations investigated. Instead, changes in fracture behavior with hydrogen are correlated with deformation behavior and  $\alpha$  precipitation. The susceptibility of Ti-15Mo-3Nb-3Al is attributed to a high temperature, long time solution treatment which affects deformation behavior in the SHT condition and promotes grain boundary  $\alpha$  precipitation in the PA condition. The high temperature solution treatment reduced  $\alpha$  nucleation sites in grain interiors and promoted planar slip. Subsequent  $\alpha$  precipitation occurred preferentially on  $\beta$  grain boundaries and, lastly, in grain interiors resulting in fine intragranular precipitates. It is hypothesized that fine intragranular  $\alpha$  plates as well as aligned boundary  $\alpha$  colonies are readily sheared and also promote planar slip in the PA condition. In contrast, a lower temperature, shorter duration solution treatment for Ti-15V-3Cr-3Al-3Sn resulted in wavy slip after SHT and more homogeneous, slightly coarser  $\alpha$  precipitates upon aging, which may be less prone to slip localization by dislocation shearing. Localized planar slip and grain boundary  $\alpha$  colonies are believed to promote both internal hydrogen embrittlement and aqueous environmentally assisted cracking. These factors are more closely linked to thermomechanical processing than to alloy composition in the present study.



keywords:  $\alpha$  precipitation,  $\beta$ -titanium alloys, Bridgman's analysis, cleavage, deformation mode, fracture path, hydriding, hydrogen embrittlement, hydrogen trapping, intergranular cracking, multiple slip, planar slip, stress corrosion cracking, transgranular cracking

## INTRODUCTION

Modern  $\beta$ -titanium alloys are candidates for room temperature marine and aerospace applications due to their excellent strength, toughness, formability, and resistance to general and crevice corrosion<sup>(1-5)</sup>. Although the stress corrosion cracking resistance (SCC) of  $\alpha$  and  $\alpha + \beta$  titanium alloys is well characterized, the environmental cracking resistance of aged  $\beta$  titanium alloys is less well reported in the literature<sup>(6-8)</sup>.  $\beta$ -titanium alloys (Ti-11.5Mo-6Zr-4.5Sn, Ti-13V-11Cr-3Al, and binary Ti-Mo compositions) are susceptible to stress corrosion cracking in ambient temperature neutral halide containing solutions in fracture mechanics experiments<sup>(7,9,10)</sup>. Fracture occurs both intergranularly and by  $\{100\}$  cleavage<sup>(9)</sup>.

SCC susceptibility is a strong function of electrochemical potential and increasing yield strength<sup>(7,8,10)</sup>. However, the potential dependency observed for SCC of  $\beta$ -titanium differs from that observed for *bcc* ferrous alloys long known to be prone to hydrogen embrittlement cracking in halide containing aqueous environments. Specifically, cracking is exacerbated at potentials near -600 mV vs. SCE for  $\beta$ -titanium alloys<sup>(7,8)</sup>. Cracking also occurs at more positive potentials but is not observed at potentials more negative than approximately -1000 mV<sup>(7,8,11)</sup>. In contrast, a different trend is observed in the case of steels of similar yield strengths. Greater susceptibility is observed at increasingly negative potentials relative to -600 mV vs. SCE as well as at more positive potentials<sup>(12-14)</sup>. In fact, the minimum in susceptibility occurs in the range of approximately -500 to -700 mV vs. SCE in neutral  $\text{Cl}^-$  containing solutions. The increasing susceptibility trend with cathodic polarization in the case of steel occurs due to the strong correlation between embrittlement susceptibility and fracture process zone hydrogen concentration which depends, in turn, on the rate of hydrogen production from the reduction of water reaction<sup>(13-15)</sup>. The anodic trend is attributed to ferrous and ferric ion hydrolysis, local acidification, enhanced hydrogen production and its absorption from the environment established at occluded sites<sup>(13)</sup>. In the case of  $\beta$ -titanium, different controlling electrochemical parameters may allow hydrogen production and entry to occur within the -500 to -700 mV potential range, or entirely different mechanisms may govern aqueous room temperature SCC.

Based on the observed lack of SCC susceptibility at -1000 mV, the ability of titanium's compact surface oxide film to limit hydrogen entry<sup>(8)</sup>, its rapid repassivation rate<sup>(16,17)</sup>, and the high hydrogen solubility of the beta matrix<sup>(18)</sup>, hydrogen may be prematurely dismissed as an unlikely embrittling agent for  $\beta$ -titanium alloys. However, the role of hydrogen in the room temperature aqueous SCC of  $\beta$ -titanium alloys at potentials near -600 mV SCE requires more thorough examination for the following reasons. Hydrogen production is thermodynamically assured at the transiently bare crack tip in the case of Ti due to the negative equilibrium potentials associated with the  $\text{Ti}/\text{Ti}^{+2}$  and  $\text{Ti}/\text{Ti}^{+3}$  oxidation reactions (e.g. -1.87 and -1.21 V vs. SCE at 1 M  $\text{Ti}^{+2}$  and 1 M  $\text{Ti}^{+3}$  concentrations, respectively)<sup>(19)</sup> and the likelihood of significant IR-based voltage differences between transiently bare cracks and external surfaces<sup>(16)</sup>.  $\text{Ti}^{+3}$  cations are hydrolyzable; a pH < 1.3 has been reported at pit sites while a pH as low as zero is measured when dissolving  $\text{TiCl}_3$  under deaerated conditions simulating an occluded crack<sup>(16,17,20)</sup>. Moreover, hydrogen transport rates in  $\beta$ -titanium (e.g.  $-1.8 \times 10^{-7} \text{ cm}^2/\text{sec}$  at  $25^\circ\text{C}$ ) are similar to those in *bcc* steels<sup>(21-23)</sup> and, consequently,



are not expected to limit fracture process zone hydrogen accumulation in monotonic loading experiments at slow strain rate. Finally, hydrogen embrittlement susceptibility is well established for high strength *bcc* materials particularly as yield strength is increased<sup>(24,25)</sup>. For these reasons, internal hydrogen should be examined as a possible contributor to room temperature aqueous SCC phenomena.

To date, the relative importance of internal hydrogen as either a contributor or the root cause of room temperature aqueous embrittlement of  $\beta$ -titanium alloys has not been unambiguously distinguished from aqueous dissolution. Clearly, binary beta titanium alloys as well as early developmental  $\beta$  alloys (Ti-13V-11Cr-3Al) can be susceptible to hydrogen embrittlement. Shih and Birnbaum have shown that the solution treated beta alloy Ti-30Mo is extrinsically embrittled through the formation of the *fcc*  $\delta$  hydride containing 66 at% hydrogen<sup>(26)</sup>. Solution treated beta alloys are also intrinsically embrittled by hydrogen at bulk concentrations well below that required to produce hydriding of the  $\beta$  matrix<sup>(21-27)</sup>. Gerberich et al. have shown a continuous decrease in the fracture stress of solution annealed Ti-30Mo containing 20-1800 ppm by weight of hydrogen without the formation of a hydride<sup>(27)</sup>. Nakasa and co-workers found a decrease in bending strength for both the solution annealed and peak-aged Ti-13V-11Cr-3Al, again without detection of hydriding in either the  $\alpha$  or  $\beta$  phase at hydrogen concentrations up to 15,000 wt. ppm<sup>(28)</sup>. A {100} cleavage plane was identified on flat fracture surfaces in both the solution annealed and aged conditions. The *fcc*  $\epsilon$  hydride was detected under extreme autoclave conditions at hydrogen concentrations of the order of 40,000 ppm<sup>(28)</sup>. Hydrogen was also implicated in the aqueous cracking of aged  $\beta$ -titanium alloy Beta-C (Ti-3Al-8V-6Cr-4Mo-4Zr)<sup>(29)</sup>. In this study, embrittlement was only observed when pre-cracked specimens were cathodically polarized in H<sub>2</sub>S containing acidified chloride solutions. Previous studies of  $\alpha$ - $\beta$  and metastable  $\beta$ -titanium alloys in aqueous solutions also attribute environmental cracking to a hydrogen environment assisted cracking mechanism<sup>(11,30,31)</sup>. Coincidentally, {100} cleavage<sup>(9)</sup> and intergranular separation<sup>(9,11)</sup> are observed. Factors supporting a time dependent hydrogen embrittlement phenomenon for Ti-15Mo-3Nb-3Al in aqueous solutions include (a) electrochemical conditions at the crack tip which favor hydrogen production, (b) a loading rate dependency suggesting the need for dynamic strain, (c) and discontinuous crack bursts<sup>(11)</sup>.

This paper seeks to define the effects of a broad range of internal hydrogen concentrations on the room temperature mechanical properties of solution annealed, single step peak aged, and duplex aged beta titanium alloys Ti-15Mo-3Nb-3Al and 15V-3Cr-3Al-3Sn and to correlate hydrogen assisted cracking to observed aqueous, environmentally assisted cracking<sup>(11)</sup>. Here, electrochemical pre-charging of aged or solution heat treated material is conducted near ambient temperature to avoid the complications of hydrogen induced  $\beta$  phase stabilization common to high temperature gaseous charging studies<sup>(32-34)</sup>. Mechanical testing of pre-charged specimens is performed in air, to decouple hydrogen effects from other aqueous embrittlement mechanisms which may complicate in-situ SCC studies. The strong permeation barrier provided by the titanium oxide is exploited to minimize outgassing of precharged hydrogen during the duration of these tests. Embrittlement is quantified as a function of maximum longitudinal stress, plastic strain at maximum load, and total hydrogen concentration. Hydriding of the  $\alpha$  and  $\beta$  phases is investigated through x-ray diffraction. Metallographic, plastic deformation mode and fractographic features are correlated with mechanical property data and likely fracture scenarios are discussed.

## EXPERIMENTAL

### *Metallurgy*

Cross rolled plates, nominally 10 mm thick, of Ti-15V-3Cr-3Sn-3Al (composition expressed in wt pct., referred to as 15-3) and Ti-15Mo-3Nb-3Al (composition expressed as wt. pct., referred to as 21S) were received in the solution annealed condition. The Ti-15V-3Cr-3Sn-3Al alloy was solution heat treated (SHT) at 816°C for 0.5 h while the Ti-15Mo-3Nb-3Al alloy was SHT at 871°C for 8 h (Table 1). Average grain sizes of 90 and 100  $\mu\text{m}$  were determined for 15-3 and 21S, respectively. Solution annealed (SHT), single step peak aged (PA), and duplex aged (DA) heat treatments were investigated. Duplex aging was performed in an attempt to promote a finer, more homogenous  $\alpha$  distribution and avoid preferential precipitation on  $\beta$  grain boundaries<sup>(35)</sup>. Preferential  $\alpha$  precipitation has previously been associated with increased susceptibility to stress corrosion cracking, hydrogen embrittlement, and intergranular cracking<sup>(36,38)</sup>. Table 1 details the heat treatments and corresponding hardness of each condition. Air tensile properties are reported elsewhere<sup>(11,37)</sup>. For single step PA Ti-15V-3Cr-3Sn-3Al and Ti-15Mo-3Nb-3Al, yield strengths of 1315 and 1364 MPa and % reductions in area of 13 and 2 were produced, respectively, for smooth tensile specimens. Both PA and DA 21S exhibited preferential nucleation of  $\alpha$  plates at  $\beta$  grain boundaries while  $\alpha$  plates nucleated intragranularly in both PA and DA 15-3. This difference in nucleation behavior is identified metallographically after a one hour age at 538°C as shown in Figure 1a and b. Dark field transmission electron microscopy (TEM) analysis also revealed a 0.1  $\mu\text{m}$  thick  $\alpha$  film along  $\beta$  grain boundaries in both 21S and 15-3 after aging at 538°C. Aligned plate-like  $\alpha$  colonies were observed perpendicular to  $\beta$  grain boundaries in the 21S alloy both metallographically (Fig. 1a) and by dark field TEM<sup>(37)</sup>. Subsequent aging to peak strength at 538°C or duplex aging resulted in a uniform high density of intragranular  $\alpha$  plates in both alloys. X-ray diffraction (XRD) after SHT, PA and DA heat treatments indicated presence of the  $\beta$  phase (SHT), or  $\beta$ + secondary  $\alpha$  phases (PA and DA). The  $\omega$  phase was neither detected by TEM-selected area diffraction nor by X-ray diffraction in PA alloys.

### *Hydrogen charging*

Electrochemical pre-charging of hydrogen was conducted in a solution of 10ml  $\text{H}_2\text{SO}_4$ , 1000ml  $\text{H}_2\text{O}$  and 0.8 g  $\text{Na}_4\text{P}_2\text{O}_7$  at 90°C<sup>(39)</sup>. Previously heat treated and machined tensile specimens were cathodically polarized to 100 A/m<sup>2</sup> for various times, as described elsewhere<sup>(36)</sup>, to facilitate hydrogen uptake and were tested in air. Upon removal from the charging bath, the oxide which forms in air is an effective barrier to hydrogen egress. Hydrogen concentrations reported for each tensile specimen were obtained from a section of the same tensile bar adjacent to the notch by thermal emission (LECO) and represent an average total concentration for the volume of metal tested. The hydrogen uptake rate of 15-3 was approximately 5-6 times greater than that of 21S for all the heat treatments investigated which was attributed, in part, to a higher hydrogen overpotential and fugacity on the surface of 15-3 at equal cathodic current density. At 25°C, galvanostatic measurements in the charging solution indicate that 15-3 develops a potential approximately 200 mV cathodic to 21S at an equivalent current density of 100 A/m<sup>2</sup>.

### *Notched tensile testing*

Circumferentially notched "Bridgman" tensile bars were employed to quantify the effects of hydrogen on the mechanical properties of the alloys investigated<sup>(40)</sup>. Degree of embrittlement was quantified by determining the maximum longitudinal stress developed at the centerline of the notched region and the effective plastic strain across the notch diameter at maximum load following the procedures of Hancock et al.<sup>(41,42)</sup>. All tensile tests were conducted at a crosshead displacement rate of  $2.5 \times 10^{-5}$  cm/s and at ambient laboratory temperature. The effect of constraint on the failure stress and strain in PA material was determined as a function of hydrogen concentration at four different initial constraint levels (0.52, 0.62, 1.03, 1.43) where the triaxial constraint is defined as the ratio of mean to effective stress,  $(\sigma_m/\bar{\sigma})$ <sup>(40-42)</sup>. These constraint levels correspond to notch radii of 7.9 mm, 4.8 mm, 1.6 mm, and 0.79 mm respectively at a constant initial diameter across the notch of 6.4 mm. Additional tensile tests, conducted at the constraint level of 1.43 (0.33 = uniaxial tension, 2.50 = sharp notch), compared the effects of hydrogen on SHT, single step PA, and DA heat treatments.

### *Deformation mode*

The slip behavior of each alloy was investigated by deforming electropolished cubes of SHT material (approximately 1 cm<sup>3</sup>) in compression and observing the surface slip lines via optical microscopy. This procedure produced similar trends as obtained from microscopic examination of regions of metal flow associated with hardness indentation. Quantified levels of plastic deformation were achieved with compression testing.

### *Detection of hydriding*

X-ray diffraction experiments were performed with a Scintag automated diffractometer utilizing copper K<sub>α</sub> radiation, which was continuously scanned over 30-80° 2θ at a rate of 1° per minute. Both the heat treated and heat treated + hydrogen charged conditions were investigated. Diffraction spectra of electrochemically charged plate were taken both at the charged surface and well into the specimen interior. The latter was achieved by sectioning and grinding.

## **RESULTS**

### *Notched tensile testing - influence of constraint and hydrogen*

The maximum longitudinal tensile stress increased and the corresponding plastic strain decreased with increasing level of constraint for uncharged PA 15-3 and 21S (Figure 2). The maximum longitudinal tensile stress and plastic strain developed in PA 15-3 decreased almost linearly with hydrogen concentration. The slope of the nearly linear relationship between stress and total hydrogen became more negative with constraint. For instance, a ratio of the maximum longitudinal stress with 3400 ppm hydrogen relative to the as received condition of < 0.6 was observed at the 1.43 constraint level. In contrast, a ratio of 0.7 is found at the 0.52 constraint level for the Ti-15V-3Cr-3Al-3Sn alloy. Ti-15Mo-3Nb-3Al, however, exhibited a more abrupt decrease in longitudinal tensile stress and plastic strain at hydrogen concentrations greater than approximately 1000 wt. ppm. Moreover, the threshold hydrogen concentration required to produce the distinct decrease was a function of constraint. For instance, a ratio of maximum longitudinal stresses with hydrogen relative to the as received condition of <0.6 was observed at the 1.43

constraint level with only 1000 ppm hydrogen. A greater hydrogen concentration than 1000 wt. ppm is clearly required for the 1.03 constraint level (Figure 2). Similarly, larger relative reductions in plastic strain occur for 21S at the highest constraint (Figure 2b). As reported previously, the fracture appearance of 21S at a constraint of 1.03 changed from a process completely governed by microvoid initiation, growth and coalescence to transgranular and intergranular separation processes with increasing hydrogen concentration<sup>(36)</sup>. In contrast, the fracture mode of PA 15-3 was relatively insensitive to hydrogen concentration as will be detailed below. Given the influence of constraint on the effects of internal hydrogen, SHT, PA and DA metallurgical conditions were investigated at the high constraint level of 1.43.

#### *Notched tensile testing - influence of heat treatment*

Solution heat treated alloys were tensile tested over a total hydrogen concentration range extending from the as-received levels to almost 3000 wt. ppm at the highest constraint level investigated (1.43). The failure stress and strain of 15-3 were unaffected by hydrogen concentrations up to 2900 wt. ppm as shown in Figure 3. In contrast, 21S was embrittled at 2900 wt. ppm (Figure 3). Although the maximum longitudinal stresses were nearly equal for each alloy in the SHT condition, 15-3 displayed approximately twice the plastic strain at maximum load as 21S for low hydrogen concentrations and more than five times the plastic strain at the hydrogen concentration of 2900 wt. ppm. It should be noted that the difference in the hardness of the two alloys is only slight in the solution heat treated condition as shown in Table 1.

In the PA condition (Fig. 4), both 15-3 and 21S exhibited a decrease in strength and ductility above approximately 1000 wt. ppm total hydrogen. This decrease was more pronounced for 21S as was the change in fracture mode which will be discussed below. Again, Table 1 indicates that 21S is of only slightly greater hardness than the 15-3 alloy.

Duplex aged 15-3 and 21S both indicated susceptibility to hydrogen embrittlement at similar total hydrogen concentrations (Fig. 5). The 15-3 material exhibited greater intrinsic ductility than 21S at all hydrogen concentrations and, therefore, the exact effects of hydrogen are less certain from analysis of notched tensile properties. However, fractography indicates a more brittle fracture appearance in the case of 21S relative to 15-3 as will be shown in the next section. Comparison of material at equivalent hardness levels (as in the case of DA 15-3 at Rockwell C 41.4 versus PA 21S at Rockwell C 42.1) clearly shows that 15-3 still exhibits superior resistance to hydrogen embrittlement at the same total hydrogen concentration. In support of this claim, comparison of Figures 2 and 5 indicate only a slight decrease in the maximum longitudinal stress at 4000 wt. ppm hydrogen for DA 15-3 (Figure 5), while a severe reduction is observed for PA 21S (Figure 2).

#### *Fractography*

All fractography reported was examined at approximately equivalent radial distances from the notch surface. The fracture mode of SHT 15-3 was relatively insensitive to hydrogen concentration. At all hydrogen levels investigated SHT 15-3 failed by transgranular microvoid processes. In PA material, the fracture mode of 15-3 was also transgranular microvoid coalescence at all constraint and hydrogen levels investigated. One effect of increasing hydrogen and constraint for the 15-3 alloy was to increase the density of microvoids per given fracture area and decrease the depth and

width of the microvoids. Such a trend has also been associated with decreased fracture toughness of Beta III, but as a function of aging time<sup>(10)</sup>. The fracture mode of DA 15-3 also consisted of progressively finer microvoids up to its highest hardness (Rockwell C 41) and hydrogen concentration (3793 ppm H) where the fracture mode changed to transgranular ductile tearing characterized by fine undetermined features as shown in Figure 6.

In contrast to 15-3, the fracture modes of the SHT, PA and DA 21S alloys all changed significantly as the hydrogen concentration was increased (Fig. 7). The fracture mode of SHT 21S changed from large microvoids at approximately 100 ppm hydrogen, the as-received hydrogen concentration (Fig. 7a), to small microvoids and ductile tearing features at 680 ppm hydrogen (not shown). At 3000 ppm a flat fracture appearance characterized by three distinct fracture modes was observed: (1) fine voids and tearing features similar to the 680 ppm hydrogen level, (2) flat transgranular fracture, and (3) transgranular fracture displaying relatively straight parallel markings (Fig. 7b). These parallel markings typically extend across an entire grain diameter and are consistent with hydrogen induced slip band fracture which has been observed in hydrogen charged bcc steels, pure nickel, and nickel and iron base alloys<sup>(43-46)</sup>. The transgranular fracture surfaces at other grains within the notch region contained almost entirely the fracture modes described by (1) and (2) above. The variations in fracture mode between individual grains is believed to be caused by differences in slip system orientation relative to the tensile axis.

The fracture mode in PA 21S is influenced by both level of constraint and hydrogen concentration as detailed elsewhere<sup>(36)</sup>. At the highest constraint levels, peak aged 21S exhibits a transgranular microvoid fracture appearance with a bimodal distribution of dimple sizes in the uncharged condition. This changed to a mixture of intergranular and transgranular fracture as hydrogen concentration is increased (Fig. 7c). The flat featureless areas of the PA 21S at 4664 ppm hydrogen (Fig. 7d) suggest that slip plane decohesion has occurred. However, this hypothesis still requires crystallographic confirmation. The distinct changes in fracture mode with hydrogen concentration and increasing constraint support the notion of a hydrogen/constraint based threshold for embrittlement in 21S as indicated in Figure 2.

Duplex aged 21S fails by transgranular fracture with approximately 10  $\mu\text{m}$  wide irregular terraces at 75 ppm hydrogen, the as-received level. Flat transgranular fracture characterized by parallel arrays of ridges containing micro-voids is observed across entire grains at 3800 ppm (Fig. 7e). Cleavage (Fig. 7f) apparently occurs at 5600 ppm as evidenced by a flat transgranular fracture appearance with markings. This result is consistent with the notion that the hydrogen affected ductile to brittle transition temperature for bcc titanium has been shifted above the test temperature.

### *Deformation Mode*

Compression tests on SHT alloys revealed that both alloys were prone to highly localized planar slip at low plastic strains (3%). At strains on the order of 8%, extensive multiple or wavy slip occurred in 15-3. In contrast, localized planar slip persisted in the SHT 21S material at high plastic strains. Figure 8a and b compares the surface slip observed in SHT 15-3 and 21S at approximately 8% plastic strain and illustrates the difference.

### *X-ray Diffraction*



Analysis of x-ray diffraction (XRD) data was undertaken for both peak aged 21S and 15-3. A  $\beta$  phase lattice parameter of 0.325 nm was determined for uncharged 21S ( $\approx 75 \pm 25$  wt. ppm hydrogen), 0.328 for 24 hour charging ( $\approx 1400 \pm 400$  wt. ppm) and 0.331 nm for 64 hour charging ( $\approx 2600 \pm 800$  wt. ppm) using the (110) reflection. In contrast, very little change in the *hcp*  $\alpha$  phase lattice parameter is observed. These results suggest partitioning of hydrogen to the  $\beta$  phase. Paton et al. also correlated  $\beta$  lattice parameter to hydrogen concentration in solution annealed Ti-18 Mo<sup>(47)</sup>. Lattice parameters equal to 0.328 and 0.331 nm were obtained at 1000 and 2100 wt. ppm hydrogen, respectively, in good agreement with the data presented here. No evidence of hydriding of the  $\beta$  phase was found.

Regarding the possibility of massive hydriding of  $\alpha$  precipitates, x-ray diffraction analysis was conducted on (a) specimen surfaces, (b) several micrometers beneath the specimen surface, and (c) at a position as near as possible to the centerline of the notched region of a high constraint, high hydrogen 21S tensile bar. The latter two conditions were achieved by surface grinding and sectioning, respectively. Neither  $\alpha$  nor  $\beta$  phase hydride formation was detected at (a), (b) or (c) for charged and plastically strained PA 21S. Instead, diffraction peaks coinciding with the  $\alpha$  and  $\beta$  phases are observed, except for immediately at the charged surface where neither the  $\alpha$  phase nor its corresponding hydride was observed (Figure 9a). An increase in the  $\beta$  lattice parameter was observed at interior positions confirming the presence of hydrogen, although the increase was somewhat less than at the surface. Electron microscopic examination revealed that selective removal of the  $\alpha$  phase occurred due to spalling of the near surface  $\alpha$  precipitates (Fig. 9b). Such spalling might be expected based on the 18% volume increase which occurs upon hydriding of the  $\alpha$  phase<sup>(27,47)</sup>. Spalling of hydrided  $\alpha$  phase has previously been reported by Nakasa in Ti-6Al-4V during electrochemical hydrogen charging<sup>(48)</sup>. To confirm the notion that surface  $\alpha$  could be hydrided under the electrochemical conditions used here, commercially pure Ti was charged under identical charging conditions used for Ti-15Mo-3Nb-3Al. Hydride formation was indeed confirmed by XRD and metallography.

Diffraction spectra taken from the surface of as-charged PA 15-3 indicated that surface-exposed  $\alpha$  also became hydrided but did not spall (Fig. 10). Hydriding appears to be a phenomenon associated with surface exposed  $\alpha$  for both alloys since no hydride peaks were detected in the interior of either material when diffraction spectra were taken after serial grinding of the hydrogen charged surface. Instead, partitioning of hydrogen to the  $\beta$  phase is again observed as indicated by increases in the  $\beta$  lattice parameter. An increase in the  $\beta$  lattice parameter indicates the presence of a significant hydrogen concentration in the bcc phase at depths where hydriding of  $\alpha$  was not observed. However, this does not preclude the possibility of localized deformation assisted hydriding in slip bands or localized hydriding of  $\alpha/\beta$  interfaces as discussed by Boyd<sup>(49)</sup>, if the volume fraction of hydride formed was too small for detection by XRD. To summarize, our findings suggest that hydriding of  $\alpha$  precipitates occurs at the free surface but that hydriding of a large volume fraction of the subsurface  $\alpha$  does not occur due to partitioning of hydrogen to the high solubility  $\beta$  phase. Local hydriding at  $\alpha/\beta$  interfaces remains possible.

## DISCUSSION

### *Metallurgical factors affecting embrittlement susceptibility*

Both preferential grain boundary  $\alpha$  precipitation and localized planar slip can be circumstantially correlated with the greater susceptibility to internal hydrogen embrittlement (IHE) of the Ti-15Mo-3Nb-3Al alloy. Recall that preferential grain boundary  $\alpha$  precipitation was noted in aged 21S (Fig. 1a) and intergranular cracking occurred (Fig. 7c). Planar slip was observed for SHT 21S (Fig. 8b) and is suggested by the fracture appearances in SHT (Fig 7b) as well as aged 21S (Fig. 7e). In contrast, wavy slip was observed in SHT 15-3, intragranular  $\alpha$  precipitation was observed in aged 15-3 and transgranular fracture occurred. At issue are the governing metallurgical factors.

It is difficult to attribute the hydrogen embrittlement susceptibility of 21S exclusively to the mere presence of grain boundary  $\alpha$  in the aged condition for two reasons. Firstly, aged 15-3 contained a 0.1  $\mu\text{m}$  thick  $\alpha$  film along  $\beta$  grain boundaries, although preferential formation of  $\alpha$  colonies perpendicular to boundaries did not occur. The thin  $\alpha$  film did not render the alloy susceptible. Secondly, 21S was more susceptible than 15-3 in the SHT condition where a solid solution  $\beta$  microstructure was preserved upon cooling from above the  $\beta$  transus. The parallel, linear features shown on the fracture surfaces of hydrogen charged 21S in the SHT and DA conditions (Figures 7b and 7e) and previously observed in hydrogen charged PA material<sup>(36)</sup> suggest an interaction between hydrogen, slip and fracture mode.

In the present study, planar slip has been observed for SHT 21S but not yet confirmed for aged 21S. However, it is reasonable to expect that aging would exacerbate the planar slip tendency seen in the SHT condition since (a)  $\alpha$  plates are fine and, perhaps, shearable, (b) well aligned  $\alpha$  colonies at grain boundaries might promote shearing, and (c) TEM/electron diffraction experiments show that both 15-3 and 21S exhibit Burger's  $\alpha$  (i.e.  $(110)_{\beta} \parallel (0001)_{\alpha}$ ,  $[111]_{\beta} \parallel [11\bar{2}0]_{\alpha}$ )<sup>(51)</sup>. This suggests that transfer of slip from  $\beta$  to  $\alpha$  may be possible and also that shearing of  $\alpha$  precipitates may occur. In support of this view, Okada, Banerjee, and Williams found that slip transfer from  $\beta$  to  $\alpha$  was a function of precipitate morphology in Ti-15V-3Cr-3Al-3Sn<sup>(52)</sup>. Slip initiates in the  $\beta$  phase and parallel  $\alpha$  plates of the same variant (colony type structure) allow dislocations to shear the  $\alpha$  phase while  $\alpha$  plates of differing physical orientations promote homogeneous slip<sup>(52)</sup>. High magnification SEM of aged, metallographically prepared 21S and 15-3 show a difference in the size and physical orientation of  $\alpha$  plates for the two alloys<sup>(37)</sup>. It is plausible that the coarseness of intragranular  $\alpha$  in aged 15-3, which has nucleated first and grown for a longer time, is a more effective slip barrier than the fine  $\alpha$  of 21S. A greater impedance to planar slip would promote more homogeneous deformation in the form of multiple or wavy slip in aged alloys.

Hydrogen segregation to dislocations and transport by slip is well documented in bcc metals<sup>(53,54)</sup>. Recall that hydrogen has been shown to partition to and is relatively mobile in the bcc lattice<sup>(36,55)</sup> which provides a readily available source for hydrogen pickup by dislocations and possible deposition of this hydrogen at grain boundaries. In the case of 15-3, which appears more prone to wavy or multiple slip, we hypothesize that less hydrogen is transported to  $\beta$  grain boundaries and the locally high hydrogen concentrations possible along the intense planar slip bands seen in 21S (Fig. 8b) are avoided. In this way slip mode would also contribute to the

observation of intergranular cracking in 21S. This explanation for intergranular cracking is well supported by the fracture modes observed for 21S but not found for 15-3 in this study and is consistent with the work of Thompson, Bernstein et al. in aluminum alloys<sup>(56-59)</sup>.

Ti-15Mo-3Nb-3Al, which is prone to planar slip, undergoes slip band, possibly slip plane, intergranular, and cleavage cracking depending on microstructure, degree of constraint and hydrogen concentration. Ti-15V-3Cr-3Al-3Sn, in which multiple slip is easier to induce, exhibits a microvoid rupture fracture mode until the highest strength and hydrogen level investigated are reached where the fractographic features are on the size and order of the deformation structure seen in heavily plastically strained SHT material as shown by a comparison of Figures 6b and 8a. Correlation of the different fracture modes with the plastic slip behavior exhibited by each alloy indicates that deformation mode strongly influences the hydrogen effected fracture paths and subsequent mechanical properties. Consequently, factors influencing slip behavior should be reviewed.

It is reasonable to expect that slip behavior in *bcc* titanium is dependent on alloy composition, thermo-mechanical processing, and precipitate morphology as in the case of other alloy systems. For SHT  $\beta$  alloys it is plausible that deformation mode may be controlled by chemical composition, operative slip or twinning systems, and residual dislocation density since other factors affecting slip such as shearable  $\omega$  phase particles were not detected, nor expected. The fact that alloying additions affect stacking fault energy and subsequent slip behavior is well known and also may apply to metastable  $\beta$ -titanium alloys. Ling and co-workers noted a changed in deformation mode from wavy, multiple slip in a quenched and recrystallized Ti-28 wt. % V alloy to coarse planar slip in a 40 wt. % V alloy<sup>(60)</sup>. They traced the difference to an increasing twin fault probability with increasing V which makes cross-slip more difficult<sup>(61)</sup>. In order to compare the compositions of the two alloys studied here, equivalent molybdenum concentration provides the basis for comparison rather than vanadium content. In the present study, the equivalent Mo concentration of 15-3 is 11.9 wt. % while that of 21S is 12.8%, not a large difference. Therefore, we assert that differences in deformation mode observed here are more dependent on heat treatment than alloy composition. In support of this view it should be noted that preferential grain boundary  $\alpha$  precipitation and intergranular stress corrosion cracking have been produced in 15-3 which was solution heat treated above the  $\beta$  transus for longer times (e.g. 1038°C, 2 hours) than investigated here<sup>(37,50)</sup>. The present authors have also produced intergranular cracking in re-solutionized 15-3 (816°C, 0.5 h→Air cool, 950°C, 12 h→Air cool) with room temperature hydrogen charging<sup>(62)</sup>. Of important note, this condition was also more prone to planar slip than SHT 15-3 after 816°C for 0.5 h<sup>(62)</sup>. Therefore, solution heat treatment temperature and time appear to affect both slip behavior and  $\alpha$  precipitation in 15-3 and 21S more strongly than compositional differences.

The temperature and time associated with solution heat treatments (Table 1) affect residual dislocation density, vacancy concentration, and grain growth. Since minimal grain growth was observed, vacancy concentration and dislocation density are implicated as key factors. Fujii has shown that a high excess vacancy concentration created by very high SHT temperatures (i.e. > 1000°C) and a low density of vacancy sinks (grain boundaries, twin boundaries and dislocations) accelerate aging and promote fine homogeneous  $\alpha$  precipitation<sup>(63)</sup>. However, a balance exists between the opposing roles of dislocations as vacancy sinks and as heterogeneous  $\alpha$  nucleation sites<sup>(63)</sup>. Dislocations remaining from prior working clearly readily serve as strong  $\alpha$  nucleation sites



as shown by studies of the effect of cold work on aging<sup>(63,64)</sup>. In this study, the differences in excess vacancy concentration following heat treatment at 816, 871 or 950°C are probably minor. However, long solutionizing times at 871°C (21S: 8h) and 950°C (Re-solution heat treated 15-3: 12h) are likely to lower dislocation density, given temperatures of about one-half the melting temperature. We speculate that residual dislocation substructure is a dominate factor affecting slip mode and aging behavior in the present study and that composition and vacancies play secondary roles. Solution treatment has also been identified as the controlling factor in hot salt stress corrosion cracking susceptibility of the metastable  $\beta$  alloy Beta-III but the mechanism of embrittlement was not discussed<sup>(38)</sup>. In the present study, solution treatment time and temperature are implicated as important factors affecting the internal hydrogen embrittlement (IHE) susceptibility of  $\beta$ -titanium alloys.

#### *Other factors possibly affecting embrittlement susceptibility*

Two other important differences have been reported for Ti-15V-3Cr-3Al-3Sn and Ti-15Mo-3Nb-3Al that pertain to hydrogen embrittlement susceptibility. Pound reports a higher apparent hydrogen trapping constant associated with the single step peak aged 21S as compared to peak aged 15-3<sup>(65)</sup>. The materials analyzed were identical to those used in the present study. The controlling trap site is thought to be the  $\alpha/\beta$  interfaces, in particular those associated with grain boundary  $\alpha$  colonies<sup>(65)</sup>. The intrinsic trap capability of  $\alpha/\beta$  interfaces may depend on their degree of coherency and lattice misfit. In general, coherent interfaces are viewed as reversible hydrogen trap sites that rely on local stress state and dislocations to promote trapping<sup>(66)</sup>. Noncoherent interfaces are often regarded as irreversible trap sites which also may possess lower cohesive strengths<sup>(66)</sup>. Interestingly, hydrogen partitioning alters the  $\beta$  lattice parameter but the low levels present in the *hcp* phase prior to hydriding lead to minimal changes in the  $\alpha$  lattice parameter<sup>(67)</sup>. This suggests that the misfit strain of an  $\alpha/\beta$  interface may be a function of hydrogen content as well as  $\alpha$  and  $\beta$  phase compositions which also affect their lattice parameters. It is unclear whether or not differences in misfit strain exist between the intragranular and grain boundary  $\alpha/\beta$  interface structures, or whether differences exist in the case of 21S relative to 15-3. Recall that a Burger's orientation relationship was observed between the  $\beta$  matrix and  $\alpha$  plates in both 21S and 15-3 suggesting the presence of some misfit strain and therefore some intrinsic trapping capability in the case of both alloys<sup>(51)</sup>. An alternative view is that local hydriding occurs more readily at grain boundary  $\alpha/\beta$  interfaces and accounts for the irreversible trapping reported by Pound<sup>(49,65)</sup>. It is unclear why either hydriding or intrinsic trapping capability is preferentially more severe at grain boundary  $\alpha/\beta$  interfaces since the misfit strain along these plates should not differ from that at  $\alpha/\beta$  interfaces associated with intragranular precipitates. One theory is that the tips of well aligned  $\alpha$  colonies at the grain boundary provide the noncoherent interface responsible for irreversible trapping and form a well-connected fracture path. However, this notion is not consistent with intergranular fracture facets (Figure 7c) which do not show indications of following the tips of the parallel  $\alpha$  colonies shown in Figure 1a. Moreover, it is difficult to attribute all of the differences in IHE susceptibility between 15-3 and 21S exclusively to a difference in the irreversible trapping capability of  $\alpha/\beta$  interfaces in the two alloys since (a) SHT 21S is more susceptible to IHE than SHT 15-3 even in the absence of  $\alpha$  precipitates, (b) re-solution heat treated 15-3 and re-solution heat treated and aged 15-3 are rendered susceptible to IHE and SCC<sup>(37)</sup>, respectively, and no  $\alpha$  precipitates are present in re-SHT 15-3, and (c) irreversible trapping at  $\alpha/\beta$  interfaces does not account for many of the other fracture paths reported in the present study. It is also difficult to attribute the difference in susceptibility

to just the presence of boundary  $\alpha$ , since aged 15-3 contained a  $0.1 \mu\text{m}$   $\alpha$  film but did not crack intergranularly in aqueous testing<sup>(37)</sup> or with internal hydrogen.

The second factor is the effect of hydrogen on the ductile to brittle transition temperature (DBTT) for the  $\beta$  matrix<sup>(1,67)</sup>. Lederich reports a  $50^\circ\text{C}$  difference in DBTT for 15-3 versus 21S, with 21S experiencing the higher of the two transition temperatures at a given  $\beta$  phase hydrogen concentration<sup>(67)</sup>. Calculations show<sup>(62)</sup> it to be unlikely that the DBTT has been shifted above room temperature for either of the two alloys in the present study for the majority of the hydrogen levels studied. This conclusion is reached even after taking into consideration a correction in hydrogen concentration due to hydrogen partitioning in the  $\beta$  matrix of  $\beta + \alpha$  Ti microstructures<sup>(62)</sup>.  $\beta$  phase hydrogen concentrations of 5333 and 7586 wt. ppm would be required to raise the DBTT above  $25^\circ\text{C}$  for 21S and 15-3, respectively. Only in the case of DA 21S at 5600 wt. ppm total hydrogen (Figure 7f) is cleavage induced by an increased DBTT suspected. Consequently, we conclude that this particular intrinsic difference between 15-3 and 21S is not the operative reason for the susceptibility of 21S over the range of hydrogen concentrations reported in the present study.

Finally, it is possible that hydrogen assisted intergranular cracking in *bcc-ti* is attributable to some, as yet unidentified, boundary segregation phenomenon. It is interesting to note that the intergranular fracture facets produced show some indications of deformation (Figure 7c) supporting the notion of a role for planar slip in intergranular separation. However, intergranular fracture surfaces do not follow the morphology of well aligned  $\alpha$  colonies at grain boundaries suggesting that some other factor plays a role in intergranular cracking. The synergistic negative role of phosphorus, sulfur and hydrogen on the intergranular cracking behavior of steel has been well reported<sup>(68,69)</sup>. A detrimental segregation tendency, involving an as yet unidentified alloying impurity, is consistent with the observation of a solutionizing time and temperature dependency in the *bcc* titanium system.

#### *Correlations with aqueous stress corrosion cracking*

Hydrogen has previously been suggested as the embrittling species in aqueous chloride testing of PA  $\beta$  titanium alloys<sup>(10,11)</sup>. Hydrogen-slip interactions may explain the superior SCC resistance of PA 15-3 vs. PA 21S in aqueous sodium chloride solution<sup>(11,37)</sup>. Young and Gangloff have suggested that dislocation motion is a requisite for EAC in 21S based on J-integral resistance curve testing conducted at varying load-line displacement rates and "ripple" loaded tests of PA 15-3 and 21S in aqueous saltwater<sup>(37)</sup>. This statement fits well with the observations made in this paper. Consider the production of hydrogen at an acidified crack tip and absorption of this hydrogen into the fracture process zone. Under a "ripple" load designed to rupture the surface oxide film (but well below the fatigue  $\Delta K$  threshold for crack growth in moist air) hydrogen may enter the metal if elastic strains are capable of rupturing the oxide film and partitions primarily in the  $\beta$  phase where it is highly soluble. Localized planar slip band formation does not occur, however, below the moist air fatigue  $\Delta K$  threshold.

Under a rising load test, however, where dislocation motion is occurring, hydrogen may be transported by dislocations and deposited at the dislocation sinks (i.e. grain boundaries) where it is trapped and promotes intergranular separation. The differences in the SCC resistance between 15-3 and 21S may also be traced to the tendency of 21S toward planar slip which might promote

hydrogen transport over long distances to grain boundaries. Multiple or wavy slip, which has been shown to occur more readily in SHT 15-3 than 21S, hinders the transport and deposition of hydrogen to grain boundaries and concurrently disperses hydrogen as dislocations transport hydrogen to newly activated slip systems. Planar slip may also promote film rupture phenomena to stimulate crack tip hydrogen entry in aqueous SCC testing.

## CONCLUSIONS

1. Hydriding of a large volume fraction of the  $\alpha$  and  $\beta$  phases is not required for hydrogen embrittlement to occur in  $\beta$  titanium alloy Ti-15Mo-3Nb-3Al. Reduction in the maximum longitudinal tensile stress and plastic strain developed in solution annealed Ti-15Mo-3Nb-3Al at hydrogen concentrations < 2900 wt. ppm suggest that the  $\beta$  phase is intrinsically embrittled by hydrogen especially when deformation occurs by localized planar slip.
2. Embrittlement is a function of hydrogen concentration, constraint, and yield strength for alloys which have a susceptible microstructure. Susceptible microstructures are caused by high solution treatment temperatures and times which remove heterogeneous nucleation sites from grain interiors to promote grain boundary  $\alpha$ , delay intragranular  $\alpha$  precipitation and promote planar slip. In aged alloys it is speculated that fine  $\alpha$  precipitates may be sheared by dislocations to promote planar slip, concentrate hydrogen along planar slip bands and transport hydrogen to grain boundaries.
3. The relationships between microstructure, deformation mode and speculated hydrogen transport behavior can account for the observed cracking in  $\beta$  titanium which was precharged with hydrogen and slowly strained in air as well as simultaneously polarized and slowly strained in aqueous chloride solution. This correlation supports a hydrogen embrittlement/dislocation transport mechanism for aqueous saltwater stress corrosion cracking of metastable  $\beta$  titanium alloys.

## ACKNOWLEDGMENTS

This research was supported by the Office of Naval Research (Grant N00014-91-J-4164) with Dr. A. John Sedriks as Scientific Monitor and by the Virginia Center for Electrochemical Science and Engineering at the University of Virginia. The material used in this study was graciously donated by TIMET. The authors wish to acknowledge the invaluable assistance and discussions with R.P. Gangloff, B.P. Somerday, L.M. Young, K. Lawless and J.M. Howe.

## REFERENCES

1. H.G. Nelson, "Hydrogen Environment Effects on Advanced Alloys and Composites in Aerospace Structures," pp. 301-311, (Charlottesville, VA: First Thermal Structures Conference, 1990).
2. P.J. Bania, G.A. Lenning and J. A. Hall, "Development and Properties of Ti-15V-3Cr-3Sn-3Al (Ti-15-3)," pp. 209-299, (Warrendale, PA: Beta Titanium Alloys in the 80's, 1983).
3. A.G. Hicks and H. W. Rosenberg, "Ti-15-3 Foil Properties and Applications," pp. 231-238, (Warrendale, PA: Beta Titanium Alloys in the 80's, 1983).
4. P.J. Bania and W.M. Parris, "BETA-21S: A High Temperature Metastable Beta Titanium Alloy," (Orlando, FL: Titanium Development Association International Conference, 1990).

5. T.W. Duerig and J.C. Williams, "Overview: Microstructure and Properties of Beta Titanium Alloys," pp. 19-67, (Warrendale, PA: Beta Titanium Alloys in the 80's, 1983).
6. R.J. H. Wanhill, *British Corrosion J.*, 10(2)(1975): pp. 69-78.
7. M.J. Blackburn, J.A. Feeney, T.R. Beck, *Stress Corrosion Cracking of Ti Alloys* (New York, NY: Advances in Corrosion Science and Technology, 1972), pp. 67-292.
8. R.W. Schutz and D.E. Thomas, *Corrosion of Titanium and Titanium Alloys* (Metals Park, OH: Metals Handbook, 9th edition, Vol. 13, 1987), pp. 669-706.
9. D.N. Fager and W.F. Spurr, *Trans. ASM*, 61(1968): pp. 283-292.
10. J.A. Feeney, M.J. Blackburn, *Metall. Trans.*, 1(1970): pp. 3309-3323.
11. L.M. Young, *Environment Assisted Cracking in  $\beta$ -Titanium Alloys* (Charlottesville, VA: Master's Thesis, 1993).
12. H.J. Bhatt, E.H. Phelps, *Corrosion J.*, 17(1961): pp. 430t-434t.
13. B.E. Wilde, *Corrosion J.*, 27(8)(1971): p. 326.
14. J.R. Scully, P.J. Moran, *Corrosion J.*, 44(3)(1988): pp. 176-186.
15. R.P. Gangloff, "Corrosion Prev. and Control," pp. 64-111, (Watertown, MA: Proc. of the 33rd Sagamore Army Materials Research Conf., 1986).
16. D. Kolman, and J.R. Scully, Unpublished research, The University of Virginia, Charlottesville, VA, 1993.
17. T.R. Beck, *Localized Corrosion* (Houston, TX: NACE, 1974), pp. 644-652.
18. A.D. McQuillan, "An Experimental and Thermodynamic Investigation of the Hydrogen-Titanium System," pp. 309-323, (*Proceedings of the Royal Society of London*, Vol. A204, 1950).
19. M. Pourbaix, *Atlas of Electrochemical Equilibria in Aqueous Solutions* (Houston, TX: NACE, 1974).
20. B.F. Brown, C.T. Fujii, and E.P. Dahlberg, *J. Electrochem. Soc.*, 116(1969): pp. 218-219.
21. J.J. DeLuccia, "Electrolytic Hydrogen Permeation in Beta Titanium," Report No. NADC-76297-30, Naval Air Development Center, 1976.
22. W.R. Holman, R.W. Crawford, F. Paredes, Jr., *Hydrogen Diffusion in a Beta-Titanium Alloy*, *Trans. TMS-AIME*, (233)(1965): pp. 1836-1839.
23. R.L. Schulte, P.N. Adler, "Stress Induced hydrogen Redistribution in High Purity Ti-31V Alloy," pp. 177-185, (Warrendale, PA: Hydrogen Effects in Metals, 1980).
24. K.N. Akhurst, T.J. Baker, *Metall. Trans. A*, 12A(1981): pp. 1059-1071.
25. N. Bandyopadhyay, J. Kameda, C.J. McMahon, *Metall. Trans. A*, 14A(1983): pp. 881-888.
26. D.S. Shih, and H.K. Birnbaum, *Evidence of FCC Titanium Hydride Formation in  $\beta$  Titanium Alloy: An X-Ray Diffraction Study*, *Scripta Met.*, Vol 20(1986): pp 1261-1264.

27. W.W. Gerberich, N.R. Moody, C.L. Jensen, C. Hayman, and K. Jatavallabhula, "Hydrogen in  $\alpha/\beta$  and all  $\beta$  Titanium Systems," pp. 731-745, (Warrendale, PA: Hydrogen Effects in Metals, 1981).
28. K. Nakasa and J. Liu, Bending Strength of Hydrogen Charged Ti-13V-11Cr-3Al Alloy (J Japan Inst. Metals, Vol 55, No. 9(1991): pp. 922-927.
29. D.E. Thomas and S.R. Seagle, "Stress Corrosion Cracking Behavior of Ti-38-6-44 in Sour Gas Environments," Titanium Science and Technology, Vol. 4, pp.2533-2540, (1984).
30. M.J. Blackburn and W.H. Smyrl, Stress Corrosion and Hydrogen Embrittlement (New York, NY: Titanium Science and Technology, 1973), pp. 2577-2609.
31. H.G. Nelson, "Aqueous Chloride Stress Corrosion Cracking of Titanium - A Comparison with Environmental Hydrogen Embrittlement," pp.445-464, (Hydrogen in Metals, 1973).
32. N.E. Paton and O. Buck, "Effect of Hydrogen Behavior of Materials," pp. 83-89, (Warrendale, PA: 1975).
33. N.E. Paton, R.A. Spurling and C.G. Rhodes, pp.269-279, "Hydrogen Effects in Metals," pp. 269-279, (Warrendale, PA 1981).
34. J.E. Costa, D. Banerjee, and J.C. Williams, "Hydrogen Effects in  $\beta$ -Titanium Alloys," pp. 69-84, (Warrendale, PA: Beta Titanium Alloys in the 80's, 1983).
35. L. Wagner, J.K. Gregory, "Improvement of the Mechanical Behavior in Ti-3Al-8V-6Cr-4Mo-4Zr by Duplex Aging," pp. 199-209, (Denver, CO: Proc. of the TMS Beta-Titanium Symposium, TMS Annual Meeting, 1993).
36. G.A. Young Jr. and J.R. Scully, Effects of Hydrogen on the Mechanical Properties of a Ti-Mo-Nb-Al Alloy, Scripta Met., (28)(1993): pp. 507-512.
37. L.M. Young, G.A. Young, Jr., J.R. Scully, R.P. Gangloff, "Aqueous Environment Enhanced Crack Propagation in High Strength Beta-Titanium Alloys," in review, Metall. Trans., 1993.
38. J.B. Guernsey, V.C. Petersen, and F.H. Froes, Discussion of Effect of Microstructure on the Strength, Toughness, and Stress-Corrosion Cracking Susceptibility of a Metastable  $\beta$  Titanium Alloy, Met. Trans. A, (3)(1972): pp. 339-340.
39. Z.A. Foroulis, "Factors Affecting Absorption of Hydrogen in Titanium from Aqueous Electrolytic Solutions," pp. 2705-2711, (Warrendale, PA: Ti'80, Science and Technology, 1980).
40. P.W. Bridgman, Studies in Large Plastic Flow, McGraw-Hill Inc.(1952): pp. 9-37.
41. J.W. Hancock and A.C. Mackenzie, On the Mechanisms of Ductile Failure in High-Strength Steels Subjected to Multi-Axial Stress-States, J. Mech. Phys. Solids, (24)(1976): pp. 147-169.
42. A.C. Mackenzie, J.W. Hancock and D.K. Brown, On the Influence of State of Stress on Ductile Failure Initiation in High Strength Steels, Engineering Fracture Mechanics, (9)(1977): pp. 167-188.
43. J. Eastman et al., "Hydrogen Effects in Nickel--Embrittlement or Enhanced Ductility," Hydrogen Effects in Metals, pp. 397-409, (The Metallurgical Society of AIME, 1980).
44. R.E. Stoltz and A.J. West, "Hydrogen Assisted Fracture in FCC Metals and Alloy," Hydrogen Effects in Metals, pp. 541-553, (The Metallurgical Society of AIME, 1980).
45. N.R. Moody and F.A. Greulich, Hydrogen Induced Slip Band Fracture in an Fe-Ni-Co Superalloy, Scripta Met., (19)(1985): pp. 1107-1111.

46. N.R. Moody, R.E. Stoltz, and M.W. Perra, The Effect of Hydrogen on Fracture Toughness of the Fe-Ni-Co Superalloy IN903, *Met Trans A*, (18A)(1987): pp. 1469-1482.
47. N.E. Paton, O. Buck, J.C. Williams, *Scripta. Met.*, 2(1978): p. 669.
48. K. Nakasa and J. Liu, Surface Peeling of Ti-6Al-4V Alloy Specimens during Hydrogen Charging, *J. Japan Inst. Metals*, 54 (11)(1990): pp. 1261-1269.
49. J.D. Boyd, Precipitation of Hydrides in Titanium Alloys, *Trans ASM*, (62)(1969): pp. 977-988.
50. D.A. Meyn and P.S. Pao, "Slow Strain Rate Testing of Precracked Titanium Alloys in Salt Water and Inert Environments", *Slow Strain Rate Testing: Research and Engineering Applications*, ASTM STP 1210, R. Kane, ed., ASTM 1993.
51. K.R. Lawless, Unpublished Research, The University of Virginia, Charlottesville, VA, 1993.
52. M. Okada, D. Banerjee, and J.C. Williams, "Tensile Properties of Ti-15-V-3Al-3Cr-3Sn Alloy," pp. 1835-1842, (*Titanium Science and Technology*, 1980).
53. J.P. Hirth, Effects of Hydrogen on the Properties of Iron and Steel, *Met Trans A*, (11A)(1980): pp. 861-890.
54. C.J. MacMahon Jr., "Effects of Hydrogen on Plastic Flow and Fracture in Iron and Steel," *Hydrogen Effects in Metals*, pp. 219-233, (The Metallurgical Society of AIME, 1980).
55. R.L. Shulte and P.N. Adler, "Stress-Induced Hydrogen Redistribution in High Purity Ti-31V Alloy," *Hydrogen Effects in Metals*, pp. 177-185, (The Metallurgical Society of AIME, 1980).
56. J.K. Tien et al., Hydrogen Transport by Dislocations, *Met. Trans. A*, (7A)(1976): pp. 821-829.
57. J. Albrecht, I.M. Bernstein, and A.W. Thompson, Evidence for Dislocation Transport of Hydrogen in Aluminum, *Met. Trans. A*, (13A)(1982): pp. 811-820.
58. D.A. Hardwick, A.W. Thompson, and I.M. Bernstein, The Effect of Copper Content and Microstructure on the Hydrogen Embrittlement of Al-6Zn-2Mg Alloys, *Met. Trans. A*, (14A)(1983): pp. 2517-2526.
59. D. Nguyen, A.W. Thompson, and I.M. Bernstein, Microstructural Effects on Hydrogen Embrittlement in a High Purity 7075 Aluminum Alloy, *Acta Met.*, (35) 10(1987): pp. 2417-2425.
60. F.W. Ling, E.A. Starke, Jr., and B.G. LeFevre, *Metall. Trans.*, 5(1974): pp. 179-187.
61. F.W. Ling, H.J. Rack, E.A. Starke, Jr., *Metall. Trans.*, 4(1973): pp. 1671-1676.
62. G.A. Young, Jr., *Hydrogen Effects in Metastable Beta Titanium Alloys* (Charlottesville, VA: Master's Thesis, 1993).
63. H. Fujii, H.G. Suzuki, "Effect of Solution Treatment Conditions on Aging Response," pp. 249-259, (*Beta Titanium Alloys in the 1990's*, 1993).
64. M.A. Imam, P.K. Poulouse, B.B. Rath, "Modification of Alpha Phase Precipitation by Cold Work of the Ti-15-3 Alloy," pp. 261-271, (*Beta Titanium Alloys in the 1990's*, 1993).
65. B.G. Pound, "Evaluation of a Diffusion/Trapping Model for Hydrogen Ingress in High Strength Alloys," SRI Report PYU-2969, October, 1993.
66. G.M. Pressouyre, *Metall. Trans.*, 10A(1979): p. 1571.

67. R.J. Lederich, D.S. Schwartz, S.M.L. Sastry, "Effects of Internal Hydrogen on Microstructures and Mechanical Properties of  $\beta$ 21S and Ti-15-3," pp. 159-169, (Beta Titanium Alloys in the 1990's, 1993).
68. N. Bandyopadhyay, J. Kameda, C.J. McMahon, Metall. Trans. A, 14A(1983), pp. 881-888.
69. W.W. Gerberich, J. Garry, J.F. Lessar, in Hydrogen Effects on Material Behavior, A.W. Thompson, I.M. Bernstein, eds., TMS-AIME, Warrendale, PA, pp. 70-82, 1976.

TABLE 1

B-titanium alloy heat treatments and corresponding Rockwell C hardness values. Alloys were received in the SHT condition with the reported solution heat treatment temperatures and times.

| Condition: Alloy   | Heat Treatment   | HRC                      |
|--|--|--------------------------|
| <i>Solution Annealed:</i><br>Ti-15V-3Cr-3Al-3Sn<br>Ti-15Mo-3Nb-3Al | 816°C, 0.5 h → Air Cool<br>871°C, 8 h → Air Cool   | 25.2 ± 0.9<br>28.7 ± 1.2 |
| <i>Peak Aged:</i><br>Ti-15V-3Cr-3Al-3Sn<br>Ti-15Mo-3Nb-3Al         | 538°C, 8 h → Air Cool<br>538°C, 8 h → Air Cool   | 38.9 ± 0.6<br>42.1 ± 1.2 |
| <i>Duplex Aged:</i><br>Ti-15V-3Cr-3Al-3Sn<br>Ti-15Mo-3Nb-3Al       | 440°C, 20 h → Air Cool → 538°C, 0.5 h → Air Cool<br>440°C, 20 h → Air Cool → 538°C, 0.5 h → Air Cool | 41.4 ± 0.7<br>48.8 ± 0.8 |



## List of Figures

Figure 1. Optical micrographs showing the aging response of (a) Ti-15V-3Cr-3Al-3Sn and (b) Ti-15Mo-3Nb-3Al after aging for 1 hour at 538°C.

Figure 2. The effects of constraint and total internal hydrogen concentration on the maximum longitudinal stress and effective plastic strain developed in peak aged Ti-15V-3Cr-3Al-3Sn and Ti-15Mo-3Nb-3Al.  $\sigma_{YIELD}$  is the uniaxial yield strength for no intentional hydrogen additions. Note that the data points at 1.43 and 1.03 constraint with no intentional hydrogen overlay each other for the case of the Ti-15Mo-3Nb-3Al alloy.

Figure 3. The effect of total internal hydrogen concentration on maximum longitudinal stress and effective plastic strain developed in solution heat treated Ti-15V-3Cr-3Al-3Sn and Ti-15Mo-3Nb-3Al.

Figure 4. The effect of total internal hydrogen concentration on maximum longitudinal stress and effective plastic strain developed in single step peak aged Ti-15V-3Cr-3Al-3Sn and Ti-15Mo-3Nb-3Al.

Figure 5. The effect of total internal hydrogen concentration on maximum longitudinal stress and effective plastic strain developed in duplex aged Ti-15V-3Cr-3Al-3Sn and Ti-15Mo-3Nb-3Al.

Figure 6. Fracture surfaces from Ti-15V-3Cr-3Al-3Sn at a constraint level of 1.43 under (a) solution annealed conditions at the uncharged hydrogen level of 90-120 wt. ppm hydrogen, and (b) duplex aged with 3700 wt. ppm hydrogen.

Figure 7. Fracture modes produced in Ti-15Mo-3Nb-3Al at a constraint level of 1.43 after various heat treatments and different hydrogen concentrations: (a) SHT - 100 ppm, (b) SHT - 3000 ppm, (c) PA - 1000 ppm, (d) PA - 3500 ppm, (e) DA, 3800 ppm, and (f) DA, 5600 ppm.

Figure 8. Surface slip lines observed in solution heat treated (a) Ti-15V-3Cr-3Al-3Sn and (b) Ti-15Mo-3Nb-3Al both deformed to approximately 8% plastic strain in compression.

Figure 9. (a) Diffraction spectra from the surface of peak aged Ti-15Mo-3Nb-3Al charged 64 hours in  $H_2SO_4$  solution at 90°C and (b) SEM micrograph of the charged surface illustrating the spalled surface exposed secondary  $\alpha$  phase.

Figure 10. Diffraction spectra taken from the surface of PA Ti-15V-3Cr-3Al-3Sn, charged 24 hours showing the  $\alpha$ ,  $\beta$ , and  $\delta$  phase peaks.

Table 1.  $\beta$ -titanium alloy heat treatments and corresponding Rockwell C hardness values. Alloys were received in the SHT condition with the reported solution heat treatment temperatures and times.

| Condition: Alloy   | Heat Treatment   | HRC                              |
|--|--|----------------------------------|
| <i>Solution Annealed:</i><br>Ti-15V-3Cr-3Al-3Sn<br>Ti-15Mo-3Nb-3Al | 816°C, 0.5 h $\rightarrow$ Air Cool<br>871°C, 8 h $\rightarrow$ Air Cool   | 25.2 $\pm$ 0.9<br>28.7 $\pm$ 1.2 |
| <i>Peak Aged:</i><br>Ti-15V-3Cr-3Al-3Sn<br>Ti-15Mo-3Nb-3Al         | 538°C, 8 h $\rightarrow$ Air Cool<br>538°C, 8 h $\rightarrow$ Air Cool   | 38.9 $\pm$ 0.6<br>42.1 $\pm$ 1.2 |
| <i>Duplex Aged:</i><br>Ti-15V-3Cr-3Al-3Sn<br>Ti-15Mo-3Nb-3Al       | 440°C, 20 h $\rightarrow$ Air Cool $\rightarrow$<br>538°C, 0.5 h $\rightarrow$ Air Cool<br>440°C, 20 h $\rightarrow$ Air Cool $\rightarrow$<br>538°C, 0.5 h $\rightarrow$ Air Cool | 41.4 $\pm$ 0.7<br>48.8 $\pm$ 0.8 |

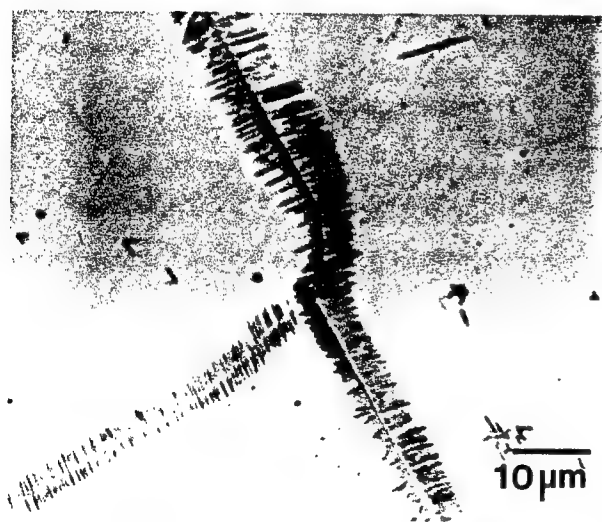


Figure 1a. Optical micrograph showing the  $\beta + \alpha$  microstructure of Ti-15Mo-3Nb-3Al after aging for 1 hour at 538°C.

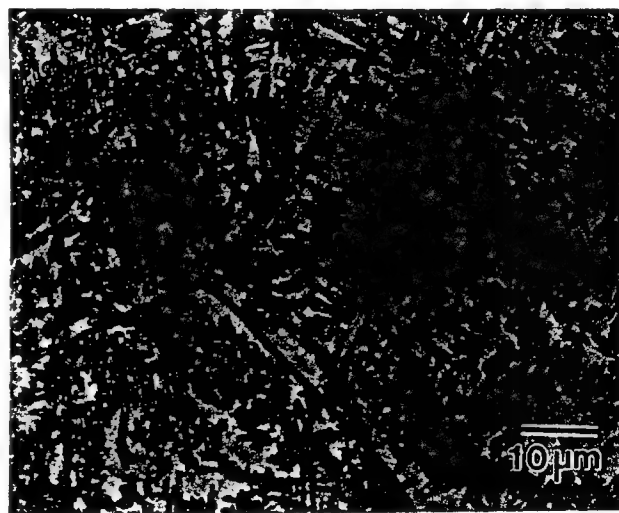


Figure 1b. Optical micrograph showing the  $\beta + \alpha$  microstructure of Ti-15V-3Cr-3Al-3Sn after aging for 1 hour at 538°C.

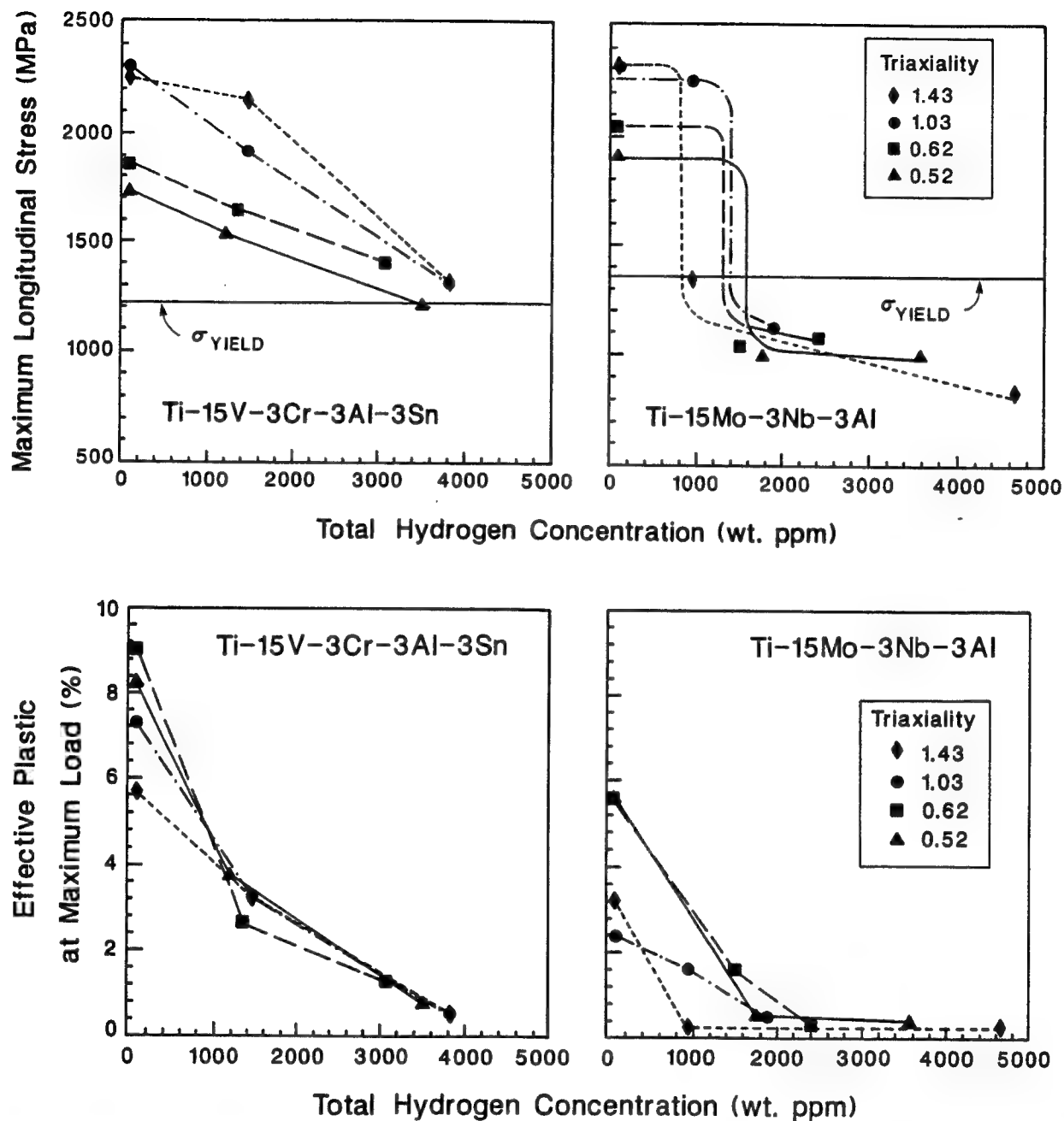


Figure 2. The effects of constraint and total internal hydrogen concentration on the maximum longitudinal stress and effective plastic strain developed in peak aged Ti-15V-3Cr-3Al-3Sn and Ti-15Mo-3Nb-3Al.  $\sigma_{YIELD}$  is the uniaxial yield strength.

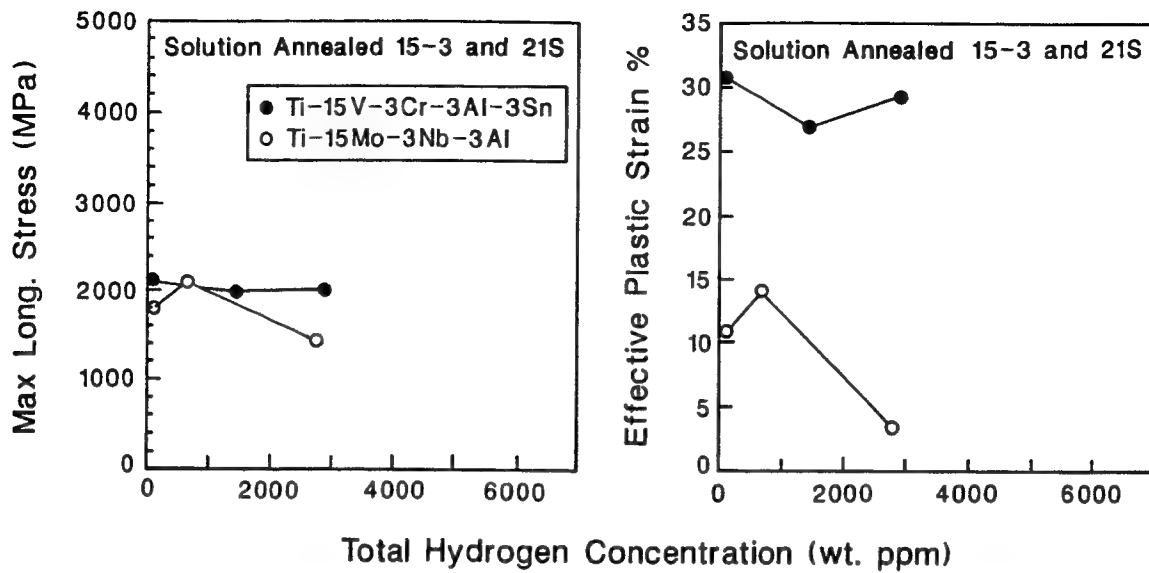


Figure 3. The effect of total internal hydrogen concentration on maximum longitudinal stress and effective plastic strain developed in solution heat treated Ti-15V-3Cr-3Al-3Sn and Ti-15Mo-3Nb-3Al.

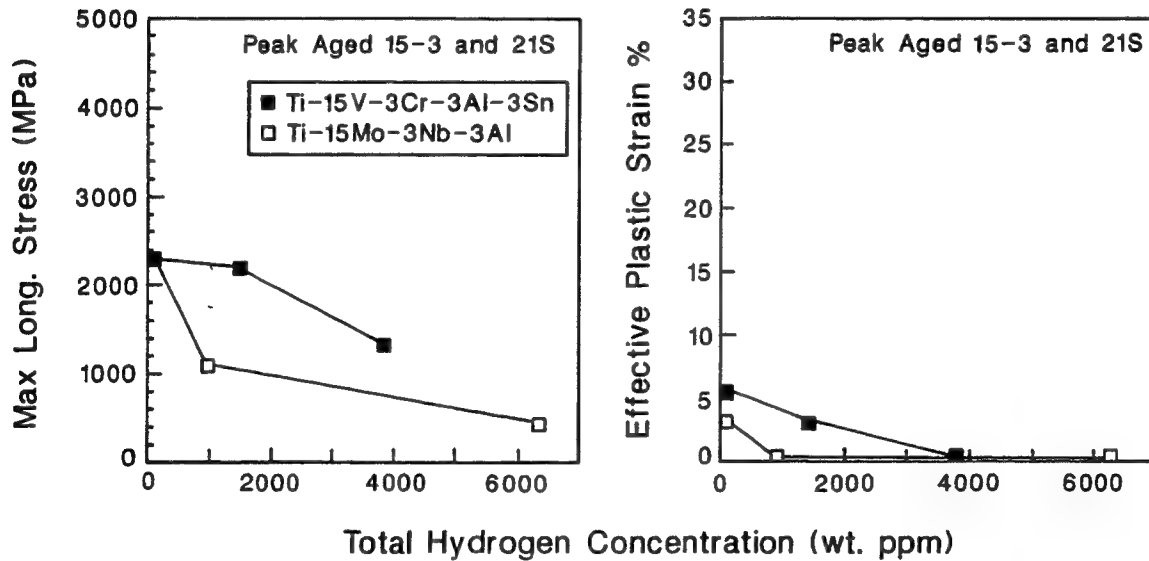


Figure 4. The effect of total internal hydrogen concentration on maximum longitudinal stress and effective plastic strain developed in single step peak aged Ti-15V-3Cr-3Al-3Sn and Ti-15Mo-3Nb-3Al.

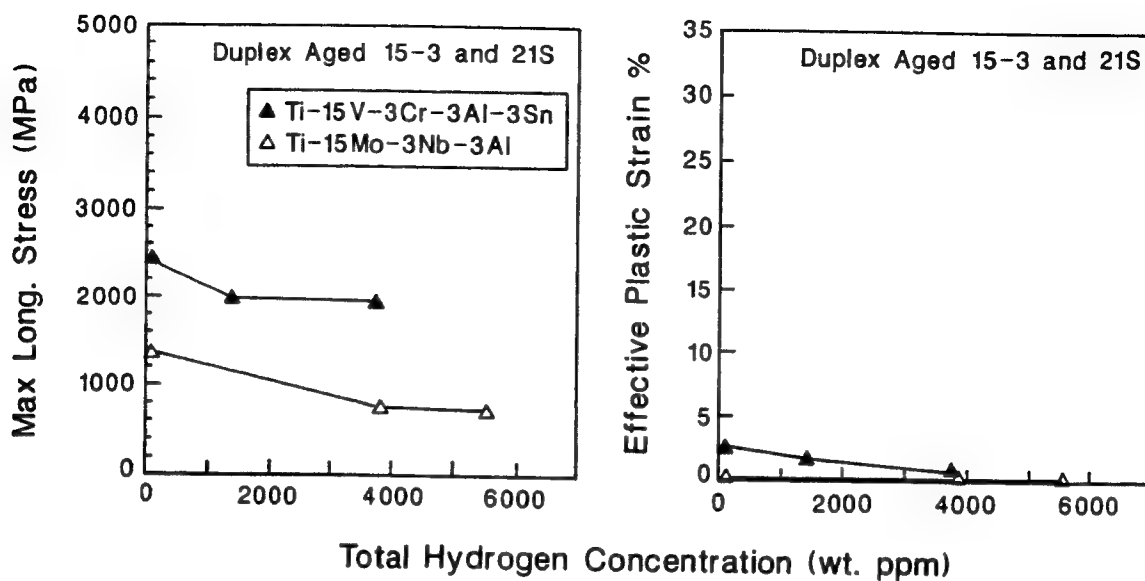


Figure 5. The effect of total internal hydrogen concentration on maximum longitudinal stress and effective plastic strain developed in duplex aged Ti-15V-3Cr-3Al-3Sn and Ti-15Mo-3Nb-3Al.

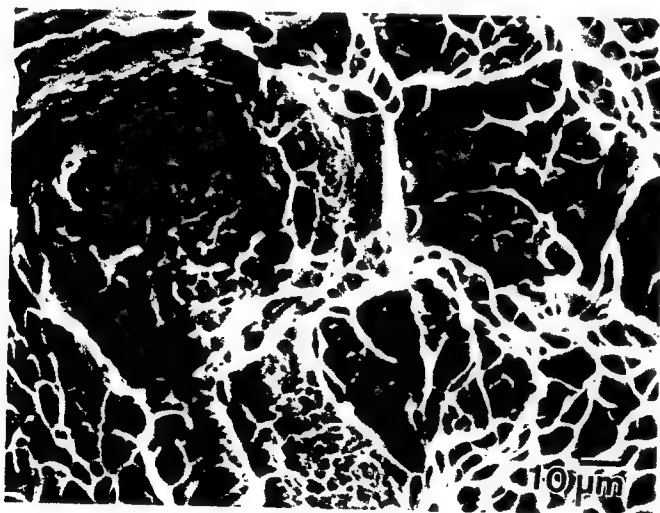


Figure 6a. Fracture surfaces from Ti-15V-3Cr-3Al-3Sn at a constraint level of 1.43 under solution heat treated conditions at the uncharged hydrogen level of 90-120 wt. ppm hydrogen.

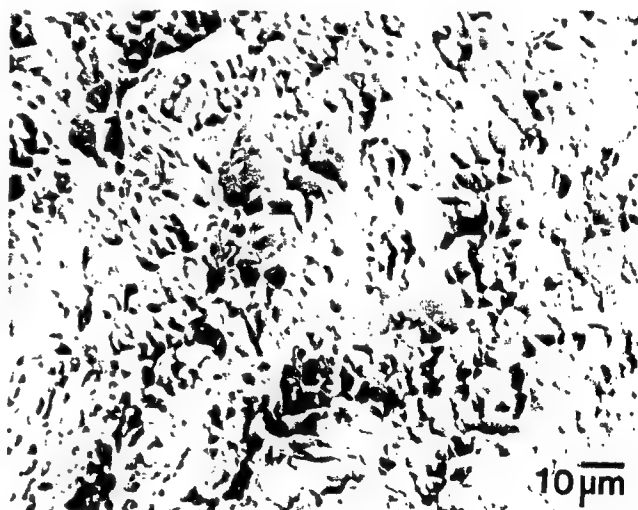


Figure 6b. Fracture surfaces from duplex aged Ti-15V-3Cr-3Al-3Sn at a constraint level of 1.43 with 3700 wt. ppm hydrogen.

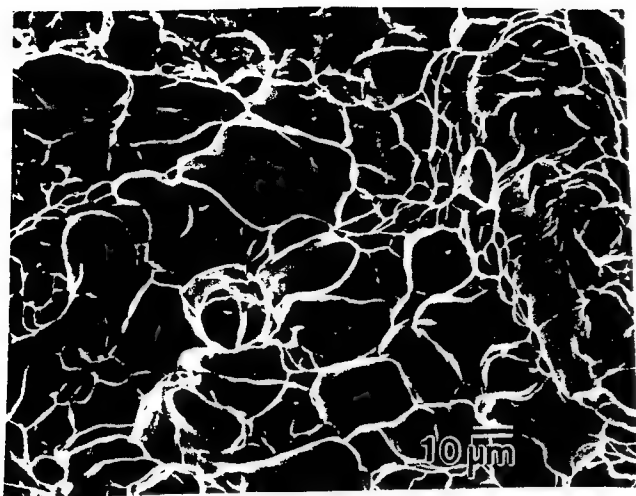


Figure 7a. Fracture mode produced in Ti-15Mo-3Nb-3Al at a constraint level of 1.43: solution heat treated - 100 wt. ppm hydrogen.

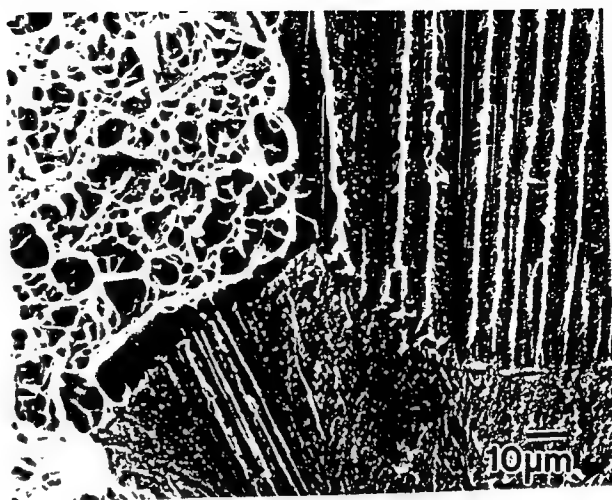


Figure 7b. Fracture mode produced in Ti-15Mo-3Nb-3Al at a constraint level of 1.43: solution heat treated - 3000 wt. ppm hydrogen.

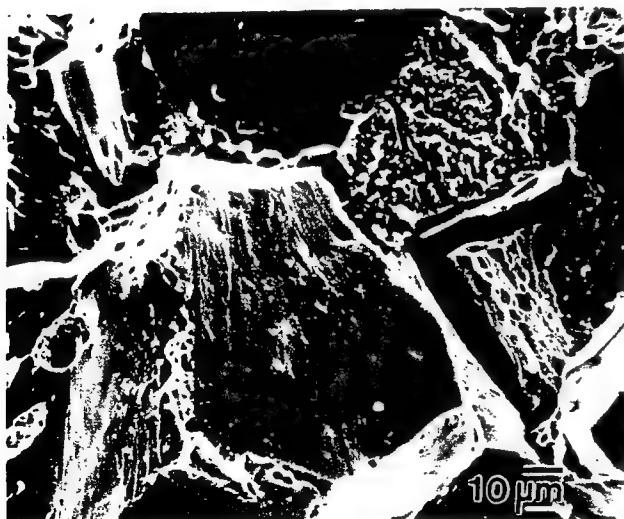


Figure 7c. Fracture modes produced in Ti-15Mo-3Nb-3Al at a constraint level of 1.43: peak aged - 1000 wt. ppm hydrogen.

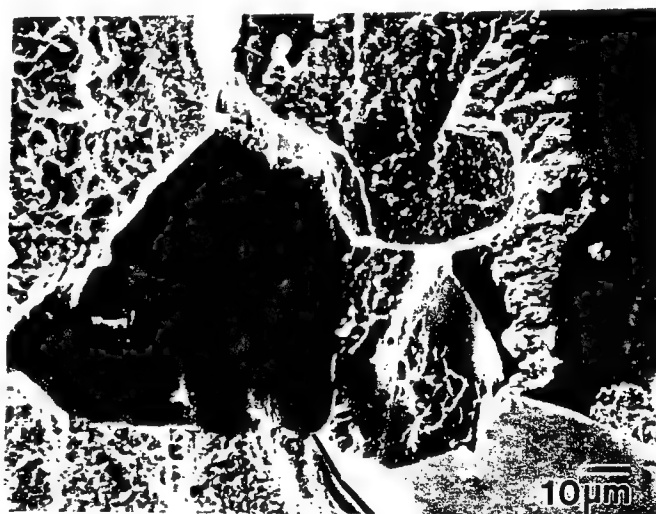


Figure 7d. Fracture modes produced in Ti-15Mo-3Nb-3Al at a constraint level of 1.43: peak aged - 3500 wt. ppm hydrogen.

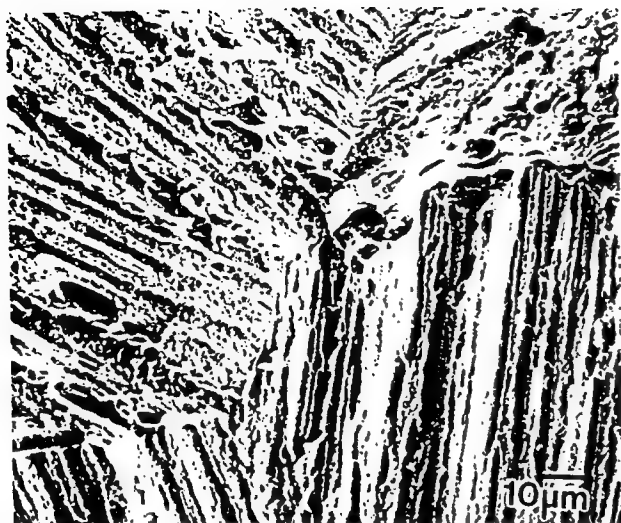


Figure 7e. Fracture modes produced in Ti-15Mo-3Nb-3Al at a constraint level of 1.43: duplex aged - 3800 wt. ppm hydrogen.

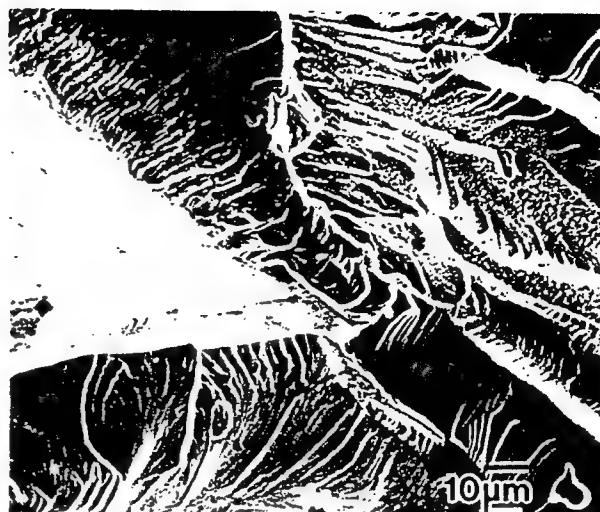


Figure 7f. Fracture modes produced in Ti-15Mo-3Nb-3Al at a constraint level of 1.43: duplex aged - 5600 wt. ppm hydrogen.

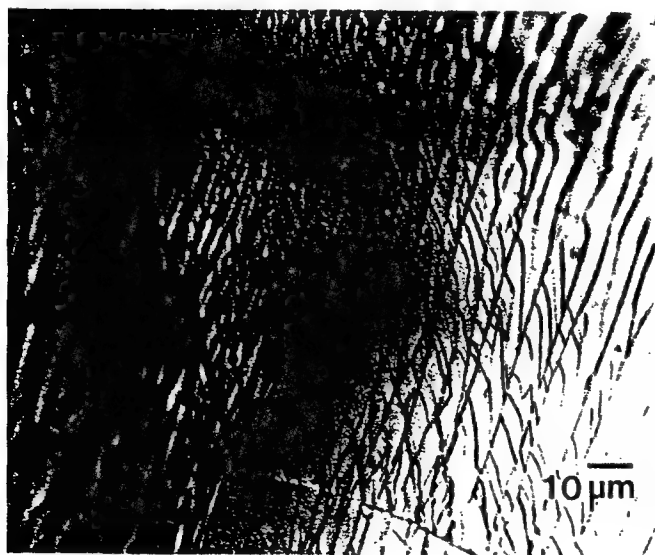


Figure 8a. Surface slip lines observed in solution heat treated Ti-15V-3Cr-3Al-3Sn deformed to approximately 8% plastic strain in compression.

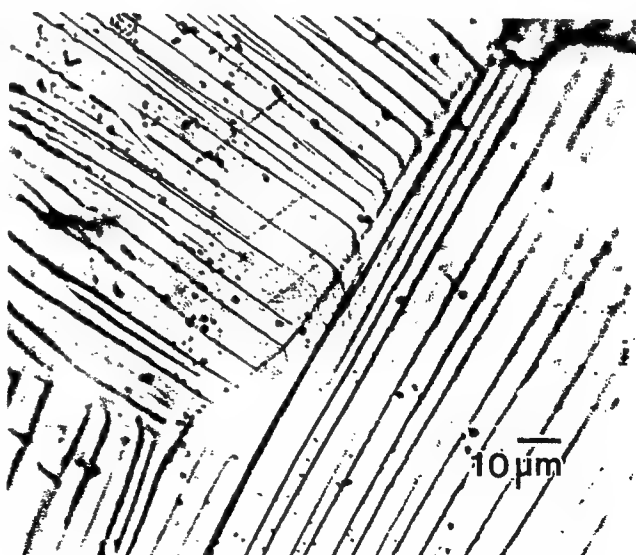


Figure 8b. Surface slip lines observed in solution heat treated Ti-15Mo-3Nb-3Al deformed to approximately 8% plastic strain in compression.

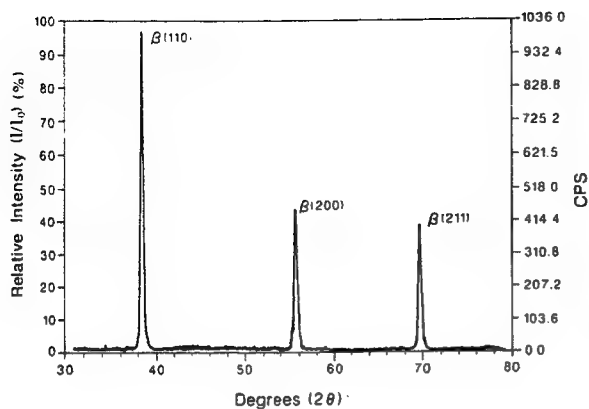


Figure 9a. Diffraction spectra from the surface of peak aged Ti-15Mo-3Nb-3Al charged 64 hours in  $H_2SO_4$  solution at 90°C.

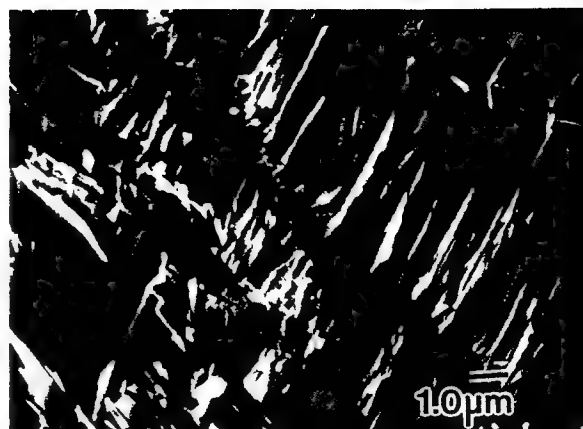


Figure 9b. SEM micrograph of the charged peak aged Ti-15Mo-3Nb-3Al surface illustrating the spalled surface exposed secondary  $\alpha$  phase.

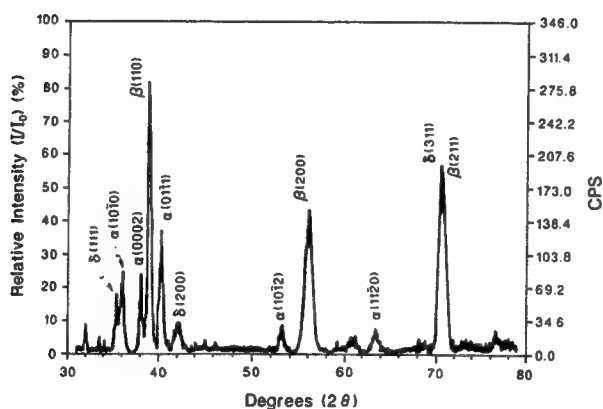


Figure 10. Diffraction spectra taken from the surface of PA Ti-15V-3Cr-3Al-3Sn, charged 24 hours showing the  $\alpha$ ,  $\beta$ , and  $\delta$  phase peaks.



**THE EFFECTS OF HYDROGEN ON THE MECHANICAL PROPERTIES  
OF A Ti-Mo-Nb-Al ALLOY**

**George A. Young, Jr.  
John R. Scully**

**THE EFFECTS OF HYDROGEN ON THE ROOM TEMPERATURE MECHANICAL  
PROPERTIES OF Ti-15V-3Cr-3Al-3Sn AND Ti-15Mo-3Nb-3Al**

George A. Young Jr. and John R. Scully

Materials Science & Engineering  
The University of Virginia  
Charlottesville, VA 22903

**Abstract**

The effects of electrochemically introduced hydrogen on the room temperature mechanical properties of two  $\beta$  titanium alloys, TIMETAL 15-3 (Ti-15V-3Cr-3Al-3Sn, wt%) and TIMETAL 21S (Ti-15Mo-3Nb-3Al, wt%) are compared. Solution annealed, peak aged (538°C, 8h), and duplex aged (440°C, 20h, 538°C, ½h) conditions are investigated. Bridgman notched tensile bars are employed to quantify the degree of embrittlement both by reduction in the maximum longitudinal stress developed at the centerline of the notch and the average effective plastic strain across the notch diameter at maximum load. Fracture paths are correlated with the slip behavior observed in solution annealed material. Possible hydriding of the  $\alpha$  and  $\beta$  phases is investigated through x-ray diffraction. Results show that TIMETAL 21S is more susceptible to hydrogen embrittlement than TIMETAL 15-3 as evidenced by reductions in the longitudinal stress, plastic strain, and changes in fracture mode at hydrogen concentrations above 1000 wt. ppm. Possible hydriding of a large volume fraction of the  $\alpha$  or  $\beta$  phases was not observed over the range of hydrogen concentrations investigated. The increased susceptibility of TIMETAL 21S to hydrogen embrittlement is attributed to a high temperature, long time, solution treatment which removed heterogeneous nucleation sites from the grain interiors. Subsequent aging occurs preferentially on  $\beta$  grain boundaries and lastly in the grain interiors, resulting in fine intragranular precipitates. These fine  $\alpha$  plates are readily sheared and promote planar slip. In contrast, a lower temperature, shorter duration solution treatment for TIMETAL 15-3, results in a material with more homogeneous, larger  $\alpha$  precipitates, which, in turn, promote wavy slip. Results indicate that persistent planar slip exacerbates both hydrogen embrittlement and aqueous environmentally assisted cracking in metastable  $\beta$  titanium alloys.

## Introduction

Modern  $\beta$  titanium alloys are candidates for many hydrogen environment applications due to their desirable mechanical properties, protective oxide film, and high hydrogen solubility [1-4]. However,  $\beta$  titanium alloys are susceptible to hydrogen embrittlement. Both  $\beta$  and  $\alpha$  titanium form a brittle hydride phase and recent reports suggest that the bcc  $\beta$  phase is intrinsically embrittled by hydrogen [5-9]. The present study seeks to compare and contrast the effects of a range of electrochemically charged hydrogen concentrations on the room temperature mechanical properties of the metastable  $\beta$  titanium alloys TIMETAL 15-3 and TIMETAL 21S in both the solution annealed and  $\beta + \alpha$  aged conditions. Duplex aging was performed in an attempt to promote a finer, more homogenous  $\alpha$  distribution and avoid preferential precipitation on  $\beta$  grain boundaries. Preferential  $\alpha$  precipitation has previously been associated with increased susceptibility to stress corrosion cracking, hydrogen embrittlement, and intergranular cracking [9-12].

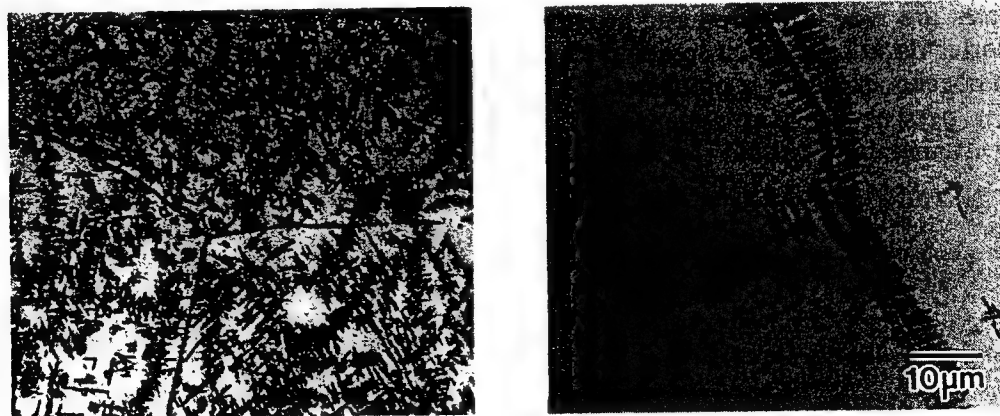
## Experimental

Cross rolled plate, nominally 10 mm thick, of TIMETAL 15-3 (Ti-15V-3Cr-3Sn-3Al) and TIMETAL 21S (Ti-15Mo-3Nb-3Al) was received in the solution annealed condition. Solution annealed (SA), single step aged (referred to hereafter as peak aged (PA)), and duplex aged (DA) heat treatments were investigated. Table I details the heat treatments and corresponding hardness of each condition. Both PA and DA 21S exhibited preferential nucleation of  $\alpha$  along  $\beta$  grain boundaries while  $\alpha$  nucleated intragranularly in 15-3 after one hour at 538°C as shown in Figure 1.

Table I. Heat treatments and corresponding hardnesses of the conditions investigated.

| Condition: Material                            | Heat Treatment   | HRC                              |
|--|--|----------------------------------|
| Solution Annealed: TIMETAL 15-3<br>TIMETAL 21S | 816°C, 0.5 h - Air Cool<br>871°C, 8 h - Air Cool   | 25.2 $\pm$ 0.9<br>28.7 $\pm$ 1.2 |
| Peak Aged: TIMETAL 15-3<br>TIMETAL 21S         | 538°C, 8 h - Air Cool<br>538°C, 8 h - Air Cool   | 38.9 $\pm$ 0.6<br>42.1 $\pm$ 1.2 |
| Duplex Aged: TIMETAL 15-3<br>TIMETAL 21S       | 440°C, 20 h - Air Cool - 538°C, 0.5 h - Air Cool<br>440°C, 20 h - Air Cool - 538°C, 0.5 h - Air Cool | 41.4 $\pm$ 0.7<br>48.8 $\pm$ 0.8 |

Figure 1. Optical micrographs showing the aging response of (a) TIMETAL 15-3 and (b) TIMETAL 21S after aging for 1 hour at 538°C.



Electrochemical pre-charging of hydrogen was conducted in a solution of 10cc  $\text{H}_2\text{SO}_4$ , 1000cc  $\text{H}_2\text{O}$  and 0.8 g  $\text{Na}_4\text{P}_2\text{O}_7$  at  $90^\circ\text{C}$  [13]. Previously machined and heat treated tensile specimens were cathodically polarized to  $100 \text{ A/m}^2$  for various times to promote hydrogen uptake and were tested in air, as described elsewhere [9]. Upon removal from the charging bath, the oxide which forms in air is an effective barrier to hydrogen egress. Hydrogen concentrations reported for each tensile specimen were obtained from a section of the tensile bar adjacent to the notch and represent an average total concentration for the volume of metal tested. Note that the hydrogen uptake rate of 15-3 was approximately 5-6 times greater than that of 21S for all the heat treatments investigated. This increase in hydrogen uptake is attributed, in part, to a higher hydrogen fugacity on the surface of 15-3. At  $25^\circ\text{C}$ , galvanostatic measurements in the charging solution indicate that 15-3 develops a potential approximately 200 mV cathodic to 21S at an equivalent current density of  $100 \text{ A/m}^2$ .

Circumferentially notched "Bridgman" tensile bars were employed to quantify the effects of hydrogen on the mechanical properties of the alloys investigated [14]. Degree of embrittlement was quantified by determining the maximum longitudinal stress developed at the centerline of the notched region and the effective plastic strain across the notch diameter at maximum load following the procedures of Hancock et al. [15-16]. All tensile tests were conducted at a crosshead displacement rate of  $1.5 \times 10^{-2} \text{ mm/min}$ . The effect of constraint on the failure stress and strain in PA material was determined as a function of hydrogen concentration at four different initial constraint levels (0.52, 0.62, 1.03, 1.43) where the triaxial constraint is defined as the ratio of mean to effective stress,  $(\sigma_m/\bar{\sigma})$  [14-16]. These constraint levels correspond to notch radii of 7.9mm, 4.8mm, 1.6mm, and 7.9mm respectively at a constant initial diameter across the notch of 6.4mm. Additional tensile tests, conducted at the constraint level of 1.43 (0.33 = uniaxial tension, 2.50 = sharp notch), compared the effects of hydrogen on SA, PA, and DA heat treatments.

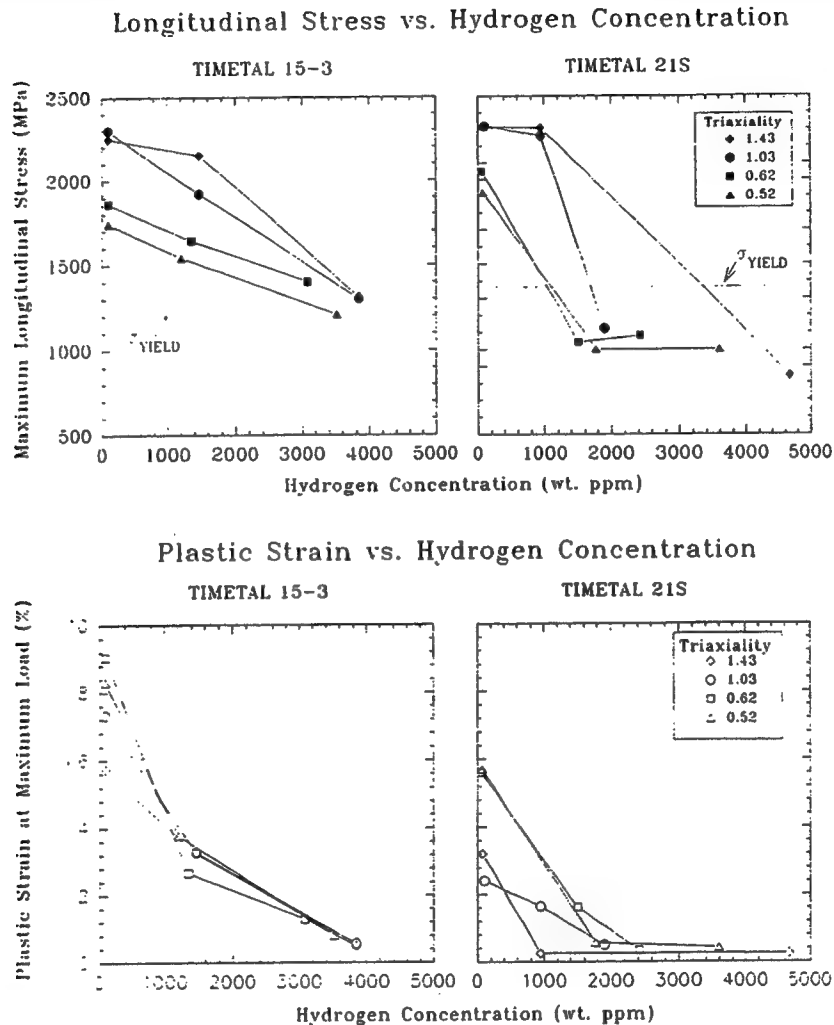
The slip behavior of each alloy was investigated by deforming electropolished cubes of SA material (approximately  $1 \text{ cm}^3$ ) in compression and observing the surface slip lines via optical microscopy. X-ray diffraction experiments were performed with a Scintag automated diffractometer utilizing copper K- $\alpha$  radiation, which was continuously scanned over  $30\text{-}80^\circ 2\theta$  at a rate of  $1^\circ$  per minute. Both the heat treated and heat treated + hydrogen charged conditions were investigated. Diffraction spectra of electrochemically charged plate were taken both at the charged surface and well into the specimen interior by sectioning and grinding.

## Results

### Mechanical Testing

Constraint and Hydrogen The longitudinal stress increased and the plastic strain decreased as level of constraint increased for both uncharged, PA 15-3 and 21S as shown in Figure 2. The longitudinal stress and plastic strain developed in 15-3 decreased linearly with increasing hydrogen concentration. TIMETAL 21S, however, exhibited a sharp decrease in longitudinal stress and plastic strain at hydrogen concentrations greater than 1000 wt. ppm. Note that the largest reductions in plastic strain for 21S occur at the highest constraint.

Figure 2. The effects of constraint and hydrogen on the stress and strain developed in peak aged TIMETAL 15-3 and TIMETAL 21S.  $\sigma_{YIELD}$  is the uniaxial yield strength.



**Heat Treatment** Concerning SA material at the highest constraint level investigated (1.43), the failure stress and strain of 15-3 are unaffected by hydrogen concentrations up to 3000 wt. ppm. In contrast, 21S is embrittled at less than 3000 wt. ppm as shown in Figure 3a. Although the failure stresses for each material in the SA condition are nearly equal, 15-3 displays approximately twice the plastic strain of 21S and nearly three times the plastic strain at high hydrogen concentrations. In the PA condition (Fig. 3b), both 15-3 and 21S exhibit a decrease in strength and ductility at approximately 1000 ppm H. This decrease is more pronounced for 21S. Duplex Aged 15-3 also exhibits greater resistance to hydrogen embrittlement than DA 21S (Fig. 3c). Comparison of material at equivalent hardness levels (as in the case of DA 15-3 versus PA 21S) shows that 15-3 still exhibits superior resistance to hydrogen embrittlement.

**Deformation Mode** Compression tests on SA material revealed that both alloys are prone to planar slip at low plastic strains (3%) while at strains on the order of 8%, extensive cross slip occurred in 15-3 but not in 21S. Figure 4 compares the surface slip observed in SA 15-3 and 21S at approximately 8% plastic strain and illustrates the difference.

Figure 3. The effects of hydrogen on the stress and strain developed in TIMETAL 15-3 and TIMETAL 21S in the (a) solution annealed, (b) peak aged, and (c) duplex aged conditions.

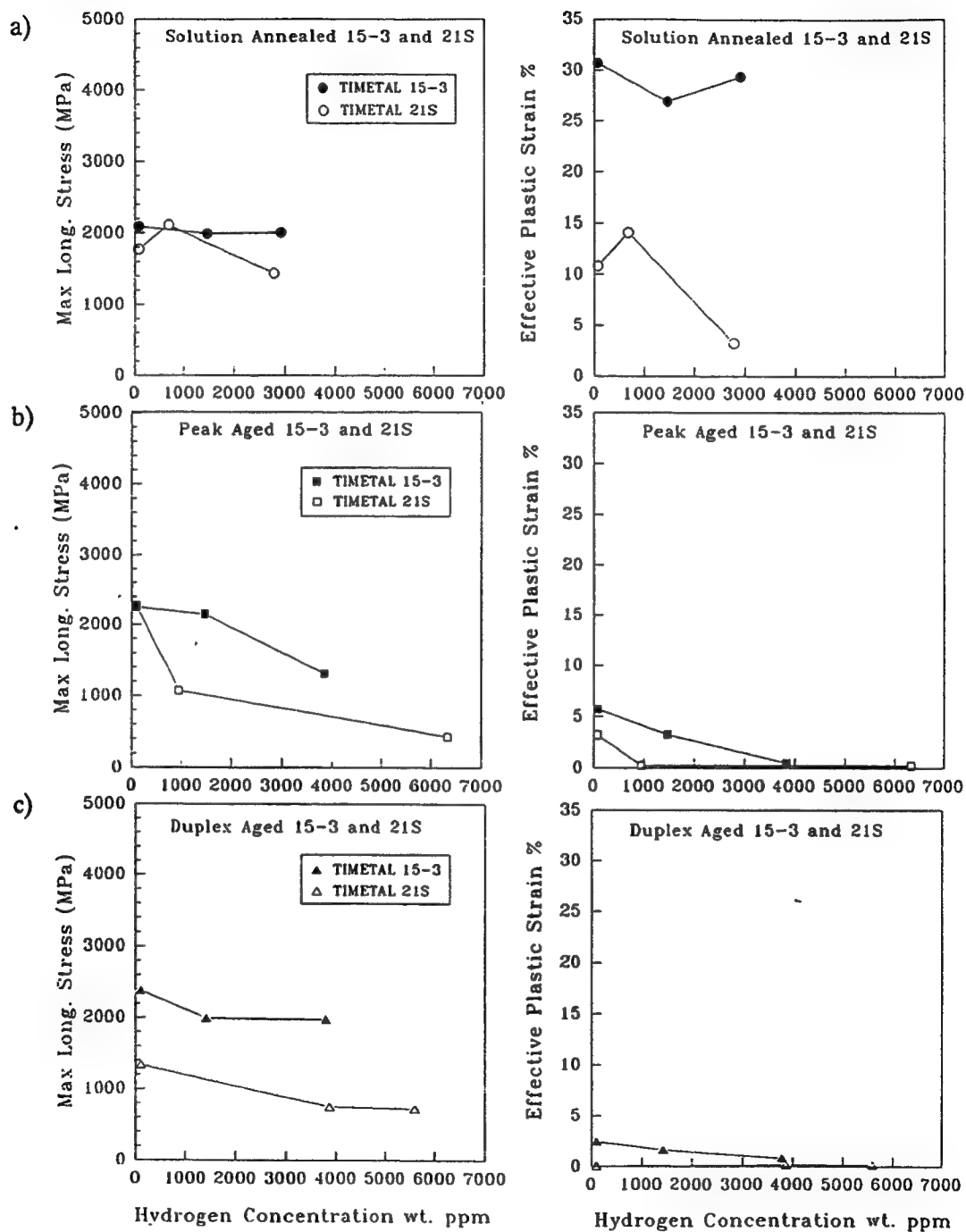
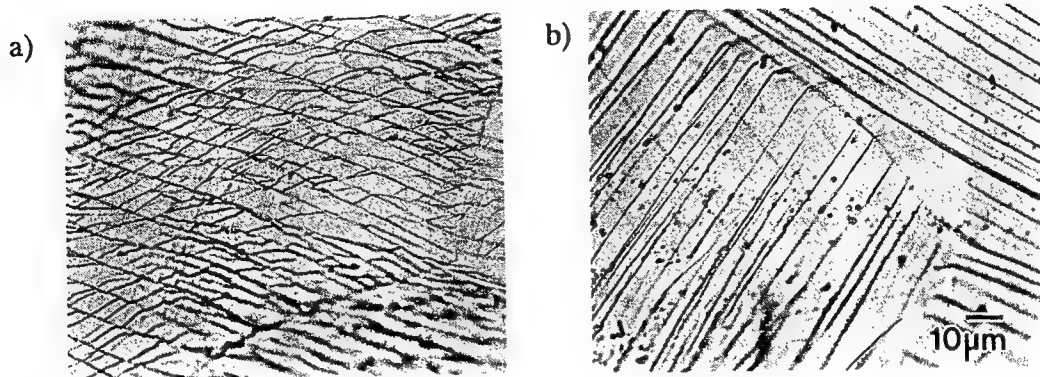


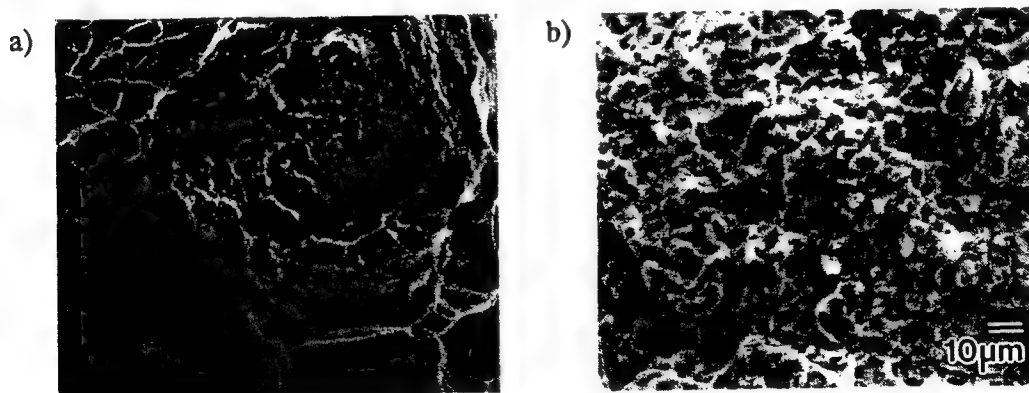
Figure 4. Surface slip lines observed in solution annealed (a) TIMETAL 15-3 and (b) TIMETAL 21S deformed to approximately 8% plastic strain in compression.



#### Fractography

The fracture mode of SA 15-3 was relatively insensitive to hydrogen concentration. At all hydrogen levels investigated SA 15-3 failed by microvoid coalescence. In PA material, the fracture mode of 15-3 was also microvoid coalescence at all constraint and hydrogen levels investigated. The only noticeable effect of increasing hydrogen and constraint was to decrease the depth and width of the microvoids. The fracture mode of 15-3 consists of fine equiaxed microvoids up to its highest hardness and hydrogen concentration (DA to  $R_C$  41, 3793 ppm H) where the fracture mode changed to transgranular ductile tearing as shown in Figure 5.

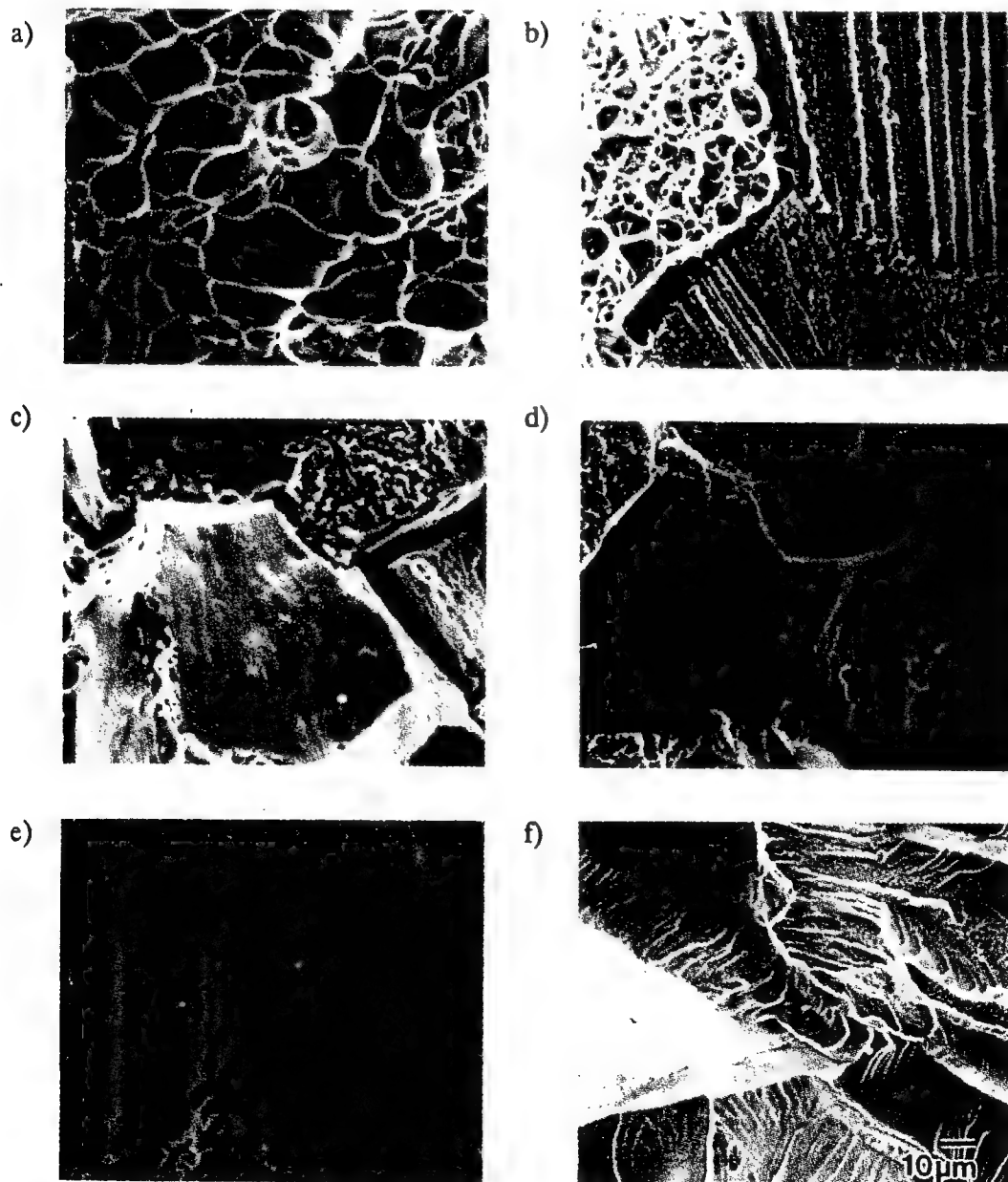
Figure 5. Fracture surfaces from TIMETAL 15-3 (a) uncharged, solution annealed and (b) duplex aged, 3700 wt. ppm hydrogen.



In contrast to 15-3, the fracture mode of SA, PA, and DA 21S changed as the hydrogen concentration was increased (Fig. 6). The fracture mode of SA 21S progressed from large microvoids at approximately 100 ppm hydrogen (Fig. 6a), to small microvoids and ductile tearing features at 680 ppm H, and finally at 3000 ppm to flat fracture characterized by three distinct fracture modes; 1) fine voids and tearing features similar to the 680 ppm hydrogen level, 2) flat transgranular fracture, and 3) transgranular fracture displaying parallel markings (Fig. 6b). These parallel markings typically extend across an entire grain diameter and are consistent with hydrogen induced slip band fracture which has been observed in hydrogen charged bcc steels, pure nickel, and nickel & iron base alloys, [17-20]. The difference in fracture mode between individual grains is believed to be caused by differences in slip system orientation relative to the tensile axis.

The fracture mode in PA 21S is strongly influenced by both level of constraint and hydrogen concentration as detailed elsewhere [9]. At the highest constraint levels, peak aged 21S exhibits a duplex microvoid structure in the uncharged condition, which progresses to a mixture of intergranular and transgranular fracture as H concentration is increased (Fig. 6c). The flat featureless areas of 4664 ppm PA 21S (Fig. 6d) indicate that some slip plane decohesion has occurred. Duplex aged 21S fails by ductile tearing at 75 ppm H progressing to flat fracture characterized by elongated, but microscopically ductile voids at 3800 ppm (Fig. 6e), and finally by cleavage (Fig. 6f) at 5600 ppm.

Figure 6. Fracture modes produced in TIMETAL 21S at a constraint level of 1.43 and different hydrogen levels and heat treatments (a) SA, 100 ppm, (b) SA, 3000 ppm, (c) PA, 1000 ppm, (d) PA, 3500 ppm, (e) DA, 3800 ppm, and (f) DA, 5600 ppm.





## X-ray Diffraction

Diffraction spectra taken from the surface of as charged PA plate indicated that surface exposed  $\alpha$  of 21S spalled off while that of 15-3 did not (Fig. 7). Spalling of the  $\alpha$  phase has previously been reported by Nakasa in Ti-6Al-4V during electrochemical hydrogen charging [21]. TIMETAL 15-3, however, exhibited some evidence of hydriding as shown by diffraction spectra of Figure 8. Hydriding appears to be a phenomena associated with surface exposed  $\alpha$  for both alloys since no hydride peaks were detected in the interior of either material when diffraction spectra were taken after serial grinding of the charged surface. Instead, partitioning of hydrogen to the  $\beta$  phase was suspected as indicated by large changes in the  $\beta$  lattice parameter. However, this does not preclude the possibility of deformation assisted hydriding or localized hydriding of the  $\alpha/\beta$  interfaces as discussed by Boyd [22].

Figure 7. (a) Diffraction spectra from the surface of peak aged TIMETAL 21S charged 64 hours in  $H_2SO_4$  solution and (b) SEM micrograph of the charged surface illustrating the spalled  $\alpha$  phase.

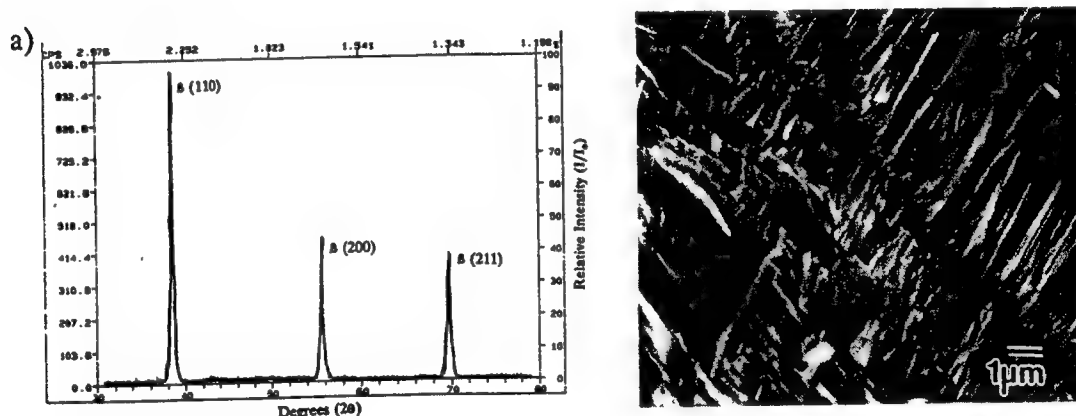
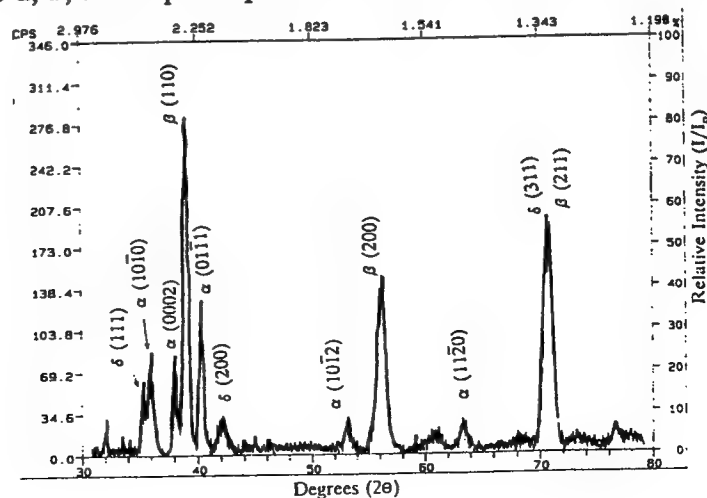


Figure 8. Diffraction spectra taken from the surface of PA TIMETAL 15-3, charged 24 hours showing the  $\alpha$ ,  $\beta$ , and  $\delta$  phase peaks.

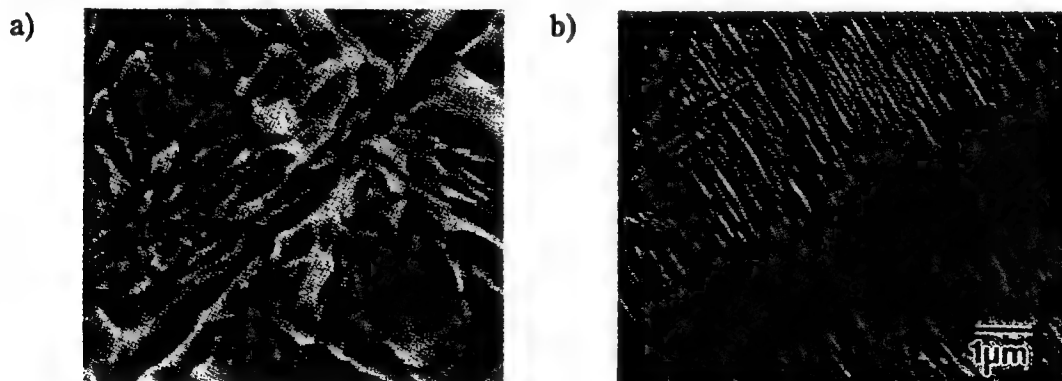


## Discussion

Embrittlement appears to be exacerbated by persistent planar slip in 21S. Slip behavior is dependent on both alloy composition and precipitate morphology. The fact that alloying additions affect stacking fault energy (SFE) and subsequent slip behavior is well known but the authors know of no reports of the effects of alloying additions on SFE in  $\beta$ -Ti alloys. Furthermore, hydrogen affected fracture modes such as intergranular cracking appear to be primarily affected by heat treatment. Alloying elements may play a secondary role. Both L.M. Young and Meyn & coworkers have produced intergranular cracking in 15-3 which was heat treated above the  $\beta$  transus for longer times than investigated here (e.g. 2 hours) [10,23].

Heat treatment, specifically solution treatment and its effects on the resulting microstructure and slip behavior may dominate hydrogen embrittlement resistance in metastable  $\beta$  titanium alloys. Solution treatment has been identified as the controlling factor in hot salt stress corrosion cracking susceptibility of the metastable  $\beta$  alloy Beta-III but the mechanism of embrittlement was not discussed [12]. Okada, Banerjee, and Williams studied the transfer of slip from  $\beta$  to  $\alpha$  as a function of precipitate morphology in Ti-15V-3Cr-3Al-3Sn. They demonstrated that slip initiates in the  $\beta$  phase and that parallel  $\alpha$  plates of the same variant (colony type structure) allow dislocations to shear the  $\alpha$  phase while  $\alpha$  plates of differing orientations promote homogeneous slip [24]. While TEM/SAD experiments have shown that both 15-3 and 21S exhibit Burger's  $\alpha$  (i.e.  $(110)_{\alpha}$ ,  $\parallel (0001)_{\alpha}$ ,  $\parallel [111]_{\alpha}$ ,  $\parallel [11\bar{2}0]_{\alpha}$ ) [25], high magnification SEM of PA metallographic specimens (Figure 9) show a difference in the size and orientation of the  $\alpha$ , especially at the grain boundaries [10].

Figure 9. High magnification SEM micrographs of  $\alpha$  in peak aged (a) TIMETAL 15-3 and (b) TIMETAL 21S (from ref 10).



The parallel, linear features shown on the fracture surfaces of hydrogen charged 21S in the SA and DA conditions (Figures 6b and 6e) and previously observed in hydrogen charged PA material [9] suggest an interaction between hydrogen, slip, and fracture mode. Hydrogen segregation to dislocations and transport along slip lines is well documented in bcc metals [26-27]. Recall that hydrogen has been shown to partition to, and is relatively mobile in, the bcc lattice which provides a readily available source for hydrogen pickup by dislocations and possible deposition of this hydrogen at grain boundaries [9,28].

It is plausible that rather than crystallographic orientation, physical alignment at grain boundaries and coarseness of  $\alpha$  in the 15-3 (which has nucleated first and grown for a longer time) is a more effective slip barrier than the fine  $\alpha$  of the 21S. A greater

impedance to planar slip promotes more homogeneous deformation (i.e. cross slip). In turn, less hydrogen is transported to  $\beta$  grain boundaries and the locally high hydrogen concentrations along persistent planar slip bands is reduced. This explanation is well supported by the fracture modes observed in this study and is consistent with the work of Albrecht, Thompson, and Bernstein in aluminum alloys [29-32].

TIMETAL 21S which is prone to planar slip (at the investigated heat treatment) undergoes slip line, slip plane, and intergranular cracking depending on microstructure, degree of constraint and hydrogen concentration. In contrast, 15-3, in which wavy slip is easier to induce, exhibits a microvoid rupture fracture mode until the highest strength and hydrogen level investigated where the fractographic features are on the size and order of the deformation structure seen in SA material as shown by a comparison of Figures 4a and 5b. Correlation of the different fracture modes with the mechanical properties exhibited by each alloy indicate that deformation mode strongly influences the hydrogen effected fracture paths and subsequent mechanical properties.

Hydrogen has previously been suggested as the embrittling species in aqueous chloride testing of PA  $\beta$  titanium alloys [10-11]. Hydrogen-slip interactions may explain the superior EAC resistance of PA 15-3 vs. PA 21S in aqueous sodium chloride solution [10-11]. L.M. Young and R.P. Gangloff have suggested that dislocation motion is a requisite for EAC in 21S based on J-integral resistance curve testing conducted at varying load-line displacement rates and "ripple" loaded tests of PA 15-3 and 21S in aqueous saltwater [10]. This statement fits well with the observations made in this paper. Consider the production of hydrogen at an acidified crack tip and absorption of this hydrogen into the fracture process zone. Under a "ripple" load designed to rupture the surface oxide film (but well below the fatigue  $\Delta K$  threshold for crack growth in moist air) hydrogen enters the metal and diffuses through the lattice, partitioning primarily to the  $\beta$  phase where it is highly soluble. Persistent planar slip band formation does not occur, however, below the moist air fatigue  $\Delta K$  threshold.

Under a rising load test, however, where dislocation motion is occurring, hydrogen is transported by dislocations and deposited at the dislocation sinks (i.e. grain boundaries) where it is trapped and promotes intergranular separation. The difference in the EAC resistance between 15-3 and 21S is attributed to the tendency of 21S toward planar slip (which promotes hydrogen transport over long distances to grain boundaries). Cross slip, which has been shown to occur more readily in SA 15-3 than 21S, retards the transport and deposition of hydrogen to grain boundaries and concurrently lowers local hydrogen concentrations as dislocations transport hydrogen to newly activated slip systems.

### Conclusions

1. Hydriding of a large volume fraction of the  $\alpha$  and  $\beta$  phases is not required for embrittlement to occur in  $\beta$  titanium. Reduction in the longitudinal stress and plastic strain developed in solution annealed TIMETAL 21S at hydrogen concentrations  $< 3000$  wt. ppm suggest that the  $\beta$  phase is intrinsically embrittled by hydrogen especially when deformation occurs by persistent planar slip.

2. Embrittlement is a function of hydrogen concentration, constraint, and yield strength for material (21S) which has a susceptible microstructure. Susceptible microstructures are caused by excessive solution treatment temperatures which remove heterogeneous nucleation sites from grain interiors, delaying the onset of intragranular  $\alpha$  precipitation. The resulting fine  $\alpha$  precipitates are readily sheared by dislocations, promoting planar slip, concentration of hydrogen along persistent planar slip bands, and transport of hydrogen to grain boundaries.

3. The relationships between hydrogen transport, microstructure, and deformation behavior described in this paper accurately account for the observed effects on specimens which were precharged with hydrogen and tested in air as well as specimens which were simultaneously polarized and tested in aqueous chloride environments. This correlation supports a hydrogen embrittlement/dislocation transport mechanism for aqueous saltwater stress corrosion cracking of metastable  $\beta$  titanium alloys.

#### Acknowledgements

This research was supported by the Office of Naval Research (Grant N00014-91-J-4164) with Dr. A. John Sedriks as Scientific Monitor and by the Virginia Center for Electrochemical Science and Engineering at the University of Virginia. The material used in this study was graciously donated by TIMET. The authors wish to acknowledge the invaluable assistance of R.P. Gangloff, R.J. Kilmer, S.S. Kim, D.G. Kolman, B.P. Somerday, and L.M. Young.

#### References

1. H.G. Nelson, First Thermal Structures Conference, E. Thornton, ed., Nov 13-15, The University of Virginia, Charlottesville, VA, (1990) 301-311.
2. P.J. Bania, G.A. Lenning and J.A. Hall, Beta Titanium Alloys in the 80's, R.R. Boyer and H.W. Rosenberg eds., TMS-AIME, Warrendale, PA, (1983) 209-237.
3. P.J. Bania and W.M. Parris, "Beta-21S: A High Temperature Metastable Beta Titanium Alloy", paper presented at the Titanium Development Association Conference, Orlando, FL (1990).
4. R.W. Schütz and D.E. Thomas, "Corrosion of Titanium and Titanium Alloys," Metals Handbook, 9th ed. 13, ASM, Metals Park, Ohio, (1987) 669-706.
5. J.E. Costa, J.C. Williams, and A.W. Thompson, "The Effects of Hydrogen in Mechanical Properties in Ti-10V-2Fe-3Al" Met. Trans. A, (18A) (1987), 1421-1430.
6. J.J. DeLuccia, Report No. NADC-76297-30, Naval Air Development Center, Warminster, PA (1976).
7. K. Nakasa and J. Liu, "Bending Strength of Hydrogen Charged Ti-13V-11Cr-3Al alloy", J. Japan Inst. Metals, 55 (9) (1991) 922-927.
8. D.S. Shih and H.K. Birnbaum, "Evidence of FCC Titanium hydride Formation in  $\beta$  Titanium Alloy: An X-ray Diffraction Study," Scripta Met., (20) (1986), 1261-1264.
9. G.A. Young Jr. and J.R. Scully, "Effects of Hydrogen on the Mechanical Properties of a Ti-Mo-Nb-Al Alloy", Scripta Met., (28) (1993) 507-512.
10. L.M. Young, "Hydrogen Environment Embrittlement of Beta Titanium Alloys," to be published in Proceedings of the Seventh World Conference on Titanium, F.H. Froes and I.L. Caplan, eds., TMS-AIME, Warrendale, PA (1993).
11. L.M. Young, "Environment Assisted Cracking in  $\beta$ -Titanium Alloys," Master's Thesis, The University of Virginia, Charlottesville, VA (1993).
12. J.B. Guernsey, V.C. Petersen, and F.H. Froes, "Discussion of Effect of Microstructure on the Strength, Toughness, and Stress-Corrosion Cracking Susceptibility of a Metastable  $\beta$  Titanium Alloy" Met. Trans. A, (3) (1972) 339-340.
13. Z.A. Foroulis, "Factors Affecting Absorption of Hydrogen in Titanium from Aqueous Electrolytic Solutions," Ti'80, Science and Technology, H. Kimura and O. Izumi eds., TMS-AIME, Warrendale, PA, (1980) 2705-2711.
14. P.W. Bridgman, Studies in Large Plastic Flow, McGraw-Hill Inc., New York, NY (1952) 9-37.

15. J.W. Hancock and A.C. Mackenzie, "On the Mechanisms of Ductile Failure in High-Strength Steels Subjected to Multi-Axial Stress-States," J. Mech. Phys. Solids, (24) (1976) 147-169.
16. A.C. Mackenzie, J.W. Hancock and D.K. Brown, "On the Influence of State of Stress on Ductile Failure Initiation in High Strength Steels," Engineering Fracture Mechanics, (9) (1977) 167-188.
17. J. Eastman et al., "Hydrogen Effects in Nickel--Embrittlement or Enhanced Ductility," Hydrogen Effects in Metals, I.M. Bernstein and A.W. Thompson eds., The Metallurgical Society of AIME (1980) 397-409.
18. R.E. Stoltz and A.J. West, "Hydrogen Assisted Fracture in FCC Metals and Alloy," Hydrogen Effects in Metals, I.M. Bernstein and A.W. Thompson eds., The Metallurgical Society of AIME (1980) 541-553.
19. N.R. Moody and F.A. Greulich, "Hydrogen Induced Slip Band Fracture in an Fe-Ni-Co Superalloy," Scripta Met., (19) (1985) 1107-1111.
20. N.R. Moody, R.E. Stoltz, and M.W. Perra, "The Effect of Hydrogen on Fracture Toughness of the Fe-Ni-Co Superalloy IN903," Met Trans A, (18A) (1987) 1469-1482.
21. K. Nakasa and J. Liu, "Surface Peeling of Ti-6Al-4V Alloy Specimens during Hydrogen Charging" J. Japan Inst. Metals, 54 (11) (1990) 1261-1269.
22. J.D. Boyd, "Precipitation of Hydrides in Titanium Alloys" Trans ASM, (62) (1969) 977-988.
23. D.A. Meyn and P.S. Pao, "Slow Strain Rate Testing of Precracked Titanium Alloys in Salt Water and Inert Environments", to be published in Slow Strain Rate Testing: Research and Engineering Applications.
24. M. Okada, D. Banerjee, and J.C. Williams, "Tensile Properties of Ti-15-V-3Al-3Cr-3Sn Alloy," Titanium Science and Technology, G. Lütjering, U. Zwicker, and W. Buck, eds., (3) (1980) 1835-1842.
25. K.R. Lawless, Unpublished Research. University of Virginia, Charlottesville, VA (1993).
26. J.P. Hirth, "Effects of Hydrogen on the Properties of Iron and Steel", Met Trans A, (11A) (1980) 861-890.
27. C.J. MacMahon Jr., "Effects of Hydrogen on Plastic Flow and Fracture in Iron and Steel," Hydrogen Effects in Metals, I.M. Bernstein and A.W. Thompson, eds., The Metallurgical Society of AIME (1980) 219-233.
28. R.L. Shulte and P.N. Adler, "Stress-Induced Hydrogen Redistribution in High Purity Ti-31V Alloy," Hydrogen Effects in Metals, I.M. Bernstein and A.W. Thompson eds., The Metallurgical Society of AIME (1980) 177-185.
29. J.K. Tien et al., "Hydrogen Transport by Dislocations," Met. Trans. A, (7A) (1976) 821-829.
30. J. Albrecht, I.M. Bernstein, and A.W. Thompson, "Evidence for Dislocation Transport of Hydrogen in Aluminum," Met. Trans. A, (13A) (1982) 811-820.
31. D.A. Hardwick, A.W. Thompson, and I.M. Bernstein, "The Effect of Copper Content and Microstructure on the Hydrogen Embrittlement of Al-6Zn-2Mg Alloys," Met. Trans. A, (14A) (1983) 2517-2526.
32. D. Nguyen, A.W. Thompson, and I.M. Bernstein, "Microstructural Effects on Hydrogen Embrittlement in a High Purity 7075 Aluminum Alloy," Acta Met., (35) 10 (1987) 2417-2425.

**HYDROGEN INTERACTIONS AND EMBRITTLEMENT IN  
METASTABLE BETA Ti-3Al-8V-6Cr-4Mo-4Zr**

**Michelle A. Gaudett  
John R. Scully**

# Hydrogen Interactions and Embrittlement in Metastable Beta Ti-3Al-8V-6Cr-4Mo-4Zr

Michelle A. Gaudett and John R. Scully

Center for Electrochemical Sciences and Engineering  
Department of Materials Science and Engineering  
University of Virginia  
Charlottesville, VA 22903-2442

## Abstract

The effects of electrochemically pre-dissolved hydrogen on the room temperature mechanical properties of Beta-C titanium (Ti-3Al-8V-6Cr-4Mo-4Zr, wt%) have been investigated using circumferentially notched tensile specimens. The as-received, solutionized condition ( $\sigma_{y,2\%} = 830$  MPa) and the solutionized + peak aged condition ( $\sigma_{y,2\%} = 1280$  MPa) were compared to define the relationships between the fracture process zone hydrogen concentration, hydrogen-metal interactions (i.e. trapping, hydriding) and the resulting mechanical properties. Finite element based analysis of notch stress fields was used to define relationships between threshold stress for crack initiation versus internal hydrogen concentration. Solutionized + peak aged ( $\beta + \alpha$ ) Beta-C fractured intergranularly at total hydrogen concentrations  $\geq 1400$  wt. ppm. Solutionized Beta-C resisted hydrogen assisted cracking but was not immune: a fracture mode resembling slip line fracture was observed at  $\sim 4000$  wt. ppm. and cleavage cracking was provoked at 6900 wt. ppm. A comparison of the hydrogen trapping behavior between solutionized and solutionized + peak aged Beta-C revealed an additional trapping state in the aged condition. However, it is unclear whether the additional trapping state, or some other factor such as yield strength controls the fracture resistance.

Acknowledgements: This work is supported by the Office of Naval Research (Grant N00014-91-J-4164) and the Virginia Center for Electrochemical Sciences and Engineering at the University of Virginia. Michelle Gaudett is partially supported by the National Science Foundation. Alloys were donated by RMI Titanium, Niles, OH.

## Introduction

Beta titanium alloys are embrittled by hydrogen, as demonstrated by smooth specimen tensile experiments in high pressure  $H_2$  [1]. Ambient to elevated temperature hydrogen charging, by either cathodic polarization or gaseous hydrogen, followed by static or monotonic loading at room temperature, embrittles solution heat treated (ST) and solution heat treated and age hardened (STA)  $\beta$ -titanium alloys (i.e., Ti-30Mo, Ti-15Mo-3Nb-3Al, Ti-15V-3Cr-3Al-3Sn and Ti-10V-2Fe-3Al, wt.%), as determined by changes in tensile ductility, cleavage fracture stress, and fracture morphology [2-5]. A continuous decrease in the fracture stress of solution heat treated Ti-30Mo containing 20-1800 wt. ppm hydrogen occurred without the formation of a hydride [3]. Similarly, embrittlement was observed in ST and STA Ti-15Mo-3Nb-3Al and, to a lesser extent, Ti-15V-3Cr-3Al-3Sn at >500 wt. ppm hydrogen without detection of hydriding by X-ray diffraction (XRD). A decrease in bending strength was observed for both ST and STA Ti-13V-11Cr-3Al, without detection of hydriding in either the  $\alpha$  or  $\beta$  phase, at hydrogen concentrations up to 15,000 wt. ppm [6]. A {100} cleavage plane was identified on flat fracture surfaces in both the solution annealed and aged ( $\beta + \alpha$ ) conditions. However, the fct  $\epsilon$  hydride was detected in Ti-13V-11Cr-3Al under extreme autoclave conditions at hydrogen concentrations on the order of 40,000 ppm [6] and ST Ti-30Mo was extrinsically embrittled through the formation of the fcc  $\delta$  hydride containing 66 at% hydrogen [7]. Hydrogen was also implicated in the aqueous cracking of aged  $\beta$ -titanium alloy Beta-C (Ti-3Al-8V-6Cr-4Mo-4Zr) [8]. In this study, embrittlement was only observed when pre-cracked specimens were cathodically polarized in  $H_2S$  containing acidified chloride solutions. Previous studies of  $\alpha$ - $\beta$  and metastable  $\beta$ -titanium alloys in aqueous solutions also attribute aqueous environmental cracking to a hydrogen environment assisted cracking mechanism [9-11]. A {100} cleavage plane [12] and intergranular separation [12,13] have been observed. The relationships between beta phase hydrogen concentration and ductile to brittle transition temperature (DBTT) in Ti-15Mo-3Al-3Nb (Beta-21S) as well as Ti-15V-3Cr-3Al-3Sn has been established for smooth tensile specimens [2]. Hence, it is reasonable to conclude that many reports of environmentally-induced cleavage fracture in metastable bcc  $\beta$ -titanium are a result of hydrogen-induced shifts in the ductile to brittle transition temperature (DBTT) above the mechanical test temperature. Intergranular cracking, however, suggests a different controlling mechanism.

Exposure of  $\beta$ -titanium alloys at elevated temperature to gaseous hydrogen followed by fracture at room temperature can result in other complicating effects. Here a competition exists between the rate of hydrogen accumulation to lower the beta transus below the charging temperature and the kinetics of diffusional phase transformations operative in the metastable titanium system (e.g.  $\beta \rightarrow \omega \rightarrow \alpha$ ,  $\beta \rightarrow \beta' \rightarrow \alpha$ ). One effect of dissolved hydrogen is alloy softening due to  $\beta$  phase stabilization and the retardation of  $\alpha$  and  $\omega$  precipitation [1,4,14]. Consequently, possible hydrogen interactions in the metastable Beta-Ti system include (a) microstructural effects, (b) extrinsic hydrogen effects: cleavage and hydriding, and (c) intrinsic hydrogen embrittlement in which trapping can play a part. Elevated temperature gaseous charging is not directly relevant to the room temperature environmental hydrogen embrittlement of ST and STA  $\beta$ -titanium where hydrogen uptake occurs from either cathodic charging at near ambient temperatures or dynamic straining in an aqueous hydrogen producing environments. Here microstructural effects are not operative and hydrogen trapping may play a role. At room temperature a variety of intrinsic hydrogen induced fracture paths are possible in Ti-15Mo-3Al-3Nb (Beta-21S) as well as Ti-15V-3Cr-3Al-3Sn depending on hydrostatic constraint and hydrogen concentration including (a) intergranular, (b) slip band and (c) hydrogen affected



microvoid initiation, growth and linkage [5,15].

This paper seeks to define the effects of a range of internal hydrogen concentrations on the room temperature mechanical properties of ST and STA beta titanium alloy Ti-3Al-8V-6Cr-4Mo-4Zr (Beta-C). Here, electrochemical pre-charging ST or STA material is conducted near ambient temperature to avoid the complications of hydrogen induced  $\beta$  phase stabilization common to high temperature gaseous charging studies. Mechanical testing of pre-charged specimens is performed in air, to decouple hydrogen effects from other aqueous embrittlement mechanisms which may complicate in-situ stress corrosion cracking studies. The strong permeation barrier provided by the titanium oxide is exploited to minimize outgassing of precharged hydrogen during the duration of these tests. We seek to understand the origins of the difference in HE susceptibilities for  $\beta$  and  $\beta + \alpha$  microstructures. In particular, analysis of the possible role of hydrogen trapping sites is presented to aid in elucidating differences between ST and STA material.

### Materials and Procedures

#### Titanium Alloy

The composition of the Beta-C alloy studied was 3.42Al, 8.30V, 5.86Cr, 4.44Zr, 12Nb, 4.12Mo, <.1 O, C, N, and Fe in wt%. The product was provided as a hot-rolled, 4.1 cm diameter round bar that was solutionized above the  $\beta$  transus and air cooled. The two conditions examined were the as received beta solutionized form, (1h at 815°C,  $\sigma_{y,2\%} = 830$  MPa), and the beta solutionized + peak aged condition (30h at 500°C,  $\sigma_{y,2\%} = 1280$  MPa).

Metallography conducted on three mutually perpendicular surfaces of the ST material revealed equiaxed beta grains 85  $\mu\text{m}$  in diameter. Decoration aging at 500°C for 1h confirms intragranular precipitation of the  $\alpha$  phase. High magnification scanning electron microscopy (SEM) performed on the decoration and peak aged material revealed homogeneous  $\alpha$  precipitation within the grains and a very limited amount of grain boundary  $\alpha$ . The presence of a thin  $\alpha$  film (.1  $\mu\text{m}$ ) at the grain boundary as observed in Beta-21S and Ti-15-3 has not as yet been verified by transmission electron microscopy [16].

#### Hydrogen Charging

ST and STA specimens were pre-charged with hydrogen in a solution of 1000 ml distilled  $\text{H}_2\text{O}$ , 10 ml  $\text{H}_2\text{SO}_4$  and .8g  $\text{Na}_2\text{P}_2\text{O}_7$  at 90°C. Hydrogen uptake was promoted by cathodically polarizing the specimen galvanostatically using a PAR Model 362 potentiostat and a platinized Nb counter electrode. The concentration of predissolved H was controlled by varying the applied cathodic current density from .1 to 10  $\text{mA}/\text{cm}^2$  while maintaining a constant charging time of 64h. Fickian diffusion calculations using a diffusion coefficient of  $1.9 \times 10^{-7} \text{ cm}^2/\text{sec}$  for H in  $\beta$  Ti at 90°C assures that a nearly homogeneous concentration exists across a cylindrical diameter of .42 cm for this charging time [17]. The total H concentration was determined via a hot vacuum extraction method by LECO Corporation. All total hydrogen concentrations were determined from sections taken from machined rods or from the fractured tensile bars and give a maximum uncertainty of  $\pm 20$  wt. ppm.

#### Mechanical Testing

The tensile testing was conducted on round, circumferentially notched bars with a

diameter of .417 cm remote from the notch, a minimum diameter of .241 cm at the notch root and a notch root radius of .054 cm. The resulting constraint factor (1.02) is sufficient to trigger hydrogen assisted cracking in Beta-21S [18]. Tensile testing was conducted at a constant stroke rate of  $2 \times 10^{-5}$  cm/sec. This stroke rate has been shown in prior studies to be sufficiently slow to observe embrittlement in Ti-based alloys [18-20].

A computer program which employs an ABACUS finite element calculation was used to obtain the distribution of stresses across the notch diameter at the maximum applied remote stress measured during each mechanical test. Following Hancock [21], this maximum in load prior to a load drop was assumed to indicate crack initiation. Also, crack initiation was assumed to occur at the position of the maximum longitudinal stress. This value of stress was used to establish the relationship between fracture stress and total hydrogen concentration.

Fracture surfaces were investigated using a JOEL scanning electron microscope at a working distance of 39 mm in SEI mode. The fractographs presented represent the fracture surfaces at the location of crack initiation, which was assumed to be the position of the maximum longitudinal stress given by the finite element analysis.

### Thermal Desorption Spectroscopy

A thermal desorption spectroscopy (TDS) system designed and developed at the University of Virginia was used to investigate the H trapping behavior of both ST and STA  $\beta$ -C Ti. A schematic of the system is shown in Figure 1. Rods .24 cm in diameter were charged 64h at cathodic current densities which yielded hydrogen concentrations ( $C_H$ ) of 5650 wt. ppm for the ST material and 1750 wt. ppm for the STA condition. Desorption data was collected over a temperature range from 30°C to 890°C at constant heating rates of .5, 2, 5 and 10 °C/min. The uncharged condition was studied using constant heating rates of 2 and 5 °C/min only.  $C_H$  was 186 wt. ppm for the uncharged, ST condition and 89 wt. ppm for the uncharged, STA condition. The  $H_2$  detrapped and desorbed was monitored mass selectively in the form of  $H_2^+$  and  $H^+$  pressure by a Dycor quadrapole gas analyzer (QMS) and converted to desorption rate using the known cracking patterns and H pumping speed. Asymmetrical double sigmoidal peak fitting was performed and was used to identify and deconvolute overlapping trapping states. Total hydrogen concentrations determined by LECO subsequent to TDS shows that all but a residual amount equal to 6-10 wt. ppm hydrogen is desorbed during TDS.

### X-Ray Diffraction

XRD was performed on charged TDS samples in order to determine the shift the  $\beta$  lattice parameter ( $\Delta a$ ) with hydrogen concentration in the  $\beta$  lattice ( $[H]_\beta$ ). The increase in lattice parameter from the uncharged condition is linearly related to the concentration of hydrogen in the  $\beta$  lattice. XRD was performed on a Scintag automated diffractometer utilizing Cu  $K_\alpha$  radiation and continuously scanned over a  $2\theta$  range of 38 to 40 degrees at .1 °/min. The (110)  $\beta$  lattice peak was used to determine  $\Delta a$ . The change in metal volume with atomic hydrogen concentration ( $\Delta v$ ) is similar for many alloy systems and the values found in the literature range from  $2.9 \text{ \AA}^3/\text{atom}$  for various hcp, fcc and bcc alloys [22] to  $2.31 \text{ \AA}^3/\text{atom}$  for the  $\beta$  Ti alloy Ti-30Mo [23]. The relationship between  $\Delta a$  and

$[H]_{\beta}$  is given by:

$$\frac{\Delta a}{a_0} = [H]_{\beta} \frac{\Delta v}{3\Omega} \quad (1)$$

where  $[H]_{\beta}$  is the ratio of hydrogen atoms to metal atoms in the  $\beta$  phase,  $a_0$  is the lattice parameter in the uncharged condition and  $\Omega$  is the mean atomic volume of the metal (e.g.,  $a_0^3/2$ ). Hence, whereas LECO gives total concentrations that include contributions from all phases present and trapped hydrogen,  $\Delta a$  can be used to determine the true  $\beta$  lattice hydrogen concentration.

## Results and Discussion

### Mechanical Behavior with Hydrogen

The maximum longitudinal stress as a function of  $C_H$  for heat treatments is shown in Figure 2. The STA material showed a large decrease in the local longitudinal stress at crack initiation as  $C_H$  was increased to approximately 1500 wt. ppm. The ST material, however, did not show a decrease in the local initiation stress until  $C_H$  was increased to at least 2580 wt. ppm.

Figure 3 shows the fractography for selected hydrogen concentrations. Regarding the STA material, five distinct fracture modes were observed. In the uncharged condition, cracking initiated primarily by transgranular microvoid coalescence (MVC). A very limited amount of ductile cracking, possibly at planar slip bands, was also observed. At a level of approximately 430 wt. ppm, the portion of fracture area associated with ductile slip line fracture increased and a different flat, transgranular fracture mode was observed (Figure 3(a)). Microscopically ductile features were observed on these transgranular surfaces when viewed at higher magnification (1000x). Also, linear markings that could correspond to slip bands are visible on these surfaces. The spacing of these linear markings are consistent with slip lines observed subsequent to compression testing of electropolished cubes [18].

The large decrease in the local maximum longitudinal stress with hydrogen correlated with the introduction of an intergranular fracture mode at a  $C_H$  of approximately 1500 wt. ppm (Figure 3(b)). The previously described fracture modes were also present in small amounts, and linear markings resembling slip lines due to similar spacing were present on some of the intergranular facets, which also revealed some microscopic ductility at higher magnification. At greater than 2000 wt. ppm hydrogen, a transgranular, microscopically ductile yet macroscopically brittle fracture mode dominated the surface. At 3000 wt. ppm or greater cleavage was observed (Figure 3(c)).

At hydrogen concentrations greater than 3000 wt. ppm where cleavage is observed, it is presumed that the DBTT has been increased to above room temperature, resulting in lower shelf behavior. Nelson related the DBTT to  $C_H$  for solutionized Beta-21S [24]. However, this relation cannot be directly applied to STA material without taking into account hydrogen partitioning between the  $\beta$  and  $\alpha$  phases. Calculations were performed to estimate the concentration in the  $\beta$  lattice of an aged alloy containing 50 vol%  $\alpha$  saturated to 200 wt. ppm hydrogen. [25] The calculated H concentration in the  $\beta$  phase was approximately twice the total hydrogen concentration. Using Nelson's relation, a DBTT of 51°C is calculated for a total hydrogen concentration of 3000 wt. ppm,

substantiating that we are indeed observing lower shelf behavior at these hydrogen concentrations.

Four major fracture modes are observed for the ST material (Figure 4). In the uncharged condition, the material separates by transgranular microvoid processes. As  $C_H$  was increased to 500 wt. ppm, a flat transgranular mode was observed (Figure 4(a)). This mode was similar to that observed in the STA material except that the extent of microscopic ductility was greater and linear features resembling slip lines were not observed. At hydrogen concentrations of 4100 wt. ppm, ductile failure along slip bands was the predominant fracture mode (Figure 4(b)). This indicates that ST Beta-C was resistant but not immune to HE at concentrations below levels which produce cleavage. Lastly, a cleaved fracture surface was observed at approximately 6900 wt. ppm (Figure 4(c)).

### Thermal Desorption Spectroscopy and X-Ray Diffraction

Figures 5(a) and 5(b) show the peak fits for TDS experiments conducted at .5 °C/min, for the ST and STA conditions, respectively. The peak fits are more accurate at the slowest ramp rate due to the slightly greater peak separation. After fitting the data, three distinct trapping states are observed for the ST condition (labelled 1-3) and four trapping states are observed for the STA condition (labelled 1-4). It should be noted that one of the trapping states corresponds to lattice hydrogen in the  $\beta$  matrix. This hydrogen is retained in the lattice until such temperatures because of the  $TiO_2$  surface oxide which act as a permeation barrier [26].

The other microstructural trap sites remain unidentified as yet. However, comparison of the fractions of the total hydrogen concentration associated with each peak (Table I) were made with upper bound calculations of the expected H concentration at particular traps ( $C_H^T$ ). In this preliminary work, the absolute concentrations derived from the QMS are not well calibrated. Instead, the concentrations associated with each peak were determined by multiplying the fractional area occupied by each peak with the total hydrogen concentration measured independently by LECO. Calibration uncertainties do not affect this approach.

Table I-Measured Hydrogen Concentrations Associated With Peaks in Figure 5.

| ST<br>Peak # | Measured $C_H^P$ wt.<br>ppm*, (fraction of<br>total H) | STA<br>Peak # | Measured $C_H^P$ wt.<br>ppm*, (fraction<br>of total H) |
|--------------|--|---------------|--|
| 1            | 214, (.04)   | 1             | 280, (.16)   |
| 2            | 5019, (.89)  | 2             | 578, (.33)   |
| 3            | 417, (.07)   | 3             | 752, (.43)   |
| -            | -  | 4             | 140, (.08)   |

\*Hydrogen concentrations are given in gH per g of alloy sample (i.e., per g  $\beta$  in the ST case and per g ( $\alpha + \beta$ ) in the STA case).

XRD was performed in order to determine the concentration in the  $\beta$  lattice. For the ST material (uncharged),  $a_0$  was measured to be 3.2442Å. The shift in lattice parameter

correlates with a hydrogen concentration which can range from 4790 to 6010 wt. ppm based on the range of values found for  $\Delta v$  in the literature. This agrees with the concentration given by peak #2.

For the STA material (uncharged)  $a_0$  was measured to be 3.2173Å and the lattice parameter shift gives a H concentration of 740 to 930 wt. ppm per unit  $\beta$ , or gH per  $10^6$  g of  $\beta$  phase. However, in order to compare to the results given by TDS, the concentration must be converted to gH per  $10^6$  g of  $\alpha + \beta$ . Assuming 50 vol%  $\alpha$ , we would expect the  $\beta$  lattice desorption peak to give a hydrogen concentration of 380 to 480 wt. ppm. This concentration is in between the concentrations associated with peak #1 and peak #2.

The similarity in  $T_{max}$  for the high temperature peak in both the ST (peak #3) and STA condition (peak #4) indicate a microstructural trap site common to both conditions. This trapping state also corresponds to the same desorption peak observed in the uncharged condition of both ST and STA material. Speculatively, a point defect site in the  $\beta$  lattice is implicated. Furthermore, the O and N concentrations in this material, (800 and 160 wt. ppm respectively), are in agreement with the concentrations associated with peak #3 (ST) and peak #4 (STA) assuming one H atom associated with each impurity atom.

Upper bound calculations can be performed to determine the H concentration arising from trapping at the  $\alpha/\beta$  interfaces assuming 50 vol%  $\alpha$ . The resulting hydrogen concentration ( $C_H^{\alpha/\beta}$ ) would be approximately 73 wt. ppm. For hydrogen trapping at dislocations, the calculated concentration ( $C_H^L$ ) is 35 wt. ppm for a dislocation density of  $10^{12} \text{ cm}^{-1}$ . We see from Table I that the measured concentrations are larger than that expected for  $\alpha/\beta$  interface and/or dislocation trapping. [25]

Trapping at the metal/oxide interface was considered:

$$C_H^{interface} = (10^6) \frac{\lambda 2A \theta n_H}{N_A M} = .033 \text{ wt. ppm} \quad (2)$$

where  $\lambda$  = number of trap sites per unit area ( $\{011\}$  type plane assumed)

$2A$  = specimen surface area (doubled due to surface roughness)

$\theta$  = fraction of sites occupied by H (assumed to be 1)

$n_H$  = atomic weight of hydrogen (1.0079 g/mole)

$N_A$  = Avogadro's number

$M$  = specimen mass

From Table I it is seen that the measured concentrations are too large to be associated solely with trapping at the oxide/metal interface.

Spalling of the  $\alpha$  phase of the charged surfaces of the STA material is attributed to the 18% volume expansion associated with hydriding [25,27]. However, internal hydriding of the STA material was not observed by XRD. TDS performed on hydrided Grade 2 titanium foil shows that the temperature at which the hydride decomposes is within the temperature range over which the desorption peaks occur for Beta-C. Assuming that the volume fraction of hydride is below the XRD detection limit of approximately 2 vol% hydride, a calculation of the H measured from the decomposition of a small amount of

TiH<sub>2</sub> during the temperature ramp can be calculated:

$$C_H^\delta = (10^6) \frac{2n_H \rho_\delta (.02V)}{(2n_H + n_T)M} = 656 \text{ wt. ppm} \quad (3)$$

where V = specimen volume

$\rho_\delta$  = hydride density (3.9 g/cm<sup>3</sup>)

These results indicate that the hydriding of a small amount of  $\alpha$  and its subsequent decomposition cannot be ruled out as a source for one of the observed desorption peaks (peak #2 or #3).

Although an additional trapping state is observed in the STA material, it cannot be concluded that the differences in susceptibility between ST and STA Beta-C is solely related to the presence of this trapping state. In order to improve the resolution of the thermal desorption spectra so that the smaller desorption peaks can be studied with accuracy and in more detail, the  $\beta$  lattice hydrogen concentration must be reduced. Future testing will involve baking the samples prior to TDS analysis to reduce this concentration while retaining hydrogen trapped in sites of higher binding energy.

### Conclusions

- The STA material shows a large decrease in the maximum longitudinal stress at hydrogen concentrations of approximately 1500 wt. ppm. The evolution of fracture mode with increased hydrogen concentration progresses from transgranular microvoid coalescence, ductile slip line fracture and a less ductile transgranular fracture, to intergranular fracture at 1500 wt. ppm. At higher concentrations a granulated fracture surface appears followed by cleavage fracture observed at 3000 wt. ppm.
- The ST material shows a decrease in the maximum longitudinal stress above a concentration of approximately 2600 wt. ppm. The fracture mode here is characterized by microvoid coalescence and a less ductile transgranular fracture with increasing hydrogen. Ductile slip line fracture appears at 4100 wt. ppm hydrogen. Cleavage fracture is observed at approximately 6900 wt. ppm.
- The similarity of  $T_{\max}$  for the high temperature peak in both the ST and STA condition indicate a microstructural trap site common to both conditions.
- The microstructural trap sites remain unidentified as yet. However, calculations indicate the following:
  - (1) Measured concentrations are too large to be associated with trapping at the oxide/metal interface.
  - (2) The concentrations measured by XRD are consistent with the concentration associated with peak #2 in the ST desorption spectrum.
  - (3) Although bulk hydriding in the STA material was not detected with x-ray diffraction, the concentrations measured are on the order of that calculated assuming the decomposition of a small amount of hydride during TDS (<2 vol. %). Also, the concentrations in the  $\beta$  lattice determined by XRD for the STA material can account for either peak #1 or #2 in the STA desorption spectrum but suggests the presence of a small amount of hydride as one of the remaining peaks.



## References

1. N.E. Paton, R.A. Spurling and C.G. Rhodes, Hydrogen Effects in Metals, ed. I.M. Bernstein and A.W. Thompson, (Warrendale, PA: TMS-AIME, 1981), 269-279.
2. R.J. Lederich, D.D. Schwartz and S.M.L. Sastry, Beta Titanium Alloys in the 1990's, ed. D. Eylon, R.R. Boyer, and D.A. Koss, (Warrendale, PA: TMS, 1993), 159-169.
3. W.W. Gerberich et. al., "Hydrogen in  $\alpha/\beta$  and all  $\beta$  Titanium Systems," Hydrogen Effects in Metals, ed. I. M. Bernstein and A.W. Thompson, (Warrendale, PA: TMS-AIME, 1981), 731-745.
4. J.E. Costa, D. Banerjee and J.C. Williams, "The Effect of Hydrogen on Microstructure and Properties of Ti-10V-2Fe-3Al," Titanium Science and Technology, vol. 4, ed. G. Lutjering, U. Zwicker, and W. Bunk, (Germany: Deutsche Gesellschaft Fur Metallkunde E.V., 1984), 2479-2487.
5. G.A. Young and J.R. Scully, Beta Titanium Alloys in the 1990's, ed. D. Eylon, R.R. Boyer and D.A. Koss, (Warrendale, PA: TMS, 1993), 147-158.
6. K. Nakasa and J. Liu, "Bending Strength of Hydrogen Charged Ti-13V-11Cr-3Al Alloy" J. Japan Inst. Metals, 55 (9) (1991), 922-927.
7. D.S. Shih and H.K. Birnbaum, "Evidence of FCC Titanium Hydride Formation in  $\beta$  Titanium Alloy: An X-Ray Diffraction Study", Scripta Met., 20 (1986), 1261-1264.
8. D.E. Thomas and S.R. Seagle, "Stress Corrosion Cracking Behavior of Ti-38-6-44 in Sour Gas Environments," Titanium Science and Technology, vol. 4, ed. G. Lutjering, U. Zwicker, and W. Bunk, (Germany: Deutsche Gesellschaft Fur Metallkunde E.V., 1984), 2533-2540.
9. L.M. Young, "Environmentally Assisted Cracking in  $\beta$ -Titanium Alloys" (MS thesis, University of Virginia, 1993).
10. M.J. Blackburn and W.H. Smyrl, "Stress Corrosion and Hydrogen Embrittlement", Titanium Science and Technology, vol. 4, ed. R.I Jaffee and H.M. Burte, (New York, NY: Plenum Publishing Corp., 1973) 2577-2609.
11. H.G. Nelson, "Aqueous Chloride Stress Corrosion Cracking of Titanium - A Comparison with Environmental Hydrogen Embrittlement," Hydrogen in Metals, (1973), 445-464.
12. D.N. Fager and W.F. Spurr, Trans. ASM, 61 (1968), 283-292.
13. J.A. Feeney and M.J. Blackburn, Metall. Trans., 1 (1970), 3309-3323.
14. N.E. Paton and O. Buck, Effect of Hydrogen on Behavior of Materials, ed. I.M. Bernstein and A.W. Thompson, (Warrendale, PA: TMS-AIME, 1975), 83-89.
15. G.A. Young and J.R. Scully, Scripta Metall., accepted for publication, 1993.
16. L.M. Young, G.A. Young, J.R. Scully and R.P. Gangloff, "Aqueous Environment-Enhanced Crack Propagation in High Strength Beta Titanium Alloys", accepted for publication in Metallurgical Transactions A, (1994).
17. J.L. Waisman, G. Sines and L.B. Robinson, "Diffusion of Hydrogen in Titanium Alloys Due to Composition, Temperature and Stress Gradients", Metallurgical Transactions, 4 (1973), 291-302.
18. G.A. Young and J.R. Scully, "Internal Hydrogen Embrittlement of Solution Heat Treated and Aged Ti-15V-3Cr-3Al-3Sn and Ti-15Mo-3Nb-3Al", (Paper No. 347 presented at Corrosion '94, National Association of Corrosion Engineers, Baltimore, MD).
19. D.N. Williams, "The Hydrogen Embrittlement of Titanium Alloys", Journal of the Institute of Metals, 91 (1962), 147-152.
20. H.G. Nelson, D.P. Williams and J.E. Stein, "Environmental Hydrogen Embrittlement of an  $\alpha$ - $\beta$  Titanium Alloy: Effect of Microstructure", Metallurgical

- Transactions A, 4A (1972), 469-475.
21. J.W. Hancock and A.C. Mackenzie, "On the Mechanisms of Ductile Fracture in High Strength Steels Subjected to Multi-Axial Stress States," J. Mech. Phys. Solids, 24 (1976), 147-169.
  22. H. Peisl, "Lattice Strains Due to Hydrogen in Metals," Topics in Applied Physics vol. 28, ed. G. Alefeld and J. Volkl, (where:publ, 1978), 53-74.
  23. W.W. Gerberich et. al., "Hydrogen in  $\alpha/\beta$  and All  $\beta$  Titanium Systems: Analysis of Microstructure and Temperature Interactions on Cracking," Hydrogen Effects in Metals, ed I.M. Bernstein and A.W. Thompson, (Warrendale, PA: TMS-AIME, 1980), 732-744.
  24. H.G. Nelson, "Hydrogen Materials Compatibility," NASP Government Work Package #92, Monterey, CA, (1992).
  25. G.A. Young, "Hydrogen Effects in Metastable  $\beta$  Titanium Alloys" (MS thesis, University of Virginia, 1993).
  26. R.W. Schutz and L.C. Covington, "Effect of Oxide Films on the Corrosion Resistance of Titanium", Corrosion, 37 (10) (1981), 585-591.
  27. K. Nakasa and J. Liu, "Surface Peeling of Ti-6Al-4V Alloy Specimens During Hydrogen Charging," J. Japan Inst. Metals, 54 (11) (1990), 1261-1269.



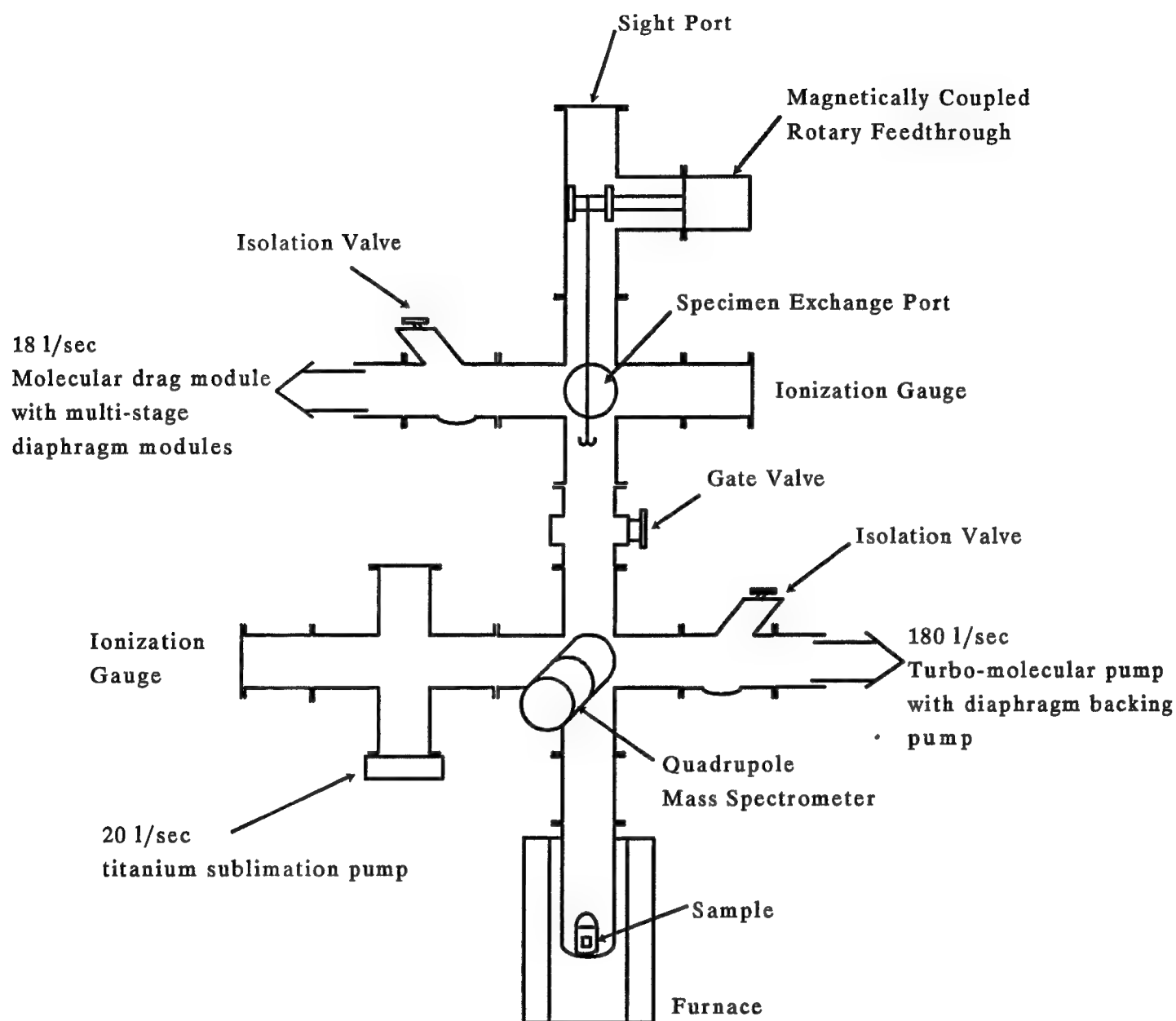


Figure 1 - Schematic of the thermal desorption spectroscopy system developed at the University of Virginia.

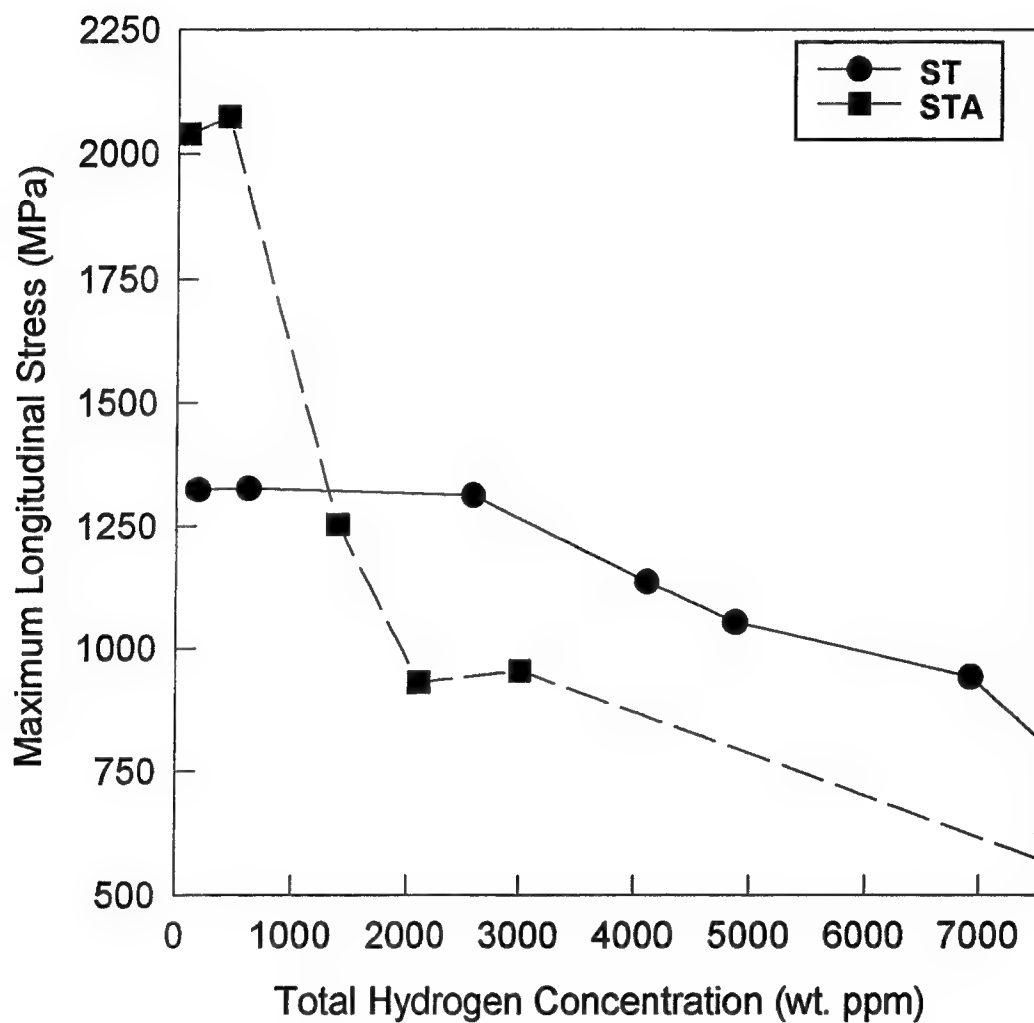
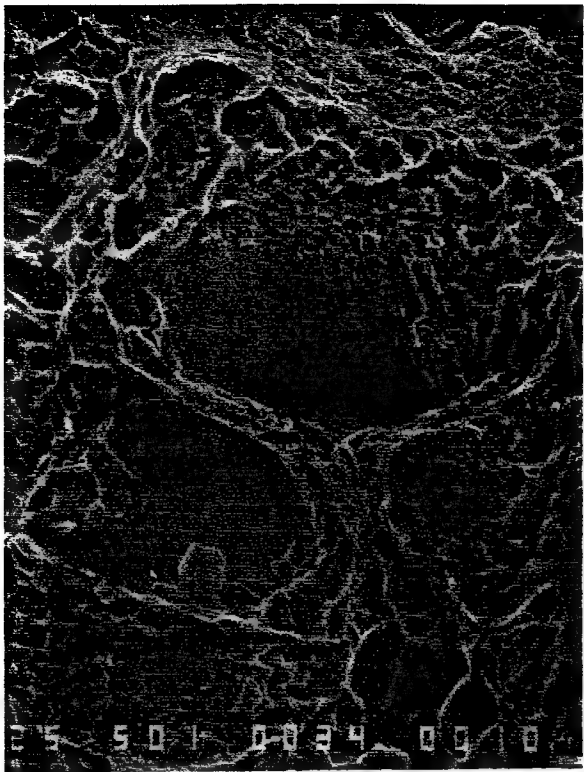
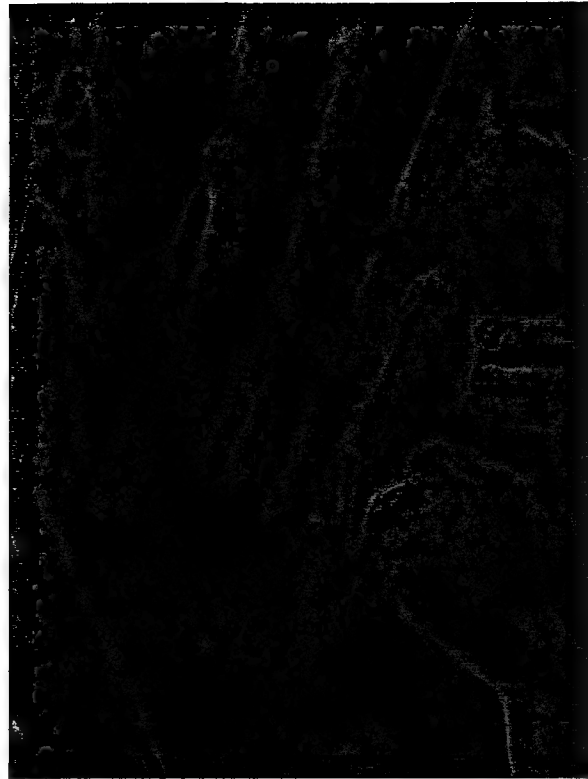


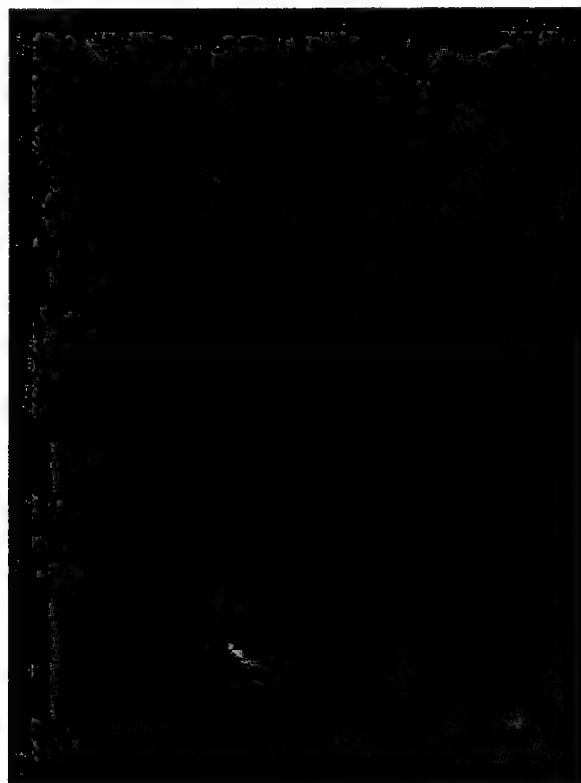
Figure 2 - Maximum longitudinal stress at crack initiation as a function of the total internal hydrogen concentration for ST and STA Beta-C.



(a)



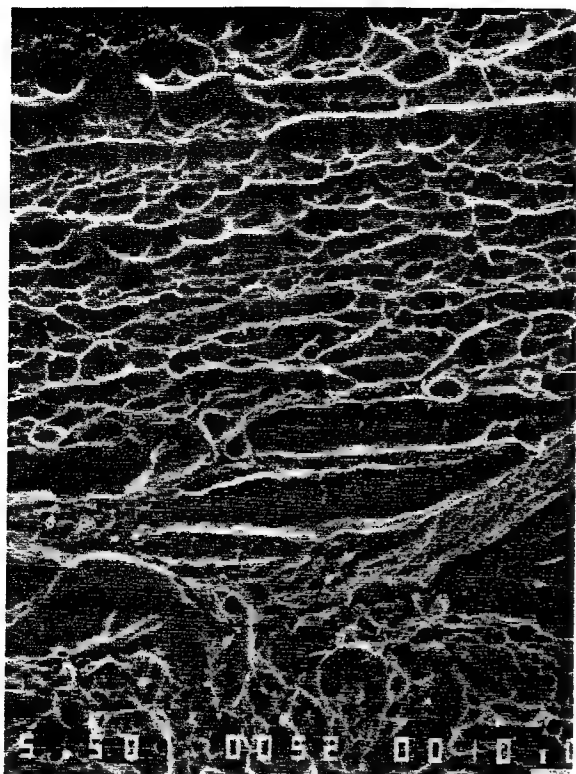
(b)



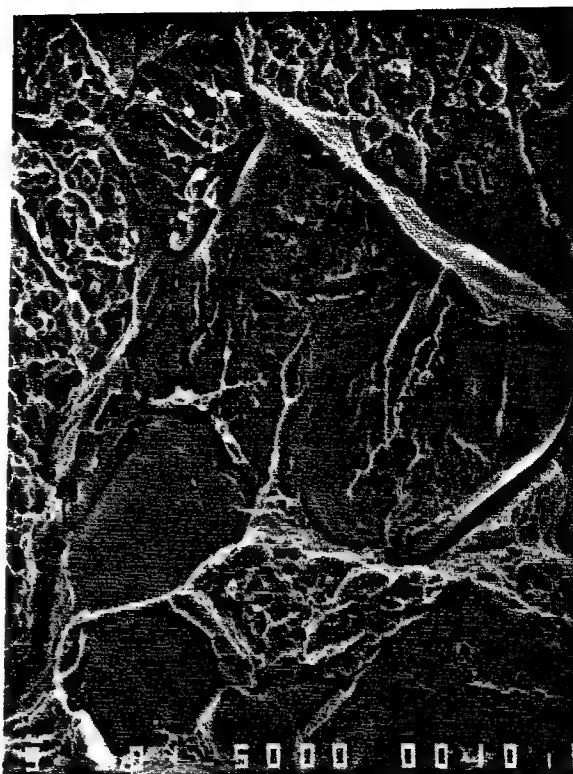
(c)

— 20 microns

Figure 3 - SEM fractographs of ST Beta-C circumferentially notched tensile bars charged to total hydrogen concentrations of (a) 620 wt. ppm, (b) 4100 wt. ppm and (c) 6920 wt. ppm.

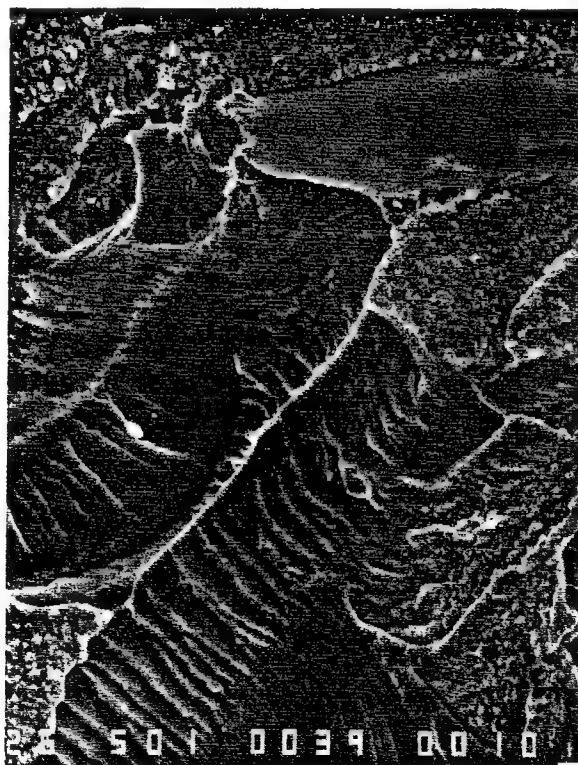


(a)



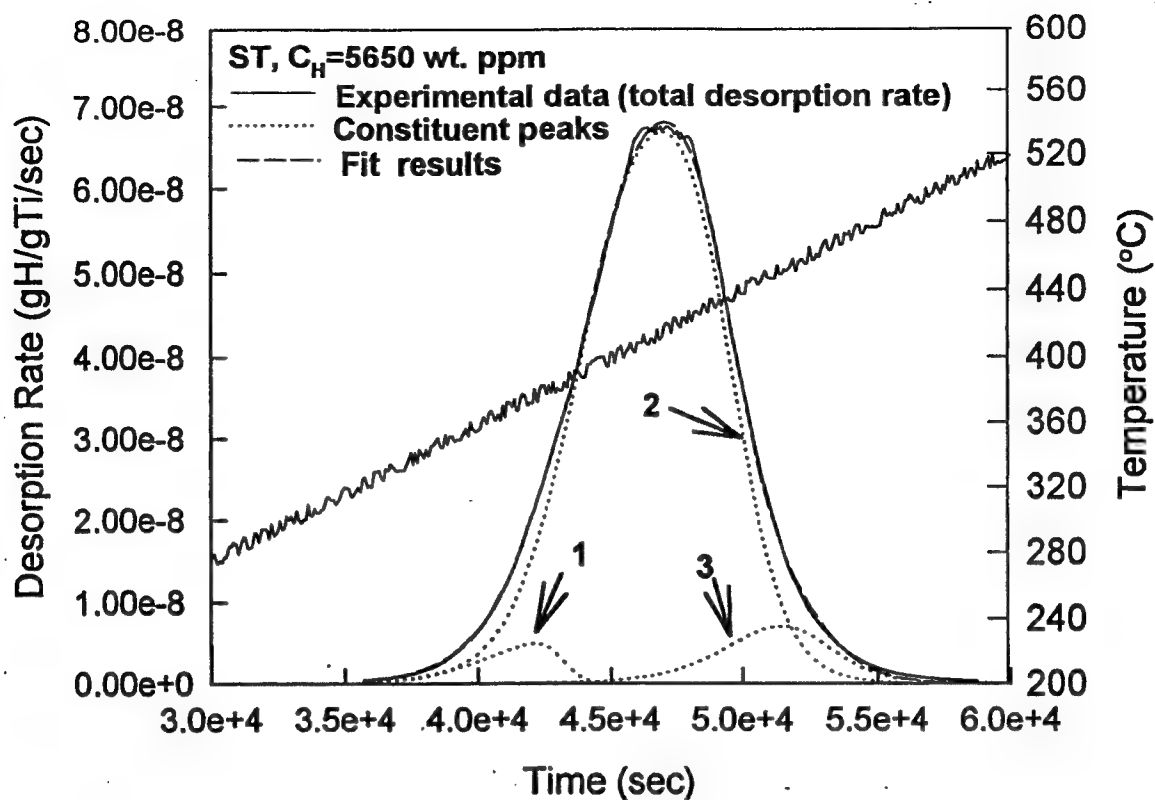
(b)

— 20 microns

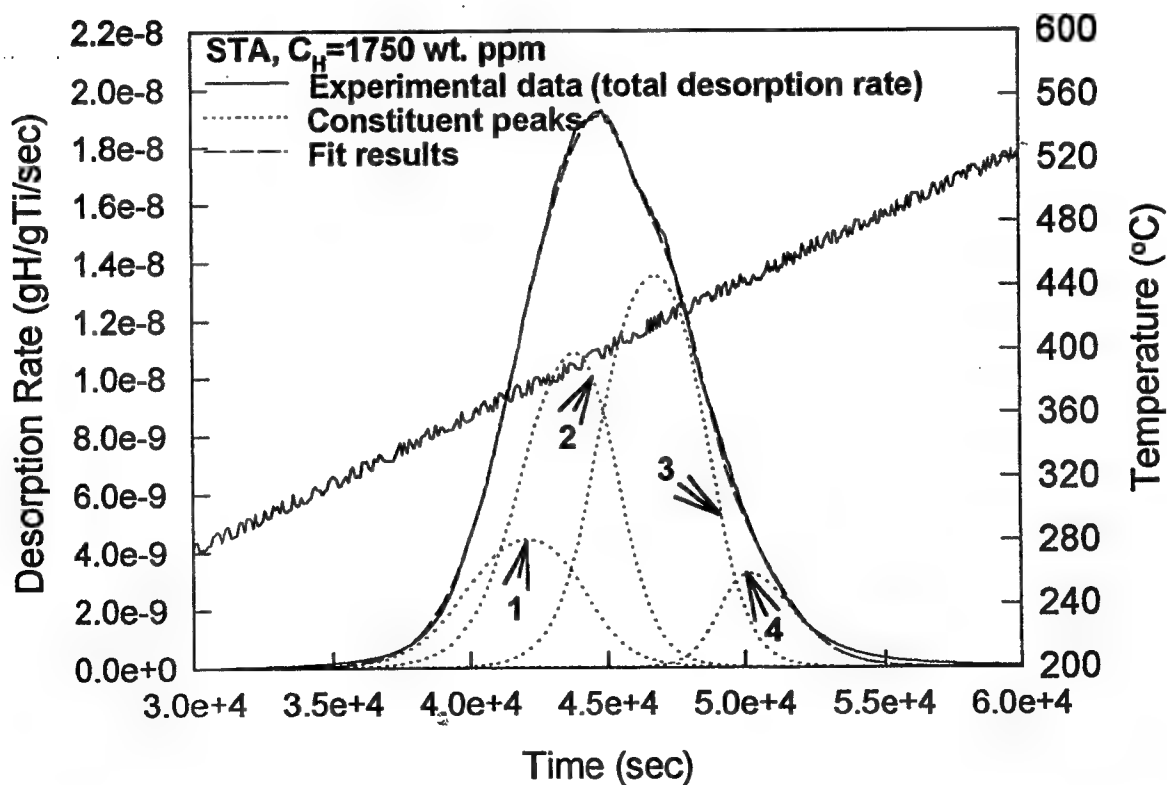


(c)

Figure 4 - SEM fractographs of STA Beta-C circumferentially notched tensile bars charged to total hydrogen concentrations of (a) 430 wt. ppm, (b) 1380 wt. ppm and (c) 3020 wt. ppm.



(a)



(b)

Figure 5 - Desorption spectra, peak fit and constituent peaks at a constant temperature rate of .5 °C/min for (a) ST and (b) STA Beta-C.

**MICROBE ENHANCED ENVIRONMENTAL FATIGUE CRACK  
PROPAGATION IN HY130 STEEL**

**Richard P. Gangloff  
Robert G. Kelly**

# Microbe-Enhanced Environmental Fatigue Crack Propagation in HY130 Steel<sup>☆</sup>

R.P. Gangloff and R.G. Kelly<sup>\*</sup>

## ABSTRACT

Research was undertaken to characterize the effect of sulfate-reducing bacteria (SRB) on aqueous environment-enhanced fatigue cracking in a high-strength alloy steel. *Desulfovibrio vulgaris* in Postgate C solution greatly increased rates of ambient-temperature fatigue crack propagation (FCP) in tempered martensitic HY130 steel (MIL-S-24371A) under cathodic polarization and low-frequency, constant stress intensity range ( $\Delta K$ ) loading. Crack growth rates (da/dN) in the SRB solution increased 50- to 1,000-fold relative to FCP in sterile sodium chloride (NaCl) solution at  $-1,000$  mV<sub>SCE</sub> and under vacuum, respectively. The presence of microbes shifted fatigue cracking from a transgranular path (typical in sterile NaCl) to an intergranular crack path consistent with the enhanced growth rates. The SRB reduced fatigue crack initiation resistance, countering the beneficial effect of cathodic polarization for sterile NaCl. Metal embrittlement and increased hydrogen uptake at the occluded crack tip caused by bacterially produced hydrosulfide (HS<sup>-</sup>) and sulfide (S<sup>2-</sup>) ions were implicated. SRB did not appear to colonize the occluded alkaline crack tip. At constant  $\Delta K$ , transient environmental FCP in the SRB solution was substantial and was most likely a result of time-dependent bacterial growth and enhanced metabolically produced sulfides. Other time-dependent hydrogen sources may have been important.

**KEY WORDS:** aqueous environments, crack tip, cracking, fatigue, fracture mechanics, hydrogen embrittlement, microbiologically influenced corrosion, sodium chloride, steels, sulfate-reducing bacteria

## INTRODUCTION

Reduced sulfur (S) species dissolved in aqueous chloride solution have been shown to have the most deleterious effect on environment-enhanced fatigue crack propagation (FCP) in steels of the variables studied to date.<sup>1</sup> In conjunction with cathodic polarization, gaseous hydrogen sulfide (H<sub>2</sub>S) in chloride solution increased FCP rates in low-strength, carbon (C)-manganese (Mn) steels by 300-fold over rates in vacuum.<sup>2</sup> This dramatic increase overwhelms a 15-fold increase in growth rates for freely corroding specimens in seawater and a 40-fold increase for FCP under cathodic protection.<sup>3</sup> Sulfide-bearing environments also degrade the monotonic load cracking (stress corrosion cracking [SCC]) resistance of steels, particularly for higher strength levels.<sup>4</sup> S species are present in sour gas wells and papermaking process solutions. They also develop as a result of the metabolic action of sulfate-reducing bacteria (SRB).<sup>5-7</sup>

The deleterious effect of SRB on FCP in C-Mn steels has been documented.<sup>8-10</sup> However, data and a mechanistic understanding have been limited. Thomas, et al., showed decomposition of marine algae in estuary silt by SRB led to a 60- to 120-fold increase in FCP rates under free corrosion conditions or under

<sup>\*</sup> Submitted for publication April 1993; in revised form, October 1993.

<sup>\*</sup> Department of Materials Science and Engineering, University of Virginia, Charlottesville, VA, 22903.

mild cathodic polarization.<sup>8</sup> SRB effects on cracking in moderate- to high-strength alloy steels have not been characterized.<sup>1,11</sup>

An understanding of SRB effects has been hindered by several factors. Fatigue experiments generally yield steady-state cracking kinetics and neglect transient growth rates. The bacterial environment chemistry generally changes with time as the bacteria population progresses through different growth stages.<sup>12-13</sup> The chemical composition of the solutions is complex, biologically and electrochemically. SRB may populate test chamber surfaces, boldly exposed fatigue specimen surfaces, and areas within the occluded crack. The relative importance of SRB at each location has not been defined. Finally, the basic chemomechanical mechanisms for environment-enhanced fatigue cracking have not been quantified, even for steels in sterile sodium chloride (NaCl) solutions.<sup>1</sup> Both anodic dissolution and cathodic hydrogen production processes are important.

Cathodic protection is used to retard both general corrosion and fatigue crack initiation (FCI) in steels exposed to sterile and SRB-containing marine environments.<sup>1,14-16</sup> Protection against general corrosion in SRB environments requires larger applied cathodic potentials than in sterile solutions,<sup>15-16</sup> supporting the cathodic depolarization theory of SRB-influenced corrosion. Since SRB prefer near-neutral pH, the local alkalinity produced by cathodic polarization might retard their growth.<sup>10</sup> The anodic reaction rate (iron [Fe] dissolution) also is decreased by cathodic polarization. The contributions of each effect have not been delineated. Cathodic polarization effects on FCP are complex in sterile environments<sup>1</sup> and have not been characterized for biologically inoculated solutions.

The objectives of the present work were to characterize the effect of SRB, including the influence of cathodic polarization, on environmental FCP in an alloy steel of moderate strength and to assess the probable locations of embrittling bacteria colonies and their metabolites with respect to the fatigue crack tip process zone.

## EXPERIMENTAL PROCEDURE

### Material

Quenched and tempered HY130 alloy steel (Fe, 0.1% C, 0.4% Mn, 5.3% nickel [Ni], 0.5% chromium [Cr], 0.6% molybdenum [Mo], 0.2% silicon [Si], and 0.06% vanadium [V] by wt%; MIL-S-24371A) was investigated. Oversized specimen blanks were austenitized at 830°C for 90 min in flowing argon (Ar), water-quenched, and tempered in a salt bath at 610°C for 60 min to produce a Rockwell hardness (HRC) of 33, a prior austenite grain size of 30  $\mu\text{m}$ , and a calculated tensile yield strength of 1,040 MPa.<sup>11</sup>

### Fatigue Crack Growth Rate Measurement

Fracture mechanics single-edge, notched tension (SENT) specimens (5.1 mm thick and 38.1 mm wide with an edge notch 10.2 mm deep) in the long transverse (LT) orientation were used for fatigue crack growth rate (da/dN) measurements. Pin gripping with free rotation and maximum load levels were consistent with the boundary conditions of the stress intensity solution and small scale yielding, respectively.<sup>11</sup>

Fatigue experiments were conducted in a computer-controlled servohydraulic test machine operated in load control. Crack growth was monitored continuously by direct current (DC) electrical potential measurements. Real-time computer control guaranteed a constant applied stress intensity (K) range ( $\Delta K = K_{\text{max}} - K_{\text{min}}$ ) at low constant stress ratio ( $R = K_{\text{min}}/K_{\text{max}} = 0.10$ ) and a constant loading frequency of either 1 Hz (for crack initiation) or 0.1 Hz (for FCP). Additional experiments were conducted using a single specimen at R values between 0.10 and 0.85.  $K_{\text{max}}$  was constant as  $\Delta K$  levels were decreased incrementally to avoid delay retardation. A constant frequency of 1 Hz or 5 Hz was maintained. Electrical potential-derived crack lengths were corrected linearly based on the difference between predicted and optically measured crack lengths from the fractured specimen. Fatigue da/dN were calculated by linear regression of crack length vs load cycle data for each constant  $\Delta K$  and R condition.

### Aqueous Environment Control

Two aqueous environments, 3% NaCl and a bacteriological medium, were investigated. Both were at near-neutral pH and at 23°C. To create the bacteriological medium, *Desulfovibrio vulgaris* bacteria were cultivated in deaerated Postgate medium C containing (per liter of distilled water) 6.0 g lactic acid, 4.5 g sodium sulfate ( $\text{Na}_2\text{SO}_4$ ), 1.0 g yeast extract, 1.0 g ammonium chloride ( $\text{NH}_4\text{Cl}$ ), 0.5 g monobasic potassium phosphate ( $\text{KH}_2\text{PO}_4$ ), 0.3 g hydrated sodium citrate, 0.06 g hydrated calcium chloride ( $\text{CaCl}_2$ ), 0.06 g hydrated magnesium sulfate ( $\text{MgSO}_4$ ), and 0.004 g hydrated ferrous sulfate ( $\text{FeSO}_4$ ) stored in 15-mL vials.

For each environment, the central portion of the edge-cracked specimen was immersed in a sealed 1-L polymethyl methacrylate chamber (Figure 1). No dissimilar metal contacted the immersed portion of the specimen. All tubing and fittings were polytetrafluoroethylene (PTFE). The electrolyte was deaerated with Ar. The grounded specimen was maintained at a constant electrode potential of  $-1,000 \text{ mV}_{\text{SCE}}$  by a potentiostat in conjunction with a silver-silver chloride (Ag-AgCl) reference electrode and two platinum (Pt) counterelectrodes. The reference electrode was adjacent to the notch mouth, while the two counter-



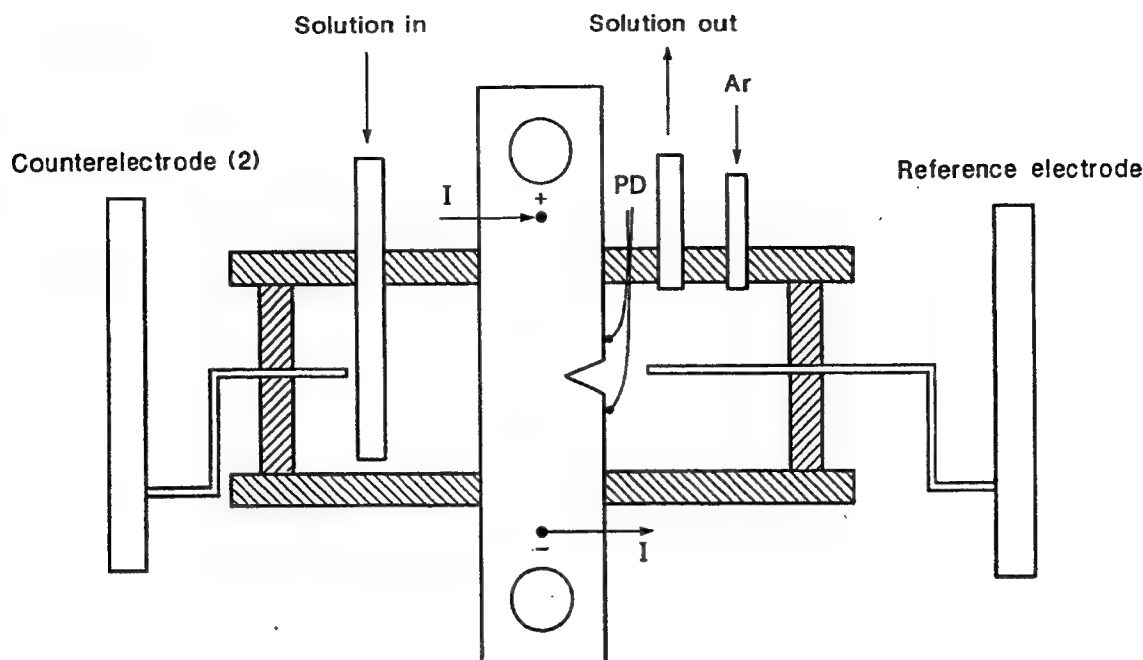


FIGURE 1. Environmental cell used in fatigue cracking experiments. "PD" indicates the location of probes for measuring electrical potential difference caused by passage of DC ( $I$ ) through the uncracked portion of the specimen.

electrode compartments were normal to and  $\sim 5$  cm from the broad faces of the SENT specimen. The reference and counterelectrodes contained 3% NaCl and were isolated from the test solution by asbestos frits. The sterile 3% NaCl solution was pumped peristaltically at 30 mL/min through the chamber, and solution in the chamber was deaerated continuously with Ar. For experiments with SRB, 45 mL of bacteria solution was added to the cell, which contained 550 mL of Postgate medium C diluted by 400 mL of distilled water and fully deaerated with Ar. This environment was maintained statically during the FCP experiment. Specimens were immersed in the bacteria solution for 4 h before fatigue loading.

The corrosion fatigue procedures have been detailed previously.<sup>11,17</sup>

## RESULTS AND DISCUSSION

### SRB-Enhanced Fatigue Crack Growth

The strong and damaging effect of SRB on FCP in HY130 steel was demonstrated by the  $da/dN$ -vs.-applied stress intensity range ( $\Delta K$ ) data in Figure 2. The FCP behavior of HY130 steel in moist air and vacuum is shown by the two dashed lines, which represent extensive historical data for C-Mn and alloy steels.<sup>1-11</sup> Growth rates at  $\Delta K$  above 20 MPa $\sqrt{m}$  were measured at several constant  $\Delta K$  levels, a constant  $R$  value of 0.10, and at a constant loading frequency of

0.1 Hz. Below  $\Delta K$  of 20 MPa $\sqrt{m}$ ,  $K_{max}$  was maintained at 33 MPa $\sqrt{m}$  as  $\Delta K$  was step-reduced (and  $R$  was step-increased) after each increment of steady-state FCP was obtained at a frequency of 1 Hz or 5 Hz. This procedure minimized the complicating mechanical effect of fatigue crack closure and produced unique growth rate relationships for fatigue in moist air and vacuum where intrinsic  $R$ -value effects were not likely.<sup>1,11</sup> Limited FCP data for HY130 steel in moist air (O), obtained with this constant  $\Delta K/K_{max}$  procedure, were in excellent agreement with previous results (Figure 2).

The sterile NaCl environment with cathodic polarization at  $-1,000$  mV<sub>SCE</sub> increased  $da/dN$  by 4-fold relative to moist air and 30-fold relative to vacuum for HY130 steel at a wide range of  $\Delta K$  and  $R$ .<sup>(1)</sup> The  $da/dN$  value depended on  $\Delta K$  raised to the 2.9 power below 20 MPa $\sqrt{m}$  and to the 1.6 power above this  $\Delta K$  level. This environmental effect was typical of the behavior of a wide variety of C-Mn and alloy steels in aqueous chloride.<sup>1,11,17-18</sup>

*Desulfovibrio vulgaris* in diluted Postgate medium C ( $-1,000$  mV<sub>SCE</sub>) enhanced  $da/dN$  values up to 1,000 times relative to vacuum, 100-fold relative to air and 40-fold compared to 3% NaCl, as indicated by the filled

<sup>(1)</sup> Polarization to  $-1,000$  mV<sub>SCE</sub> required application of cathodic currents on the order of 500  $\mu A/cm^2$  for each deaerated aqueous environment.

triangular data points in Figure 2.<sup>(2)</sup> While crack growth experiments were not conducted in diluted medium without SRB, this environment was likely to enhance  $da/dN$  similar to sterile NaCl.<sup>1</sup> The deleterious effect of SRB demonstrated in Figure 2, specific to cathodic polarization at  $-1,000 \text{ mV}_{\text{SCE}}$ , was comparable to published data for SRB-enhanced crack growth in C-Mn steels under freely corroding and mildly cathodic conditions ( $-850 \text{ mV}_{\text{SCE}}$ ).<sup>8-9</sup> Substantial cathodic protection did not mitigate the deleterious effect of SRB on environmental FCP in HY130 steel.

The importance of the deleterious SRB effect is demonstrated in Figure 3. Trend lines from extensive literature data represent the environmental FCP behavior of a wide range of C-Mn and alloy steels, cyclically loaded at  $R$  of 0.05 and a frequency of 0.1 Hz in 3.5% NaCl (sterile) at a fixed cathodic potential of  $-1,000 \text{ mV}_{\text{SCE}}$ .<sup>1</sup> The two data points for the steady-state, low  $R$ -low frequency SRB environment are replotted from Figure 2 and are represented by a power law ( $da/dN \propto \Delta K^{1.6}$ ) parallel to the sterile NaCl results in Figure 2. These two  $da/dN$  values for HY130 exposed to SRB were equally consistent with a relationship parallel to the  $\Delta K^{1.2}$  dependence indicated by the historical results for HY130 steel in sterile NaCl (Figure 3.) While the effects of steel yield strength and microstructure were less than a factor of 2 on FCP rate at any  $\Delta K$ , the SRB dramatically enhanced  $da/dN$  by up to 2 orders of magnitude.

Environmentally enhanced FCP in steels of yield strength  $< \sim 1,200 \text{ MPa}$  that are exposed to sterile aqueous chloride at various cathodic electrode potentials (Figure 3) generally occurs at cyclic stress intensity levels well below the threshold stress intensity for monotonic load cracking ( $K_{\text{ISCC}}$ , or where  $K_{\text{max}}$  and  $K_{\text{min}}$  in the fatigue cycle are below  $K_{\text{ISCC}}$ ).<sup>1</sup> For such cases, environmental FCP is both time- and load-cycle dependent. Considering HY130 in sterile NaCl ( $-1,000 \text{ mV}_{\text{SCE}}$ ),  $K_{\text{ISCC}}$  equals  $110 \text{ MPa}\sqrt{\text{m}}$ .<sup>19</sup> Data in Figure 2 represent FCP at  $K$  levels well below this monotonic threshold.  $K_{\text{ISCC}}$  for steels at this yield strength is lowered to perhaps  $20 \text{ MPa}\sqrt{\text{m}}$  by acid and gaseous  $\text{H}_2\text{S}$  additions to NaCl (e.g., the solution defined in NACE Standard MR0175, "Sulfide Stress

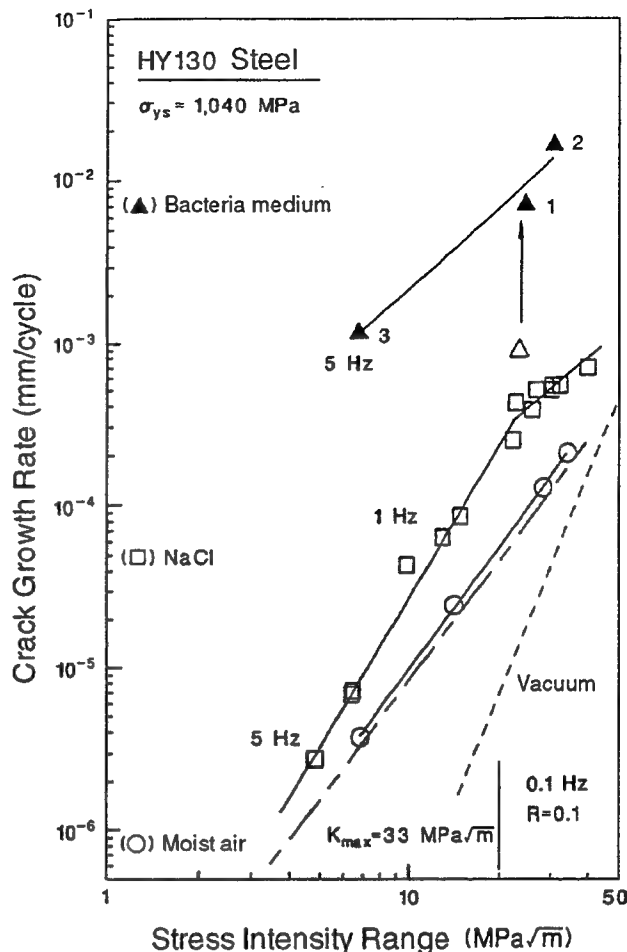


FIGURE 2. Fatigue  $da/dN$  vs applied  $\Delta K$  for tempered martensitic HY130 steel in vacuum,<sup>11</sup> in moist air, sterile NaCl at  $-1,000 \text{ mV}_{\text{SCE}}$ , and Postgate medium C at  $-1,000 \text{ mV}_{\text{SCE}}$ . Stress ratio and frequency were varied as shown. Arrow indicates transient crack growth at constant  $\Delta K$  and during the approach to steady state in the bacteria solution.

Cracking Resistant Metallic Materials for Oilfield Equipment"). Time-dependent crack growth rates ( $da/dt$ ) are rapid.<sup>4</sup>  $K_{\text{ISCC}}$  is, however, unknown for quenched and tempered steels in SRB solution. The potency of SRB-enhanced FCP indicated SCC could be produced by particular metallurgical, biological, and electrochemical conditions. This issue must be examined.<sup>(3)</sup>

When the applied  $\Delta K$  is maintained at a constant level, FCP in steels exposed to sterile NaCl generally is steady state after minimal short-term transient growth. Crack length increases linearly with the number of load cycles for constant applied  $\Delta K$ . In sterile NaCl (as well as moist air and vacuum), each point in Figure 2 resulted from such a linear record. Transient FCP was not observed.

In sharp contrast to results in sterile NaCl, transient crack growth occurred in the SRB

<sup>(2)</sup> The  $da/dN$ - $\Delta K$  dependence for the steady-state SRB case in Figure 2 was plotted parallel to the data for HY130 steel in sterile NaCl and should be interpreted with caution because  $R$  increased with decreasing  $\Delta K$ . The intrinsic effect of stress ratio on environmental FCP in steels was not defined.

<sup>(3)</sup> For environmental FCP above  $K_{\text{ISCC}}$ , and with high  $da/dt$ ,  $da/dN$  depended on  $\Delta K$  raised to a power between 10 and 40 at cyclic  $K$  levels near  $K_{\text{ISCC}}$ , followed by essentially  $\Delta K$ -independent behavior at higher  $\Delta K$ .<sup>1</sup> The HY130 in SRB growth rates in Figure 2 were only of the above- $K_{\text{ISCC}}$  type if  $K_{\text{ISCC}}$  was  $< 10 \text{ MPa}\sqrt{\text{m}}$ . Alternately, since similar power-law  $da/dN$ - $\Delta K$  relationships were observed for HY130 in moist air ( $\Delta K$  exponent of 2.5), sterile NaCl (2.9 and 1.6), and the SRB environment (1.6), the FCP behavior in Figure 2 may have been of the below- $K_{\text{ISCC}}$  type.

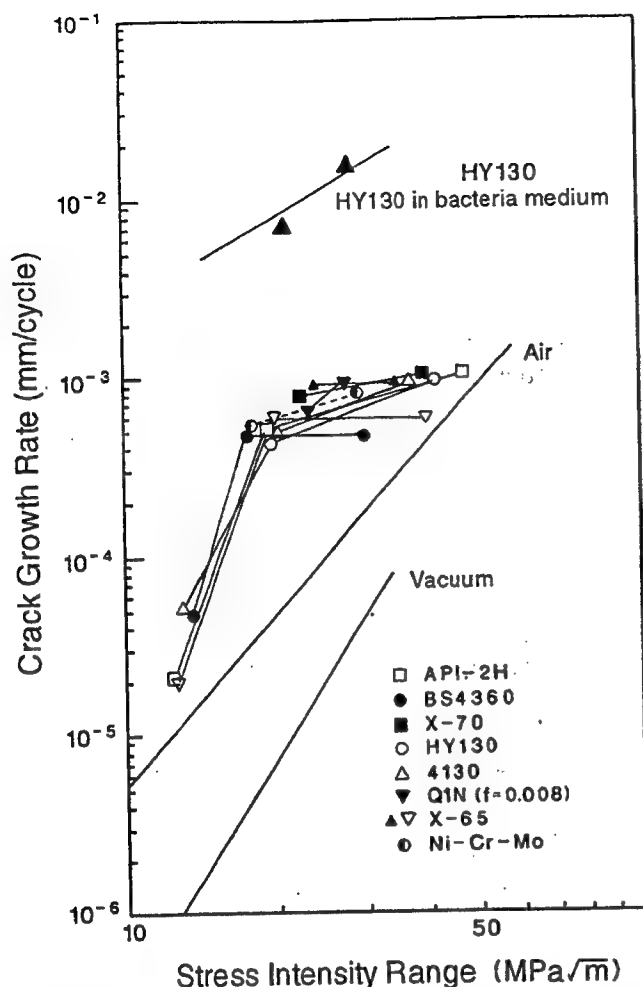


FIGURE 3. Environmental FCP in C-Mn and alloy steels exposed to sterile 3.5% NaCl and bacterially active solutions at  $-1,000$  mV<sub>SCE</sub> at a fixed loading frequency (0.1 Hz) and constant  $R$  (0.05).<sup>1</sup>

environment. Figure 4 shows measured values of fatigue crack length vs loading cycles (analyzed to yield a portion of the  $da/dN$  vs  $\Delta K$  data in Figure 2). In this experiment, a single HY130 specimen was immersed in SRB plus diluted Postgate C with cathodic polarization at  $-1,000$  mV<sub>SCE</sub> for 4 h without loading. The fatigue crack was grown from the notch (depth of 10.2 mm) to a depth of 1.46 mm (total notch plus crack length = 11.66 mm) over 8,100 cycles at 1 Hz (2.3 h exposure). After this initial crack growth, constant  $\Delta K$  (20.8 MPa $\sqrt{m}$ ,  $R = 0.10$ ) loading commenced at 0.1 Hz. As this loading continued from 8,100 to 10,800 cycles (over 7.5 h), the FCP rate accelerated from  $8.9 \times 10^{-4}$  mm/cycle to  $2.0 \times 10^{-3}$  mm/cycle. Since crack length did not increase linearly with loading cycles, steady-state FCP was not achieved during the first day. The specimen was maintained in the SRB solution for 12 h without load, and the experiment was

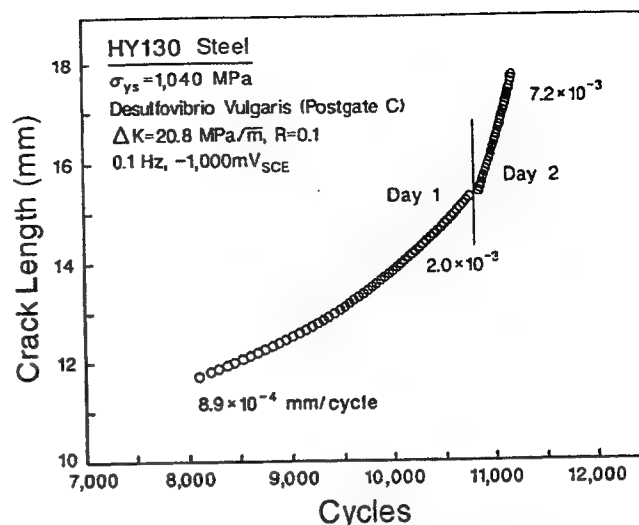


FIGURE 4. Fatigue crack length vs loading cycles for tempered martensitic HY130 steel in Postgate medium C at  $-1,000$  mV<sub>SCE</sub>, constant  $\Delta K$  of 20.8 MPa $\sqrt{m}$ , frequency of 0.1 Hz, and stress ratio of 0.1.

reinitiated at the same constant  $\Delta K$  and frequency (Day 2, Figure 4). The resultant crack advance essentially was linear for 1.2 h at an average rate of  $7.2 \times 10^{-3}$  mm/cycle, indicating steady state was achieved.

The initial SRB rate on Day 1 (open triangle, Figure 2) was slightly higher than the  $da/dN$  value typical of FCP in sterile NaCl. Increasingly rapid rates were observed during Day 1 (as shown by the arrow from the open triangle). The steady-state behavior observed during Day 2 is represented by the filled triangle labelled "1" in Figure 2. Subsequent sequential crack growth experiments, labelled "2" and "3," were conducted over 48 h at different  $\Delta K$  and  $R$  and yielded essentially linear  $a$  vs  $N$  data. The trend line in Figure 2 approximated steady-state FCP for HY130 in the SRB solution. The  $da/dN$  value depended on  $\Delta K$  raised to the 1.6 power, similar to the behavior of C-Mn steel in  $H_2S$ -saturated chloride solution. However, a wider range of  $\Delta K$  must be examined to better characterize this behavior.<sup>2</sup>

Bacteria concentrations and dissolved  $H_2S$  levels were not measured during these experiments. The SRB solution darkened continuously during the first day of the experiment, and odor indicated  $H_2S$  was formed in the cell. These observations indicated increasing bacterial activity, coincident with the accelerating  $da/dN$  values. A constant SRB environment likely was achieved, but only after the first day.<sup>12-13</sup> Additional factors may cause transient FCP in the presence of SRB, as considered later in this work.

Results demonstrated that SRB-related environment effects must be considered in damage

tolerant analyses of fatigue in marine structures.<sup>20</sup> Such work will be complicated because  $da/dN$  can change with exposure time at constant  $\Delta K$  as a result of varying biological environment chemistry. Fracture mechanics growth rate similitude, in conjunction with steady-state  $da/dN$ -vs- $\Delta K$  data, may not describe component performance adequately.<sup>(4)</sup>

Data in Figure 2 may provide a reasonable upper-bound  $da/dN$ - $\Delta K$  relationship for HY130 steel in SRB of essentially constant activity. Studies of metallurgical effects on corrosion fatigue (i.e., weld heat-affected zone behavior) must include SRB chemical variables such as the cultivating medium. From a practical perspective, significant cathodic polarization did not mitigate the deleterious effects of SRB on FCP, in agreement with the work of Edyvean, et al.<sup>10</sup> FCP may be enhanced more severely by SRB in the presence of mild anodic polarization or under free corrosion conditions.

### SRB-Sensitive Fatigue Crack Surface Morphology

Environmental fatigue crack surfaces were examined by scanning electron microscopy (SEM). Photomicrographs (Figure 5) demonstrated the strong embrittling effect of *Desulfovibrio vulgaris* on FCP in HY130 steel. All fractographs are oriented with the fatigue crack growth direction from top to bottom and the crack front parallel to the horizontal direction. Figure 5(a) shows the crack morphology typical of environmental FCP in sterile NaCl at  $-1,000$  mV<sub>SCE</sub>. Cracking was entirely transgranular and most probably was associated with environment-enhanced martensite lath interface cracking and crystallographic cracking along a low index plane through the tempered martensite.<sup>11</sup> The environmental crack path illustrated in Figure 5(a) was not typical of FCP in HY130 steel stressed in moist air or vacuum. In these benign environments, FCP was transgranular but involved crack tip plasticity damage independent of environment-embrittled martensite.

In contrast to the vacuum and sterile NaCl cases, *Desulfovibrio vulgaris* in diluted Postgate medium C

promoted intergranular cracking, the increasing proportion of which correlated with increasing FCP rates.<sup>(5)</sup>

Figure 5(b) illustrates that SRB-enhanced cracking on Day 1 progressed by a mixture of transgranular and intergranular separation. Qualitatively, the proportion of transgranular cracking was equal to or greater than the amount of intergranular separation. This mixed morphology was consistent with the modestly enhanced  $da/dN$  relative to fully transgranular FCP in sterile NaCl (Figure 2). Crack growth in the SRB medium during Day 2 (Figure 5[c]) occurred by a larger proportion of intergranular separation, correlating with increased bacterial activity and the increased  $da/dN$ . Portions of the Day 2 crack surface were nearly 100% intergranular.

Apart from severe temper embrittlement and abiotic sulfides, no chemical or mechanical variable has been reported previously to induce intergranular fatigue cracking in low- to moderate-strength quenched and tempered alloy steels.<sup>1</sup>

### SRB-Enhanced FCI

The effect of environment on notch-tip FCI in HY130 steel was measured at the beginning of each crack propagation experiment and was based on a fracture mechanics estimate of the local pseudo-elastic stress and total strain ranges.<sup>23-24</sup> SENT specimens for experiments in moist air, sterile NaCl, and the SRB in Postgate C were notched similarly (with a root radius [ $\rho$ ] of 0.25 mm and by grinding without additional polishing), and subjected to a constant  $\Delta K$  of 20.8 MPa $\sqrt{m}$  (calculated as if the blunt notch was a crack of the same length) at a frequency of 1 Hz and R of 0.1.<sup>(6)</sup> After a period of no measurable crack formation, FCI progressed from the notch, as indicated by electrical potentials measured during cyclic loading.

The chloride environments affected FCI in tempered martensitic HY130 steel, as demonstrated in Figure 6. This figure presents the number of load cycles required for FCI at constant  $\Delta K/\sqrt{\rho}$ , where a crack growth increment of 1 mm was taken as an approximation of the initiation stage of cracking. Results are given for FCI in moist air and in three aqueous chloride environments. It is well known that, compared to fatigue in moist air, sterile NaCl degrades the FCI resistance of C-Mn and alloy steels.<sup>23-24</sup> This environmental effect is severe for electrode potentials near free corrosion ( $-600$  mV<sub>SCE</sub> to  $-750$  mV<sub>SCE</sub>) and is mitigated by applied cathodic potentials near  $-1,000$  mV<sub>SCE</sub>.<sup>25</sup> The detrimental effect of sterile NaCl at  $-600$  mV<sub>SCE</sub> and the beneficial effect of applied cathodic polarization are reflected in Figure 6. The result for HY130 steel in NaCl at  $-1,000$  mV<sub>SCE</sub> was measured in the current study, and the free corrosion result was estimated from data reported for a similar

<sup>(4)</sup> Paris<sup>21</sup> and Wei, et al.,<sup>22</sup> experimentally demonstrated the principle of fracture mechanics similitude for FCP; that is, equal  $da/dN$  are produced for equal applied  $\Delta K$  independent of applied load, crack size, and component or specimen geometry. Similitude enables integration of laboratory  $da/dN$ - $\Delta K$  data to predict component fatigue behavior; in terms of applied stress range vs total life or crack length vs applied load cycles for any initial defect size and component configuration.

<sup>(5)</sup> Fatigue cracking in the SRB environment is intergranular with respect to prior austenite boundaries in HY130 steel.

<sup>(6)</sup> This loading condition corresponded to a notch-root, pseudo-elastic stress range of 1,315 MPa, calculated from  $\Delta K/\sqrt{\rho}$ ,<sup>24</sup> and to a proportional local plastic strain range that was not determined. FCI was governed by plastic strain, however, the stress-based approach provided a basis for comparing environment effects.

high-strength steel loaded at a frequency of 0.2 Hz and  $R$  of 0.1.<sup>24</sup> For this latter case, FCI life may be higher for a loading frequency of 1 Hz.

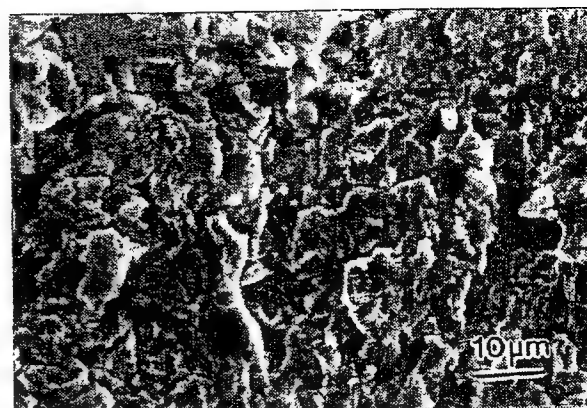
*Desulfovibrio vulgaris* in Postgate medium C with cathodic polarization reduced the FCI resistance of HY130 steel relative to moist air and sterile aqueous chloride at  $-1,000 \text{ mV}_{\text{SCE}}$ . This result is important technologically because cathodic polarization is used widely to mitigate corrosion FCI in the steel and chloride system. SRB appeared to reduce its effectiveness.

Compared to sterile NaCl at the free corrosion potential, the bacterial solution enhanced FCP but reduced FCI susceptibility in HY130 steel at  $-1,000 \text{ mV}_{\text{SCE}}$ . The SRB-stimulated hydrogen embrittlement may have contributed to the environmental effects on crack initiation and propagation. The aggressive character of the sterile solution at  $-600 \text{ mV}_{\text{SCE}}$  suggested an increased role of pitting-based FCI compared to SRB at  $-1,000 \text{ mV}_{\text{SCE}}$ .<sup>25</sup> Pitting as a result of SRB-produced reduced sulfide species at  $-600 \text{ mV}_{\text{SCE}}$  and the associated FCI life were not characterized. SRB also may degrade FCI resistance of freely corroding steels in bacterially active electrolytes with reduced near-electrode-surface alkalinity.

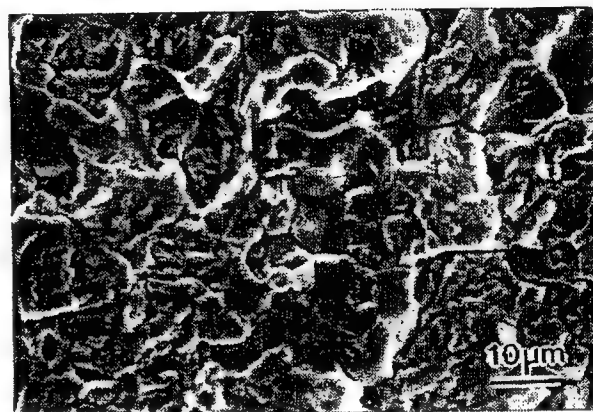
### Mechanism for the SRB Effect on Environmental FCP

Hydrogen environment embrittlement (HEE) is a likely mechanism for enhanced FCP in steels exposed to many gaseous and electrolytic environments near  $25^\circ\text{C}$ .<sup>1</sup> For sterile aqueous electrolytes, atomic hydrogen (H) forms on metal surfaces by cathodic reduction of hydrogen ions and water. The H that does not recombine to molecular hydrogen ( $\text{H}_2$ ) can enter the metal lattice, diffuse to the crack tip region, segregate at microstructural trap sites, and enhance fatigue damage and  $\text{da}/\text{dN}$  by one of several controversial mechanisms. The H source for crack tip embrittlement depends on environment chemistry.<sup>27</sup> The crack tip surface is dominant when occluded crack acidification occurs or when crack surface strain stimulates electrochemical reactions. H production on specimen surfaces that are exposed boldly to the bulk environment can be important for aggressive solutions, particularly those containing reduced S species, and for prolonged exposures.

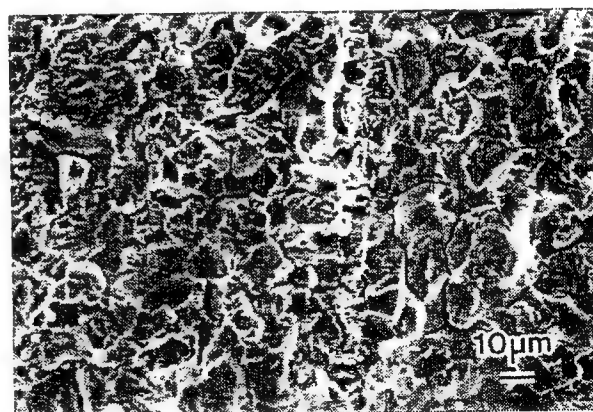
FCP rates are controlled by the kinetics of the slow step(s) in the sequence that produces and delivers embrittling H to the crack tip process zone.<sup>22</sup> An environmental factor (i.e., cathodic polarization,  $\text{H}_2\text{S}$ , decreasing loading frequency) that increases H uptake to the crack tip process zone is likely to increase FCP rates. For example,  $\text{H}_2\text{S}$  dissolved in chloride solution increases H uptake by reducing the rate of H



(a)



(b)



(c)

FIGURE 5. SEM fractographs of high  $\Delta K$  FCP in HY130 exposed to sterile chloride and SRB solutions at  $-1,000 \text{ mV}_{\text{SCE}}$  ( $\Delta K = 20.8 \text{ MPa}\sqrt{\text{m}}$ ,  $R = 0.1$ , and  $f = 0.1 \text{ Hz}$ ). Crack growth direction was from top to bottom, and the crack front was parallel to the horizontal direction.

recombination to  $\text{H}_2$  and greatly enhances rates of FCP.<sup>25,28</sup> Scully and Moran demonstrated that this mechanism promotes H permeation in tempered martensitic type 4340 steel, but only in acid environments ( $\leq \text{pH } 3$ ).<sup>25</sup>



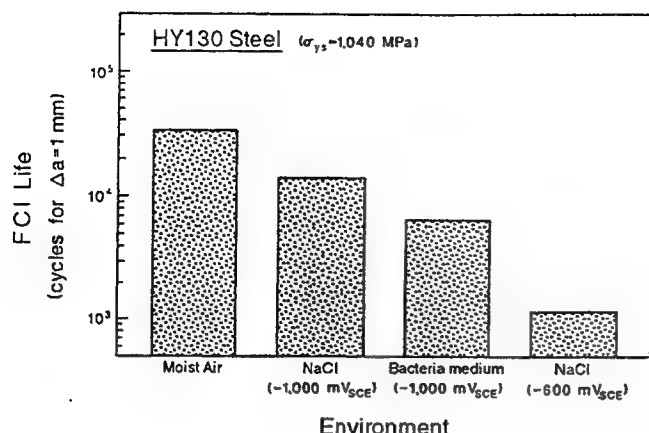
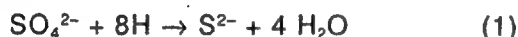


**FIGURE 6.** FCI life ( $\Delta N$  for 1 mm of crack extension from a notch tip) as a function of environment for HY130 steel at constant loading conditions ( $\Delta K_{I\text{P}} = 1,315 \text{ MPa}$ ,  $R = 0.1$ , and  $f = 1 \text{ Hz}$ ). The free corrosion result ( $-600 \text{ mV}_{\text{SCE}}$ ) was reported for similar martensitic steels at a frequency of  $0.2 \text{ Hz}$ .<sup>1,24</sup>

SRB may affect H production and uptake through metabolic action.<sup>30-32</sup> SRB generate energy by coupling the reduction of sulfate ions and the oxidation of a food source (often an organic molecule such as lactate).<sup>13</sup> Bacterial sulfate ( $\text{SO}_4^{2-}$ ) reduction involves H according to the reaction:



The cathodic depolarization theory of SRB-influenced corrosion is based on the idea that bacterial utilization of H removes the cathodic product in the corrosion reaction couple and thus increases the open-circuit corrosion rate of steel.<sup>15,33-35</sup> This effect lowers the amount of H available to enter the metal. Countering the potentially beneficial effect of the consumption of H in SRB metabolism, the production of sulfide or other metabolites may increase the uptake efficiency of H produced on the occluded crack tip or boldly exposed metal surfaces. Walch, et al., showed H uptake into palladium and steel is enhanced in near-neutral solutions containing SRB.<sup>30-31</sup> The net effect of SRB on H production and environmental FCP depends on the relative strengths of these individual processes.

This result led to speculation that the HEE mechanism describes the deleterious effect of SRB on  $da/dN$  in HY130 steel. Increased H uptake and environmental cracking rates may be caused by the metabolic production of sulfide overwhelming any beneficial effect of H consumption by the bacteria. In this regard, SRB may play a role analogous to hydrogen recombination poisons,<sup>36</sup> promoting H uptake efficiency and brittle cracking.<sup>(7)</sup>

The observed intergranular FCP indicated SRB-enhanced hydrogen production resulted in increased H

partitioned to trap sites at prior austenite grain boundaries within the fracture process zone, over the amount produced in sterile chloride.<sup>37</sup> The fracture strength of the austenite grain boundaries had to be more strongly dependent on local hydrogen concentration, compared to the behavior of coherent lath interfaces, to rationalize the transgranular to intergranular fatigue crack path transition. However, this speculation was not proved.

It was necessary to determine whether SRB acted directly at the crack tip or on boldly exposed specimen surfaces or whether ions from SRB metabolism in the bulk solution migrated to these locations to enhance hydrogen uptake.

### Transient FCP in the SRB Environment

The long-term transient crack propagation in HY130 steel in the SRB solution raised important issues for fatigue in bioactive environments. Since the SRB population grew during the fatigue experiment in the statically contained environment,  $da/dN$  may have increased at constant  $\Delta K$  over a 24-h period because of increased concentrations of metabolic S species. The extent to which a solution concentration transient dominated the transient FCP was not measured. It is difficult to maintain bacterial solutions at constant activity, compared to solutions used in typical environmental cracking experiments. Experiments must be developed to characterize the importance of biological environment chemistry changes.

Additional causes for time-dependent  $da/dN$  at constant  $\Delta K$  can be assessed by diffusion calculations within the HEE framework. The effective diffusivity of hydrogen ( $D_H$ ) in HY130 steel is  $4 \times 10^{-7} \text{ cm}^2/\text{s}$ ,<sup>38</sup> and the diffusivity of ions ( $D_i$ ) in the electrolyte is  $10^{-5} \text{ cm}^2/\text{s}$ .<sup>39</sup> For FCP in sterile NaCl (at free corrosion to modest cathodic polarization), no transient crack propagation was observed because the elements of the embrittlement process were localized at the crack tip. Crack solution transport, crack surface electrochemical reactions, and crack tip process zone H diffusion<sup>(8)</sup> are relatively fast, and H diffusion from boldly exposed surfaces is not important.<sup>1,11,22,27</sup>

If SRB migrated rapidly and populated the crack tip, steady-state FCP should have resulted, similar to

<sup>(7)</sup> Sulfide does not promote hydrogen uptake on unstrained, filmed steel surfaces in neutral to alkaline solutions,<sup>29</sup> and therefore, may not enhance  $da/dN$  for the cathodic polarization case where the crack tip is alkaline.<sup>38</sup> If cyclic plastic strain destabilizes a crack tip surface film, formed by reaction with high-pH solution, then  $\text{HS}^-$  from SRB activity could promote hydrogen uptake at the crack tip.

<sup>(8)</sup> The distance ( $x$ ) for hydrogen diffusion from the crack tip surface to the point of maximum stress within the process zone is on the order of  $5 \mu\text{m}$  ( $K = 25 \text{ MPa}\sqrt{\text{m}}$ , yield strength =  $1,040 \text{ MPa}$ , and elastic modulus =  $200 \text{ GPa}$ ).<sup>1,11</sup> Hydrogen will penetrate to a level of 95% of the surface concentration in a time ( $t$ ) of  $0.2 \text{ s}$  ( $x = 2[D_H t]^{1/2}$ ).

sterile NaCl. The occurrence of the long-term transient suggested the SRB did not colonize surfaces, presumably because the occluded crack solution was alkaline for chloride at  $-1,000 \text{ mV}_{\text{SCE}}$ .<sup>40</sup> This conclusion was contingent on a constant SRB population.

$\text{HS}^-$  and  $\text{S}^{2-}$ , produced by bacteria throughout the bulk solution and on specimen and chamber surfaces, can cause a FCP transient, but ion diffusion times are relatively short. For example, if S species are produced on or near boldly exposed notch surfaces, 1 h is required for diffusion to the tip of a 4-mm-deep fatigue crack. Since ion migration and convective mixing promote ion transport to the crack tip,<sup>40</sup> this and shorter times were not consistent with the observed 24-h transient FCP.

Metabolite diffusion could limit FCP for transport distances on the order of 25 mm or larger. Remote SRB colony sites were important if cathodic polarization reduced SRB metabolism on and near the steel specimen due to local alkalinity. For the current experiments with low cathodic current density and buffered Postgate C solution, only solution within hundreds of micrometers of specimen surfaces should have been sufficiently alkaline to hinder SRB metabolism.

Finally, S metabolites may stimulate H production on boldly exposed steel surfaces with subsequent diffusion to the crack tip process zone. Diffusion calculations<sup>(6)</sup> indicated 11 h are required for H to diffuse through the steel over a distance equal to half of the single-edge-crack specimen thickness. This "lag time" for hydrogen supply was consistent with the transient cracking response of HY130 steel in SRB solution, but not with the observed crack profiles. Similar crack front shapes were observed for HY130 in sterile NaCl and SRB at  $-1,000 \text{ mV}_{\text{SCE}}$ . The environmental fatigue cracks did not advance preferentially near specimen surfaces compared to crack penetration at the specimen midplane. Such inverse crack tunneling is likely when hydrogen uptake at boldly exposed surfaces is substantial relative to that at the crack tip.<sup>27</sup> Austin<sup>2</sup> and others<sup>10</sup> have reported equal rates of FCP for bare and painted fracture mechanics specimens of a C-Mn steel loaded cyclically in gaseous  $\text{H}_2\text{S}$ -doped seawater. This suggested that sulfide enhanced crack tip H production, while hydrogen from boldly exposed specimen surfaces was not important.

Determining whether organic molecules from the Postgate medium adsorbed on metal surfaces to hinder H production and uptake is important.<sup>10</sup> The concentration of dissolved  $\text{H}_2\text{S}$  in solution provides a means to assess SRB activity and an indication of HEE severity. Media-cultured SRB such as *Desulfovibrio vulgaris* have produced on the order of 500 ppm to 2,000 ppm  $\text{H}_2\text{S}$ .<sup>10</sup> Thomas and others reported that

FCP rates in a C-Mn steel exposed to 200 ppm and 600 ppm  $\text{H}_2\text{S}$  dissolved from the gas were increased by factors of 20 and 100, respectively, compared to  $da/dN$  in pure seawater.<sup>2,10</sup> These enhancement factors were only factors of 10 and 15 for similar levels of dissolved  $\text{H}_2\text{S}$  produced by SRB from algae decomposition in seawater. These results indicated the biological environment produced substantial sulfide species but interfered with hydrogen uptake compared to abiotic  $\text{H}_2\text{S}$ . The inhibiting behavior of Postgate medium C was uncharted.

## CONCLUSIONS

- ❖ The SRB *Desulfovibrio vulgaris* in diluted Postgate medium C solution greatly enhanced FCP rates and reduced FCI life in the martensitic alloy steel HY130 under cathodic polarization ( $-1,000 \text{ mV}_{\text{SCE}}$ ). Metabolic sulfide-enhanced H uptake and crack tip process zone hydrogen embrittlement were implicated.
- ❖ Transgranular cracking, typical of fatigue in sterile NaCl solution, changed to intergranular cracking as a result of the presence of SRB.
- ❖ The severity of the SRB effect on growth rates and intergranular cracking is paramount among those variables that influence environmental fatigue in C-Mn and alloy steels.
- ❖ The deleterious effects of SRB on FCP and FCI were not mitigated by cathodic polarization.
- ❖ Transient environmental FCP in the SRB solution likely was a result of time-dependent bacterial growth and enhanced metabolically reduced sulfides. Transient FCP at constant  $\Delta K$  also may have been a result of diffusion of metabolites from the bulk to the crack tip solution and hydrogen penetration from boldly exposed specimen surfaces. SRB may not have colonized the occluded alkaline crack tip.
- ❖ Transient fatigue cracking in SRB solutions compromised life prediction based on stress intensity similitude.

## ACKNOWLEDGMENTS

The authors acknowledge the financial support of the Virginia Center for Innovative Technology Technology Development Center on Electrochemical Science and Engineering (grant no. CIT-TDC-88-01) and by the Office of Naval Research (grant no. N00014-91-J-4164, project monitor A.J. Sedriks). The experiments were conducted by R. Krishnamurthy and S. Huettner.

## REFERENCES

1. R.P. Gangloff, "Corrosion Fatigue Crack Propagation in Metals," in Environment-Induced Cracking of Metals, eds. R.P. Gangloff, M.B. Ives (Houston, TX: NACE, 1990), p. 55.

2. I.M. Austin, E.F. Walker, "Corrosion Fatigue Crack Propagation in Steels Under Simulated Offshore Conditions," in *Fatigue 84*, ed. C.J. Beevers (West Midlands, U.K.: EMAS, 1984), p. 1,457.
3. T.W. Thorpe, P.M. Scott, A. Rance, D. Silvester, *Intl. J. Fat.* 5 (1983): p. 123.
4. R.P. Gangloff, "A Review and Analysis of the Threshold for Hydrogen Environment Embrittlement of Steel," in *Corrosion Prevention and Control*, 33rd Sagamore Army Materials Research Conf., eds. M. Levy, S. Isserow (Watertown, MA: U.S. Army Laboratory Command, 1986), p. 64.
5. D.H. Pope, et al., "Microbiologically Influenced Corrosion: A State-of-the-Art Review," MTI Publication No. 13, 2nd ed. (Houston, TX: NACE, 1989).
6. F. Mansfeld, B. Little, *Corros. Sci.* 32 (1991): p. 247.
7. W.A. Hamilton, *Ann. Rev. Microbiol.* 39 (1985): p. 195.
8. C.J. Thomas, R.G.J. Edyvean, R. Brook, *Biofouling* 1 (1988): p. 65.
9. M.J. Cowling, R.J. Appleton, "Corrosion Fatigue of a C-Mn Steel in Sea Water Solutions," in *Proc. Inst. Mech. Engrs. Conf. on Fatigue and Crack Growth in Offshore Structures* (London, U.K.: Inst. Mech. Engrs., 1986), p. 77.
10. R.G.J. Edyvean, C.J. Thomas, R. Brook, I.M. Austen, "The Use of Biologically Active Environments for Testing Corrosion Fatigue Properties of Offshore Structural Steels," in *Biologically Induced Corrosion*, ed. S.C. Dexter (Houston, TX: NACE, 1986), p. 254.
11. R. Krishnamurthy, "Microstructure and Yield-Strength Effects on Hydrogen Environment Fatigue of Steels" (Ph.D. diss., University of Virginia, 1991).
12. I.P. Pankhania, *Biofouling* 1 (1988): p. 27.
13. J.R. Postgate, *The Sulfate Reducing Bacteria* (Cambridge, U.K.: Cambridge University Press, 1979).
14. J. Horvath, M. Novak, *Corros. Sci.* 4 (1964): p. 159.
15. G.H. Booth, L. Eford, D.S. Wakerley, *Brit. Corros. J.* 11 (1976): p. 105.
16. D.J. Duquette, R.E. Ricker, "Electrochemical Aspects of Microbiologically Induced Corrosion," in *Biologically Induced Corrosion*, ed. S.C. Dexter (Houston, TX: NACE, 1986), p. 121.
17. R. Krishnamurthy, C.N. Marzinsky, R.P. Gangloff, "Microstructure and Yield Strength Effects on Hydrogen Environment Enhanced Fatigue of Steels," in *Hydrogen Effects on Material Behavior*, eds. N.R. Moody, A.W. Thompson (Warrendale, PA: TMS-AIME, 1990), p. 891.
18. O. Vosikovskiy, *J. Test. Eval.* 6 (1978): p. 175.
19. T.W. Crooker, J.A. Hauser, R.A. Bayles, "Ripple-Loading Effects on Stress-Corrosion Cracking in Steels," in *Environmental Degradation of Engineering Materials 3*, eds. M.R. Louthan Jr., R.P. McNitt, R.D. Sisson Jr. (University Park, PA: Pennsylvania State University, 1987), p. 521.
20. P.L. Andresen, R.P. Gangloff, L.F. Coffin, F.P. Ford, "Applications of Fatigue Analyses: Energy Systems," in *Fatigue 87*, 3-A, eds. R.O. Ritchie, E.A. Starke Jr. (West Midlands, U.K.: EMAS, 1987), p. 1,723.
21. P.C. Paris, M.P. Gomez, W.E. Anderson, *The Trend in Engineering* 13, 1 (1961): p. 9.
22. R.P. Wei, R.P. Gangloff, "Environmentally Assisted Crack Growth in Structural Alloys: Perspectives and New Directions," in *Fracture Mechanics: Perspectives and Directions*, ASTM STP 1020, eds. R.P. Wei, R.P. Gangloff (Philadelphia, PA: ASTM, 1989), p. 233.
23. S.S. Rajpathak, W.H. Hartt, "Keyhole Compact Tension Specimen Fatigue of Selected High-Strength Steels in Seawater," in *Environmentally Assisted Cracking: Science and Engineering*, ASTM STP 1049, eds. W.B. Lisagor, T.W. Crooker, B.N. Leis (Philadelphia, PA: ASTM, 1990), p. 425.
24. S.R. Novak, "Corrosion Fatigue Crack Initiation Behavior of Four Structural Steels," in *Corrosion Fatigue: Mechanics, Metallurgy, Electrochemistry, and Engineering*, ASTM STP 801, eds. T.W. Crooker, B.N. Leis (Philadelphia, PA: ASTM, 1983), p. 26.
25. H.H. Lee, H.H. Uhlig, *Met. Trans.* 3 (1972): p. 2,949.
26. R.A. Cottis, A. Markfield, "The Role of Inclusions in Corrosion Fatigue Crack Initiation in Q1N," in *Fatigue 87*, eds. R.O. Ritchie, E.A. Starke Jr. (West Midlands, U.K.: EMAS, 1987), p. 587.
27. A. Turnbull, *Scrip Metal.* 20 (1986): p. 365.
28. R.N. Iyer, I. Takeuchi, M. Zamanzadeh, H.W. Pickering, *Corrosion* 46 (1990): p. 460.
29. J.R. Scully, private communication, University of Virginia, Charlottesville, VA, 1993.
30. M. Walch, R. Mitchell, "Microbial Influence on Hydrogen Uptake by Metals," in *Biologically Induced Corrosion*, ed. S.C. Dexter (Houston, TX: NACE, 1986), p. 201.
31. M. Walch, T.E. Ford, R. Mitchell, *Corrosion* 45 (1989): p. 705.
32. T.E. Ford, R. Mitchell, "Hydrogen Embrittlement: A Microbiological Perspective," *CORROSION/89*, paper no. 189 (Houston, TX: NACE, 1989).
33. C.A.H. von Wolzogen Kuhr, *Corrosion* 17 (1961): p. 293t.
34. W.P. Iverson, *Nature* 217 (1968): p. 1,265.
35. G.H. Booth, A.K. Tiller, *Corros. Sci.* 8 (1968): p. 583.
36. R.D. McCright, in *Stress Corrosion Cracking and Hydrogen Embrittlement of Iron Base Alloys*, eds. R.W. Staehle, J. Hochmann, R.D. McCright, J.E. Slater (Houston, TX: NACE, 1977), p. 306.
37. M. Gao, R.P. Wei, *Metall. T-A* 16A (1985): p. 2,039.
38. J.R. Scully, P.J. Moran, "Influence of Strain on Hydrogen Assisted Cracking of Cathodically Polarized High-Strength Steel," in *Environmentally Assisted Cracking*, ASTM STP 1049, eds. W.B. Lisagor, T.W. Crooker, B.N. Leis (Philadelphia, PA: ASTM, 1990), p. 5.
39. J. Newman, *Electrochemical Systems* (Englewood Cliffs, NJ: Prentice-Hall Inc., 1973), p. 230.
40. A. Turnbull, D.H. Ferriss, *Corros. Sci.* 27 (1987): p. 1,323.



**CORROSION FATIGUE CRACKING**

**Richard P. Gangloff**

# CORROSION FATIGUE CRACKING

Richard P. Gangloff

Department of Materials Science and Engineering  
University of Virginia  
Charlottesville, VA 22903

Accepted for Publication:

*Manual on Corrosion Tests and Standards: Application and Interpretation*, Robert Baboian, Ed,  
ASTM, Philadelphia, PA (1994).

April, 1994

Revised: August, 1994

# CORROSION FATIGUE CRACKING

Richard P. Gangloff<sup>1</sup>

Corrosion fatigue (CF) is an important but complex mode of failure for high performance structural metals operating in aggressive environments. This view is based on the likelihood of cyclically varying loads and chemical environments in service, the need for predictable long-life component performance and life extension, the universal susceptibility of pure metals and alloys to CF damage, and the time-dependent multi-variable character of corrosion fatigue. For example, stress corrosion cracking (SCC) immune alloys are susceptible to CF. Corrosion fatigue has affected nuclear power systems, steam and gas turbines, aircraft, marine structures, pipelines, and bridges; CF issues are central to the behavior of many aging systems [1-3].

The objective of this chapter is to highlight modern laboratory methods for characterizing the corrosion fatigue behavior of metals in aqueous electrolytes. The principles and mechanisms of CF are summarized in Section I, followed by discussions of experimental methods in Section II. Specimen design and loading, environment control, strain and crack size measurement, and computer automation are discussed. The emphasis throughout is on exemplary experimental methods and results, as well as on CF data analysis and interpretation. Section III cites applications of CF data to service, the advantages and limitations of the experimental methods, and directions for research on CF experimentation. Symbols and terms are defined in Section IV. This Chapter, with extensive references, extends previous reviews of corrosion fatigue test techniques [4,5].

## I. Basic Principles

### IA. Fundamentals of Corrosion Fatigue

#### IA1. Definition

Corrosion fatigue is defined as the sequential stages of metal damage that evolve with accumulated load cycling, in an aggressive environment compared to inert or benign surroundings, and resulting from the interaction of irreversible cyclic plastic deformation with localized chemical

---

---

<sup>1</sup> *Professor, Department of Materials Science and Engineering, University of Virginia, Charlottesville, VA, 22903.*

or electrochemical reactions. Environment-enhanced fatigue is a modern term, however, corrosion fatigue is traditionally used when emphasizing electrochemical environments. Mechanical fatigue experiments and analyses, detailed in recent textbooks [6-8], provide the basis for understanding CF.

### IA2. Stages of Corrosion Fatigue

CF damage accumulates with increasing load cycle count ( $N$ ) and in four stages: (1) cyclic plastic deformation, (2) microcrack initiation, (3) small crack growth to linkup and coalescence, and (4) macrocrack propagation. A cardinal principle is to design a CF experiment to isolate and quantitatively characterize one of these four stages. The methods in this chapter are organized as follows: (1) smooth specimen life for high cycle fatigue (HCF) described by  $\Delta\sigma$  versus  $N$  data, (2) smooth uniaxial or notched specimen life for low cycle fatigue (LCF) described by  $\Delta\epsilon_p$  versus  $N$  or  $\Delta K/\sqrt{\rho}$  versus  $N$ , respectively, and (3) fatigue crack propagation (FCP) kinetics described by  $da/dN$  versus the fracture mechanics  $\Delta K$ .

### IA3. Mechanisms

It is important to understand damage mechanisms in order to correctly interpret and extrapolate laboratory CF data. Similar to SCC, the mechanism for CF may involve hydrogen embrittlement; film rupture, dissolution and repassivation; enhanced localized plasticity; interactions of dislocations with surface dissolution, films or adsorbed atoms; and complex combinations of these processes [9-16]. The contribution of each mechanism is controversial, and depends on metallurgical and environment chemistry variables. While providing significant insight, existing mechanism-based models are generally not capable of accurately predicting CF behavior beyond the range of laboratory data.

Hydrogen environment embrittlement (HEE) is an important mechanism for CF crack propagation in ferritic and martensitic steels, as well as aluminum, titanium and nickel-based alloys exposed to gases and electrolytes near 25°C [15-21]. This hypothesis is supported by extensive but circumstantial evidence, and is most readily accepted for high strength alloys in strong hydrogen-producing environments. In HEE atomic hydrogen (H) chemically adsorbs on strained-clean initiation sites or crack surfaces as the result of electrochemical reduction of hydrogen ions or water. (Adsorbed H is also produced by the reactions of  $H_2$ ,  $H_2O$ ,  $C_2H_2$  or  $H_2S$  molecules with metal surfaces.) Hydrogen production follows mass transport within the occluded crack (pit or crevice) solution, crack tip dissolution, and hydrolysis of cations for local acidification; and precedes H diffusion by lattice, interface or dislocation processes in the initiation-volume or crack tip plastic zone.

Fatigue damage is promoted by hydrogen-affected lattice bonding, grain or dislocation cell boundary decohesion, enhanced localized plasticity, or metal hydride formation (in certain alloys such as HCP titanium-based). H-enhanced CF cracking is either intergranular or transgranular; with the latter involving dislocation substructure, low index crystallographic planes, or interfaces.

A second mechanism for CF is based on damage by passive film rupture and transient anodic dissolution at a surface initiation site or crack tip. This model was developed with several necessary empirical elements to predict CF propagation in carbon and stainless steels in high temperature pure water environments [22,23], and is sometimes applied to titanium and aluminum alloys in aqueous chloride solutions. Localized plastic straining, described by continuum mechanics or dislocation plasticity, ruptures the protective film. Crack advance occurs by transient anodic dissolution of metal at the breached film, and at a decreasing rate while the surface repassivates pending repetition of this sequence. The increment of CF growth depends Faradaically on the anodic charge (transient current-time integral) passed per load cycle. Charge is governed by clean-repassivating surface reaction kinetics for the CF-sensitive alloy microstructure in occluded crack solution, and by the time between ruptures given by local strain rate and film ductility. As with the hydrogen mechanism, film rupture modeling is complex and controversial; confirming data exist [22,23], but other research shows the model to be untenable for specific alloy/environment systems [24].

Several CF mechanisms were proposed based on interactions between dislocations and environment-based processes at initiation sites or crack tip surfaces. For example, *in-situ* transmission electron microscopy and dislocation modeling show that adsorbed H localizes plastic deformation in several pure metals and alloys [25]. Second, reaction-product films are not capable of extensive plastic deformation relative to the underlying metal, and may cause CF damage by one or more processes, viz: (1) interference with the reversibility of slip, (2) localization of persistent slip bands, (3) reduction of near-surface plasticity leading to reduced or enhanced CF depending on the cracking mechanism, (4) localization of near-surface dislocation structure and voids, or (5) film-induced cleavage [14,15,26-28]. Adsorbed cations could similarly affect fatigue [29]. Finally, anodic dissolution may eliminate near-surface work hardening and hence stimulate fatigue damage [30]. These mechanisms have not been developed and tested quantitatively.

## **IB. Factors Controlling Corrosion Fatigue**

Two considerations are central to understanding the effects of mechanical, metallurgical and

chemical variables on CF. The influences of electrolyte composition, conductivity, pH, electrode potential, temperature, viscosity and biological activity are governed by the mass transport and electrochemical reaction conditions within occluded pits, crevices or cracks; including the role of strain in creating reactive clean surfaces [31,32]. Second, CF can be time-dependent. Crack growth is often rate-limited by one or more of the slow steps in the mass transport and crack surface reaction sequence; slow loading rates enhance CF damage [17]. Increased crack tip strain rate is deleterious when the extent of per-cycle electrochemical reaction is promoted [22-24].<sup>2</sup>

Variables that affect CF were reviewed elsewhere [15-17]. Important factors are cited here to illustrate important CF test methods and to guide data interpretation.

### IB1. Mechanical Variables

An important issue is the influence of an electrochemical environment on the cyclic deformation behavior of metals [14,33-35]. As illustrated by the data in Fig. 1 for a C-Mn steel in high temperature water, environment does not typically affect the relationship between stresses and strains derived from the maximum tensile (or compressive) points of steady-state (saturation) hysteresis loops [36]. Such loops should relate to elastic and plastic deformation prior to substantial CF microcracking. CF data of the sort shown in Fig. 1 are produced by either stress or total strain controlled uniaxial fatigue experiments, identical to the methods developed for measuring purely mechanical cyclic stress-strain data [8,37]. While macroscopic constitutive properties may not be environment sensitive, slip localization can be affected by electrochemical reactions [14,33].

**Mechanical Driving Forces:** Considering smooth specimens, the range of applied true stress or true plastic strain control the fatigue and CF responses of metals for HCF and LCF conditions, respectively. For HCF, smooth specimen CF life increases with decreasing elastic stress range, at cycles in excess of the transition fatigue life,  $N_T$ , according to the Basquin equation:

$$\Delta\sigma = \sigma'_f (N_f)^{-b} \quad (1)$$

---

---

<sup>2</sup> Considering HEE, it is important to consider the primary hydrogen source when designing CF experiments and interpreting results. In addition to occluded crack tip H-production, mobile H can diffuse over long distances from production sites at mildly strained bulk-solution-exposed specimen surfaces to the propagating CF crack tip. Bulk-surface H production is important for ferrous alloys at long exposure times in acidic or H<sub>2</sub>S-bearing solutions, and with cathodic polarization [21]. This H-source is less important for aluminum and titanium alloys in electrolytes that form passive surface films capable of blocking H uptake.

and due to decreasing globally plastic strain at cycles less than  $N_T$ , according to the Coffin-Manson equation for LCF:

$$\Delta \epsilon_p = \epsilon'_f (N_f)^{-c} \quad (2)$$

Alternatively, Eq. 1, divided by  $E$  to relate  $N_f$  to elastic strain range ( $\Delta \sigma/E$ ), is added to Eq. 2 in order to relate  $N_f$  to total applied strain range, the sum of the elastic and plastic strain ranges.

The material property parameters for HCF and LCF ( $b$ ,  $c$ ,  $\sigma'_f$ , and  $\epsilon'_f$ ) depend on metallurgical, environmental and time variables. Data in Fig. 2 show that the HCF life of AISI 4140 steel is degraded by aerated neutral NaCl solution, compared to similar fatigue lives for dry and moist air as well as deaerated chloride [38,39]. The data in Fig. 3 show that distilled water and aqueous 3% NaCl similarly degrade the LCF resistance of an unrecrystallized precipitation hardened aluminum alloy [35]. The Basquin and Coffin-Manson laws are generally obeyed for fatigue in electrochemical environments, however, multiple power law segments may occur. Critically, the HCF endurance limit or threshold stress range can be eliminated by the action of the electrolyte, as illustrated in Fig. 2. A common explanation for this effect is pitting-based CF crack initiation.

Rates of CF crack propagation are uniquely defined by the linear elastic fracture mechanics stress intensity factor range that combines the effects of applied load, crack size and geometry [17,40]. The *similitude principle* states that fatigue and CF cracks growth at equal rates when subjected to equal values of  $\Delta K$  [6-8]. The  $da/dN$  versus  $\Delta K$  relationship may be complex, however, an effective approach is based on a power (or Paris) law of the form [41]:

$$\frac{da}{dN} = A \Delta K^m \quad (3)$$

$\Delta K$  is limited to stress intensity changes above zero because compressive loads do not cause appreciable crack tip plastic strain and damage. The material properties ( $A$  and  $m$ ) depend on environmental and time variables. For metals in vacuum and moist air, FCP is described by a single power law and an apparent threshold stress intensity range below which  $da/dN$  tends to zero [42]. More complex cracking behavior is observed for CF, as illustrated for aqueous chloride solution-enhanced FCP in titanium (Fig. 4) and advanced Al-Li-Cu alloys (Fig. 5) [43,44]. Note the complex  $\Delta K$ -dependence of  $da/dN$  for FCP in chloride solution, but not vacuum or moist air. Environmental effects on Paris regime FCP have been characterized broadly, however, data on near-threshold CF

( $da/dN < 10^{-6}$  mm/cycle) are scarce [16,42].

Crack closure can strongly affect fatigue and CF [45]. This phenomenon is based on crack surface contact during unloading, critically at stress intensity levels above zero and applied-positive  $K_{min}$  values. Crack wake contact is caused by corrosion debris, plasticity, crack path roughness, or phase transformation products; each mechanism may be sensitive to aqueous environmental reactions [6]. To account for closure,  $da/dN$  is correlated with an effective stress intensity range that is defined operationally as the difference between applied  $K_{max}$  and the  $K_{cl}$  level where surface contact is resolved (Section IID6).

CF crack initiation in notched specimens is most effectively characterized by the notch-root plastic strain range calculated by Neuber's method, elastic-plastic finite elements, or fracture mechanics approximation [7,8]. The latter approach is illustrated in Fig. 6, showing the results of over one-hundred experiments with C-Mn and alloy steels in aqueous chloride solution compared to moist air [8,46-48]. The load cycles to produce 1 mm of fatigue crack extension, measured optically, increase with decreasing  $\Delta K/\sqrt{\rho}$ , an estimate of notch root  $\Delta\epsilon_p$ , for air and chloride solution.<sup>3</sup> At fixed  $\Delta K/\sqrt{\rho}$ ,  $N_i$  is reduced by chloride exposure at free corrosion, relative to fatigue in moist air. An endurance limit is observed for moist air, but not this CF case. Cathodic polarization (CP) restores a portion of the moist air fatigue initiation/early growth life, as discussed in an ensuing section.

**Loading Frequency:** Slow frequency CF experiments are necessary because of mass transport and electrochemical reaction rate limitations on damage, but are challenging because of prolonged test time. The generally deleterious effect of decreasing  $f$  on smooth specimen CF life is illustrated in Fig. 7 for an LCF case involving a C-Mn pressure vessel steel, corroding freely in high temperature water with varying dissolved oxygen levels between 0.01 and 8 ppm. (The free corrosion potential for these steel CF specimens increases as the dissolved oxygen concentration increases.) For fixed  $\Delta\epsilon_p$ , the ratio of  $N_f$  for fatigue in water to that for air, each at 270°C, declines with decreasing average total strain rate (proportional to frequency) [36]. (LCF lives are rate independent for fatigue in laboratory air at low to moderate temperatures where creep is minimal.)

Frequency effects on CF crack propagation have been characterized broadly and modeled

---

<sup>3</sup>  $\Delta K$  is calculated assuming a sharp crack of length and geometry equivalent to the notch. This method is a reasonable alternative to a finite element or Neuber analysis of notch strain, but only for crack-like notches of the sort shown by the insert in Fig. 6 [7].



based on the HEE and film rupture mechanisms [16-18,22-24]. FCP rates are  $f$ -independent for alloys in moist air or vacuum at low to moderate temperatures. For CF, there are three possible frequency responses: (1) purely time-dependent, where  $da/dN$  increases with decreasing frequency proportional to  $(1/\alpha f)$ , (2) cycle-time-dependent, where  $da/dN$  increases with decreasing frequency proportional to  $(1/\alpha f)^\beta$  with  $\beta$  on the order of 0.5, and (3) cycle-dependent, where  $da/dN$  is environmentally-enhanced, but  $da/dN$  is frequency-independent. The parameter  $\alpha$  gives the proportion of the load-cycle time that produces CF damage, and is often taken as 2 for a symmetrical cycle, since environmental cracking may not occur during unloading [16]. An alternative model of the frequency effect considers that electrochemical reactions occur throughout the entire load-cycle [17]. A single alloy/environment system can exhibit each  $da/dN$ - $f$  relationship, depending on  $\Delta K$ ,  $f$  and alloy composition, as illustrated for aged 7000 series aluminum alloys (AA) (Figs. 8) and steels (Fig. 9) [18,49-51]. These plots illustrate the two usual ways of presenting frequency-dependent CF  $da/dN$  data, with the abscissa as either  $\log(f)$  or  $\log(1/\alpha f)$ .

Time-dependent cracking is observed for high strength SCC-prone alloys when  $K_{max}$  in the fatigue cycle is above  $K_{ISCC}$  and  $da/dt$  is rapid. This case, illustrated in Fig. 8 for AA7079 at  $f < 1$  Hz and for AA7075 at  $f < 0.001$  Hz, is modeled by linear superposition of SCC  $da/dt$  and inert environment  $da/dN$  data [49,52,53]. Cycle-time-dependent CF (or *cyclic stress corrosion cracking*) involves substantial CF at  $\Delta K$  levels that are below  $K_{ISCC}$  or where  $da/dt$  is slow. This response is illustrated for AA7017 and AA7475 (Fig. 8) in seawater and acidified NaCl respectively, and for two steels in neutral NaCl with cathodic polarization (Fig. 9), each at fixed  $\Delta K$  and  $R$  [18,50,51]. In both systems,  $\beta$  is 0.3 to 0.6. Note (Fig. 9) that cycle-time-dependent  $da/dN$  achieves a plateau or saturation level at slow frequencies below a critical value that depends on steel composition. The third case,  $f$ -independent CF, is illustrated for AA7075 in 80°C chloride solution (Fig. 8) and for the two steels at high frequencies in NaCl at 25°C (Fig. 9) [49,51]. This response (*true corrosion fatigue*) is often observed at low  $\Delta K$ , at high loading frequencies, or for alloys that resist environmental cracking. In some cases CF  $da/dN$  increases with increasing  $f$ . This behavior is illustrated in Fig. 4 for a titanium alloy at low  $\Delta K$ , in addition a crossover to time-dependent CF above 20 MPa/m and time-cycle-dependent CF at intermediate  $\Delta K$  [43].

Figure 10 illustrates the nil effect of loading frequency on CF crack initiation for blunt notched steel specimens in aqueous chloride solution at free corrosion [46]. These data are notable for the rare combination of low  $f$  and high cyclic lives (175 days were required to obtain  $3 \times 10^6$  cycles at 12

cpm), and for the lack of a frequency effect on the cycles required to produce 1 mm of CF cracking. This result indicates that one or more of the early stages of CF (cyclic plastic deformation, pitting, crack nucleation, and small crack growth) are frequency-insensitive, consistent with the frequency-independence of long crack CF at low  $\Delta K$  for many alloys including steels in NaCl [16,51]. Results of the sort shown in Fig. 10 are limited and this behavior has not been modeled.

**Other Mechanical Factors:** Applied load or strain waveform, stress ratio, load spectrum, and overloads can affect CF [16,22,23,54-56]. This chapter emphasizes uniaxial tensile loading of CF specimens because environmental effects on fatigue under torsional or multiaxial loading have not been studied. An exception is illustrated in Fig. 11, showing fatigue life data for smooth specimens of AA7075 in moist air and aqueous NaCl [57]. Note the strong environmental degradation for uniaxial loading, but a reduced effect for torsion. Such results can be explained based on the deleterious role of triaxial tensile stresses, and the associated high hydrostatic (mean) tension, in CF propagation by HEE; this stress state is present for uniaxially loaded Mode I cracks, but not for torsional loading and Mode II or III cracks. Fatigue initiation may be similarly environment-enhanced for uniaxial tensile and torsional loading, explaining the modest reduction in  $N_f$  for torsion (Fig. 11).

## IB2. Electrochemical Variables

**Electrode Potential:** Both anodic and cathodic polarization can affect CF, with different trends observed for crack initiation compared to propagation, and for steels compared to either aluminum or titanium alloys. For ferritic and martensitic steels in aqueous chloride solution, high cycle CF occurs at electrode potentials near free corrosion for aerated solution ( $E_c \approx -650$  mV<sub>SCE</sub>), but is often reduced in severity or eliminated by cathodic polarization to near  $-1000$  mV<sub>SCE</sub> [58]. This behavior is illustrated in Figs. 6 and 12 for notched and smooth-uniaxial fatigue specimens, respectively [47,59]. CF of polished specimens of 1020 and 4140 steels, exposed to NaCl during high frequency rotating bending, occurred only if a critical anodic current was exceeded [38,39]. In this study, CF was essentially eliminated by solution deaeration which reduced the steel corrosion rate current and free corrosion potential (Fig. 2). Applied cathodic polarization similarly reduced CF of polished specimens.

Understanding the effect of applied polarization on CF propagation requires a description of crack tip electrochemistry; particularly local pH and potential, as affecting the kinetics of passive film formation, dissolution, hydrogen production and hydrogen entry. Occluded crack processes are

complex, as are the observed dependencies of CF  $da/dN$  on electrode potential. For example, CF crack growth rates for steels in chloride increase with increasing cathodic polarization, with a modest minimum in  $da/dN$  at about 200 mV active to the free corrosion potential [16,20]. As an example, Fig. 13 illustrates that the environmental enhancement of  $da/dN$  increases with the total rate of H production at the crack tip, raised to the 1/4 power, for C-Mn steel in NaCl ( $E_C = -675 \text{ mV}_{SCE}$ ), polarized between -750 and -1325  $\text{mV}_{SCE}$  [16]. H production was calculated from a crack chemistry model [60]. For this system, solution deaeration does not affect CF  $da/dN$  when electrode potential is fixed potentiostatically [61]. The opposite effects of polarization on smooth specimen CF life and crack propagation in steel can be reconciled. Dissolution and pitting probably govern environment-enhanced fatigue crack initiation [14,38,39]; H plays a secondary role for the fast loading frequencies, near-threshold stress intensities and uniaxial stress states typical of smooth specimen studies. Slow loading frequencies and crack tip hydrostatic tension promote crack growth by HEE. Here, important contributions to crack tip H production are from crack acidification near free corrosion and water reduction at cathodic potentials [16,60].

Cathodic polarization of aluminum and titanium alloys in chloride provides an interesting contrast to steels. Duquette and others reported that the fatigue lives of smooth specimens of AA7075 and Al-Mg-Li in NaCl solution were maximum at potentials mildly active of free corrosion; both anodic and highly cathodic polarization degraded corrosion fatigue life [15,57,58]. CF propagation occurs at the free corrosion potential, is exacerbated by either anodic polarization or extreme cathodic polarization, and is arrested by modest cathodic polarization. This trend was demonstrated for AA7079, AA7075 and AA2090 in NaCl and explained based on HEE [19,62,63]. At negative potentials from cathodic polarization, crack tip H production may be reduced by the effect of alkaline occluded-crack solution on the overpotential and exchange current density for H production on strain-bared surfaces, and H uptake may be blocked by crack surface films.

**Sulfur ion content:** Sulfur ions in electrolytes exacerbate CF crack propagation in many alloys. Various forms of sulfur are important in sour oil or gas well and geothermal brine environments, and are also produced in unlikely ways. For example, the  $da/dN$  versus  $\Delta K$  data in Fig. 14 show the CF behavior of martensitic HY130 steel in sterile 3.5% NaCl solution with CP, an environment which enhances cracking by two to eight-fold relative to moist air and more compared to FCP in vacuum. Note the strong environmental effect caused by a sulfate reducing bacteria (SRB; *desulfrovibrio vulgaris*) cultured in Postgate C food-medium and with cathodic polarization [64].

These, and similar data for both biologically active and abiotic gaseous  $H_2S$  saturated sterile chloride solutions, are interpreted based on sulfide-stimulated HEE [64,65]. Bacteria metabolize the food-source and consume H to produce sulfide ions and other sulfur species. These anions poison recombinant H desorption to reduce  $H_2$  production and increase H entry into the metal at the crack tip, similar to the deleterious effect of dissolved  $H_2S$ .

In a second example, CF is promoted by increased impurity-sulfur in ferritic steels subjected to low frequency loading in pressurized pure water at 288°C (Fig. 15) [22,23]. MnS inclusions which intersect crack flank surfaces dissolve to enrich the occluded crack solution in sulfide. These anions promote crack advance by increasing the anodic charge that is passed per film rupture event, or perhaps by the HEE mechanism. This effect of steel sulfur content is severe for a stagnant environment within the autoclave, and is eliminated by turbulent solution flow which reduces sulfide buildup within the crack [66].

*Other Chemical Factors:* Solution pH, ionic composition, conductivity, and temperature can affect CF [14-17,22,23,43,58].

### IB3. Metallurgical Variables

Metallurgical factors can influence CF crack initiation and growth. Prominent in this regard are sensitization of grain boundaries in austenitic stainless steels [22,23], locally intense slip in aluminum alloys from dislocation interactions with shearable precipitates [67], and metalloid impurities segregated to grain boundaries in steels [68]. CF crack initiation often occurs at surface intersecting inclusions that concentrate strain and may dissolve to produce a locally aggressive environment [69]. CF crack propagation in the ferritic steel/aqueous chloride system is apparently not affected by substantial changes in steel composition, microstructure and yield strength [51]. In another case aluminum alloy processing route, and the resulting degree of recrystallization and grain size, did not substantially affect aqueous environmental LCF life and FCP kinetics [35,44,70]. Increasing copper content in precipitation hardened Al-Zn-Mg alloys reduced the environmental enhancement of  $da/dN$ , with the importance of the effect depending on aging condition [67].

### IC. Relationship Between CF and SCC

Corrosion fatigue is related to, but uniquely distinct from stress corrosion cracking [71]. Purely time-dependent CF crack propagation in SCC-prone alloys is governed by the integrated amount of time-based crack extension per fatigue load cycle. In such cases CF and SCC occur by

the same mechanism, and are affected by the same variables, as modeled by simple linear superposition [49,52,53]. SCC is discussed elsewhere in this volume.

Time-cycle- and cycle-dependent CF are more complex, involve unique mechanisms, and occur at stress intensities where SCC is insignificant. In these cases the CF damage mechanism is unique for reasons traceable to cyclic loading, and including: a) increased crack tip strain rate [22-24], b) resharpening of the blunted crack geometry during unloading, particularly at high  $\Delta K$ , c) altered crack chemistry by convective mixing [72], d) evolution of persistent slip band, slip step, and dislocation cell structures into embryonic damage, often at low  $\Delta \epsilon_p$  or low  $\Delta K$  [73,74], and e) mobile dislocation transport of hydrogen in the crack tip process zone [18,50]. These additional factors must be considered when interpreting and modeling CF data [16].

## ID. Literature Sources for CF Data and Mechanisms

In addition to the examples presented in Figs. 1 through 15, extensive CF data have been published in several volumes [1,2,9-12,58,75-78].

## **II. Testing Techniques**

### IIA. Common Elements of a Corrosion Fatigue Experiment

An experiment to characterize the CF properties of a metal involves cyclic straining of a precisely machined specimen in an electrolyte. (Precorrosion effects on fatigue are not considered.) Environment containment about the specimen must guarantee constant solution purity and composition. Specimen potential should be monitored, often controlled potentiostatically, and not affected by galvanic coupling to the grips or test machine. The mechanical parameters that must be measured depend on the experiment; be it HCF, LCF, LEFM-crack propagation or notched; and are progressively more difficult to monitor from the HCF to notched cases. CF experiments follow directly from procedures for mechanical tests with benign environments; the latter are well-developed and standardized, while CF experiments are not. For example, ASTM Committee G1 has published 14 standards or practices for SCC experiments (see Volume 03.02, Section 3 of the *Annual Book of ASTM Standards*), but none for corrosion fatigue.

CF experiments are hindered by several common factors. Aggressive environments are difficult to contain at a constant condition, and hinder precise measurements of specimen

displacement, load and crack size. CF is influenced by many interactive mechanical, chemical and microstructural variables that must be factored into experimental design. It is often necessary to investigate slow-rate deformation and cracking phenomena in a realistic time; experiments must be conducted for 1 day to 1 year or more. CF damage is localized at surface slip structure and near the crack tip; high resolution observations are not generally available and behavior must be interpreted from indirect measurements.

## IIB. Smooth Specimen $\Delta\sigma$ -Life Method for High Cycle CF

### IIB1. Governing Standards

Experiments to characterize high cycle CF life according to the Basquin Law (Eq. 1) follow from ASTM standards for metals in moist air [79,80]. Such methods were detailed for steels and aluminum alloys in aqueous chloride solutions [38,39,57-59,69,81,82]. Typical data are presented in Figs. 2, 11 and 12.

### IIB2. Specimens and Loading

High cycle CF specimens focus failure in a carefully prepared reduced-uniform or mild-blend-radius gauge section, often of circular cross-section and with ends for gripping in the fatigue machine. Typical specimen designs are shown elsewhere, including methods for low-damage gauge machining and polishing [79,83]. HCF specimens are loaded in uniaxial tension or bending (3-point, 4-point, or cantilevered) with electromechanical, servohydraulic or rotating wheel/mass machines, and grips of various designs [79,83]. Elastic straining is load or displacement controlled; involves either negative, zero or positive mean stress; and varies with time symmetrically in a sinusoidal or linear-ramp waveform. Since CF is dominated by electrochemical surface damage,  $N_f$  could decrease and variability may increase with increasing surface area that is stressed.

High cycle corrosion fatigue experiments are conducted for  $10^5$  to  $10^9$  cycles to failure, at a relatively high frequency of 25 to 100 Hz to conserve time. ( $N_f$  of  $10^6$  cycles requires 5.5 hours, while  $10^9$  cycles require 230 days of continuous loading at 50 Hz.) Multiple, reliable and inexpensive rotating-bend machines are often dedicated to these experiments.

### IIB3. Environmental Cell Design

The design of the environmental cell depends on electrolyte and temperature. A typical cell is illustrated in Fig. 16 for containing aqueous chloride solution at ambient temperature [81]. Glass,

plexiglass, teflon, or other plastics are adequate cell materials. The specimen is gripped outside of the test solution to preclude galvanic effects, and the cell is sealed to the round or square/rectangular specimen with O-rings away from the high-stress gauge section. Solution can be circulated from a large storage volume and at a constant flow rate. The cell should include reference and counter electrodes to enable specimen (working electrode) polarization with standard potentiostatic (or galvanostatic) procedures [38,39,59,81]. When fixing potential or current, care should be taken to correctly ground or isolate the test specimen, to uniformly polarize the gauge surface, to account for IR effects when necessary, and to isolate counter electrode reaction products. Provided that potential is controlled, there is probably no reason to control the oxygen content of the solution. Temperature is maintained between sub-zero and boiling levels with a heater or cooling coil, a specimen thermocouple, control electronics and a condensation apparatus. Cells for more complex environments are detailed in Section IIC3.

#### IIB4. Parameter Measurement, Control and Computer Automation

The maximum and minimum applied loads (or alternately, displacements) are measured with a load cell (or remotely attached extensometer/LVDT) and controlled during a HCF experiment.  $\Delta\sigma$  is calculated from standard elastic solutions for bars under uniaxial tension, or beams subjected bending. Elastic strain range is calculated from  $\Delta\sigma/E$  and gauge displacement is not typically measured.

#### IIB5. Crack Detection

Total load cycles to failure are measured, but crack initiation and growth are not monitored during an HCF experiment. Information on these stages of HCF is critical, but difficult to obtain. Methods for CF crack detection are discussed in Section IIF.

#### IIB6. Data Analysis and Evaluation

High cycle CF data are presented in a logarithmic plot of stress range versus cycles to failure according to the Basquin Law (Eq. 1). (Data are also plotted as stress amplitude ( $\Delta\sigma/2$ ) versus reversals to failure ( $2N_f$  for simple wave-forms).) The Basquin Law is based on the initial applied elastic stress range and does not consider the complicating effect of a growing crack on  $\Delta\sigma$ . Material property constants;  $\sigma'_f$ ,  $b$ , and the endurance limit (or fatigue strength at a given number of cycles); are environment sensitive. The mechanical information that should be reported with HCF data is standardized [80], and electrochemical factors should be cited as discussed in this book.

Design and alloy development studies require mean as well as minimum (lower bound)

Basquin Laws, and statistics on the distribution of  $\Delta\sigma-N_f$  data. This distribution depends on the fatigue damage mechanism. Most CF studies have not provided such information, often because of time-intensive slow frequency experiments and the many important variables. A sense of the variability in CF data is portrayed by the extensive HCF results collected for C-Mn and alloy steels in marine environments [58]. The distribution of HCF lives at a given stress range was analyzed based on Weibull statistics applied to a data base of 30,000 points for steels in benign environments [84]. While instructive, these statistical results are not necessarily relevant to high cycle CF where electrochemical reactions introduce additional variability.

Future work must address two areas to provide the foundation for statistically-based analyses of high cycle CF (as well as environmental LCF and FCP). For simple laboratory conditions, the Weibull analysis of mechanical HCF failure probability [84] must be extended to include CF. Second, variable load, temperature and environment chemistry histories are likely to be complex in applications and significantly affect CF life. Such history effects have not been studied. The scaling of Basquin Law data to predict the life of a structure is qualitative and uncertain. Either the local strain approach to CF crack initiation life, or the fracture mechanics analysis of CF propagation, provide a better foundation for life prediction and failure analysis.

## IIC. Smooth Specimen $\Delta\epsilon_p(N)$ Method for Low Cycle CF

### IIC1. Governing Standards

Experiments to characterize low cycle CF life according to the Coffin-Manson Law (Eq. 2) follow from an ASTM standard for LCF of metals in air, and a classic ASTM manual on laboratory methods [37,85]. Low cycle CF experiments are detailed elsewhere [33-36,74,86], and typical data are presented in Figs. 3 and 7.

### IIC2. Specimens and Loading

Uniform-gauge or mild-radius (hourglass) round specimens are subjected to uniaxial tensile loading with rigid gripping and a test machine that provides for either tension-compression or tension-tension strain cycling. (Square or rectangular specimens have also been successfully employed.) Specimen alignment is critical for this rigid gripping system [83]. Total axial displacement is generally controlled, with regard to maximum and minimum limits as well as time-dependence, while load is measured, often with a computer-automated servoelectric or servohydraulic closed-loop test machine. Such machines provide a variety of strain-time profiles. Loading frequencies are typically less than



those employed for HCF experiments because failure occurs in less than  $10^4$  cycles. Low cycle CF experiments differ from the HCF case in that gauge displacement must be measured with sufficient resolution to apply  $\Delta\epsilon_p$  between  $10^{-4}$  and  $10^{-1}$ .

### IIC3. Environmental Cell Design

Cells for environment containment and control are identical for LCF and HCF (Section IIB.3). LCF cells are more complicated, because of the requirement to measure specimen gauge displacement, as illustrated in Fig. 17 [33,36]. For simple aqueous environments, diametral or axial displacement is measured by a contacting (but galvanically insulated) extensometer, perhaps employing pointed glass or ceramic arms extending from a body located outside of the solution. A hermetically sealed extensometer or LVDT can be submerged in many electrolytes over a range of temperatures and pressures. Alternately, the specimen can be gripped in a horizontally mounted test machine, and half-submerged in the electrolyte, with the extensometer contacting the dry side of the gauge (Fig. 17a) [33]. For both simple and aggressive environments, grip displacement can be measured external to the cell-contained solution, as shown in Fig. 17b for high temperature water in a pressurized autoclave [34,36]. It is necessary to conduct LCF experiments in air (at temperature), with an extensometer mounted directly on the specimen gauge, to relate grip displacement and specimen strain.

### IIC4. Parameter Measurement, Control and Computer Automation

Applied load and gauge displacement are measured throughout an LCF experiment. From these data, it is possible to calculate true  $\Delta\sigma$ ,  $\Delta\epsilon_T$ , and  $\Delta\epsilon_p$ , where axial plastic strain range equals  $(\Delta\epsilon_T - \Delta\sigma/E)$ . For the hourglass specimen, true total diametral strain can be measured at any time, and converted to axial strain according to [37]:

$$\epsilon = (\sigma / E) (1 - 2\nu_g) - 2\epsilon_d \quad (4)$$

If  $\Delta\epsilon_T$  or  $\Delta\epsilon_d$  is maintained constant by the test machine, then  $\Delta\sigma$  increases and  $\Delta\epsilon_p$  decreases until the hysteresis loop stabilizes at a constant form for a cyclically hardening material, and vice-versa for a softening alloy [7,37]. The stabilized-loop value of axial  $\Delta\epsilon_p$  is used in the Coffin-Manson Law to correlate  $N_f$ . When substantial crack growth occurs, these stress and strain range calculations are not accurate. Experiments are often terminated and failure is defined for a percent decline in  $\Delta\sigma$ . Total strain rate, average plastic strain rate, or the frequency of displacement cycling should be maintained constant during the low cycle corrosion fatigue experiment.

Personal computer programs are available commercially to control the closed-loop test machine during an LCF experiment, and to analyze load-displacement-time data.

#### IIC5. Crack Detection, Data Analysis and Evaluation

These procedures are identical for LCF and HCF, as discussed in Sections IIB5 and IIB6.

### IID. Fracture Mechanics Methods for Corrosion Fatigue Crack Propagation

#### IID1. Governing Standards

Experiments to characterize CF crack propagation kinetics, in terms of LEFM Paris Law (Eq. 3) and near- $\Delta K_{TH}$  data, are guided by an ASTM standard for metals in air [87], a compilation of laboratory experience with this standard [88], and a review of inert environment FCP testing [89]. The ASTM standard contains an appendix specific to CF crack growth in marine environments [87,90]. Procedures for CF in other environments are not standardized, however, methods have evolved for specific technologies [2,4]. CF  $da/dN$  data are presented in Figs. 4, 5, 8, 9 and 13 to 15.

#### IID2. Specimens and Loading

CF crack propagation data are obtained with a variety of notched and precracked specimen geometries that are well characterized in terms of stress intensity and compliance functions [17,91]. The Mode I compact tension, single-edge crack, 3 or 4-point bend, and center-cracked tension specimens are used commonly, and are prepared based on standardized procedures [87]. Specimen in-plane dimensions are selected to guarantee elastic deformation with limited small-scale crack tip plasticity. Specimen thickness, and the plane stress or plane strain deformation state, is a variable. Closed-loop servohydraulic test machines are most effective for CF propagation experiments, with the control parameter being either load, load-line displacement, or crack mouth opening displacement. Such machines provide a range of load or displacement waveforms (sinusoidally time-dependent is typical) and frequencies ( $10^{-4}$  to 100 Hz are typical values).

#### IID3. Environmental Cell Design

Cells for CF crack propagation experiments are designed to control solution composition and specimen electrochemistry analogous to HCF and LCF (Sections IIB3 and IIC3), while allowing for measurements of applied load, crack opening displacement, and crack length. A variety of approaches are reviewed elsewhere, including electrochemical details for several environments [4]. Two cells for ambient temperature electrolytes are shown in Fig. 18. If the test machine and loading

axis are mounted in a horizontal plane ( $90^\circ$  to the normal orientation), then the compact tension crack tip can be dipped into solution which is exposed to air without complex sealing (Fig. 18a). The alternate approach in Fig. 18b employs a vertical loading axis with a segmented plexiglass or teflon cell, sealed to the faces of the compact tension specimen with O-rings and including a short segment in the notch mouth. Solution flow is through the notch, parallel to the crack front. Small cells clamped to specimen surfaces (Fig. 18b) are equally effective for center-through-cracked plate specimens. Specimens with surface cracks or single-edge cracks are effectively contained in environmental cells which are large and sealed to the round or flat ends inboard from the gripping points [92]. Compact tension and surface crack specimens have been contained in pressurized metal autoclaves with electrolytes or steam at elevated temperature (Fig. 19) [93]. In this particular study, a yoke was employed to simultaneously test two specimens in one autoclave and load frame.

Reference and counter electrodes are readily employed in the various cells (e.g., Fig. 18b), perhaps with salt bridges to remote containers and including high pressure and temperature compensation capabilities. Procedures to eliminate galvanic couples and to maintain solution purity and composition are identical to those employed in HCF and LCF experiments. Crack opening displacement is measured with a remote or immersed extensometer or LVDT. The cell must not interfere with specimen loading or displacement. For example in Fig. 18b, the shaded mid-portion is a flexible membrane designed so that cell clamping forces do not alter specimen compliance. This is important for accurate measurements of crack closure.

#### IID4. Crack Length Measurement

CF propagation experiments are unique in the need to monitor crack length, often over long-time. Much has been written on two widely employed methods, direct or alternating current electrical potential difference and compliance [87,88,94,95]; as well as on less-tried methods such as eddy current, acoustic wave, optical, or crack surface marking [96]. Compliance and EPD are broadly calibrated and well-suited for precision ( $\pm 25 \mu\text{m}$  or better), long-term-stable monitoring of crack length in many common fracture mechanics specimens and aggressive CF environments. These methods can be computer-automated for test machine and stress intensity control (see Section IID5). The principles and instrumentation for each method are detailed elsewhere [87,88].

Several points are pertinent to CF. First, compliance allows monitoring of both crack length and crack closure [97]. The advantage of the EPD method is simplicity; it is not necessary to immerse a displacement gauge in the electrolyte. (The compliance scheme illustrated in Fig. 18b

avoids this complication.) The EPD method is best-suited for monitoring the growth of surface fatigue cracks. Second, there is no evidence that the 1 to 50 ampere direct or alternating current used in the potential difference method affects CF kinetics. Presumably, the current path through the metal is of orders of magnitude lower resistance compared to that of even the more conductive solutions in an occluded crack. Voltage differences along a crack surface, and due to this current distribution in the metal, are small (less than 1 mV) and probably unimportant. None-the-less, prudence dictates that the influence of applied current be tested by employing an independent monitor of crack length in limited qualification and calibration experiments. Finally, the electrical potential signal often increases with increasing load in the fatigue cycle because electrically conductive crack surfaces are parted. Accordingly, potential should be measured at maximum load, and errors in crack length due to residual "crack surface-shortening contact" should be corrected based on post-test crack length measurements [98]. Finally, solution flow or temperature changes can upset the stability of the electrical potential signal due to thermally-induced voltages and material resistance changes.

Ground-loops between potentiostat and electrical potential crack monitoring electronics degrade the quality of polarization, as well as CF crack length and growth rate measurements. A successful approach to this problem is based on a specimen (working electrode) that is grounded commonly with the test machine, constant-current power supply and EPD amplifier; coupled with a potentiostat that utilizes a grounded working electrode. (In this case the specimen should not be grounded virtually through an operational amplifier.) With this procedure, and the several-ohm (or larger) alternate current path through the typical loading system and test machine, it is not necessary to electrically isolate the CF specimen from the grips. As a test of ground-loop integrity in CF, guarantee no resolvable specimen electrochemical current changes, at fixed electrode potential, upon reversing of the polarity of the crack monitoring current.

Given the success of the direct-EPD method, with current applied through the bulk of the CF specimen, there is generally no need to employ an indirect method based on a foil gauge bonded to the specimen surface and solely carrying the applied current. This latter method eliminates the effect of applied current on crack electrochemistry (if such an effect exists), however, long-term crevice and galvanic corrosion associated with the attached foil may be important. CF crack growth in the mid-region of a specimen is reasonably indicated by compliance or direct EPD, but not by the surface-mounted foil gauge method.

#### IID5. Parameter Measurement, Control and Computer Automation

Applied load and crack length from electrical potential or compliance are measured as a function of load cycles during a CF experiment. Apart from simple constant load range (increasing  $\Delta K$ ) loading, modern FCP and CF experiments are computer-automated to control the  $\Delta K$ -history, with the mode selection based on the goal of the work, be it mechanism or application-based. Load is computer-varied, in real time and at frequencies between  $10^{-4}$  and 50 Hz, to maintain the crack length dependence of stress intensity range according to [87]:

$$\Delta K = \Delta K_0 \exp [C (a - a_0)] \quad (5)$$

R-value is typically maintained constant as  $\Delta K$  changes. A programmed C of 0 yields a constant  $\Delta K$  experiment, which is useful for establishing transient and steady state CF growth rates for mechanistic research. Negative C-values provide for a  $\Delta K$ -decreasing experiment for measuring near- $\Delta K_{TH}$  CF, while positive C gives a  $\Delta K$ -increasing experiment which confirms stress-intensity governed cracking and which yields data in a reasonable time. Guidance on those values of C that minimize the effect of prior load history is standardized [87].<sup>4</sup>

#### IID6. Data Analysis and Evaluation

Applied stress intensity range and CF crack growth rate are calculated at regular crack length intervals, based on standardized analytical procedures [87]. For continuously increasing or decreasing  $\Delta K$  experiments,  $da/dN$  is calculated by either a point-to-point difference (secant) or incremental polynomial method. For constant  $\Delta K$ ,  $da/dN$  is determined by linear regression of cyclic crack length data. The simple secant calculation amplifies  $da/dN$  variability, while polynomial methods average the growth kinetics over seven (typically)  $a$  versus  $N$  points. Growth rate variations depend on the size of the crack growth interval. It is particularly challenging to establish physically meaningful variations in growth rates from an average law. FCP variability was considered in conjunction with an interlaboratory test program that measured  $da/dN$  versus  $\Delta K$  for a very well-behaved high strength

---

---

<sup>4</sup> During fatigue and CF crack propagation, a sudden large decrease in the maximum stress intensity level of the load cycle produces a strong reduction in subsequent growth rates, or so-called delay retardation. These growth rates are important, but are not steady-state and not simply governed according to Eq. 3 [6-8]. Most CF experiments are designed and conducted to avoid such overload effects.

steel in moist air [99]. For this best case and fourteen laboratories,  $da/dN$  variability from replicate standardized experiments within a single laboratory equalled between  $\pm 13\%$  and  $\pm 50\%$  ( $\pm$  two residual standard deviations about the mean regression curve) at fixed  $\Delta K$ . Variability in CF experiments has not been addressed quantitatively, however, the results from the moist air FCP program provide a lower bound. The increased complexity and prolonged test times typical of CF experiments, as well as the FCP behavior of more complex alloys, should lead to increased variability and uncertainty.

Two complications are notable for CF experimentation. CF  $da/dN$  vs applied  $\Delta K$  data may be affected by a crack closure mechanism that depends on aqueous environment exposure (see Section IB1) [6,45]; such CF growth kinetics are defined as an extrinsic property that may be test method-specific. As a diagnostic, if CF  $da/dN$  depends strongly on  $R$ , if environmental  $\Delta K_{TH}$  value is high and increases with decreasing loading frequency, or if crack arrest occurs during CF propagation at constant applied  $\Delta K$ , then environment-sensitive crack closure phenomena should be suspected. A bilinear specimen compliance trace (of applied load vs crack mouth or load line displacement) confirms the presence of crack closure. Closure is characterized and eliminated approximately for a given  $da/dN$  by reducing the applied  $\Delta K$  to  $\Delta K_{eff}$ , the difference between  $K_{max}$  and  $K_{cl}$  rather than  $K_{max}$  and  $K_{min}$ .  $K_{cl}$  is determined by a global compliance method that is nearing standardization [100]. CF  $da/dN$  vs  $\Delta K_{eff}$  data, as well as results obtained at high constant  $R$  (above about 0.7) or high constant  $K_{max}$  (see Fig. 5 and Section IIE1), are reasonably closure free and are an intrinsic property for a given material-environment system [62]. Closure-free CF data are necessary for basic studies of crack tip process zone damage mechanisms, while crack closure phenomena may be important to applications. As an example, corrosion fatigue cracks in steels exposed to seawater at low  $R$  are arrested by cathodic polarization, because calcareous corrosion products precipitate within the growing crack and cause crack surface closure contact at  $K$  levels well zero [20,101].  $\Delta K_{eff}$  is substantially less than both the applied  $\Delta K$  and the intrinsic  $\Delta K_{TH}$ . Rough intergranular CF crack surfaces, coupled with local Mode II displacements, may also promote crack closure. Closure benefits may, however, be limited to simply loaded laboratory specimens. For example, compression elements of a complex load history can crush corrosion debris and crack surface roughness asperities, and can thus reduce crack closure.

As a second complication, crack tip stress, strain and strain rate within the process zone are more fundamental than  $\Delta K$  or  $\Delta K_{eff}$  and govern CF crack growth kinetics. It is not presently possible

to unambiguously calculate the stress intensity dependence of these more fundamental parameters [16,22-24]. Shoji and coworkers argue that the time-based rate of mechanical fatigue propagation in an inert environment is proportional to the rate of dislocation emission from the crack tip, or equivalently to the crack tip strain rate [102]. The value of  $da/dt$  for FCP in vacuum, or more typically moist air, is therefore an indirect crack tip driving force parameter for correlating CF  $da/dN$  data which are also often stated with respect to a time-rate. In this approach  $da/dt$  is the product of  $da/dN$  and  $f$ . An example of this correlation is shown in Fig. 20 which represents the CF enhancement in  $da/dN$  relative to the air case for three high-sulfur-content heats of a C-Mn steel in elevated temperature water [103]. The speculation is that this relationship between the benign and CF time-based rates of cracking is followed independent of  $\Delta K$ ,  $R$ ,  $f$  and loading waveform, as demonstrated for several material-environment systems [102]. In Fig. 20 these parameters are varied widely; for example  $f$  between  $10^{-4}$  Hz and  $10^{-1}$  Hz, and  $R$  between 0.2 and 0.7, but a single CF crack growth law is observed. Based on the film rupture (and perhaps HEE) mechanism, environmental  $da/dt$  should increase with increasing crack tip strain rate [22-24], and hence with the mechanical  $da/dt$ , as suggested in Fig. 20. A complication is that crack tip strain rate depends on several mechanical terms, including the environmental  $da/dt$ .

### IIE. Specialized Corrosion Fatigue Experiments

Several new CF experimental methods have evolved over the past decade.

#### IIE1. Programmed Stress Intensity Experimentation

Real-time computer-control of stress intensity during a CF experiment provides important benefits. For example, CF experiments can be designed with a large negative  $C$ -value (Eq. 5) to produce continuously decreasing  $\Delta K$  at constant applied  $K_{max}$  and increasing  $R$  [62,104]. This approach minimizes the complicating effect of crack closure and provides near- $\Delta K_{TH}$  data, albeit at high  $R$ . The CF results presented in Fig. 5 were obtained based on this method [44]. Since both  $\Delta K$  and  $R$  change during this type of experiment, the effects of these two mechanical parameters must be characterized and understood when using the constant  $K_{max}$  method in CF [16]. Second, variables such as electrode potential, solution composition or frequency are easily changed as the crack grows at constant  $\Delta K$  to probe subtle growth rate changes for basic research [61,64]. A constant  $\Delta K$  segment can be conducted over an interval of CF crack extension, then  $\Delta K$  can be step-increased or decreased at constant  $K_{max}$  [51,62,64]. The data presented in Figs. 9, 13, and 14 were obtained with

this method.

## IIE2. Cyclic Strain-Induced Dissolution

The *cyclic-mechanical depassivation method* involves measurement of transient electrochemical current during cyclic plastic straining of a smooth specimen in an electrolyte at fixed potential [34,105]. A three electrode cell, coupled with a fast-response potentiostat and the mechanical LCF procedures described in Section IIC, are employed in this regard. Data include time-dependent applied plastic strain, stress and anodic current density. The phase difference between the mechanical and electrochemical parameters, the strain dependence of the current density during repeated repassivation repair of ruptured surface films, the anodic charge passed per fatigue cycle, and the charge accumulation with increasing cycles and time are interpreted to probe CF damage mechanisms. For example, peak anodic current density and the cycle-cumulative charge increased with increasing strain rate for LCF of a ferritic stainless steel in NaCl, consistent with the film rupture model [34]. (This current reflects metal oxidation to produce cations in solution and in formation of the passive film; or collectively, metal removal.) Additionally, the time dependence of repassivation and the magnitude of current transients depended on the sign of the plastic strain, and the repassivation characteristics for this system varied with cycle count, demonstrating the complexity of CF. This method was employed to rank the susceptibility of alloys to CF, based on the stability of surface passive films [105].

## IIE3. Small Crack CF Methods

An important goal of CF experimentation and modeling is to quantitatively couple smooth specimen and fracture mechanics approaches to understand the total life of components with microscopic defects. Studies of the so-called *small crack problem* have contributed in this regard [6]. Small crack size can be a particularly important variable that affects CF propagation rates [106,107]. For example, CF cracks sized between 100 and 1000  $\mu\text{m}$  grew up to 1000-fold faster than predicted compared to long crack compact tension specimen  $da/dN$  data at fixed  $\Delta K$ , for the case of a high strength martensitic steel in NaCl [108]. Such crack geometry effects are traced to differences in crack solution mass transport and crack surface electrochemical reactions that govern HEE and film rupture processes [16,106,107].

Both electrical potential and high magnification optical methods have been developed to monitor the formation and growth of CF cracks smaller than 500  $\mu\text{m}$  [109,110]. Each method is capable of micron-level resolution. The electrical potential approach monitors average short crack



growth into the specimen bulk, while microscopic methods focus on surface crack interactions with specific microstructural features including inclusions and corrosion pits. The data presented in Fig. 21 were obtained from *in situ* monitoring of AA2024 in aqueous chloride solution with a long focal length (15 to 40 cm) and high magnification (500 times with 1  $\mu\text{m}$  resolution) optical microscope interfaced with a servohydraulic test machine and video system [110]. Microstructurally small CF cracks initiated at constituent particles and grew at rates that were equal to values obtained with the standard LEFM method discussed in Section IID. While the *chemically small crack* effect is not observed for the system in Fig. 21 [110], data of this type are lacking for a range of materials and environments [106-109].

The use of short crack specimens provides an important benefit for corrosion fatigue experimentation. Since high resolution crack monitoring is employed, crack growth rates are quantitatively defined with small crack extensions and the associated reduced  $N$ . It is possible to obtain accurate low growth rate CF data at low loading frequencies. For example, a short crack specimen was employed to measure a  $da/dN$  value of 0.5  $\mu\text{m}/\text{cycle}$  at constant  $\Delta K$  and  $f$  of 0.0002 Hz during a CF test time of 10 days [16,109]. Perhaps 10 to 20-fold longer test time is required to obtain this measurement with a standard long crack method.

#### IIE4. Measurement of CF Crack Solution pH and Potential

It is important to measure occluded crack pH, potential and solution composition because these factors govern CF by either HEE or film rupture mechanisms. Several experimental approaches have succeeded in this regard for simple ambient temperature and complex high temperature pressurized water electrolytes [111,112]. Reference and pH electrodes were located in small holes drilled in the compact tension specimen to intersect the CF crack plane growing from the notch, as shown in Fig. 22 [112]. This method provides information on the crack size and position dependence of local pH and potential, as well as on the effects of  $\Delta K$ ,  $R$  and  $f$ . Additionally, crack solution can be sampled from crack-intersecting holes for composition analysis by ion chromatography and capillary electrophoresis [113]. Important data were obtained to test models of crack chemistry [72,112] and to understand solution dissolved oxygen and metal sulfide effects on CF [22,23,113]. Given the very small volume of a typical CF crack, solution extraction methods are likely to upset crack electrochemistry and alter  $da/dN$ .

### III. Applications of Corrosion Fatigue Test Results

#### IIIA. Modern Approach to CF Life Prediction

A cardinal principle is to design the CF experiment to isolate and characterize quantitatively each of the four stages of fatigue damage defined in Section IA1. The choice of stage depends on the problem; be it pitting-based crack nucleation in a polished and rigorously inspected medical implant or steam turbine blade, or macrocrack propagation from a weld defect in a large offshore marine structure. If a CF experiment measures total life, without quantifying the four damage stages, then basic understanding and component life prediction are compromised. This is the situation for standardized high and low cycle fatigue experiments which measure total  $N_f$  of a small laboratory specimen. The CF material properties embodied in the Basquin and Coffin-Manson Laws (Eqs. 1 and 2) are not directly scalable to predict the lives of components of alternate geometries and perhaps containing preexisting flaws. These data can not be used to test models of CF because  $N_f$  embodies cyclic deformation, microcrack nucleation and coalescence, small/short crack growth and long crack propagation.

Implementing the correct method for CF life prediction and CF-resistant alloy development is often controversial, as existing approaches (often based on smooth specimen HCF data) are challenged by more modern approaches. A consensus is perhaps developing; an effective method couples the local strain approach to CF crack initiation with the LEFM approach to propagation in order to calculate the summed total component life. The recommendation is that the Coffin-Manson approach be employed, but that the number of cycles to initiate a (reasonably) resolvable crack size (perhaps 0.1 to 1 mm) be measured in place of total cycles to failure. Equation 2 then describes the CF crack initiation resistance of a given alloy-environment system, with the size of the initiated crack defined operationally. These material-environment property data are coupled with Neuber's method or finite element calculations of local plastic strain range in a component to define service initiation life [7]. The fracture mechanics approach should be employed to characterize CF crack propagation kinetics, with emphasis on both the microstructurally small, physically short, and conventional long crack regimes [6,8]. The Paris Law (Eq. 3), or more complex formulations, are employed with stress intensity similitude and an analysis of the stress and stress intensity conditions of the component to predict CF propagation life, integrated from the size of the crack formed in the initiation stage [41]. A variety of desktop computer programs have been developed for the LEFM portion of the fatigue life prediction problem [114]. If nondestructive testing so indicates, then the LCF initiation portion

of the problem can be equated to zero, and the fracture mechanics integration started at the appropriate existing flaw size.

The output of an integrated CF prediction method is plots of total cyclic life as a function of applied stress range, or crack length versus load cycles at constant applied  $\Delta\sigma$ , for specific material, time and environment chemistry variables. Coffin-Manson and Paris Law data depend on the variables cited in Section II. Since a legion of variables is important, and since prolonged CF test times are often required, mechanistic modeling of the nucleation and crack propagation processes is a critical tool to develop algorithms for extrapolating the results of limited laboratory experiments [115].

### IIIB. Examples of Component Service Life Prediction with Laboratory CF Data

Corrosion fatigue problems have been attacked aggressively in several technologies over the past decade. The coupled local strain-initiation and LEFM-propagation approach has not, however, been broadly employed. Early codified design predictions, utilizing elastic smooth-specimen fatigue data (HCF-SN) adjusted empirically for deleterious time-dependent environmental effects, are being replaced by LEFM predictions of crack propagation from an inspection-based or estimated initial crack size [115]. Examples of this procedure were reported for CF in welded offshore structures in the marine environment [1,3,58,115-117], in-core and out-of-core components in commercial light water nuclear reactors [2,22,115,117], oil and gas pipelines [118], and aircraft [119,120]. Emphases focused on the conflicting effect of cathodic polarization on CF crack initiation and growth (marine structures), the unifying role of crack tip strain rate (nuclear reactors), the deleterious effect of sulfur contaminants (nuclear reactor systems and pipelines), and the CF kinetics of small multiple fatigue cracks (aircraft). Tens of man-years are typically required to address a complex CF problem, and large data bases for SCC and CF resulted from these efforts [58,121].

### IIIC. Future Research Needs in CF Experimentation

Environmental effects have not been rigorously incorporated in fatigue life prediction procedures [114]. The time-dependence of CF, the many important interacting variables, and several uncertainties confound the problem. From the experimental perspective, LCF and LEFM-based laboratory CF methods must be improved to address the following uncertainties.

- (1) Methods must be further developed to probe the growth of single small CF cracks sized

below 500  $\mu\text{m}$ , and the interaction and coalescence of multiple small cracks must be characterized. Both LCF and LEFM approaches must be modified in this regard.

- (2) Near-threshold CF crack initiation and propagation, and environment-dependent crack closure, must be characterized including the important effect of low loading frequency [122].
- (3) Load- and environment-spectrum history effects on CF crack initiation and propagation must be characterized.
- (4) The statistical distribution of CF initiation and crack propagation properties must be defined.
- (5) High-resolution probes must be developed to measure occluded crack chemistry, transient crack surface electrochemical reactions, crack tip process zone damage processes, and microcrack advance.
- (6) Fractographic analyses of CF must be improved, including quantitative measurement of crack surface crystallography [123], and computerized image analysis methods to characterize and reconstruct the CF process [124].
- (7) For mechanistic modeling, CF results must be coupled with transient electrochemical reaction kinetics, hydrogen permeation, and hydrogen trapping analyses described elsewhere in this book.

#### IV. Symbols

|                     |   |
|---------------------|---|
| $\Delta \sigma$     | Applied true stress range in a fatigue load cycle; $\sigma_{\max} - \sigma_{\min}$ , where $\sigma$ is load/instantaneous cross-sectional area. |
| $\Delta \epsilon_p$ | True plastic axial strain range in a fatigue load cycle; $\epsilon_{p\max} - \epsilon_{p\min}$ .  |
| $\Delta \epsilon_T$ | Applied true total axial strain range in a fatigue load cycle; $\epsilon_{T\max} - \epsilon_{T\min}$ .  |
| $\epsilon$          | True axial strain; $\ln (l/l_0)$  |
| $\epsilon_d$        | True diametral strain; $\ln (d/d_0)$  |
| $l, d$              | Gauge length and specimen diameter, respectively.   |
| $\sigma_f', b$      | Basquin law material property parameters.   |
| $\epsilon_f', c$    | Coffin-Manson law material property parameters.   |
| $N_f$               | Number of load cycles for specimen failure by fatigue.  |
| $N_i$               | Number of load cycles for fatigue crack initiation.   |
| $N_T$               | The transition fatigue life, or the number of load cycles where the magnitudes of the elastic and plastic axial strain ranges are equal.        |
| $da/dN$             | Macroscopically averaged fatigue crack growth rate.   |
| $a$                 | Fatigue crack length.   |
| $N$                 | Fatigue load cycle count.   |

|                  |  |
|------------------|--|
| $\Delta K$       | Applied stress intensity factor range; $K_{\max} - K_{\min}$ .   |
| A, m             | Paris law material property constants.   |
| $\Delta K_{TH}$  | Threshold stress intensity range.  |
| R                | Stress ratio; $K_{\min}/K_{\max}$ .  |
| $\rho$           | Notch tip radius.  |
| f                | Loading frequency in cycles per second or Hertz.   |
| $1/\alpha f$     | Time-portion of the load cycle where CF damage occurs.   |
| $K_{ISCC}$       | Threshold stress intensity for monotonic load SCC.   |
| da/dt            | Velocity of monotonic load SCC.  |
| $E_c$            | Free corrosion potential.  |
| E                | Modulus of elasticity.   |
| $\Delta K_{eff}$ | Effective stress intensity range; $K_{\max} - K_{cl}$ .  |
| $K_{cl}$         | Stress intensity value in a fatigue load cycle where crack-surface closure contact is experimentally resolved and operationally defined. |
| $\Delta K_o$     | Stress intensity range at a fixed crack length, $a_o$ .  |
| C                | Constant in the $\Delta K$ -control equation with units of $\text{mm}^{-1}$ .  |
| da/dt            | Time-based crack growth rate; often approximated by $(da/dN)(f)$ .   |
| CF               | Corrosion fatigue.   |
| SCC              | Stress corrosion cracking.   |
| HCF              | High cycle fatigue.  |
| LCF              | Low cycle fatigue.   |
| FCP              | Fatigue crack propagation.   |
| HEE              | Hydrogen environment embrittlement.  |
| H                | Atomic hydrogen.   |
| HCP              | Hexagonal-closed-packed.   |
| LEFM             | Linear elastic fracture mechanics.   |
| SN               | Stress range vs Life.  |
| CP               | Cathodic polarization.   |
| Mode I           | Applied load perpendicular to the crack plane and growth direction [6-8].  |
| Mode II          | Applied load parallel to the crack plane and the crack growth direction.   |
| Mode III         | Applied load parallel to the crack plane and perpendicular to the growth direction.  |
| $\nu_e$          | Poisson's ratio for isotropic elastic deformation, often taken as 0.33.  |
| LVDT             | Linear Variable Differential Transformer.  |
| EPD              | Electrical Potential Difference.   |

## V. Acknowledgements

This chapter was written based on the support of the Office of Naval Research (Grant N00014-91-J-4164, with Dr. A. John Sedriks as the Scientific Officer), the NASA Langley Research

Center (Grant NAG-1-745, with Mr. D.L. Dicus as Grant Monitor), and the Virginia Center for Innovative Technology (Technology Development Center for Electrochemical Science and Engineering, with Professor G.E. Stoner as Director).

## VI. References

1. Proceedings Institute of Mechanical Engineers Conference on Fatigue and Crack Growth in Offshore Structures, Inst. Mech. Engr., London, England (1986).
2. Proceedings of the Second International Atomic Energy Agency Specialists Meeting on Subcritical Crack Growth, Volumes I and II, U.S. Nuclear Regulatory Commission Document, NUREG CP-0067, Washington, DC (1986).
3. S.J. Hudak, O.H. Burnside and K.S. Chan, J. Energy Resources Tech., ASME Trans., Vol. 107., pp. 212-219 (1985).
4. R.P. Gangloff, in Metals Handbook: Mechanical Testing, 9th edition, Vol. 8, ASM International, Metals Park, Ohio, pp. 403-410 (1985).
5. A. Turnbull, Test Methods for Environment-Assisted Cracking, National Physical Laboratory Report DMM(A)66, Teddington, UK (1992).
6. Fatigue of Materials, Subra Suresh, Cambridge University Press, Cambridge, UK (1991).
7. Mechanical Behavior of Materials, N.E. Dowling, Prentice Hall Inc., Englewood Cliffs, NJ (1993).
8. Fatigue and Fracture Control in Structures, J.M. Barsom and S.T. Rolfe, 2nd Ed., Prentice-Hall, Inc., Englewood Cliffs, NJ (1987).
9. Environment Induced Cracking of Metals, R.P. Gangloff and M.B. Ives, eds., NACE, Houston, TX (1990).
10. Corrosion Fatigue, Chemistry, Mechanics and Microstructure, O. Devereux, A.J. McEvily and R.W. Staehle, eds., NACE, Houston, TX (1972).
11. Stress Corrosion Cracking and Hydrogen Embrittlement of Iron Based Alloys, J. Hochmann, J. Slater, R.D. McCright and R.W. Staehle, eds., NACE, Houston, TX (1977).
12. Hydrogen Effects on Material Behavior, N.R. Moody and A.W. Thompson, eds., TMS-AIME, Warrendale, PA (1990).
13. Chemistry and Physics of Fracture, R.M. Latanision and R.H. Jones, eds., Martinus Nijhoff Publishers BV, Netherlands (1987).
14. D.J. Duquette, in Environment Induced Cracking of Metals, R.P. Gangloff and M.B. Ives, eds., NACE, Houston, TX, pp. 45-53 (1990).
15. D.J. Duquette, Mechanisms of Corrosion Fatigue of Aluminum Alloys, AGARD Report No. AGARD-CP-316 (1981).
16. R.P. Gangloff, in Environment Induced Cracking of Metals, R.P. Gangloff and M.B. Ives, eds., NACE, Houston, TX, pp. 55-109 (1990).
17. R.P. Wei and R.P. Gangloff, in Fracture Mechanics: Perspectives and Directions, ASTM STP 1020, R.P. Wei and R.P. Gangloff, eds., ASTM, Philadelphia, Pa, pp. 233-264 (1989).
18. N.J.H. Holroyd and D. Hardie, Corr. Sci., Vol. 23, pp. 527-546 (1983).
19. M.O. Speidel, M.J. Blackburn, T.R. Beck and J.A. Feeney, in Corrosion Fatigue, Chemistry, Mechanics and Microstructure, O. Devereux, A.J. McEvily and R.W. Staehle, eds., NACE, Houston, TX, pp. 324-345 (1972).
20. P.M. Scott, T.W. Thorpe and D.R.V. Silvester, Corr. Sci., Vol. 23., pp. 559-575 (1983).
21. A.J. Griffiths, R. Hutchings and A. Turnbull, Scripta Metall., Vol. 29, pp. 623-626 (1993).
22. F.P. Ford, J. Press. Ves. Tech., Trans. ASME, Vol. 110, pp. 113-128 (1988).
23. F.P. Ford, in Environment Induced Cracking of Metals, R.P. Gangloff and M.B. Ives, eds., NACE, Houston, TX, pp. 139-166 (1990).

24. S.J. Hudak, *Corrosion Fatigue Crack Growth: The Role of Crack-Tip Deformation and Film Formation Kinetics*, PhD Dissertation, Lehigh University, Bethlehem, PA (1988).
25. H.K. Birnbaum, in *Environment Induced Cracking of Metals*, R.P. Gangloff and M.B. Ives, eds., NACE, Houston, TX, pp. 21-29 (1990).
26. T.S. Sudarshan and M.R. Louthan, Jr., *Intl. Metall. Rev.*, Vol. 32, pp. 21-151 (1987).
27. N.M. Grinberg, *Intl. J. Fatigue*, April, pp. 83-95 (1982).
28. K. Sieradzki, in *Environment Induced Cracking of Metals*, R.P. Gangloff and M.B. Ives, eds., NACE, Houston, TX, pp. 125-137 (1990).
29. D.J. Duquette, in *Environment Sensitive Fracture of Engineering Materials*, Z.A. Foroulis, ed., TMS-AIME, Warrendale, PA, pp. 521-537 (1979).
30. D.A. Jones, in *Environment Induced Cracking of Metals*, R.P. Gangloff and M.B. Ives, eds., NACE, Houston, TX, pp. 265-270 (1990).
31. *Embrittlement by the Localized Crack Environment*, R.P. Gangloff, ed., TMS-AIME, Warrendale, PA (1984).
32. *Corrosion Chemistry Within Pits, Crevices and Cracks*, A. Turnbull, ed., National Physical Laboratory, Teddington, UK (1987).
33. B. Yan, G.C. Farrington and C. Laird, *Acta Metall.*, Vol. 33, pp. 1533-1545 (1985).
34. T. Magnin and L. Coudreuse, *Matls. Sci. and Engr.*, Vol. 72, pp. 125-134 (1985).
35. F.S. Lin and E.A. Starke, Jr., *Matls. Sci. and Engr.*, Vol. 39, pp. 27-41 (1979).
36. H.M. Chung, et al., *Environmentally Assisted Cracking in Light Water Reactors*, US Nuclear Regulatory Commission Report NUREG/CR-4667, Vol. 16, ANL-93/27 (1993).
37. *Manual on Low Cycle Fatigue Testing*, ASTM STP 465, American Society for Testing and Materials, Philadelphia, PA (1969).
38. H.H. Lee and H.H. Uhlig, *Met. Trans.*, Vol. 3, pp. 2949-2957 (1972).
39. D.J. Duquette and H.H. Uhlig, *Trans. ASM*, Vol. 61, pp. 449-456 (1968).
40. J.A. Feeney, J.C. McMillan and R.P. Wei, *Met. Trans.*, Vol. 1, pp. 1741-1757 (1970).
41. P.C. Paris, M.P. Gomez and W.E. Anderson, *The Trend in Engineering*, University of Washington, Vol. 13, pp. 9-14 (1961).
42. *Fatigue Thresholds*, D. Taylor, EMAS, Ltd., Warley Heath, U.K. (1982).
43. D.B. Dawson and R.M. Pelloux, *Metall. Trans. A*, Vol. 5A, pp. 723-731 (1974).
44. D.C. Slavik, *Environmental Fatigue Crack Growth and Microscopic Damage Mechanisms in AA2090*, PhD Dissertation, University of Virginia, Charlottesville, VA (1993).
45. *Mechanics of Fatigue Crack Closure*, ASTM STP 982, J.C. Newman and W. Elber, eds., ASTM, Philadelphia, PA (1988).
46. M.E. Taylor and J.M. Barsom, in *Fracture Mechanics: Thirteenth Conference*, ASTM STP 743, R. Roberts, Ed., ASTM, Philadelphia, PA, pp. 599-622 (1981).
47. S.S. Rajpathak and W.H. Hartt, in *Environmentally Assisted Cracking: Science and Engineering*, ASTM STP 1049, W.B. Lisagor, T.W. Crooker and B.N. Leis, eds., ASTM, Philadelphia, PA, pp. 425-446 (1990).
48. S.R. Novak, in *Corrosion Fatigue Technology*, ASTM, STP 642, H.L. Craig, Jr., T.W. Crooker and D.W. Hoepfner, eds., ASTM, Philadelphia, PA, pp. 26-63 (1978).
49. M.O. Speidel, in *Stress Corrosion Research*, Hans Arup and R.N. Parkins, eds., Sijthoff & Noordhoff, Alphen aan den Rijn, Netherlands, pp. 117-183 (1979).
50. M.E. Mason and R.P. Gangloff *Modeling Time-Dependent Corrosion Fatigue Crack Propagation in 7000 Series Aluminum Alloys*, in *Proceedings, International Symposium on Advanced Structural Integrity Methods for Airframe Durability and Damage Tolerance*, C.E. Harris, ed., NASA-Langley Research Center, Hampton, VA, in press (1994).
51. R. Krishnamurthy, *Microstructure and Yield Strength Effects on Hydrogen Environment Fatigue of Steels*, PhD Dissertation, University of Virginia, Charlottesville, VA (1991).
52. R.P. Wei and J.D. Landes, *Matls. Res. Stds.*, Vol. 9, pp. 25-28 (1969).
53. R.J. Bucci, PhD Dissertation, Lehigh University, Bethlehem, PA (1970).



54. R.J. Selines and R.M. Pelloux, Met. Trans., Vol. 3, pp. 2525-2531 (1972).
55. O. Vosikovsky, J. Test. Eval., Vol. 8, pp. 68-73 (1980).
56. J.M. Barsom, in Corrosion Fatigue, Chemistry, Mechanics and Microstructure, O. Devereux, A.J. McEvily and R.W. Staehle, eds., NACE, Houston, TX, pp. 424-436 (1972).
57. D.J. Duquette, in Environment Sensitive Fracture of Metals, R.P. Wei, D.J. Duquette, T.W. Crooker and A.J. Sedriks, eds., Office of Naval Research, Arlington, VA, pp. 1-16 (1987).
58. Corrosion Fatigue of Metals in Marine Environments, C.E. Jaske, J.H. Payer and V.S. Balint, Metals and Ceramics Information Center, MCIC-81-42 (1981).
59. K. Endo, K. Komai and S. Kinoshita, in Proceedings of the 22nd Japan Congress on Materials Research, Kyoto, Japan, pp. 193-198 (1978).
60. A. Turnbull and M. Saenz de Santa Maria, Metall. Trans. A, Vol. 19A, pp. 1795-1806 (1988).
61. R.P. Gangloff, in Embrittlement by the Localized Crack Environment, R.P. Gangloff, ed., TMS-AIME, Warrendale, PA, pp. 265-290 (1984).
62. R.S. Piascik and R.P. Gangloff, Metall. Trans. A, Vol. 22A, pp. 2415-2428 (1991).
63. R.E. Stoltz and R.M. Pelloux, Met. Trans., Vol. 3, pp. 2433-2441 (1972).
64. R.P. Gangloff and R.G. Kelly, Corrosion, Vol. 50, pp. 345-354 (1994).
65. C.J. Thomas, R.G.J. Edyvean and R. Brook, Biofouling, Vol. 1, pp. 65-77 (1988).
66. P.M. Scott, A.E. Truswell and S.G. Druce, Corrosion, Vol. 40, pp. 350-357 (1984).
67. F.S. Lin and E.A. Starke, Jr., Matls. Sci. and Engr., Vol. 45, pp. 153-165 (1980).
68. C.A. Hipsley, Hydrogen and Temper Embrittlement Interactions in Fatigue of 2 1/4Cr-1Mo Steel, Harwell Laboratory Report AERE R 12322, Oxon, UK (1986).
69. R.A. Cottis, A. Markfield, A. Boukerrou and P. Haritopoulos, in Environment Induced Cracking of Metals, R.P. Gangloff and M.B. Ives, eds., NACE, Houston, TX, pp. 223-227 (1990).
70. F.S. Lin and E.A. Starke, Jr., Matls. Sci. and Engr., Vol. 43, pp. 65-76 (1980).
71. R.P. Wei and M. Gao, Scripta Metall., Vol. 17, pp. 959-962 (1983).
72. A. Turnbull and D.H. Ferriss, Corr. Sci., Vol. 27, pp. 1323-1350 (1987).
73. T. Magnin and L. Coudreuse, Matls. Sci. and Engr., Vol. 72, pp. 125-134 (1985).
74. B. Yan, G.C. Farrington, and C. Laird, Fat. and Fract. of Engr. Matls. and Struct., Vol. 8, pp. 259-273 (1985).
75. Atlas of Stress-Corrosion and Corrosion Fatigue Curves, A.J. McEvily, ed., ASM International, Metals Park, OH (1990).
76. Corrosion Fatigue Technology, ASTM STP 642, H.L. Craig, Jr., T.W. Crooker and D.W. Hoepfner, eds., ASTM, Philadelphia, PA (1978).
77. Corrosion Fatigue: Mechanics, Metallurgy, Electrochemistry and Engineering, ASTM STP 801, T.W. Crooker and B.N. Leis, eds., ASTM, Philadelphia, PA (1984).
78. Proceedings of the Conference on Low Frequency Cyclic Loading Effects in Environment Sensitive Fracture, Corr. Sci., Vol. 23, No. 6 Pergamon Press, Oxford, UK (1983).
79. Standard Practice for Conducting Constant Amplitude Fatigue Tests of Metallic Materials, Designation E466-82, Annual Book of ASTM Standards, Vol. 03.02, Section 3, ASTM, Philadelphia, PA, pp. 564-568 (1992).
80. Standard Practice for Presentation of Constant Amplitude Fatigue Test Results for Metallic Materials, Designation E468-90, Annual Book of ASTM Standards, Vol. 03.01, Section 3, ASTM, Philadelphia, PA, pp. 574-579 (1992).
81. W.J. Derrick Jones and A.P. Blackie, in Environmentally Assisted Cracking: Science and Engineering, ASTM STP 1049, W.B. Lisagor, T.W. Crooker and B.N. Leis, eds., ASTM, Philadelphia, PA, pp. 447-462 (1990).
82. E.U. Lee, in Corrosion Cracking, V.S. Goel, ed., ASM International, Metals Park, OH, pp. 123-128 (1986).
83. E.J. Czyryca, in Metals Handbook: Mechanical Testing, 9th edition, Vol. 8, ASM International, Metals Park, Ohio, pp. 366-375 (1985).



84. T. Tanaka, T. Sakai and T. Iwaya, in Fatigue Lives and Fatigue Strengths of Ferrous Metals, pp. 125-157 (1986).
85. Standard Recommended Practice for Constant Amplitude Low Cycle Fatigue Testing, Designation E606-80, Annual Book of ASTM Standards, Vol. 03.01, Section 3, ASTM, Philadelphia, PA, pp. 629--641 (1992).
86. H. Bernstein and C. Loeb, in Offshore and Arctic Operations, I. Konuk, ed., PD-Vol. 10, ASME, New York, NY, pp. 253-259 (1987).
87. "Standard Test Method for Measurement of Fatigue Crack Growth Rates", Designation E647-91, Annual Book of ASTM Standards, Vol. 03.01, Section 3, ASTM, Philadelphia, PA, pp. 674-701 (1992).
88. Fatigue Crack Growth Measurement and Data Analysis, ASTM STP 738, S.J. Hudak and R.J. Bucci, eds., ASTM, Philadelphia, PA (1981).
89. D.A. Utah et al., in Metals Handbook: Mechanical Testing, 9th edition, Vol. 8, ASM International, Metals Park, Ohio, pp. 376-402 (1985).
90. T.W. Crooker, F.D. Bogar and G.R. Yoder, Standard Method of Test for Constant-Load-Amplitude Fatigue Crack Growth Rates in Marine Environments, Naval Research Laboratory Report 4594, Washington, DC (1981).
91. H.R. Smith and D.E. Piper, in Stress Corrosion Cracking in High Strength Steels and in Titanium and Aluminum Alloys, B.F. Brown, ed., Naval Research Laboratory, Washington, DC, pp. 17-78 (1972).
92. L.M. Young, Environment-Assisted Cracking in Beta Titanium Alloys, MS Thesis, University of Virginia, Charlottesville, VA (1993).
93. L.J. Ceschini, P.K. Liaw, G.E. Rudd and W.A. Logsdon in Environment-Sensitive Fracture: Evaluation and Comparison of Test Methods, ASTM STP 821, S.W. Dean, E.N. Pugh and G.M. Ugiansky, eds., ASTM, Philadelphia, PA, pp. 426-442 (1984).
94. Advances in Crack Length Measurement, C.J. Beevers, ed., EMAS, Cradley Heath, Warley, West Midlands, UK (1982).
95. Fatigue Crack Measurement: Techniques and Applications, K.J. Marsh, R.A. Smith and R.O. Ritchie, eds., EMAS, Cradley Heath, Warley, West Midlands, UK (1991).
96. Small Crack Test Methods, ASTM STP 1149, J.M. Larsen and J.E. Allison, eds., ASTM, Philadelphia, PA, pp. 116-168 (1992).
97. L.A. James and L.J. Ceschini, J. Test. Eval. JTEVA, Vol. 13, pp. 409-415 (1985).
98. J.K. Donald and J. Ruschau, in Fatigue Crack Measurement: Techniques and Applications, K.J. Marsh et al., Eds., EMAS, West Midlands, UK, pp. 11-37 (1991).
99. W.G. Clark, Jr. and S.J. Hudak, Jr., J. Test. Eval., Vol. 3, pp. 454-476 (1975).
100. E.P. Phillips, Results of the Second Round Robin on Opening-Load Measurement, NASA TM 109032, Langley Research Center, Hampton, VA (1993).
101. R. Van der Velden, H.L. Ewalds, W.A. Schultze and A. Punter, in Corrosion Fatigue: Mechanics, Metallurgy, Electrochemistry and Engineering, ASTM STP 801, T.W. Crooker and B.N. Leis, eds., ASTM, Philadelphia, PA, pp. 64-80 (1984).
102. T. Shoji, H. Takahashi, M. Suzuki and T. Kondo, J. Engr. Matls. Tech., Trans. ASME, Vol. 103, pp. 298-304 (1981).
103. L.A. James, Effect of Temperature and Cyclic Frequency Upon Fatigue Crack Growth Behavior of Several Steels in an Elevated Temperature Aqueous Environment, J. Press. Vess. Technol., in press (1994).
104. W.A. Herman, R.W. Hertzberg and R. Jaccard, J. Fat. and Frac. of Engr. Matls. and Struc., Vol. 11, pp. 303-320 (1988).
105. C. Amzallag, B. Mayonobe and P. Rabbe, in Electrochemical Corrosion Testing, ASTM STP 727, F. Mansfeld and U. Bertocci, eds., ASTM, Philadelphia, PA, pp. 69-83 (1981).
106. R.P. Gangloff and R.P. Wei, in Small Fatigue Cracks, R.O. Ritchie and J. Lankford, eds., TMS-AIME, Warrendale, PA, pp. 239-264 (1986).
107. S.J. Hudak and F.P. Ford, in Small Fatigue Cracks, R.O. Ritchie and J. Lankford, eds., TMS-AIME, Warrendale, PA, pp. 289-310 (1986).

108. R.P. Gangloff, Metall. Trans. A., Vol. 16A., pp. 953-969 (1985).
109. R.P. Gangloff, D.C. Slavik, R.S. Piascik and R.H. Van Stone, in Small Crack Test Methods, ASTM STP 1149, J.M. Larsen and J.E. Allison, eds., ASTM, Philadelphia, PA, pp. 116-168 (1992).
110. R.S. Piascik and S.A. Willard, *The Growth of Small Corrosion Fatigue Cracks in Alloy 2024*, NASA TM 107755, Langley Research Center, Hampton, VA (1993). Also: Fatigue and Fracture of Engineering Materials and Structures, in press (1994).
111. G. Gabetta and R. Rizzi, Corr. Sci., Vol. 23, pp. 613-620 (1983).
112. A. Turnbull, A.S. Dolphin and F.A. Rackley, Corrosion, Vol. 44, pp. 55-61 (1988).
113. P.L. Andresen and L.M. Young, *Crack Tip Chemistry and Growth Rate Measurements in Low Alloy Steel in High Temperature Water*, Corrosion, in review (1994).
114. R.G. Forman, V. Shivakumar, J.C. Newman, Jr., S.M. Piotrowski and L.C. Williams, in Fracture Mechanics: Eighteenth Symposium, ASTM STP 945, ASTM, Philadelphia, PA, pp. 781-803 (1988).
115. P.L. Andresen, R.P. Gangloff, L.F. Coffin and F.P. Ford, in Fatigue 87, Vol. III-A, R.O. Ritchie and E.A. Starke, Jr., eds., EMAS, West Midlands, UK, pp. 1723-1751 (1987).
116. P.M. Scott, Memoires et Etudes Scientifiques Revue de Metallurgie, November, pp. 651-660 (1983).
117. W.D. Dover, Intl. J. Fatigue, Vol. 3, pp. 52-60 (1981).
118. O. Vosikovsky and R.J. Cooke, Int. J. Pres. Ves. & Piping, Vol. 6, pp. 113-129 (1978).
119. R.P. Gangloff, R.S. Piascik, D.L. Dicus and J.C. Newman, *Fatigue Crack Propagation in Aerospace Aluminum Alloys*, Journal of Aircraft, in press (1994).
120. *Durability of Metal Aircraft Structures*, S.N. Ataluri, C.E. Harris, A. Hoggard, N. Miller and S.G. Sampath, eds., Atlanta Technology Publishers, Atlanta, GA (1992).
121. *EPRI Database for Environmentally Assisted Cracking*, Project RP2006-2, J. Gilman, manager, Electric Power Research Institute, Palo Alto, CA.
122. *Threshold Corrosion Fatigue of Welded Shipbuilding Steels*, Ship Structures Committee Report SSC-366, Washington, DC (1992).
123. D.C. Slavik, J.A. Wert and R.P. Gangloff, J. Matls. Res., Vol. 8, pp. 2482-2491 (1993).
124. T. Kobayashi and D.A. Shockey, *Computational Reconstruction of Environmentally Accelerated Cyclic Crack Growth in Reactor Steels*, Paper No. 563, Corrosion 89, NACE, Houston, TX (1989).

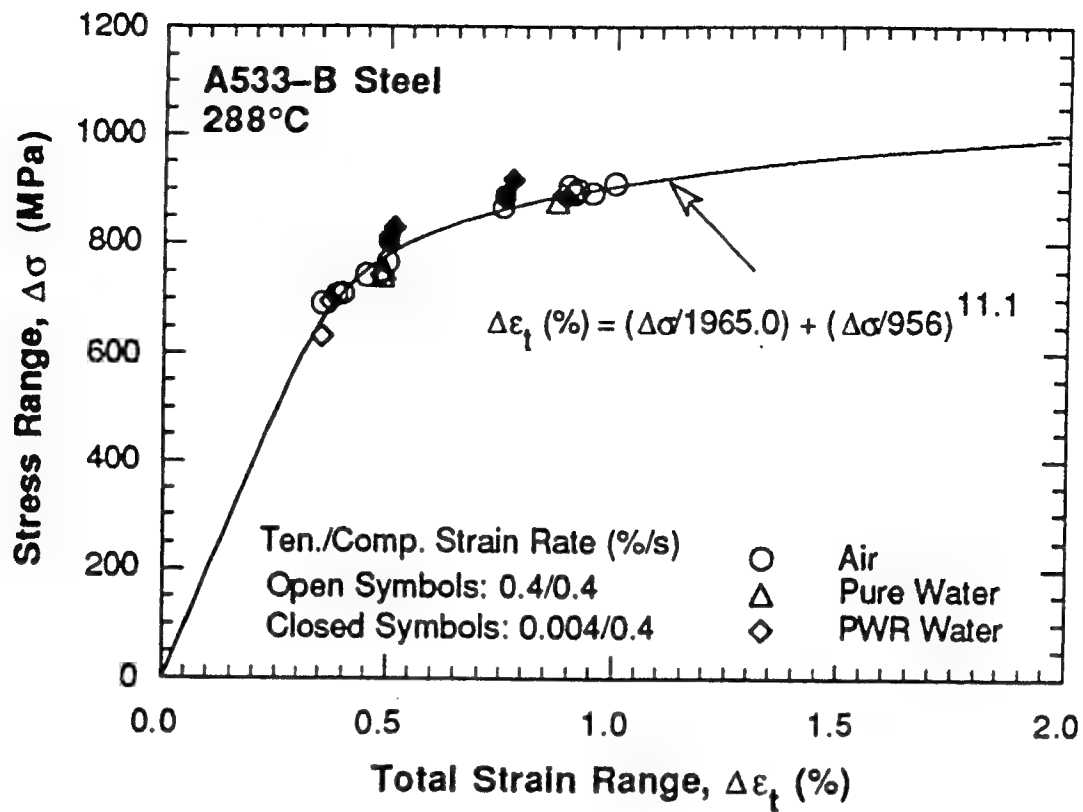


Figure 1 The nil effect of environment on the cyclic stress-strain response of a C-Mn steel in moist air and pressurized water at 288°C. (After Chopra, Michaud and Shack [36])

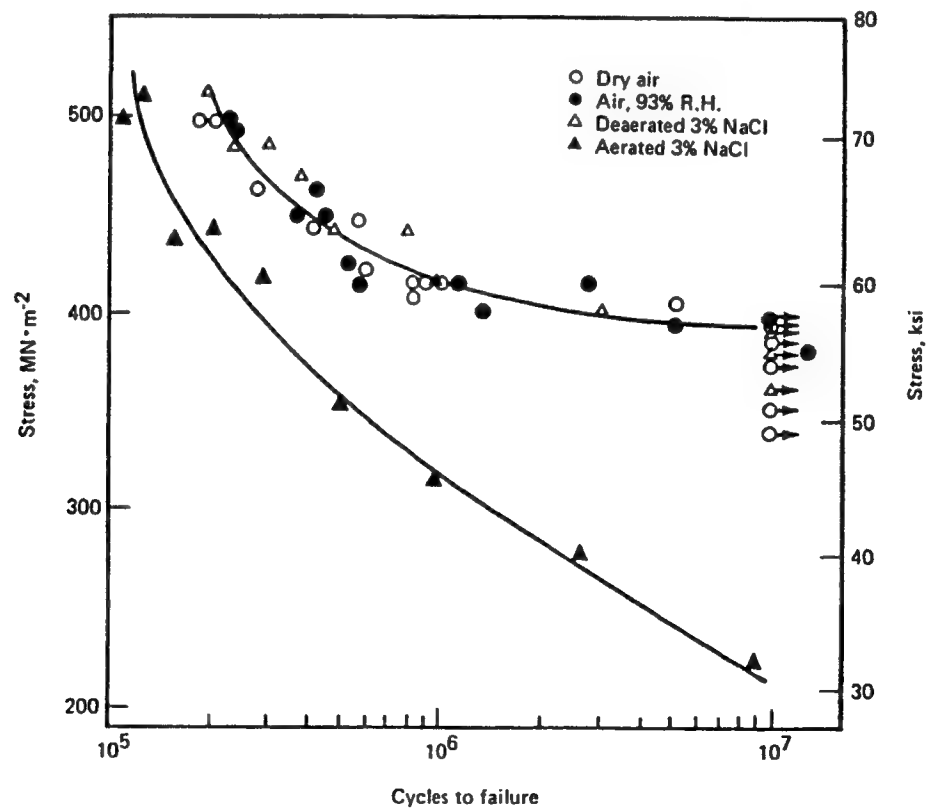


Figure 2 The deleterious effect of aerated aqueous chloride solution on the HCF life of smooth specimens of tempered martensitic AISI 4140 steel. Symbols with horizontal arrows indicate that CF failure has not occurred after  $10^7$  load cycles. (After Lee and Uhlig [38])

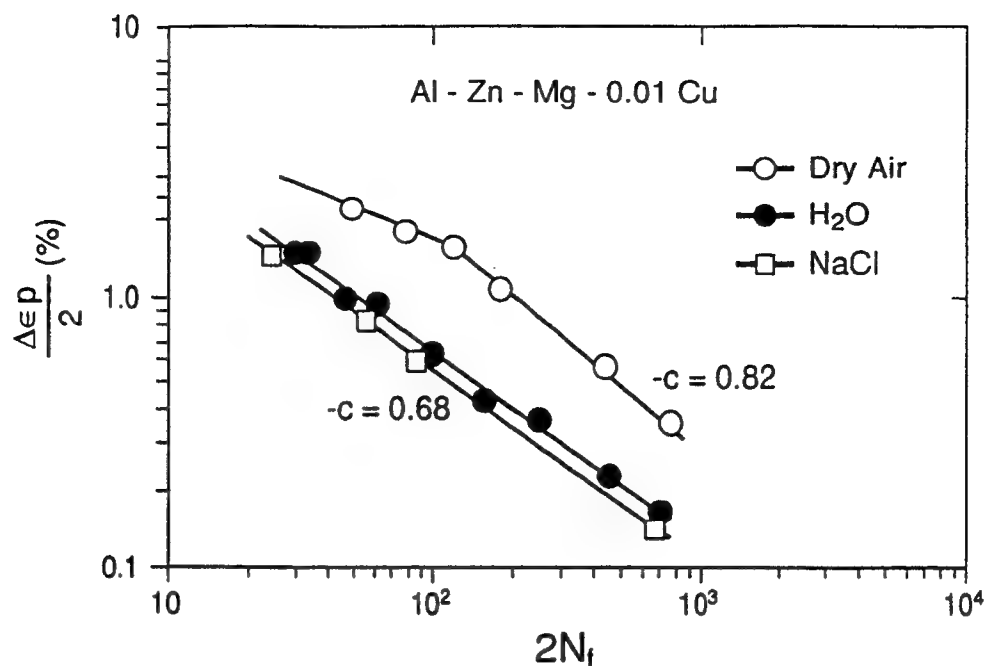


Figure 3 The deleterious effect of aqueous chloride solution on the LCF life of a precipitation hardened aluminum alloy. (After Lin and Starke [35])

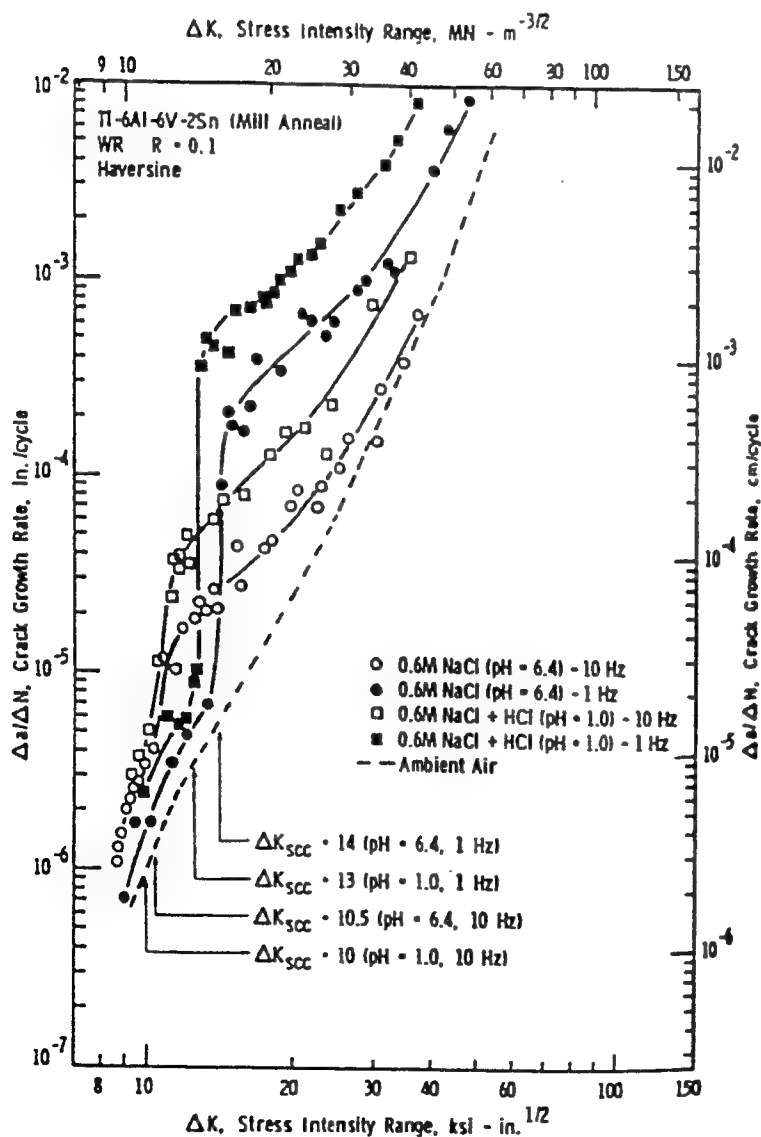


Figure 4 The effect of solution pH and loading frequency on CF crack propagation in an α/β titanium alloy exposed to aqueous chloride. (After Dawson and Pelloux [43])

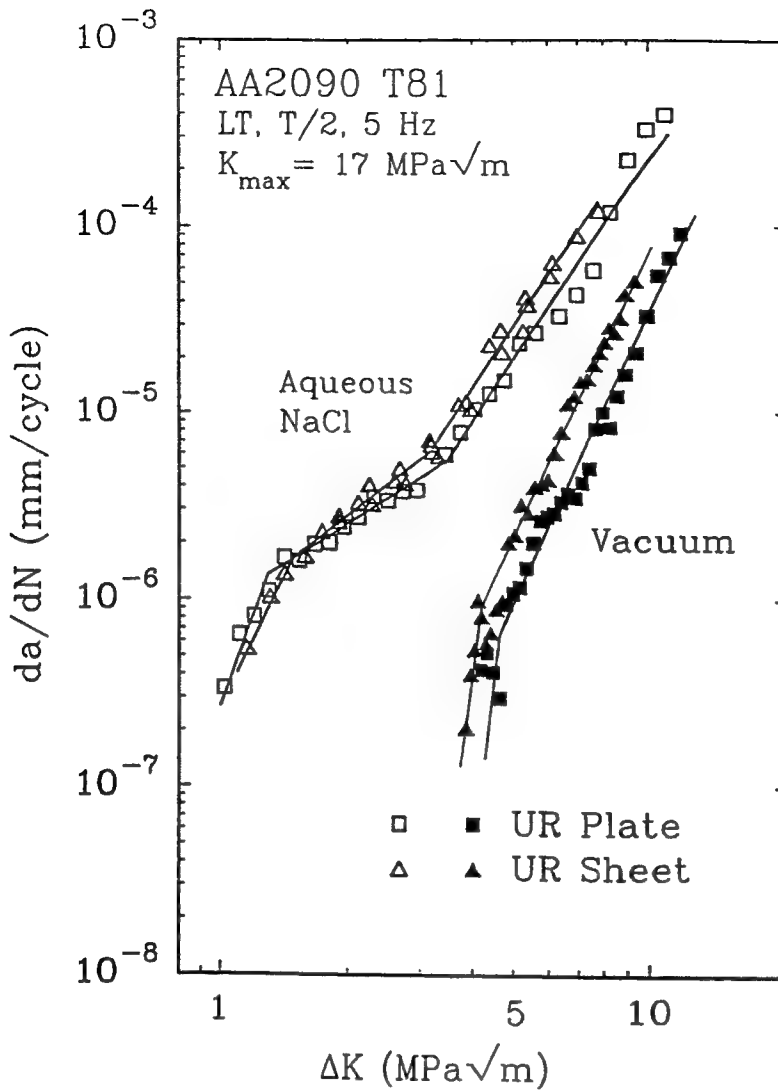


Figure 5

The effect of aqueous NaCl on the CF crack propagation response of unrecrystallized sheet and plate of an advanced Al-Li-Cu-Zr alloy. (After Slavik and Gangloff [44])

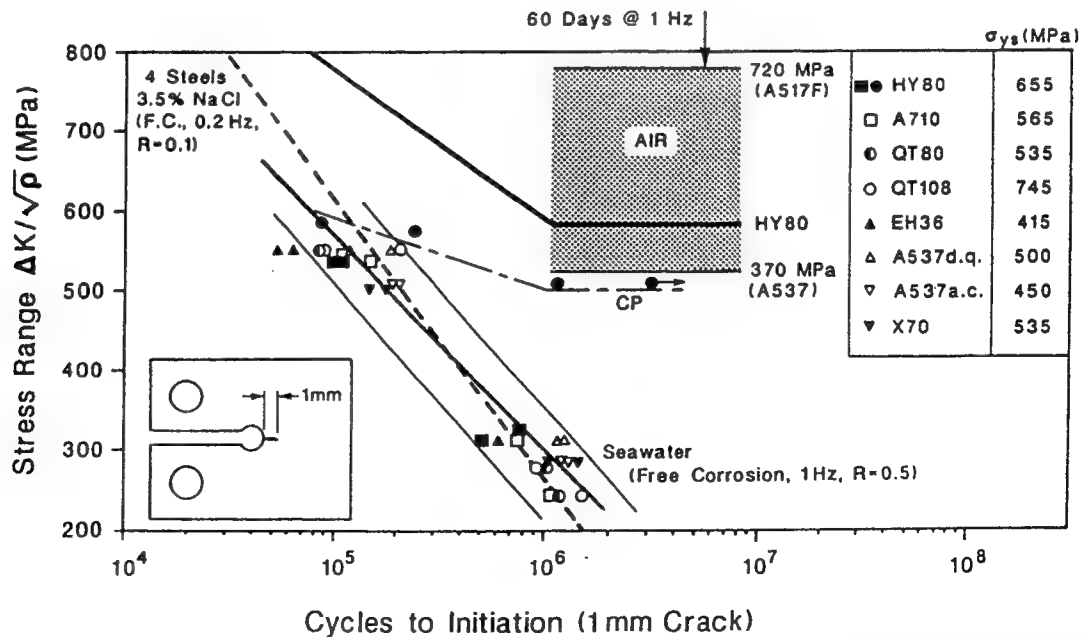


Figure 6

The effect of chloride on the CF crack initiation resistance of notched steel specimens. (After Taylor and Barsom--solid line for 4 steels in NaCl, Rajpathak and Hartt--data points for seawater, and Novak--dashed line for 4 steels in NaCl [46-48])

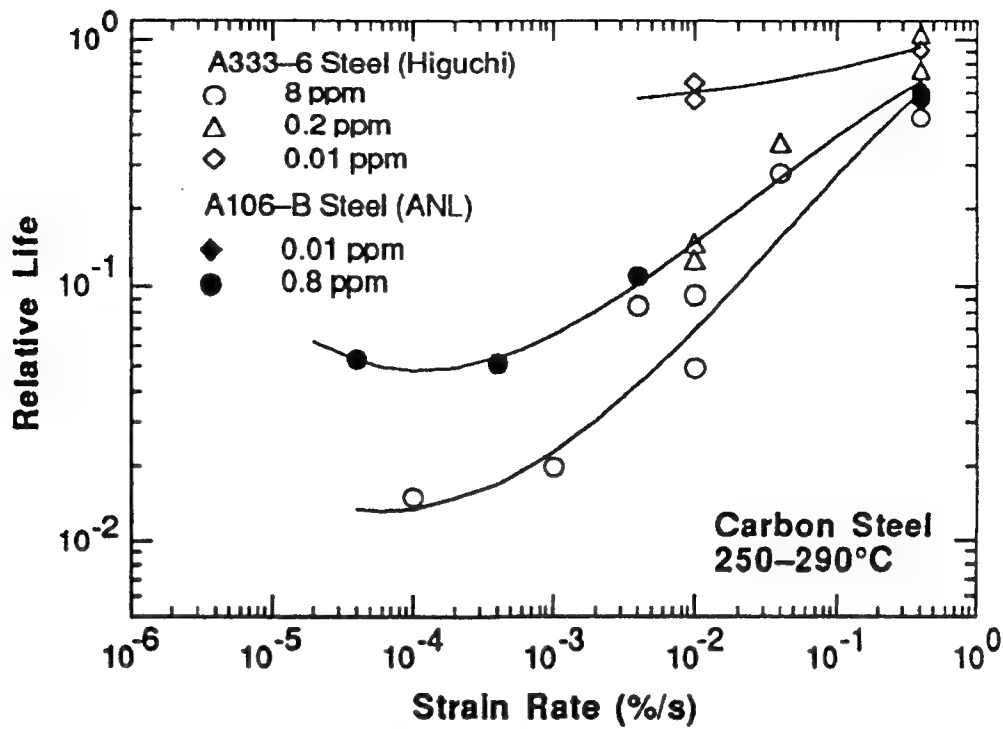


Figure 7 The effect of strain rate on low cycle CF in the C-Mn steel/high temperature water system. The dissolved oxygen content of the pure water environment was varied, as indicated by the weight-parts-per-million values in the legend. (After Chopra, Michaud and Shack [36])

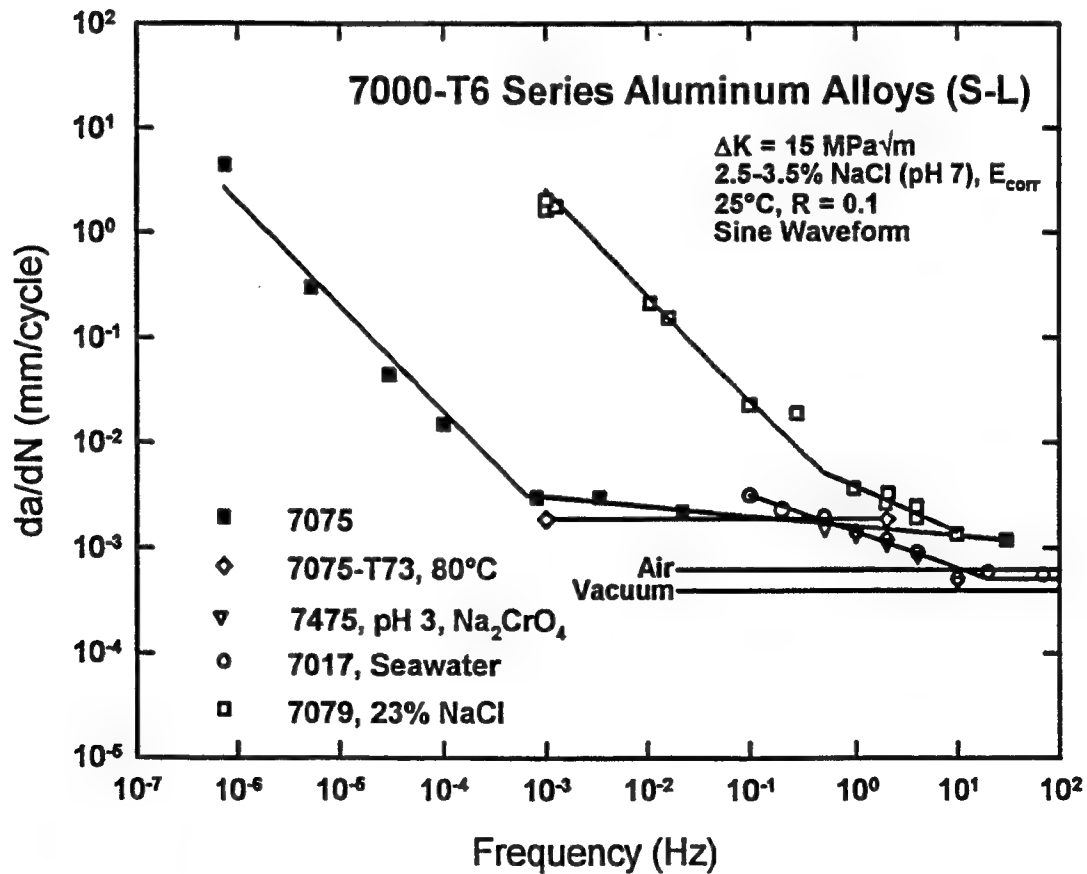


Figure 8 The varied effects of loading frequency on CF crack propagation rate in peak aged AA7075, 7017, 7475 and 7079 exposed to aqueous chloride solution (free corrosion) at constant  $\Delta K$  and  $R$ . The fatigue crack is parallel to the plate rolling plane, in the SCC sensitive S-L orientation (After Mason and Gangloff [50])

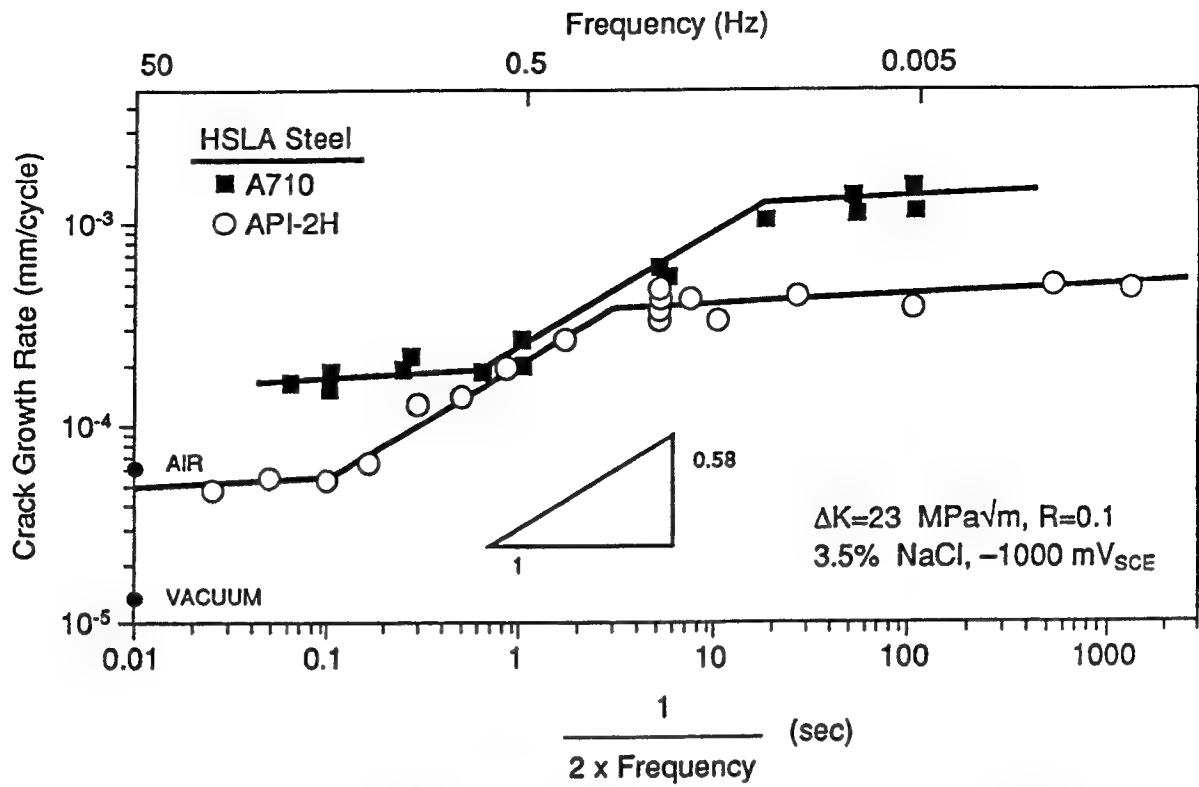


Figure 9 The effect of loading frequency on CF propagation in API-2H and A710 steels, at the 625 to 750 MPa yield strength level, exposed to aqueous NaCl solution with CP to -1000 mV<sub>SCE</sub> at constant ΔK and R. (After Krishnamurthy and Gangloff [51]).

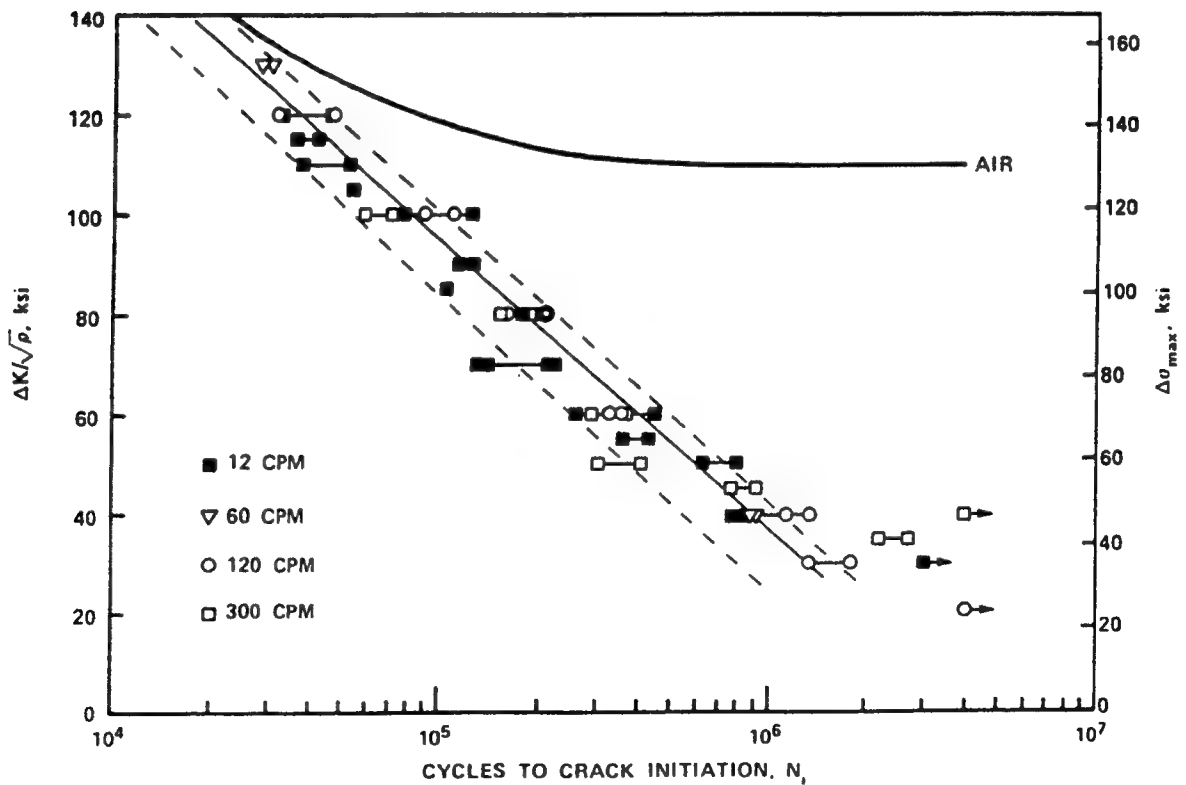


Figure 10 The frequency independence of CF life for blunt notch specimens of A517 steel, freely corroding in aqueous 3.5% NaCl as a function of notch root strain range. (After Taylor and Barsom [46])

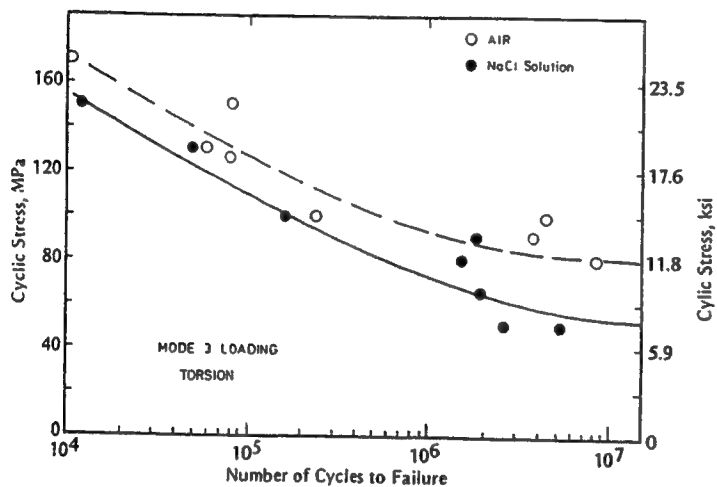
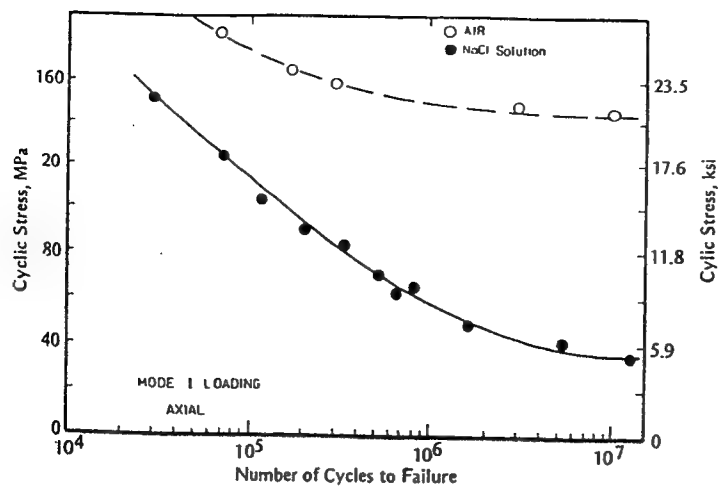


Figure 11

The effect of environment on tensile and torsional high cycle corrosion fatigue in the 7075/NaCl solution system. (After Duquette [57])

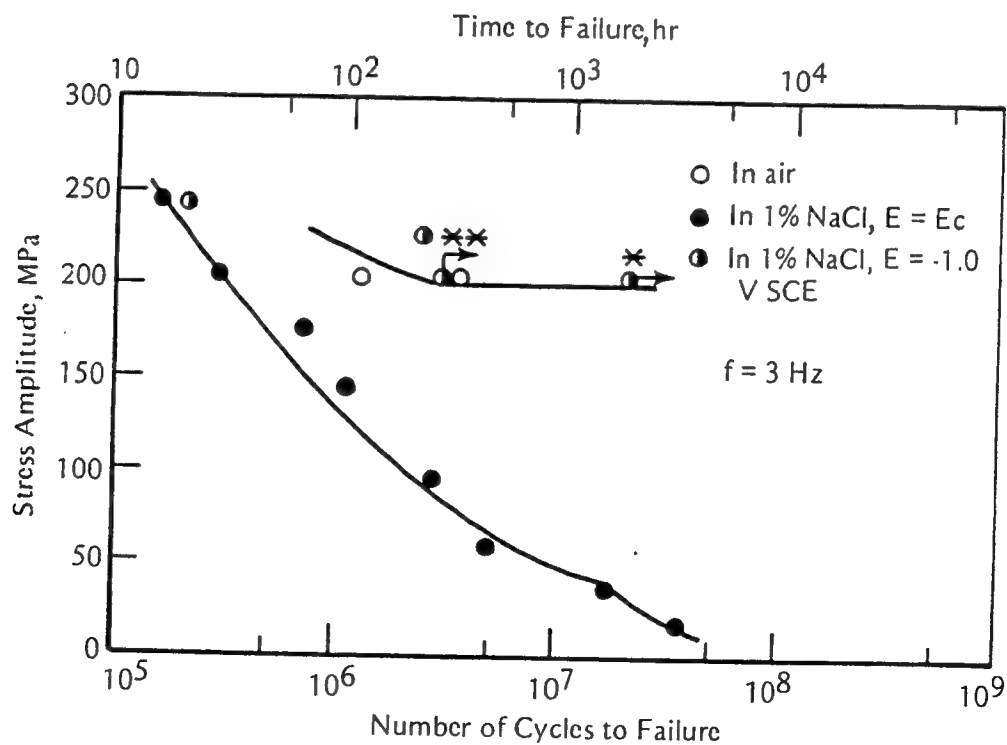


Figure 12

The beneficial effect of cathodic polarization on high cycle CF crack initiation in a C-Mn steel in 1% NaCl solution. (After Endo, Komai and Kinoshita [59])



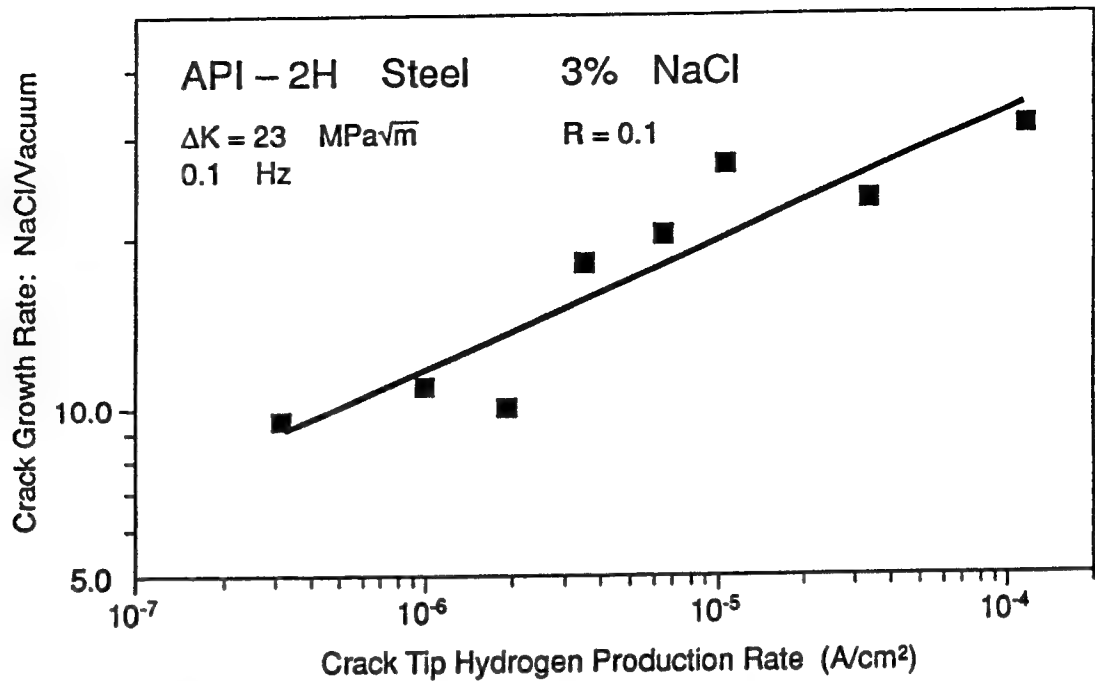


Figure 13 The effect of electrode potential on relative CF crack propagation rate in the C-Mn steel/chloride system, as portrayed by the crack tip hydrogen production current calculated from a crack chemistry model. The equation of the line from regression analysis is:  $y = 2.39 + 0.22 x$ , where  $y$  is the normalized (dimensionless) crack growth rate and  $x$  is crack tip hydrogen production rate in  $A/cm^2$ . (After Gangloff [16])

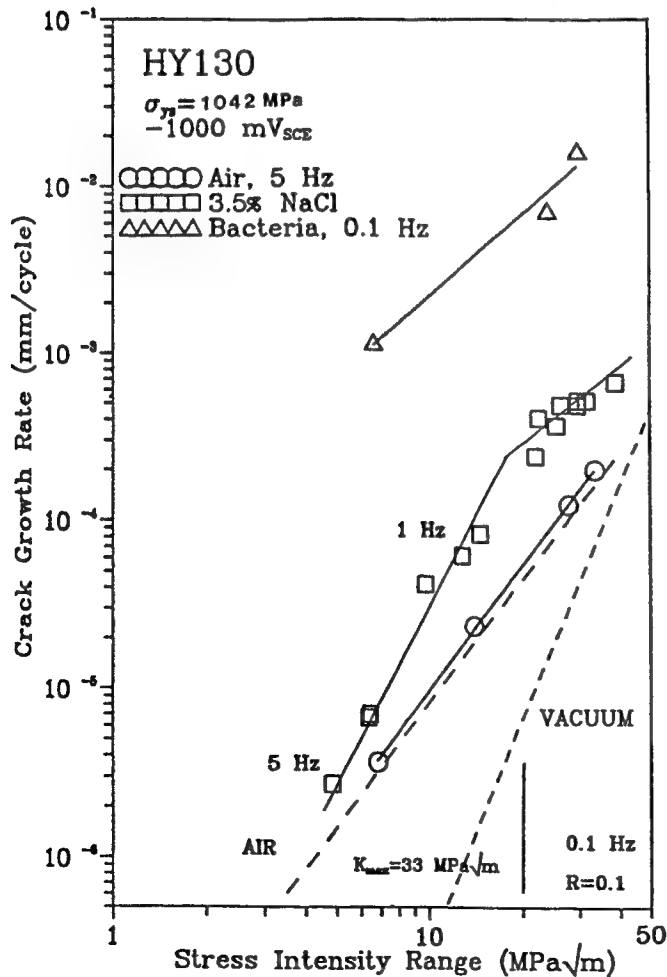


Figure 14 CF crack propagation in HY130 steel in aqueous (sterile) chloride and active sulfate-reducing bacteria environments, both with CP to  $-1000 mV_{SCE}$ .  $\Delta K$  values above  $20 MPa\sqrt{m}$  were applied at  $R$  of  $0.1$  and  $f$  of  $0.1 Hz$ , while  $\Delta K < 20 MPa\sqrt{m}$  were applied at constant  $K_{max}$  of  $33 MPa\sqrt{m}$  and  $f$  of  $1$  or  $5 Hz$ . The dashed line represents literature data for FCP in the steel/vacuum system. (After Gangloff and Kelly [64])

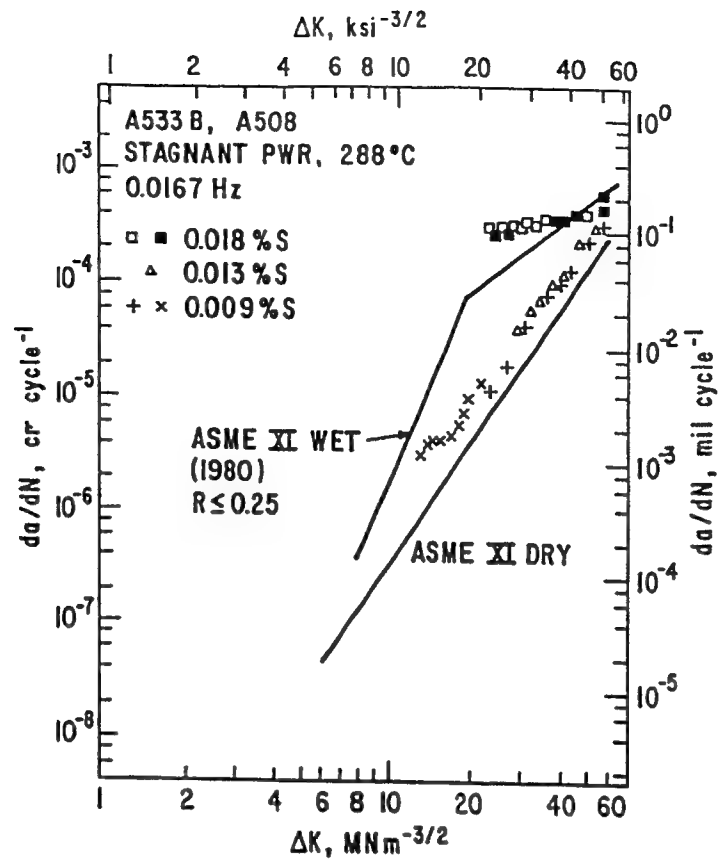


Figure 15 The effect of alloy impurity-sulfur content on CF crack propagation in the C-Mn steel/high temperature pure water system. (Reported by C. Amzallag and J.L. Bernard in Ford [22])

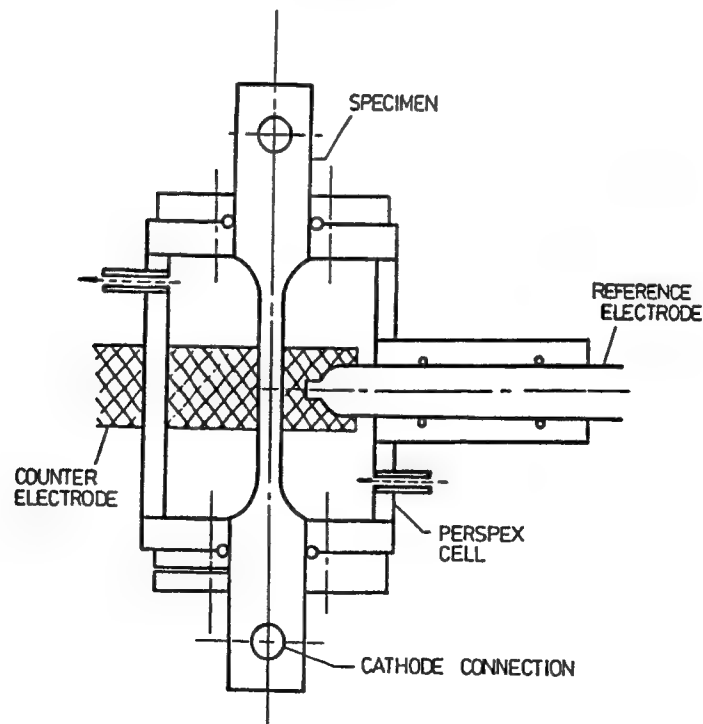
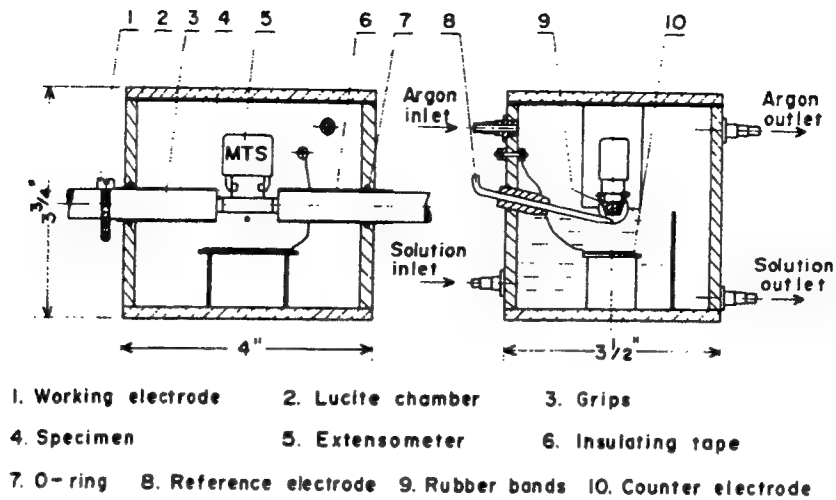
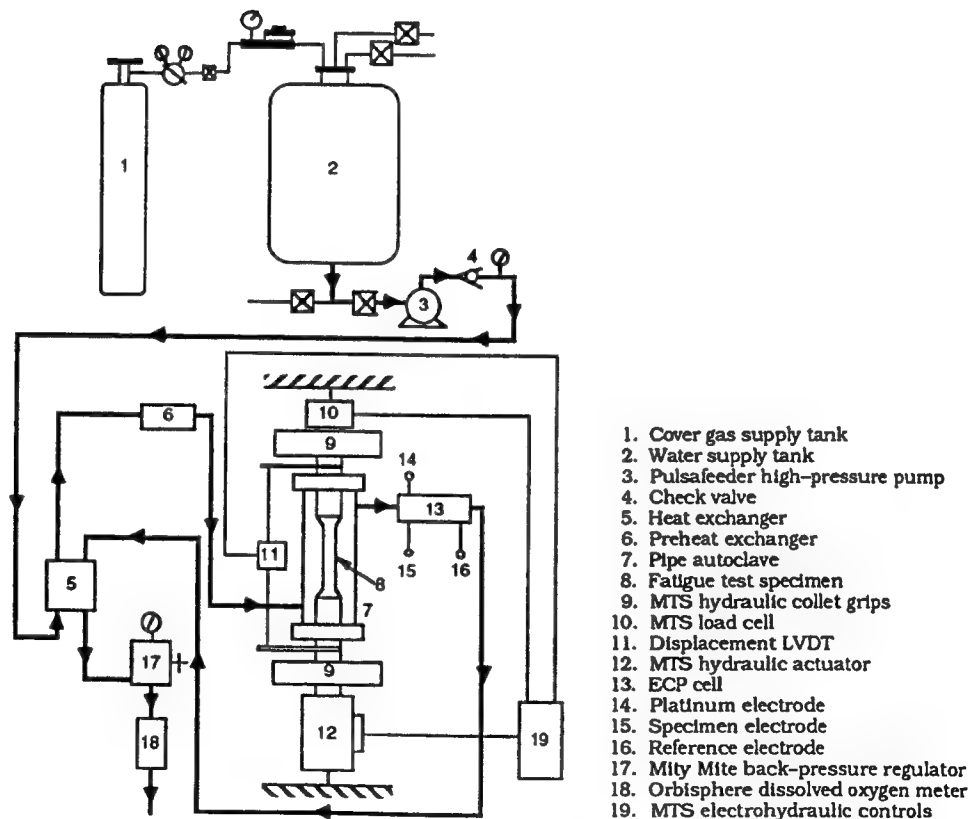


Figure 16 Uniaxially loaded smooth-gauge specimen and environmental chamber for high cycle CF experimentation with aqueous chloride solutions at near ambient temperatures. (After Jones and Blackie [81])

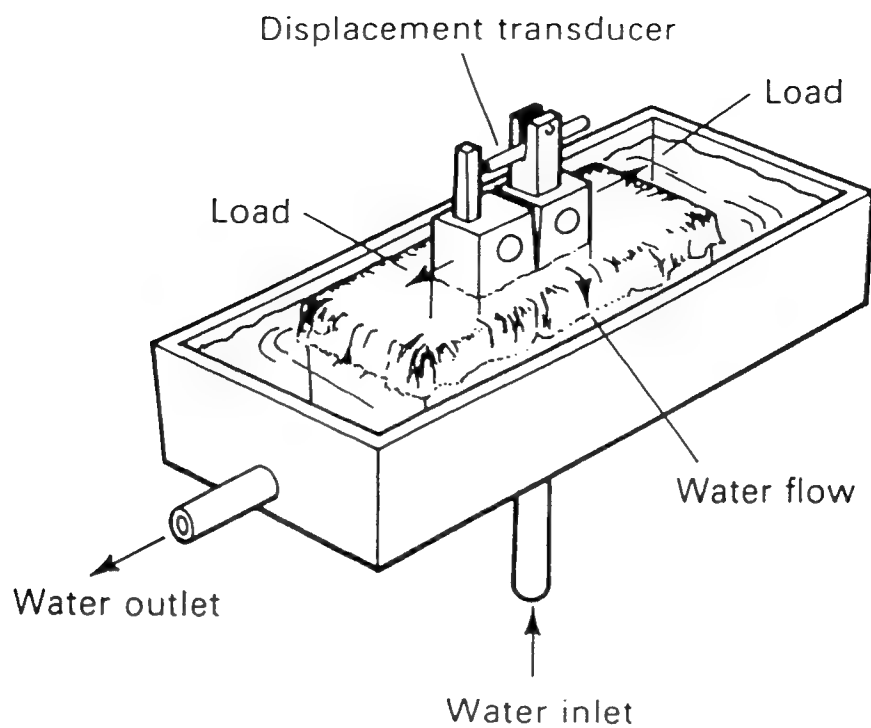


(a)

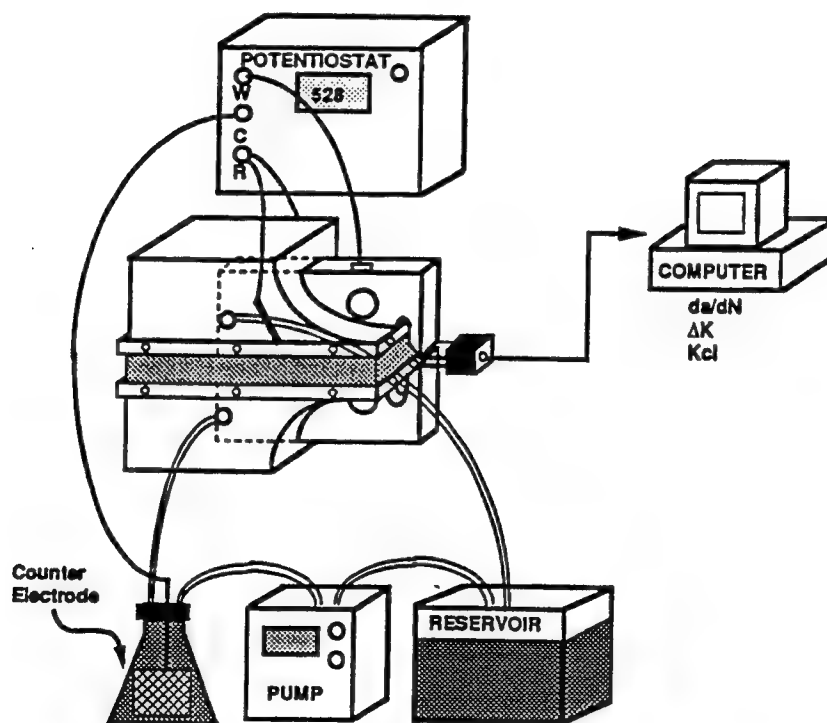


(b)

Figure 17 Environmental chambers for low cycle CF in: a) an electrolyte at ambient temperature (after Yan et al. [33]), and b) high temperature water. (After Chopra et al. [36])



(a)



(b)

Figure 18

Environmental chambers for CF in electrolytes where: a) the CT specimen is loaded horizontally and dipped into solution, (after Turnbull and Scott [4]), and b) the CT crack is enclosed by a clamped cell and polarized potentiostatically. In part b load (P)-displacement ( $\delta$ ) data are recorded by computer and autographically for compliance measurement of crack length and  $K_{Ic}$ . (After Kim and Gangloff, unpublished research)

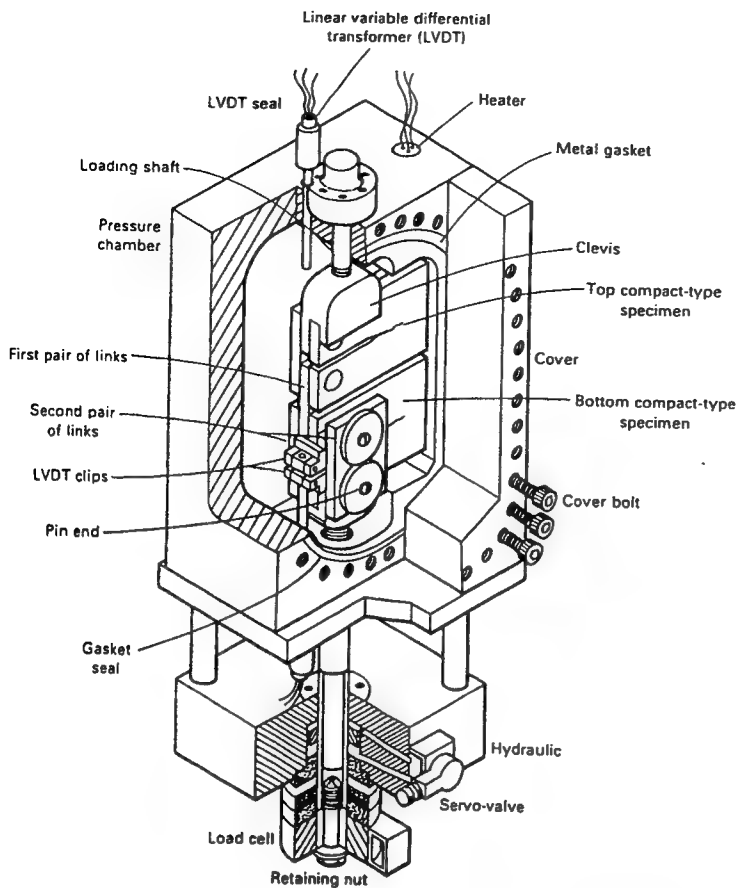


Figure 19

Two compact tension specimens mounted in a high pressure-temperature stainless steel autoclave containing water, steam, or acidified  $H_2S$  bearing brine environments. (After Liaw et al. [4,93])

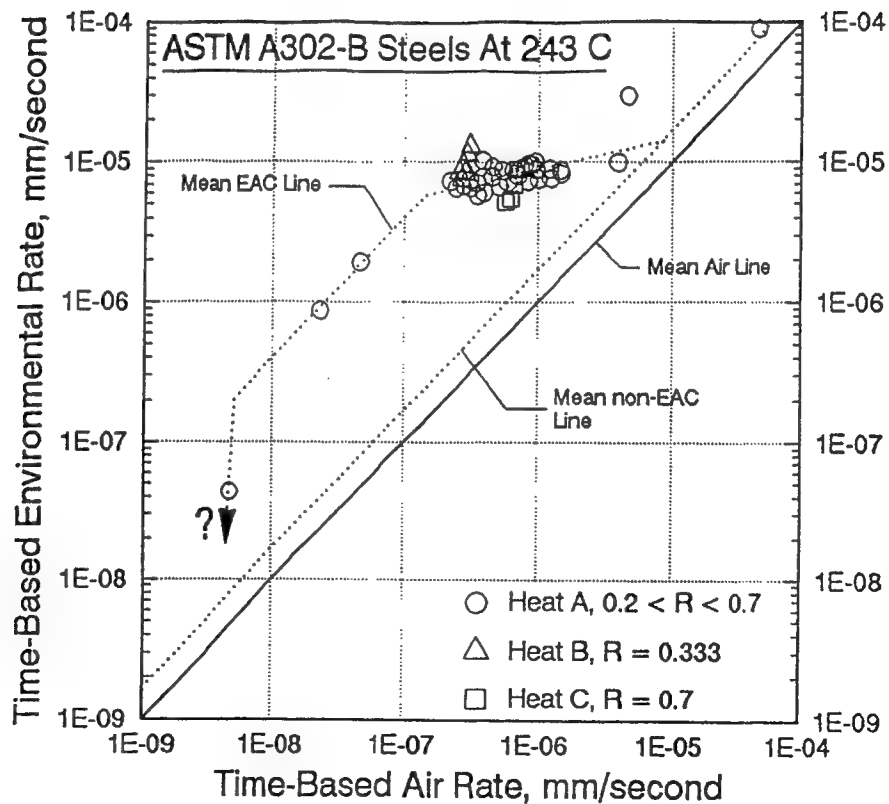


Figure 20

Time-based CF propagation rate for several heats of A302-B steel in high temperature water versus mechanical  $da/dt$  for the same alloy in moist air and at several  $R$  values. (After James [103])

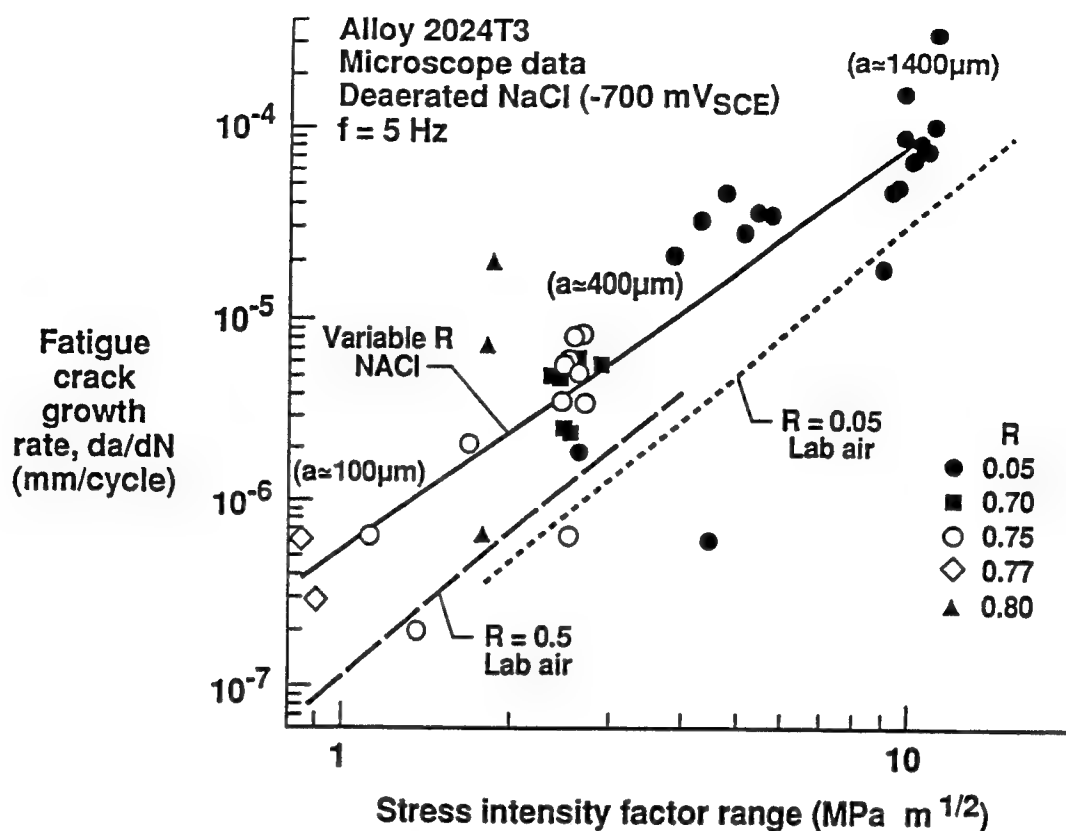


Figure 21 Propagation rate vs  $\Delta K$  for microstructurally small cracks in AA2024 exposed to deaerated aqueous chloride at fixed potential. Crack growth was monitored by *in situ* optical microscopy. (After Piascik and Willard [110])

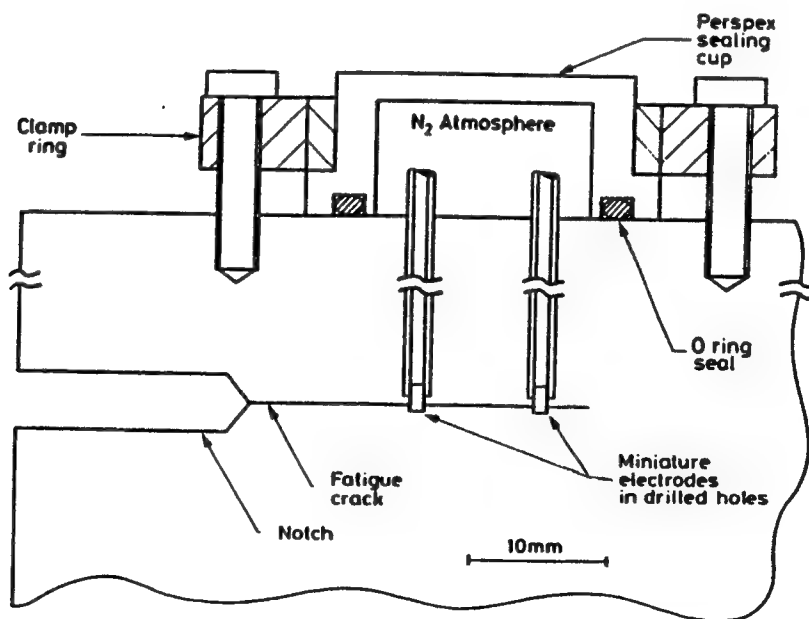


Figure 22 Compact tension specimen and electrode arrangement for *in situ* measurement of crack electrode potential, pH, and solution composition during CF growth. (After Turnbull et al. [112])

## DISTRIBUTION LIST

|         |   |
|---------|---|
| 1 - 3   | Dr. A. John Sedriks<br>Materials Division, Code 1131M<br>Office of Naval Research<br>800 N. Quincy Street<br>Arlington, VA 22217-4660   |
| 4       | Mr. Michael Karp<br>Administrative Contracting Officer<br>Office of Naval Research<br>Resident Representative<br>101 Marietta Tower, Suite 2805<br>101 Marietta Street<br>Atlanta, GA 30303 |
| 5 - 6   | H. Earnhardt  |
| 7       | Director, Naval Research Laboratory<br>Code 2627<br>Washington, DC 20375  |
| 8       | Naval Research Laboratory<br>Code 6000<br>Washington, DC 20375  |
| 9       | Naval Research Laboratory<br>Code 6300<br>Washington, DC 20375  |
| 10      | Naval Research Laboratory<br>Code 5227<br>Washington, DC 20375  |
| 11 - 12 | Defense Technical Information Center, S47031<br>Building 5, Cameron Station<br>Alexandria, VA 22314   |
| 13 - 14 | Naval Air Warfare Center<br>White Oak Detachment<br>Attention: Library, Code R33<br>Silver Spring, MD 20903-5000  |
| 15      | Naval Postgraduate School<br>Mechanical Engineering Department<br>Monterey, CA 93940  |

- 16            Naval Air Systems Command  
              Code 5304  
              Washington, DC 20361
- 17            Naval Sea Systems Command  
              Code 05M  
              Washington, DC 20362
- 18            Naval Sea Systems Command  
              Code 05R  
              Washington, DC 20362
- 19            Naval Air Warfare Center  
              Library  
              Aircraft Division, Trenton  
              Trenton, NJ 08628
- 20            Naval Facilities  
              Materials Division  
              Engineering Service Center  
              Port Hueneme, CA 94043
- 21            Naval Surface Warfare Center  
              Library  
              Carderock Division  
              Bethesda, MD 20084
- 22            Naval Underwater Warfare Center  
              Library  
              Newport, RI 02840
- 23            Naval Air Warfare Center  
              Library  
              Weapons Division  
              China Lake, CA 93555-6001
- 24            National Aeronautics and Space Administration  
              Library  
              Lewis Research Center  
              21000 Brook Park Road  
              Cleveland, OH 44135
- 25            National Institute of Standards and Technology  
              Metallurgy Division  
              Gaithersburg, MD 20899
- 26            National Institute of Standards and Technology  
              Ceramics Division  
              Gaithersburg, MD 20899



- 27            National Institute of Standards and Technology  
Fracture and Deformation Division  
Gaithersburg, MD 20899
- 28            Naval Command, Control and Ocean Surveillance Center  
Attention: Library  
R & D Division  
San Diego, CA 92152-5000
- 29            Office of the Assistant Commander HQ Marine Corps  
Attention: Scientific Advisor  
2 Navy Annex  
Washington, DC 20380-1775
- 30            Army Research Office  
Metallurgy and Ceramics Program  
P.O. Box 12211  
Research Triangle Park, NC 27709
- 31            Army Materials Technology Laboratory  
SLCMT-TMM  
Watertown, MA 02172-0001
- 32            Air Force Office of Scientific Research  
Electronics and Materials Science Directorate  
Building 410  
Bolling Air Force Base  
Washington, DC 20332
- 33            National Aeronautics and Space Administration  
Headquarters  
Code RN  
Washington, DC 20546
- 34            Naval Surface Warfare Center  
Port Hueneme Division  
Attention: Library  
4363 Missile Way  
Port Hueneme, CA 93043-4307
- 35            Metals Information Analysis Center  
Purdue University  
2595 Yeager Road  
West Lafayette, IN 47906
- 36            Naval Facilities Engineering Command  
Code 03  
Alexandria, VA 22331

- 37 Oak Ridge National Laboratory  
Metals and Ceramics Division  
P.O. Box X  
Oak Ridge, TN 37380
- 38 Los Alamos Scientific Laboratory  
Attention: Report Librarian  
P.O. Box 1663  
Los Alamos, NM 87544
- 39 Argonne National Laboratory  
Metallurgy Division  
P.O. Box 229  
Lemont, IL 60439
- 40 Brookhaven National Laboratory  
Research Laboratory  
Upton, Long Island, NY 11973
- 41 Lawrence Berkeley Laboratory  
Attention: Library  
1 Cyclotron Road  
Berkeley, CA 94720
- 42 Naval Surface Warfare Center  
Code 61  
Annapolis Detachment  
Annapolis, MD 21402-5067
- 43 Naval Surface Warfare Center  
Code 613  
Annapolis Detachment  
Annapolis, MD 21402-5067
- 44 Naval Surface Warfare Center  
Cod 0115  
Annapolis Detachment  
Annapolis, MD 21402-5067
- 45 Professors G. H. Meier and F. S. Pettit  
Department of Materials Science and Engineering  
848 Benedum Hall  
University of Pittsburgh  
Pittsburgh, PA 15261
- 46 Professor Gordon P. Bierwagen  
North Dakota State University  
Department of Polymers and Coatings  
Box 5227  
Fargo, ND 58105

- 47            Professor H. W. Pickering  
              The Pennsylvania State University  
              209 Steidle Building  
              University Park, PA 16802
- 48            Professor D. J. Duquette  
              Department of Metallurgical Engineering  
              Rensselaer Polytechnic Institute  
              Troy, NY 12181
- 49            Professor D. Tomanek  
              Michigan State University  
              Department of Physics and Astronomy  
              East Lansing, MI 48824-1116
- 50            Dr. M. W. Kendig  
              Rockwell International Science Center  
              1049 Camino Dos Rios  
              P.O. Box 1085  
              Thousand Oaks, CA 91360
- 51            Professor R. A. Rapp  
              Department of Metallurgical Engineering  
              The Ohio State University  
              116 West 19th Avenue  
              Columbus, OH 43210-1179
- 52            Dr. R. D. Granata  
              Sinclair Laboratory #7  
              Lehigh University  
              Bethlehem, PA 18015
- 53            Dr. G. D. Davis  
              Martin Marietta Laboratories 848  
              1450 South Rolling Rd.  
              Baltimore, MD 21227-3898
- 54            Dr. S. M. Lipka  
              Department of Ocean Engineering  
              Florida Atlantic University  
              Boca Raton, FL 33431-0991
- 55            Dr. D. D. Macdonald  
              The Pennsylvania State University  
              517 Deike Building  
              University Park, PA 16802

- 56 Dr. B. G. Pound  
SRI International  
333 Ravenswood Ave.  
Menlo Park, CA 94025
- 57 Professor C. R. Clayton  
Department of Materials Science and Engineering  
State University of New York  
Stony Brook  
Long Island, NY 11794
- 58 Dr. J. W. Oldfield  
Cortest Laboratories Ltd.  
23 Shepherd Street  
Sheffield, S3 7BA, U.K.
- 59 Ms. D. M. Aylor  
Code 613  
Naval Surface Warfare Center  
Annapolis, MD 21402-5067
- 60 Professor K. Sieradzki  
Department of Materials Science and Engineering  
The Johns Hopkins University  
Baltimore, MD 21218
- 61 Dr. P. S. Pao  
Code 6326  
Naval Research Laboratory  
Washington, DC 20375-5343
- 62 Dr. W. P. Allen  
United Technologies Research Center  
East Hartford, CT 06108
- 63 Dr. B. A. Shaw  
Department of Engineering Science and Mechanics  
207 Hallowell Building  
The Pennsylvania State University  
University Park, PA 16802-1484
- 64 Dr. P. Cox  
SRI International  
333 Ravenswood Ave.  
Menlo Park, CA 94025-3493
- 65 Dr. R. E. Ricker  
National Institute of Standards and Technology  
Building 223, Room B-266  
Gaithersburg, MD 20899

- 66 Dr. F. B. Mansfeld  
Department of Materials Science  
University of Southern California  
University Park  
Los Angeles, CA 90089-0241
- 67 Professor R. E. White  
Department of Chemical Engineering  
University of South Carolina  
Columbia, SC 29208
- 68 Professor R. A. Buchanan  
Department of Materials Science and Engineering  
University of Tennessee  
Knoxville, TN 37996-2200
- 69 Dr. B. J. Little  
NRL Detachment  
Building 1105, Room D415  
Stennis Space Center, MS 39529-5004
- 70 Professor M. E. Orazem  
Department of Chemical Engineering  
University of Florida  
Gainesville, FL 32611
- 71 Professor J. O'M. Bockris  
Department of Chemistry  
Texas A & M University  
College Station, TX 77843
- 72 Dr. V. S. Agarwala  
Code 6062  
Naval Air Warfare Center  
Warminster, PA 18974-0591
- 73 Professor R. C. Newman  
UMIST  
Corrosion and Protection Center  
P.O. box 88  
Manchester M60 1QD, U.K.
- 74 Professor S. C. Dexter  
College of Marine Studies  
University of Delaware  
700 Pilottown Rd.  
Lewes, DE 19958

|                |   |
|----------------|---|
| 75             | Dr. R. Brown<br>Department of Chemical Engineering<br>University of Rhode Island<br>Kingston, RI 02881-0805             |
| 76             | Dr. J. Jones-Meehan<br>Code R301<br>Naval Surface Warfare Center<br>10901 New Hampshire Ave.<br>Silver Spring, MD 20903 |
| 77             | Dr. P. Natishan<br>Code 6322<br>Naval Research Laboratory<br>Washington, DC 20375-5343                                  |
| 78             | Dr. R. L. Jones<br>Code 6170<br>Naval Research Laboratory<br>Washington, DC 20375-5342                                  |
| 79 - 81        | Office of Naval Research<br>Code 3310<br>800 North Quincy Street<br>Arlington, VA 22217-5660                            |
| 82 - 87        | R. P. Gangloff  |
| 88 - 92        | J. R. Scully  |
| 93             | R. G. Kelly   |
| 94             | W. A. Jesser  |
| *              | SEAS Postaward Administration   |
| 95             | SEAS Preaward Administration  |
| * Cover Letter |   |

JO#6064:pa